MIXED CONVECTION IN VERTICAL ROD BUNDLES

by

PAUL DOUGLAS SYMOLON
B.S., M.S., Rensselaer Polytechnic Institute
(1978)

SUBMITTED TO THE DEPARTMENT OF
MECHANICAL ENGINEERING IN PARTIAL
FULFILLMENT OF THE
REQUIREMENTS FOR THE
DEGREE OF
DOCTOR OF PHILOSOPHY
at the
MASSACHUSETTS INSTITUTE OF TECHNOLOGY
August 1982

© Massachusetts Institute of Technology 1982

Signature of Author: Signature redacted
Department of Mechanical Engineering
August 13, 1982

Certified by: Signature redacted
Neil E. Todreas
Thesis Supervisor

Accepted by: Signature redacted
Warren M. Rohsenow
Chairman, Department Committee

Archives
MASSACHUSETTS INSTITUTE OF TECHNOLOGY
NOV 12 1982

MITLibraries

77 Massachusetts Avenue
Cambridge, MA 02139
http://libraries.mit.edu/ask

DISCLAIMER NOTICE

Due to the condition of the original material, there are unavoidable flaws in this reproduction. We have made every effort possible to provide you with the best copy available.

Thank you.

The following pages were not included in the original document submitted to the MIT Libraries.

This is the most complete copy available.

p. 425

MIXED CONVECTION IN VERTICAL ROD BUNDLES

by

Paul D. Symolon

Submitted to the Department of Mechanical Engineering
In August 1982 in partial fulfillment of the
requirements for the Degree of Doctor of Philosophy in
Mechanical Engineering

ABSTRACT

In recent years, there has been increased interest in predicting the temperature and flow fields in nuclear reactor rod bundles operating under low flow conditions, where buoyancy effects become important. In particular, the LMFBR blanket assembly is of interest since large radial power gradients exist. The radial power gradients result in buoyancy induced flow redistribution within the rod bundle. In this paper, criteria are developed to predict the onset of mixed convection and the onset of flow recirculation in vertical rod bundles, thus identifying three flow regimes, forced convection, mixed convection, and recirculation. In forced convection the flow field may be determined independent of the temperature field, while in mixed convection the momentum and energy equations become coupled through the buoyancy term. The recirculation regime is actually a subset of the mixed convection regime, but the solution method must allow for the existence of flow reversal, and strong transverse flows in the rod bundle.

The two criteria are based on a two channel model of the rod bundle. Conservation equations for mass, momentum and energy are written for each channel under the assumption of (1) negligible axial conduction, (2) Boussinesq approximation, and (3) neglect unsteady terms in the energy equation. The resulting equations are solved analytically by the method of trial solution with undetermined parameters. The two undetermined parameters are the integrated buoyancy induced crossflow, and the crossflow profile shape. The correct crossflow profile shape is determined from results of standard multichannel numerical codes. The buoyancy induced crossflow is then calculated with the two channel model.

The criteria is intended for use with existing numerical tools to aid the user in selecting the code most appropriate for a given set of operating conditions. For example, the onset of mixed convection criteria determines when a forced convection code is no longer valid, so that a code with mixed convection capability must be employed.

Thesis Supervisor: Dr. Neil E. Todreas

Title: Professor of Nuclear Engineering

ACKNOWLEDGEMENTS

The authors would like to express his graditude to Professor Neil Todreas for his guidance throughout the course of this work. Professor Rohsenow is also acknowledged for many helpful and enlightening technical discussions. The helpful suggestions of Professors Mikic and Sonin were also appreciated. Dr. Ehsan Khan is also thanked for providing COBRA runs for this work.

Special thanks are due to my associates on the mixing project and my office mates. The expert typing of the thesis by Donna Dutton, and diligent drafting work by Judy Symolon is warmly appreciated. The timely assistance of Kevin Burns is also acknowledged.

Finally, I thank my wife, Judy, for her support and encouragement during my years as a graduate student. The strong support, both moral and financial, of Stan, Marion, Jack and Vivian is sincerely appreciated.

TABLE OF CONTENTS

		Page
ABSTRACT		ii
ACKNOWLEDGEMENTS		iii
TABLE OF CONTENTS		iv
LIST OF FIGURES		x
LIST OF TABLES		xxi
NOMENCLATURE		xxiii
CHAPTER 1	INTRODUCTION	1
	1.1 Buoyancy Effects in Reactor Heat Transfer	1
	1.2 Contribution of This Work	8
CHAPTER 2	VERTICAL MIXED CONVECTION FLOWS	12
	2.1 Fundamental Mechanisms in Mixed Convection	13
	2.1.1 Nondimensionalization of the Governing Equations	13
	2.1.2 The Effects of Buoyancy on Laminar and Turbulent Flows Near Vertical Surfaces	21
	2.2 Literature Review of Mixed Convection	26
	2.2.1 Review of Data and Correlations for Mixed Convection	26
	2.2.2 Prandtl Number Effects in Mixed Convection	42
	2.2.3 Flow Regime Identification and Criteria	47
	2.2.4 Instability and Transition to Turbulence	52
	2.3 Comparison of Correlations With Data	57
	2.4 Comparison of Data with Criteria	67
CHAPTER 3	MIXED CONVECTION IN VERTICAL ROD BUNDLES	70
	3.1 Literature Review of Mixed Convection in Rod Bundles	70
	3.1.1 Local Buoyancy Effects	71
	3.1.2 Bundle Buoyancy Effects	74

Page

3.2 Numerical Tools for Analysis of LMFBR Rod Bundles 77
3.2.1 The ENERGY Series of Codes . . 79
3.2.2 Input Parameters for Subchannel Analysis Codes 84
3.2.3 Structure of the Numerical Tools 84

CHAPTER 4 EXPERIMENTAL APPARATUS 87

4.1 Flow Loop 87
4.2 Test Section 89
4.3 Heater Rod Instrumented With a Thermocouple Probe 89

CHAPTER 5 DEVELOPMENT OF A TWO-CHANNEL MODEL FOR A VERTICAL ROD BUNDLE 94

5.1 Governing Equations 94
5.1.1 Derivation of Conservation Equations for the Two Channel Model. 94
5.1.2 Simplification of the Governing Equations 109

5.2 Method of Solution of Equations . . 121
5.2.1 Velocity Profile Assumptions For the Two Channel Model. . 122
5.2.2 Integration of the Momentum Equation 126
5.2.3 Evaluation of the Buoyancy Term . 132

5.3 Governing Equation of the Two Channel Model 141

CHAPTER 6 VALIDATION OF THE TWO CHANNEL MODEL . . . 144

6.1 Comparison of the two channel model Results to the BNWL 2x6 Test Results and COBRA predictions 145
6.1.1 Steady State Results . . . 145
6.1.2 Assessment of the Transient Term in the Two Channel Model . . 169

6.2 Comparison of the Two Channel Model Results to ENERGY code Predictions . 189
6.2.1 Comparison of the Results of ENERGY IV with the WARD Data . 189

TABLE OF CONTENTS (continued)

		Page
	6.2.2 Determination of Model Input Parameters for LMFBR Bundles	190
	6.2.3 Comparison of the ENERGY Code and Two-Channel Model Results	199
CHAPTER 7	CRITERIA FOR ONSET OF FLOW RECIRCULATION IN VERTICAL ROD BUNDLES	215
	7.1 Literature Review	216
	7.2 Experimental Determination of the Onset of Flow Recirculation in the MIT 4x4 Rod Bundle	217
	7.2.1 Bundle Instrumentation . .	217
	7.2.2 Dye Injections Method versus Outlet Thermocouple Technique for Determining the Onset of Recirculation .	222
	7.2.3 Onset of Recirculation Data .	228
	7.3 Onset of Recirculation Criteria Based on a Two-Channel Model of the Rod Bundle	240
	7.3.1 Equations and Solution Method	240
	7.3.2 Alternate Approaches for Specification of the Onset of Recirculation . .	240
	7.4 Comparison of Onset of Recirculation Criteria with Data	243
	7.4.1 Discussion of Effect of Input Parameters on the Onset of Recirculation	243
	7.4.2 Comparison of Criteria with MIT Data	249
	7.4.3 Improved Predictions Based on a Mixing Model, and a Model for Local Buoyancy Effects	270
	7.4.4 Comparison with BNWL Recirculation Data . .	281
	7.5 Flow Regime Map and Hand Calculation for the Onset of Recirculation .	286

TABLE OF CONTENTS (continued)

		Page
	7.5.1 Onset of Recirculation Criteria Expressed as a Flow Regime Map	288
	7.5.2 Hand Calculation Procedure for the Onset of Recirculation	293
	7.5.3 Recommended Input Parameters and Sample Calculation .	295
CHAPTER 8	CRITERIA FOR THE ONSET OF MIXED CONVECTION IN VERTICAL ROD BUNDLES	299
	8.1 Literature Review and Previous Work in Criteria Development . . .	299
	8.2 Alternate Approaches for Predicting the Onset of Mixed Convection .	303
	8.2.1 Criteria for the Onset of Mixed Convection Based on the Buoyancy Induced Crossflow	305
	8.2.2 Criteria for Onset of Mixed Convection Based on Buoyancy Induced Energy Transport	306
	8.2.3 Criteria for Onset of Mixed Convection Based on the Peak Temperature Rise . .	309
	8.2.4 Discussion of the Three Approaches	312
	8.3 Calculation of the Onset of Mixed Convection in LMFBR Bundles . .	313
	8.3.1 Input Parameters for LMFBR Rod Bundles	314
	8.3.2 Calculation of the Onset of Mixed Convection . . .	319
	8.3.3 Comparison of Model Results to the Westinghouse Criteria	322
	8.4 Calculation of the Onset of Mixed Convection in a Bare Rod Water-Cooled Bundle	327
	8.5 Discussion of the Alternate Approaches for Specifying the Onset of Mixed Convection . .	328

TABLE OF CONTENTS (continued)

		Page
	8.6 Flow Regime Map and Hand Calculation for the Onset of Mixed Convection	331
	8.6.1 Flow Regime Map for the Onset of Mixed Convection . .	332
	8.6.2 Hand Calculation of the Onset of Mixed Convection . .	335
	8.6.3 Recommended Input Parameters and Sample Calculation of the Onset of Mixed Convection	336
CHAPTER 9	FLOW REGIME MAP FOR MIXED CONVECTION IN ROD BUNDLES	338
CHAPTER 10	SUMMARY, CONCLUSIONS AND RECOMMENDATIONS FOR FUTURE WORK	341
	10.1 Summary and Limitations of the Model	341
	10.2 Conclusions	341
	10.3 Recommendations for Future Work .	345
REFERENCES	. . . . .	347
APPENDIX A	KENNING'S DATA FOR MIXED CONVECTION IN A VERTICAL TUBE	353
APPENDIX B1	ASSESSMENT OF THE IMPORTANCE OF THE AXIAL CONDUCTION TERM	358
APPENDIX B2	ASSESSMENT OF THE IMPORTANCE OF THE TRANSIENT TERM	364
APPENDIX C1	ANALYTICAL SOLUTIONS OF THE ENERGY EQUATION	373
APPENDIX C2	NUMERICAL SOLUTION OF THE ENERGY EQUATION	377
APPENDIX D	COMPUTER PROGRAMS FOR SOLUTION OF THE TWO-CHANNEL MODEL EQUATIONS	382
APPENDIX E1	COBRA PREDICTION FOR THE 2x6 ROD BUNDLE STEADY STATE TEST	395
APPENDIX E2	THE VERSION OF ENERGY EMPLOYED IN THIS STUDY	402

TABLE OF CONTENTS (continued)

		Page
APPENDIX E3	DETERMINATION OF w_t^* FOR AN LMFBR WIRE WRAPPED BUNDLE	403
APPENDIX E4	COMPARISON OF ENERGY RESULTS TO THE WESTINGHOUSE BLANKET BUNDLE DATA . . .	413
APPENDIX F1	DETERMINATION OF THE TEMPERATURE DEPENDENT FLOW PARAMETERS FOR THE 4x4 ROD BUNDLE .	433
APPENDIX F2	ONSET OF RECIRCULATION DATA	437
APPENDIX F3	ANALYSIS OF ERRORS IN THE ONSET OF RECIRCULATION EXPERIMENT	485
APPENDIX F4	MODEL FOR THE CRITICAL VALUE OF C AT THE ONSET OF RECIRCULATION	491
APPENDIX F5	MODEL FOR THE CRITICAL VALUE OF C AT THE ONSET OF RECIRCULATION ALLOWING FOR LOCAL BUOYANCY EFFECTS	498
APPENDIX F6	DEVELOPMENT OF A MIXING MODEL FOR BUOYANCY DOMINATED FLOWS THROUGH ROD BUNDLES	506
APPENDIX F7	DETERMINATION OF THE DOMINANT DIMENSION-LESS PARAMETERS FOR THE ONSET OF MIXED CONVECTION AND ONSET OF RECIRCULATION CRITERIA	514

LIST OF FIGURES

		Page
1.1.1	Typical Primary Loop of a LMFBR	2
1.1.2	Cross Section of LMFBR Reactor Core	4
1.1.3	Typical LMFBR Assembly	6
1.1.4	Local Buoyancy Effects	7
1.2.1	Overview of Work	9
2.1.1	Effect of Buoyancy on Heat Transfer for Aiding and Opposing Flow	22
2.1.2	Effect of Buoyancy on Heat Transfer for Aiding Turbulent Flow	24
2.2.1	Experimental Results of Kenning	27
2.2.2	Experimental Results of Buhr	29
2.2.3	Data and Correlations of Petukhov	32
2.2.4	Experimental Results of Connor	33
2.2.5	Experimental Results of Byrne and Ejiogu	36
2.2.6	Experimental Results of Alferov	37
2.2.7	Analytical Results of Lloyd and Sparrow	43
2.2.8	Prandtl Number Effects in Mixed Convection	45
2.2.9	Flow Regime Map for Flow in Vertical Tubes	48
2.2.10	Flow Regime Map of Alferov	51
2.2.11	Results of Scheele and Hanratty	55
2.2.12	Results of Sherwin and Wallis	56
2.2.13	Experimental Transition Data of Lawrence	58
2.2.14	Velocity Profile Shape Transition Parameter of Lawrence	59

LIST OF FIGURES (Continued)

		Page
2.3.1	Comparison of Correlations and Data in Terms of Ra_A/Re^2	60
2.3.2	Comparison of Correlations and Data in Terms of Gr_A/Re^2	62
2.3.3	Comparison of Data and Correlations in Terms of Gr_A/Re^2	64
2.3.4	Nusselt Number Variation with L/D and Gr_A/Re^2 For Runs 10 to 20 of Kenning's Data	65
2.3.5	Nusselt Number Variation with L/D and Gr_A/Re^2 For Runs 98 to 106 of Kenning's Data	66
2.4.1	Flow Regime Map for Mixed Convection in Tubes With Experimental Data	68
3.1.1	Numerical Results of Yang For Aiding Mixed Convection Flow in Rod Arrays	72
3.1.2	Numerical Results of Tsai for Mixed Convection in a Thin Rectangular Channel	75
3.2.1	Typical Computation Grid Employed by BODYFIT for Distributed Parameter Analysis of a 19 Pin Bundle	78
3.2.2	Subchannel Analysis of a Rod Bundle	80
3.2.3	Effect of Wire Wrap on Coolant Flow	82
3.2.4	Energy Model of an LMFBR Rod Bundle	83
4.1.1	Schematic of Flow Loop	88
4.2.1	Side View of MIT 4x4 Bundle	90
4.2.2	Cross Section of MIT 4x4 Bundle	91
4.3.1	Instrumented Heater Rod	92
4.3.2	Thermocouple Probe	94
5.1.1	Two Channel Model of a Rod Bundle	96
5.1.2	Control Volume Analysis for Mass Conservation	98

LIST OF FIGURES (Continued)

		Page
5.1.3	Control Volume Analysis for Momentum Conservation	100
5.1.4	Control Volume Analysis for Energy Conservation	106
5.1.5	Control Volume for Bundle Energy Balance	119
5.2.1	V_2^* and w_c^* versus x* for Various Choices of f(x*)	125
5.2.2	K_1 and K_2 as a Function of C and E* for $f(x^*) = x^*$	137
5.2.3	Effect of f(x*) on K_1 and K_2 for E*=0	138
5.2.4	Effect of Inlet Velocity Profile and Axial Power Profile on K_1 and K_2 for E*=0 and $f(x^*) = x^*$	140
6.1.1	Test Section of BNWL 2x6 Test	146
6.1.2	Experimental and COBRA predicted Velocities for Case 1	148
6.1.3	Experimental and COBRA predicted Velocities for Case 2	149
6.1.4	Experimental and COBRA predicted Velocities for Case 3	150
6.1.5	Two Channel and COBRA Noding Scheme for BNWL 2x6 Rod Bundle	152
6.1.6	COBRA Predicted Crossflow	154
6.1.7	COBRA Predicted Axial Velocity	155
6.1.8	COBRA Versus Model Predictions of Axial Velocity for Case 1	158
6.1.9	COBRA Versus Model Predictions of Crossflow for Case 1	159
6.1.10	COBRA Versus Model Predictions of the Axial Velocity for Case 3	161

LIST OF FIGURES (Continued)

		Page
6.1.11	COBRA Versus Model Predictions of Cross-flow for Case 3	162
6.1.12	Comparison of Data with COBRA and Two Channel Model Predictions for Case 1 at x*=.5 and x*=1.0	163
6.1.13	Comparison of Data with COBRA and Two Channel Model Predictions for Case 3 at x*=.5 and x*=1.0	164
6.1.14	Comparison of COBRA with Data for Case 2 at x*=.50 and x*=1.00	165
6.1.15	COBRA Predictions of the Axial Velocity Profile Shape Function	167
6.1.16	Measured and Predicted Subchannel Velocities for Cases 6 and 9	172
6.1.17	Bundle Noding Scheme for Two Channel COBRA Run	173
6.1.18	Transient Bulk Temperature Rise and Bundle Velocity for 1:0 and 4:1 Power Gradients	175
6.1.19	V_1^* and V_2^* as Functions of Axial Distance for 4:1 Power Gradient	176
6.1.20	V_1^* Versus Axial Distance for 1:0 Power Gradient	177
6.1.21	w_c^* Versus Axial Distance for 1:0 Power Gradient	178
6.1.22	w_c^* Versus Axial Distance for 4:1 Power Gradient	179
6.1.23	Crossflow Parameter and Power Delivered To The Coolant as Predicted by COBRA for 1:0 and 4:1 Power Gradients	182

LIST OF FIGURES (Continued)

		Page
6.1.24	$f(x^*)$ Versus x^* as Predicted by COBRA for 1:0 Power Gradient	183
6.1.25	$f(x^*)$ Versus x^* as Predicted by COBRA for 4:1 Power Gradient	184
6.1.26	Model Versus COBRA Prediction of C as a Function of Transient Time	185
6.1.27	Assessment of the Transient Term of the Two Channel Model	187
6.2.1	ε^*_{1L} and C_{1L} Versus Re for the Blanket Bundle	193
6.2.2	Flowsplit Prediction for the WARD Blanket Bundle	194
6.2.3	ε^*_{1L} and C_{1L} Versus Re for the ORNL Fuel Bundle	195
6.2.4	Flowsplit Prediction for the ORNL Fuel Bundle	196
6.2.5	ENERGY Versus Model Prediction of θ_{2e} and V^*_{2e}	204
6.2.6	ENERGY Versus Model Prediction of the Hot Channel Exit Temperature and Velocity For $F_g = .75$	207
6.2.7	ENERGY Versus Model Prediction of θ_{2e}	208
6.2.8	Axial Velocity Profiles Predicted by ENERGY	210
6.2.9	Crossflow Profiles Predicted by ENERGY	211
6.2.10	Axial Velocity Profile Shape Function Predicted by ENERGY	212
6.2.11	Model Versus ENERGY Prediction of the Axial Temperature Profile	213

LIST OF FIGURES (Continued)

		Page
7.2.1	Upper Region of Bundle	218
7.2.2	Cross Section of Test Section	219
7.2.3	Power Gradients Used in Recirculation Experiments	220
7.2.4	Power Gradients Used in Recirculation Experiments	221
7.2.5	Dye Injection and Thermocouple Data with Two Rows Heated at 500 Watts Per Rod	223
7.2.6	Dye Injection and Thermocouple Data with One Row Heated at 1500 Watts Per Rod	226
7.2.7	Dye Injection Data for Profile # 1	229
7.2.8	Dye Injection Data for Profile # 2	230
7.2.9	Dye Injection Data for Profile # 3	231
7.2.10	Dye Injection Data for Profile # 5	232
7.2.11	Dye Injection Data for Profile # 6	233
7.2.12	Combined Upflow and Downflow	235
7.2.13	Measured Versus Calculated Bulk Temperature Rise	239
7.3.1	Alternate Approaches For Specifying the Onset of Recirculation	241
7.4.1	COBRA Predictions of f(x*) at the Onset of Recirculation	244
7.4.2	Bundle Noding for Variable R Approach	250
7.4.3	Bundle Noding for Variable R Approach	251
7.4.4	Onset of Recirculation Data and Predictions for Power Profile # 2	253

LIST OF FIGURES (Continued)

		Page
7.4.5	Onset of Recirculation Data and Predictions for Power Profile # 1	256
7.4.6	Onset of Recirculation Data and Predictions for Power Profile # 3	258
7.4.7	Onset of Recirculation Data and Predictions for Power Profile # 4	259
7.4.8	Onset of Recirculation Data and Predictions for Power Profile # 6	260
7.4.9	Recirculation Data and Predictions for Power Profile # 5	263
7.4.10	C as a Function of Re Calculated from the Two Channel Model	265
7.4.11	Recirculation Data and Predictions With Cold Wall	269
7.4.12	Predictions for Power Profile # 6 including the Effect of Mixing	272
7.4.13	Recirculation Data and Predictions for Power Profile # 5 With Mixing Model	274
7.4.14	Recirculation Predictions for Power Profile # 4 With and Without Mixing Model	276
7.4.15	Recirculation Predictions for Power Profile # 3 With and Without Mixing Model	277
7.4.16	Determination of C_{crit} and Re_{crit} with Local Buoyancy Effects	280
7.4.17	Recirculation Data With Model Predictions for Power Profile # 5	282
7.4.18	BNWL 2x6 Test Recirculation Data and Model Predictions	285

LIST OF FIGURES (Continued)

		Page
7.5.1	Uncorrelated Recirculation Data	289
7.5.2	Correlated Recirculation Data With Model Predictions	291
7.5.3	Recirculation Data on Onset of Recirculation Flow Regime Map	292
7.5.4	Power Distribution in a Blanket Bundle	297
8.1.1	Normalized Peak Temperature Rise Versus Gr_A/Re for the WARD Blanket Bundle	302
8.2.1	Two Channel Model of An LMFBR Rod Bundle	304
8.2.2	Temperature and Flow Fields for Forced Convection and Mixed Convection with Two Channel Model Approximations	310
8.3.1	Dimensionless Mixing and Conduction Parameters and Normalized Forced Convection Solution for the Blanket Bundle	315
8.3.2	Dimensionless Mixing and Conduction Parameters and Normalized Forced Convection Solution for the Fuel Bundle	316
8.3.3	Dimensionless Mixing and Conduction Parameters and Normalized Forced Convection Solution for the Fuel and Blanket Assembly	317
8.3.4	Determination of the Onset of Mixed Convection in the Blanket Bundle	320
8.3.5	Determination of the Onset of Mixed Convection for the Fuel Bundle	321
8.3.6	Effect of Power Gradient on the Onset of Mixed Convection	323

LIST OF FIGURES (Continued)

		Page
8.4.1	θ_{2e} and C Versus Re for the MIT 4x4 Bundle	328
8.6.1	Onset of Mixed Convection Criteria with Results from ψ = .01 Approach	333
8.6.2	Onset of Mixed Convection Criteria with Westinghouse Data	334
9.2.1	Flow Regime Map for Mixed Convection in Rod Bundles	340
10.1.1	Summary of Modes Development	344

LIST OF FIGURES

Appendix

		Page
B1.1	Axial Conduction in a Heated Channel	359
B1.2	Effect of Axial Conduction on the Coolant Temperature	362
B2.1	T^*, V_b^* and Δ as Functions of t^*	367
B2.2	T^*, V^* and Δ Versus Time for Pump Coastdown and Pipe Rupture Transient	370
B2.3	T^* and V^* Versus Transient Time	372
D.1	Flowchart for Bisection Algorithm	384
E3.1	Mixing Across The Channel Boundary For an LMFBR Rod Bundle	404
E3.2	Physical Significance of F_g	407
E4.1	Subchannel Numbering Scheme Using in Ward-ENERGY Comparison	415
E4.2	Comparison of ENERGY Predictions to Ward Data Run 218	416
E4.3	Comparison of ENERGY Predictions to Ward Data Run 221	417
E4.4	Comparison of ENERGY Predictions to Ward Data Run 223	418
E4.5	Comparison of ENERGY Predictions to Ward Data Run 224	419
E4.6	Comparison of ENERGY Predictions to Ward Data Run 232	420
E4.7	Comparison of ENERGY to Ward Data - Run 227	421
E4.8	Comparison of ENERGY to Ward Data - Run 719	422
E4.9	Comparison of ENERGY to Ward Data - Run 401	423
E4.10	Comparison of ENERGY to Ward Data - Run 725	424
E4.11	Comparison of ENERGY to Ward Data - Run 720	425

LIST OF FIGURES (Continued)

Appendix

		Page
E4.12	Comparison of ENERGY to Ward Data - Run 229	426
E4.13	Comparison of ENERGY to Ward Data - Run 702	427
E4.14	Comparison of ENERGY to Ward Data - Run 716	428
E4.15	Comparison of ENERGY to Ward Data - Run 712	429
E4.16	Comparison of ENERGY to Ward Data - Run 546	430
E4.17	Comparison of ENERGY to Ward Data - Run 547	431
E4.18	Comparison of ENERGY to Ward Data - Run 530	432
F1.1	Temperature Dependent Fluid Properties	436
F4.1	Bundle Geometry - Lumped Subchannels	493
F4.2	Assumed Exit Velocity Profiles at the Onset of Recirculation for Power Profiles 1 to 3	495
F4.3	Assumed Exit Velocity Profiles at the Onset of Recirculation for Power Profiles 4 to 6	496
F5.1	Local Flow Recirculation in an Edge Subchannel	499
F5.2	Velocity Field at Onset of Recirculation	503
F6.1	Mixing Length Turbulence Model	507
F7.1	Flow Regime Map in Terms of Re and B_D^*	518
F7.2	Flow Regime Map in Terms of B_L^* and Re	522
F7.3	Flow Regime Map in Terms of B* and Re	524

LIST OF TABLES

		Page
2.2.1	Dimensionless Parameters from Nondimensionalization of Governing Equations	17
2.1.2	Definitions of Important Dimensionless Parameters in Mixed Convection	20
2.2.1	Burh's Data and Connor's Data	30
2.2.2	Criteria for Turbulent Mixed Convection for Aiding Flow in Vertical Circular Tubes	49
3.2.1	Subchannel Codes for Analysis of LMFBR Rod Bundles	86
5.2.1	Axial Velocity Profile Shape Functions	127
5.2.2	Friction Factor Correlations Used in the Two Channel Model	131
5.2.3	Energy Equation Integrals for $g(x^*)=1$, $E^*=0$, and $V^*_{1i}=V^*_{2i}=S=1$	135
6.1.1	BNWL 2x6 Steady State Runs	147
6.1.2	COBRA Predicted Velocities and Crossflows	153
6.1.3	COBRA and Model Predictions of C for BNWL 2x6 Steady State Runs	157
6.1.4	Run Conditions for BNWL 2x6 Transient Runs	170
6.2.1	Bundle Geometric Perimeters	191
6.2.2	Hawley-Chiu Friction Factors for Blanket and Fuel Bundles	197
6.2.3	Row Power Factors and Channel Power Inputs for Three Power Gradients	198
6.2.4	ENERGY Results	201
6.2.5	Two Channel Results	202
7.2.1	Data for Determining Onset of Recirculation for Two Rows Heated at 500 Watts per Rod	224
7.2.2	Data for Determining Onset of Recirculation for One Row Heated at 1500 Watts per Rod	227

LIST OF TABLES (Continued)

		Page
7.2.3	Onset of Recirculation Data	237
7.4.1	Model Predictions of Recirculation Reynolds Number for IVP = 4	246
7.4.2	Onset of Recirculation Predictions for Profiles 1 to 4.	254
7.4.3	Recirculation Data and Predictions for Power Profiles # 5	264
7.4.4	Recirculation Data and Predictions With Cold Wall	268
7.4.5	Onset of Recirculation Predictions for Power Profile 6	273
7.4.6	Onset of Recirculation Data From BNWL 2x6 Transient and Steady State Runs	283
8.3.1	Onset of Mixed Convection Results for ψ = .01 Approach	324
A.1	Kennings data for mixed convection in a tube	354
E1.1	Case 1 COBRA subchannel average velocities	396
E1.2	Case 2 COBRA subchannel average velocities	397
E1.3	Case 3 COBRA subchannel average velocities	398
E1.4	Case 1 subchannel temperatures	399
E1.5	Case 2 subchannel temperatures	400
E1.6	Case 3 subchannel temperatures	401
E4.1	Westinghouse data compared with ENERGY	414

NOMENCLATURE

A_i	area of channel i
A_b	bundle area
A_D^*	defined by Eq. F7.11
A^*	defined by Eq. 7.5.3
B_D^*	defined by Eq. 7.8
B_L^*	dimensionless buoyancy term defined by Eq. F7.15
B^*	dimensionless buoyancy term defined by Eq. F7.19
c_{1L}	swirl velocity ratio
C	buoyancy induced crossflow parameter defined by Eq. 5.2.1
C_f	skin friction coefficient in friction factor correlation $f = C_f/Re^m$
D_{ei}	hydraulic diameter of channel i = $4A_i/P_{wi}$, where P_{wi} is wetted perimeter of channel i
D_{eb}	bundle hydraulic diameter = $4A_b/P_{wb}$
D_H	bundle heated diameter = $4A_b/P_{Hb}$, where P_{Hb} is the bundle heated perimeter
E^*	dimensionless lateral energy transport due to mixing and conduction = $w_t^* + K^*$
f_i	friction factor for channel i
f_b	bundle friction factor
$f(x^*)$	velocity profile shape function
$f_1(x^*)$	function defined by Eq. 5.2.44
$f_2(x^*)$	function defined by Eq. 5.2.45

NOMENCLATURE (continued)

F_c	integrated friction term defined by Eq. F7.2
F_g	factor on temperature gradient in Eq. E3.6
Gr_q	$= D_e^4 g\beta q''/K\nu^2$ Grashof number based on heat flux
g	gap between rod and duct wall
g(x*)	axial power profile shape function
K_1, K_2	defined by Eqs. 5.2.56 and 5.2.57
K	thermal conductivity
K_0	defined by Eq. 8.6.2
K*	dimensionless conduction term defined by Eq. 8.3.1
ℓ	centroid to centroid distance between channels 1 and 2
L	bundle heated length
m	exponent in friction factor correlation $f = C_f/Re^m$
N_R	number of rings of pins
P	rod to rod pitch
$P_f(x^*)$	fraction of the bundle power input up to x* defined by Eq. 5.1.73
P_H	heated perimeter
P_{wi}	wetted perimeter of channel i
P_i	fraction of bundle power input to channel i
p_i	pressure in channel i
Pr	$= \mu c_p/K$ Prandtl number
q_i'	power input per unit axial length for channel i
Q*	power input parameter defined by Eq. 5.1.58 or Eq. F4.2
R	$= A_1/A_2$: ratio of channel areas

NOMENCLATURE (continued)

Re	$= DeV_b/\nu$: bundle Reynolds number
SF	conduction shape factor
T_i	temperature in channel i
t	time (sec)
V_i	velocity in channel i
w_c	mass crossflow rate per unit length
w_t	mixing parameter
w	width available for conduction and mixing
x	axial distance
x_i	flow split parameter for region i (i = 1,2)
y_1, y_2	defined by Eqs. 5.2.52 and 5.2.53

Greek Symbols:

β	volumetric expansion coefficient
ΔT_B	bulk temperature rise
∇T	temperature gradient
ε^*_{1L}	interior region mixing parameter
θ_i	dimensionless temperature defined by Eq. 5.1.72
$\mu(x)$	defined by Eq. 5.2.49
ν	kinematic viscosity
ρ	density
τ	wall shear stress
ϕ	defined by Eq. 8.2.7
ψ	defined by Eq. 8.2.18

NOMENCLATURE (continued)

Subscripts

1,2	pertaining to channel 1 or 2
crit	critical value
e	exit value
edg	pertaining to edge subchannel
i	inlet value
in,out	inlet or outlet value
int	pertaining to interior subchannel
L,T	pertaining to laminar or turbulent flow respectively
max	maximum value
min	minimum value

Superscripts

fc	forced convection
mc	mixed convection
*	indicates dimensionless parameter

CHAPTER 1

INTRODUCTION

One of the most urgent research needs in reactor safety and design has been identified as the need to develop the capability to accurately predict a wide range of postulated transient and accident conditions. Of particular interest in the present study is the loss of flow or small break LOCA event which causes a reduction in coolant flow through the core. For these events, buoyancy effects become an important thermal-hydraulic phenomena which must be modeled correctly for codes to accurately predict the peak temperatures which will occur during the transient.

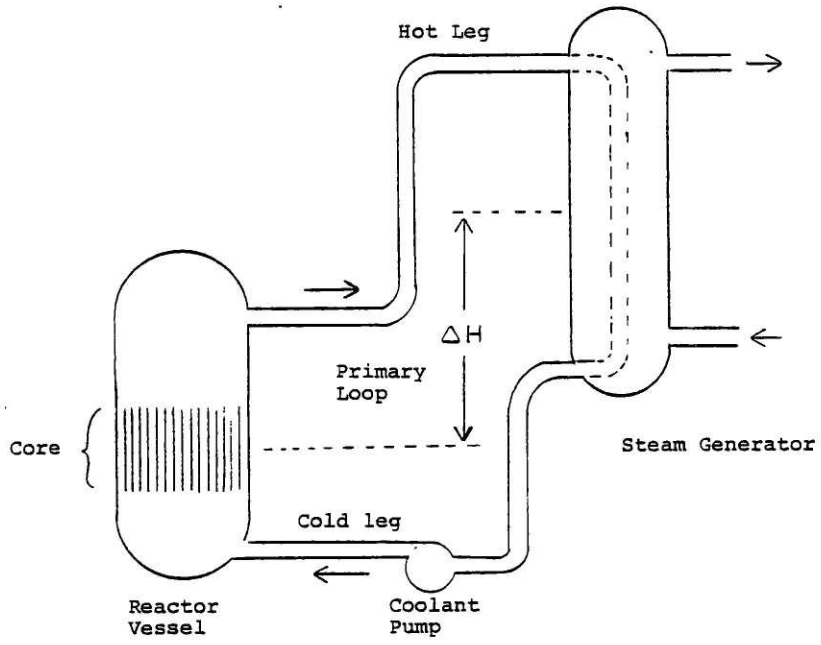
1.1 BUOYANCY EFFECTS IN REACTOR HEAT TRANSFER

In this section, the effects of buoyancy on reactor heat transfer will be discussed for the LMFBR case, though many of the comments are applicable to other types of reactors. The discussion will proceed from global to local buoyancy effects.

Figure 1.1.1 gives a schematic of a typical primary coolant loop. In the event of a pump failure, the flow will coast down with time, decreasing the coolant flow through the core. Even with reactor scram, decay heat will be generated for some time and the system must be designed to remove this heat without exceeding peak temperature limits.

FIGURE 1.1.1

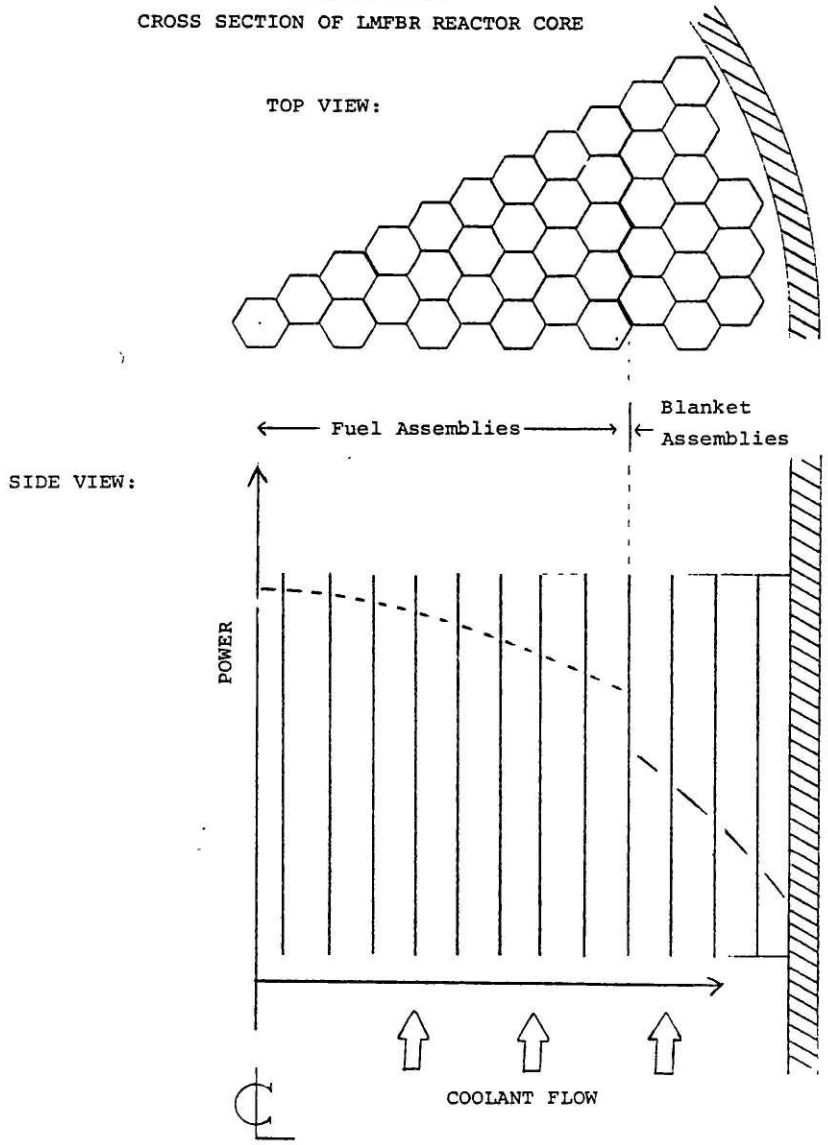
TYPICAL PRIMARY LOOP OF AN LMFBR



One way to help maintain coolant flow for the order of minutes is to build a pump with a flywheel which stores kinetic energy to continue turning the pump. If the pump has stopped, a flow bypass line would allow the large flow resistance of the stalled pump to be avoided. For long times after scram the elevation difference between the thermal centers of the core and the steam generator will produce a buoyancy head which can maintain flow through the core via natural circulation. However, if the flow resistance through the loop is too large natural circulation will not be maintained, but only local recirculation will occur within the core, and overheating will eventually occur if no other heat sink is provided. Also there are a range of potential situations useful to examine in which the reactor vessel becomes isolated from the steam generator. In all of these cases a heat sink must be provided to maintain safe core conditions.

In Figure 1.1.2 we focus attention on the core itself, which for an LMFBR consists of a number of and blanket assemblies which behave as coolant flow channels. A power gradient exists across the core as shown. The power gradient results in different assembly average temperatures, and different coolant densities. If the flow through the core is low, the buoyancy force becomes important, and causes the hotter assemblies to get more flow. This phenomena is termed inter-assembly flow redistribution. Under extreme conditions, the flow may reverse in the coldest assemblies, causing flow

FIGURE 1.1.2
CROSS SECTION OF LMFBR REACTOR CORE



recirculation to exist in the core. Radial heat conduction from a hot assembly to a cold assembly through the duct wall also becomes more important for low flows. This is termed inter-assembly heat transfer.

Note that a large radial power gradient exists across the blanket assemblies of Figure 1.1.2. One such assembly is shown in more detail in Figure 1.1.3. The fluid on the high power side of the bundle is hotter and less dense. Therefore, for low flows it is accelerated to a higher velocity than the fluid on the lower power side. For a uniform inlet flow distribution, a buoyancy induced crossflow transports fluid to the hot side of the bundle. This is termed intra-assembly flow redistribution. Under severe power skew and flow conditions, the flow may reverse at the cold side of the bundle, resulting in flow recirculation within the assembly.

For the LMFBR, each assembly consists of a number of wire wrapped fuel rods. The wire wrap provides spacing for the rods, and enhances coolant mixing between the subchannels. In Figure 1.1.4 a wire wrapped rod is shown along with axial velocity profiles corresponding to increasing buoyancy effect. For larger buoyancy forces, the hot fluid near the surface of the pin is accelerated, while the channel centerline velocity decreases. Knowledge of these local buoyancy effects is necessary to properly model the coolant mixing and form drag due to the wire, along with the heat transfer and frictional resistance at the rod surface.

FIGURE 1.1.3
TYPICAL LMFBR ASSEMBLY

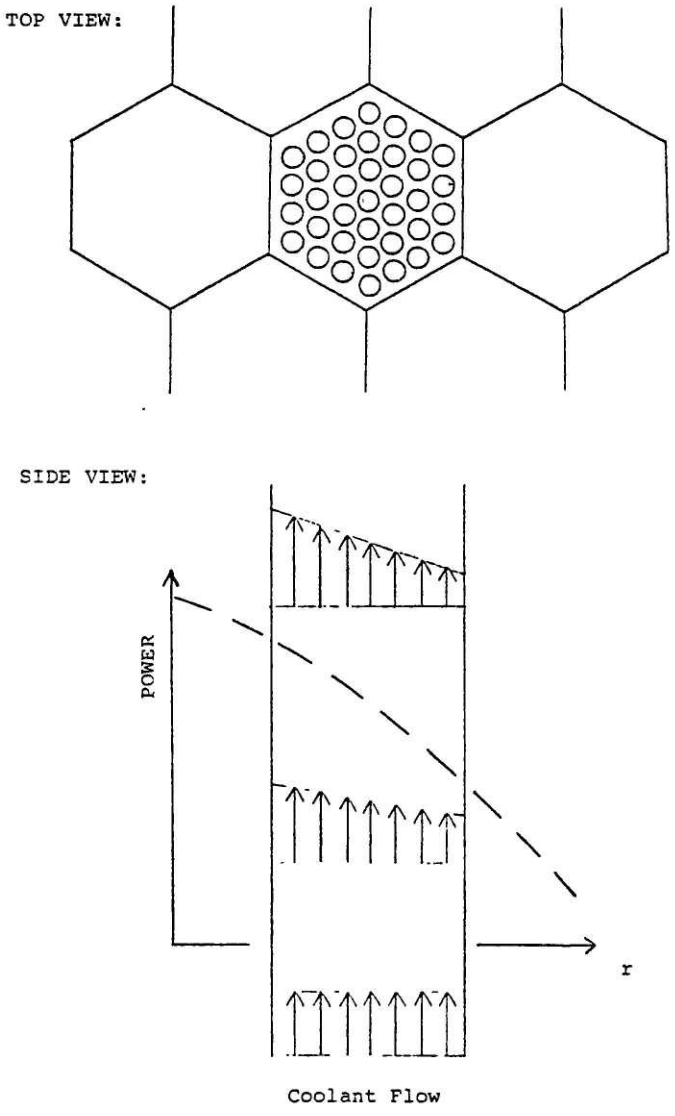
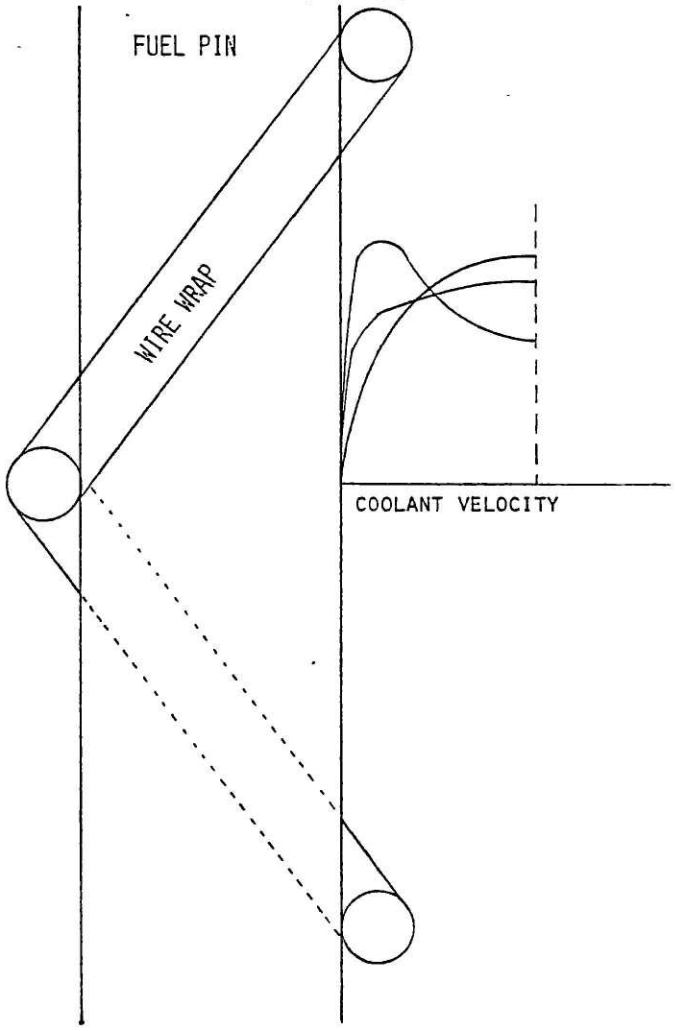


FIGURE 1.1.4
LOCAL BUOYANCY EFFECTS



Considering a single assembly it is necessary to distinguish between local (subchannel) and global (bundle) buoyancy effects. Local buoyancy effects are produced by density variations within a subchannel, which cause the velocity profile to distort as shown in Figure 1.1.4. Global buoyancy effects are produced by density variations within a bundle, and cause a buoyancy induced crossflow to the hot side of the bundle and a flattening of the radial temperature profile. We require a criteria for each. The local mixed convection criteria tells us when the correlations for input parameters (such as friction factor) must account for the effect of buoyancy. The global mixed convection criteria tells us when the overall code structure itself must account for buoyancy by providing for coupling of the governing conservation equations.

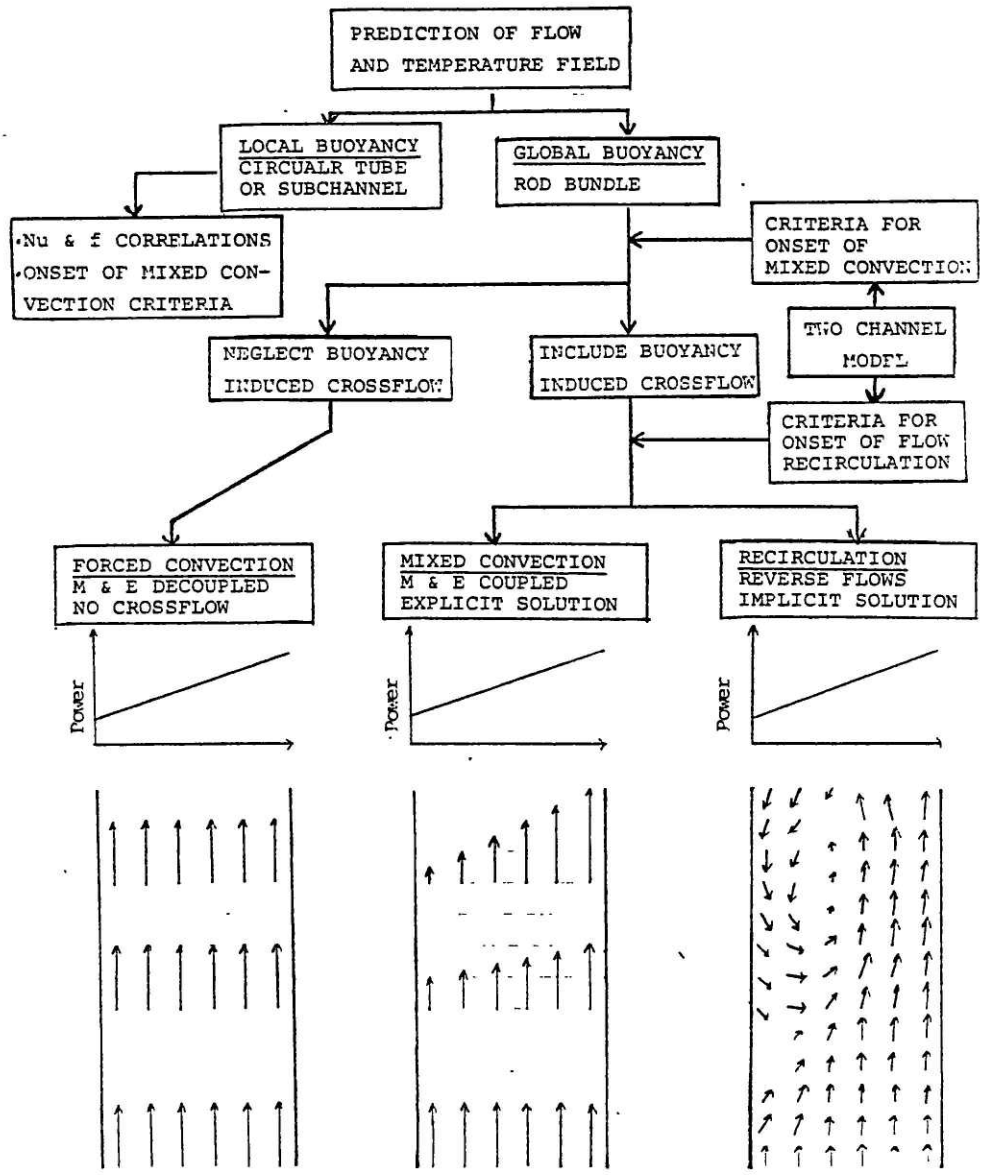
1.2 CONTRIBUTION OF THIS WORK

Figure 1.2.1 outlines the key technical issues which will be addressed in this thesis. The overall goal is to provide models to improve the capability of existing numerical tools which predict the flow and temperature field in rod bundles.

Both local buoyancy effects (subchannels and circular tubes) and global buoyancy effects (rod bundles) are considered. A literature review of mixed convection in circular tubes and other simple geometries will be presented. The purpose of this review is two-fold. First, it will provide physical insight into the phenomena of mixed convec-

FIGURE 1.2.1

OVERVIEW OF WORK



tion which will be helpful in the study of rod bundles. Second, circular tube correlations are often used in rod bundle analysis through use of the hydraulic diameter concept. The review will identify the important correlations (for friction factors and Nusselt numbers), and assess their validity through comparisons with data. Existing criteria for onset of mixed convection in tubes will be compared, and necessary improvements will be recommended.

For the case of rod bundles, criteria will be developed to predict the onset of mixed convection and onset of flow recirculation based on a two channel model of the rod bundle. Note that the global mixed convection criteria for rod bundles is different than the local mixed convection criteria for tubes or subchannels. The local mixed convection criteria determines when local buoyancy effects cause a significant departure of the correlations for circular tube Nusselt numbers or friction factors from their forced convection values. The rod bundle criteria determines when global buoyancy effects become important, and cause a buoyancy induced crossflow in the rod bundle. The rod bundle criteria thus determines when buoyancy effects must be accounted for in the numerical solution. A fundamental similarity between local and bundle mixed convection will be identified.

The criteria for onset of recirculation determines the conditions under which reverse flows will occur in a rod

bundle. It identifies a regime which should be avoided since the accuracy of subchannel codes (which assume that the flow is predominately axial) has not been confirmed for recirculating flows. It also gives a means of determining what type of numerical tool is required for detailed analysis of the rod bundle. If no recirculation exists, explicit methods may be employed, whereas reverse flows require implicit methods.

As indicated in Figure 1.2.1, a two channel model of the rod bundle will be used to develop the two criteria. An approximate analytical solution is obtained for the governing equations by the method of trial solution with undetermined parameters. In dimensionless form, the analytical solution allows identification of the key dimensionless parameters governing mixed convection in rod bundles. The analytical solution can then be expressed in the form of a flow regime map, giving the dividing lines between the forced convection, mixed convection and recirculation flow regimes.

CHAPTER 2

VERTICAL MIXED CONVECTION FLOWS

Before addressing the problem of mixed convection in vertical rod bundles, a thorough understanding of mixed convection in less complex geometries should exist. Many of the thermal hydraulic phenomena which occur in rod bundles also occur in more simple geometries which have already received much attention both experimentally and analytically. In some instances, these results may be applied directly to the rod bundle case. An example of this is the application of circular tube friction factor and Nusselt number correlations to flow in rod bundles by employing the hydraulic diameter transformation. Even if not directly applicable, results for simple geometries will certainly shed light on some of the important thermal hydraulic aspects of mixed convection in rod bundles.

In this literature review, attention will be focused on aiding mixed convection flows adjacent to vertical surfaces since this is the type of flow which occurs for upflow in rod bundles. The geometry of greatest interest is the circular tube since flow in an isolated subchannel can be expected to exhibit similar characteristics to flow in circular tubes.

2.1 FUNDAMENTAL MECHANISMS IN MIXED CONVECTION

2.1.1 Nondimensionalization of the Governing Equations

The general governing equations for determination of the velocity and temperature fields in a fluid near a vertically aligned solid surface are:

$$\frac{D\rho}{Dt} + \rho\nabla\cdot\bar{V} = 0 \qquad 2.1.1a$$

$$\rho\frac{D\bar{V}}{Dt} = -\nabla P + (\rho-\rho_o)g\bar{e} + \mu\nabla^2\bar{V} + \frac{\mu}{3}\nabla(\nabla\cdot\bar{V}) \qquad 2.1.1b$$

$$\rho C_p\frac{DT}{Dt} = \nabla\cdot K\nabla T + \beta T\frac{DP}{Dt} + \mu\Phi_V \qquad 2.1.1c$$

where $\bar{e}$ is a unit vector in the direction of gravity. The above equations constitute a set of coupled elliptic partial differential equations, and are very difficult to solve. Several approximations may be employed to simplify the equations.

For the Boussinesq approximation, density variations are neglected everywhere but in the gravity term of the momentum equation. This allows us to write:

$$-(\rho - \rho_0) = \rho\beta(T - T_0) \qquad 2.1.2$$

It has been shown in Reference 3 that this approximation is valid if:

$$\beta(T-T_o) << 1 \qquad 2.1.3$$

and:

$$\left(\frac{\partial \rho}{\partial P}\right)_T gL << 1 \qquad (2.1.4)$$

With the Boussinesq approximation the equations (2.1.1a to 2.1.1c) are:

$$\nabla \cdot \bar{V} = 0 \qquad (2.1.5a)$$

$$\rho \frac{D\bar{V}}{Dt} = -\rho g \beta (T-T_o)\bar{e} - \nabla P + \mu \nabla^2 \bar{V} \qquad (2.1.5b)$$

$$\rho C_p \frac{DT}{Dt} = K\nabla^2 T + \beta T \frac{DP}{Dt} + \mu \Phi_V \qquad (2.1.5c)$$

An additional approximation which is often made for external flows is the boundary layer approximation. The key assumption in the boundary layer approximation is that gradients parallel to the surface are neglected with respect to gradients normal to the surface. This approximation will not be made since internal flows are considered here.

The dimensionless parameters governing mixed convection may be obtained from dimensional analysis (Buckingham π theorem). This gives us the dimensionless parameters, but does not attach physical meaning to them. A better approach is to nondimensionalize the governing equations. This has been done by many investigators (1, 2, 3, 4). Their results will be outlined here.

In mixed convection, both the forced convection flow and

natural convection (buoyancy induced) flow are significant. Hence, it is not obvious what to use as a characteristic velocity in mixed convection. Two limiting cases will be considered: flows dominated by forced convection effects, and flows dominated by free convection effects.

In forced convection, we know the characteristic velocity from the forced flow. In natural convection the characteristic velocity may be estimated by assuming that the inertia force balances the buoyancy force. This gives the maximum possible velocity since viscous effects are ignored. This force balance gives

$$V_{free} = \sqrt{g\beta L(T-T_0)} \qquad (2.1.6)$$

Assume for now that the characteristic velocity V_C is known through some physical argument. The governing equations will now be made dimensionless by utilizing the characteristic velocity V_C, the characteristic dimension L, the characteristic time t_C, and characteristic temperatures T_1 and T_0. It follows that:

$$V^* = \frac{\bar{V}}{V_C} \qquad \Phi_V^* = \Phi_V \frac{L^2}{V_C^2}$$

$$\nabla^* = L\nabla$$

$$P^* = P/\rho V_C^2 \qquad \nabla^{*2} = L^2\nabla^2 \qquad (2.1.7)$$

$$\theta = \frac{T-T_0}{T_1-T_0} \qquad t^* = t/t_C$$

where the stars indicate dimensionless quantities. If the conservation equations are written in terms of the above dimensionless quantities, the following equations result:

$$\nabla^* \cdot \bar{V}^* = 0 \qquad (2.1.8a)$$

$$\textcircled{1}\ \frac{\partial V^*}{\partial t^*} + \bar{V}^* \cdot \nabla^* \bar{V}^* = -\nabla^* P^* + \frac{\nabla^{*2} \bar{V}^*}{\textcircled{2}} - \textcircled{3}\ \theta \bar{e} \qquad (2.1.8b)$$

$$\textcircled{1}\ \frac{\partial \theta}{\partial t^*} + \bar{V}^* \cdot \nabla^* \theta = \textcircled{4} \nabla^{*2} \theta + \beta T \left[\textcircled{5}\ \frac{\partial P^*}{\partial t^*} + \textcircled{6}\ \bar{V}^* \cdot \nabla^* P^* \right] + \textcircled{7}\ \Phi_V^* \qquad (2.1.8c)$$

where the coefficients ① through ⑦ are given in Table 2.1.1. The physical significance attached to each coefficient is given. For dominant forced convection $V_C = V$, and the seven coefficients form 5 independent dimensionless parameters upon which the velocity and temperature fields will depend (Sr, Re_L, Gr, Pr, Ec). For dominant free convection, $V_C = \sqrt{g\beta L(T_1 - T_0)}$ and the seven coefficients form four independent dimensionless parameters (Sr, Gr, Pr, $\frac{g\beta L}{C_P}$). Note that for dominant free convection the dimensionless parameters are the same with the exception that Re is replaced by $\sqrt{Gr}$ and Ec is replaced by $\frac{g\beta L}{C_P}$. The Strouhal number retains the same name, but a different characteristic velocity is used.

If appropriate characteristic length, time, velocity and temperature scales are selected the dimensionless

TABLE 2.1.1

DIMENSIONLESS PARAMETERS FROM NONDIMENSIONALIZATION OF GOVERNING EQUATIONS

		DOMINANT FORCED CONVECTION $V_C = V$		DOMINANT FREE CONVECTION $V_C = \sqrt{g\beta L(T_1-T_o)}$	
COEFFICIENT	PHYSICAL SIGNIFICANCE	DIMENSIONLESS GROUP		DIMENSIONLESS GROUP	
(1) $= \frac{L}{V_c t_c}$	$\frac{\text{fluid particle residence time}}{\text{characteristic time}}$	Sr	Strouhal number	Sr	Strouhal number
(2) $= \frac{V_c L}{\nu}$	$\frac{\text{inertia force}}{\text{viscous force}}$	Re_L	Reynolds number	$\sqrt{Gr}$	Grashov number
(3) $= \frac{g\beta L(T_1-T_o)}{V_c^2}$	$\frac{\text{buoyancy force}}{\text{inertia force}}$	$\frac{Gr_{\Delta T}}{Re^2} = Ri$	Richardson number	1	--
(4) $= \frac{\alpha}{V_c L}$	$\frac{\text{conduction heat transfer}}{\text{convection heat transfer}}$	$\frac{1}{Pe} = \frac{1}{RePr}$	Peclet number	$\frac{1}{\sqrt{Gr}\,Pr}$	--
(5) $= \frac{V_c L}{C_p t_c (T_1-T_o)}$	$\frac{\text{viscous dissipation energy}}{\text{convective energy}} \frac{\text{particle residence time}}{\text{characteristic time}}$	Ec Sr	--	$(\frac{g\beta L}{C_p})$ Sr	--
(6) $= \frac{V_c^2}{C_p(T_1-T_o)}$	$\frac{\text{viscous dissipation energy}}{\text{convective energy}}$	Ec	Eckert number	$(\frac{g\beta L}{C_p})$	--
(7) $= \frac{\nu V_c}{C_p L(T_1-T_o)}$	$\frac{\text{viscous dissipation energy x viscous force}}{\text{convective energy x inertia force}}$	$\frac{Ec}{Re}$	--	$\frac{g\beta L}{C_p}\frac{1}{\sqrt{Gr}}$	--

parameters of Equations 2.1.7 are all of order one. It follows that the order of magnitude of the terms in Equations 2.1.8a to 2.1.8c are given by the coefficients (1), (2), (3), (4) and (7), and the coefficients (5) and (6) multiplied by βT where T is the absolute temperature. Terms in the equations which are preceded by coefficients which are small relative to the others may be neglected.

In Reference 4 it was shown that the Eckert number is significant only when the characteristic velocity is of the order of the speed of sound, so coefficients (5) through (7) may be neglected for our purposes. For transient flows Sr may be negligible if the characteristic time is large in comparison to the fluid particle residence time (L/V_C). This is the quasi-steady state approximation. Under these conditions the governing equations are:

$$\nabla^* \cdot \bar{V}^* = 0 \qquad (2.1.9a)$$

$$\bar{V}^* \cdot \nabla^* \bar{V}^* = -\nabla^* P^* + \frac{1}{(2)} \nabla^{*2} \bar{V}^* - (3)\,\theta \bar{e} \qquad (2.1.9b)$$

$$\bar{V}^* \cdot \nabla^* \theta = (4) \nabla^{*2} \theta \qquad (2.1.9c)$$

For the case of dominant forced convection, the velocity and temperature fields are functionally expressed as:

$$\bar{V}^*, \theta = f(Re, Pr) \qquad (2.1.10)$$

while for dominant free convection

$$\bar{V}^*, \theta = f(Gr, Pr) \qquad (2.1.11)$$

For the case of mixed convection, which is the transition between the above two cases, we expect all three parameters to be of importance:

$$\bar{V}^*, \theta = f(Gr, Re, Pr) \qquad (2.1.12)$$

The dimensionless parameters which have been identified from the governing equations are given in Table 2.1.2. Note that D has been selected as the characteristic dimension in Re and $Gr_{\Delta T}$ since we are concerned primarily with internal flows. Other dimensionless parameters which have been found in the literature are also given, along with conversion relations.

TABLE 2.1.2

DEFINITIONS OF IMPORTANT DIMENSIONLESS PARAMETERS IN MIXED CONVECTION

NAME	DIMENSIONLESS GROUP
Reynolds number	$Re = \frac{VD_e}{\nu}$
Prandtl number	$Pr = \frac{C_p \mu}{K}$
Grashof number	$Gr_{\Delta T} = \frac{\beta g \Delta T D_e^3}{\nu^2}$
Eckert number	$Ec = \frac{V^2}{C_p \Delta T}$
Strouhal number	$Sr = \frac{L}{Vt_c}$
Richardson number	$Ri = \frac{Gr_{\Delta T}}{Re^2}$
Peclet number	$Pe = RePr$
Boussinesq number	$Bo = GrPr^2$
Rayleigh number	$Ra = GrPr$
Grashof number based on heat flux	$Gr_q = \frac{\beta g q'' D_e^4}{K\nu^2}$
Grashof number based on axial temp. gradient	$Gr_A = \frac{\beta g D_e^4}{\nu^2} \frac{\Delta T_b}{L} = \frac{4Gr_q}{RePr} \frac{D_e}{D_H}$

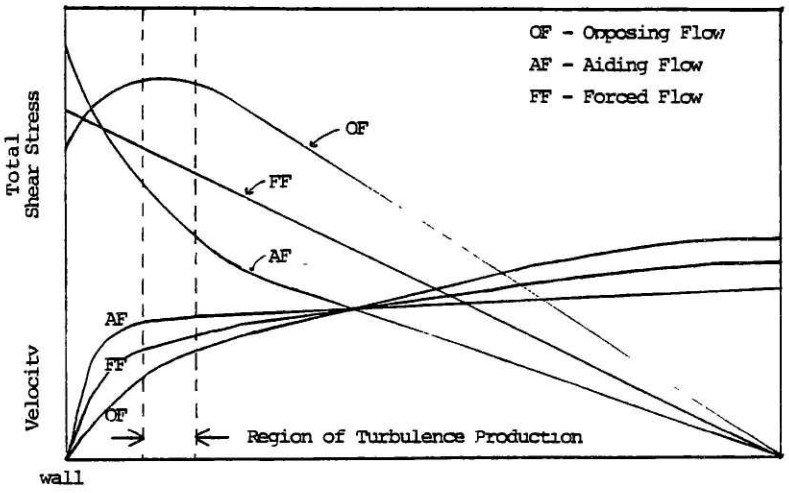
2.1.2 The Effects of Buoyancy on Laminar and Turbulent Flows Near Vertical Surfaces

Figure 2.1.1 shows qualitatively the velocity and shear stress distributions in a vertical tube for aiding and opposing flow, along with isothermal forced flow profiles. The distributions are different in detail for laminar and turbulent flows, but the manner in which they are affected by buoyancy is similar. It is then surprising that for laminar aiding flow, buoyancy increases Nu, while for a turbulent aiding flow, buoyancy decreases Nu (initially, at least). Both effects reverse for an opposing flow. This behavior can be explained qualitatively in the following manner.

The heat transfer coefficient is in general determined by two factors: the distribution of the velocity, and the distribution of the diffusivity for heat in the fluid. For a laminar flow, the diffusivity for heat is a constant so the effect of buoyancy on heat transfer is determined by the velocity distribution. The higher the velocity close to the wall, the higher heat transfer coefficient is obtained. Figure 2.1.1 shows that for aiding flow, buoyancy will increase the velocity close to the wall, and increase Nu and f. For opposing flow the opposite will initially occur. For large buoyancy forces a point may be reached when the flow near the wall reverses direction, and increasing the buoyancy decreases Nu and f; but this type of profile is highly unstable, and the flow is not likely to remain laminar.

FIGURE 2.1.1

EFFECT OF BUOYANCY ON VELOCITY AND SHEAR STRESS
FOR AIDING AND OPPOSING FLOW.

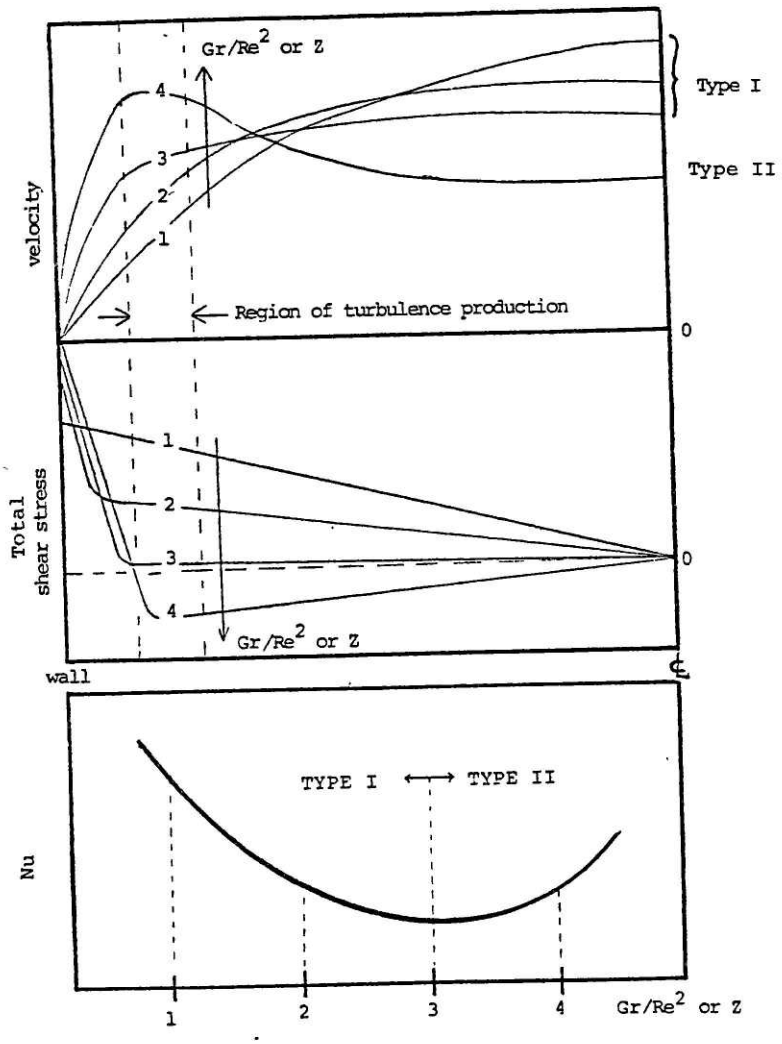


The same effect on the velocity profiles exist for turbulent flow, but in this case the change in turbulent diffusivity dominates. In a turbulent pipe flow, turbulence kinetic energy is produced close to the wall and diffuses out to the core (turbulence energy production is equal to the product of the turbulent shear stress and the gradient of the mean velocity). The region of high turbulence production (given as $Y^+ = 10$ to 30 in Reference 5) is shown in Figure 2.1.1 with dotted lines close to the wall. It follows from these profiles that an aiding flow creates lower turbulence production and a reduction in heat transfer. The turbulence production in an opposing flow is increased, enhancing the heat transfer (initially).

The case of turbulent aiding flow merits closer study, as it is the flow obtained in reactor applications. The velocity and shear stress profiles of Figure 2.1.2 represent profiles for increasing buoyancy effects, or increasing Gr/Re^2. If the buoyancy forces are sufficient to reduce the turbulence production to zero (see profile number 3) the flow will become laminar. This phenomena also occurs in turbulent boundary layers undergoing strong acceleration (6), or suction at the wall and has been termed laminarization. It was observed in buoyant flows of supercritical fluids (see the review article by Hall (7)) in which the density is a strong function of temperature, and large buoyancy forces are easily generated. It was later shown to occur in noncritical fluids (8). Further increase in the buoyancy forces will cause the

FIGURE 2.1.2

EFFECT OF BUOYANCY ON HEAT TRANSFER FOR AIDING TURBULENT FLOW



shear stress to reverse sign (see profile number 4) and the maximum velocity to shift from the channel center line. (This was called a Type II flow by Connor (9), as opposed to a Type I flow where the maximum velocity is along the channel centerline). If this occurs the turbulence production increases, improving the heat transfer.

This laminarization and subsequent transition to turbulence has been observed to cause a localized deterioration in heat transfer in developing aiding flow in vertical pipes, and peaks in wall temperature. Many examples of this phenomena are given by Jackson and Hall (10).

Since the laminarization phenomena can cause local overheating, it is of interest to predict the heat transfer under these conditions. Launder and Jones (11) employed a two equation turbulence model to predict laminarization in a boundary layer undergoing acceleration. Abdelmeguid and Spalding (12) calculated laminarization due to buoyance forces with the same type of turbulence model. Their code predicted well the Nusselt number data of Buhr (13) which exhibited buoyancy induced laminarization. Oosthuizen (14) modified the mixing length model to account for the effect of buoyancy. His numerical results predicted deterioration in heat transfer (Laminarization) for turbulent flow over a vertical flat plate.

2.2 LITERATURE REVIEW OF MIXED CONVECTION

2.2.1 Review of Data and Correlations for mixed convection

Kenning et al. (8) performed an experimental study of turbulent mixed convection in a vertical tube with upflow for uniform heat flux. Wall temperature measurements were made at ten axial locations in a tube of 80 heated lengths, with a 22 L/D unheated entrance. Figure 2.2.1 summarizes some of his results. Wall temperature peaking was observed to occur for larger heat fluxes. The peak first appears near the tube exit, and moves upstream for increasing heat flux. Correlations were developed for the wall temperature peaking regime, the distance for development of the peak temperature, and the minimum Nussult number. One hundred and six experimental runs were made where the heat flux, flow rate, and inlet temperature were varied. Kenning's data are given in Appendix A along with a program which will be used to calculate Re, Pr, Gr and Nu for each data point of each run. Correlations were given for the conditions under which wall temperature peaking occurred:

$$\frac{Gr_q}{Re^{3.4}Pr^{.4}} > 4 \times 10^{-5} \qquad (2.2.1)$$

The value of the minimum heat transfer coefficient:

$$Nu = .75(Gr_q Pr)^{.25} \qquad (2.2.2)$$

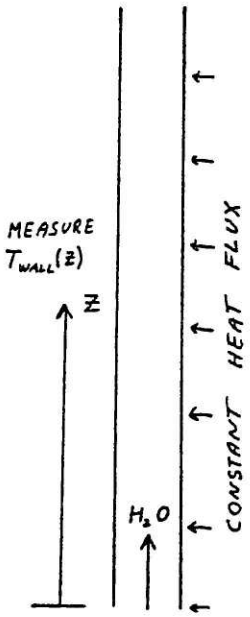
and the distance for development of the peak wall temperature:

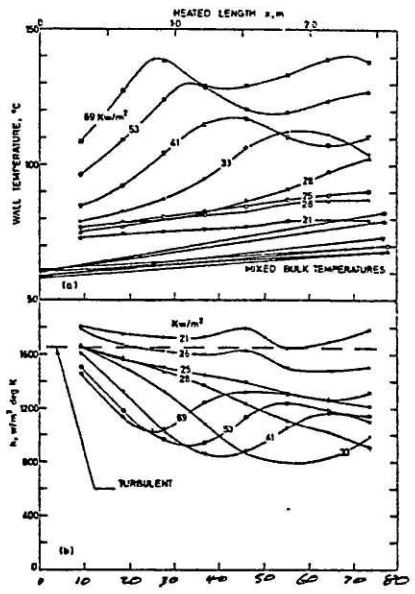
$$\frac{x}{d} = .07 \frac{Re^3 Pr^{1.2}}{Gr_q} \qquad (2.2.3)$$

FIGURE 2.2.1

EXPERIMENTAL RESULTS OF KENNING

Circular tube





Re = 16,000

Pr = 2.7

T_{in} = 60°C

Figure 2.2.2 presents some of the results of Buhr (13) for flow of mercury in a vertical tube. Velocity and temperature profiles were measured at a fixed distance from the start of heating of L/D = 74 for Reynolds numbers of 19,000, 30,000 and 60,000. Even for Re = 60,000 significant distortion of the velocity profile due to buoyancy is observed. The Nusselt number was also measured for each of 16 runs. The Nusselt number data is presented in Table 2.2.1. Additional data for mercury can be found in Reference 15, but only temperature profiles were measured.

An experimental study of mixed convection in a vertical tube with water was made by Petukhov and Strigin (16, 17). Correlations were obtained for Nusselt numbers and friction factors for both upflow and downflow. Only the upflow results will be given here. Two test sections were employed. Test section #1 had an unheated entrance length of 26 L/D, and a heated length of 99 L/D. Test section #2 had a smooth converging nozzle at the inlet, and a heat length of 80 L/D.

For type I flows, the Nusselt number depended on the test section inlet length. For either test section, the type I flow Nusselt number was correlated by:

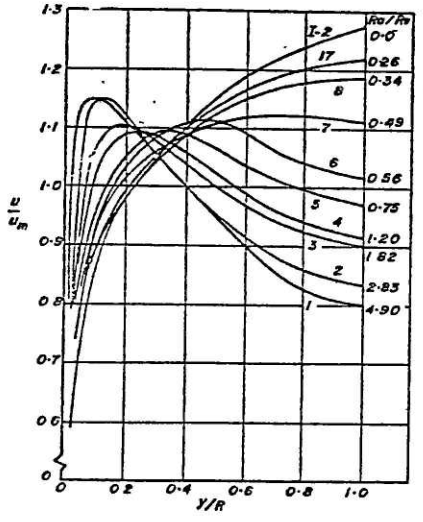
$$\frac{Nu}{Nu_T} = \left(1 + B \frac{Ra_A}{Re^2}\right)^{-1} \qquad (2.2.4)$$

where:

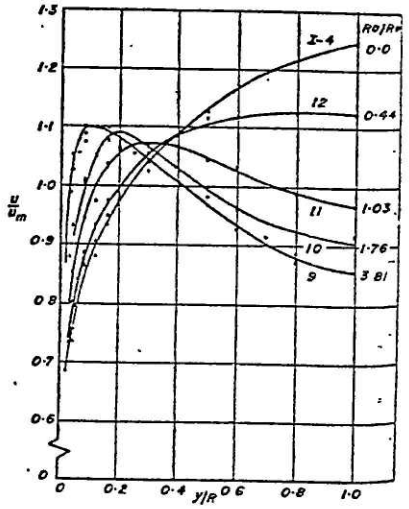
$$\text{If } \left.\frac{L}{D}\right|_{in} = 0 \quad B = 94, \quad Ra_A/Re^2 < 4.8 \times 10^{-3}$$

FIGURE 2.2.2

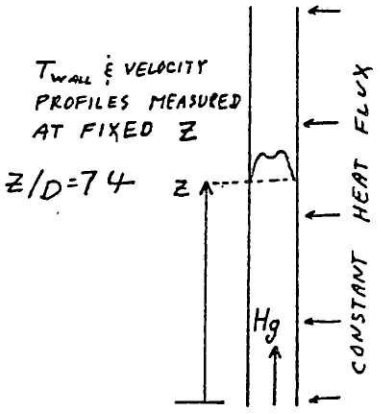
EXPERIMENTAL RESULTS OF BUHR

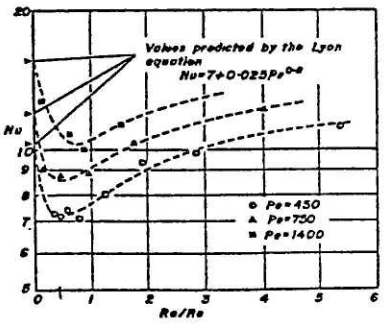


Re = 19,000



Re = 30,000





Variation of Nusselt number with heat flux

TABLE 2.2.1

BUHR'S DATA AND CONNOR'S DATA

Run #	Re x 10^{-3}	Gr_A/Re^2	Nu/Nu_T
1	19.6	1.19E-2	1.07
2	19.4	6.39E-3	.95
3	19.3	4.30E-3	.90
4	19.0	2.88E-3	.77
5	19.0	1.83E-3	.69
6	18.8	1.34E-3	.72
7	18.9	1.08E-3	.70
8	19.0	8.00E-4	.71
9	35.0	5.00E-3	.98
10	33.6	2.28E-3	.84
11	33.1	1.26E-3	.73
12	30.8	6.65E-4	.74
20	32.2	2.16E-4	.74
13	62.4	6.26E-4	.64
15	61.6	4.39E-4	.69
16	61.0	8.57E-5	.82
N10	5.4	3.81E-4	.76
N11	5.3	5.87E-4	.51
N12	5.3	7.80E-4	.55
N13	5.0	1.02E-3	.58

Runs 1-20: Buhr's mercury data
Runs N10-N13: Connor's air data
E-n means x 10^{n}

$$\text{If } \left.\frac{L}{D}\right|_{in} = 26 \qquad B = 719, \quad Ra_A/Re^2 < 1.6 \times 10^{-3}$$

For type II flows, the heat transfer is independent of the inlet length, and for either test section, the Nusselt number is given by:

$$\frac{Nu}{Nu_T} = 3.97 \left(\frac{Ra}{Re^2}\right)^{1/3} \tag{2.2.5}$$

For Equations 2.2.4 and 2.2.5 Nu_T is the Nusselt number for fully developed turbulent forced convection:

$$Nu_T = .023\ Re^{.8} Pr^{.4} \tag{2.2.6}$$

The Nusselt number correlations above are plotted in Figure 2.2.3 along with the experimental data. For low values of Ra_A/Re^2 the forced convection limit is achieved ($\frac{Nu}{Nu_T} = 1$).

For test section number 2, pressure drop data was taken, and correlated in terms of the friction factor. The data was correlated by:

$$\frac{f}{f_o} = \left[1 + 3.5\left(\frac{Ra_A}{Re^{3/2}}\right)^2\right]^{.4} \tag{2.2.7}$$

where:

$$f_o = \frac{.316}{Re^{1/4}}$$

Some of the results of Connor and Carr (9) for the aiding flow of air in a vertical tube are given in Figure 2.2.4. Curves 1-4 show the effect of increasing the heat flux on

FIGURE 2.2.3

DATA AND CORRELATIONS OF PETUKHOV

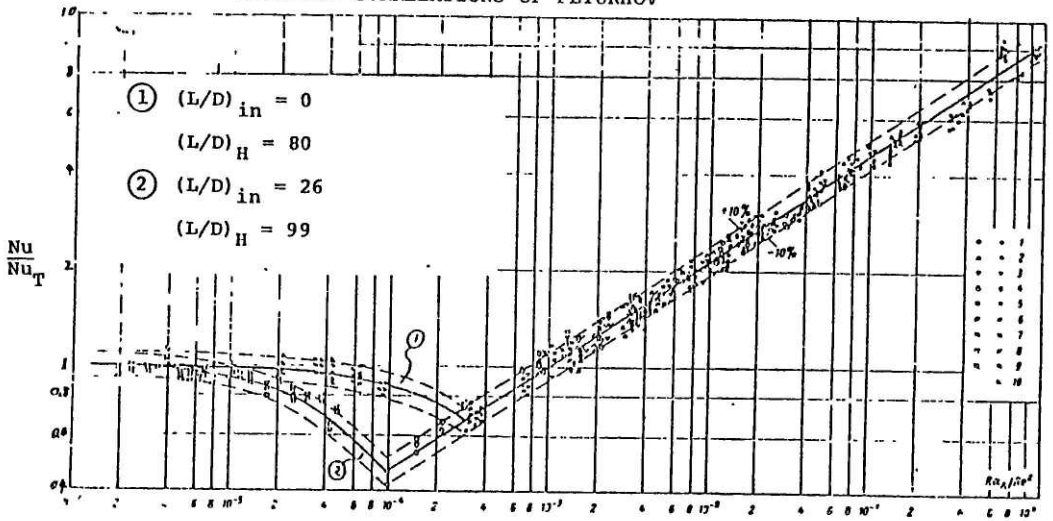
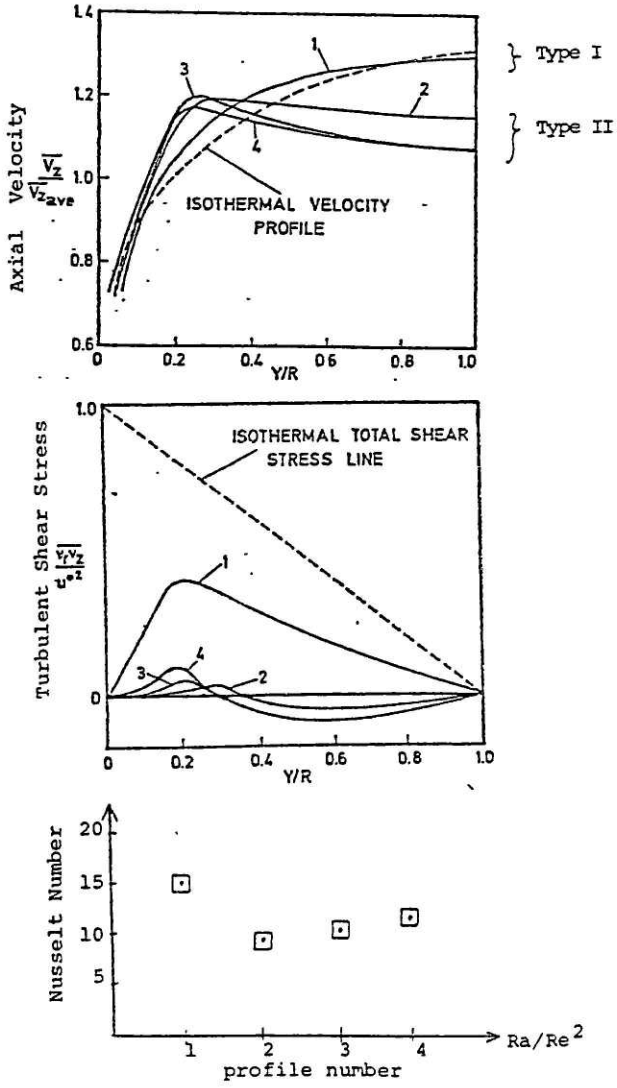


FIGURE 2.2.4

EXPERIMENTAL RESULTS OF CONNOR



velocity, turbulent shear stress, and turbulent velocity intensity profiles. The Nusselt numbers corresponding to profiles 1-4 are 14.8, 9.8, 10.6, and 10.7, respectively. As expected, the minimum Nusselt number corresponds to the flat velocity profile (#2) and the nearly zero shear stress profile. The improvement in heat transfer results when the type II profile develops, and the turbulent shear stress near the wall (and hence the turbulence production) starts to increase. The minimum heat transfer corresponds also to a minimum turbulent intensity profile. Connor presented a correlation valid only for Type II flows which appeared to correctly account for Pr:

$$Nu/Nu_T = 4.26 \left(Gr_A/Re^2 \right)^{.263} \qquad 2.2.8$$

An experimental and theoretical study of heat transfer in vertical tube flows was performed by Greif (18) for aiding flow with air and argon. Temperature profiles were measured for laminar ($1850 < Re < 2100$) and turbulent ($10{,}000 < Re < 19{,}500$) flows. Measurements were taken at $\frac{x}{D} = 108$, where the flow was observed to be fully developed. The turbulent flow results were in the forced convection regime, while buoyancy effected the laminar flow results (16% decrease in Nusselt number from forced convection value of 4.364).

In Reference 19 Greif extended his numerical analysis to account for the effect of thermal radiation. The radiation heat transfer coefficient was found to be about 10% of

the total heat transfer coefficient for a flow of carbon dioxide in the tube. The effect of radiation caused a flattening of the radial temperature profile, and a decrease in the effect of buoyancy.

Figure 2.2.5 summarizes some of the results of Byrne and Ejiogu (20) for air flow in a vertical pipe with a uniform wall temperature boundary condition. Figure 2.2.5a shows the effect of Grashof number on a Nu vs Re plot. For higher Gr, a minima occurs in the Nusselt number due to laminarization. Figure 2.2.5b shows the same data with a plot of constant Nu on a Gr-Re plane. It also shows that the minima in heat transfer corresponds closely to their criteria (see Table 2.2.2). The turbulence intensity and velocity profiles across the tube are given in Figures 2.2.5c and 2.2.5d, respectively. Note that for the $Gr_{\Delta T} = 1.34 \times 10^9$ run of Figure 2.2.5a the minimum Nu occurs at $Re = 4 \times 10^4$, which also corresponds with the minima in turbulence intensity of Figure 2.2.5c and the flat velocity profile of Figure 2.2.5d. This is in agreement with the turbulence production agrument given earlier.

Some of the results of Alferov, et al. (21) are presented in Figure 2.2.6. The first plot shows the wall temperature distribution for both upflow and downflow of water and the second plot shows the corresponding heat transfer coefficients ($\alpha_t/\alpha_f = Nu/Nu_T$) for a typical run. Note that

FIGURE 2.2.5

EXPERIMENTAL RESULTS OF BYRNE AND EJIOGU

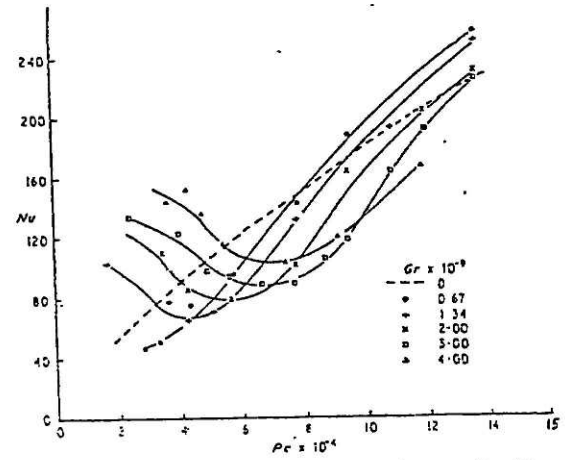
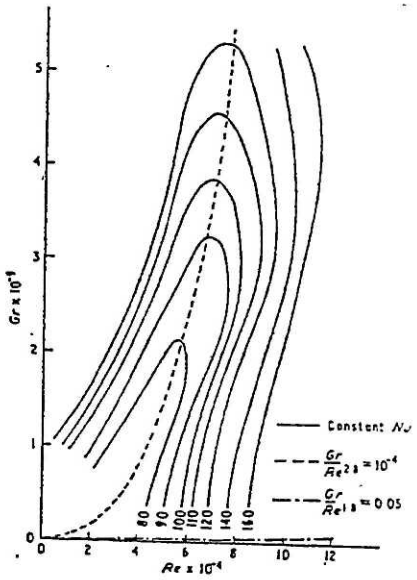


Fig. A Effect of Grashof number on the heat transfer with forced convection



B Contours of constant Nusselt number on grid of Grashof and Reynolds numbers

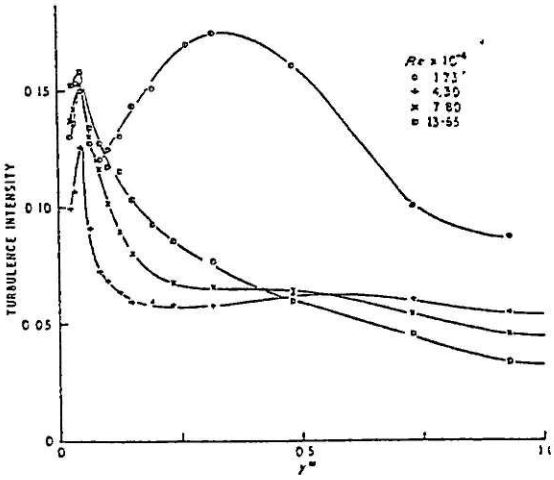


Fig. C Distribution of turbulence intensity across the pipe at a Grashof number of 1·34×10⁵ and various Reynolds numbers

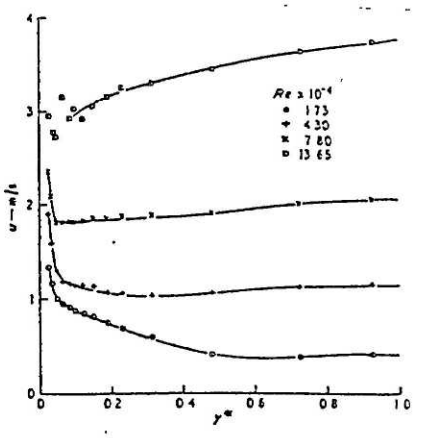
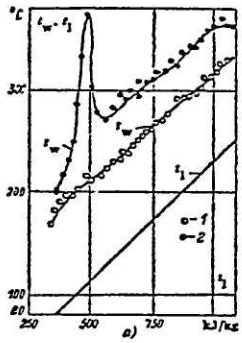


Fig. D Velocity distribution across the pipe for a Grashof number of 1·34×10⁵ at various Reynolds numbers

FIGURE 2.2.6

EXPERIMENTAL RESULTS OF ALFEROV

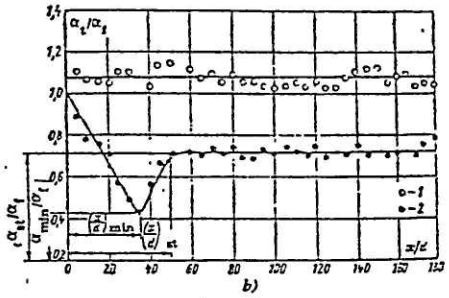


t_w - wall temperature

t_l - bulk temperature

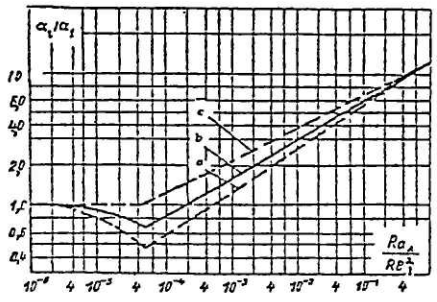
O - 1 downflow

● - 2 upflow



$$(x/d)_{min} = 52(Ra_A/Re)_{in}^{-.5}$$

$$(x/d)_{st} = 1.5(x/d)_{min}$$



curve a - α_{min}/α_f (upflow)

curve b - α_{st}/α_f (upflow)

curve c - downflow

Generalised dependence $\alpha/\alpha_l = f(Ra_A/Re_l^2)$

for downflow, α_t/α_f is constant with x/d, but for upflow, local deterioration in heat transfer is observed due to laminarization. This is followed by a region of stabilized (fully-developed) heat transfer. The final plot shows a best-fit of the Nusselt number data plotted against Ra_A/Re^2. Curve "a" is a plot of the minimum Nusselt number (α_{MIN}/α_f) which occurs at $(x/d)_{MIN}$, curve "b" is a plot of the fully developed Nusselt number (α_{st}/α_f which occurs for $(x/d) > (x/d)_{ST}$), and curve "c" is the Nusselt number for downflow.

This plot displays vividly the three regimes of heat transfer:

(1) When $Ra_A/Re^2 < 3 \cdot 10^{-6}$, the three curves converge into one where $\alpha_t/\alpha_f = 1$. This is the forced convection regime, where the heat transfer depends on Re only.

(2) When $Ra_A/Re^2 > 1$, the three curves converge into one which is Reynolds number independent. This is the natural convection regime.

(3) When $Ra_A/Re^2 = 3 \times 10^{-6}$ to 1, both Re and Ra_A are important in determining heat transfer. This is the mixed convection regime.

Correlations were also presented for the distance to the heat transfer minima $(x/d)_{MIN}$, and the distance to fully developed heat transfer $(x/d)_{st}$.

The effects of buoyancy on laminar upflow friction factors was studied by Bishop et al. (22). An analytical solution of the conservation equations was found for fully developed flow. The velocity field was expressed in terms of B_{er} and B_{ei} functions, and the parameter Gr_q/Re. The analytical solution was in good agreement with the velocity profiles measured by Greene and Scheele. From the velocity field, the friction factor was obtained. An algebraic fit to the analytical result was found to be:

$$\frac{f}{f_o} = \left[1 + 2.97 \times 10^{-3} \frac{Gr_q}{Re} \right]^{.655} \equiv F \qquad (2.2.9)$$

From the friction factor data of Greene and Scheele (23) and Kemeny and Somers (24), a best fit correlation was found which accounts for the effect of flow development:

$$\frac{f}{f_o} = 1 + \frac{F-1}{1+.36Z^{-3}} \qquad (2.2.10)$$

where:

$$Z = 50\left(\frac{L}{D}\right)$$

This reduces to Equation 2.2.9 for large $\frac{L}{D}$. Since the data of (23) and (24) were for water, the correlation is only valid

for $2<Pr<6$. The analysis by Brown (25) for fully developed upflow yielded:

$$\frac{f}{f_o} = .1\left[\frac{Gr_q}{Re}\right]^{.475}, \quad \frac{Gr_q}{Re} > 135 \tag{2.2.11}$$

Mixed Convection - Opposing Flow

The case of opposing flow (downflow in a heated channel) has received considerable attention, since in an HTGR the coolant flows vertically downward in the core. Turbulent downflow in a pipe was investigated experimentally by Easby (26) for uniform wall temperature. The friction factor was correlated by:

$$\frac{f}{f_{iso}} = 1.006 - 5.13\,\frac{Gr}{Re^2} \tag{2.2.12}$$

and heat transfer by:

$$\frac{st}{st_{iso}} = 1 + 8.9\,\frac{Gr}{Re^2} \tag{2.2.13}$$

where iso indicates isothermal flow and Gr is defined as:

$$Gr = \frac{g(T_w-T_B)D^3}{\nu^2 T_B} \tag{2.2.14}$$

The Reynolds number range was $2,000<Re<10,000$ and $Gr<10^6$. Note that buoyancy increases heat transfer and decreases friction. The decrease in friction is caused by the decrease in the velocity gradient at the wall, and the increase in heat transfer is due to enhanced turbulence production which was discussed in Section 2.1.

Laminar upflow and downflow was studied numerically by Collins (27) for uniform heat flux. His results for downflow indicated that both f and Nu decrease with Gr/Re. This confirms the discussion of Section 2.1 regarding buoyancy effects in opposing laminar flow.

The entrance region for turbulent downflow of air in a heated pipe with uniform wall temperature was investigated by Khosla et al. (28). His results indicated that buoyancy increased turbulent transport, and that isothermal eddy diffusivity models are inadequate for buoyancy dominated flows. An additional test was run with water to identify local flow reversal for upflow with a cold wall.

A Nusselt number correlation for opposing flow was given by Petukhov and Strigin (16) as:

$$\frac{Nu}{Nu_T} = \left(1 + .5\,\frac{Ra_A}{16Re}\right)^{1/3} - 0.15\,\exp\left[-8\left(\frac{Ra_A}{16Re} - .5\right)^2\right] \qquad (2.2.15)$$

For: $300 < Re < 25{,}000$

$300 < \frac{Ra_A}{16} < 8 \times 10^5$

$2 < Pr < 8$

As Ra_A/Re^2 increases the above correlation predicts a slight decrease in heat transfer (due to a decrease in velocity near the wall), than an increase in heat transfer (due to enhanced turbulence production). For $Ra_A/16Re > 1$ the second term of Equation 2.2.15 is small, giving

$$\frac{Nu}{Nu_T} = \left(1 + .5\,\frac{Ra_A}{16Re}\right)^{1/3} \qquad (2.2.16)$$

The quantity 16 appears under Ra_A because Reference 16 defined Ra_A different than does this work.

Additional studies of downflow have been performed by Axcell and Hall (29), Herbert and Sterns (30), and Jackson and Fewster (31).

2.2.2 Prandtl Number Effects in Mixed Convection

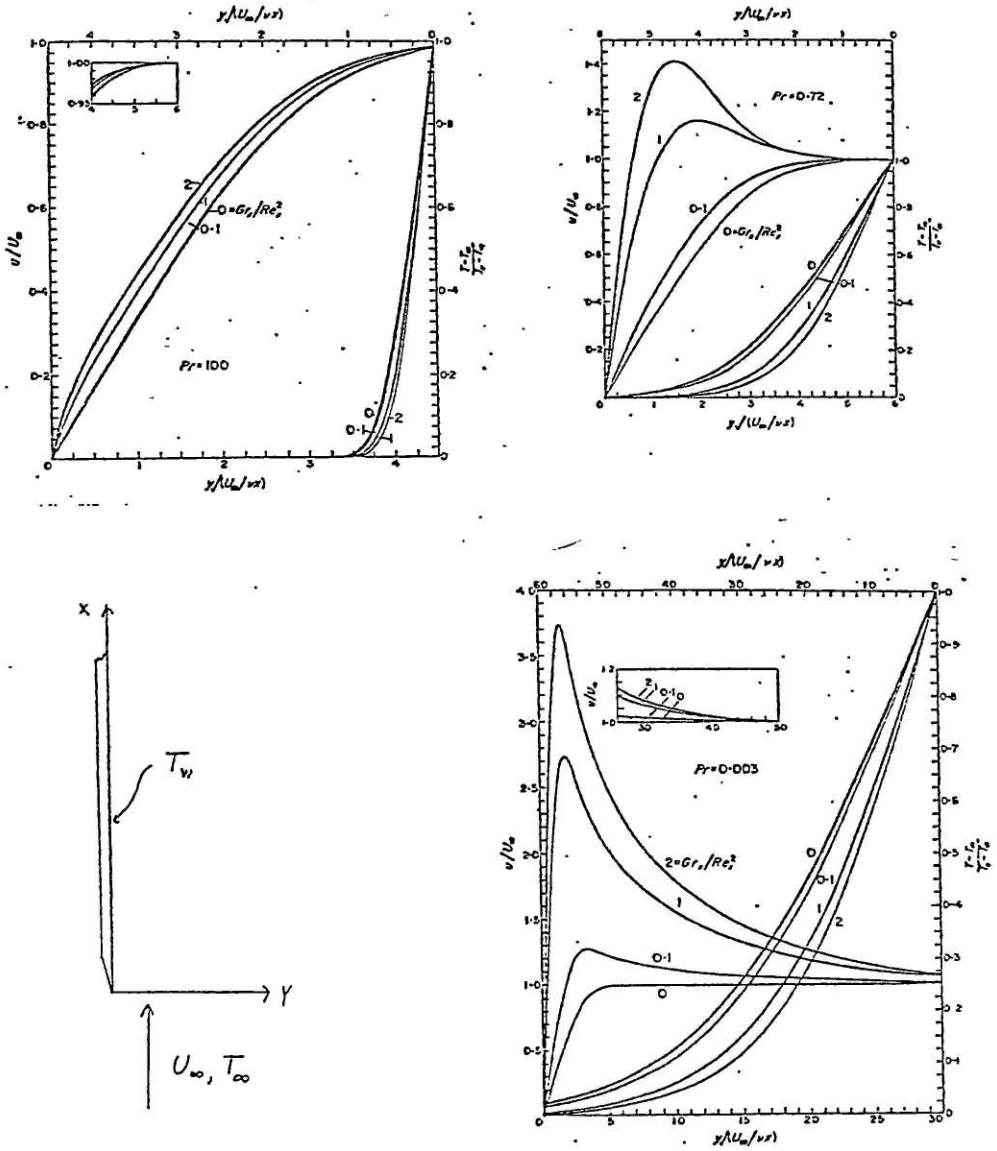
Since the present research effort is directed toward LMFBR applications (low Prandtl number fluid) the determination of the effect of Prandtl number on mixed convection is of importance, particularly since much of the existing data are for water and air (moderate Prandtl number).

Lloyd and Sparrow (32) analytically determined velocity and temperature profiles for laminar mixed convection flow adjacent to a heated vertical flat plate at a uniform wall temperature by the method of local similarity. Their results for dimensionless velocity and temperature profiles are given in Figure 2.2.7 for Pr=100, .72, and .003. It can be seen that for a given Gr_x/Re_x^2, the distortion of the velocity and temperature profiles is much larger for the smaller Prandtl number flows.

Laminar mixed convection near a flat plate was studied by Sparrow and Minkowycz (33) who considered values of Pr of .01, .7 and 10. Buoyancy effects were found to be significantly larger for lower Pr. As Pr was changed from 10 to .01,

FIGURE 2.2.7

ANALYTICAL RESULTS OF LLOYD AND SPARROW



skin friction was increased by a factor of forty, and heat transfer by a factor of 18. For Pr = .7, a 5% change in heat transfer due to buoyancy was observed at $Gr_x/Re_x^{5/2} \geq .041$.

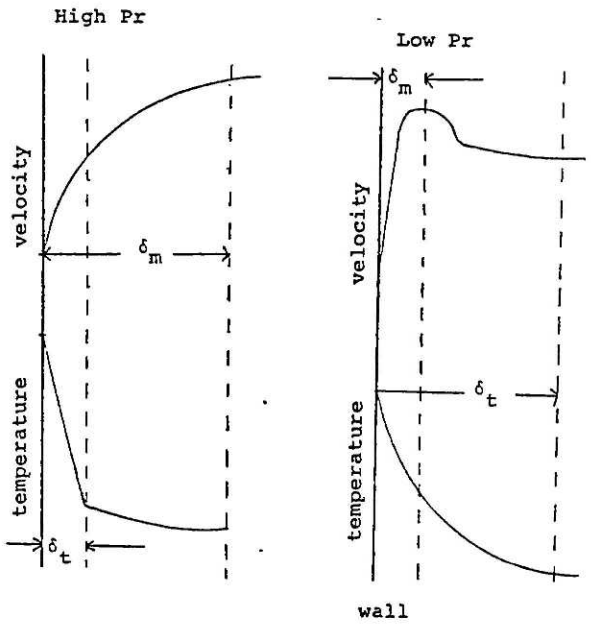
Hommel (34) and Szewczyk (35) also conclude that buoyancy effects are more predominant for fluids with low Pr.

Turbulent aiding flow in a tube was studied by Polyakov (36), who developed equations for friction and heat transfer when the influence of buoyancy on the forced flow was small. He found that for turbulent flow, the influence of buoyancy appears earlier for low Pr. The same conclusion was obtained by Bishop (22) for laminar flow in a tube.

These results may seem contrary to expectation, since larger conductivity would seem to prevent buoyancy forces from appearing near the wall. However the relative boundary layer thickness must also be considered. A physical explanation of the effect of Pr on mixed convection follows. The "velocity overshoot" near the wall, or type II profile observed for the lower Pr of Figure 2.2.7 is a result of buoyancy forces near the wall, which in turn is a result of the temperature profile. For a high Prandtl number, the thermal boundary layer is thin with respect to the momentum boundary layer, as exhibited in Figure 2.2.8. Within the momentum boundary layer, the dynamics of the flow are dominated by viscous effects. The thermal boundary layer can be considered to be a region enclosing the buoyancy effects. Therefore, for high Prandtl number, all of the buoyancy effects

FIGURE 2.2.8

PRANDTL NUMBER EFFECTS IN MIXED CONVECTION



lie in a region dominated by viscosity, so no velocity overshoot occurs (viscous forces balance buoyancy forces). For a low Prandtl number, the momentum boundary layer is thin, so much of the buoyancy effects lie in the inertia dominated region (see Figure 2.2.8). In this region, inertia forces balance buoyancy forces, and velocity overshoot can occur. The inertia force is proportional to u^{du}/dx so large buoyancy forces in the outer region causes u^{du}/dx to be large, and overshoot occurs (small Pr), zero buoyancy force in the outer region causes u^{du}/dx to be zero, and no overshoot occurs. The same argument may be applied to an internal flow, but the overshoot phenomena may be more dramatic, because any increase in velocity near the wall will be accompanied by a decrease in the centerline velocity, due to mass conservation.

Buoyancy induced laminarization in liquid metals has been observed experimentally by Wendling (37) and Buhr (13). Buhr observed significant distortion of the velocity profile for Reynolds numbers as high as 60,000.

A numerical study of the simultaneous effects of free convection and axial conduction on a laminar forced flow between vertical parallel plates was performed by Husain et al. (38). Axial conduction caused buoyancy effects to penetrate upstream of the heated length, causing a distortion of the velocity profile. Free convection increased heat transfer, but to a lesser extent for lower Pe.

2.2.3 Flow Regime Identification and Criteria

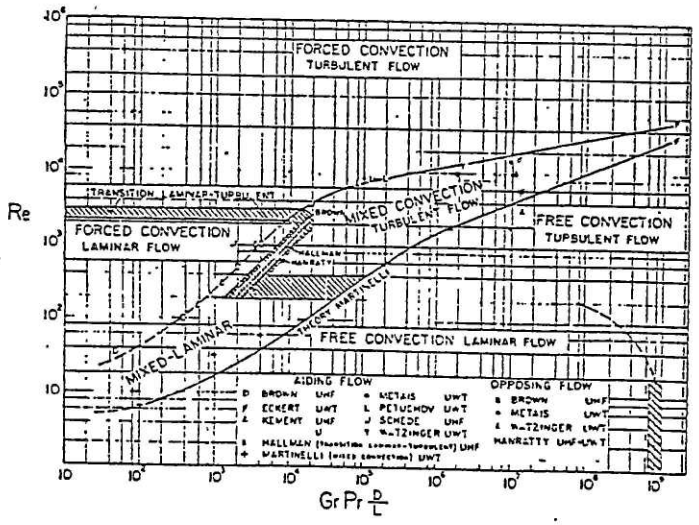
Since buoyancy plays an important role in many practical heat transfer calculations, it is important to know when the buoyant flow can be neglected with respect to the forced flow (forced convection regime); when the forced flow can be neglected with respect to the buoyancy driven flow (free convection regime); and when both are important (mixed convection regime). In each of the above cases, it is also of interest to determine if the flow is laminar or turbulent. The flow regime map of Metais and Eckert (39, 40) given in Figure 2.2.9 allows these regimes to be identified for flow through vertical tubes based on the parameters Re and Gr_A Pr (D/L) for $10^{-2} < Pr < 1$.

Additional criteria which have been proposed for mixed convection are presented in Table 2.2.2. The criteria of Jackson and Hall (10) was derived by expressing the fractional reduction in shear stress due to buoyancy at $y^+ = 30$ in terms of fluid properties and flow properties (Re and C_f). The effect of the shear stress on heat transfer was estimated, and C_f was expressed as $.046\ Re^{-.2}$ to give the criteria shown. The criteria is difficult to apply, because the wall temperature must be known to evaluate the Grashof number.

The criteria of Polyakov (36) was derived by working with the turbulent energy equation, keeping the generation, dissipation, and buoyancy terms. He derived equations for friction factor and Nusselt number under mixed convection conditions when the influence of buoyancy is small. From

FIGURE 2.2.9

FLOW REGIME MAP FOR FLOW IN VERTICAL TUBES



Regimes of free, forced, and mixed convection for flow through vertical tubes

$\left(10^{-1} < Pr\frac{d}{L} < 1\right)$

TABLE 2.2.2

CRITERIA FOR TURBULENT MIXED CONVECTION
FOR AIDING FLOW IN VERTICAL CIRCULAR TUBES

Author(s) (Reference)	Criteria	Equation	Range of Applicability
Jackson and Hall (10)	Criteria for when buoyancy reduces heat transfer coefficient from forced convection value by less than 5%.	$\frac{\overline{G}_r \left(\frac{\mu_w}{\mu_b}\right)\left(\frac{\rho_b}{\rho_w}\right)^{1/2}}{Re_b^{2.7} Pr_b^{.5}} < 10^{-5}$ $(\overline{Gr}=Gr_{\Delta T})$	$.7 < Pr_b < 5$
Polyakov (36)	For when a 1% deviation of Nu from its forced convection value occurs	$Gr_q = \frac{1.3\times10^{-4} Re^{2.75} Pr\left[Re^{1/8}+2.4(Pr^{2/3}-1)\right]}{\log Re + 1.15\log(5Pr+1)+\frac{1}{2}Pr-1.8}$	$Pr \geq 1$
	For when a 1% deviation of friction factor from forced convection occurs	$Gr_q = 2\times10^{-4} Pr\, Re^{2.75}$ $(Gr_b^{*}=Gr_q)$	
Kenning, et al (8)	For when wall temperature peaks (local reductions in heat transfer coefficient) occur	$\frac{Gr_b^{*}}{Re_b^{3.4} Pr_b^{.4}} > 4\times10^{-5}$	$0 < x/d < 80$ $1.5 < Pr_b < 7$
Hall (7)	For when heat transfer is impaired by buoyancy	$\frac{G_r}{Re^{2.7}} \cong .7\times10^{-4}$	None given
Byrne and Ejiogu (20)	Criteria for significant buoyancy effect on heat transfer	$Gr/Re^{1.8} \cong .05$ $(Gr=Gr_{\Delta T})$	None given
	For minimum heat transfer	$Gr/Re^{2.8} \cong 10^{-4}$ $(Gr=Gr_{\Delta T})$	

these equations he derived the two criteria given in Table 2.2.2. His results show that for smaller Pr, the influence of buoyancy appears earlier.

Kenning et al. (8) experimentally determined a criteria for when wall temperature peaking occurs. This regime can be considered a subset of the mixed convection regime.

Hall (5) derived a criteria for when heat transfer is significantly impaired by buoyancy by deriving an expression for when the shear stress at $y^+ = 30$ is approximately zero, and hence the turbulence production nearly zero.

Figure 2.2.10 shows the flow regime criteria of Alferov et al. (21). Figures a-d correspond to pipe diameters of 30 mm, 20 mm, 14 mm, and 8 mm, respectively. For given heat flux (q), and mean bulk temperature (t_1) a point can be located on the plot. If the point lies above the boundary line for the particular mass velocity, buoyancy forces must be considered.

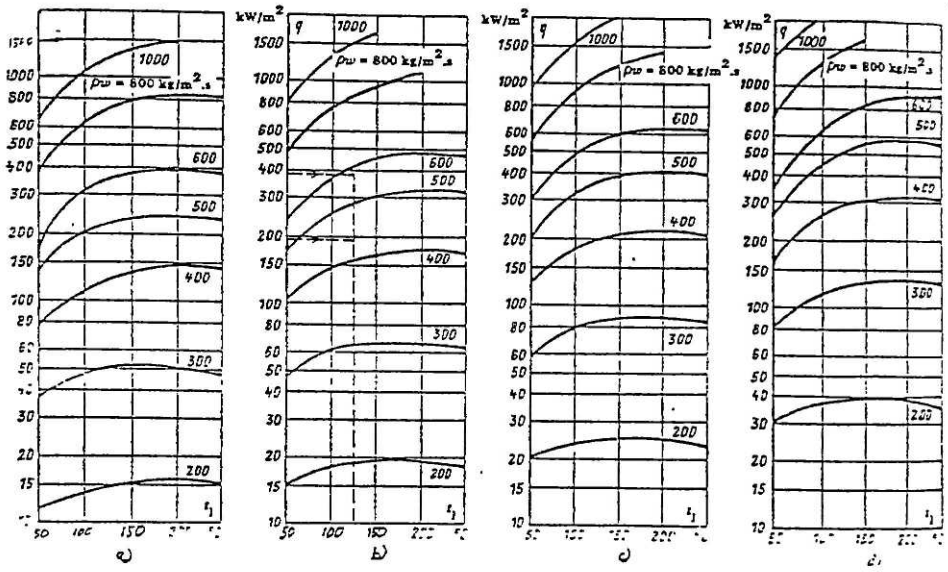
From Table 2.2.2 it can be seen that the key parameter governing the onset of mixed convection and the heat transfer minima is given by:

$$\frac{Gr}{Re^{\alpha}Pr^{\beta}} \simeq \text{const}$$

As suggested by nondimensionalization of the governing equations in Section 2.1.1, the dimensionless parameters of Equation 2.1.12 appear. However, examination of the governing equations alone could not give the functional form of the relation.

FIGURE 2.2.10

FLOW REGIME MAP OF ALFEROV



D = 30mm D = 20mm D = 14mm D = 8mm

2.2.4 Instability and Transition to Turbulence

Since the heat transfer and frictional characteristics of a turbulent flow are considerably different from that of a laminar flow, it is important to accurately predict the transition from laminar to turbulent flow. Mathematically, this prediction is based on the following question: can a given laminar flow withstand a disturbance and still return to its original state? If so, it is stable and the laminar flow will remain. If not, a transition to turbulence will eventually occur.

The analytical tool used to investigate this question is linear stability theory. First, it is assumed that there is a known solution Q_o to the governing differential equation. The terms in Q_o can be subtracted since it identically satisfies the equation. What remains is the disturbance equation for Q', which is a nonlinear partial differential equation. If Q' is assumed small, and products and powers of disturbance variables are neglected, a set of linear partial differential equations result. Further simplification occurs if the flow is assumed to depend on only one space coordinate (parallel flow assumption). For a given disturbance frequency the equations can be solved for the neutral curves, which form the boundary between the stable and unstable regions.

For a forced convection flow, the resulting equations (known as the Orr-Sommerfeld equations) are of fourth order, but when buoyancy forces are accounted for they are of sixth

order. Because of their complexity, they have been unresolved until the development of high capacity machines and sophisticated numerical techniques. If viscosity is neglected, a somewhat simpler set of second order equations result. For this case it can be shown (41) that a necessary condition for instability is that the velocity profile has a point of inflection. This is known as the "inviscid instability".

Gebhart (42) studied the stability of a natural convection flow over a vertical flat plate. He calculated the neutral stability curves allowing for the effect of wall heat capacity.

Stability theory tells us that the critical Reynolds number depends only on the velocity profile shape for the inviscid instability. Many investigators replace stability analysis with an experimental measurement of the onset of instability plus a laminar flow computer solution for the velocity profile. The onset of instability is then correlated with a particular profile shape calculated by the code. Some examples of this follow:

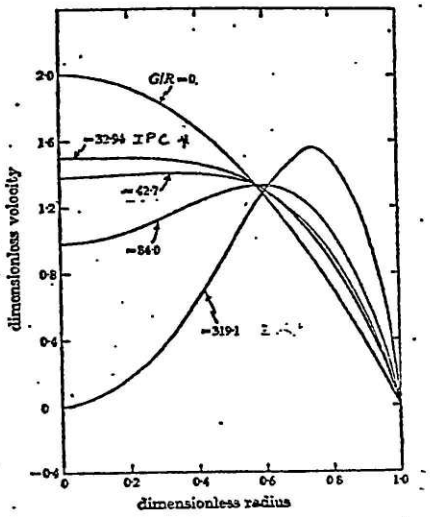
Scheele and Hanratty (43) investigated experimentally the stability of fully developed mixed convection flow in a vertical pipe 762 diameters long. They found that stability depends primarily on the shape of the velocity profile, which in turn depends on the power to flow ratio (Gr/Re). For aiding flow, instability occurs when the velocity profile develops a point of inflection, and transition to turbulence involves the gradual growth of small disturbances. For

opposing flow instability is associated with separation (flow reversal) at the wall. Transition to turbulence occurred shortly thereafter. Figure 2.2.11 shows the velocity distributions for aiding and opposing flow. For aiding flow the inflection point at the tube centerline occurs at Gr_q/Re = 32.94, and moves toward the wall for increasing Gr_q. At Gr_q/Re = 319.1, the velocity at the centerline is zero and further increases in heat flux will cause reverse flow near the tube center. For opposing flow an inflection point at the wall occurs at Gr_q/Re = 9.87, and moves toward the tube center for increasing Gr_q/Re. For Gr_q/Re = 52.2, the velocity gradient at the wall is zero and further increases in Gr_q/Re result in reverse flow near the wall. These results infer that an inflection point at the wall is not as destabilizing as an inflection point at the centerline.

Sherwin and Wallis (44) studied developing laminar aiding flow in a heated vertical annulus. Figure 2.2.12a and 2.2.12b show their developing axial and radial velocity profiles for Gr_q/Re = 400 (the inner rod was heated, and the outer duct insulated). For X ≃ 3 the velocity gradient at the outer surface was nearly zero. The magnitude of the radial velocities decreases with X until X = 2.9, above which it increases. This behavior near X = 3 was associated with the initiation of unstable flow. Figure 2.2.12c shows the numerical analysis of onset of flow instabilities along with their experimental results, which were obtained by the dye injection flow visualization method. The agreement is reasonable, and differences

FIGURE 2.2.11

Results of Scheele and Hanratty



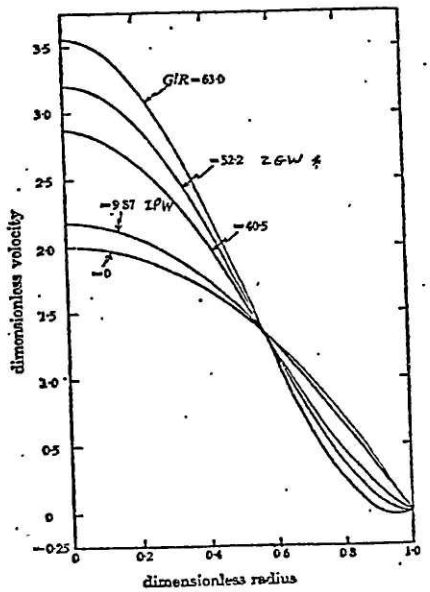
IPC - Inflection Point at the Centerline

IPW - Inflection Point at the Wall

ZGW - Zero gradient at the wall

* - Onset of Instability

Velocity profiles for laminar upflow with constant-flux heating.



Velocity profiles for laminar downflow with constant-flux heating.

FIGURE 2.2.12

RESULTS OF SHERWIN AND WALLIS

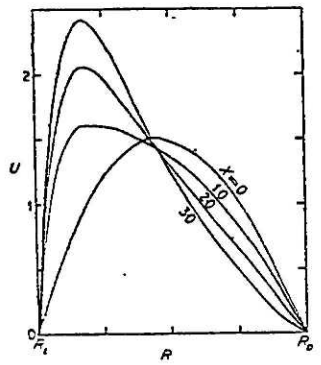


Fig. 112.1. Developing axial velocity profiles—
$Gr_q/Re = 400$

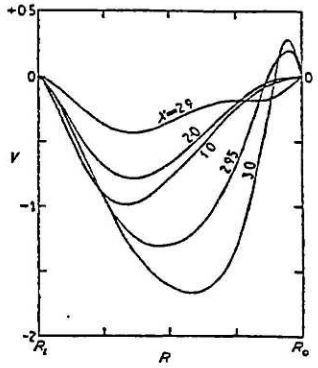


Fig. 112.2. Developing radial velocity profiles—
$Gr_q/Re = 400$

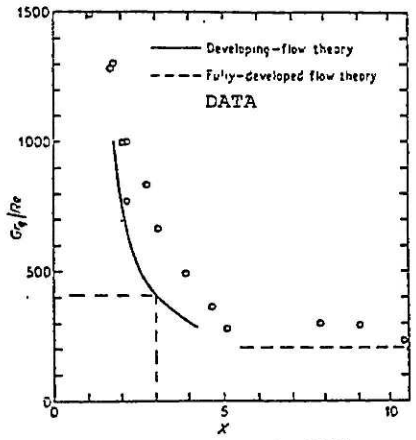


Fig. 112.3. Onset of flow instabilities

were attributed to asymmetry in the flow field near the unstable region. This asymmetry was also observed by Scheele and Hanratty (43).

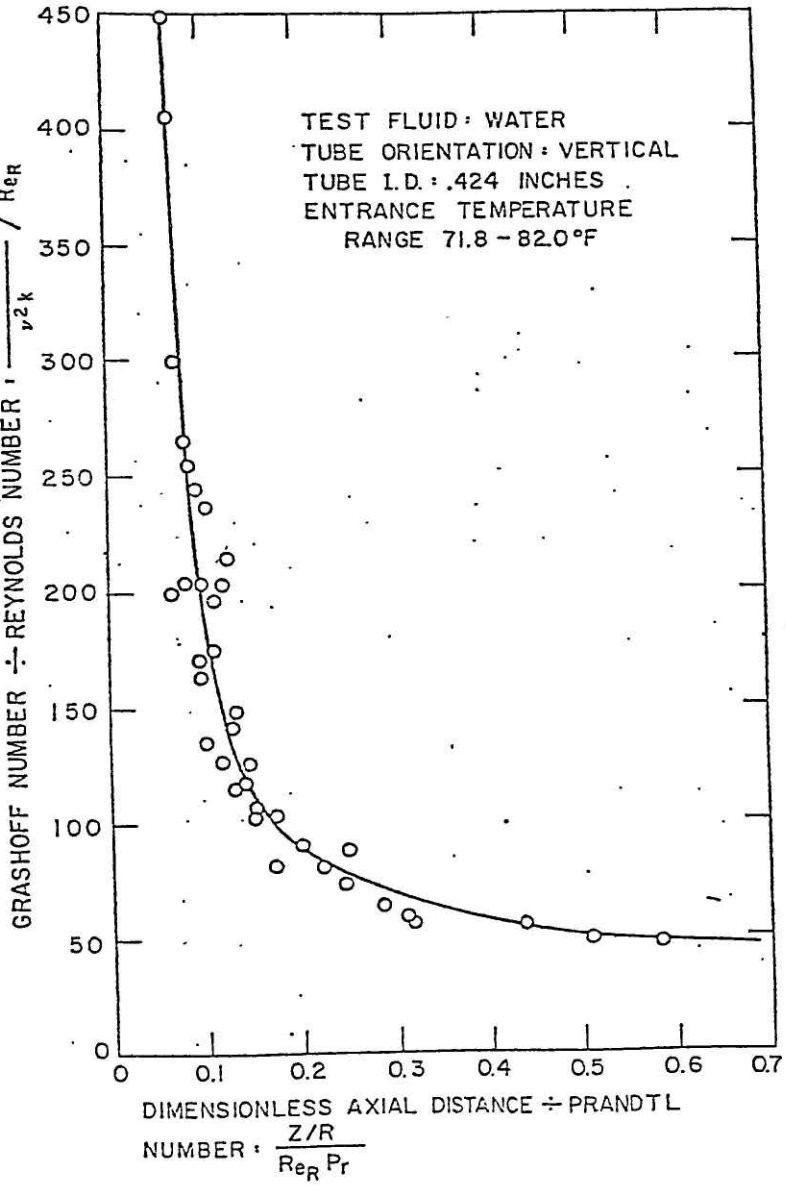
Lawrence (45) investigated laminar developing flow in a circular tube. His theoretical solution was used to obtain developing axial velocity profiles for the cases shown in Figure 2.2.13. The experimental data gave the axial position at which instability began. Thus calculated, unstable profiles were obtained for different Reynolds numbers. His results showed that transition always occurred after the profile had developed an inflection point with a type II profile. This corresponds to the results of Scheele and Hanratty. By trial and error, Lawrence found a transition parameter based on the velocity profile shape, and correlated it against entrance Reynolds number as shown in Figure 2.2.14. It was later shown by Collins (46) that the velocity profile transition parameter did not correlate the transition data of Scheele (43) very well.

2.3 COMPARISON OF CORRELATIONS WITH DATA

Figure 2.3.1 gives a plot of Petukov's correlations along with the data of Kenning at L/D = 80 (see Appendix A for Kenning's data) and the data of Buhr and Connor (Table 2.2.1). The Nusselt number minima for Kenning's data is quite close to the minima predicted by the Petukhov correlations for $\frac{L}{D}\Big|_{in} = 26$. The minima for Connor's air

FIGURE 2.2.13

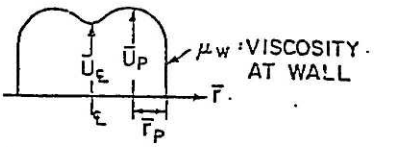
EXPERIMENTAL TRANSITION DATA OF LAWRENCE



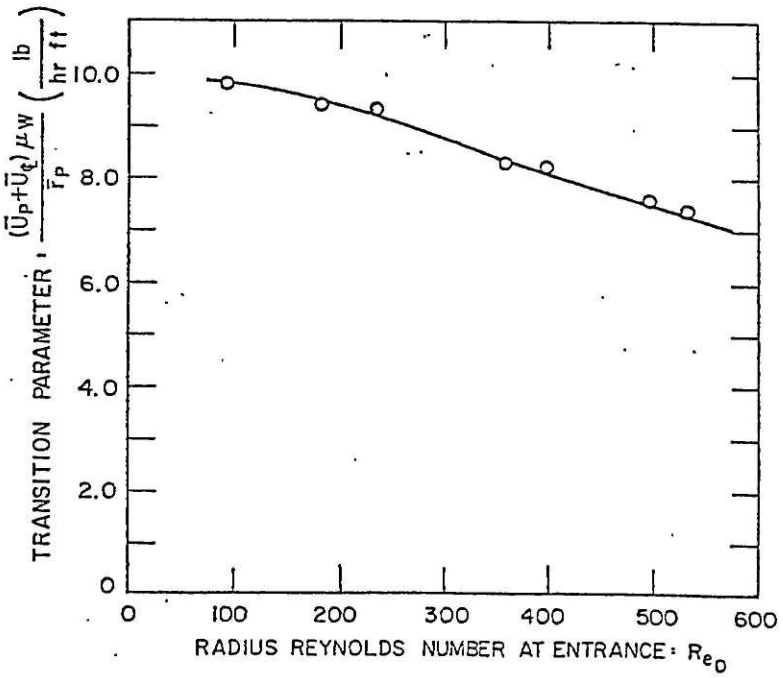
EXPERIMENTAL TRANSITION DATA.

FIGURE 2.2,14

VELOCITY PROFILE SHAPE TRANSITION PARAMETER OF LAWRENCE

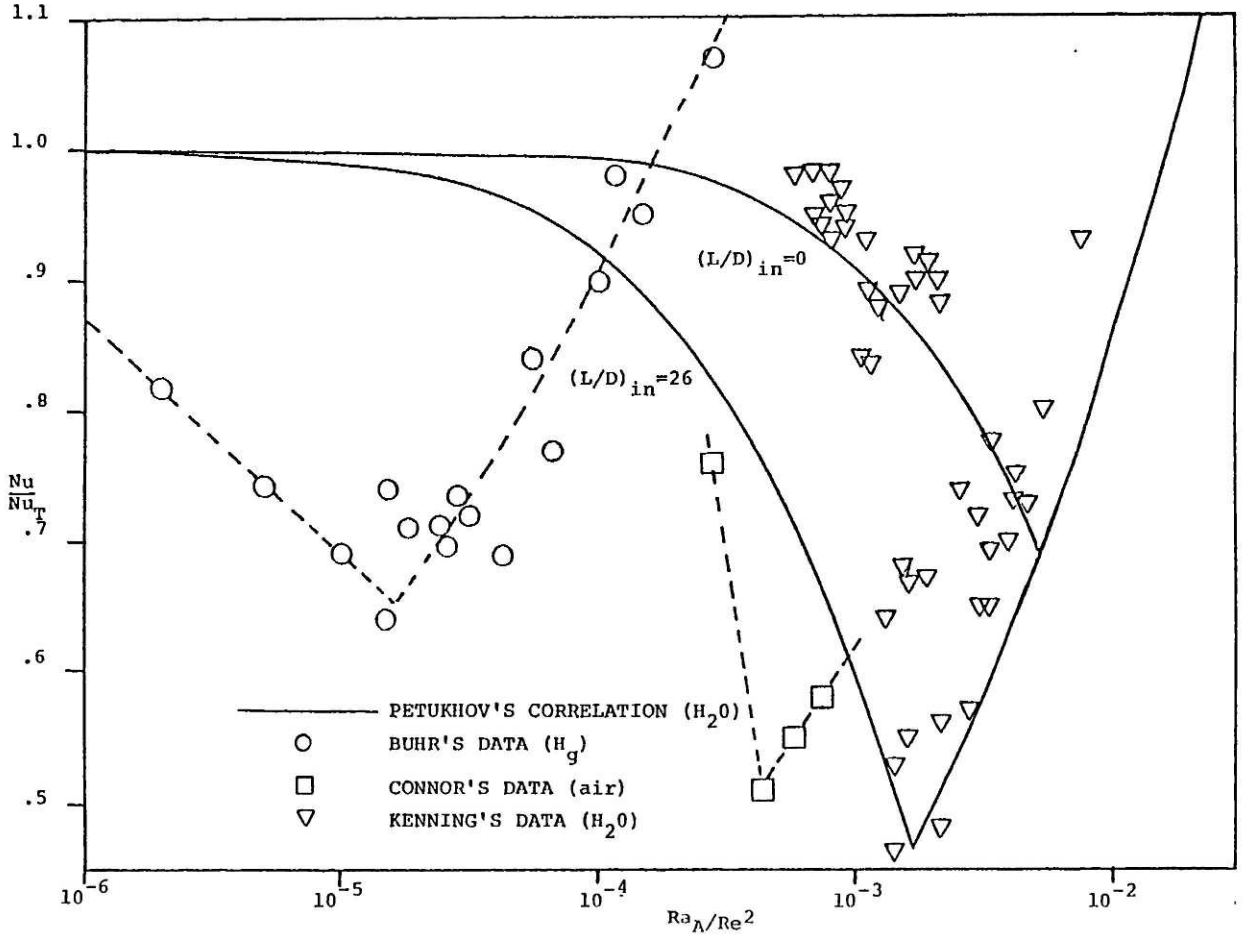


TRANSITION PROFILE NOMENCLATURE SHOWN ON AXIAL VELOCITY PROFILE



VELOCITY PROFILE SHAPE TRANSITION PARAMETER AS A FUNCTION OF ENTRANCE REYNOLDS NUMBER.

FIGURE 2.3.1
COMPARISON OF CORRELATIONS AND DATA IN TERMS OF Ra_A/Re^2



data is displaced further to the left, and has a higher $\left.\frac{Nu}{Nu_T}\right|_{min}$. The Nusselt number minima for Buhr's mercury data is displaced to the left by about two orders of magnitude, and the value of $\left.\frac{Nu}{Nu_T}\right|_{min}$ is significantly higher for mercury than for the air and water data. These results support the conclusion obtained in Section 2.2.2 that buoyancy effects appear earlier (lower power or higher flow) for fluids of lower Pr. It is also observed in Figure 2.3.1 that the value of $\left.\frac{Nu}{Nu_T}\right|_{min}$ decreases with increasing Pr. This is due to the increased importance of conduction heat transfer for fluids of low Pr.

In Figure 2.3.2 the data of Figure 2.3.1 is plotted against Connors correlating parameter (Gr_A/Re^2). For simplicity only Kenning's Type I data is included, and data points for constant Re are connected with a straight line. Connor's correlation (Equation 2.2.8) which is valid for Type II velocity profiles only is plotted. Petukhov's correlation (valid for water) was also plotted by assuming $Pr = 5$ to convert Ra_A to Gr_A ($Ra_A = Gr_A Pr$). Two significant observations may be made:

1) The first is that Gr_A/Re^2 correlates the data for various Pr much better than Ra_A/Re^2. The spread in $(Nu/Nu_T)_{min}$ for the various Pr fluids is a factor of 330 for Figure 2.3.1 but only a factor of 3 for Figure 2.3.2.

2) The second observation is that Kenning's data

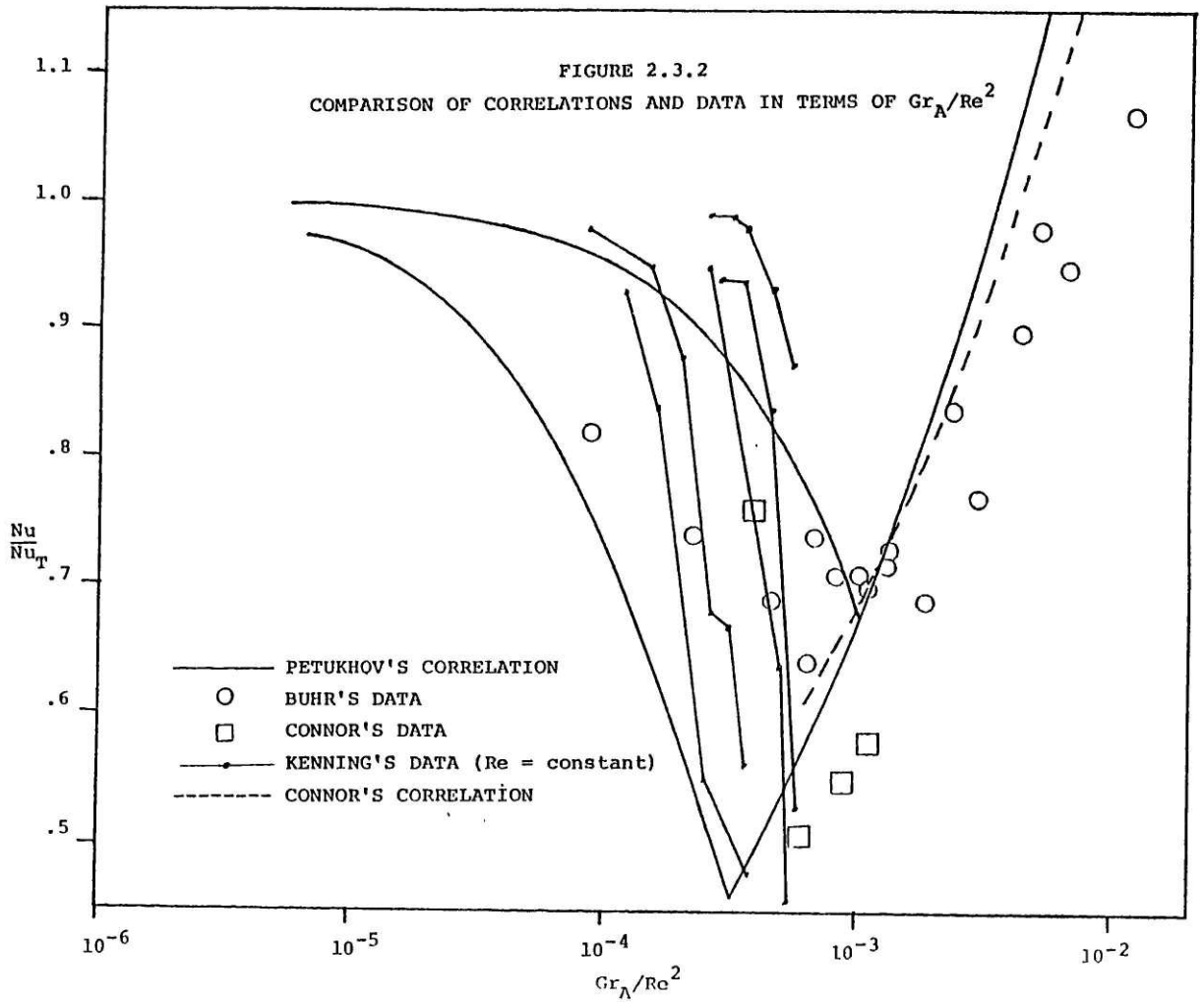


FIGURE 2.3.2
COMPARISON OF CORRELATIONS AND DATA IN TERMS OF Gr_A/Re^2

forms a family of curves for different values of Re. This may be seen more readily on Figure 2.3.3, which is the same graph, but on an expanded scale.

The first observation clearly illustrates that the parameter for correlating data for various Pr is Gr_A/Re^2, and not Ra_A/Re^2.

The second observation suggests that a flow development effect exists in the data. The $\frac{L}{D}\Big|_{in}$ effect in Petukhov's correlation is consistent with the Re effect in Kenning's data if one thinks of velocity profile development. In forced convection, the Nusselt number for developing flow is often expressed as:

$$\frac{Nu}{Nu_\infty} = 1 + C\,\frac{RePr}{L/D} \qquad (2.3.1)$$

where C is a constant. It follows from Equation 2.3.1 that increasing L/D has the same effect on Nu as decreasing Re. This behavior is also exhibited in Figure 2.3.3.

The effect of flow development can also be shown by plotting Kenning's data for X/D = 10 to 80 on the same set of coordinates as Figure 2.3.3. This was done for runs 10 to 20 on Figure 2.3.4 and runs 98 to 106 on Figure 2.3.5. The data points for various axial locations for each run are connected with straight lines. The fact that Nu/Nu_T is changing with X/D indicates that the flow is still developing. For the low power runs, Nu/Nu_T decreases with X/D.

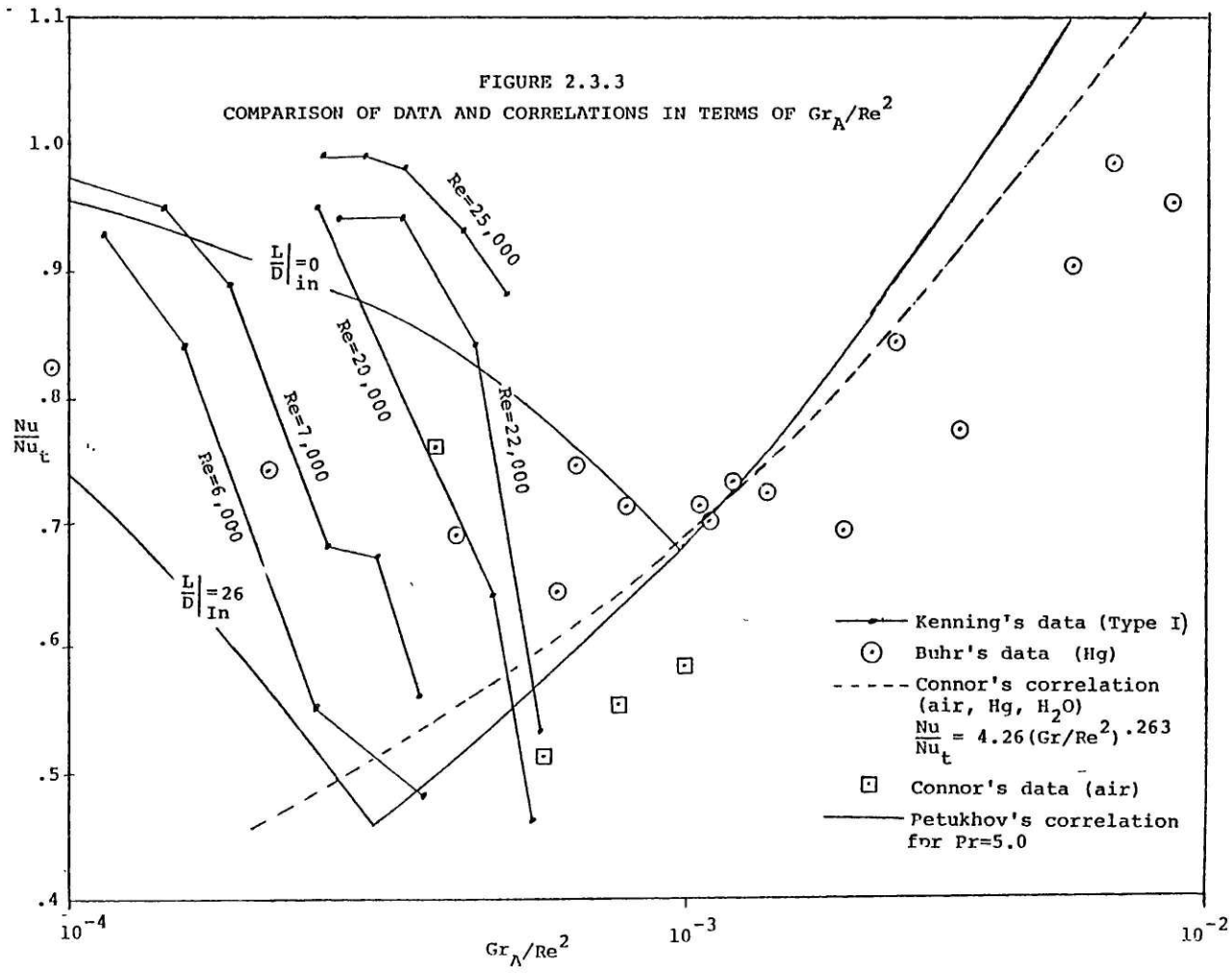


FIGURE 2.3.3

COMPARISON OF DATA AND CORRELATIONS IN TERMS OF Gr_A/Re^2

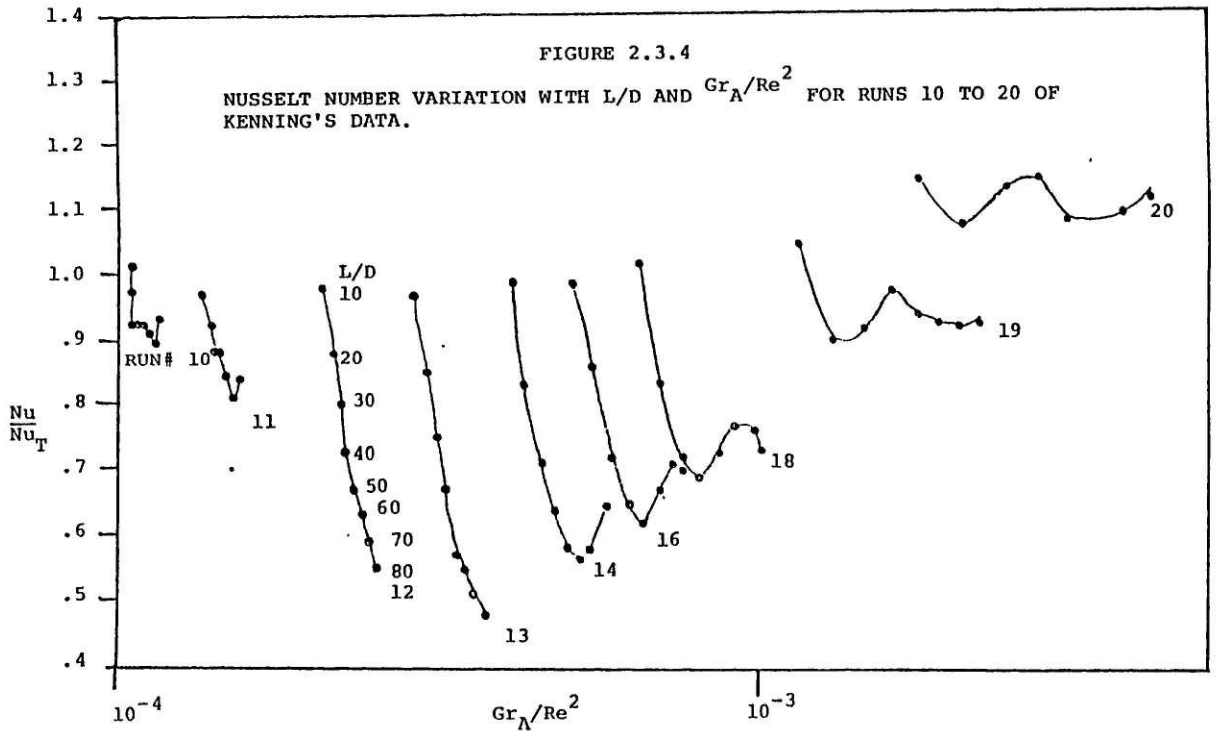
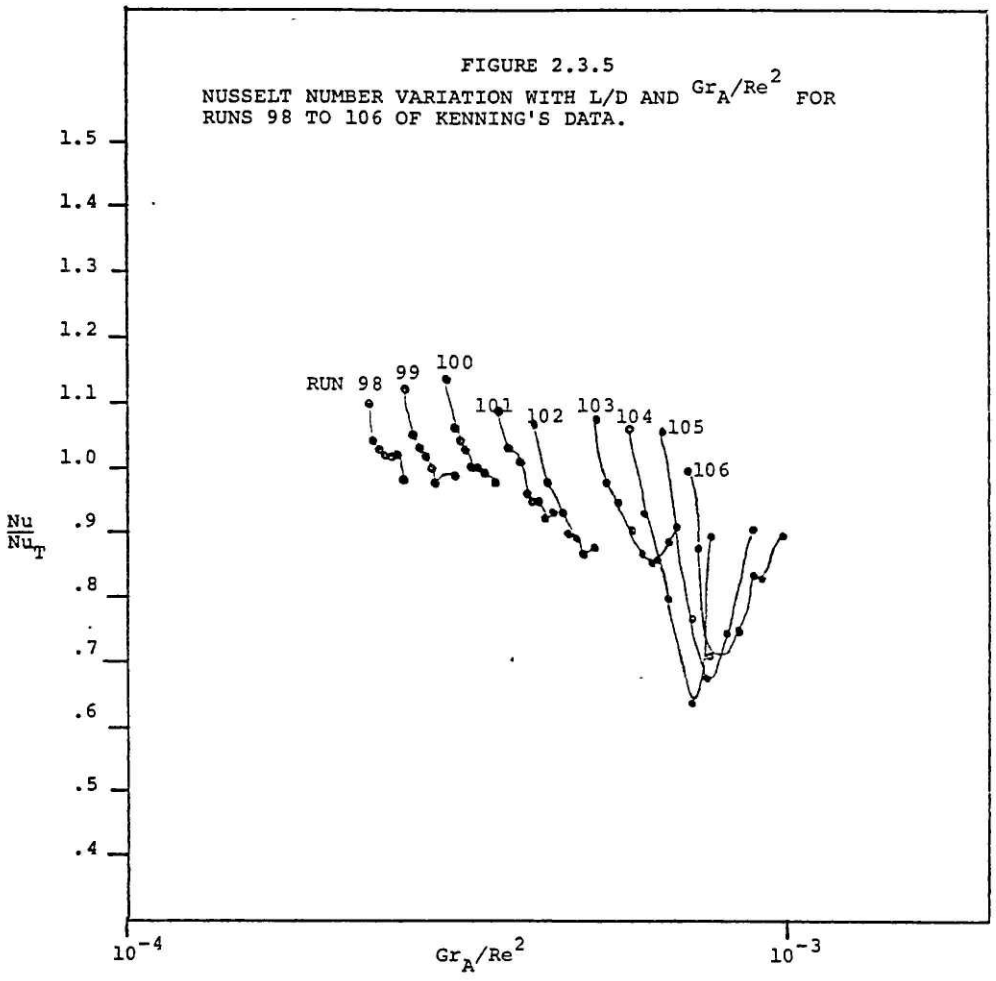


FIGURE 2.3.4

NUSSELT NUMBER VARIATION WITH L/D AND Gr_A/Re^2 FOR RUNS 10 TO 20 OF KENNING'S DATA.

FIGURE 2.3.5
NUSSELT NUMBER VARIATION WITH L/D AND Gr_A/Re^2 FOR RUNS 98 TO 106 OF KENNING'S DATA.



For the higher power runs local minima are observed, indicating wall temperature peaking.

The results presented above suggest that flow development effects should be incorporated in mixed convection correlations for reasonable values of L/D. Recall that Petukhov correlated his Type I data by Equation 2.2.4:

$$\frac{Nu}{Nu_T} = (1 + B \frac{Ra_A}{Re^2})^{-1} \qquad (2.3.2)$$

where different values for B were used for each of his two test sections. It may be possible to account for the effects of flow development defining B as a flow development factor:

$$B = C \frac{L/D}{Re^{\alpha} Pr^{\beta}} \qquad (2.3.3)$$

and calibrating the constants C, α and β against existing data.

2.4 COMPARISON OF DATA WITH CRITERIA

It follows from Figure 2.3.1 that all of Buhr's mercury data is in the mixed convection regime since the Nusselt number has changed by more than 10% of the fully developed value. Buhr's data was plotted on the Metais-Eckert flow regime map in Figure 2.4.1. It is observed that all of his data lies in the forced convection regime of the map. Lines $\overline{AA}$ and $\overline{BB}$ represent the onset of mixed

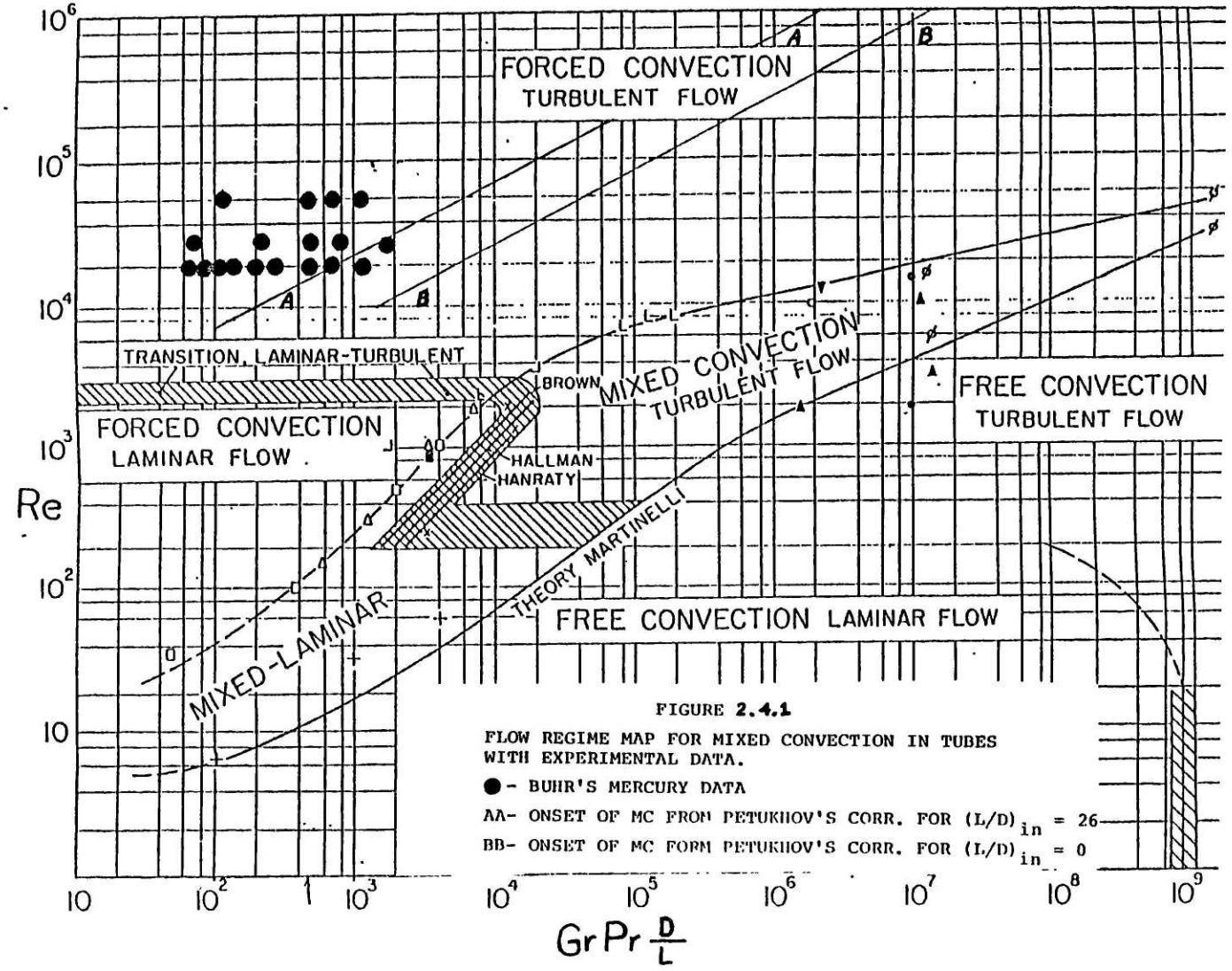


FIGURE **2.4.1**

FLOW REGIME MAP FOR MIXED CONVECTION IN TUBES WITH EXPERIMENTAL DATA.

● - BUHR'S MERCURY DATA

AA- ONSET OF MC FROM PETUKHOV'S CORR. FOR $(L/D)_{in} = 26$

BB- ONSET OF MC FORM PETUKHOV'S CORR. FOR $(L/D)_{in} = 0$

convection as predicted by Petukhov's correlation for $\frac{L}{D}\Big|_{in} = 26$ and $\frac{L}{D}\Big|_{in} = 0$, respectively. These lines were obtained by equating Nu/Nu_T of Equation 2.2.4 to .9, and solving for Ra_A/Re^2. It appears that the flow regime map significantly underestimates the onset of mixed convection for both mercury and water. It is also believed that the parameter $Gr_A Pr \frac{D}{L}$ has the wrong $\frac{L}{D}$ effect. It follows from the data of Figures 3.2.4 and 3.2.5 that mixed convection effects increase with L/D, while the flow regime map suggests that the opposite occurs (this may be the case for the uniform wall temperature boundary condition, but not uniform heat flux).

The results discussed above suggest that work still needs to be done in this area. Employing Gr_A rather than Ra_A allows correlation of data with different Pr, but an unresolved flow development effect still exists. This flow development effect does not appear to be property accounted for in the parameter $GrPr \frac{D}{L}$ used by Metais.

CHAPTER 3

MIXED CONVECTION IN VERTICAL ROD BUNDLES

As discussed in the introduction, this work focuses attention on mixed convection effects within a rod bundle. It is assumed that the bundle inlet conditions are known through prior analysis of the primary loop and reactor core. This chapter serves to outline work which has been previously done, and introduce some of the numerical tools used to analyze LMFBR rod bundles.

3.1 LITERATURE REVIEW OF MIXED CONVECTION IN ROD BUNDLES

Before proceeding to the literature review of mixed convection, some results from forced convection will be given which will be useful later. Many correlations for heat transfer and friction for laminar flows in rod bundles and other geometries are available in Reference 47. For turbulent flow, calculation of the flow and temperature is considerably more involved. Several investigators have employed the equivalent annulus method to obtain approximate results. These include the work of Rehme (48) for triangular arrays:

$$\text{For } Re = 10^4\text{: } f/f_{Ct} = 1.045 + .071\ (P/D-1) \qquad (3.1.1)$$

$$\text{For } Re = 10^5\text{: } f/f_{Ct} = 1.036 + .054\ (P/D-1) \qquad (3.1.2)$$

and for square arrays Marek (49) found that:

$$\text{For } Re = 10^5\text{: } f/f_{Ct} = 1.04 + .06\ (P/D-1) \qquad (3.1.3)$$

where f_{Ct} is the friction factor for turbulent flow in a circular tube.

The work done in mixed convection will be outlined next. First local buoyancy effects will be considered, then global (bundle) buoyancy effects.

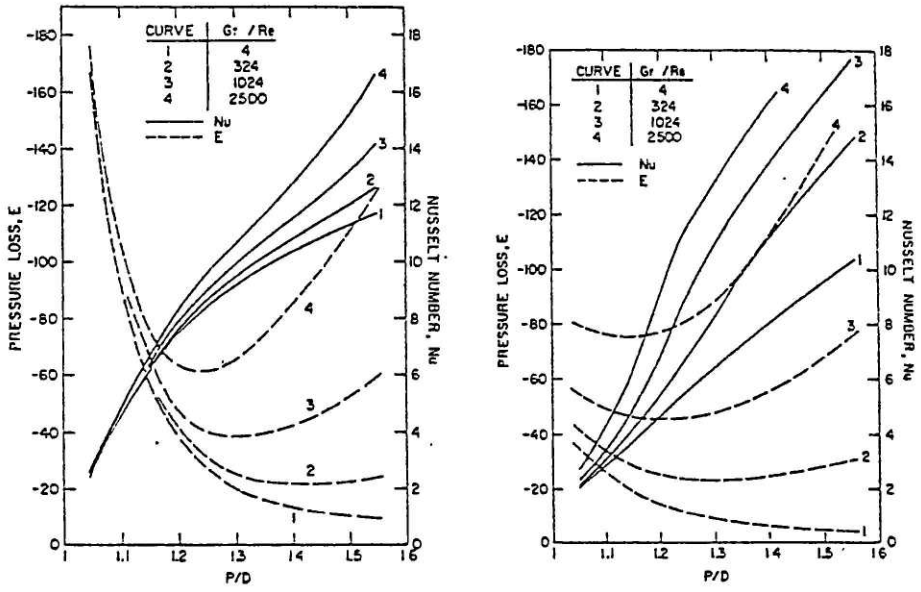
3.1.1 Local Buoyancy Effects

Yang (50) performed a numerical study of fully developed aiding flow through isolated interior subchannels of square and triangular rod arrays. His results for Nusselt number (Nu) and pressure loss (E) are given in Figure 3.1.1. For a given P/D both Nu and E increase with Gr/Re, which follows directly from the discussion of Section 2.1.1. The pressure loss for the triangular array exhibits an interesting behavior. The buoyancy effect increases E significantly more for high P/D ratios, resulting in a local minima in E at P/D ≅ 1.25. It appears that there is a larger tendency for velocity profile distortion for large P/D ratios. Flow reversal at the subchannel centerline was predicted for sufficiently large Gr/Re.

Yang later analyzed the case of opposing mixed convection flows in Reference 51. Again the effects of buoyancy were more pronounced for larger P/D. For the case opposing flow, flow reversal, or flow separation occurred at the rod

FIGURE 3.1.1

NUMERICAL RESULTS OF YANG FOR AIDING MIXED CONVECTION FLOW IN ROD ARRAYS.



(a) △ ARRAY

(b) □ ARRAY

surface in the gap between two rods. The critical value of Gr/Re for flow separation was given as a function of P/D.

An experimental and numerical study of free convection in a 42 rod bundle of P/D = 2.0 and 1.68 with air flow was performed by Davis and Perona (52). Their developing laminar flow analysis predicted a decrease in Nu with increasing P/D ratio as was predicted by Yang for mixed convection. Their experimental Nusselt numbers were in good agreement with their calculated results.

Free convection in a rod bundle with mercury flow was studied experimentally by Dutton and Welty (53) for P/D = 1.1, 1.3 and 1.5. They also observed a decrease in Nu with increasing P/D.

More recently a numerical analysis of fully developed laminar mixed convection in isolated cells has been performed by Wang et al. (1, 54). Aiding and opposing flows were considered for interior, edge and corner subchannels of both triangular and square array rod bundles. Results were presented in terms of best fit polynomial correlations. The buoyancy effects on the local velocity and temperature profiles, subchannel friction factors and heat transfer coefficients were examined. Criteria were presented for the onset of mixed convection (defined as a 20% change in the friction factor from its forced convection value), and the onset of local flow recirculation.

3.1.2 Bundle Buoyancy Effects

Mixed convection of liquid sodium flowing upward in a rod bundle with a radial power gradient was investigated numerically by Tsai et al. (55). The rod bundle was simulated by a thin rectangular channel (see Figure 3.1.2a), and the rod heat input was modeled as a volumetric heat source in the coolant. The radial velocity profiles were distorted by buoyancy forces, which caused the velocity at the hot side of the bundle to increase, and a flattening of the radial temperature profile.

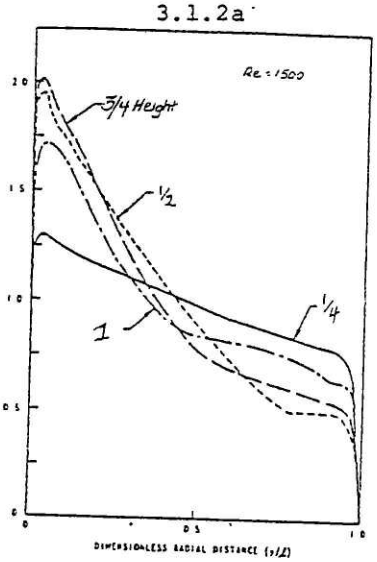
As shown in Figure 3.1.2c, a plot of maximum velocity against axial distance shows that fluctuations in the maximum velocity occurs. These fluctuations are observed to become damped for increasing axial distance, suggesting that fully developed flow may be achieved if L/De is large enough. Corresponding to the velocity fluctuations temperature reversal was observed as shown in Figure 3.1.2b for the Re= 1500 run. When temperature reversal occurs, the side of the bundle with larger heat input has a lower temperature.

A physical explanation of this phenomena was proposed. The fluid enters the rod bundle with a uniform inlet velocity, and experiences a maximum radial temperature difference due to the power skew. This causes a crossflow which increases in the hot side velocity, and hence a reduction, and possibly a reversal in the radial temperature difference. The decreased temperature difference causes a decrease in

FIGURE 3.1.2

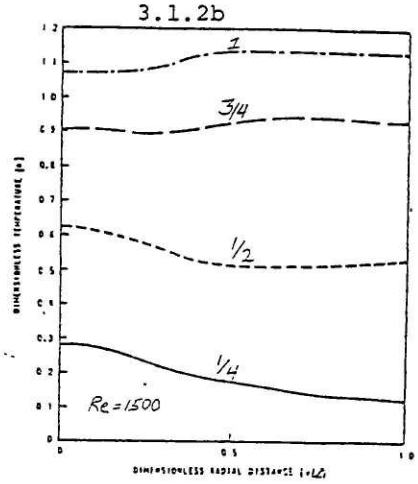
NUMERICAL RESULTS OF TSAI FOR MIXED CONVECTION IN A THIN RECTANGULAR CHANNEL

3.1.2a

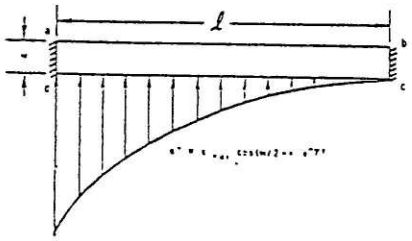


Velocity Profiles at Re = 1500

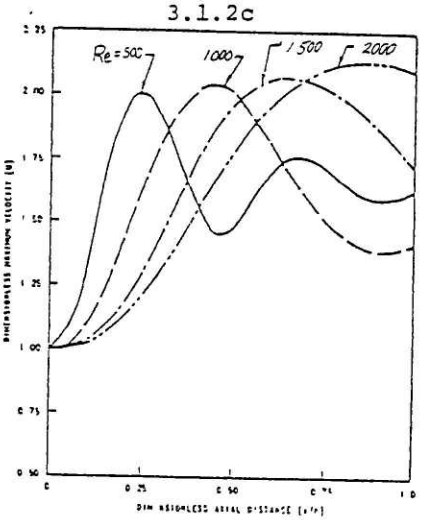
3.1.2b



Temperature Profiles at Re = 1500



3.1.2c



Fluctuations of Maximum Velocity

the buoyancy force, and hence a decrease in the hot side velocity. The cycle repeats itself with decreasing amplitude as the axial distance increases.

A similar phenomena has been predicted for flow between parallel plates (56) by Savkar. This behavior may not exist in rod bundles due to the effects of friction at the rod surface, which was neglected in Tsai's analysis.

Ramm and Johannsen (57) employed a similar approach, considering a strip section of the rod bundle. Their analysis accounted for the skin friction of the rods, but was limited to fully developed flow, so the "velocity fluctuations" observed by Tsai were not confirmed. As expected the effects of buoyancy caused distortion of the velocity field, and a flattening of the radial velocity profile.

An experimental study of mixed convection in rod bundles with severe radial power skews was undertaken at BNWL in a 2x6 rod bundle with upflow of water. Steady state results were reported in Reference 58 by Quigley et al. and transient results in Reference 59 by Khan et al. Local velocities and temperatures were measured, and compared to the predictions of the COBRA code with reasonable agreement. Buoyancy induced flow recirculation and buoyancy induced turbulence were observed at low flows. These results will be discussed in greater detail in Chapter 6.

Experimental results for mixed convection in a 4 rod bundle were presented by Efthimiadis et al. (60). Local

velocities were measured by the hydrogen bubble method, and local temperatures were measured with thermocouples. The experimental results were compared to the laminar (2D) fully developed isolated cell results of Wang (1, 54) and to the predictions of the BODYFIT code (61) which handles (3D) developing flow in interconnected subchannels. It was found that the 2D analysis overestimated the effect of buoyancy, while good agreement was obtained with the 3D prediction.

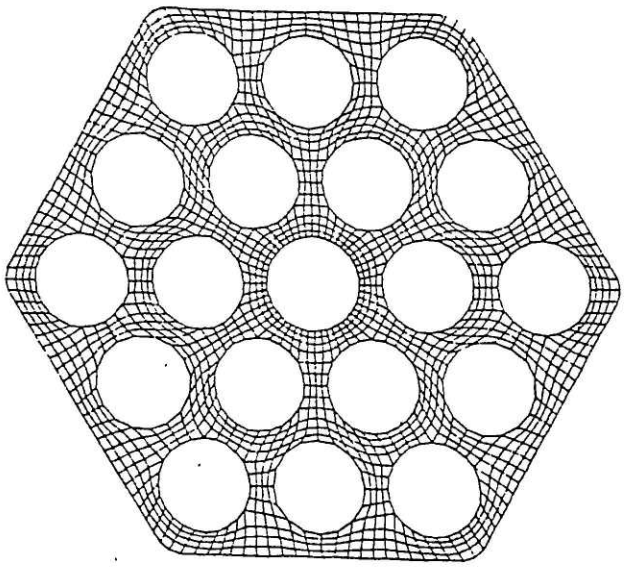
3.2 NUMERICAL TOOLS FOR ANALYSIS OF LMFBR ROD BUNDLES

To predict the thermal hydraulic performance of LMFBR rod bundles, several computer codes have been developed. These codes may be separated into two classes. The first class, known as distributed parameter analysis codes, solve for the detailed velocity and temperature distributions within the rod bundle, and require a very fine noding of the rod bundle. In general, the core storage and computational time requirements are prohibitively large for calculation of a typical LMFBR assembly, and are certainly impractical for calculating the flow and temperature field for the core. An example of a distributed parameter code is BODYFIT (61). A typical computational grid used by BODYFIT is given in Figure 3.2.1.

The second class of codes employ the lumped parameter, or subchannel analysis method. In subchannel analysis, the bundle is modeled as a number of discrete control volumes (subchannels), each with a bulk velocity and temperature

FIGURE 3.2.1

TYPICAL COMPUTATION GRID EMPLOYED BY BODYFIT FOR DISTRIBUTED PARAMETER ANALYSIS OF A 19 PIN BUNDLE.



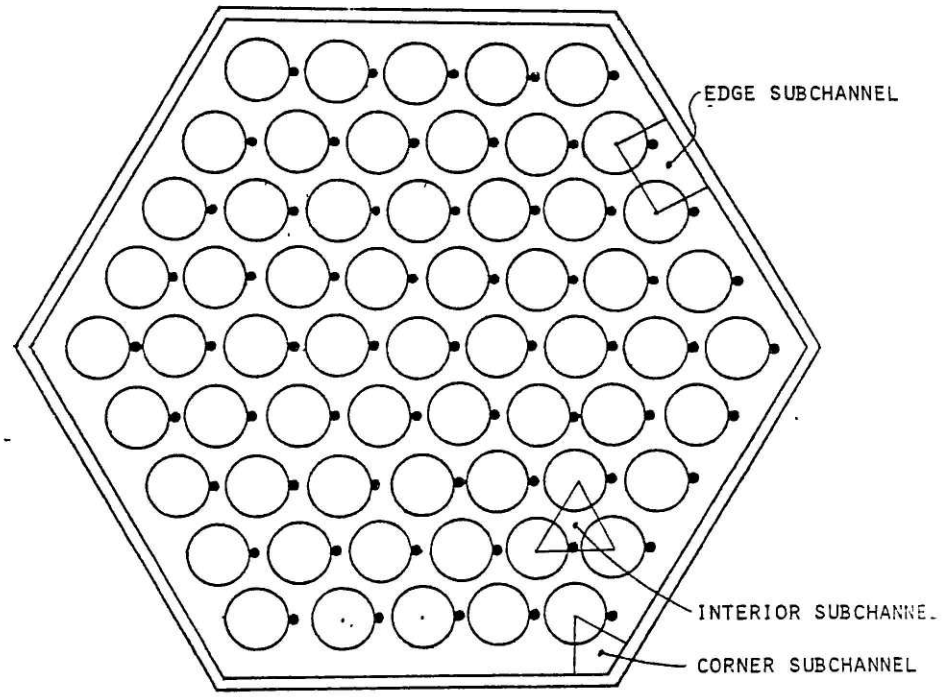
which varies axially. Conservation equations are written for the control volumes, and are solved numerically. Since bulk velocities and temperatures are employed the details of the velocity and temperature fields within the subchannel are not obtained with this technique. Hence constitutive relations for friction factor, Nussult number, and wire induced diversion crossflow must be supplied as inputs. Examples of subchannel type codes are the ENERGY (62) and COBRA (63) families of codes.

Lumped parameter analysis provides us with a more practical computational approach than distributed parameter analysis, but we pay the price of providing models for input parameters. The distributed parameter methods are often used to calculate the required input parameters. Examples of this were given in Section 3.1.1, where friction factors and Nusselt numbers were obtained from the distributed parameter approach (see, for example, the work of Wang (1)). Alternately, physical modeling and experimentation may be used to develop phenomenological correlations for the input parameters. Results from this method will be referenced in Section 3.2.2. The COBRA code has had widespread use in the nuclear industry, so will not be discussed in detail. The ENERGY code has received less attention, hence a review of the ENERGY model follows.

3.2.1 The ENERGY Series of Codes

The ENERGY family of computer codes are semi-empirical

FIGURE 3.2.2
SUBCHANNEL ANALYSIS OF A ROD BUNDLE



subchannel based computer programs which calculate the temperature and flow fields in LMFBR rod bundles. Input parameters are required for wire induced mixing and swirl flow, conduction shape factors, flow split parameters and friction factors. The single assembly steady flow version, ENERGY IV (both forced convection option and mixed convection option) will be used later in this study.

Figure 3.2.2 exhibits the three types of subchannels which exist in LMFBR rod bundles. They are referred to as edge, interior and corner subchannels. For each subchannel a bulk velocity and temperature may be calculated by solution of the appropriate governing equations. Figure 3.2.3 illustrates the effect of the wire wrap on coolant flow in the interior and edge region of the rod bundle. It can be seen that for the interior region flow is alternately swept into and out of the subchannel. Averaged over a lead length there is no net mass transfer, so the process may be modeled as an enhanced eddy diffusivity. For the edge region, the flow is always swept in the same direction, resulting in a swirl flow in the edge and corner subchannels. As exhibited in Figure 3.2.4, the bundle may be considered to consist of two regions. The interior region is characterized by an effective enhanced eddy diffusivity (ε^*_{1L}), and friction factor (f_1), and flow split parameter ($X_1 = V_1/V_b$). The edge region is characterized by a swirl velocity ration (C_{1L}), and a friction factor (f_2) and flow split parameter ($X_2 = V_2/V_b$).

FIGURE 3.2.3
EFFECT OF WIRE WRAP ON COOLANT FLOW

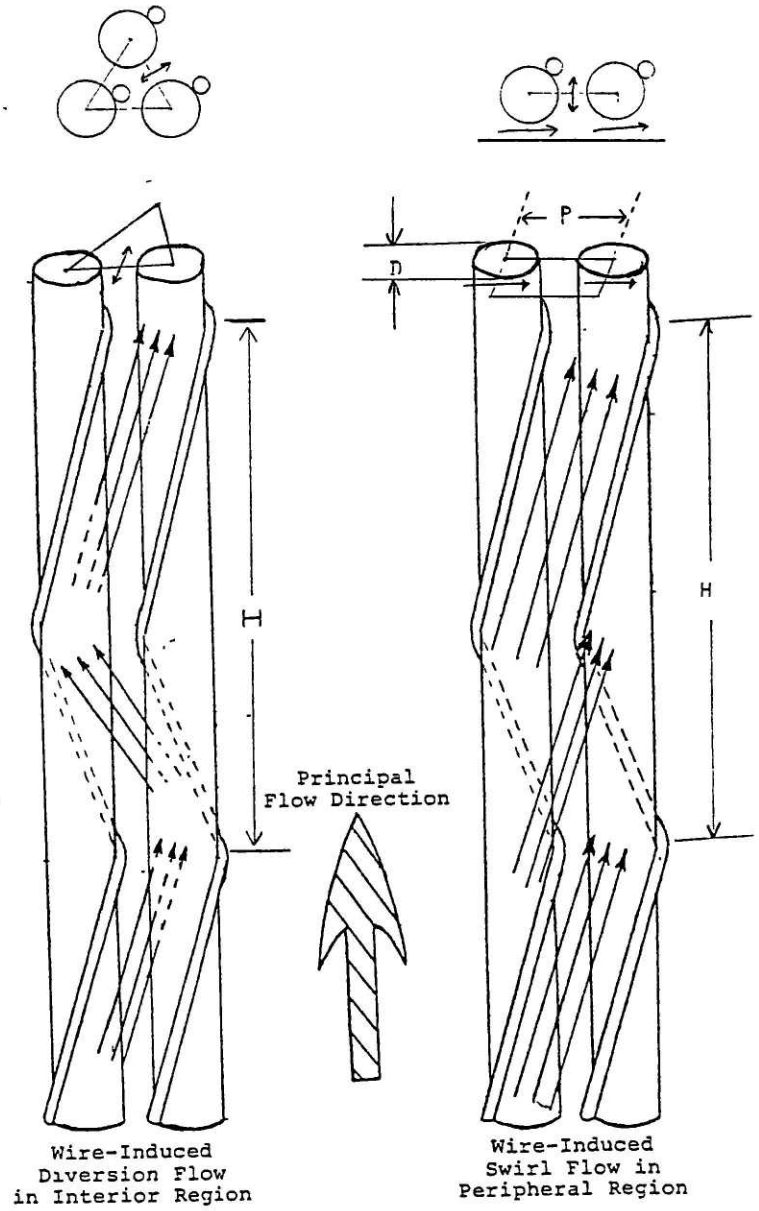
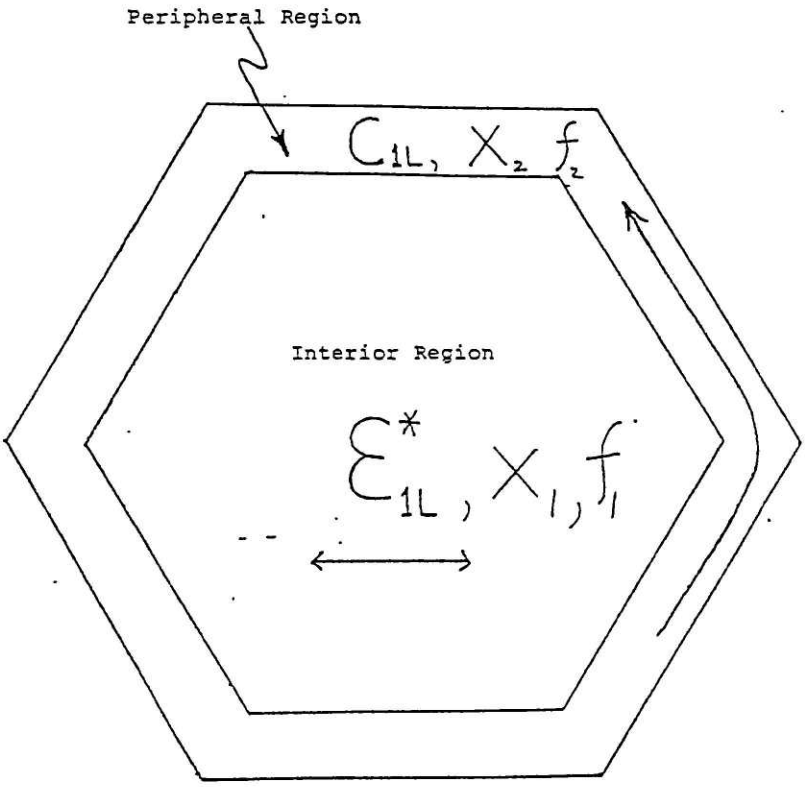


FIGURE 3.2.4
ENERGY MODEL OF AN LMFBR ROD BUNDLE



ENERGY CODE INPUT PARAMETERS:

$\varepsilon^*_{1L} = \varepsilon^*_{1L}$ (P/D, H/D, RE)

$C_{1L} = C_{1L}$ (P/D, H/D, RE)

$X_i = X_i$ (P/D, H/D, RE)

$f_i = f_i$ (P/D, H/D, RE)

3.2.2 Input Parameters For Subchannel Annalysis Codes

Phenomenological models have been developed for the interior region mixing and edge region swirl (ε^*_{1L} and C_{1L}) in Reference 64 for turbulent flow and reference 65 for laminar flow. Models for friction factors and flow split parameters for laminar, transition, and turbulent flow can be found in Reference 66. The determination of the conduction shape factor is discussed in References 67 and 68, but no correlations are available. All of the latest correlations are brought together in 69, along with a computer program for their calculation. However, all of the existing correlations are for forced convection. These correlations have also been applied to the flows in the mixed convection regime with reasonably good success (67), but how far into the mixed convection regime they are valid is an open question.

3.2.3 Structure of the Numerical Tools

Table 3.2.1 outlines the structure of the ENERGY and COBRA codes. The conservation equations solved by each are given, along with the required input parameters, and the flow regimes where each code may be applied.

The simplest type of code solves the energy equation only, and is valid in the forced convection regime. The flow field is an input parameter (X_i) determined experimentally or through prior solution of the momentum equation, and

does not vary with axial distance. Hence, the continuity and momentum equations need not be solved in the code itself. An example of such a code is ENERGY IV-FC (the forced convection option of ENERGY IV).

If the buoyancy-induced crossflow is significant, the mixed convection regime is entered, and the continuity and axial momentum equations must also be solved requiring the use of a subchannel friction factor. ENERGY IV-MC (the mixed convection option of ENERGY-IV) and COBRA are codes which are valid in both the forced and mixed convection regime. Both solve the coupled momentum and energy equations with an explicit (marching) solution scheme. COBRA provides a more comprehensive approach since it solves the transverse momentum equation and also has an option for an implicit solution scheme.

For very low flows, flow reversal may occur in the low power regions of an assembly, requiring the use of an implicit solution scheme and a recirculation model. COBRA is capable of calculating flow recirculation if the implicit solution scheme is employed. Since computation expense increases with code complexity, it is desired to use the simple code whenever possible. Therefore, criteria are needed to identify the onset

of mixed convection and the onset of flow recirculation in rod bundles. These two criteria will be developed in Chapters 5 through 8, and are based on a two channel model of the rod bundle. Both the ENERGY and COBRA codes will be used to validate the model in Chapter 6.

TABLE 3.2.1

SUBCHANNEL CODES FOR ANALYSIS OF LMFBR ROD BUNDLES

CODE (Ref)	CONSERVATION EQUATIONS				INPUT PARAMETERS					FLOW REGIME		
	Mass	Momentum		Energy	Interior Mixing	Edge Swirl	Friction	Flow Split	Conduction Shape Factor	FC	MC	Recirc
		Axial	Trans									
ENERGY IV-FC (5)				✓	ε^*_{1L}	C_{1L}		X_i	SF	✓		
ENERGY IV-MC (5)	✓	✓		✓	ε^*_{1L}	C_{1L}	f		SF	✓	✓	
COBRA (6)	✓	✓	✓	✓	Wire Model		f		1/Z	✓	✓	✓

CHAPTER 4

EXPERIMENTAL APPARATUS

The experimental apparatus employed in this work is a modification of the apparatus of Reference 1. The changes which were made will be outlined in the sections which follow.

4.1 FLOW LOOP

A schematic of the flow loop is given in Figure 4.1.1. A large water supply tank is used as a reservoir for running the tests. Prior to running a test, the water must be heated close to the boiling point using the steam supply to remove dissolved gasses in the water, which were found to occur in the tests of Reference 1. The water was then cooled by pumping the water through the heat exchanger either in a once through fashion, or by using the cooling loop to bring the reservoir to the desired temperature, then running the test without cooling from the heat exchanger. It was found that this method allowed the test section inlet temperature to be maintained at a constant value.

The water was then pumped through flowmeters FM1 or FM2 for flow measurement, and on to the test section. Either upflow or downflow could be maintained through the test section depending on the status of valves 1, 2, 3 and 4.

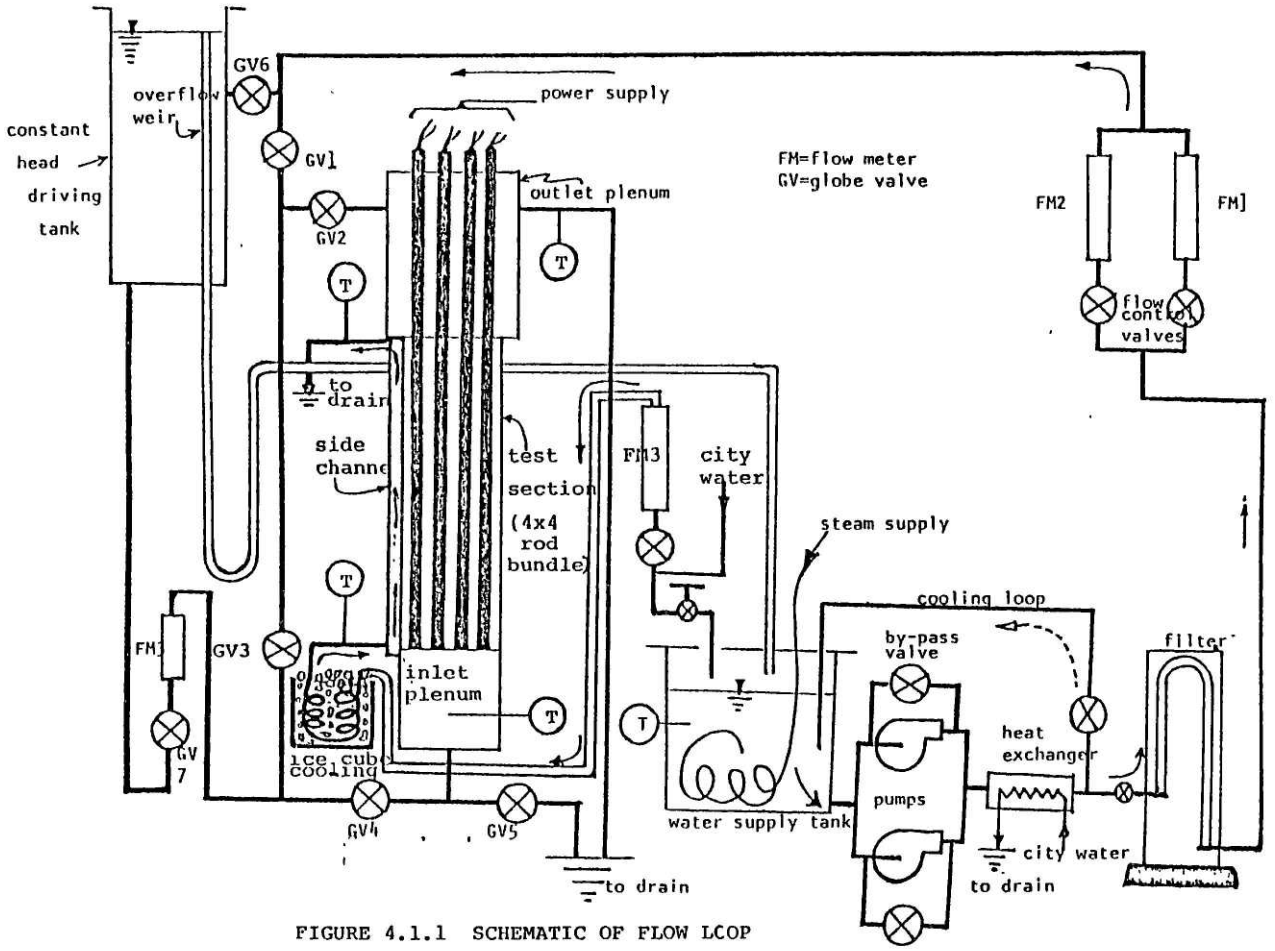


FIGURE 4.1.1 SCHEMATIC OF FLOW LCOP

The loop is also equipped with a constant head driving tank, which provides a constant inlet pressure boundary condition rather than a constant flow boundary condition.

A plexiglass side cooling channel was constructed to allow one wall of the test section to be cooled, thus simulating the effect of interassembly heat transfer. The city water was passed through flow meter 3, and through 100 feet of copper tubing immersed in ice to cool the water prior to running it through the side channel. This allowed large heat transfer rates to occur through the cold wall. The power loss from the test section could be calculated from an energy balance on the side channel flow.

4.2 TEST SECTION

A side view of the test section without the side channel is shown in Figure 4.2.1. The locations of pressure taps (P) instrument insertion locations (V,T,P) are shown. Three plexiglass windows (not shown) are located at the instrument insertion points to allow flow visualization. A cross section of the test section is shown in Figure 4.2.2 with the plexiglass side channel in place.

4.3 HEATER ROD INSTRUMENTED WITH A THERMOCOUPLE PROBE

To allow rod wall temperatures to be measured without disturbing the flow, a heater rod was designed and constructed as shown in Figure 4.3.1 The heated length was made of

FIGURE 4.2.1
SIDE VIEW - MIT 4x4 BUNDLE

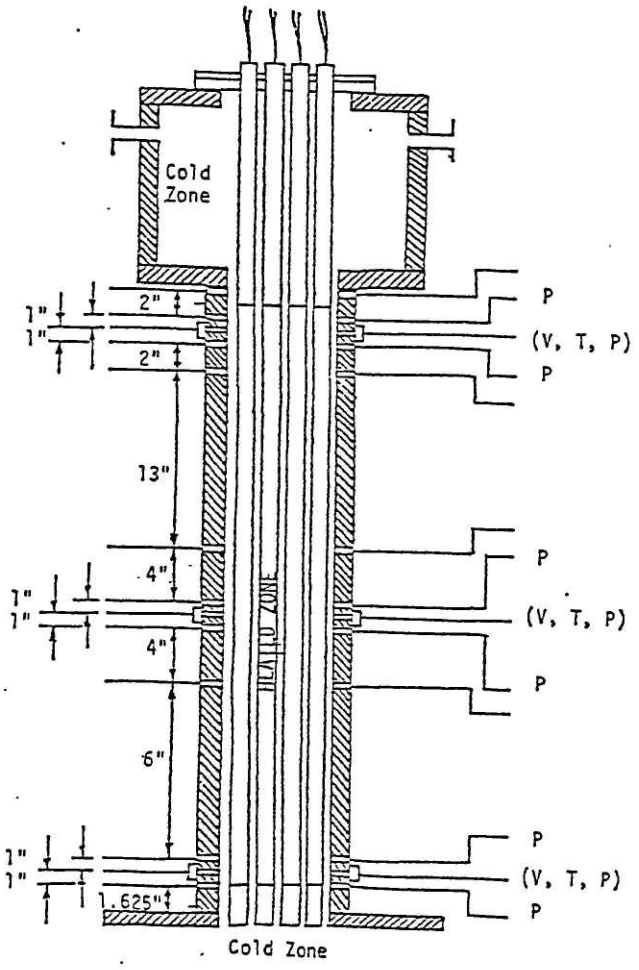
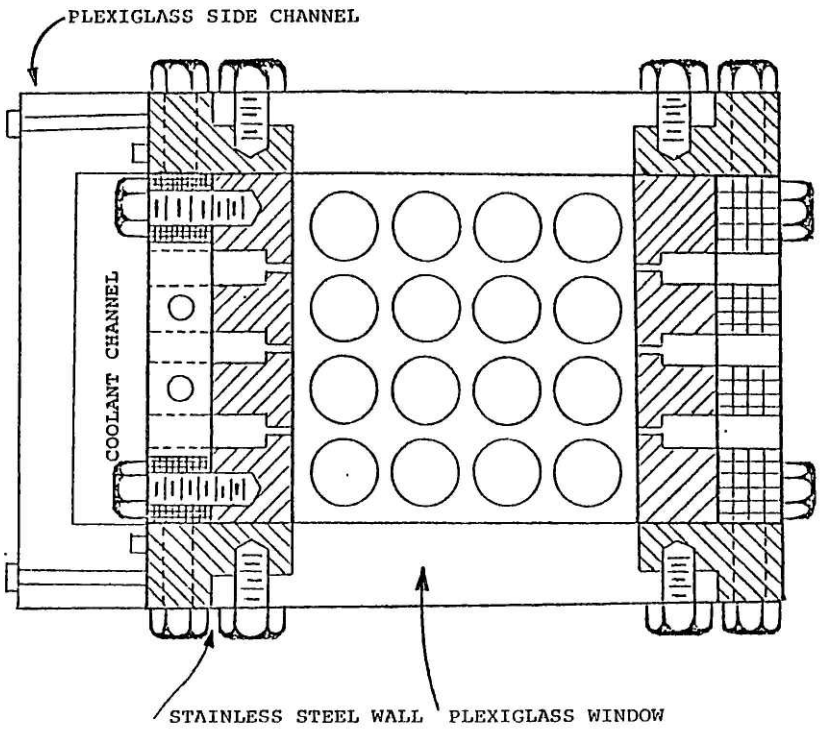


FIGURE 4.2.2

CROSS SECTION OF MIT 4x4 BUNDLE



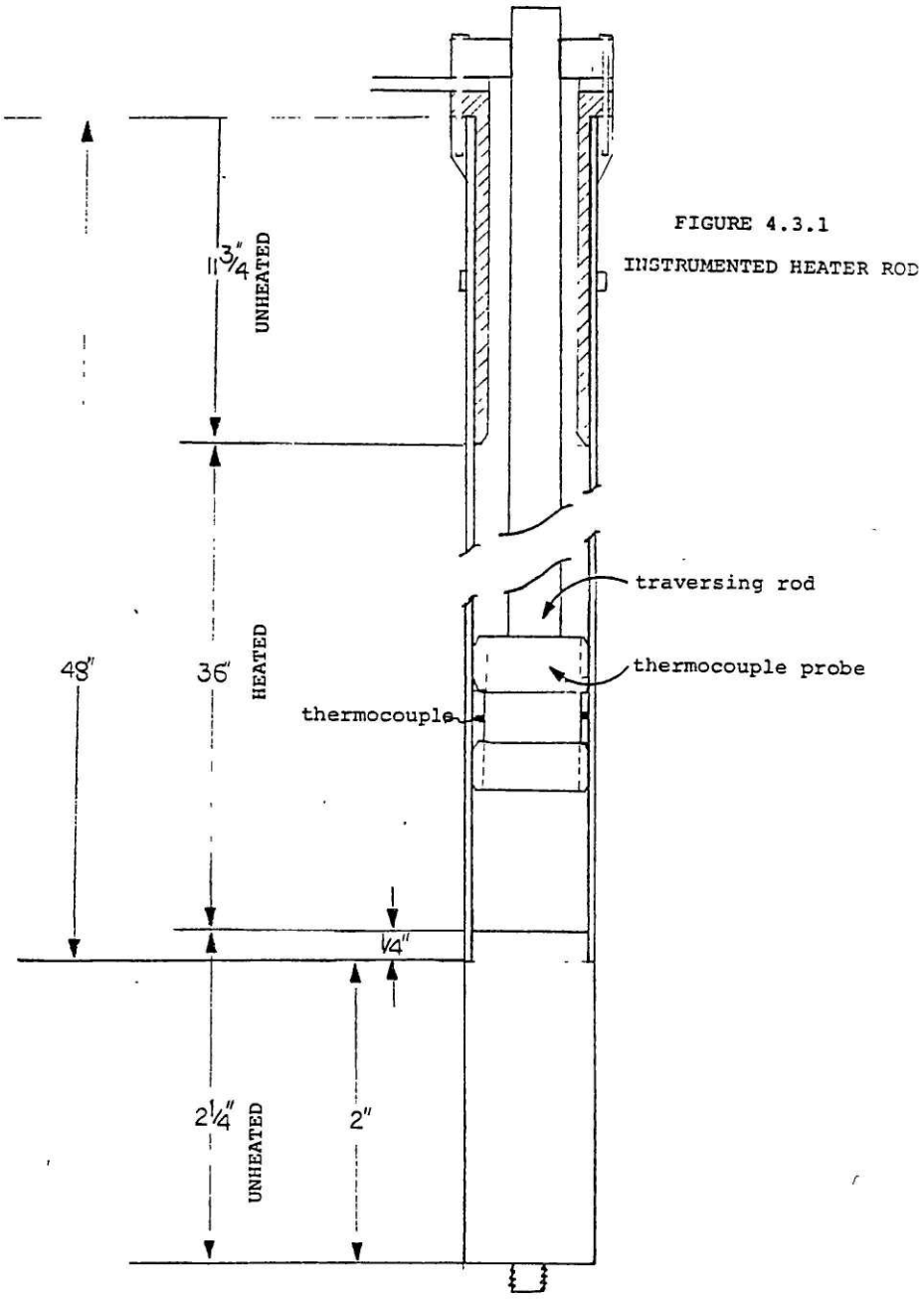


FIGURE 4.3.1

INSTRUMENTED HEATER ROD

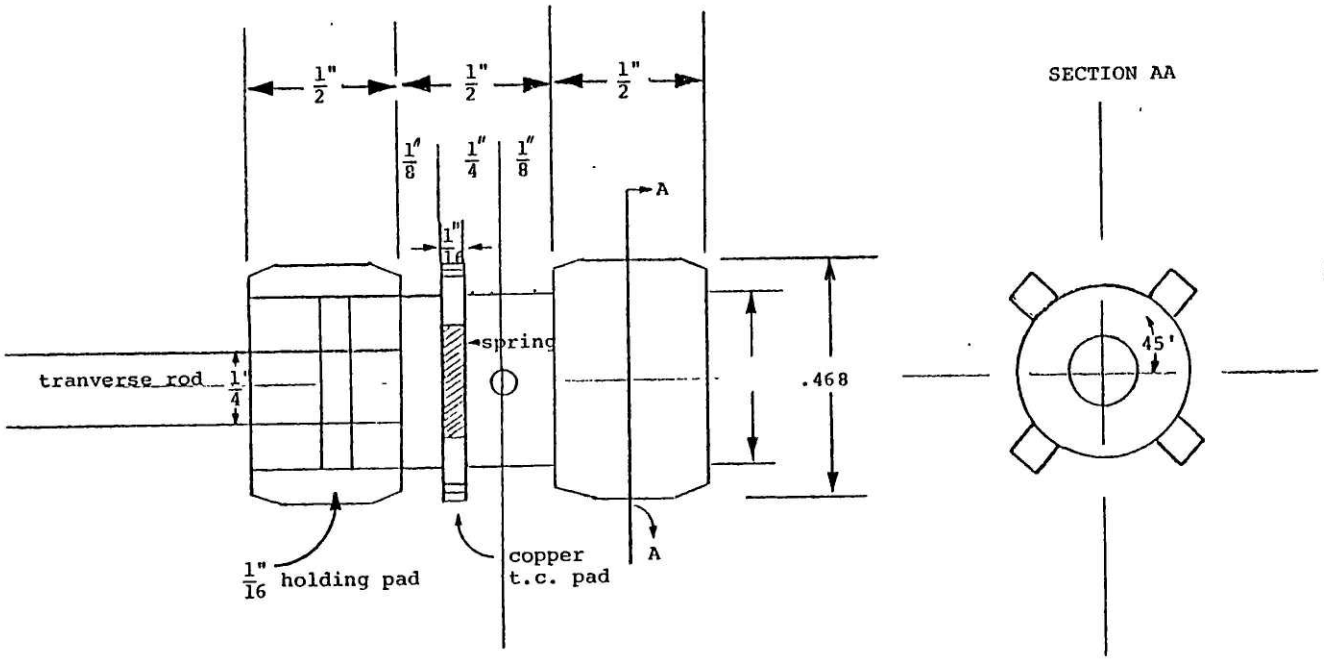
stainless steel tubing with a .016" wall. The rod was heated by direct (I^2R) heating of the tube. The lower 2¼" was made from a solid copper cylinder, so is unheated (due to the low resistance of copper). In an effort to minimize the heating in the upper 11 3/4" of the rod, a brass insert was made to closely contact the inside of the stainless steel tube. Due to the lower resistance of the brass insert, the ohmic heating was reduced.

A nylon thermocouple probe was fitted to a phenolic (insulated) traversing rod to allow the thermocouple probe to be moved axially and circumferentially in the rod bore, enabling temperature measurement at any desired location along the heated length of the rod. A detail of the thermocouple probe is given in Figure 4.3.2. The probe had two 1/16" holes drilled through at 90^{o} angles. A small spring and two copper cylinders could be inserted in each of the two holes. As shown the thermocouple was mounted in the copper cylinder, which was pushed against the heater tube wall by the spring, enabling the wall inside temperature to be measured.

The thermocouple probe was not employed in this work and remains untested, though the heater rod was tested up to a power of 4600 watts. Calibration tests should be made on the instrumented rod before loading it into the test section.

FIGURE 4.3.2

THERMOCOUPLE PROBE



CHAPTER 5

DEVELOPMENT OF A TWO CHANNEL MODEL FOR A VERTICAL ROD BUNDLE

The usual method of calculating the flow and temperature field in a rod bundle is the subchannel approach. This method involves dividing the rod bundle into a number of subchannels, and numerically solving the conservation laws for each subchannel. In the method developed here, the bundle is divided into two interacting channels, and we seek an analytical solution for the conservation equations. This is the coarsest possible noding scheme which will account for the bouyancy induced crossflow. For the LMFBR case, this requires lumping together of the interior and edge region. This approximation is acceptable since we are only interested in predicting bulk channel temperatures and velocities. The motivation for using this approach is to develop criteria for onset of recirculation and onset of mixed convection in the rod bundle. In the sections which follow, the conservation equations will be derived, and solved by an approximate analytical method.

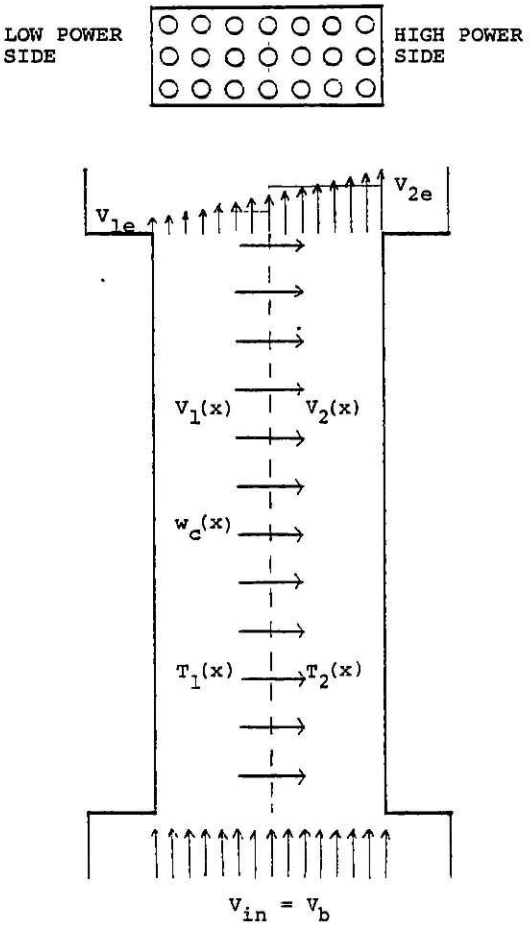
5.1 GOVERNING EQUATIONS

5.1.1 Derivation of Conservation Equations for the Two Channel Model

Figure 5.1.1 presents the two channel approach to modeling the reactor subassembly, along with the nomenclature

FIGURE 5.1.1

TWO CHANNEL MODEL OF A ROD BUNDLE



used. A mean or bulk temperature and bulk velocity which varies axially is used for each channel to approximate the bundle temperature and flow field. A channel power input which can vary axially approximates the actual power distribution. For the case of a radial power gradient, channel number 1 is the lower power channel, and channel number 2 is the higher power channel.

Mass Conservation

In words, the mass conservation law for a control volume is:

$$\left\{\begin{matrix}\text{mass outflow}\\ \text{rate}\end{matrix}\right\} - \left\{\begin{matrix}\text{mass inflow}\\ \text{rate}\end{matrix}\right\} + \left\{\begin{matrix}\text{rate of}\\ \text{storage of mass}\end{matrix}\right\} = 0$$

Applying this to the differential control volume of Figure 5.1.2 for channel 2 gives:

$$\left(\rho_2 V_2 + \frac{\partial}{\partial x}(\rho_2 V_2)dx\right)A_2 - (\rho_2 V_2 A_2 + w_c dx) + \frac{\partial}{\partial t}[\rho_2 A_2 dx] = 0 \qquad (5.1.1)$$

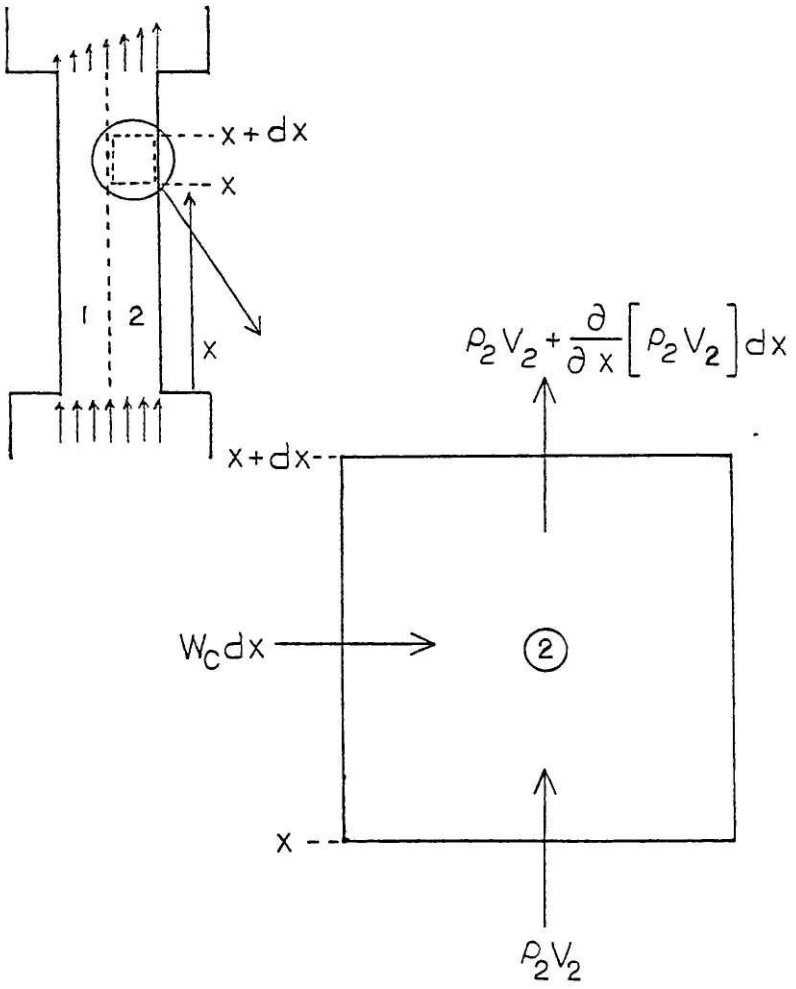
Expanding the derivative, neglecting products of differentials, and solving for the crossflow gives:

$$w_c = \rho_2 A_2 \frac{\partial V_2}{\partial x} + V_2 A_2 \frac{\partial \rho_2}{\partial x} + A_2 \frac{\partial \rho_2}{\partial t} \qquad (5.1.2)$$

$$= \rho_2 A_2 \frac{\partial V_2}{\partial x} + A_2 \frac{D\rho_2}{Dt} \qquad (5.1.3)$$

FIGURE 5.1.2

CONTROL VOLUME ANALYSIS FOR MASS CONSERVATION



where

$$\frac{D}{Dt} = \frac{\partial}{\partial t} + V \frac{\partial}{\partial x} \tag{5.1.4}$$

The crossflow is composed of two parts: one due to changes in the axial velocity ($\rho_2 A_2 \frac{\partial V_2}{\partial x}$) and the other due to changes in the density ($A_2 \frac{D\rho_2}{Dt}$). It is the former which will be of most interest in this study. Similarly, for channel 1 we obtain:

$$-w_c = \rho_1 A_1 \frac{\partial V_1}{\partial x} + V_1 A_1 \frac{\partial \rho_1}{\partial x} + A_1 \frac{\partial \rho_1}{\partial t} \tag{5.1.5}$$

$$= \rho_1 A_1 \frac{\partial V_1}{\partial x} + A_1 \frac{D\rho_1}{Dt} \tag{5.1.6}$$

Momentum Conservation

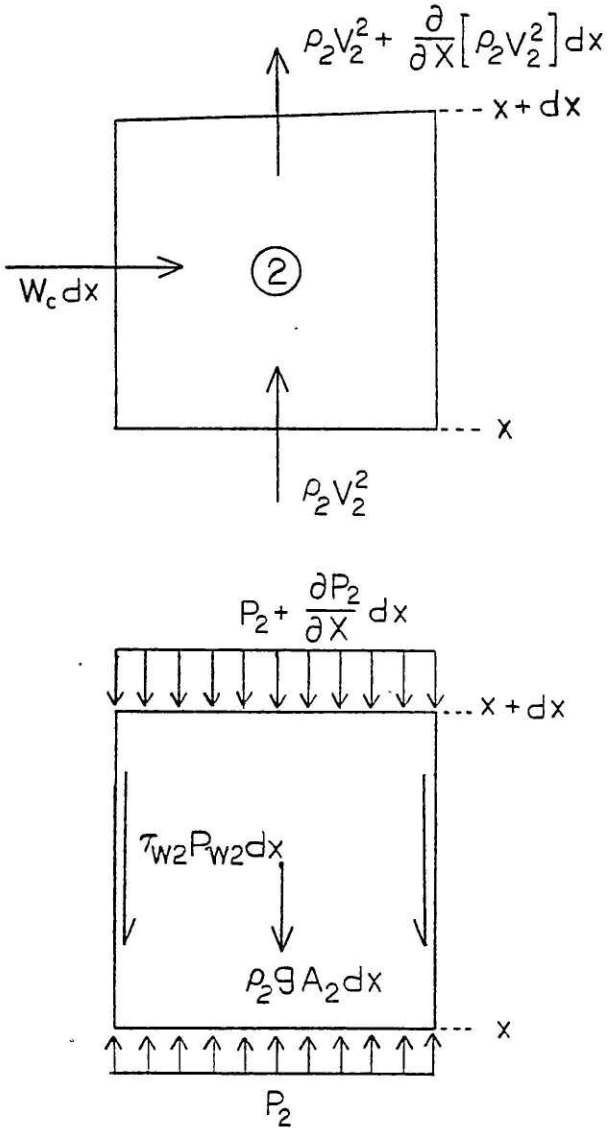
The momentum conservation law for the control volume for the x direction is:

$$\left\{\begin{array}{c}\text{sum of forces}\\ \text{on control volume}\\ \text{in x direction}\end{array}\right\} =$$

$$\left\{\begin{array}{c}\text{x direction}\\ \text{momentum}\\ \text{outflow rate}\end{array}\right\} - \left\{\begin{array}{c}\text{x direction}\\ \text{momentum}\\ \text{inflow rate}\end{array}\right\} + \left\{\begin{array}{c}\text{rate of}\\ \text{momentum}\\ \text{storage}\end{array}\right\}$$

Applying this to the control volume shown in Figure 5.1.3 gives:

FIGURE 5.1.3
CONTROL VOLUME ANALYSIS FOR MOMENTUM CONSERVATION



$$\Sigma F_x = \left(\rho_2 V_2^2 + \frac{\partial}{\partial x}(\rho_2 V_2^2)dx\right)A_2 + w_t dx V_2 -$$

$$\{\rho_2 V_2^2 A_2 + w_t V_1 dx + w_c V_1 dx\} + \frac{\partial}{\partial t}[\rho_2 A_2 V_2 dx] \quad (5.1.7)$$

Expanding terms, and dividing by $A_2 dx$:

$$\frac{\Sigma F_x}{A_2 dx} = 2\rho_2 V_2 \frac{\partial V_2}{\partial x} + V_2^2 \frac{\partial \rho_2}{\partial x} + \frac{w_t}{A_2}(V_2 - V_1) -$$

$$\frac{W_c}{A_2} V_1 + \frac{\partial}{\partial t}(\rho_2 V_2) \quad (5.1.8)$$

The corresponding equation for channel 1 is:

$$\frac{\Sigma F_x}{A_1 dx} = 2\rho_1 V_1 \frac{\partial V_1}{\partial x} + V_1^2 \frac{\partial \rho_1}{\partial x} + \frac{w_t}{A_1}(V_1 - V_2) +$$

$$\frac{w_c}{A_1} V_1 + \frac{\partial}{\partial t}(\rho_1 V_1) \quad (5.1.9)$$

For purposes of visualizing why some terms cancel for channel 1, but do not cancel for channel 2, it is useful to introduce a shorthand notation which allows both equations to be written as one. Let i indicate the channel under consideration, and j the other channel. Equations 5.1.8 and 5.1.9 can be written:

$$\frac{\Sigma F_x}{A_i dx} = 2\rho_i V_i \frac{\partial V_i}{\partial x} + V_i^2 \frac{\partial \rho_i}{\partial x} + \frac{w_t}{A_i}(V_i - V_j) \pm$$

$$\frac{w_c}{A_i} V_1 + \frac{\partial}{\partial t}(\rho_i V_i) \quad (5.1.10)$$

where the plus sign in front of the crossflow term is used for channel 1 (i=1) and the minus sign for channel 2 (i=2). Using this scheme, the continuity equations (5.1.2 and 5.1.5) can be written:

$$\pm \frac{w_c}{A_i} = - \left[\rho_i \frac{\partial V_i}{\partial x} + V_i \frac{\partial \rho_i}{\partial x} + \frac{\partial \rho_i}{\partial t} \right] \qquad (5.1.11)$$

As above, the plus sign is for i=1, and the minus sign for i=2. Substituting Equation 5.1.11 into Equation 5.1.10 to eliminate the crossflow term gives:

$$\frac{\Sigma F_x}{A_i dx} = \rho_i V_i \frac{\partial V_i}{\partial x} + \frac{w_t}{A_i}(V_i - V_j) + \rho_i \frac{\partial V_i}{\partial t} + \rho_i (V_i - V_1) \frac{\partial V_i}{\partial x} + (V_i^2 - V_1 V_i) \frac{\partial \rho_i}{\partial x} + (V_i - V_1) \frac{\partial \rho_i}{\partial t} \qquad (5.1.12)$$

For i=1, j=2 (channel 1) the last three terms are zero. For i=2, j=1 (channel 2) they remain nonzero.

The forces on the control volume are found by applying a force balance as shown in Figure 5.1.3. The net force in the x direction is:

$$\sum F_x = p_i A_i - (p_i + \frac{\partial p_i}{\partial x} dx) A_i - \tau_{wi} P_{wi} dx - \rho_i g A_i dx \qquad (5.1.13)$$

which can be written:

$$\frac{\Sigma F_x}{A_i dx} = -\frac{\partial p_i}{\partial x} - \tau_{wi}\frac{P_{wi}}{A_i} - \rho_i g \qquad (5.1.14)$$

where

$$\tau_{wi}\frac{P_{wi}}{A_i} = \frac{1}{2}\rho_i V_i^2 \frac{f_i}{De_i} \qquad (5.1.15)$$

Substituting Equations 5.1.14 and 5.1.15 into Equation 5.1.12 and solving for the pressure gradient gives:

$$-\frac{\partial p_i}{\partial x} = \rho_i V_i \frac{\partial V_i}{\partial x} + \frac{w_t}{A_i}(V_i - V_j) + \frac{1}{2}\rho_i V_i^2 \frac{f_i}{De_i} + \rho_i g + \rho_i \frac{\partial V_i}{\partial t} + \rho_i (V_i - V_1)\frac{\partial V_i}{\partial x} + (V_i^2 - V_1 V_i)\frac{\partial \rho_i}{\partial x} + (V_i - V_1)\frac{\partial \rho_i}{\partial t} \qquad (5.1.16)$$

For channel 1 (i=1, j=2), the last three terms of Equation 5.1.16 become zero, and the pressure gradient is:

$$-\frac{\partial p_1}{\partial x} = \rho_1 V_1 \frac{\partial V_1}{\partial x} + \frac{w_t}{A_1}(V_1 - V_2) + \frac{1}{2}\rho_1 V_1^2 \frac{f_1}{De_1} + \rho_1 g + \rho_1 \frac{\partial V_1}{\partial t} \qquad (5.1.17)$$

But for channel 2 (i=2, j=1), the terms are nonzero and Equation 5.16 becomes

$$-\frac{\partial p_2}{\partial x} = \rho_2 V_2 \frac{\partial V_2}{\partial x} + \frac{w_t}{A_2}(V_2-V_1) + \frac{1}{2}\rho_2 V_2^2 \frac{f_2}{De_2} + \rho_2 g +$$

$$\rho_2 \frac{\partial V_2}{\partial t} + \rho_2 (V_2-V_1)\frac{\partial V_2}{\partial x} + (V_2^2-V_1V_2)\frac{\partial \rho_2}{\partial x} + (V_2-V_1)\frac{\partial \rho_2}{\partial t} \qquad (5.1.18)$$

Introducing the coefficient of thermal expansion, $\beta = -\frac{1}{\rho}\frac{\partial \rho}{\partial T}$, into Equation 5.1.18 we obtain:

$$-\frac{\partial p_2}{\partial x} = \rho_2 V_2 \frac{\partial V_2}{\partial x} + \frac{w_t}{A_2}(V_2-V_1) + \frac{1}{2}\rho_2 V_2^2 \frac{f_2}{De_2} + \rho_2 g +$$

$$\rho_2 \frac{\partial V_2}{\partial t} + \rho_2 (V_2-V_1)\frac{\partial V_2}{\partial x} - (V_2^2-V_1V_2)\,\rho_2\beta \frac{\partial T_2}{\partial x} -$$

$$(V_2-V_1)\,\rho_2\beta \frac{\partial T_2}{\partial t} \qquad (5.1.19)$$

Equations 5.1.17 and 5.1.19 are the momentum equations for the two channel model.

Energy Conservation

The conservation of energy law for a control volume is:

$$\left\{\begin{matrix}\text{rate of outflow}\\ \text{of energy}\end{matrix}\right\} - \left\{\begin{matrix}\text{rate of inflow}\\ \text{of energy}\end{matrix}\right\} + \left\{\begin{matrix}\text{rate of storage}\\ \text{of energy}\end{matrix}\right\}$$

$$= 0$$

If we employ the subscript notation used in the momentum equation development, the energy fluxes are as shown in

Figure 5.1.4. From energy conservation, it follows that:

$$\{[\rho_i V_i h_i + \frac{\partial}{\partial x}(\rho_i V_i h_i)dx]A_i + \left[-K \frac{\partial T_i}{\partial x} + \frac{\partial}{\partial x}\left[-K \frac{\partial T_i}{\partial x}\right] dx\right] A_i$$

$$+ w_t h_i dx + KSF \frac{T_i - T_j}{\ell} w\, dx\} -$$

$$\{\rho_i V_i h_i A_i - K \frac{\partial T}{\partial x} A_i + q_i' dx \mp w_c h_l dx + w_t h_j dx\} +$$

$$\frac{\partial}{\partial t}(\rho_i e_i A_i dx) = 0 \qquad (5.1.20)$$

Neglecting kinetic and potential energy, the total energy becomes the internal energy:

$$e_i = u_i \qquad (5.1.21)$$

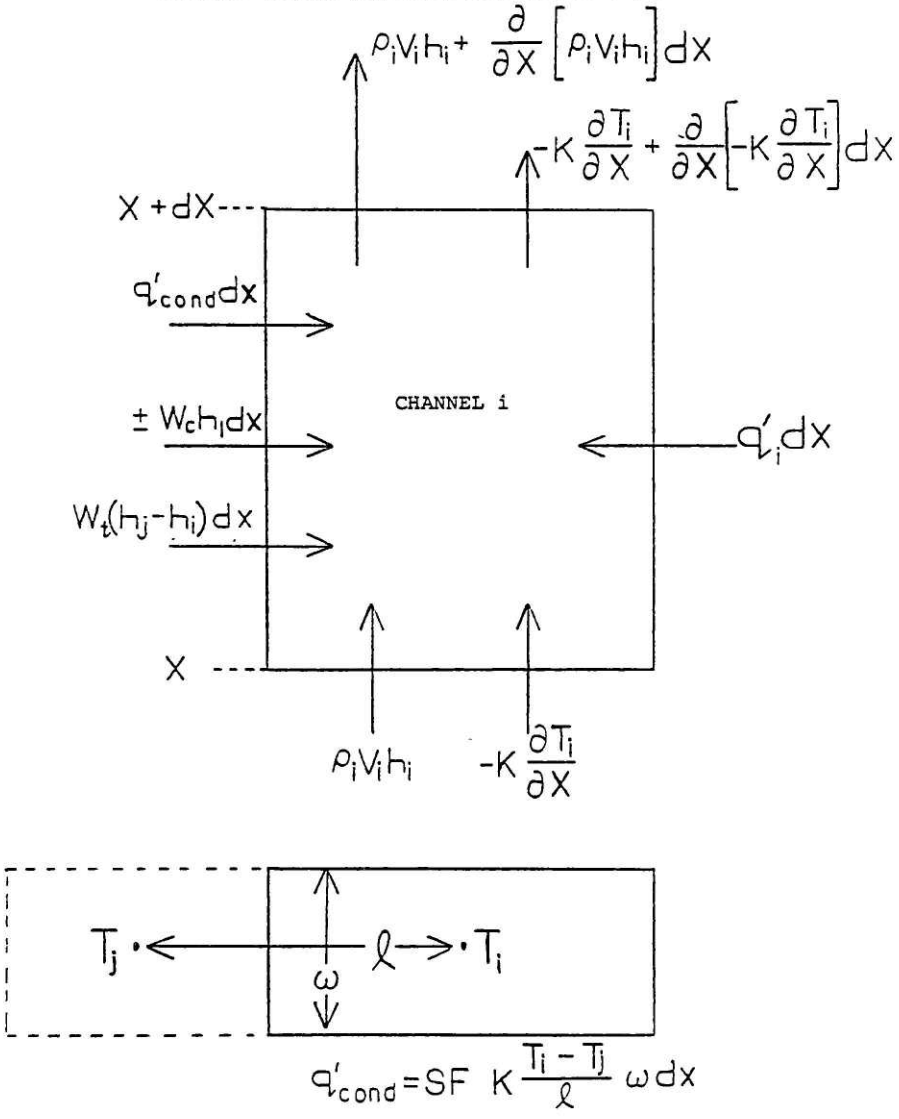
If heat capacities are assumed constant:

$$e_i = u_i = C_v T_i \qquad (5.1.22)$$

$$h_i = C_p T_i \qquad (5.1.23)$$

Substitution of Equations 5.1.22 and 5.1.23 into Equation 5.1.20 gives, for constant thermal conductivity:

FIGURE 5.1.4
CONTROL VOLUME ANALYSIS FOR ENERGY CONSERVATION



$$\frac{\partial}{\partial x}(\rho_i V_i T_i) - \frac{K}{C_p}\frac{\partial^2 T_i}{\partial x^2} + \frac{1}{A_i}\left(w_t + \frac{SFKw}{\ell C_p}\right)(T_i - T_j) - \frac{q_i'}{A_i C_p} \pm \frac{w_c}{A_i} T_1 + \frac{C_v}{C_p}\frac{\partial}{\partial t}(\rho_i T_i) = 0 \qquad (5.1.24)$$

Eliminate $\pm \frac{w_c}{A_i}$ with Equation 5.1.11 and expand derivatives to get:

$$\rho_i V_i \frac{\partial T_i}{\partial x} - \frac{K}{C_p}\frac{\partial^2 T_i}{\partial x^2} + (T_i - T_1)\left[\rho_i \frac{\partial V_i}{\partial x} + V_i \frac{\partial \rho_i}{\partial x}\right] + \left(\frac{C_v}{C_p} T_i - T_1\right)\frac{\partial \rho_i}{\partial t} + \frac{C_v}{C_p}\rho_i \frac{\partial T_i}{\partial t} + \frac{1}{A_i}\left(w_t + \frac{SFKw}{\ell C_p}\right)(T_i - T_j) - \frac{q_i'}{A_i C_p} = 0 \qquad (5.1.25)$$

Introducing the coefficient of thermal expansion, ($\beta = -\frac{1}{\rho_i}\frac{\partial \rho_i}{\partial T}$) this can be written as:

$$\rho_i V_i\left[1 - \beta(T_i - T_1)\right]\frac{\partial T_i}{\partial x} + \rho_i\left[\frac{C_v}{C_p} - \beta\left(\frac{C_v}{C_p} T_i - T_1\right)\right]\frac{\partial T_i}{\partial t} - \frac{K}{C_p}\frac{\partial^2}{\partial x^2}\frac{T_i}{} + \rho_i (T_i - T_1)\frac{\partial V_i}{\partial x} + \frac{1}{A_i}\left(w_t + \frac{SF\,K\,w}{\ell C_p}\right)(T_i - T_j) - \frac{q_i'}{A_i C_p} = 0 \qquad (5.1.26)$$

for channel number 1 (i=1, j=2) this becomes:

$$\rho_1 V_1 \frac{\partial T_1}{\partial x} - \frac{K}{C_p}\frac{\partial^2 T_1}{\partial x^2} + \rho_1 \frac{C_v}{C_p} - \left[T_1\left(\frac{C_v}{C_p} - 1\right)\right]\frac{\partial T_1}{\partial t} +$$

$$\frac{1}{A_1}\left(w_t + \frac{SF\ K\ w}{\ell\, C_p}\right)(T_1 - T_2) - \frac{q_1'}{A_1 C_p} = 0 \quad (5.1.27)$$

For channel number 2 (i=2, j=1) Eq. 5.1.26 is:

$$\rho_2 V_2\left[1-\beta(T_2-T_1)\right]\frac{\partial T_2}{\partial x} - \frac{K}{C_p}\frac{\partial^2 T_2}{\partial x^2} + \rho_2\left[\frac{C_v}{C_p} - \beta\left(\frac{C_v}{C_p}T_2 - T_1\right)\right]\frac{\partial T_2}{\partial t} +$$

$$\left[\rho_2 \frac{\partial V_2}{\partial x} + \frac{1}{A_2}\left(w_t + \frac{SF\ K\ w}{\ell C_p}\right)\right](T_2 - T_1) - \frac{q_2'}{A_2 C_p} = 0 \quad (5.1.28)$$

Note that asymmetry exists in both the momentum (Equations 5.1.17 and 5.1.19) and energy (Equations 5.1.27 and 5.1.28) equations. This is due to the assumed one-way nature of the buoyancy induced crossflow term. Since we are dealing with only two channels, we know that the buoyancy induced crossflow goes from the cold channel (channel #1) to the hot channel (channel #2). This allows us to write the buoyancy induced momentum transport as $w_c V_1$, and the buoyancy induced energy transport as $w_c C_p T_1$. This crossflow always transports momentum and energy from channel 1 to channel 2, hence channel 2 has additional terms which are not seen in channel 1.

5.1.2 Simplification of The Governing Equations

As they now stand, the conservation equations are in a form not subject to an analytical solution. Simplifying assumptions must be made to transform them into a more tractable form.

First, the Boussinesq approximation will be employed, so that the density is constant everywhere but in the gravity term of the momentum equation. Hence we set $d\rho=0$ ($\beta=0$), and drop the subscripts on ρ in all but the gravity term. Reference 2 gives a good discussion on the validity of the Boussinesq approximation. Generally speaking, it is valid if $\beta\Delta T<<1$. This is certainly valid for liquid cooled systems, but if a gas is used for the coolant, the thermal expansion may become significant. For the Boussinesq approximation, the conservation equations are:

Mass conservation:

$$w_c = \rho A_2 \frac{\partial V_2}{\partial x} = -\rho A_1 \frac{\partial V_1}{\partial x} \tag{5.1.29}$$

Momentum conservation:

$$-\frac{\partial p_1}{\partial x} = \rho V_1 \frac{\partial V_1}{\partial x} - \frac{w_t}{A_1}(V_2-V_1) + \frac{1}{2}\rho V_1^2 \frac{f_1}{D_{e1}} + \rho_1 g + \rho \frac{\partial V_1}{\partial t} \tag{5.1.30}$$

$$-\frac{\partial p_2}{\partial x} = \rho V_2 \frac{\partial V_2}{\partial x} + \frac{1}{A_2}(w_t+w_c)(V_2-V_1) + \frac{1}{2}\rho V_2^2 \frac{f_2}{D_{e2}} + \rho_2 g + \rho \frac{\partial V_2}{\partial t} \tag{5.1.31}$$

Energy conservation:

$$- \frac{K}{C_p} \frac{\partial^2 T_1}{\partial x^2} + \rho V_1 \frac{\partial T_1}{\partial x} = \frac{q_1'}{A_1 C_p} + \frac{1}{A_1}\left(w_t + \frac{SF\,K\,w}{\ell C_p}\right)(T_2 - T_1)$$

$$- \rho \frac{C_v}{C_p} \frac{\partial T_1}{\partial t} \qquad (5.1.32)$$

$$- \frac{K}{C_p} \frac{\partial^2 T_2}{\partial x^2} + \rho V_2 \frac{\partial T_2}{\partial x} = \frac{q_2'}{A_2 C_p} - \frac{1}{A_2}\left(w_c + w_t + \frac{SF\,K\,w}{\ell C_p}\right)(T_2 - T_1)$$

$$- \rho \frac{C_v}{C_p} \frac{\partial T_2}{\partial t} \qquad (5.1.33)$$

If the axial conduction term and unsteady term are negligible, the energy equations become:

$$\rho V_1 \frac{\partial T_1}{\partial x} = \frac{q_1'}{A_1 C_p} + \frac{1}{A_1}\left(w_t + \frac{SF\,K\,w}{\ell C_p}\right)(T_2 - T_1) \qquad (5.1.34)$$

$$\rho V_2 \frac{\partial T_2}{\partial x} = \frac{q_2'}{A_2 C_p} - \frac{1}{A_2}\left(w_c + w_t + \frac{SF\,K\,w}{\ell C_p}\right)(T_2 - T_1) \qquad (5.1.35)$$

The momentum equations can each be integrated to obtain the channel pressure drops. Equating the channel pressure drops gives:

$$0 = \rho\int_o^L \left[V_2\frac{\partial V_2}{\partial x} - V_1\frac{\partial V_1}{\partial x}\right]dx + w_t\left[\frac{1}{A_1} + \frac{1}{A_2}\right]\int_o^L (V_2-V_1)dx +$$

$$\int_o^L \frac{w_c}{A_2}(V_2-V_1)dx + \frac{1}{2}\rho\int_o^L \left[V_2^2\frac{f_2}{D_{e2}} - V_1^2\frac{f_1}{D_{e1}}\right]dx +$$

$$g\int_o^L (\rho_2-\rho_1)dx + \rho\int_o^L \left[\frac{\partial}{\partial t}(V_2-V_1)\right]dx \qquad (5.1.36)$$

If it is assumed that the density varies linearly with temperature, the buoyancy term can be written:

$$g(\rho_2-\rho_1) = -\rho\, g\, \beta(T_2-T_1) \qquad (5.1.37)$$

To evaluate the buoyancy term, we require (T_2-T_1) as a function of x. A differential equation for T_2-T_1 can be obtained by combining the energy equations to give:

$$\frac{\partial}{\partial x}(T_2-T_1) = \left(\frac{q_2'}{\rho V_2 A_2 C_p} - \frac{q_1'}{\rho V_1 A_1 C_p}\right) - \left[\left(\frac{1}{\rho V_1 A_1} + \frac{1}{\rho V_2 A_2}\right)\cdot \left(w_t + \frac{SF\ K\ w}{\ell\ C_p}\right) + \frac{w_c}{\rho V_2 A_2}\right](T_2-T_1) \qquad (5.1.38)$$

Note that if the axial conduction and unsteady terms are not neglected, the energy equation cannot be expressed in terms of T_2-T_1.

The unsteady terms and axial conduction terms in the energy equations were neglected to allow analytical solution of the energy equation. In Appendix B1 and B2, simple models

are developed to determine under what conditions the approximations are valid.

The analysis of Appendix B1 suggests that the axial conduction term may be neglected when:

$$\frac{L}{D_e} \text{ Re Pr} < 100$$

This corresponds to Re = 81 for the Westinghouse blanket bundle ($\frac{L}{D_e}$ = 308, Pr = .004) and Re = 88 for the ORNL fuel bundle ($\frac{L}{D_e}$ = 284, Pr = .004).

In Appendix B2, it is shown that if the flow coastdown is given by:

$$\frac{w}{w_o} = 1 - \frac{t}{t+K_t}$$

where K_t is the time constant for the flow coastdown. The transient term may be neglected if:

$$\frac{L}{2K_t V_o} \leq .10$$

where V_o is the initial bundle average velocity and L is the bundle heated length. In Appendix B2, it is shown that this criteria is satisfied for mild transients such as a pump coastdown but not more severe pipe rupture transients.

The three conservation equations will next be made dimensionless. The continuity equation (5.1.29) is made dimensionless by multiplying by $L/\rho V_b A_b$ to give:

$$w_c^* = \frac{w_c L}{\rho V_b A_b} = \frac{1}{1+R} \frac{\partial V_2^*}{\partial x^*} = \frac{-1}{1+1/R} \frac{\partial V_1^*}{\partial x^*} \qquad (5.1.39)$$

where: $R = A_1/A_2$

$x^* = x/L$

$V_i^* = V_i/V_b$

The momentum equation is made dimensionless by multiplying by $1/(\rho V_b^2)$. We will first consider the buoyancy term due to its importance in this study. The dimensionless buoyancy term is:

$$\text{Term 5} = -\frac{g\beta L}{V_b^2}\int_o^L \frac{1}{L}(T_2 - T_1)\,dx \qquad (5.1.40)$$

Making the temperature difference dimensionless by introducing the bulk temperature rise:

$$\text{Term 5} = -\frac{g\beta L\Delta T_B}{V_b^2}\int_o^L \frac{1}{L}\frac{T_2 - T_1}{\Delta T_B}\,dx \qquad (5.1.41)$$

The dimensionless group before the integral is the Richardson number:

$$Ri = \frac{g\beta\Delta T_B L}{V_b^2} \qquad (5.1.42)$$

Hence the buoyancy term is:

$$\text{Term 5} = -Ri\int_o^1 y\,dx^* \qquad (5.1.43)$$

where y is the dimensionless radial temperature difference:

$$y = \frac{T_2 - T_1}{\Delta T_B} \qquad (5.1.44)$$

The physical significance of the Richardson number is made apparent by the discussion which follows. Consider the Reynolds number based on the bundle length.

$$Re = \frac{UL}{\nu} \tag{5.1.45}$$

where U is an appropriate velocity scale. For forced convection, the appropriate velocity scale is V_b, the bundle average velocity, so that:

$$Re_{forced} = \frac{V_b L}{\nu} \tag{5.1.46}$$

For free convection, the velocity is produced by the buoyancy force. If the buoyancy forces are the same order of magnitude as the inertia forces, a force balance gives $\rho U^2/L = \rho g \beta \Delta T_B$, hence the velocity

$$U^2 = g\beta\Delta T_B L \tag{5.1.47}$$

so that the square of the Reynolds number due to free convection is:

$$Re^2_{free} = \frac{U^2 L^2}{\nu^2} = \frac{g\beta\Delta T_B L^3}{\nu^2} \equiv Gr_{\Delta T_B} \tag{5.1.48}$$

hence the Richardson number can be expressed as:

$$Ri = \left(\frac{Re_{free}}{Re_{forced}}\right)^2 = \frac{Gr_{\Delta T_B}}{Re_L^2} \tag{5.1.49}$$

The Richardson number therefore represents the square of the ratio of free convection effects to forced convection effects. The Richardson number can also be written as:

$$Ri = \frac{Gr_{\Delta T_B}}{Re^2}\left(\frac{D_e}{L}\right)^2 \tag{5.1.50}$$

where Re is based on the bundle equivalent diameter. For steady state, the bundle bulk temperature rise is:

$$\Delta T_B = \frac{q'' P_H L}{\rho V_b A_b C_p} \tag{5.1.51}$$

where P_H is the heated perimeter. Substituting the above result into Equation 5.1.50 along with the definition of $Gr_{\Delta T_B}$ from Equation 5.1.48 gives:

$$Ri = 4\,\frac{L}{D_e}\,\frac{L}{D_H}\,\frac{Gr_q}{Re^3 Pr} \tag{5.1.52}$$

where the equivalent heated diameter is:

$$D_H = \frac{4A_b}{P_H} \tag{5.1.53}$$

and the Grashof number based on heat flux is:

$$Gr_q = \frac{g\beta q'' D_e^4}{K\nu^2} \tag{5.1.54}$$

hence an alternate representation of the buoyancy term is:

$$\text{Term 5} = -4\,\frac{L}{D_e}\,\frac{L}{D_H}\,\frac{Gr_q}{Re^3 Pr}\int_o^1 y\, dx^* \tag{5.1.55}$$

This representation is particularly useful for calculational purposes, since Gr_q depends on power only. It can be determined independent of the bundle velocity.

Nondimensionalizing the other terms of the momentum equation gives:

$$0 = \int_0^1 \left(V_2^* \frac{\partial V_2^*}{\partial x^*} - V_1^* \frac{\partial V_1^*}{\partial x^*} \right) dx^* + (1+R) \int_0^1 w_c^* (V_2^* - V_1^*) dx^* +$$

$$\frac{(1+R)^2}{R} w_t^* \int_0^1 (V_2^* - V_1^*) dx^* + \frac{1}{2} \left[\frac{L}{D_{e_2}} \int_0^1 V_2^{*2} f_2 dx^* - \frac{L}{D_{e_1}} \int_0^1 V_1^{*2} f_1 dx^* \right] +$$

$$\frac{LD_e}{\nu} \frac{1}{Re^2} \int_0^1 \frac{\partial}{\partial t} [Re (V_2^* - V_1^*)] dx^* - 4 \frac{L}{D_e} \frac{L}{D_H} \frac{Gr_q}{Re^3 Pr} \int_0^1 y \, dx^* \qquad (5.1.56)$$

The energy Equation (5.1.38) is made dimensionless by multiplying by $L/\Delta T_B$ to give:

$$\frac{\partial y}{\partial x^*} = \left[(1+R) \frac{Q_2^*}{V_2^*} - (1+\frac{1}{R}) \frac{Q_1^*}{V_1^*} \right] - \left[(1+R) \frac{w_c^*}{V_2^*} + \left(\frac{SF}{RePr} \frac{w}{\ell} \frac{LD_e}{A_b} + w_t^* \right) \left(\frac{1+R}{V_2^*} + \frac{(1+1/R)}{V_1^*} \right) \right] y \qquad (5.1.57)$$

where:

$$Q_i^* = \frac{q_i'}{q_t'} \qquad (5.1.58)$$

$$w_t^* = \frac{w_t L}{\rho V_b A_b} \qquad (5.1.59)$$

Define the average dimensionless channel power input as:

$$P_i = \int_0^1 Q_i^*(x^*) dx^* = \frac{1}{q_t'} \int_0^1 q_i'(x^*) dx^* = \frac{\bar{q}_i}{q_t'} \qquad (5.1.60)$$

This is the ratio of power input into channel i to the total power input. Since $\overline{q_1'} + \overline{q_2'} = q_t'$, it follows from Equation 5.1.60 that $P_1 + P_2 = 1$. The local power input can be expressed as a product of the average power input and an axial power profile function, g(x):

$$Q_i^*(x^*) = P_i\, g(x^*) \tag{5.1.61}$$

By integrating both sides of the above relation, and applying Equation 5.1.60, it follows that:

$$\int_0^1 g(x^*)\, dx^* = 1 \tag{5.1.62}$$

For a uniform axial power distribtuion:

$$g(x^*) = 1 \tag{5.1.63}$$

For a chopped cosine axial power profile with a peak to mean power ratio of α:

$$g(x^*) = \alpha \cos \gamma (x^* - 0.5) \tag{5.1.64}$$

where γ must be obtained from the auxiliary relation:

$$\alpha \sin(\tfrac{1}{2}\gamma) - \tfrac{1}{2}\gamma = 0$$

With Equation 5.1.61 the energy equation becomes:

$$\frac{\partial y}{\partial x^*} = \left[(1+R)\frac{P_2 g}{V_2^*} - (1+\tfrac{1}{R})\frac{P_1 g}{V_1^*}\right] - \left[(1+R)\frac{w_c^*}{V_2^*} + \left(\frac{SF}{RePr}\frac{w}{\ell}\frac{LD_e}{A_b} + w_t^*\right)\left(\frac{1+R}{V_2^*} + \frac{1+1/R}{V_1^*}\right)\right] y \tag{5.1.65}$$

In addition to the dimensionless transverse temperature difference y(x), the individual channel temperatures are also of interest. These can be obtained by writing an overall energy balance for the control volume of Figure 5.1.5 For steady flow, the energy balance is:

Outflow = Inflow

$$\rho V_1 A_1 C_p T_1 + \rho V_2 A_2 C_p T_2 = \rho (V_{1i} A_1 + V_{2i} A_2) C_p T_{IN} + \int_0^x [q_1'(x) + q_2'(x)]dx \qquad (5.1.66)$$

The bundle bulk temperature rise is defined from:

$$\rho V_b A_b C_p \Delta T_B = \bar{q}_t' L \qquad (5.1.67)$$

Continuity requires that:

$$\rho V_1 A_1 + \rho V_2 A_2 = \rho V_{1i} A_1 + \rho V_{2i} A_2 \qquad (5.1.68)$$

Substitute Equation 5.1.68 into Equation 5.1.66, and rearranging gives:

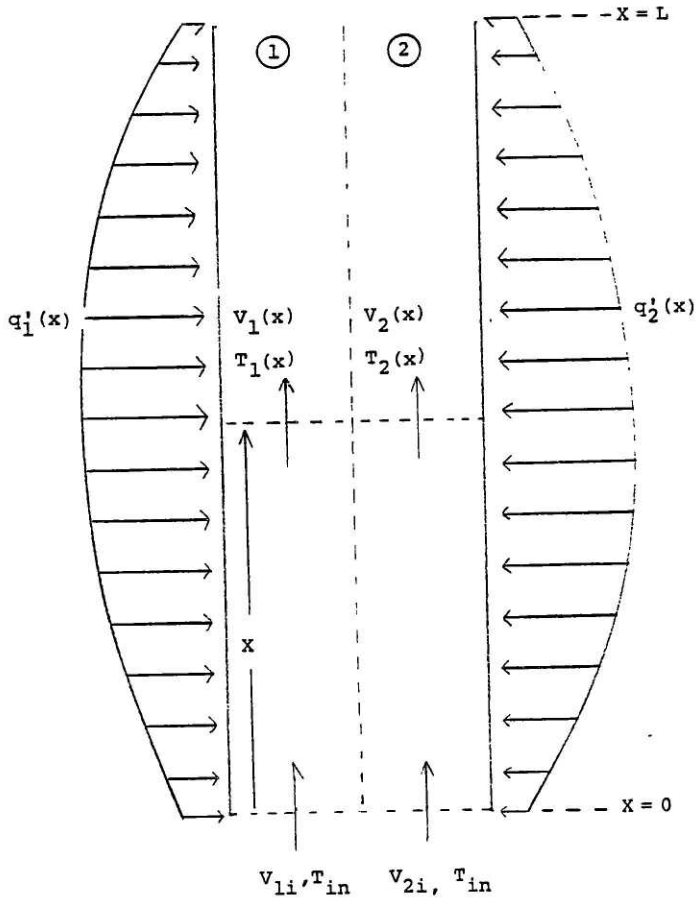
$$\rho V_1 A_1 (T_1 - T_{IN}) C_p + \rho V_2 A_2 (T_2 - T_{IN}) C_p = \int_0^x [q_1'(x) + q_2'(x)]dx \qquad (5.1.69)$$

Dividing this by Equation 5.1.67 gives:

$$V_1^* \frac{A_1}{A_b} \frac{T_1 - T_{IN}}{\Delta T_B} + V_2^* \frac{A_2}{A_b} \frac{T_2 - T_{IN}}{\Delta T_B} = \frac{1}{\bar{q}_t' L} \int_0^x [q_1'(x) + q_2'(x)]dx \qquad (5.1.70)$$

FIGURE 5.1.5

CONTROL VOLUME FOR BUNDLE ENERGY BALANCE



or

$$\theta_1 \frac{V_1^*}{1+1/R} + \theta_2 \frac{V_2^*}{1+R} = \int_0^{x^*} \left[Q_1^*(x^*) + Q_2^*(x^*) \right] dx^* \equiv P_f \qquad (5.1.71)$$

where:

$$\theta_i = \frac{T_i - T_{IN}}{\Delta T_B} \qquad (5.1.72)$$

and P_f is the fraction of the bundle power which is input up to x^*. It follows from Equation 5.1.61 that:

$$P_f = (P_1 + P_2) \int_0^{x^*} g(x^*) dx^* = \int_0^{x^*} g(x^*)\, dx^* \qquad (5.1.73)$$

From the definition of y

$$y = \theta_2 - \theta_1 \qquad (5.1.74)$$

Eliminating θ_1 from Equation 5.1.71 with Equation 5.1.74 gives:

$$\theta_2 \left(\frac{V_1^*}{1+1/R} + \frac{V_2^*}{1+R} \right) = P_f + y \frac{V_1^*}{1+1/R} \qquad (5.1.75)$$

By integrating the continuity Equation (5.1.39), the term in parenthesis can be expressed as:

$$\frac{V_1^*}{1+1/R} + \frac{V_2^*}{1+R} = \frac{V_{2i}^* + RV_{1i}^*}{1+R} \qquad (5.1.76)$$

Substituting Equation 5.1.76 into Equation 5.1.75 and solving for θ_2:

$$\theta_2 = \left[P_f + y \frac{V_1^*}{1+1/R} \right] \frac{1+R}{V_{2i}^* + RV_{1i}^*} \qquad (5.1.77)$$

Then θ_1 can be found from:

$$\theta_1 = \theta_2 - y \qquad (5.1.78)$$

In this section, we have formed a set of three integral partial differential equations in three unknowns. The three dimensionless equations are mass conservation (5.1.39), the momentum equation (5.1.56) and the energy equation (5.1.57). The three unknowns are the dimensionless velocities (V_1^* and V_2^*), and the dimensionless radial temperature difference (y). Equations 5.1.77 and 5.1.78 are auxiliary equations which allow the dimensionless channel temperatures to be calculated if they are needed. In the section which follows, an approximate analytical solution of the equations will be obtained.

5.2 METHOD OF SOLUTION OF EQUATIONS

To the author's knowledge, an analytical solution to the set of three equations can not be obtained. Since our objective is to develop an easy-to-use model, numerical methods will be avoided, and an approximate analytical approach will be used. The approach employed is trial solution with undetermined parameters (see Reference 70 for discussion).

Trial solution with undetermined parameters involves specifying a functional form for the solution with several undetermined parameters. The proposed solution is substituted into the equations, and the undetermined parameters are then obtained. For the problem at hand, the functional form of the channel axial velocity profiles will be specified in terms of two undetermined parameters, the net buoyancy induced crossflow, and the shape of the crossflow profile.

5.2.1 Velocity Profile Assumptions for The Two Channel Model

Buoyancy induced flow redistribution causes flow to move laterally to the high power side of the bundle. The two channel representation of this phenomena is shown in Figure 5.1.1. Define the crossflow parameter C as the fraction of the cold channel inlet flow which is redistributed to the hot channel:

$$C(t) = \frac{\int_0^L w_c dx}{\rho V_{1i} A_1} \tag{5.2.1}$$

Note that in general, C is a function of time. A mass balance gives the crossflow as:

$$\int_0^L w_c dx = \rho V_{1i} A_1 - \rho V_{1e} A_1 \tag{5.2.2}$$

Substituting Equation 5.2.2 into 5.2.1 gives:

$$C(t) = \frac{V_{1i} - V_{1e}}{V_{1i}} \tag{5.2.3}$$

or in dimensionless form:

$$C(t) = \frac{V^*_{1i} - V^*_{1e}}{V^*_{1i}} \tag{5.2.4}$$

where the velocities are made dimensionless with the bundle average velocity. The cold channel exit velocity is given by:

$$V^*_{1e} = V^*_{1i}(1-C) \tag{5.2.5}$$

A bundle mass balance gives:

$$V_{1i}A_1 + V_{2i}A_2 = V_{1e}A_1 + V_{2e}A_2 = V_b(A_1+A_2) \tag{5.2.6}$$

Dividing by A_2V_b gives the dimensionless equation:

$$V^*_{1i}R + V^*_{2i} = V^*_{1e}R + V^*_{2e} = 1+R \tag{5.2.7}$$

Solving for V^*_{2e} yields:

$$V^*_{2e} = V^*_{2i} + R(V^*_{1i}-V^*_{1e}) \tag{5.2.8}$$

Substituting Equation 5.2.5 into Equation 5.2.8 gives:

$$V^*_{2e} = V^*_{2i} + R\ C\ V^*_{1i} \tag{5.2.9}$$

or

$$V^*_{2e} = V^*_{2i}(1+R\ C\ S) \tag{5.2.10}$$

where:

$$S = V^*_{1i}/V^*_{2i} \tag{5.2.11}$$

when c=1, 100% of the cold channel inlet flow is redistributed to the hot channel, and $V^*_{1e}=0$. This corresponds to the onset of recirculation condition.

For a specified inlet flow split, the crossflow parameter c fixes the exit velocities. We next assume some axial velocity profile shape to give a functional relationship for the velocity variation with x*. It follows from Equation 5.2.5 and 5.2.10 that the most general form is:

$$V_1^*(x^*,T) = V_{1i}^*(1 - C(t)f(x^*)) \qquad (5.2.12)$$

$$V_2^*(x^*,t) = V_{2i}^*(1 + R\,S\,C(t)f(x^*)) \qquad (5.2.13)$$

where $f(x^*)$ must satisfy the boundary conditions $f(0) = 0$ and $f(1) = 1$. From continuity (5.1.39) the crossflow is given by:

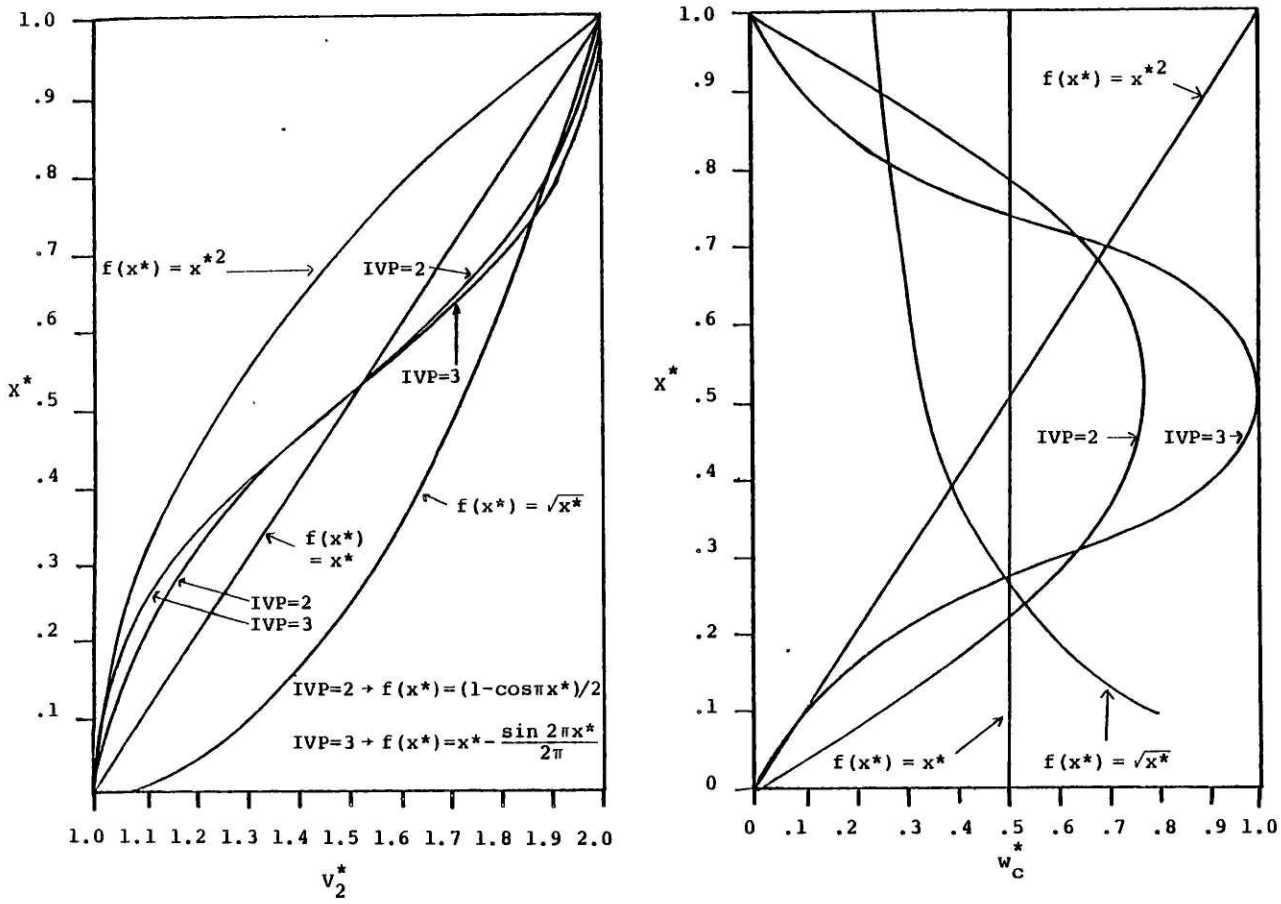
$$w_c^* = \frac{1}{1+R}\frac{\partial V_2^*}{\partial x^*} = \frac{RSC(t)f'(x^*)}{1+R}V_{2i}^* \qquad (5.2.14)$$

Equations 5.2.12 and 5.2.13 separate the space and time dependence of $V_i^*(x^*,t)$ into a space dependent function $f(x^*)$ which specifies the axial variation of the velocities and crossflow, and a time dependent parameter $C(t)$ which specifies the magnitude of the crossflow. As will be shown in the following section, this will allow the partial differential equations to be written as ordinary differential equations.

In Chapter 6 the appropriate $f(x^*)$ will be determined from subchannel codes such as COBRA and ENERGY IV . For now, we will simply assume some axial dependence functions for comparative purposes. Table 5.2.1 gives several assumed functions, each designated by an integer value of IVP. For IVP=1, $f(x^*) = x^{*n}$. With n=1, this gives a linear axial velocity variation, and a uniform crossflow as shown in Figure 5.2.1. For n=2, the velocity is parabolic, and the crossflow increases linearly with x^*. If $n = 1/2$, the crossflow is infinite at $x^*=0$, and decreases with x^*. Though physically impossible, this presents no mathematical difficulties since the discontinuity can be integrated. For IVP=2, the crossflow profile is half a sine wave,

FIGURE 5.2.1

V_2^* AND w_c^* VERSUS X^* FOR VARIOUS CHOICES OF $f(x^*)$



with zero crossflow at $x^*=0$ and $x^*=1$. For IVP=3, the slope of the crossflow profile is also zero at the endpoints, and the crossflow at the midplane ($x^*=.5$) is more peaked.

5.2.2 Integration of the Momentum Equation

The momentum equation (5.1.56) may be written:

$$0 = \text{Term 1} + \text{Term 2} + \text{Term 3} + \text{Term 4} - \text{Term 5} \qquad (5.2.15)$$

where:

$$\text{Term 1} = \int_0^1 \left[V_2^* \frac{\partial V_2^*}{\partial x^*} - V_1^* \frac{\partial V_1^*}{\partial x^*} + (1+R) w_c^* (V_2^* - V_1^*) \right] dx^* \qquad (5.2.16)$$

$$\text{Term 2} = \frac{(1+R)^2}{R} w_t^* \int_0^1 (V_2^* - V_1^*) dx^* \qquad (5.2.17)$$

$$\text{Term 3} = \frac{1}{2} \left(\frac{L}{D_{e_2}} \int_0^1 V_2^{*2} f_2 dx^* - \frac{L}{D_{e_1}} \int_0^1 V_1^{*2} f_1 dx^* \right) \qquad (5.2.18)$$

$$\text{Term 4} = \frac{L D_e}{\nu} \frac{1}{Re^2} \int_0^1 \left[\frac{\partial}{\partial t} Re (V_2^* - V_1^*) \right] dx^* \qquad (5.2.19)$$

$$\text{Term 5} = 4 \frac{L}{D_e} \frac{L}{D_H} \frac{Gr_q}{Re^3 Pr} \int_0^1 y \, dx^* \qquad (5.2.20)$$

In this section, the integration of the first four terms will be discussed. The buoyancy term (Term 5) will be addressed in Section 5.2.3.

The first term combines the inertia and crossflow terms. Employing Equation 5.1.39 to eliminate w_c^*, and rearranging gives:

TABLE 5.2.1

AXIAL VELOCITY PROFILE SHAPE FUNCTIONS

Velocity Profile Indicator (IVP)	$f(x^*)$	$f'(x^*)$	$\overline{f(x^*)} = \int_0^1 f(x^*)dx^*$
1	x^{*n}	nx^{*n-1}	$\frac{1}{n+1}$
2	$\frac{1}{2}(1 - \cos \pi x^*)$	$\frac{\pi}{2} \sin x^*$	$\frac{1}{2}$
3	$x^* - \frac{\sin 2\pi x^*}{2\pi}$	$1 - \cos 2\pi x^*$	$\frac{1}{2}$
4	Equation 6.1.2	Numerical Differentiation	Numerical Integration

$$\text{Term 1} = \int_0^1 \left[2V_2^* \frac{\partial V_2^*}{\partial x^*} - V_1 \left(\frac{\partial V_1^*}{\partial x^*} + \frac{\partial V_2^*}{\partial x^*} \right) \right] dx^* \qquad (5.2.21)$$

Substituting Equation 5.2.12 and 5.2.13 for V_1^* and V_2^* gives:

$$\text{Term 1} = \int_0^1 [2V_{2i}^{*2}(1+R\ CSf)\ R\ CSf' - V_{1i}^*(1-Cf)(-V_{1i}^* Cf' + V_{2i}^* RCSf')]\ dx^* \qquad (5.2.22)$$

$$= \int_0^1 [2V_{2i}^{*2} R\ CSf' + 2V_{2i}^{*2}(RSC)^2 ff' - V_{1i}^{*2} C(R-1)f' + V_{1i}^{*2} C^2 (R-1)f'f]dx^* \qquad (5.2.23)$$

To evaluate the above equation we require the integrals:

$$\int_0^1 f'(x^*)\, dx^* = f(1) - f(0) = 1 \qquad (5.2.24)$$

$$\int_0^1 f(x^*)f'(x^*)\, dx^* = \frac{1}{2}\left[f^2(1) - f^2(0) \right] = \frac{1}{2} \qquad (5.2.25)$$

Substituting Equations 5.2.24 and 5.2.25 into 5.2.23 gives:

$$\text{Term 1} = [2RCS + (RCS)^2]V_{2i}^{*2} - [C(R-1) - \frac{1}{2} C^2 (R-1)]V_{1i}^{*2} \qquad (5.2.26)$$

Note that this term is independent of what is chosen for $f(x^*)$ provided $f(0)=0$ and $f(1)=1$.

Integration of the second term is straightforward:

$$\text{Term 2} = \frac{(1+R)^2}{R} w_t^* \int_0^1 [V_{2i}^* - V_{1i}^* + C(1+R)V_{1i}^* f(x^*)]dx^* \quad (5.2.27)$$

$$\text{Term 2} = \frac{(1+R)^2}{R} w_t^* \left[V_{2i}^* - V_{1i}^* + C(1+R)V_{1i}^* \overline{f(x^*)}\right] \quad (5.2.28)$$

where

$$\overline{f(x^*)} = \int_0^1 f(x^*)\, dx^* \quad (5.2.29)$$

Integration of the third term requires the friction factor to be specified. The integrations can be performed for simple friction factor correlations, and simple $f(x^*)$. For more complicated correlations, an approximate technique is employed. For either the approximate or exact evaluation Term 3 can be written:

$$\text{Term 3} = \frac{1}{2}\left(\frac{L}{D_{e_2}} f_{b_2} F_2 - \frac{L}{D_{e_1}} f_{b_1} F_1\right) \quad (5.2.30)$$

where $f_{b_i} \cdot F_i = \int_0^1 V_i^{*2} f_i \, dx^* \qquad i = 1,2 \quad (5.2.31)$

For the exact evaluation, the above integration is performed analytically. For the approximate evaluation, a mean value for the friction factor is used (f_i is evaluated at the mean Reynolds number in the channel) and it is moved out in front of the integral.

$$\int_0^1 V_i^{*2} f_i \, dx^* \approx \overline{f_i} \int_0^1 V_i^{*2} dx^* \quad (5.2.32)$$

Comparison with Equation 5.2.31 gives,

$$f_{bi} = \overline{f_i}(\overline{Re_i}) \tag{5.2.33}$$

The mean channel Reynolds number is given by:

$$\overline{Re}_1 = (1 - C\overline{f(x^*)})V^*_{1i}Re_b(D_{e1}/D_{eb}) \tag{5.2.34}$$

$$\overline{Re}_2 = (1 + RCS\overline{f(x^*)})V^*_{2i}Re_b(D_{e2}/D_{eb}) \tag{5.2.35}$$

From Equation 5.2.32 it follows that:

$$F_i = \int_0^1 V_i^{*2}dx^* \tag{5.2.36}$$

Integration of the velocity profiles gives:

$$F_1 = \left[1 - 2C\int_0^1 f(x^*)dx^* + C^2\int_0^1 f^2(x^*)dx^*\right] V^{*2}_{1i} \tag{5.2.37}$$

$$F_2 = \left[1 + 2RCS\int_0^1 f(x^*)dx^* + (RCS)^2\int_0^1 f^2(x^*)\right]V^{*2}_{2i} \tag{5.2.38}$$

Table 5.2.2 gives the values of f_{bi} and F_i for various friction factor correlations. With Equations 5.2.12 and 5.2.13 substituted in for the velocities, the fourth term is:

$$\text{Term 4} = \frac{LD_e}{\nu}\frac{1}{Re^2}\int_0^1 \frac{\partial}{\partial t}\left\{Re\left[V^*_{2i}-V^*_{1i} + C(1+R)V^*_{1i}f(x^*)\right]\right\}dx^* \tag{5.2.39}$$

Taking the derivative with respect to time (keeping in mind that both Re and C may depend on time) and intergrating gives:

$$\text{Term 4} = \frac{LD_e}{\nu}\frac{1}{Re^2}\left[(1+R)V^*_{1i}\overline{f(x^*)}\left(Re\frac{dC}{dt} + C\frac{dRe}{dt}\right) + (V^*_{2i}-V^*_{1i})\frac{dRe}{dt}\right] \tag{5.2.40}$$

TABLE 5.2.2

FRICTION FACTOR CORRELATIONS USED IN THE TWO CHANNEL MODEL

IFRIC		FRICTION FACTOR CORRELATION	f(x*)	F_1	F_2	f_{bi} i = 1, 2
EXACT	1	$\frac{C_{fi}}{Re}$	any	$(1 - C\,\overline{f(x^*)}V_{1i})\cdot D_e/D_{e1}$	$(1 - RCS\,\overline{f(x^*)})V_{2i}D_e/D_{e2}$	$\frac{C_{fi}}{Re}$
	2	$\frac{C_{fi}}{Re^{mi}}$	f(x*) = x* only	$\frac{1-(1-C)^{3-m1}}{(3-m1)C}\cdot\frac{V_{1i}^{3-m1}D_e}{D_{e1}}$	$\frac{(1+RCS)^{3-m2}}{(3-m2)\,RCS}\,\frac{V_{2i}^{3-m2}D_e}{D_{e2}}$	$\frac{C_{fi}}{Re^{mi}}$
	3	$\frac{C_{f1}}{Re^{mi}}\,Gr_q^n$	f(x*) = x* only	$\frac{1-(1-C)^{3-m1}}{(3-m1)C}\cdot\frac{V_{1i}^{3-m1}D_e}{D_{e1}}$	$\frac{(1+RCS)^{3-m2}}{(3-m2)\,RCS}\,\frac{V_{2i}^{3-m2}D_e}{D_{e2}}$	$\frac{C_{fi}}{Re^{mi}}\,(Gr_qP_1)^{ni}$
APPROXIMATE	4-6	any friction factor correlation which depends on Re	any	$[1-2C\overline{f(x^*)} + C^2\overline{f^2(x^*)}]$ $\cdot V_{1i}^{*2}\cdot D_e/D_{e2}$	$[1+RC\overline{f(x^*)} + (RCS)^2$ $\cdot\overline{f^2(x^*)}]\cdot V_{2i}^{*2}\cdot D_e/D_{e1}$	evaluate f correlation at channel average Re given by: $Re_1 = Re_b(1-C\,\overline{f(x^*)})\cdot V_{1i}^*\cdot D_{e1}/D_{eb}$ $Re_2 = Re_b(1+RCS\,\overline{f(x^*)})\cdot V_{2i}^*\cdot D_{e2}/D_{eb}$
	4	Hawley/Chiu	any	as above	as above	as above
	5	Westinghouse blanket friction factor	any	as above	as above	as above
	6	Petukhov friction factor	any	as above	as above	as above

Integration of the buoyancy term is considerably more involved, and will be considered in the following section.

5.2.3 Evaluation of The Buoyancy Term

The energy equation can be written as:

$$\frac{dy}{dx^*} + \left[\frac{1}{V_2^*}\frac{dV_2^*}{dx^*} + E^*\left(\frac{1+R}{V_2^*} + \frac{1+1/R}{V_1^*}\right)\right]y = \frac{(1+R)gP_2}{V_2^*} - \frac{(1+1/R)gP_1}{V_1^*} \qquad (5.2.41)$$

$$\text{where } E^* = \frac{SF}{Re\ Pr}\ \frac{w}{\ell}\ \frac{LD_e}{A_b} + w_t^* \qquad (5.2.42)$$

since V_1^*, V_2^*, $\frac{dV_2^*}{dx^*}$, and g depend on x^* only, this equation is of the form:

$$\frac{dy}{dx^*} + f_1(x^*)y = f_2(x^*) \qquad (5.2.43)$$

Equation 5.2.43 is a first order linear ordinary differential equation with variable coefficients. $f_1(x^*)$ and $f_2(x^*)$ can be expressed as:

$$f_1(x^*) = \frac{1}{V_2^*}\frac{dV_2^*}{dx^*} + E^*\left(\frac{1+R}{V_2^*} + \frac{1+1/R}{V_1^*}\right) \qquad (5.2.44)$$

$$f_2(x^*) = a_2(x^*)P_2 - a_1(x^*)P_1 \qquad (5.2.45)$$

where:

$$a_2(x^*) = \frac{(1+R)g}{V_2^*} \qquad (5.2.46)$$

$$a_1(x^*) = \frac{(1+1/R)g}{V_1^*} \qquad (5.2.47)$$

It can be shown that the solution to Equation 5.2.43 is

$$y(x^*) = \frac{1}{\mu(x^*)}\left[\int^{x^*} \mu(x^*) f_2(x^*) + G \right] \tag{5.2.48}$$

where

$$\mu(x^*) = \exp\left[\int^{x^*} f_1(x^*)\, dx^* \right] \tag{5.2.49}$$

The constant of integration G is zero since the initial condition on y is $y(0) = 0$. Substitution of Equation 5.2.45 into 5.2.48 allows the solution for y to be expressed as the sum of two solution:

$$y(x^*) = \frac{P_2}{\mu(x^*)} \int_0^{x^*} \mu(x^*) a_2(x^*)\, dx^* - \frac{P_1}{\mu(x^*)} \int_0^{x^*} \mu(x^*) a_1(x^*)\, dx^*$$

or (5.2.50)

$$y(x^*) = y_2(x^*)P_2 - y_1(x^*)P_1 \tag{5.2.51}$$

where:

$$y_2(x^*) = \frac{1}{\mu(x^*)} \int_0^{x^*} \mu(x^*) a_2(x^*)\, dx^* \tag{5.2.52}$$

$$y_1(x^*) = \frac{1}{\mu(x^*)} \int_0^{x^*} \mu(x^*) a_1(x^*)\, dx^* \tag{5.2.53}$$

For evaluation of the buoyancy term we require the integral of $y(x^*)$:

$$\int_0^1 y(x^*)\, dx = P_2 \int_0^1 y_2(x^*)\, dx - P_1 \int_0^1 y_1(x^*)\, dx^* \tag{5.2.54}$$

$$= K_2P_2 - K_1P_1 \tag{5.2.55}$$

Where:

$$K_2 = \int_0^1 y_2\, dx^* = \int_0^1 \left[\frac{1}{\mu(x^*)} \int_0^{x^*} \mu(x^*) a_2(x^*)\, dx^* \right] dx^* \tag{5.2.56}$$

$$K_1 = \int_0^1 y_1 \, dx^* = \int_0^1 \left[\frac{1}{\mu(x^*)} \int_0^{x^*} \mu(x^*) a_1(x^*) \, dx^* \right] dx^* \quad (5.2.57)$$

In theory, Equations 5.2.56 and 5.2.57 provide us with the buoyancy term of the momentum equation. In practice, the integrations can be performed only for simple cases. Otherwise, K_1 and K_2 must be obtained numerically. The analytical and numerical approaches are discussed in detail in Appendix C1 and C2, respectively. Only the results will be presented here.

Several analytical solutions are obtained in Appendix C1. The first approach requires E* to be zero. Physically, this means that energy transport due to turbulence, wire induced mixing, and thermal conduction are neglected. For this case, it is shown that $\mu(x^*) = V_2^*$. If it is further assumed that $g(x^*) = 1$ (uniform axial power profile) several of the integrations can be expressed in closed form. The known integrations are given in Table 5.2.3. Note that even for the simplest possible profile shape $\left[f(x^*) = x^*\right]$, a closed form solution for K_1 can not be obtained. For C = 0 (no crossflow), a simple closed form solution for both K_1 and K_2 has been found for both the uniform axial power profile and chopped cosine power profile.

Since general closed form analytical solutions for both K_1 and K_2 could not be obtained, a numerical approach was employed, as discussed in Appendix C2. A subroutine was written to calculate $y_1(x^*)$, $y_2(x^*)$, K_1 and K_2 for any

TABLE 5.2.3

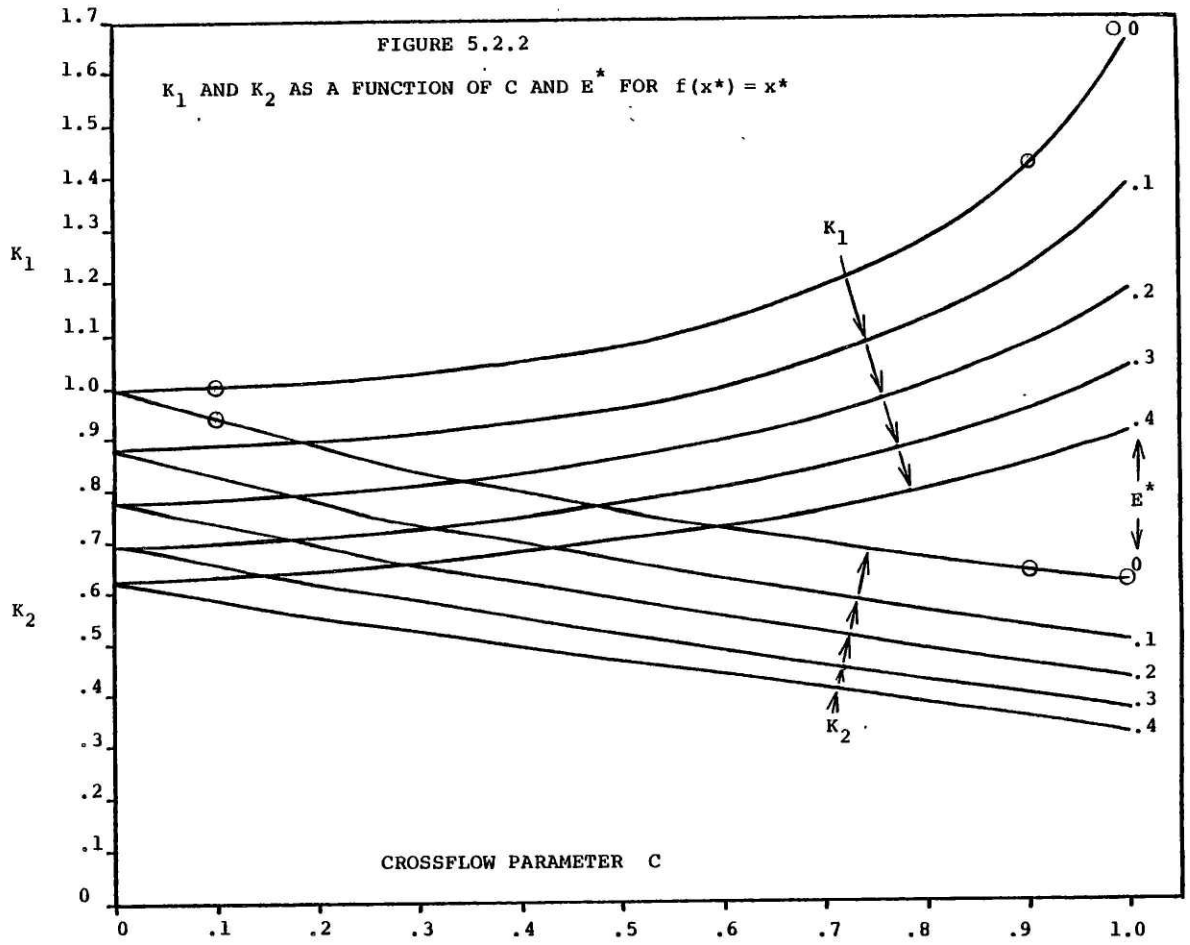
ENERGY EQUATION INTEGRALS FOR $g(x^*)=1$, $E^*=0$ and $V^*_{1i}=V^*_{2i}=S=1$

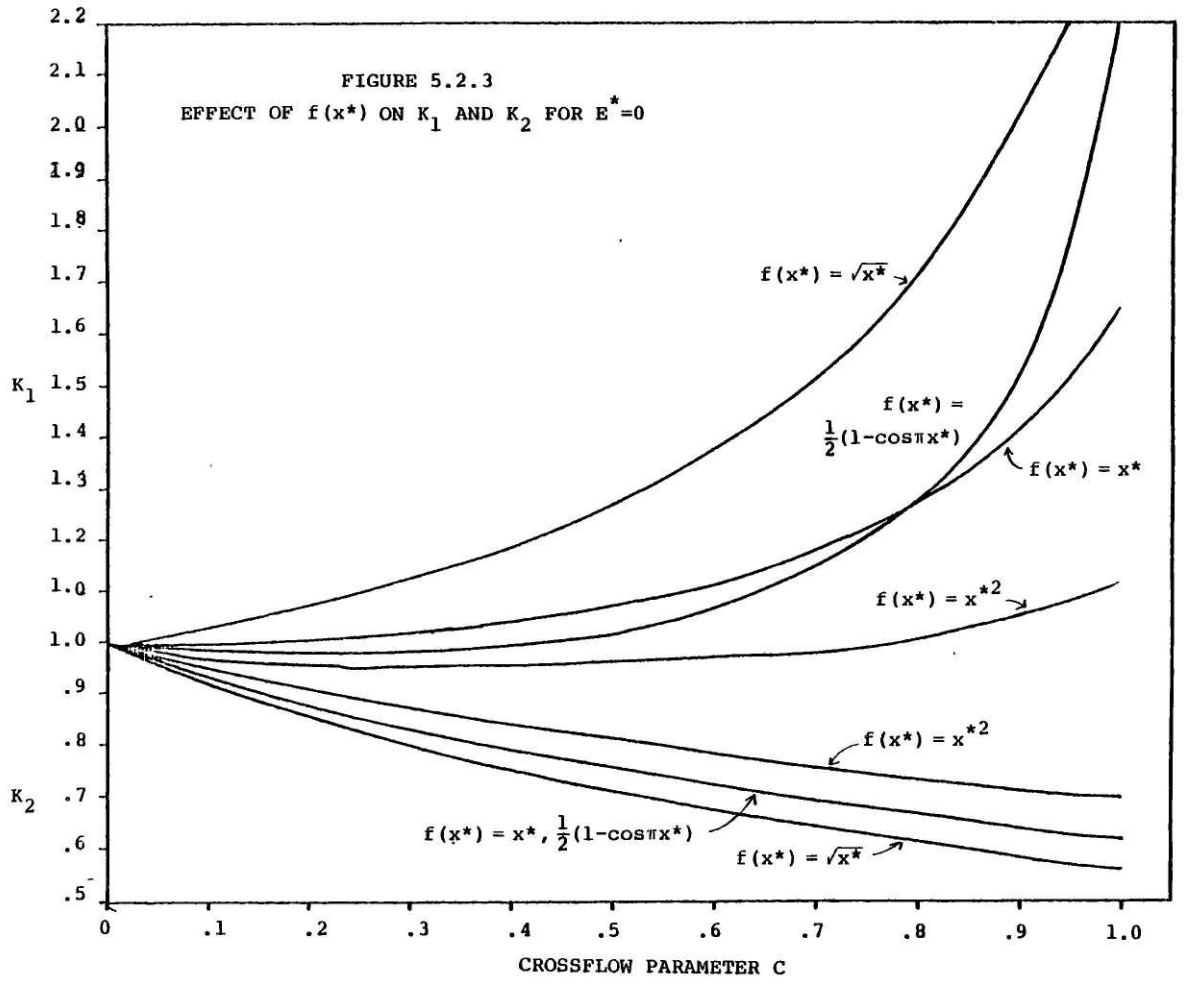
Axial Velocity Profile Function	$\frac{y_2(x^*)}{1+R}$	$\frac{K_2}{1+R}$	$\frac{y_1}{1+1/R}$	$\frac{K_1}{1+1/R}$
$f(x^*) = x^*$	$\frac{x^*}{1+RCx^*}$	$\frac{1}{RC}\left[1 - \frac{\ell n(1+RC)}{RC}\right]$	$\frac{-Rx^* - (1+R)\,\ell n(1-Cx^*)/C}{1+RCx^*}$	N.F.
$f(x^*) = x^{*2}$	$\frac{x^*}{1+RCx^{*2}}$	N.F.	N.F.	N.F.
$f(x^*) = x^{*n}$	$\frac{x^*}{1+RCx^{*n}}$	N.F.	N.F.	N.F.

N.F. - analytical solution not found

$f(x^*)$ and $g(x^*)$. Results for K_1 and K_2 are given in Figure 5.2.2 for $f(x^*) = x^*$ and $g(x^*) = 1$ with uniform inlet velocity. For c=0, $K_1 = K_2$; but as C increases, K_1 increases and K_2 decreases. Both K_1 and K_2 decrease with E* hence the buoyancy term [Term 5 = $Ri(K_2P_2 - K_1P_1)$] decreases with both C and E* for a given power skew and Richardson number. This is physically reasonable since crossflow, mixing, and radial conduction all tend to decrease the radial temperature difference, and hence decrease the buoyancy term. The circles in Figure 5.2.2 are checkpoints from the analytical solutions of Appendix C1. Since an analytical solution has not been found for K_1, the checkpoints were determined by solving for y_1 analytically (see Table 5.2.3), and numerically integrating the result with a 10 node Simpson integration. The agreement is excellent with the exception of the $c = .99\ K_1$ calculation, which is off by 3%.

In Figure 5.2.3 the effect of changing $f(x^*)$ for E*=0 is examined. It can be seen that changing $f(x^*)$ from x^* to x^{*2} will increase the buoyancy term while changing $f(x^*)$ from x^* to $\sqrt{x^*}$ will decrease the buoyancy term (see Figure 5.2.1 for how profiles change with $f(x^*)$). This is physically reasonable since for the latter case, the crossflow is large at the inlet. This causes a reduction in the radial temperature difference, hence a reduction in the buoyancy term. Conversely, for the former case the crossflow near the inlet is small, so a large radial temperature difference

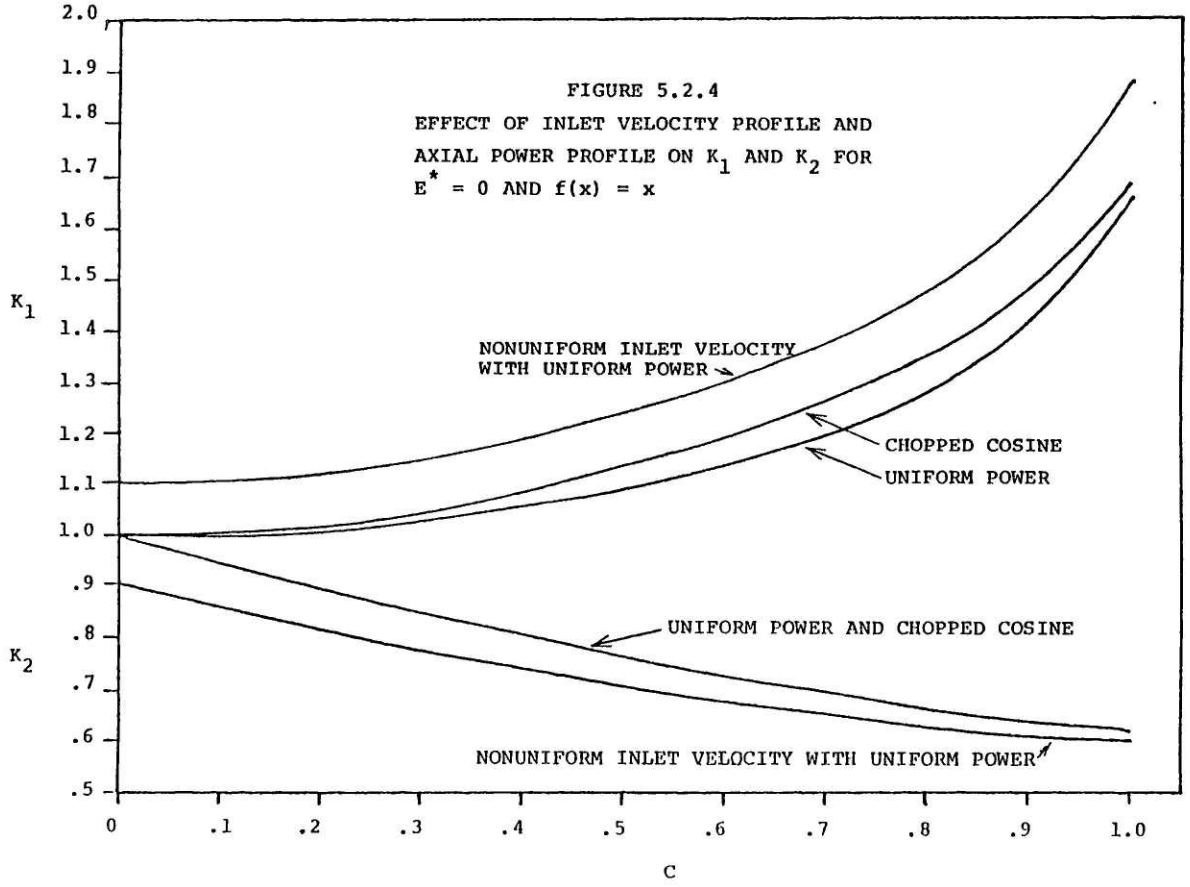

FIGURE 5.2.2
K_1 AND K_2 AS A FUNCTION OF C AND E^* FOR $f(x^*) = x^*$
K_1
K_2
K_1
K_2
E^*
0
.1
.2
.3
.4
CROSSFLOW PARAMETER C
1.7
1.6
1.5
1.4
1.3
1.2
1.1
1.0
.9
.8
.7
.6
.5
.4
.3
.2
.1
0
0
.1
.2
.3
.4
.5
.6
.7
.8
.9
1.0


FIGURE 5.2.3
EFFECT OF f(x*) ON K1 AND K2 FOR E*=0
f(x*) = √x*
f(x*) = ½(1-cosπx*)
f(x*) = x*
f(x*) = x*2
f(x*) = x*2
f(x*) = x*, ½(1-cosπx*)
f(x*) = √x*
K1
K2
2.2
2.1
2.0
1.9
1.8
1.7
1.6
1.5
1.4
1.3
1.2
1.0
1.0
.9
.8
.7
.6
.5
0
.1
.2
.3
.4
.5
.6
.7
.8
.9
1.0
CROSSFLOW PARAMETER C

develops, increasing the buoyancy term.

If $f(x^*)$ is changed from x^* to $\frac{1}{2}(1 - \cos \pi x^*)$ (uniform crossflow to half sine wave crossflow) K_2 is essentially unchanged while K_1 is nearly the same for $C \leq .9$. For $C > .9$ a significant difference exists.

In Figure 5.2.4, the effect of inlet flow split, and axial power profile is examined for $E^* = 0$ and $f(x^*) = x^*$. It is observed that the buoyancy term will decrease if the inlet flow split is changed from uniform ($V^*_{1i} = V^*_{2i} = 1$) to nonuniform ($V_{1i} = .9$, $V_{2i} = 1.1$). This is expected, since for the latter case more flow enters into the hot channel (channel #2), which decreases the radial temperature difference, and the buoyancy term. The effect of changing the axial power profile from uniform ($g(x^*) = 1.00$) to a 1.38 peak to mean chopped cosine [$g(x^*) = 1.38 \cos(2.69(x^*-0.5))$] is seen to have negligible effect on K_2, and increases K_1 slightly. This results in a slight decrease in the buoyancy term, which is expected since the power at the inlet is less for a chopped cosine, which leads to a smaller radial temperature difference.


FIGURE 5.2.4
EFFECT OF INLET VELOCITY PROFILE AND
AXIAL POWER PROFILE ON K_1 AND K_2 FOR
$E^* = 0$ AND $f(x) = x$
K_1
K_2
2.0
1.9
1.8
1.7
1.6
1.5
1.4
1.3
1.2
1.1
1.0
.9
.8
.7
.6
.5
0
.1
.2
.3
.4
.5
.6
.7
.8
.9
1.0
C
NONUNIFORM INLET VELOCITY
WITH UNIFORM POWER
CHOPPED COSINE
UNIFORM POWER
UNIFORM POWER AND CHOPPED COSINE
NONUNIFORM INLET VELOCITY WITH UNIFORM POWER

5.3 GOVERNING EQUATION OF THE TWO CHANNEL MODEL

In Sections 5.2.2 to 5.2.4 the terms of the momentum equation were evaluated. The momentum equation may now be written as:

$$0 = V_{2i}^{*2}\left[2RCS + (RCS)^2\right] - V_{1i}^{*2}\left[C(R-1) - \frac{1}{2}C^2(R-1)\right]$$

$$+ \frac{(1+R)^2}{R} w_t^*\left[(V_{2i}^* - V_{1i}^*) + C(1+R)V_{1i}^*\overline{f(x^*)}\right]$$

$$+ \frac{1}{2}\left[\frac{L}{D_{e2}} f_{b2}F_2 - \frac{L}{D_{e1}} f_{b1}F_1\right]$$

$$+ \frac{LD_e}{\nu}\frac{1}{Re^2}\left[(1+R)V_{1i}^*\overline{f(x^*)}\left(Re\frac{dC}{dt} + C\frac{dRe}{dt}\right) + (V_{2i}^* - V_{1i}^*)\frac{dRe}{dt}\right]$$

$$- 4\frac{L}{D_e}\frac{L}{D_H}\frac{Gr_q}{Re^3 Pr}(K_2P_2 - K_1P_1) \qquad (5.3.1)$$

where:

$$K_i = \int_o^1 \left[\frac{1}{\mu(x^*)}\int_o^1 \mu(x^*)a_i(x^*)\,dx^*\right] dx^* \qquad i = 1, 2$$

$$f_{bi}F_i = \int_o^1 V_i^{*2} f_i\,dx^* \qquad i = 1, 2$$

$$\overline{f(x^*)} = \int_o^1 f(x^*)\,dx^*$$

For the case of uniform inlet velocity, $V_{1i} = V_{2i} = S = 1$, Equation 5.3.1 becomes:

$$0 = 2RC + (RC)^2 - C(R-1) + \frac{1}{2}C^2(R-1) + \frac{(1+R)^3}{R} w_t^* C \overline{f(x^*)}$$

$$+ \frac{1}{2}\left[\frac{L}{D_{e2}} f_{b2} F_2 - \frac{L}{D_{e1}} f_{b1} F_1\right] + \frac{LD_e}{\nu} \frac{1}{Re^2}\left[Re\frac{dC}{dt} + C\frac{dRe}{dt}\right](1+R)\overline{f(x^*)}$$

$$- 4 \frac{L}{D_e} \frac{L}{D_H} \frac{Gr_q}{Re^3 Pr} (K_2P_2 - K_1P_1) \qquad (5.3.2)$$

Equation 5.3.1 is the key equation in the model. To solve Equation 5.3.1 we must first supply as inputs the friction factor f, the dimensionless turbulent interchange w_t^*, the conduction shape factor SF, the inlet velocity split, V_{1i} and V_{2i}, the axial power profile ($g(x^*)$), and the axial velocity profile shape function $f(x^*)$. The geometry of each channel must also be specified. The model then can be used in two ways. First as a means of predicting the flow and temperature field with a lumped subchannel approximation, C is the parameter which must be solved for. Secondly, as a criteria, C is fixed at some critical value and the corresponding Reynolds number is solved for. Once C is known, the dimensionless velocities and crossflow can be found from Equations 5.2.12, 5.2.13 and 5.2.14. The channel temperatures can also be found from Equations 5.2.50, 5.1.77 and 5.1.78. In general an iterative technique must be employed to solve 5.3.1 since it is implicit in both C and Re,

though in many instances the equation simplifies considerably. For example, for steady laminar flow with negligible radial heat conduction, Equation 5.3.1 is cubic in Re.

To perform the iterative solution of Equation 5.3.1 programs TWOCHAN and RECIRC were written. Program TWOCHAN solves for C, and program RECIRC solves for the Reynolds number. Each program solves 5.3.1 using the bisection root finding technique, and each program calls subroutine RESCALC to evaluate the terms of Equation 5.2.15. K_1 and K_2 are determined from subroutine EULER. The two programs and subroutine RESCALC are discussed in more detail in Appendix D.

CHAPTER 6

VALIDATION OF THE TWO CHANNEL MODEL

The validity of the two channel model will be demonstrated by comparison with the results of the COBRA and ENERGY codes in both the forced and mixed convection regimes. For the calculations in the chapter, we are not using the model as a criterion, but rather as a predictive tool which can calculate the flow and temperature field in a rod bundle with a lumped subchannel approximation. Direct comparison between the model and data is not practical since the model calculates lumped channel velocities and temperatures, whereas the available data is taken on a local scale. Therefore a two step validation approach will be employed. First, we compare the data with the multichannel codes to ensure their validity, then lump the multichannel code results into a two channel presentation for comparison with the model. The validity of the COBRA code is well documented, so only the results of References 58 and 59 will be outlined. The energy code will be given more careful consideration, and comparisons with the Westinghouse blanket bundle thermocouple data given.

6.1 COMPARISON OF TWO CHANNEL MODEL RESULTS TO BNWL 2 x 6 TEST RESULTS AND COBRA PREDICTIONS

Mixed convection tests were conducted in a 2 x 6 rod bundle with water flow at BNWL. The purpose of the tests was primarily for validation of the COBRA code in the mixed convection regime. Local velocity and temperature measurements were made at five axial levels. Figure 6.1.1 shows a side view and cross section of the test section. Steady state data was reported in Reference 58, and transient data in Reference 59.

6.1.1 Steady State Results

Velocity and temperature measurements were made in the BNWL 2 x 6 rod bundle operating under steady state conditions by Bates, Khan and Quigley (58). The operating conditions for the three cases considered are given in Table 6.1.1.

The LDA local velocity measurements along with the COBRA predicted subchannel average velocities for the three cases are shown in Figures 6.1.2, 6.1.3, and 6.1.4 for cases 1, 2, and 3, respectively. The COBRA predicted velocities and temperatures are given in Appendix E1. For each case comparisons are made at five axial locations for both center and edge region traverses. The results show good agreement between COBRA and the experiment. Note that for Case 2 COBRA predicts a recirculation zone near the outlet of the bundle ($Z^* = 1.00$). But no local velocity

FIGURE 6.1.1
TEST SECTION OF BNWL
2 x 6 TEST

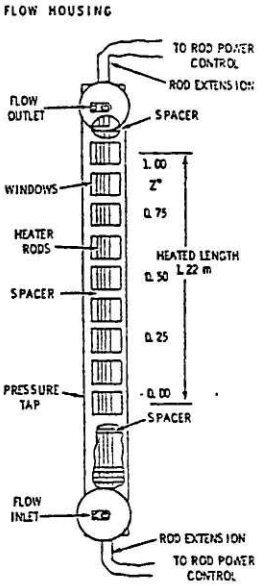
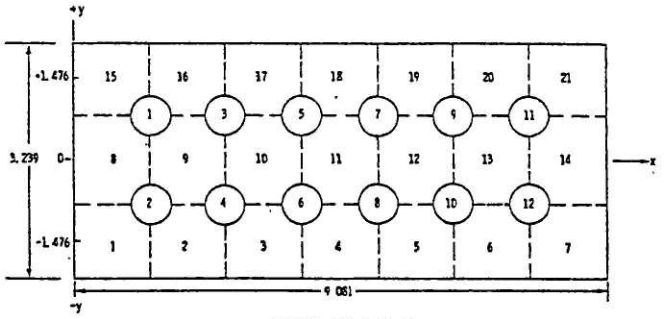


Fig. 3 Flow housing



DIMENSIONS IN cm

ROD DIAMETER, d = 12.065 mm
PITCH, p = 14.065 mm

ROD-WALL SPACING = 8.890 mm

SUBCHANNEL DIMENSIONS

TYPE	AREA (cm²)	WETTED PERIMETER (cm)	HEATED PERIMETER (cm)
CORNER	0.505	2.725	0.948
SIDE	0.727	3.355	1.895
CENTRAL	0.990	3.790	3.790

TABLE 6.1.1

BNWL 2x6 STEADY STATE RUNS

Case	Re	Gr^*	Gr_q	Skew	P_1	P_2
1	960	1.23×10^4	6.36×10^5	2;1	.333	.667
2	480	4.05×10^4	3.45×10^5	1:0	0.0	1.0
3	960	3.80×10^4	6.55×10^5	1:0	0.0	1.0

$$Gr_q = 4\, Gr_{\Delta T}\, RePr\, \frac{D_H}{L} = \frac{Gr_{\Delta T} Re}{55.66}$$

$$Gr^* = Gr_{\Delta T}(\hat{Q} - 1)$$

FIGURE 6.1.2

EXPERIMENTAL AND COBRA PREDICTED VELOCITIES FOR CASE 1

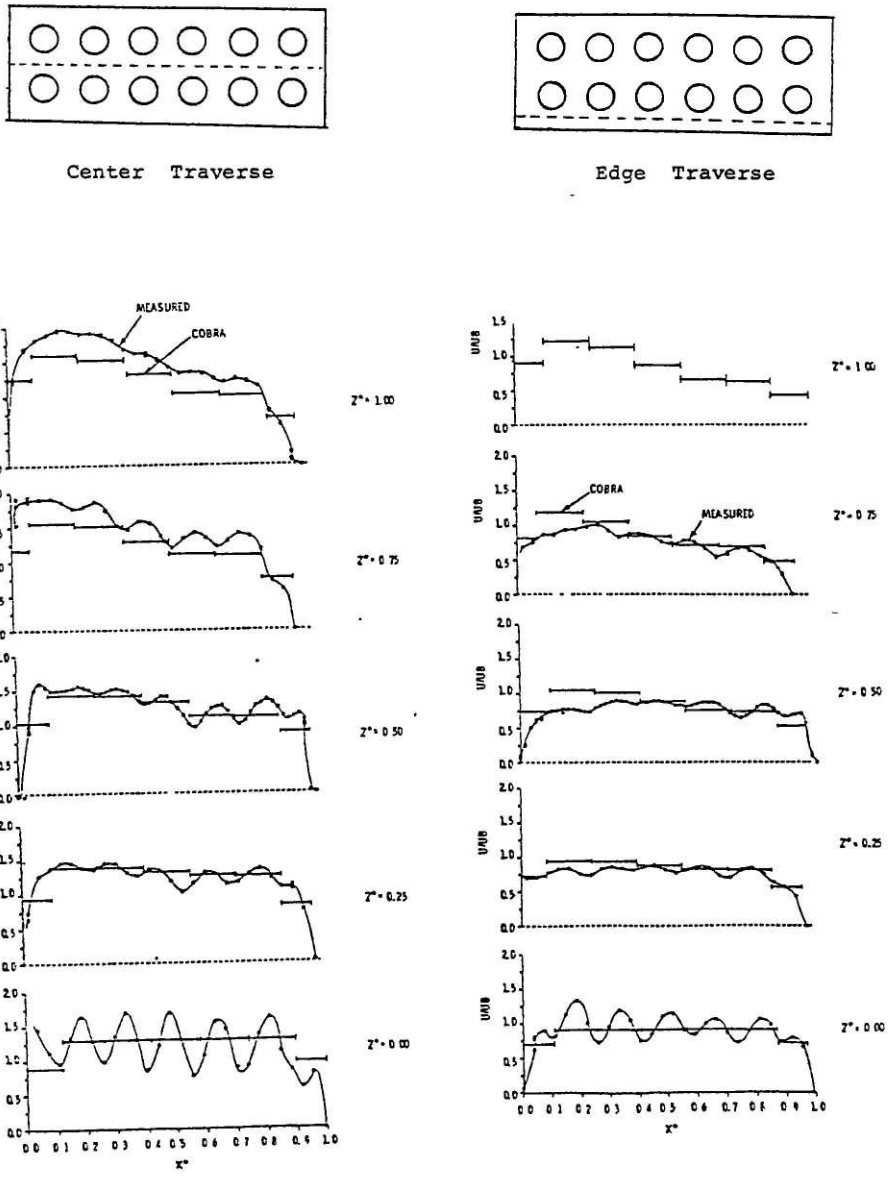
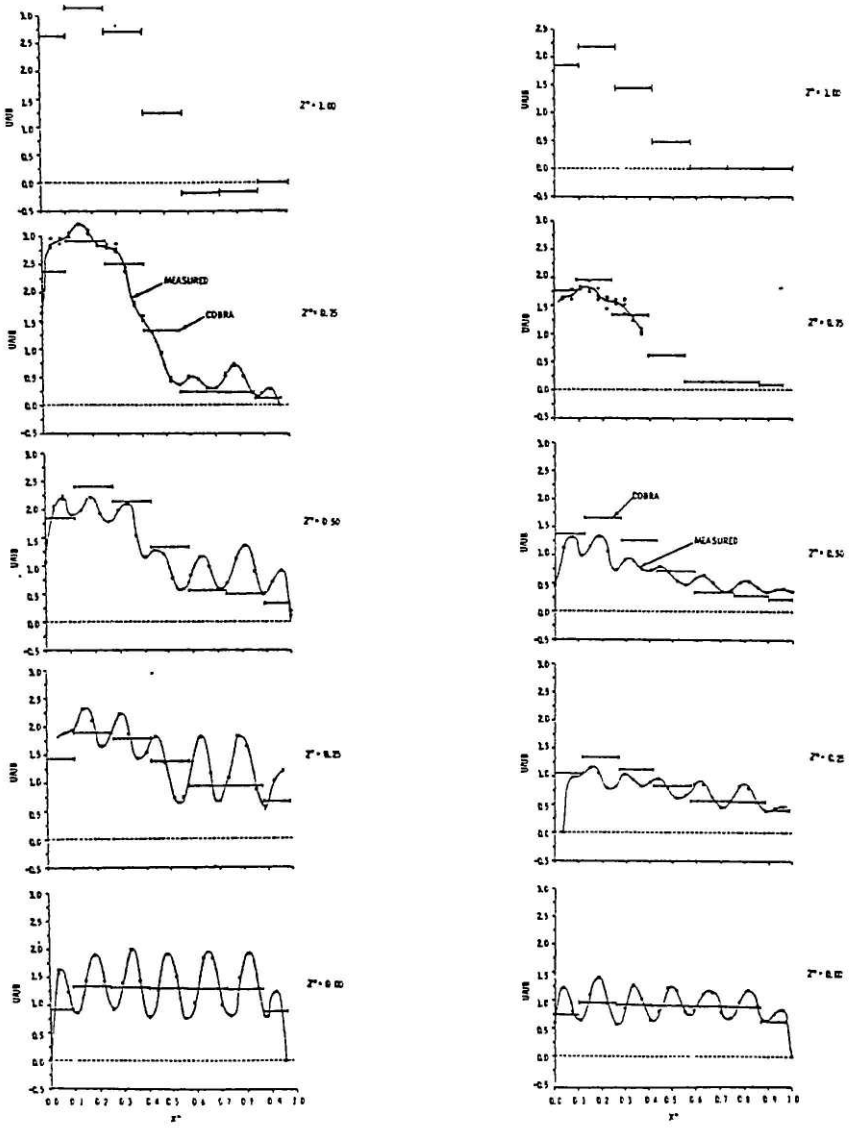


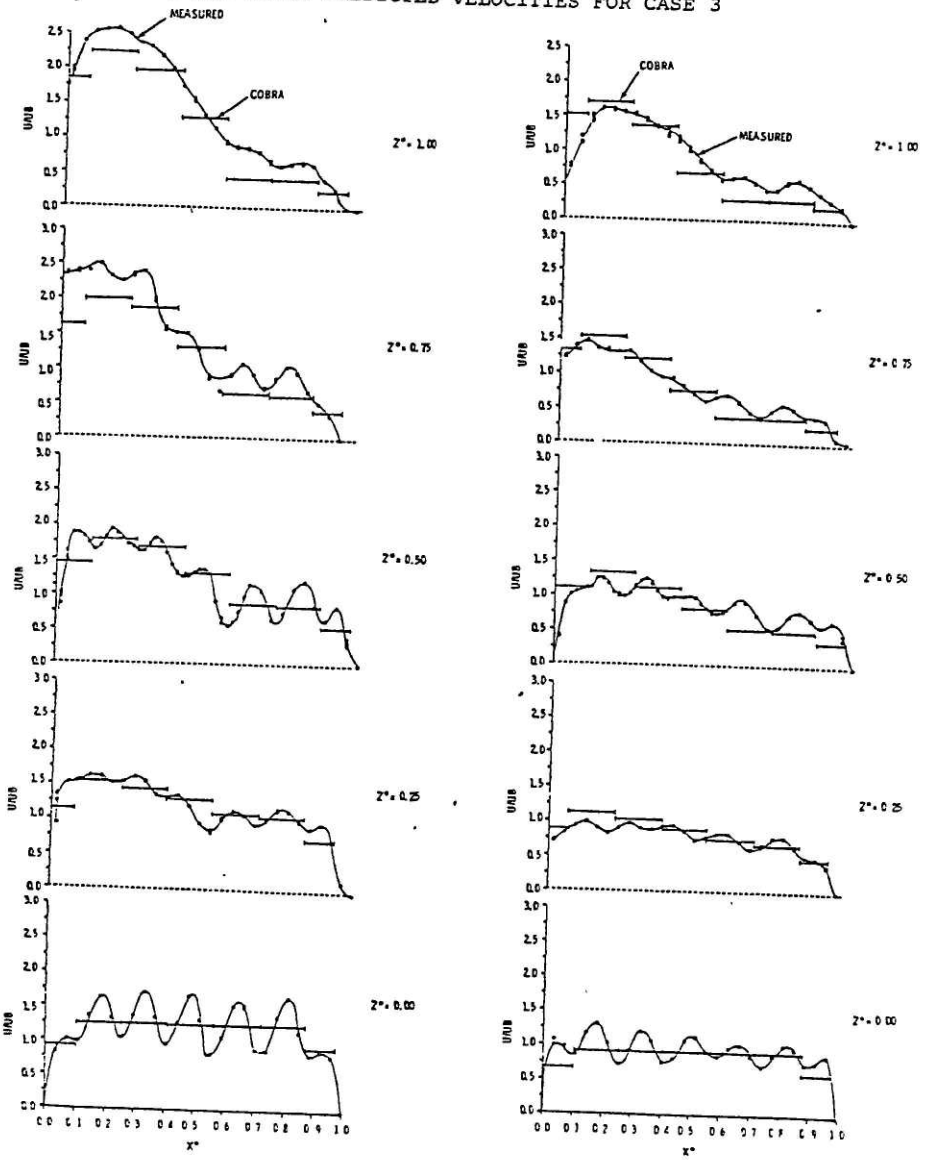
FIGURE 6.1.3
MEASURED AND COBRA PREDICTED VELOCITIES FOR CASE 2



Center Traverse

Edge Traverse

FIGURE 6.1.4
MEASURED AND COBRA PREDICTED VELOCITIES FOR CASE 3



Center Traverse

Edge traverse

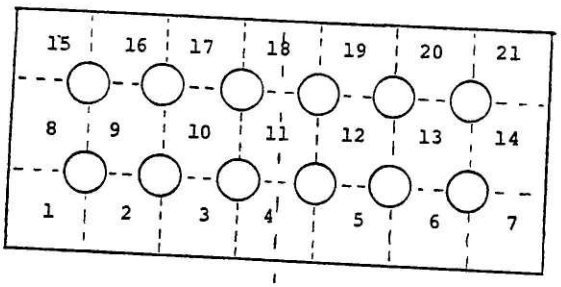
measurements were made to confirm this.

The COBRA predicted velocities and temperatures can be used to assess the validity of the two channel model. For the two channel calculation, the 2 x 6 rod bundle was modeled by two channels of equal flow area (R=1) as shown in Figure 6.1.5. The COBRA subchannel average velocities can be averaged over the area for each half of the bundle to allow direct comparison with the two channel model. This was done for the three cases at the axial levels $x^* =$ 0, .25, .50, .75 and 1.00. From continuity, the axially averaged crossflow between each of these axial levels can be obtained. Table 6.1.2 gives the results of these calculations. The averaging equations used are shown in Figure 6.1.5.

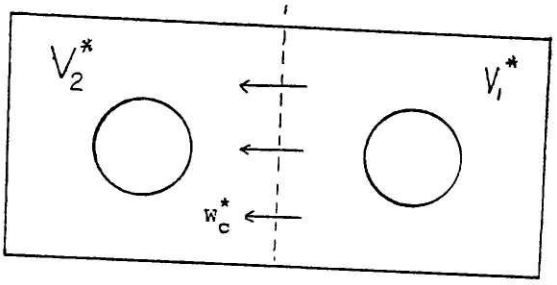
The dimensionless axial velocity and dimensionless crossflow are plotted against dimensionless axial distance in Figures 6.1.6 and 6.1.7, respectively for Cases 1, 2, and 3. The results indicate that for small crossflow (Case 1, C = .226) the axial velocity varies linearly with axial distance, and the crossflow is nearly uniform with axial distance. This suggests that $f(x^*) = x^*$ should be employed in the two channel model. However for increasing crossflow (Case 3 and 2), the axial velocity becomes nonlinear, and the crossflow profile becomes skewed toward the inlet.

FIGURE 6.1.5
COBRA AND TWO CHANNEL NODING SCHEME FOR BNWL
2 x 6 ROD BUNDLE

COBRA:



TWO CHANNEL:



CHANNEL AVERAGE VELOCITIES

$$V_2^* = \frac{2}{A_b}\left[(2V_2 + 2V_3 + V_4 + V_8)A_{edg} + 2V_1A_{cor} + (V_9 + V_{10} + \tfrac{1}{2}V_{11})A_{int}\right]$$

$$V_1^* = \frac{2}{A_b}\left[(V_4 + 2V_5 + 2V_6 + V_{14})A_{edg} + 2V_7A_{cor} + (\tfrac{1}{2}V_{11} + V_{12} + V_{13})A_{int}\right]$$

CROSSFLOW:

$$W_c^* = \frac{1}{2}\frac{\Delta V_2^*}{\Delta X^*}$$

TABLE 6.1.2

COBRA PREDICTED VELOCITIES AND CROSSFLOWS

	Case 1			Case 2			Case 3		
x^*	V_1^*	V_2^*	w_c^*	V_1^*	V_2^*	w_c^*	V_1^*	V_2^*	w_c^*
0	1.000	1.000		1.000	1.000		1.000	1.000	
			.114			.704			.338
.25	.943	1.057		.648	1.352		.831	1.169	
			.1080			.529			.336
.50	.889	1.111		.384	1.616		.663	1.337	
			.1076			.470			.290
.75	.835	1.165		.149	1.851		.518	1.482	
			.1236			.311			.250
1.00	.774	1.226		.007	2.007		.393	1.607	
	C = .226			C = 1.007			C = .607		

FIGURE 6.1.6

COBRA PREDICTED CROSSFLOW

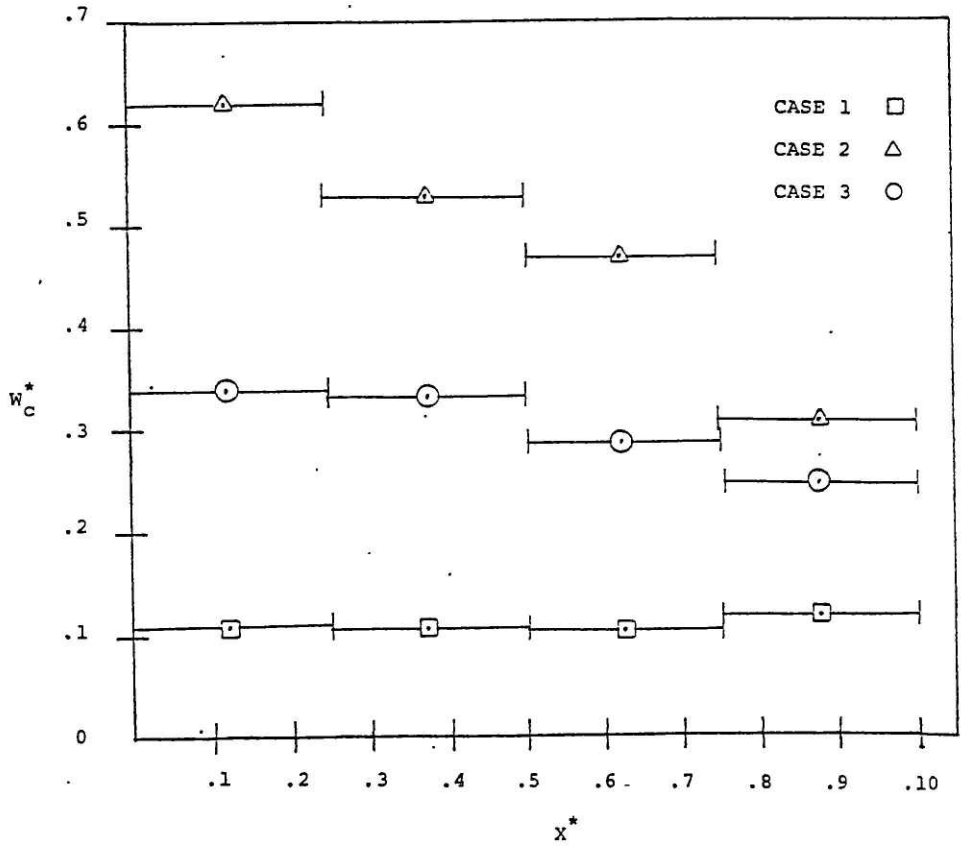
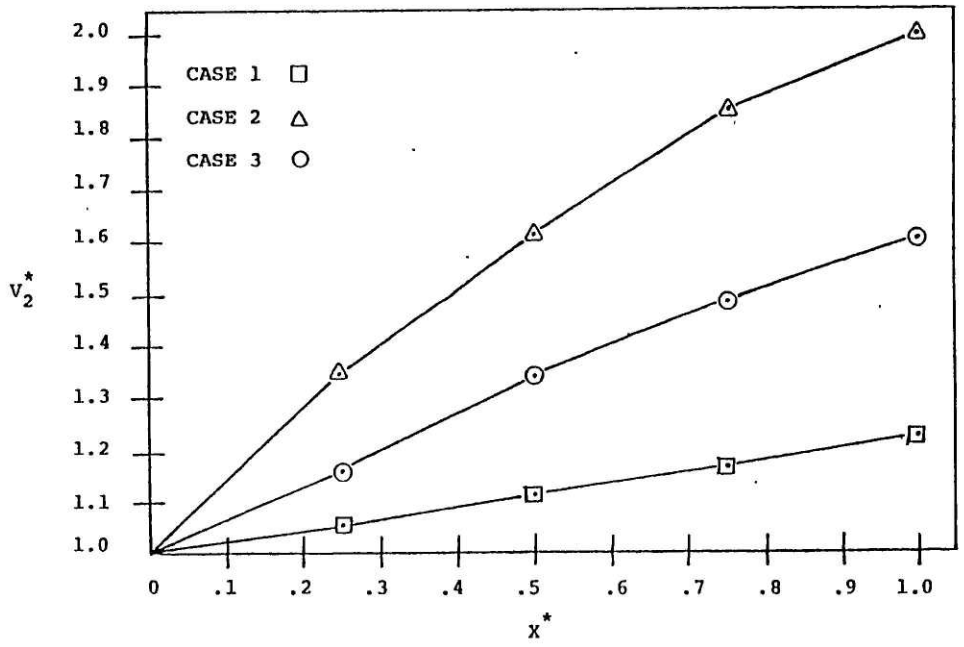


FIGURE 6.1.7

COBRA PREDICTED AXIAL VELOCITIES



The two channel model was used to predict the COBRA code calculations discussed above. The input parameters were the same as those used in the COBRA calculation, namely, no turbulent mixing ($w_t^* = 0$), and laminar friction factor ($f = 64/Re$). Various axial velocity profile functions given in Table 5.2.1 and Figure 5.2.1 were used ($f(x^*) = x^*, x^{*2}, x^{*1/2}, (1 - \cos \pi x^*)/2, x^* - (\sin 2\pi x^*)/2\pi$). The results for C are presented in Table 6.1.3 along with the COBRA results. Note that for some of the profiles the model predicts recirculation for Case 2 ($C > 1$) while COBRA predicted onset of recirculation ($C = 1$). Note also that the uniform crossflow result ($f(x^*) = x^*$) gives essentially the same value for C as the half sine wave result and the full cosine.

The axial velocity and crossflow results for Case 1 are shown in Figures 6.1.8 and 6.1.9, respectively. The results for the half sine wave are not included since they are nearly the same as the uniform crossflow case (see Table 6.1.3). It is observed that the uniform crossflow case, $f(x^*) = x^*$ gives the best results. When $f(x^*) = x^{*2}$ the crossflow is overpredicted. This is because for $f(x^*) = x^{*2}$ the crossflow near the inlet is small, allowing a large radial temperature difference to develop, thus increasing the buoyancy force. Conversely, for $f(x^*) = \sqrt{x^*}$ the crossflow near the inlet is large causing the radial temperature difference to be small, resulting in a smaller buoyancy

TABLE 6.1.3

COBRA AND MODEL PREDICTIONS OF C FOR BNWL 2x6 STEADY STATE RUNS (58)

Case #	Case Parameters			COBRA predicted C	Model Prediction of C					
					IVP = 1			IVP=2	IVP=3	IVP=4
	Re	Gr_q	Skew		n = .5	n = 1	n = 2			
1	960	6.36E5	2:1	.226	.125	.202	.273	.204	.205	.205
2	480	3.49E5	1:0	1.00	.773	R	R	R	R	R
3	960	6.55E5	1:0	.607	.421	.575	.730	.569	.570	.552
				f(x)=	x	x	x^2			

Model input parameters:

$Pr = 6.35$ $\quad f = \frac{64}{Re}$

$w_t^* = 0$ $\quad R = 1$

R - indicates recirculation (C>1)

FIGURE 6.1.8

COBRA VERSUS MODEL PREDICTIONS OF AXIAL VELOCITY FOR CASE 1

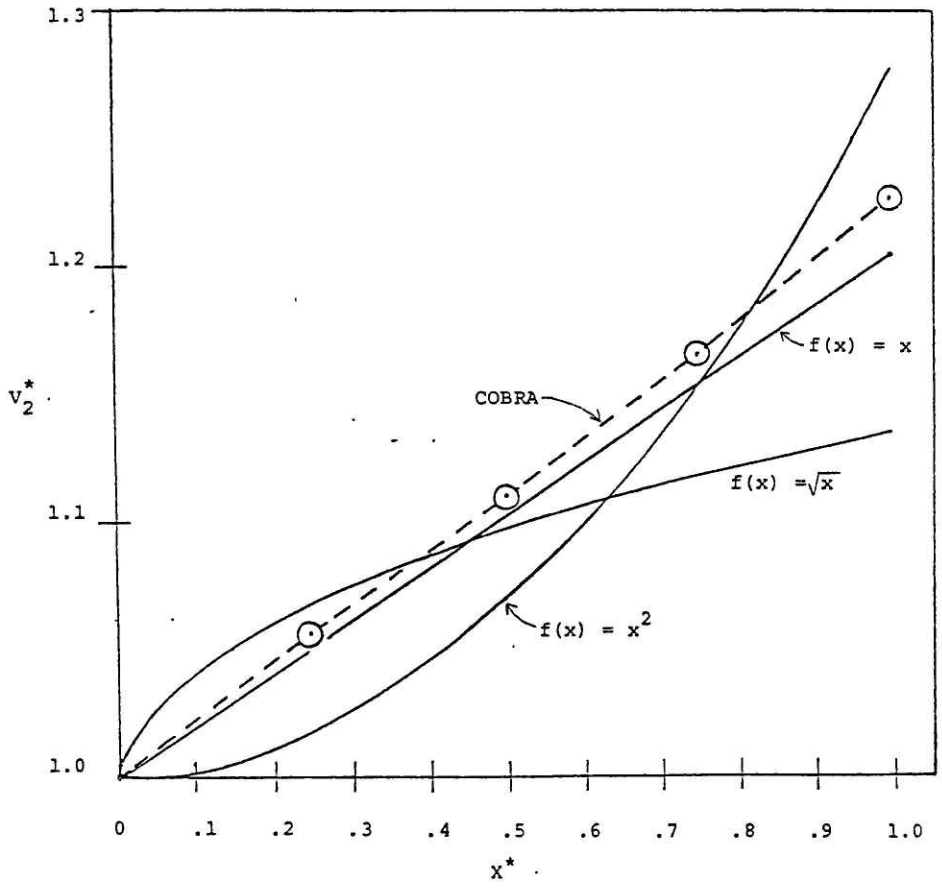
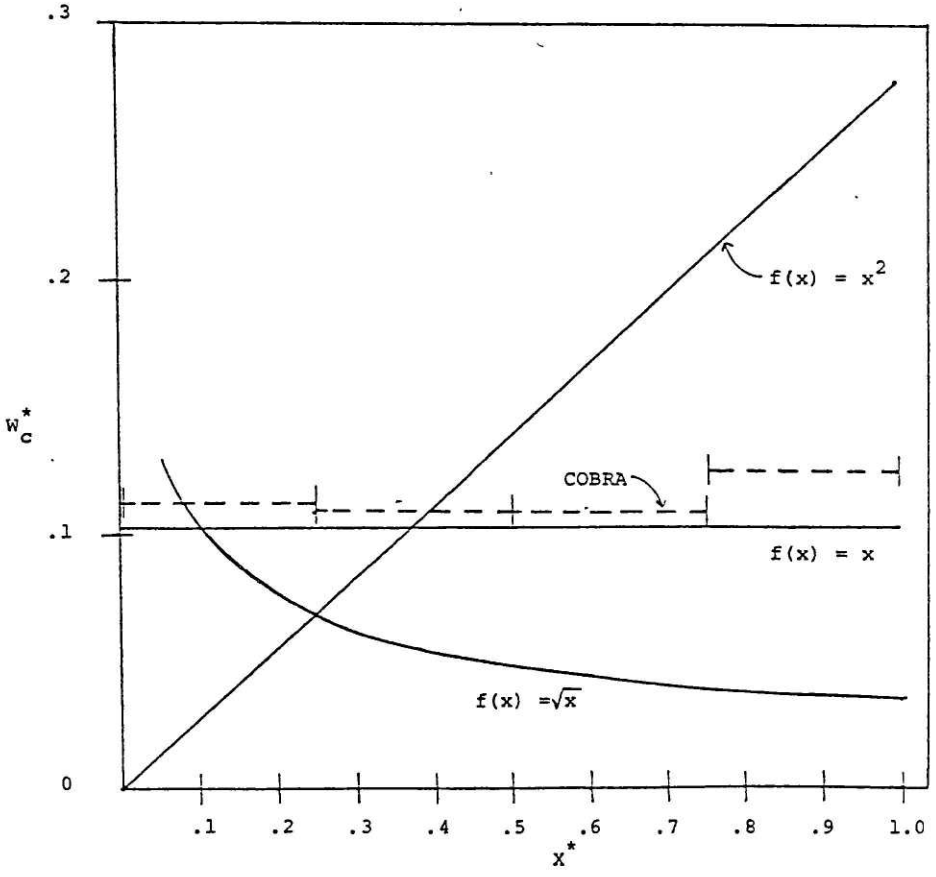


FIGURE 6.1.9

MODEL VERSUS COBRA PREDICTED CROSSFLOW FOR CASE 1



force. In fact, at $x^* = 0$ for $f(x^*) = \sqrt{x^*}$ the crossflow goes to infinity because w_c^* is proportional to $f'(x^*)$ which is $1/(2\sqrt{x^*})$. Though physically unreasonable, this presents no mathematical difficulty since the discontinuity is integrable. For Case 2, $f(x^*) = \sqrt{x^*}$ is the only profile which predicts no recirculation.

Figures 6.1.10 and 6.1.11 give the velocity and crossflow results for Case 3. The results are qualitatively the same as for Case 1, with $f(x^*) = x^*$ giving the closest prediction.

In Figures 6.1.12 and 6.1.13 the COBRA predicted subchannel temperatures and thermocouple data of Reference 58 are plotted along with the channel bulk temperatures predicted by the two channel model. The uniform crossflow profile ($f(x^*) = x^*$) was employed. The COBRA and experimental data are in good agreement with the exception of the edge channel temperatures which suggests there was heat loss at the wall. The model results for the bulk channel temperatures are qualitatively in agreement with the COBRA results, though quantitative comparison is difficult since the code and data are on a more local scale.

Figure 6.1.14 presents the results of COBRA and the experimental data. For Case 2 the COBRA and experimental results for window 9 ($x^* = 1.00$) indicate that flow recirculation has occured. This is concluded because the temperatures at the unheated side of the bundle have increased

FIGURE 6.1.10

COBRA VERSUS MODEL PREDICTIONS OF THE AXIAL VELOCITY FOR CASE 3

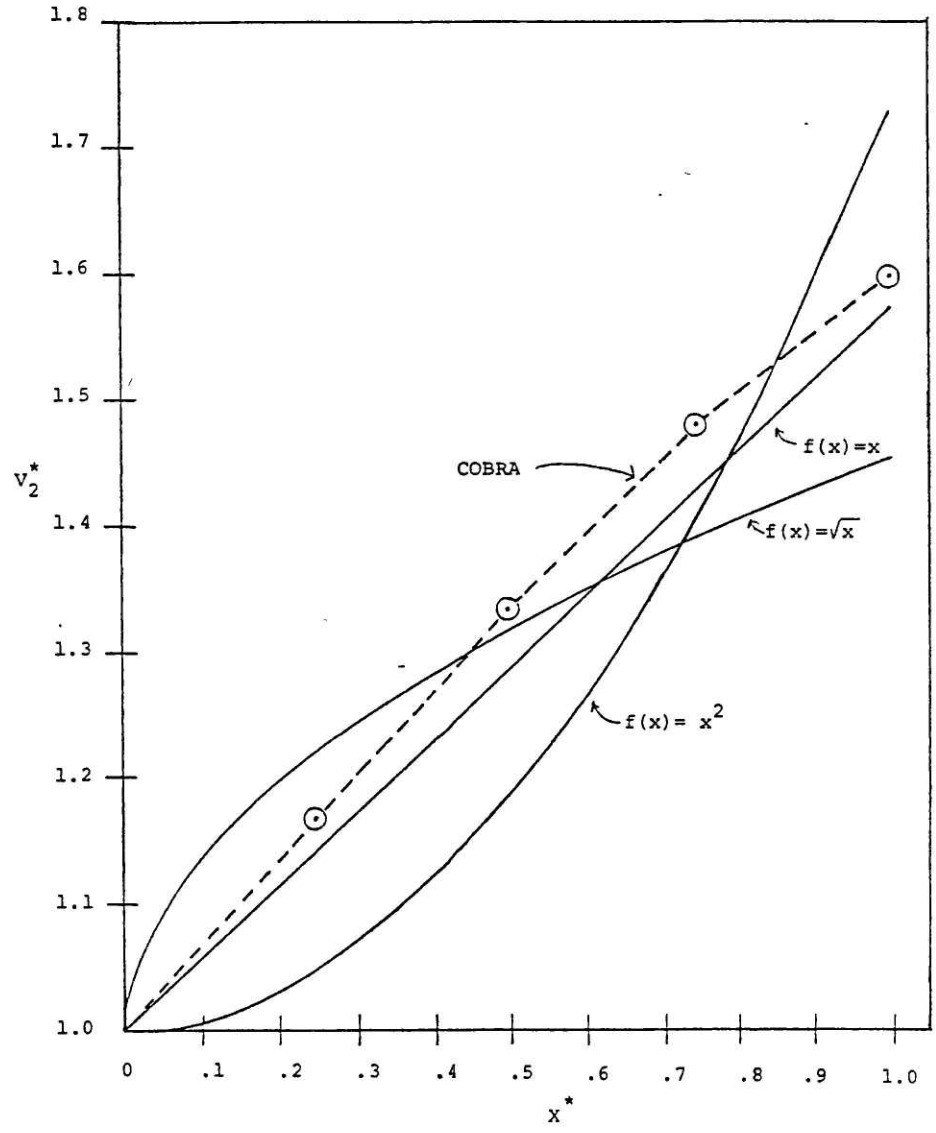


FIGURE 6.1.11

COBRA VERSUS MODEL PREDICTIONS OF CROSSFLOW FOR CASE 3

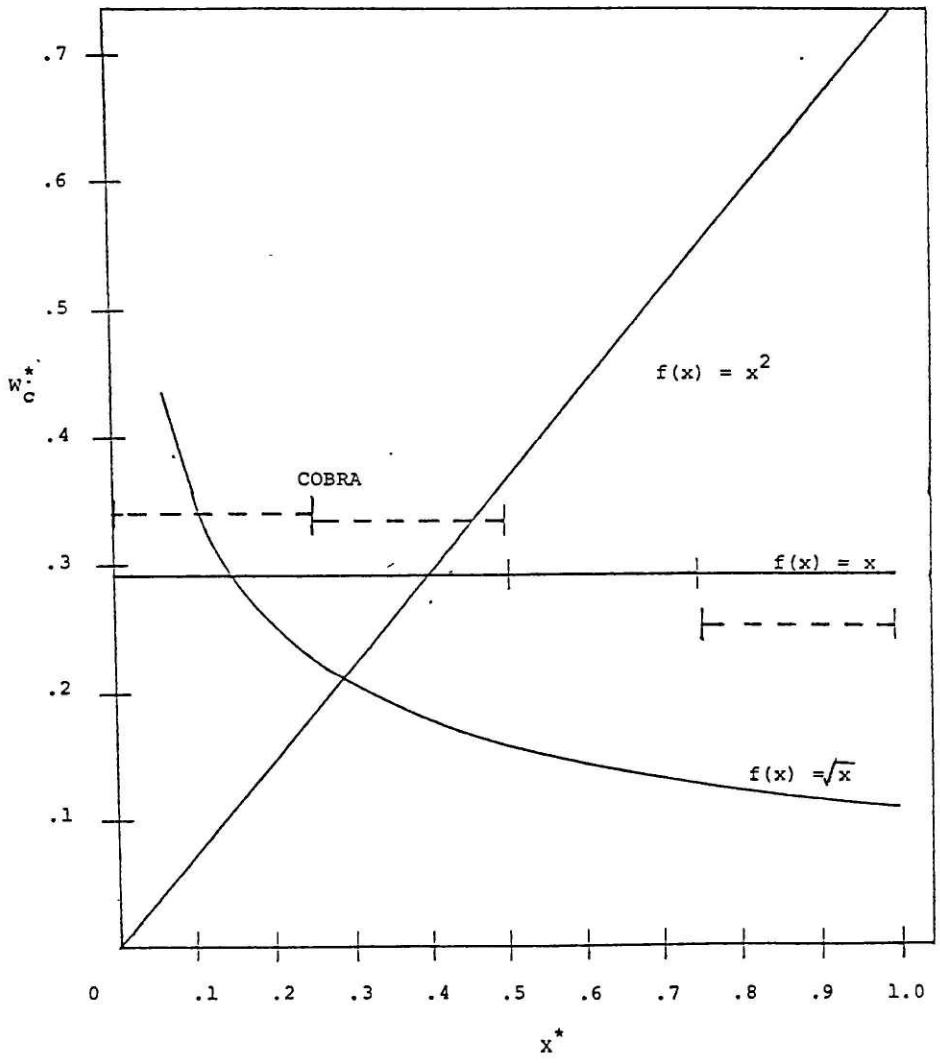


FIGURE 6.1.12

COMPARISON OF DATA WITH COBRA AND TWO CHANNEL MODEL PREDICTIONS FOR CASE 1 AT X^*=.5 and X^*=1.0

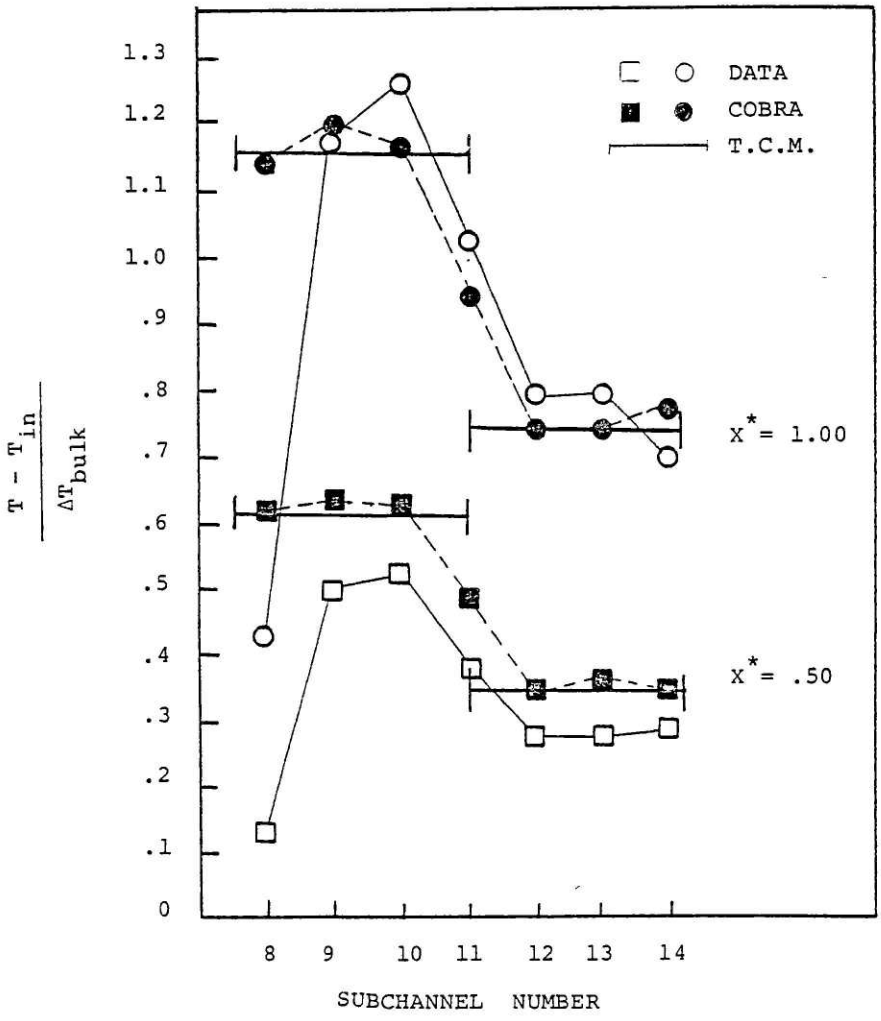


FIGURE 6.1.13

COMPARISON OF DATA WITH COBRA AND TWO CHANNEL MODEL PREDICTIONS FOR CASE 3 AT X^*=.5 AND X^* = 1.0

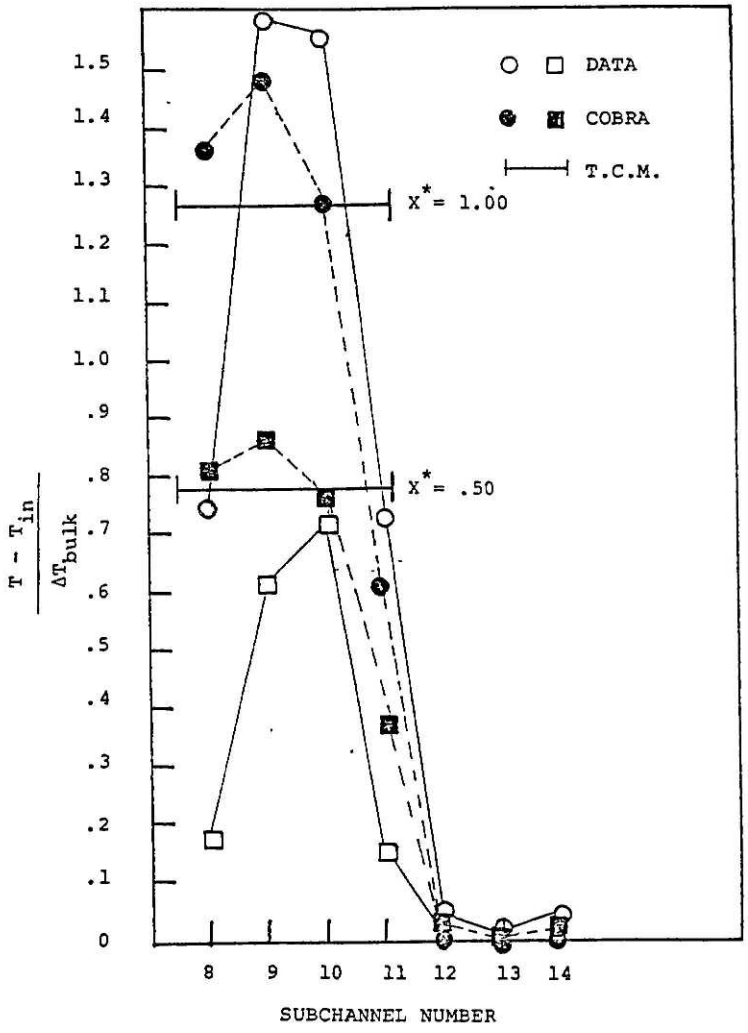
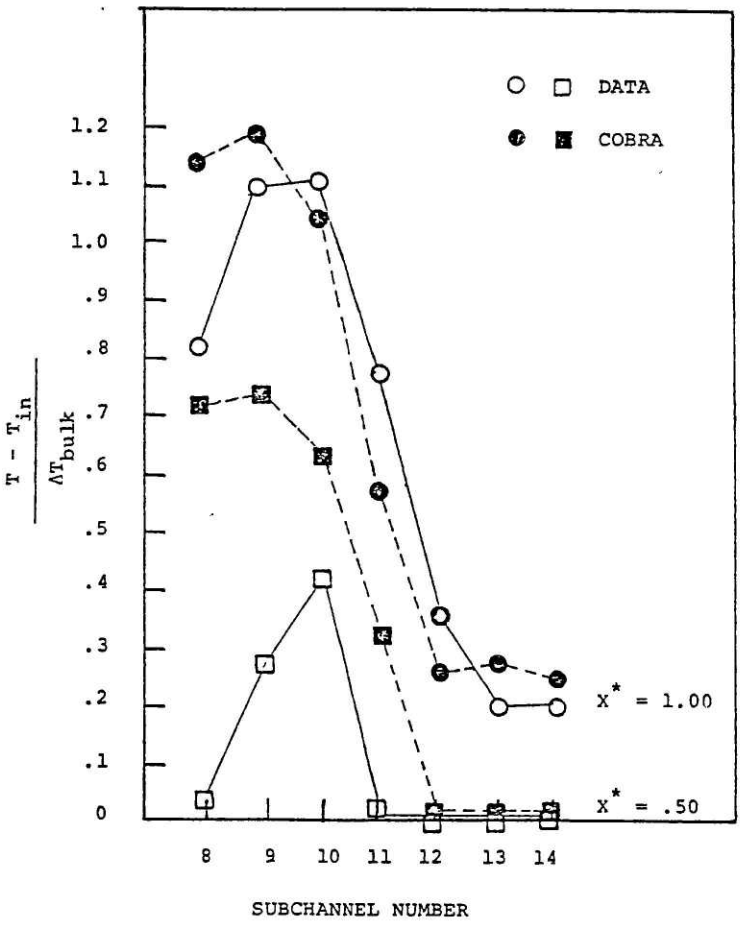


FIGURE 6.1.14

COMPARISON OF COBRA WITH DATA FOR

CASE 2 AT $X^* = .50$ AND $X^* = 1.00$



above the inlet temperature at $x^* = 1.00$, which indicates that the hot fluid in the upper plenum is flowing down in the unheated side of the bundle. However, no local velocity data was taken at window 9 to verify this, though it can be seen in Figure 6.1.3 that COBRA predicted reverse flow in two subchannels for Case 2. The value of C calculated from the COBRA subchannel velocities is one, corresponding to the onset of recirculation. Case 2 will be a data point for validating the onset of recirculation criteria in Section 7.4.

Judging by the results discussed above, it appears that the uniform crossflow approach ($f(x^*) = x^*$) gives the best results of the profiles considered so far, though the crossflow deviates from uniformity as C increases. The best way to illustrate this is to plot the COBRA predictions of $f(x^*)$ versus x^*. This is done by inverting Equation 5.2.12 to obtain:

$$f(x^*) = \frac{1}{C}\left(1 - \frac{V_1^*(x^*)}{V_{1i}^*}\right) \qquad (6.1.1)$$

The value of V_{1i}^* is unity for the cases considered here, since the inlet velocity is uniform. The COBRA predictions of C and $V_1^*(x^*)$ of Table 6.1.2 can then be used to calculate $f(x^*)$ at $x^* = 0, .25, .50, .75$ and 1.00. The results of this calculation are presented in Figure 6.1.15. As C increases, the COBRA predicted values for $f(x^*)$ deviate from the straight line representing $f(x^*) = x^*$, and approach the line for $f(x^*) = x^*$.

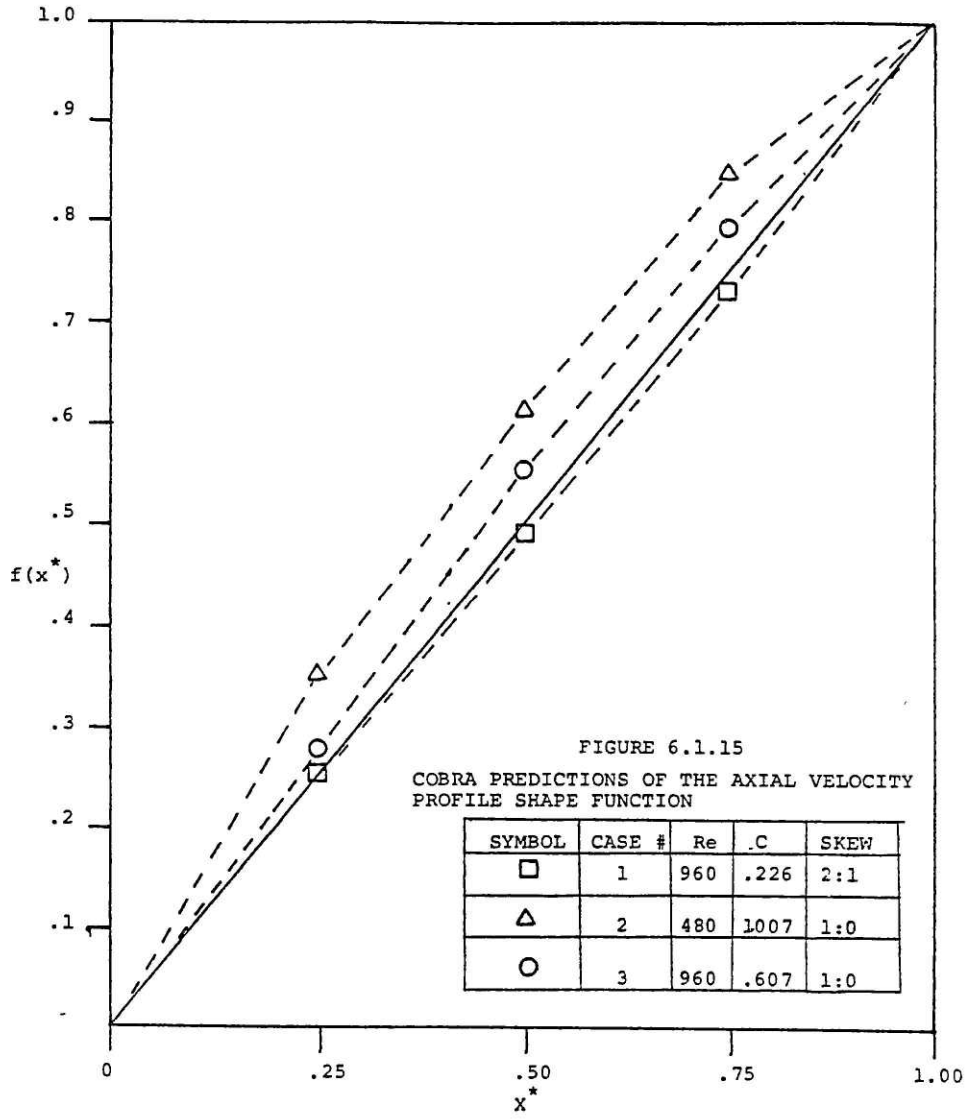


FIGURE 6.1.15

COBRA PREDICTIONS OF THE AXIAL VELOCITY PROFILE SHAPE FUNCTION

SYMBOL	CASE #	Re	.C	SKEW
□	1	960	.226	2:1
△	2	480	1007	1:0
○	3	960	.607	1:0

An additional axial velocity profile function which will be useful is one which coincides with the COBRA predicted f(x*). This will allow comparison of the two channel model results with the COBRA results for the same crossflow profile.

This profile is found by the following procedure. Let the value of f(x*) be specified at x* = 0.25, 0.50, and 0.75. As discussed in Section 5.2.1, f(x*) must satisfy the boundary conditions f(0) = 0 and f(1) = 1. Then assume a linear variation in f(x*) between these points. The function f(x*) is then given by

$$f(x^*) = 4\cdot(f(0.25)\cdot x^* \qquad 0\leq x^*\leq 0.25$$

$$f(x^*) = f(0.25) + 4\cdot(x^*-0.25)\cdot(f(0.50)-f(0.25)) \qquad 0.25\leq x^*\leq 0.50$$

$$f(x^*) = f(0.50) + 4\cdot(x^*-0.50)\cdot(f(0.75)-f(0.50)) \qquad 0.50\leq x^*\leq 0.75$$

$$f(x^*) = f(0.75) + 4\cdot(x^*-0.75)(1 - f(0.75)) \qquad 0.75\leq x^*\leq 1.00 \qquad (6.1.2)$$

The integral of f(X*) is evaluated by the trapezoidal approximation. This profile will be designated as IVP = 4.

With the values for f(x*) taken from Figure 6.1.15, this new velocity profile function was implemented in the model. The predicted values for C are given in Table 6.1.3. It is observed that the results are nearly the same as f(x*) = x*. The difference between the uniform crossflow results (f(x*) = x*) and the true (COBRA predicted) f(x*) is 1.5% for Case 1 and 4.2% for Case 3. The effect of f(x*) for Case 2 (recirculation condition) will be taken up later. It appears from the results presented here that the uniform crossflow approximation gives good agreement to the COBRA calculations.

6.1.2 Assessment of the Transient Term in the Two Channel Model

In Chapter 5 it was found that an analytical solution to the energy equation could not be found if the transient terms of the energy equation were retained. For this reason, only the transient terms of the momentum equation were included, and a model was developed in Appendix B2 to estimate when the transient terms of the energy equation could be neglected. In this section, the effect of retaining the transient terms of the momentum equation but not the energy equation will be determined. A two channel COBRA calculation (which includes all transient terms) will be used as a standard. Before proceeding with the two channel calculations, an experimental program used to validate COBRA for transient mixed convection flows will be outlined.

BNWL 2x6 Transient Experiment Versus COBRA Predictions

An experimental study has been performed at BNWL (59) to obtain local velocity and temperature measurements in the 2x6 rod bundle for controlled flow transients. Table 6.1.4 gives the operating conditions for the 9 transient runs. The flow was linearly decreased from an initially steady flow condition to a final steady flow. Power skews of 1:0 to 2:1 were used. Flow recirculation was observed in cases 4, 6 and 9, and preliminary criteria for the onset of recirculation was given.

A phenomena described as thermal plumes was observed. Thermal plumes are zones of locally heated fluid near the hot

TABLE 6.1.4

RUN CONDITIONS FOR BNWL 2x6 TRANSIENT RUNS (59)

Case Number	t Transient Time (Sec)	Power Gradient	Re (initial/final)	Gr* (initial/final)
1	S.S.	0:0	1200/1200	0.0/0.0
2	S.S.	1:1	1390/1390	0.0/0.0
3	150	0:0	1200/420	0.0/0.0
4	150	1:0	1290/520	$1.65 \times 10^4 / 7.04 \times 10^4$
5	45	0:0	1200/420	0.0/0.0
6	45	1:0	1290/520	$1.65 \times 10^4 / 7.04 \times 10^4$
7	45	2:1	1340/560	$9.20 \times 10^3 / 4.56 \times 10^4$
8	45	0:0	640/200	0.0/0.0
9	45	1:0	730/320	$3.79 \times 10^4 / 2.44 \times 10^5$

rods which rise more rapidly than the bulk fluid in the subchannel due to their lower density. The thermal plumes were observed to promote coolant mixing between the channels. A correlation for enhanced coolant mixing was presented.

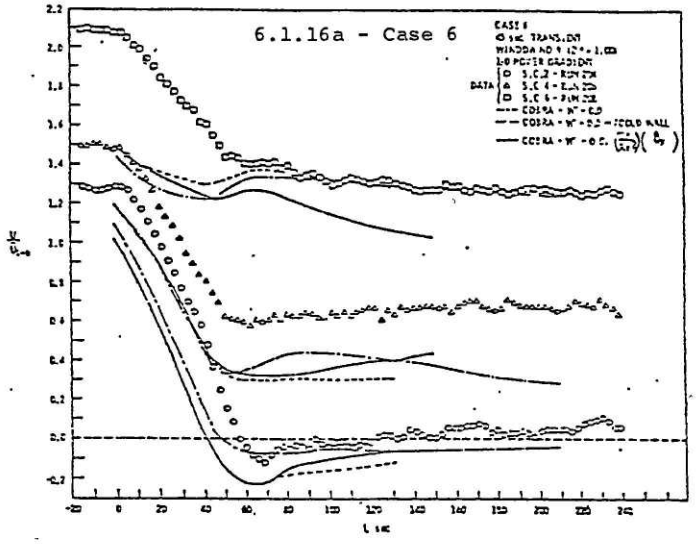
The transient velocity and temperature measurements were compared to results of the COBRA-WC code. The results for case 6 and case 9 are given in Figures 6.1.16a and 6.1.16b. respectively, where the velocity is plotted against transient time. Errors as much as 25% exist between data and prediction. Recirculation in subchannel #2 is predicted at t=40 seconds and is observed experimentally at t=60 seconds for case 6. For case 9 recirculation is predicted at t=20 seconds, and is observed at t=30 seconds. The recirculation data will be used later to validate the onset of recirculation criteria.

Two Channel COBRA Predictions Versus Model Predictions

To assess the transient capability of the two channel model 2 COBRA-WC runs were made at BNWL for this study. One run had a power skew of 1:0 and the other was a 4:1 skew. Each run was for a 45 second linear flow decay followed by a steady flow for 155 seconds as in case 9 of the BNWL runs (Table 6.1.4). The 2x6 bundle was divided into two channels as shown in Figure 6.1.17, and the geometric parameters calculated as shown. Note than an error was made in calculating the wetted perimeter of channel 2. This subsequently caused an error in the hydraulic diameters input into COBRA-WC. Though not truely representative of the case 9 run, the code

FIGURE 6.1.16

MEASURED AND PREDICTED SUBCHANNEL VELOCITIES FOR CASES 6 AND 9



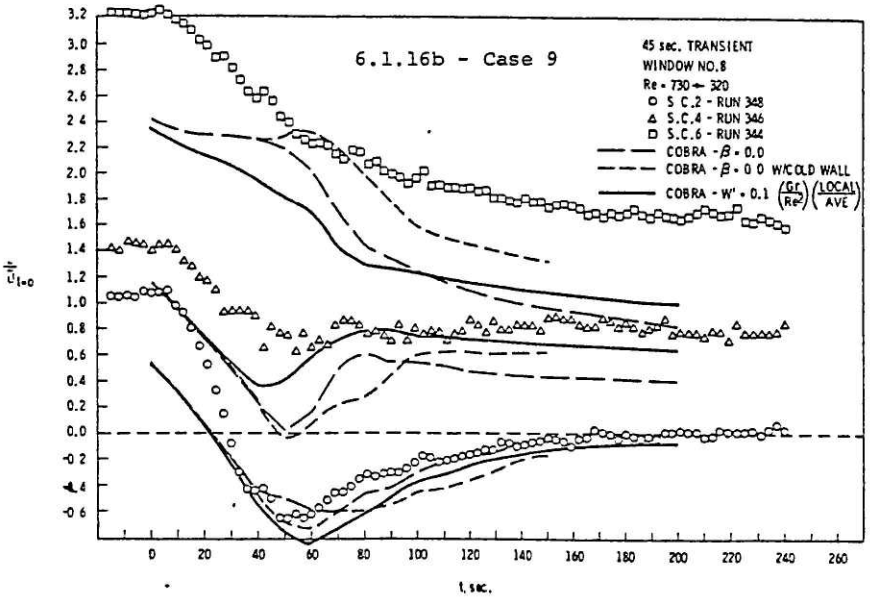
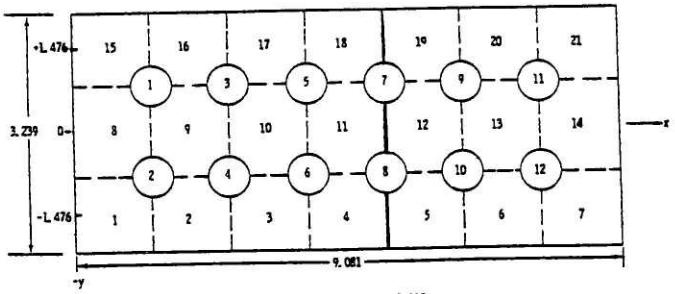


FIGURE 6.1.17

BUNDLE NODING SCHEME FOR TWO CHANNEL COBRA RUN



SUBCHANNEL DIMENSIONS

TYPE	AREA (cm^2)	WETTED PERIMETER (cm)	HEATED PERIMETER (cm)
CORNER	0.505	2.725	0.948
SIDE	0.727	3.355	1.895
CENTRAL	0.990	3.790	3.790

$$A_2 = 2(.505) + 7(.727) + 3(.990) = 9.07 \text{ cm}^2$$

$$P_{w2} = 2(2.725) + 7(3.355) + 3(3.790) = 40.31 \text{ cm}$$

$$D_{e2} = \frac{4A_z}{P_{w2}} = .90 \text{ cm} = .354 \text{ in.}$$

$$A_1 = 2(.505) + 5(.727) + 2(.990) = 6.63 \text{ cm}^2$$

$$P_{w1} = 2(2.725) + 5(3.355) + 2(3.790) = 29.81 \text{ cm} \quad (33.65 \text{ cm in COBRA})$$

$$D_{e1} = \frac{4A_1}{P_{w1}} = .890 \text{ cm} = .350 \text{ in} \quad (.310'' \text{ in COBRA})$$

$$R = A_1/A_2 = .73$$

$$D_{eb} = \frac{4A_T}{P_{wT}} = .90\text{cm} = .354 \text{ in } (.334'' \text{ in COBRA})$$

results are still useful. The full length of the bundle was modeled, including the 24 in. unheated inlet, the 48 in. heated length and the 12 in. unheated exit. Figure 6.1.18 shows the dimensionless bundle velocity ($V_b^* = V_b(t)/V_b(0)$) which was input to the code. Also shown is the COBRA calculated dimensionless bulk temperature rise ($\Delta T^* = \Delta T_B(t)/\Delta T_B(0)$) for the two runs. The single channel quasi-steady dimensionless bulk temperature rise (calculated from a heat balance with no energy storage term, or $T_{QS}^* = 1/V_b^*$), and the single channel transient calculation performed in Appendix B2 are also given. The difference between the COBRA transient ΔT^* calculation and the single channel transient calculation are largely due to the thermal response of the heater rods which was not accounted for in the single channel approach. This is demonstrated in Figure 6.1.23 by the plot of $Q^*=Q(t)/Q(0)$ ($Q(t)$ is the power delivered from the rods to the coolant). The rod power delivered to the coolant initially decreases with time, since as the velocity decreases, so does the rod heat transfer coefficient. This causes energy to be stored in the rods during the coastdown. When the flow becomes constant at t=45 seconds, Q^* increases to its initial value. As predicted by the analysis of Appendix B2, the effect of the flow coastdown is to decrease the bulk temperature rise from the quasi-steady value.

The dimensionless cold channel velocity V_1^* as a function of axial distance is shown in Figures 6.1.19 and 6.1.20 for the 1:0 and 4:1 power gradients at several times during the

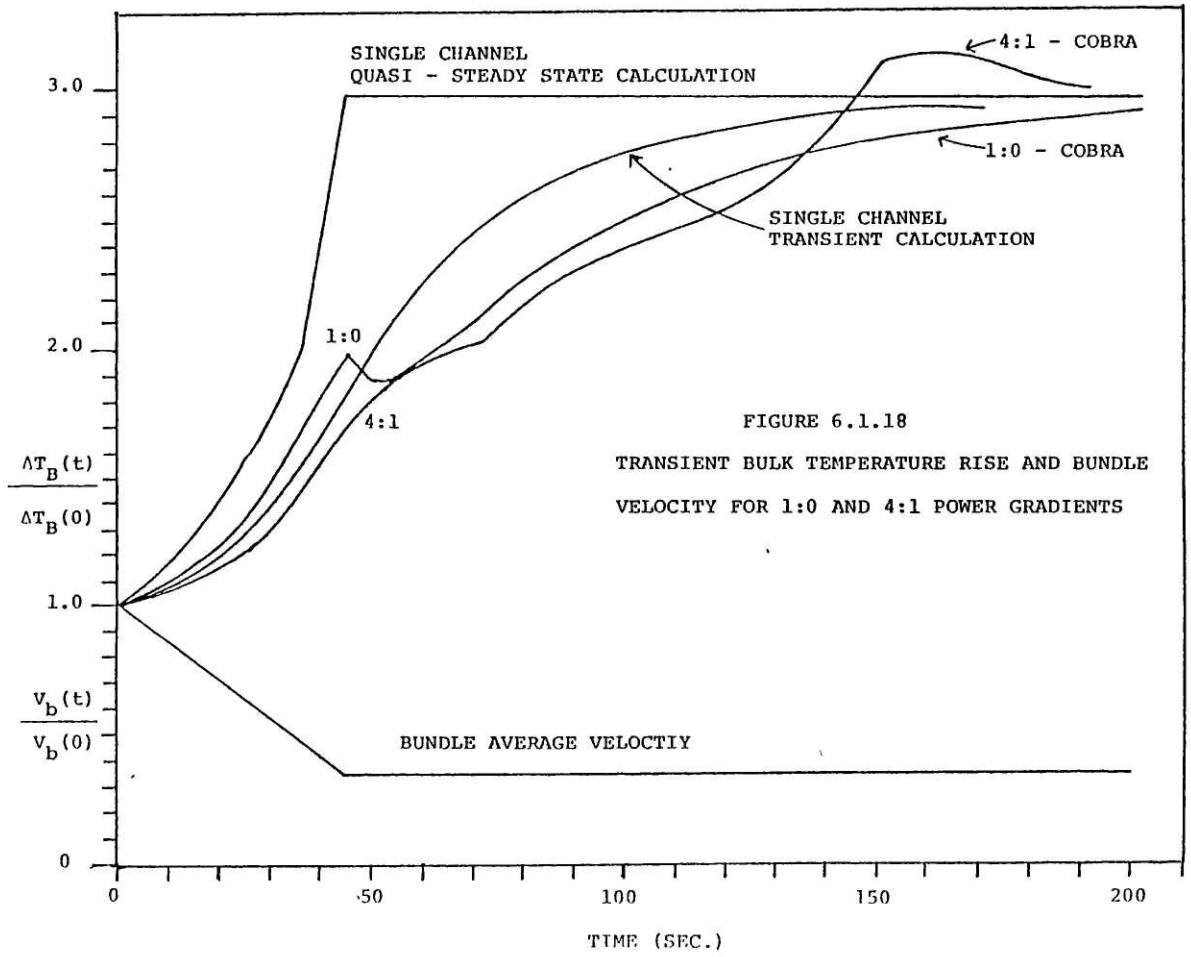
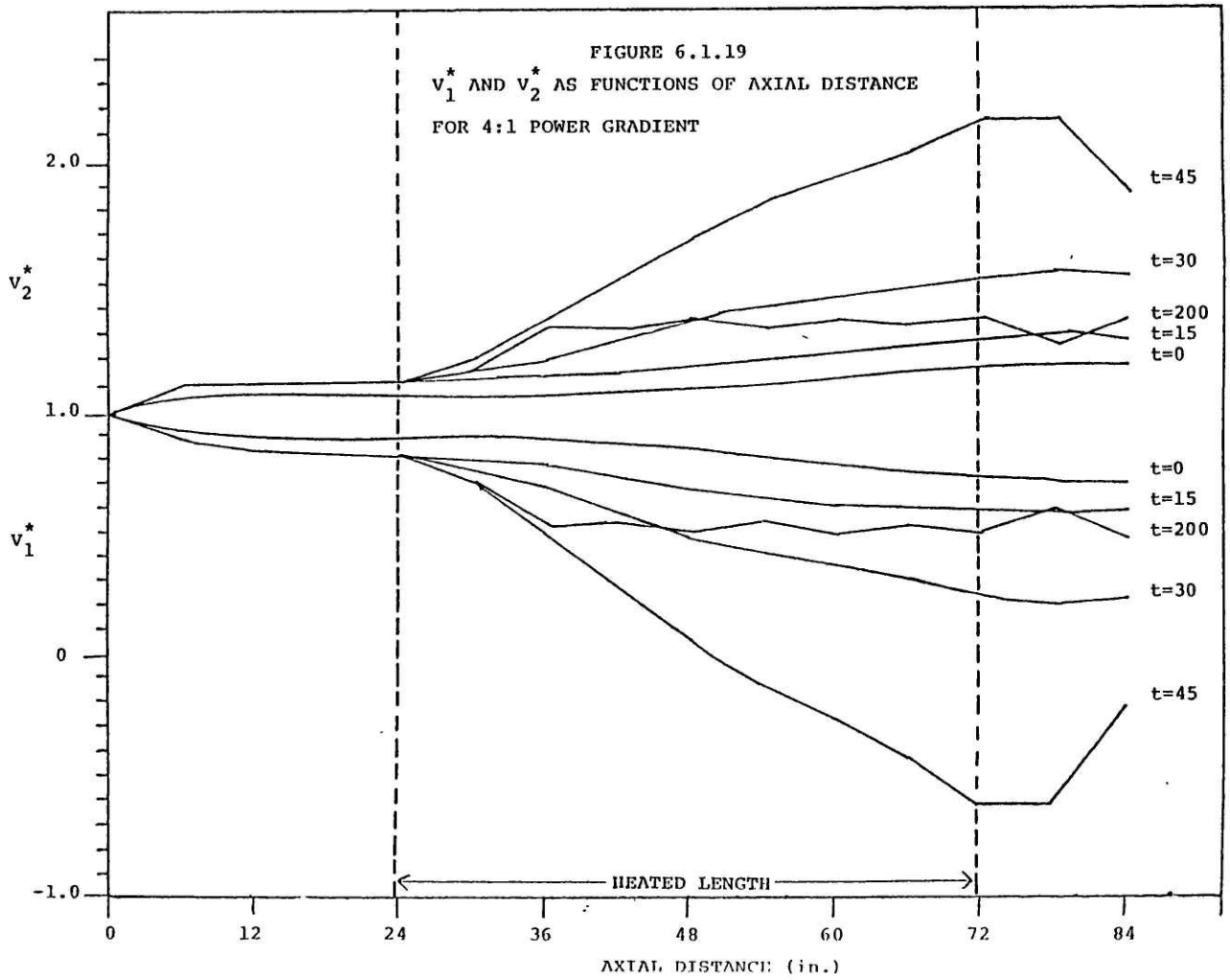
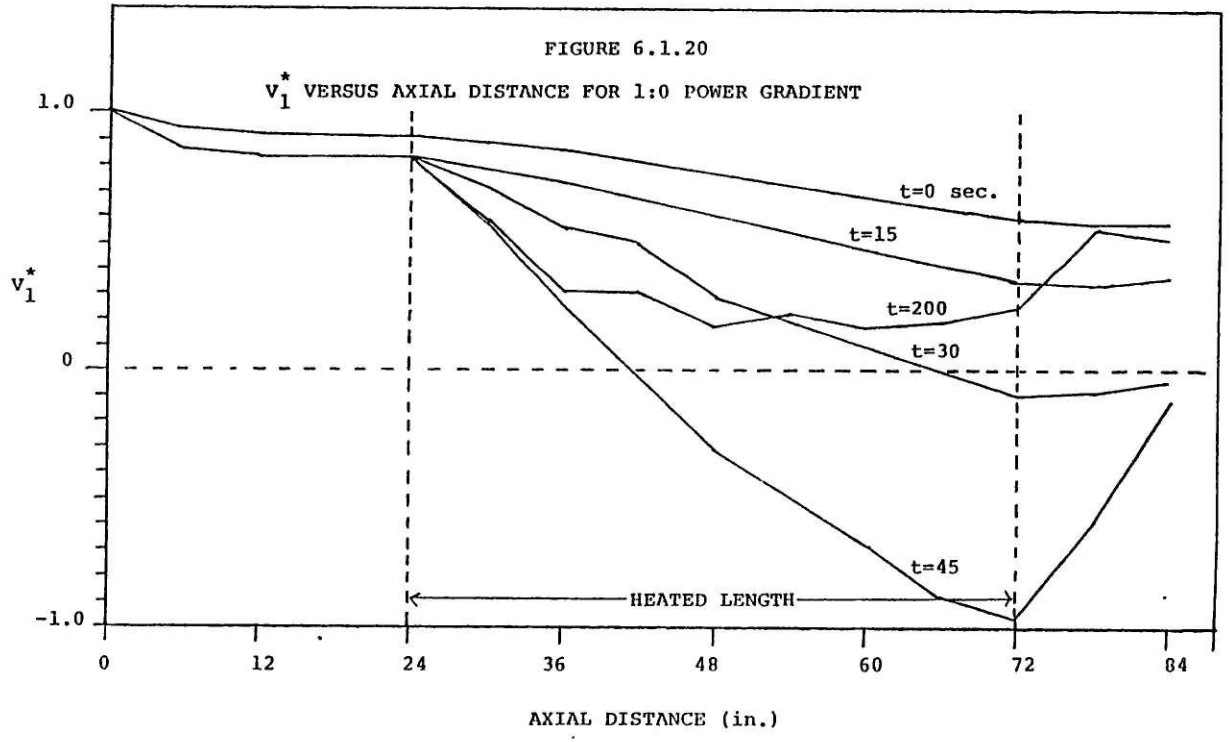


FIGURE 6.1.18

TRANSIENT BULK TEMPERATURE RISE AND BUNDLE VELOCITY FOR 1:0 AND 4:1 POWER GRADIENTS


FIGURE 6.1.19
V_1^* AND V_2^* AS FUNCTIONS OF AXIAL DISTANCE
FOR 4:1 POWER GRADIENT
2.0
1.0
0
-1.0
V_2^*
V_1^*
t=45
t=30
t=200
t=15
t=0
t=0
t=15
t=200
t=30
t=45
HEATED LENGTH
0
12
24
36
48
60
72
84
AXIAL DISTANCE (in.)


FIGURE 6.1.20
V_1^* VERSUS AXIAL DISTANCE FOR 1:0 POWER GRADIENT
1.0
0
-1.0
V_1^*
t=0 sec.
t=15
t=200
t=30
t=45
HEATED LENGTH
0
12
24
36
48
60
72
84
AXIAL DISTANCE (in.)

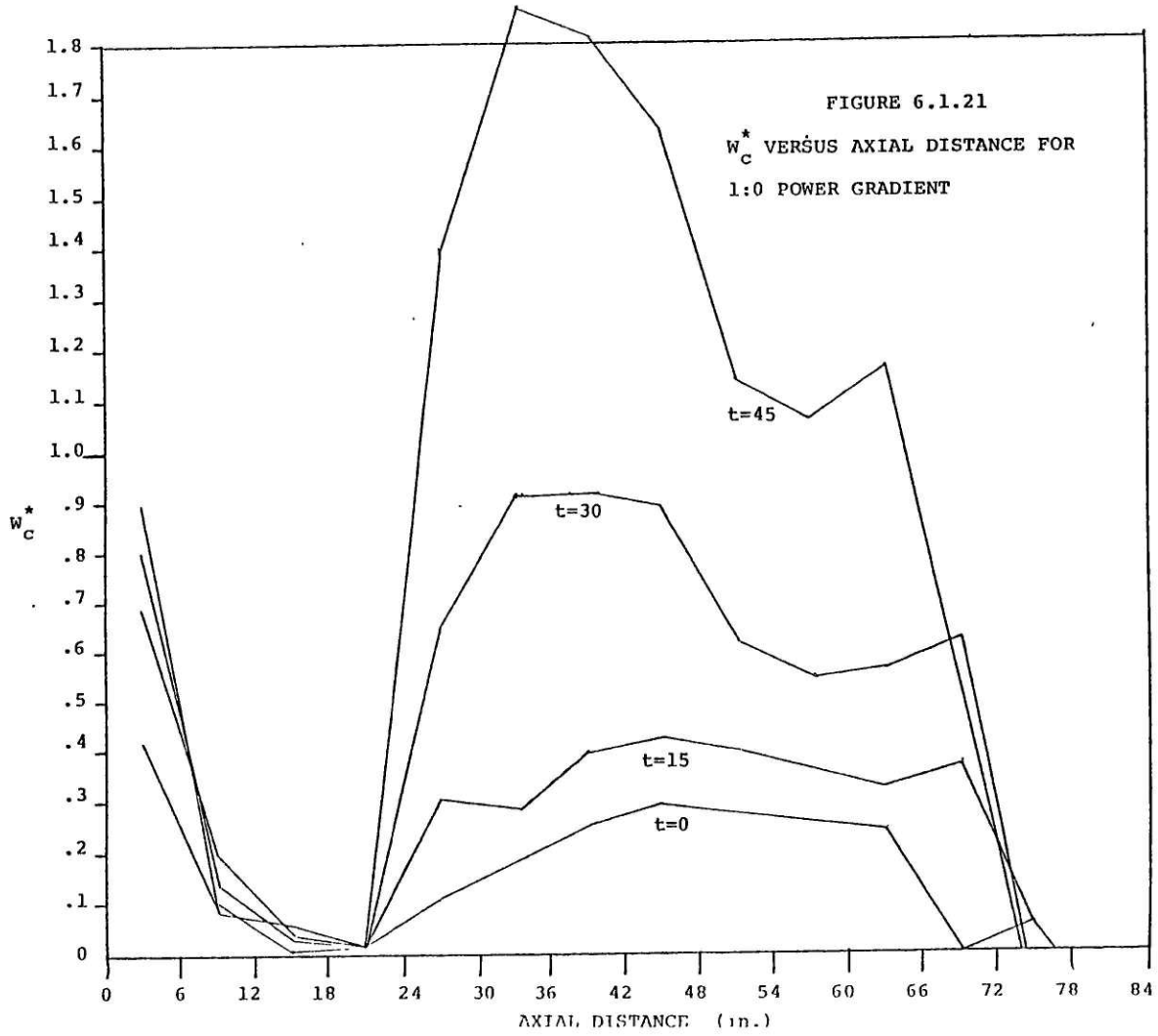
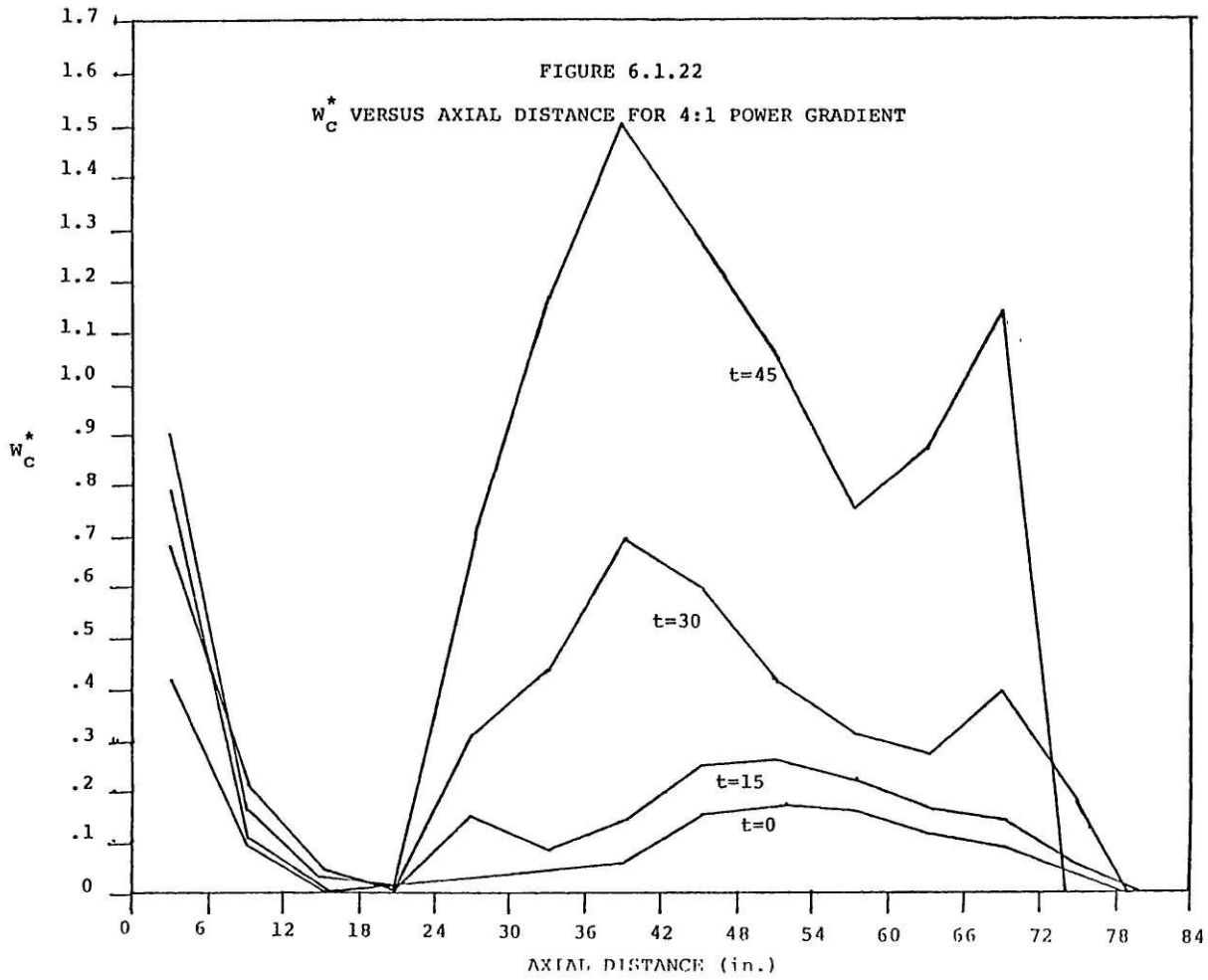


FIGURE 6.1.21

W_c^* VERSUS AXIAL DISTANCE FOR

1:0 POWER GRADIENT


FIGURE 6.1.22
W_c^* VERSUS AXIAL DISTANCE FOR 4:1 POWER GRADIENT
W_c^*
1.7
1.6
1.5
1.4
1.3
1.2
1.1
1.0
.9
.8
.7
.6
.5
.4
.3
.2
.1
0
t=45
t=30
t=15
t=0
0
6
12
18
24
30
36
42
48
54
60
66
72
78
84
AXIAL DISTANCE (in.)

transient. The corresponding crossflow profiles are given in Figure 6.1.21 and 6.1.22. Near the bundle inlet, there is a large crossflow induced by the mistakenly different channel hydraulic diameters. This results in a nonuniform inlet velocity from the inlet to the start of heating (x=24"), but does not effect the crossflow within the heated length. Over the heated length there is a buoyancy induced crossflow which increases with transient time. As was observed for the steady state run, for increasing crossflow, the crossflow profile becomes skewed toward the inlet. The recirculation is first observed at 30 seconds for the 1:0 skew and 40 seconds for the 4:1 skew.

A physical explanation of the behavior of the crossflow profile follows. At the inlet of the heated length the crossflow is zero, so the power skew causes a large radial ΔT to develop, resulting in a large crossflow. The crossflow brings more coolant to the hot side of the bundle, reducing the radial ΔT and the buoyancy forces. The reduction in buoyancy forces causes the crossflow to reduce further downstream. This effect appears to increase with decreasing Re. A similar phenomena was observed in Reference 55 by Tsai et al. though crossflow profiles were not given. Tsai's results were discussed in detail in Chapter 3. The effect of buoyancy was more pronounced in Reference 55 since friction at the rod surface was neglected.

For the two channel model, we are most interested in modeling the bundle heated length, so $x^*=0$ corresponds to

x=24", and x*=1 corresponds to x=72". From the channel velocities at the inlet and outlet of the heated length, the crossflow parameter C can be calculated from Equation 5.2.4 at each time step. The results are given in Figure 6.1.23 for the two power skews. Recall that C>1 indicates that a recirculation condition exists. For both cases recirculation occurs during the coastdown, then disappears later in the transient. This suggests that the flow coastdown provides a driving force for buoyancy induced crossflow.

From the axial velocity profiles predicted by COBRA, the velocity profile function f(x*) can be obtained from Equation 6.1.1. Figures 6.1.24 and 6.1.25 show the results of this calculation. The results are qualitatively similar to the results of Figure 6.1.15 for steady flow with the exception of f(x*) at t=200 sec, where nearly all of the crossflow occurs for x*<.25, and some oscillations in the crossflow occur for x*>.25. It is not known if this happens in reality, or if it is a numerical oscillation. Similar behavior was reported in Reference 55 , but a more detailed COBRA analysis is required to confirm the similarity.

The two channel model was used to simulate the flow coastdown for the 4:1 gradient using the quasi-steady state approximation (no transient terms retained). The model and COBRA results are given in Figure 6.1.26. The two channel model significantly overpredicts the crossflow, and predicts recirculation (C=1) at t=18 seconds (Re=454) while COBRA predicts recirculation at t=28 seconds (Re=375), giving a

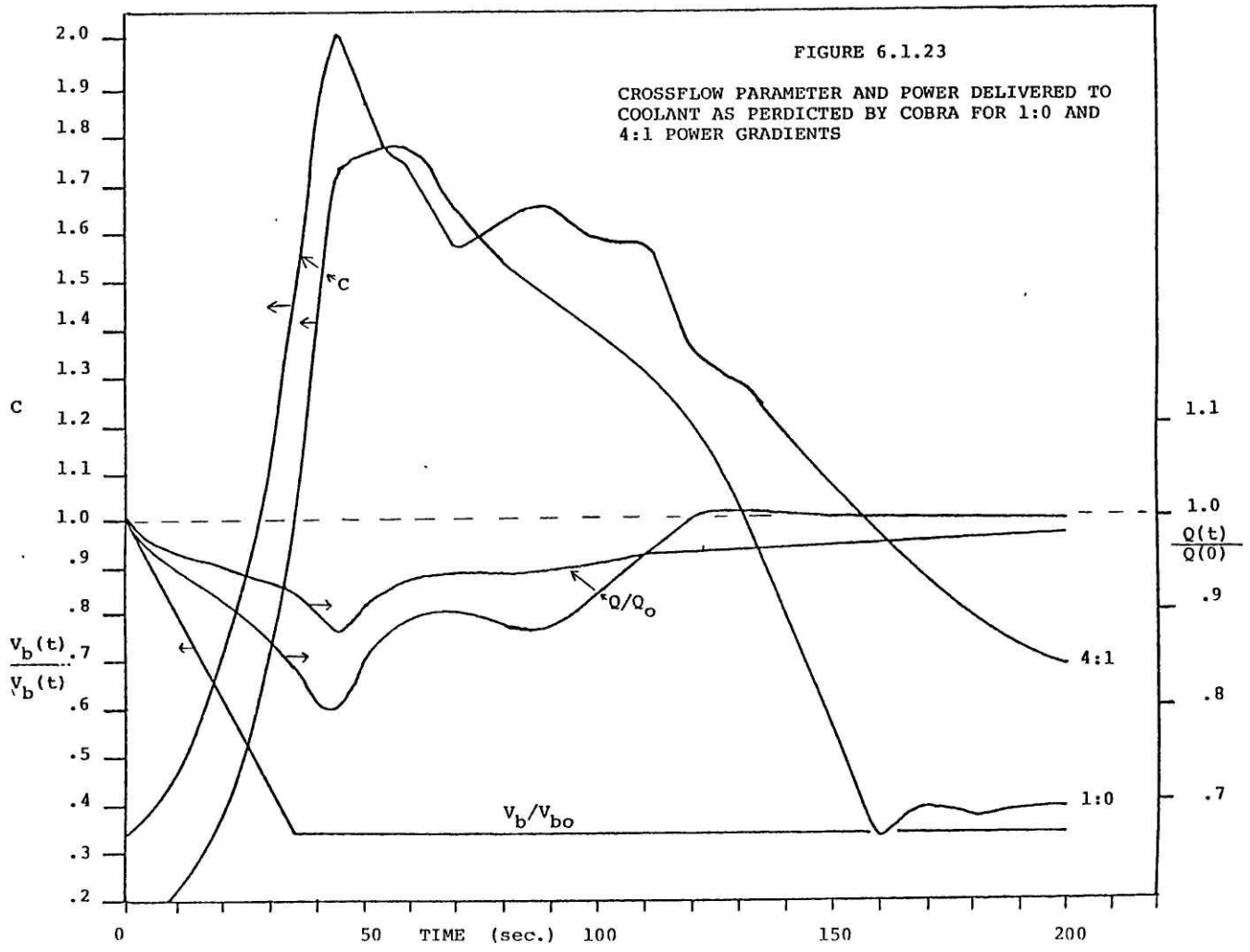


FIGURE 6.1.23

CROSSFLOW PARAMETER AND POWER DELIVERED TO COOLANT AS PERDICTED BY COBRA FOR 1:0 AND 4:1 POWER GRADIENTS

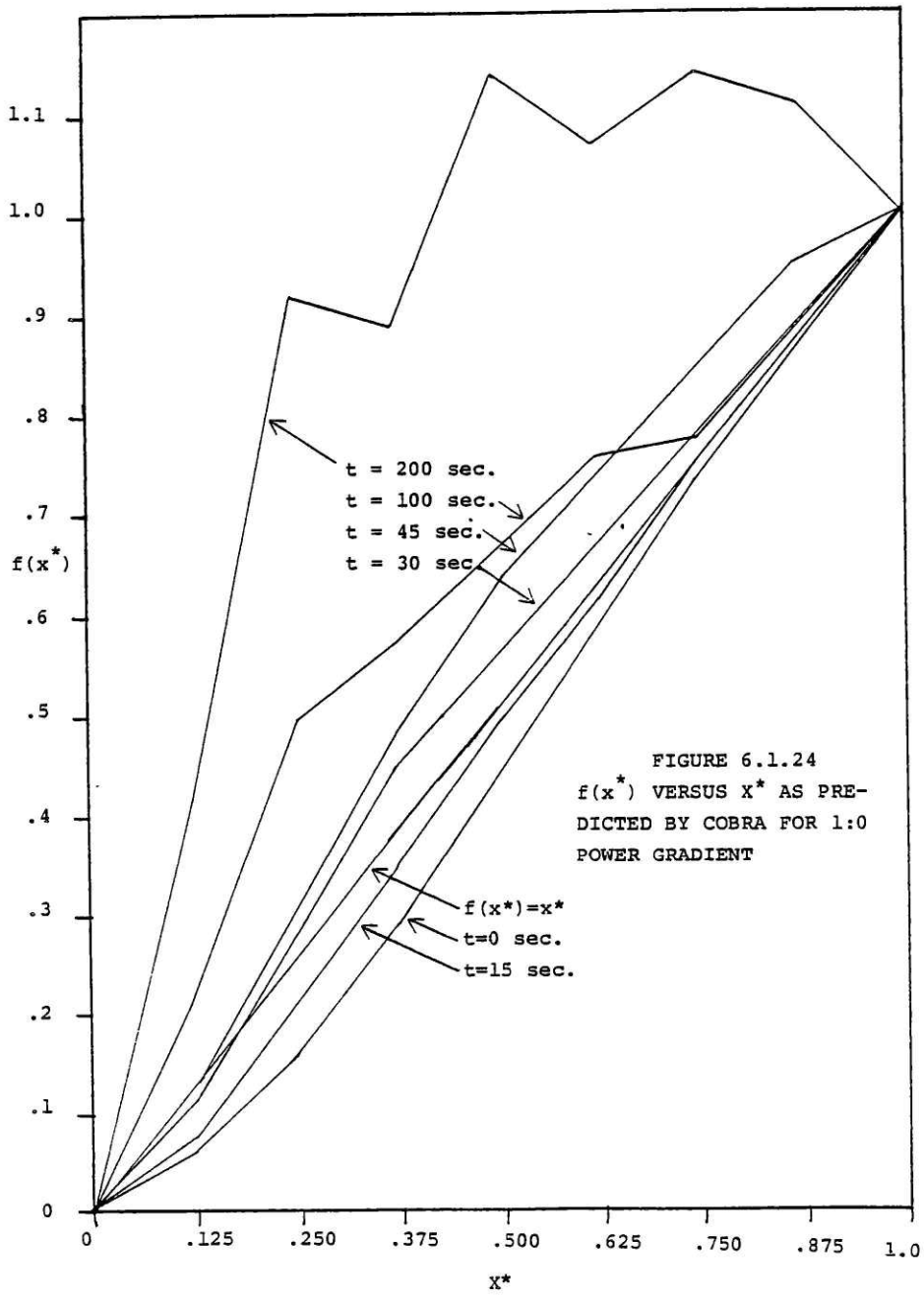


FIGURE 6.1.24
$f(x^*)$ VERSUS X^* AS PREDICTED BY COBRA FOR 1:0 POWER GRADIENT

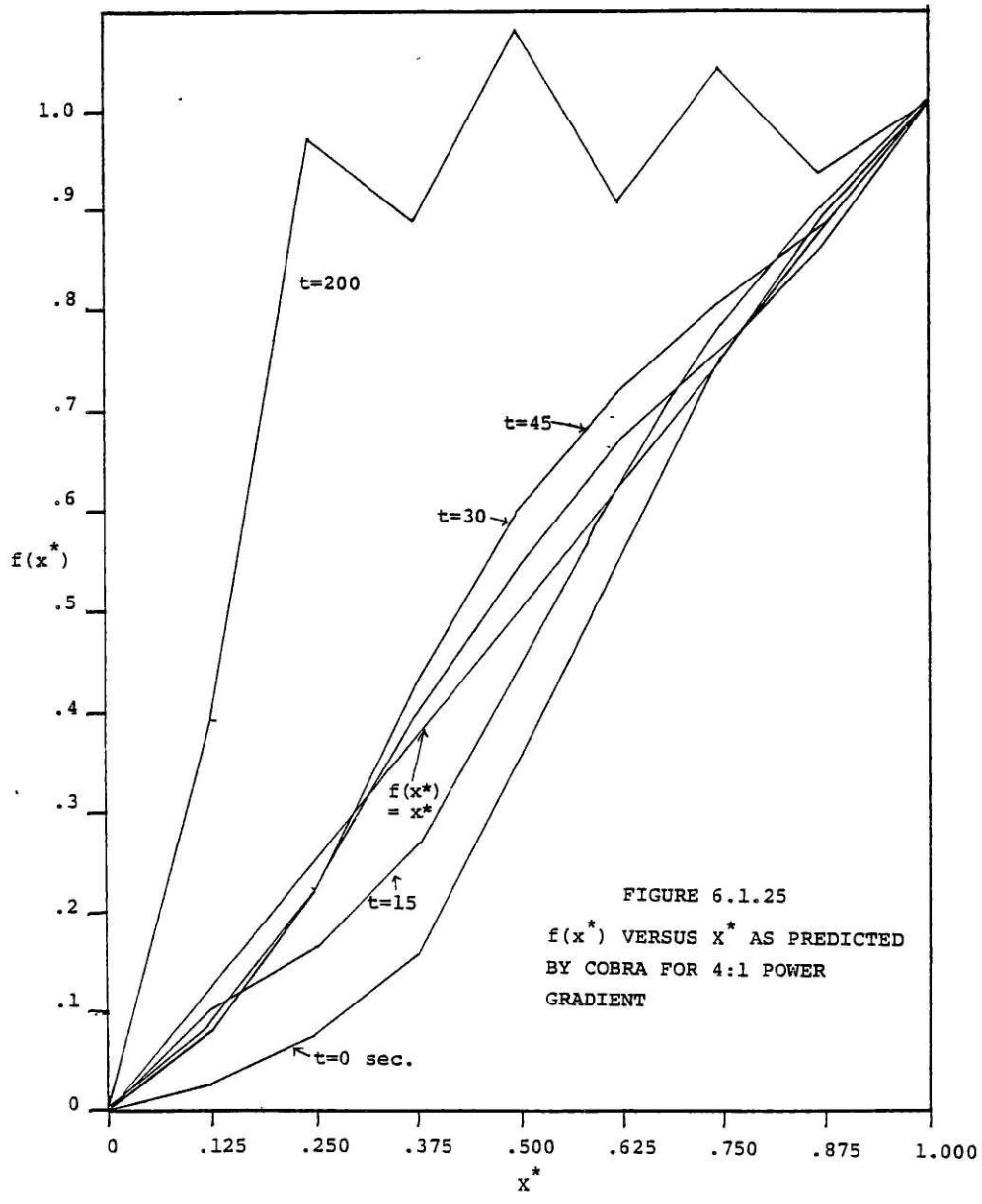


FIGURE 6.1.25

$f(x^*)$ VERSUS X^* AS PREDICTED BY COBRA FOR 4:1 POWER GRADIENT

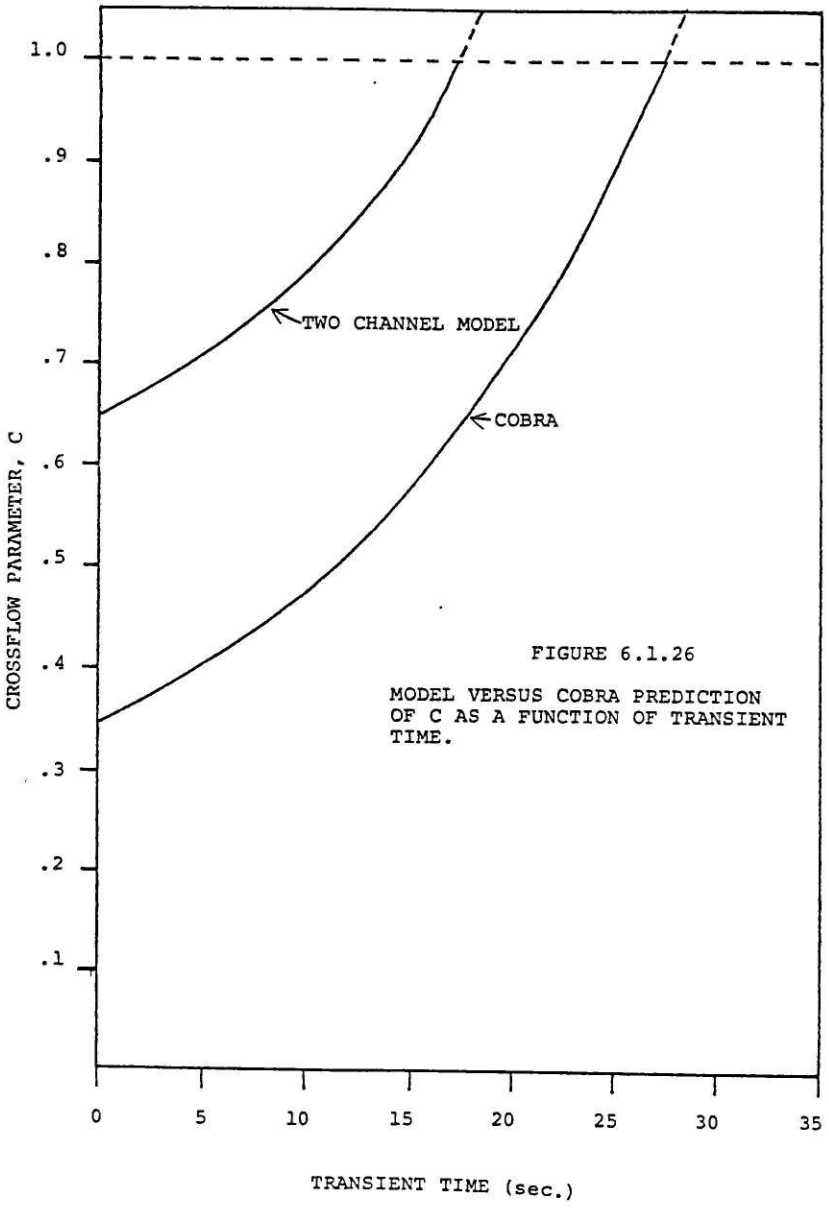


FIGURE 6.1.26

MODEL VERSUS COBRA PREDICTION OF C AS A FUNCTION OF TRANSIENT TIME.

21% error in prediction of the onset of recirculation.

The transient term in the momentum equation of the two channel model will next be calculated by COBRA to determine its effect on the above prediction. The transient term is (Equation 5.2.40):

$$\text{Term 4} = \frac{LD_e}{\nu}\frac{1}{Re^2}\left\{\left[Re\frac{dC}{dt} + C\frac{dRe}{dt}\right](1+R)V_{1i}^*\overline{f(x^*)} + (V_{2i}^* - V_{1i}^*)\frac{dRe}{dt}\right\} \qquad (6.2.1)$$

For a flow transient $\frac{dRe}{dt}$ is known, but $\frac{dC}{dt}$ is not known since C is the variable being solved for in the model. The COBRA results presented earlier may be used to evaluate the above transient term since COBRA gives us C, V_{2i}^* and V_{1i}^* as a function of time. For the linear flow decay $\frac{dRe}{dt}$ is constant at $-7.84\ \text{sec}^{-1}$, while $\frac{dC}{dt}$ is positive up to t=45 sec. Hence $C\frac{dRe}{dt}$ and $(V_{2i}^*-V_{1i}^*)\frac{dRe}{dt}$ are negative. With $\frac{LD_e}{\nu} = 9627$, R=.73 and $\overline{f(x)} = 1/2$ Equation 6.2.1 becomes:

$$\text{Term 4} = \frac{9627}{Re^2}\left\{\left[Re\frac{dC}{dt} - \left|C\frac{dRe}{dt}\right|\right]\cdot .865 - \left|(V_{2i}^*-V_{1i}^*)\frac{dRe}{dt}\right|\right\} \qquad (6.2.2)$$

The absolute values of $Re\frac{dC}{dt}$, $C\frac{dRe}{dt}$ and $(V_{2i}^*-V_{1i}^*)\frac{dRe}{dt}$ predicted by the two channel COBRA run for a 1:0 power gradient are given in Figure 6.1.27. The value of Term 4 calculated from Equation 6.2.2 is also given.

It is observed that Term 4 is positive for the first 40 seconds of the transient, and will therefore oppose flow redistribution (since it has the opposite sign of the buoyancy

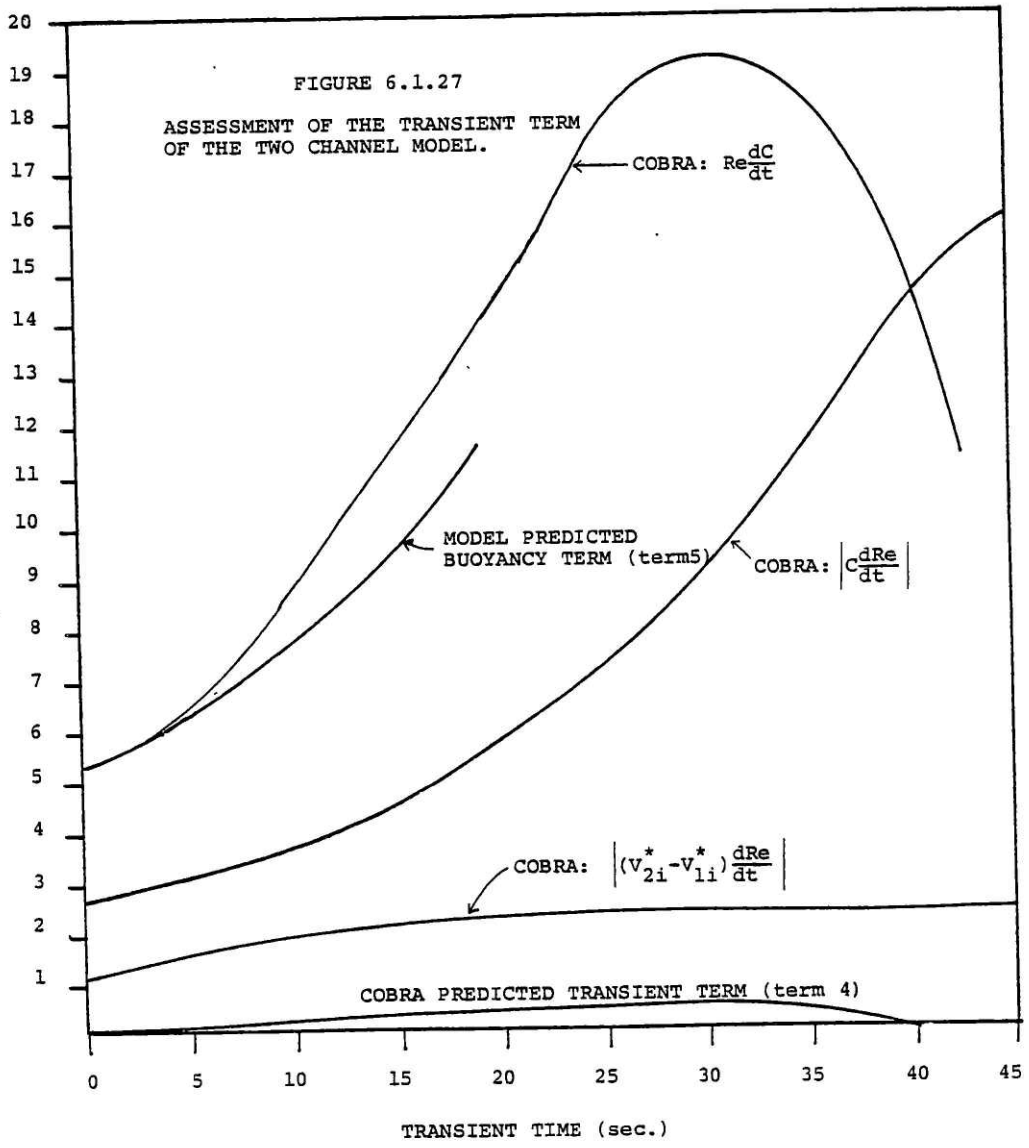


FIGURE 6.1.27

ASSESSMENT OF THE TRANSIENT TERM OF THE TWO CHANNEL MODEL.

term in Equation 5.2.15). This is contrary to the COBRA results of Figure 6.1.23, which shows a rapid decrease in the crossflow after the flow coastdown has ended. This indicates that the transient term will enhance flow redistribution. The buoyancy term calculated by the channel model is also shown in Figure 6.1.27. It is observed that the transient term is at most 2.6% of the buoyancy term, so including the transient term in the model calculation will not change the results very much. The transient term was also found to be negligible for the 4:1 power gradient. However, the COBRA results indicate that transient effects were significant for both the 1:0 power skew and and 4:1 power skew.

It can be concluded from these results that the two channel model does not adequately account for transient effects. Recall that in Chapter 5 the transient term in the energy equation was neglected to allow analytical solution of the governing equations. In Appendix B2 a criterion was derived for when this approximation was valid. The transient term in the momentum equation was retained, but it was shown in Figure 6.1.27 that it is negligible. Therefore the transient term in the model will be neglected in future calculations. The model is recommended for use in quasi-steady flows only, i.e. when Equation B.2.23 is satisfied.

6.2 COMPARISON OF THE TWO CHANNEL MODEL RESULTS TO ENERGY CODE PREDICTIONS

In the previous two sections, the validity of the two channel model was assessed by comparison to results of the COBRA code for a bare rod bundle with water flow for both transient and steady state runs. Here we will consider the case of an LMFBR assembly which has wire wrapped rods and a liquid sodium flow. This is an important step in the model validation, since now the effect of coolant mixing and radial conduction will be significant, whereas before they were negligible. The ENERGY code (62) will be employed for these cases. Since the code and correlations for the input parameters are still under development the exact version of ENERGY used here is described in Appendix E2. As discussed earlier, a two step validation procedure will be employed. First the ENERGY code predictions are compared to the data from the Westinghouse Blanket Test to demonstrate the validity of the ENERGY code. Then the two channel model results will be compared to channel averaged velocities and temperatures calculated by ENERGY.

6.2.1 Comparison of the Results of ENERGY IV With the WARD Blanket Data

Comparisons between the Westinghouse Blanket Bundle Thermocouple data and ENERGY code predictions have been made in Reference 67 and 68 . Several additional comparisons will be made in the present study. A brief description of the tests, and plots of the comparisons are given in Appendix E4.

It is concluded from these comparisons that the code predicts the data reasonably well for runs which are not far into the mixed convection regime. The reason the ENERGY predictions are not good for very low flows is due to the unavailability of mixed convection input parameters, and limited knowledge of the shape factor.

6.2.2 Determination of Model Input Parameters for LMFBR Bundles

As discussed in Section 3.3 correlations are available for ε^*_{1L} and C_{1L}. These correlations can be used to determine w^*_t for the two channel model. In Appendix E3 an approximate relationship is developed which gives w^*_t as a function of ε^*_{1L}, C_{1L}, x_1, x_2 and geometry for two different noding schemes for the LMFBR bundle. If we are interested in modeling the effect of redistribution due to a power skew, the bundle is divided into two geometrically identical channels, with channel 1 containing the lower power rods and channel 2 containing the higher power rods. For this case w^*_t is given by:

$$w^*_t = 2 \frac{D_{ei}}{\ell F_g} N_R \frac{(P-D)L}{A_b} x_1 \varepsilon^*_{1L} + \frac{2gL}{A_b} \frac{\eta_2}{\ell F_g} x_2 C_{1L} \qquad (6.2.1)$$

The first term represents the energy transport due to interior region mixing, and the second term is due to the edge region swirl. F_g is a factor which is used to match the local temperature gradient at the channel boundary with the gradient which is calculated from the two bulk temperatures obtained from the two channel model, and ℓ, the centroid to centroid distance between channels.

Table 6.2.1 gives some of the geometric parameters of

TABLE 6.2.1

BUNDLE GEOMETRIC PARAMETERS

	WARD BLANKET	ORNL FUEL
D	.519	.23
D_w	.042	.056
L_H	450	36.0
De_b	.146	.127
D_H	.180	.181
A_b	4.48	1.99
D_F	4.49	2.32
L/De_b	307.9	284.4
L/D_H	249.5	198.9
$\frac{LDe}{Ab}$	1.47	2.29
w/ℓ	.211	.54
P/D	1.08	1.24
H/D	8.0	52
Dei	.1374	.1193

the WARD blanket bundle and the ORNL fuel bundle. If the geometrical parameters are substituted into Equation 6.2.1, we obtain

$$w_t^* = (.235\ \varepsilon_{1L}^* x_1 + .258\ C_{1L} x_2)/F_g \qquad (6.2.2)$$

for the blanket bundle, and

$$w_t^* = (.939\ \varepsilon_{1L}^* x_1 + .653\ C_{1L} x_2)/F_g \qquad (6.2.3)$$

for the fuel bundle.

Program WIWRAP of Reference 69 was used to calculate ε_{1L}^*, C_{1L}, x_1 and x_2 for the WARD blanket and ORNL fuel bundles as a function of the bundle Reynolds number. The results are plotted in Figures 6.2.1 and 6.2.2 for the WARD blanket geometry, and Figures 6.2.3 and 6.2.4 for the ORNL fuel geometry. If F_g is known, these results allow w_t^* to be calculated from Equation 6.2.2 and 6.2.3 for the fuel and blanket geometries.

The coefficients of the Hawley-Chiu friction factor correlation were calculated by WIWRAP, and are given in Table 6.2.2.

The dimensionless channel powers, P_1 and P_2 must be calculated from the actual bundle power distribution. Table 6.2.3 gives the power factors for the radial power skews which will be employed in the model validation. Also shown are P_1 and P_2 which for the R=1 approach are calculated from:

$$P_1 = (5p_9 + 6p_8 + 7p_7 + 8p_6 + 4.5p_5)/61 \qquad (6.2.4)$$

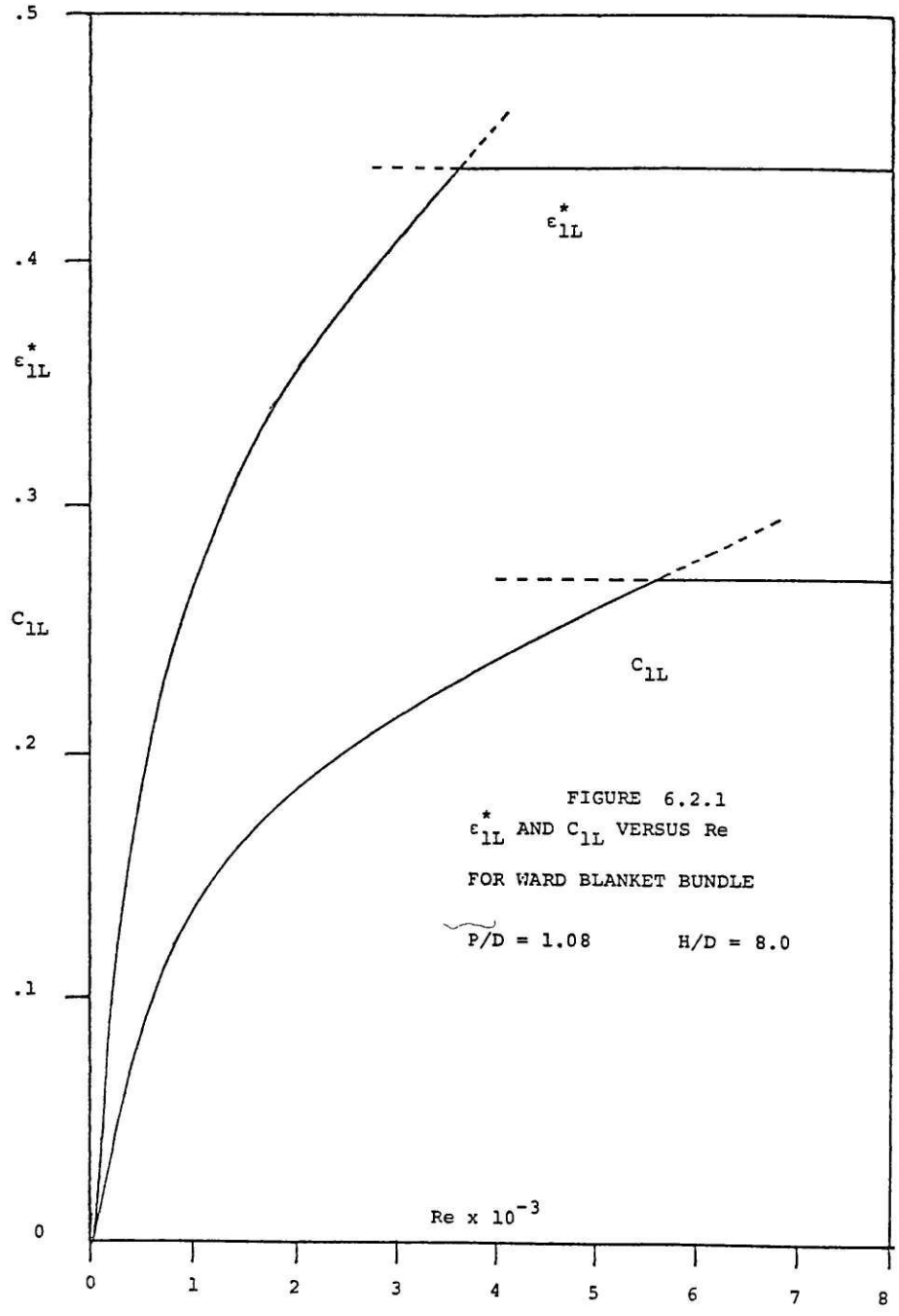


FIGURE 6.2.1

ε^*_{1L} AND C_{1L} VERSUS Re

FOR WARD BLANKET BUNDLE

P/D = 1.08 H/D = 8.0

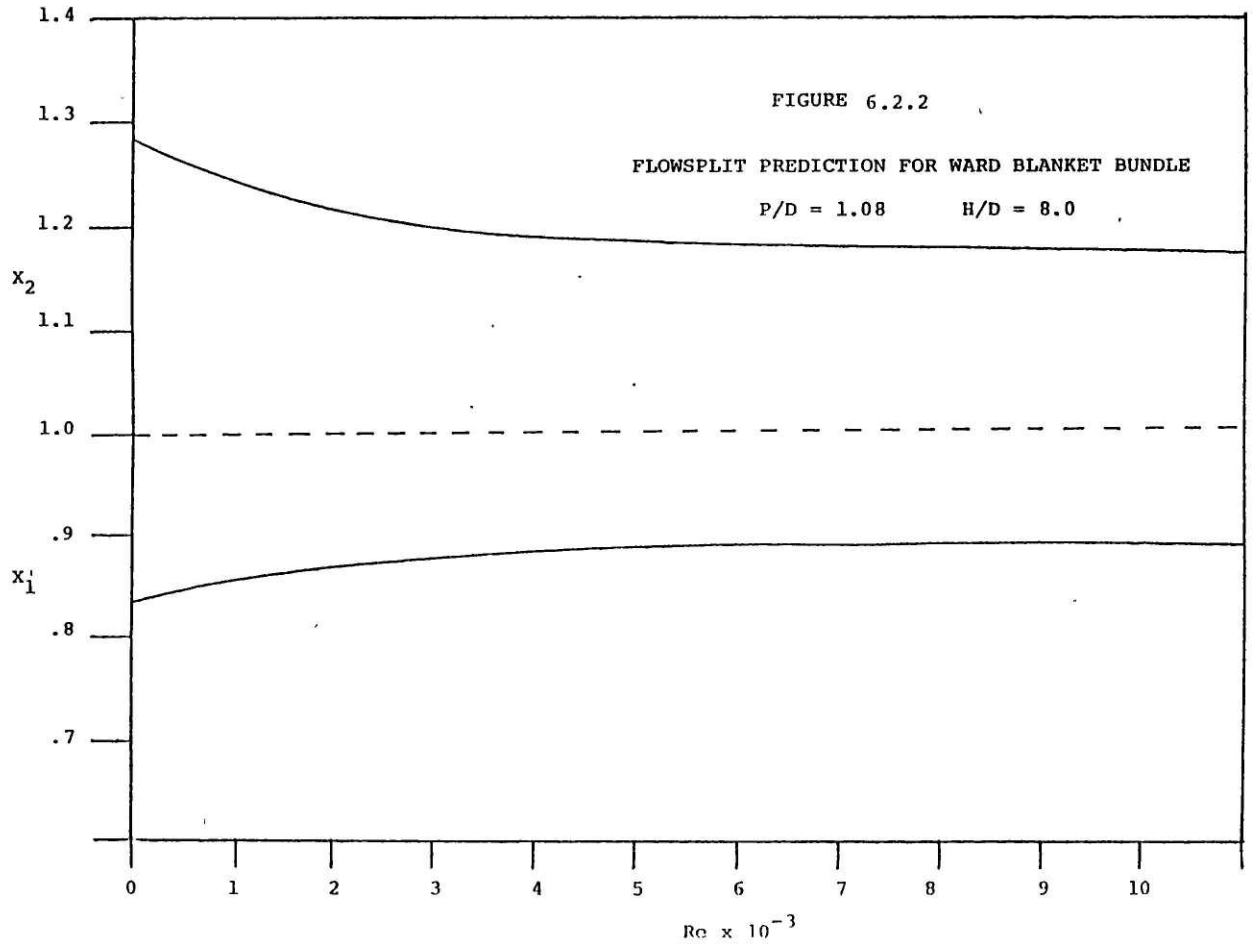


FIGURE 6.2.2

FLOWSPLIT PREDICTION FOR WARD BLANKET BUNDLE

P/D = 1.08 H/D = 8.0

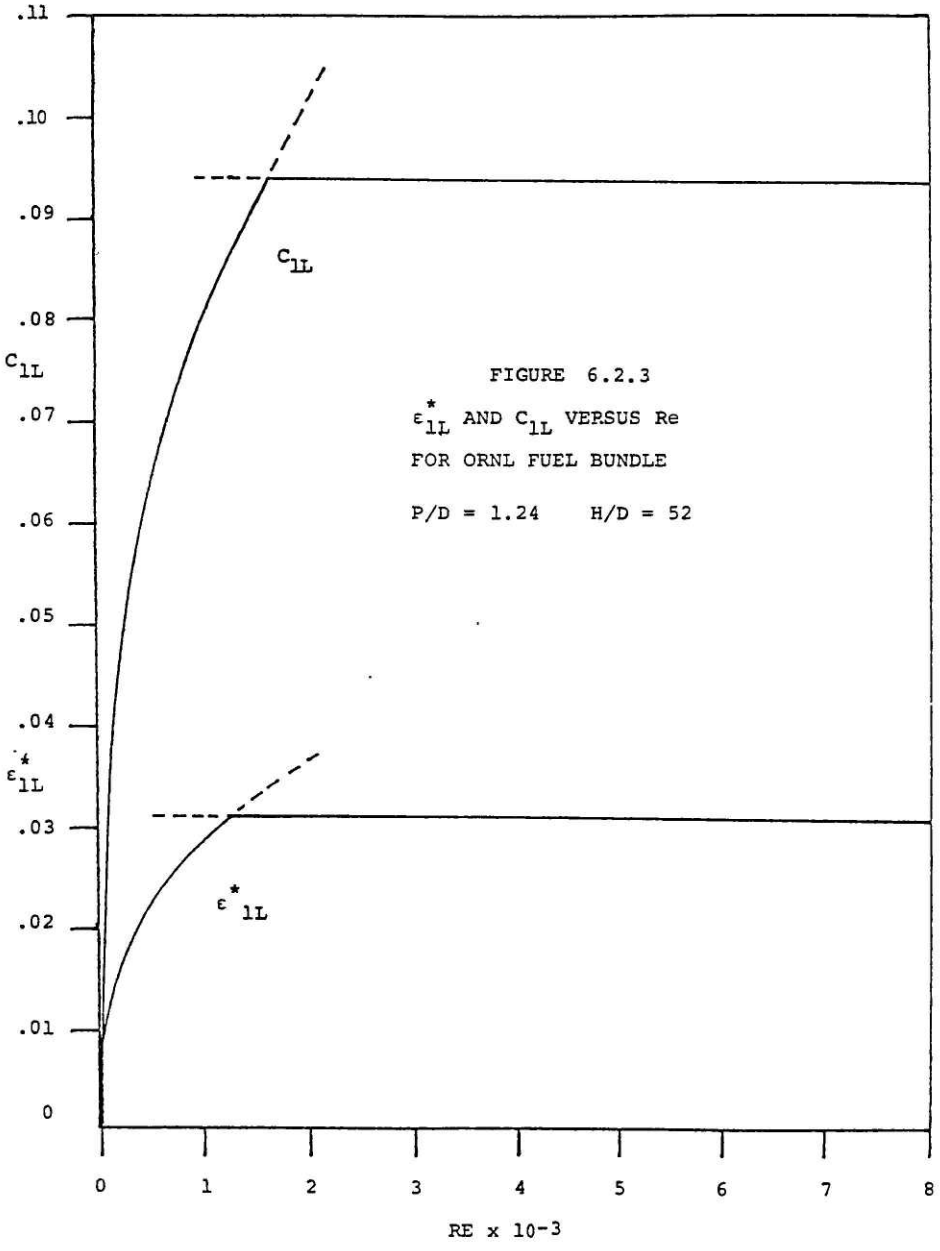


FIGURE 6.2.3

ε^*_{1L} AND C_{1L} VERSUS Re

FOR ORNL FUEL BUNDLE

P/D = 1.24 H/D = 52

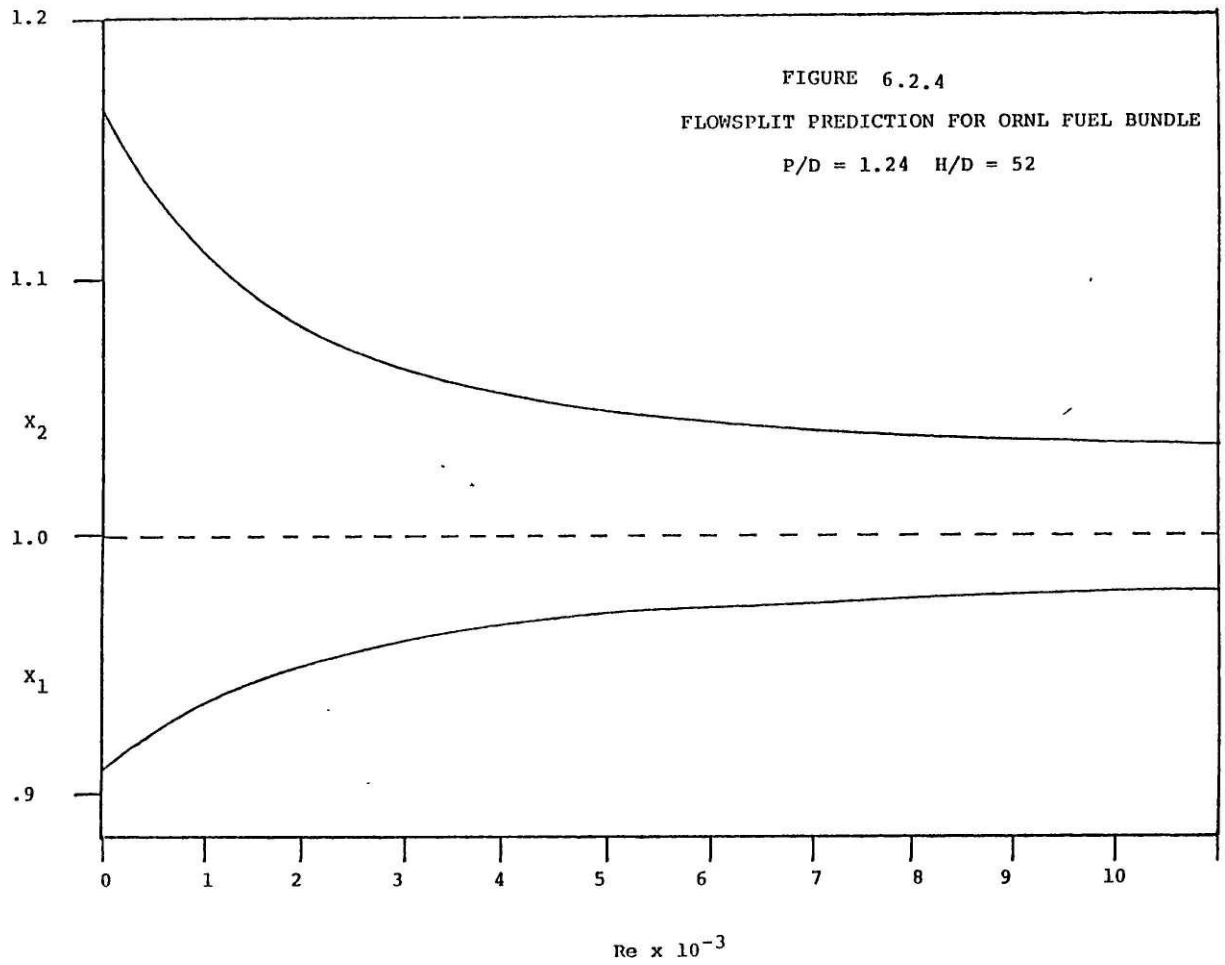


FIGURE 6.2.4

FLOWSPLIT PREDICTION FOR ORNL FUEL BUNDLE

P/D = 1.24 H/D = 52

TABLE 6.2.2

HAWLEY-CHIU FRICTION FACTORS FOR
BLANKET AND FUEL BUNDLES

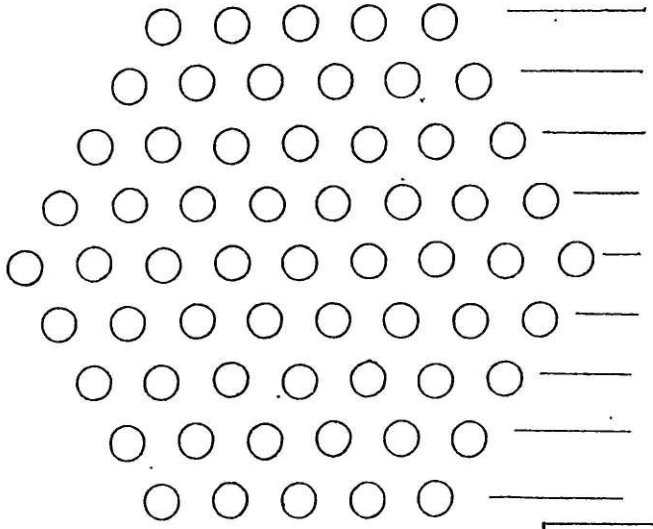
	BLANKET		FUEL	
	C_{fL}	C_{fT}	C_{fL}	C_{fT}
i = 1 Interior	121.9	.312	78.4	.161
i = 2 Edge	134.5	.264	92.7	.191
i = b Bundle	118.5	.283	80.5	.169

$$f_i = \left[\left(\frac{C_{fLi}}{Re}\right)^{\ell} + \left(\frac{C_{fTi}}{Re^{.18}}\right)^{\ell}\right]^{1/\ell}$$

$i = 1, 2, b$

TABLE 6.2.3

ROW POWER FACTORS AND CHANNEL POWER INPUTS FOR THREE POWER GRADIENTS



SKEW:	4.6:1	2.8:1	2.0:1
	.40	.635	.710
	.50	.678	.745
	.56	.713	.800
	.67	.796	.870
	.83	.882	.960
	1.06	1.026	1.060
	1.33	1.220	1.180
	1.71	1.473	1.300
	2.15	1.776	1.450
P_1 =	.302	.367	.408
P_2 =	.698	.634	.787

$$P_2 = (5p_1 + 6p_2 + 7p_3 + 8p_4 + 4.5p_5)/61 \qquad (6.2.5)$$

6.2.3 Comparison of the ENERGY Code and Two Channel Model Results

To provide a basis for direct comparison of ENERGY, and two channel model results, ENERGY was modified so that it calculated the two channel parameters T_1, T_2, V_1^* and V_2^* at each print out location. The averaging equations used are as follows:

$$V_K^* = \frac{1}{V_b A_K} \sum_{ch\ K} V_i A_i \qquad K=1,2 \qquad (6.2.6)$$

$$T_K = \frac{\sum_{ch\ K} V_i A_i T_i}{\sum_{ch\ K} V_i A_i} \qquad K=1,2 \qquad (6.2.7)$$

where $\sum_{ch\ K}$ indicates that the sum is taken over all subchannels in channel K. The dimensionless channel temperature ranges can be found from

$$\theta_K = \frac{T_K - T_{in}}{\Delta T_{bulk}} \qquad K=1,2 \qquad (6.2.8)$$

and the crossflow parameter C is found from:

$$C = 1 - V_{le}^* \qquad (6.2.9)$$

A series of runs were made with ENERGY to calibrate the mixing model (i.e. find F_g of Equation 6.2.1.) The results

of the ENERGY runs are outlined in Table 6.2.4, and the corresponding results for the two channel model are given in Table 6.2.5. A half sine wave crossflow profile [$f(x^*) = \frac{1}{2}(1 - \cos \pi x^*)$] and a 1.38 peak to mean chopped cosine axial power profile [$g(x^*) = 1.38 \cos(2.69(x^* - \frac{1}{2}))$] were used in the model.

Figure 6.2.5 compares the results of runs 1 to 5, which employed a 4.6:1 power gradient with Re=3105 and Gr_q=1209. For run #1 C_{1L}, ε^*_{1L} and SF were set equal to zero in ENERGY, and the forced convection and mixed convection options were run (1 FC and 1 MC in Table 6.2.4). For the forced convection case, this is simply a check of the energy balance, since no lateral energy transport exists. For the mixed convection run, the buoyancy induced crossflow is the only mechanism for lateral energy transport. For forced convection the ENERGY and TCM (two channel model) results are identical. For mixed convection TCM underestimates θ_{2e} and V^*_{2e} by .7% and 1.5%, respectively. This error is acceptable considering the approximate nature of the solution method employed in the two channel model (i.e., trial solution with undetermined parameters).

For run #2, conduction is included by setting SF=1.5 in both ENERGY and TCM. The lateral conduction causes a reduction in θ_{2e} and V^*_{2e}. The results of TCM are in good agreement, suggesting that the centroid to centroid distance employed in the lateral conduction term (ℓ in Equation 5.2.42) is a reason-

TABLE 6.2.4

ENERGY RESULTS

Run #	C_{1L}	ε^{*}_{1L}	SF	Re	Gr_q	Power skew	θ_{1e}	θ_{2e}	C
1 MC 1 FC	0	0	0	3105	1209	4.6:1	.608 .598	1.365 1.398	.054
2 MC	0	0	1.5	3105	1209	4.6:1	.633 .625	1.338 1.374	.052 0
3 MC 3 FC	0	.3143	1.5	3105	1209	4.6:1	.687 .679	1.291 1.319	.045 0
4 MC 4 FC	.2626	.3143	1.5	3105	1209	4.6:1	.739 .739	1.241 1.260	.038 0
5 MC 5 FC	.5252	.6286	1.5	3105	1209	4.6:1	.859 .857	1.137 1.142	.023 0
6 MC 6 FC	.2626	.3143	1.5	3105	1209	1:0	.387 .383	1.528 1.617	.091 0
7 MC 7 FC	.2626	.3143	1.5	3105	1209	2.8:1	.832 .828	1.162 1.173	.025 0
8 MC 8 EC	.2626	.3143	1.5	3105	1209	2.0:1	.881	1.114	.018
9 MC 9 FC	.1855	.2220	1.5	1223	1620	4.6:1	.839 .730	1.090 1.270	.295 0
10 MC 10 FC	.2102	.2516	1.5	1656	1400	4.6:1	.767 .728	1.169 1.273	.170 0
11 MC 11 FC	.2302	.2756	1.5	2148	1310	4.6:1	.748 .730	1.213 1.270	.096 0
12 MC 12 FC	.2681	.3549	1.5	5216	1245	4.6:1	.742 .741	1.253 1.259	.012 0

TABLE 6.2.5

TWO CHANNEL RESULTS

Run #	w_t^*	K^*	Re	Gr_q	P_2	P_1	θ_{1e}^{MC}	θ_{2e}^{MC}	C	θ_{2e}^{FC}
1A	0	0	3105	1209	.698	.302	.616	1.356	.0385	1.396
2A	0	.028	3105	1209	.698	.302	.636	1.338	.0372	--
3A B	.0675 .0900	.028	3105	1209	.698	.302	.680	1.299 1.287	.0342 .0331	1.316
4A B	.146 .1947	.028	3105	1209	.698	.302	.723	1.261 1.240	.0309 .0293	1.262
5A B	.2920 .3893	.028	3105	1209	.698	.302	.786	1.204 1.175	.0260 .0233	1.193
6A B	.1460 .1947	.028	3105	1209	1.000	0.000	.282	1.616 1.569	.0768 .0724	1.662
7A B	.1460 .1947	.028	3105	1209	.634	.367	.815	1.178 1.164	.0212 .0198	1.177
8A B	.1460 .1947	.028	3105	1209	.592	.408	.873	1.124 1.114	.0144 .0135	1.122

TABLE 6.2.5 (Continued)

Run #	w_t^*	K^*	Re	Gr_q	P_2	P_1	θ_{1e}^{MC}	θ_{2e}^{MC}	C	θ_{2e}^{FC}
9A B	.1036 .1381	.028	1223	1620	.698	.302	.831	1.088 1.086	.3160 .3105	1.262
10A B	.1171 .1709	.028	1656	1400	.698	.302	.765	1.170 1.161	.1606 .1543	1.263
11A B	.1282 .1709	.028	2148	1310	.698	.302	.741	1.219 1.205	.0837 .0797	1.261
12A B	.1562 .2083	.028	5216	1245	.698	.302	.718	1.278 1.254	.0078 .0072	1.261

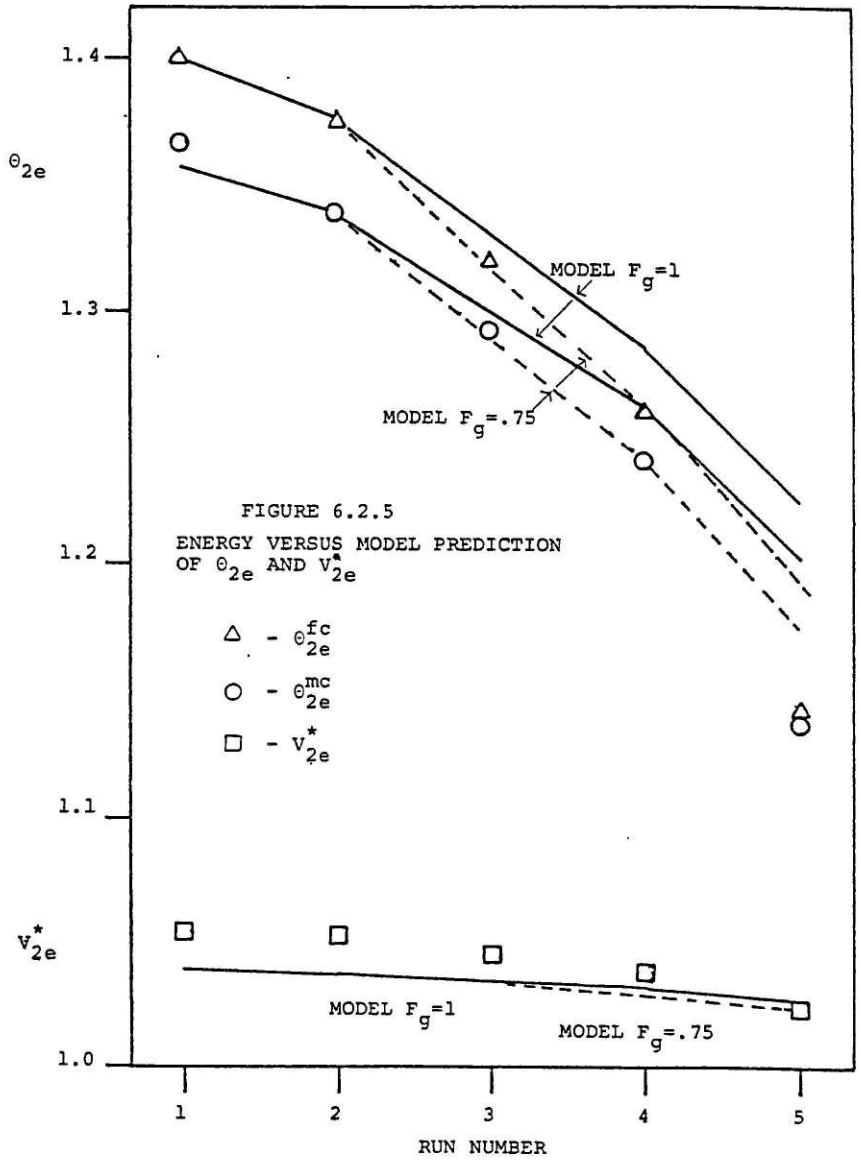


FIGURE 6.2.5
ENERGY VERSUS MODEL PREDICTION OF θ_{2e} AND V^*_{2e}

able conduction length. In run #3 interior mixing is included (ε^*_{1L} = .3143), and in run #4, the swirl is included (C_{1L} = .2626). These values for ε^*_{1L} and C_{1L} are approximately those predicted by the correlations of Reference 69 for the blanket bundle. For run #5 both ε^*_{1L} and C_{1L} were multiplied by a factor of two. The value of w^*_t calculated from Equation 6.2.2 with F_g = 1, was employed in TCM runs 3A, 4A, and 5A. It is observed that the mixing model with F_g = 1 causes TCM to overestimate θ_{2e}. It is necessary to calibrate F_g so that the mixing model (Equation 6.2.1) provides the correct lateral energy transport.

The calibration of F_g included all of the runs in Table 6.2.4, so that the effect of power skew (runs 6-8) and Reynolds number (runs 9-12) were also included, in addition to conduction and mixing (runs 1-5) as discussed above. It was found that F_g = .75 gave good agreement for most of the cases. The TCM results for F_g = 1 are given by runs 3A-12A in Table 6.2.5, and the results for F_g = .75 are given by runs 3B-12B.

Figure 6.2.5 shows the improvement which occurs for F_g = .75. Agreement is excellent for runs 3 and 4, but θ_{2e} for run 5 is still overpredicted. This indicates that F_g decreases with increasing mixing, but no efforts will be made to correlate this behavior since the mixing parameters in run #5 far exceed those which are obtained in the fuel and blanket assemblies.

The effect of changing the power skew is investigated in Figure 6.2.6 (runs 6, 7, 8 and 3 of Tables 6.2.1 and 6.2.2). Power skews of 2:1, 2.8:1, 4.6:1 (max/min linear gradient) and 1:0 (step change in power) were used. The Reynolds and Grashof numbers were held fixed. Only the mixed convection results are shown since the forced convection calculations are nearly the same as the mixed convection results. It is observed in Figure 6.2.6 that for $F_g = .75$ the ENERGY and model results are nearly identical up to a power skew of 4.6:1 or $P_2 - P_1 = .395$. For the 1:0 gradient ($P_2 - P_1 = 1.0$) the model overpredicts the ENERGY results by 3%, suggesting that F_g may be a weak function of the power gradient. Since the 1:0 gradient will not be encountered in practice, and since the dependence is not strong, the effect of power skew on F_g will be neglected.

The effect of Reynolds number on the predictions is exhibited in Figure 6.2.7 for low Re (run #9) the buoyancy induced crossflow is large, and the discrepancy between the forced and mixed convection solutions for θ_{2e} is large. As Re increases the crossflow decreases, and the forced and mixed convection predictions merge. The model gives good agreement to the ENERGY predictions. Figure 6.2.3 also shows how the onset of mixed convection may be identified by comparing the results of a forced convection and mixed convection calculation. Run #4 appears to be close to the onset since the discrepancy between the forced and mixed convection solutions is becoming significant.

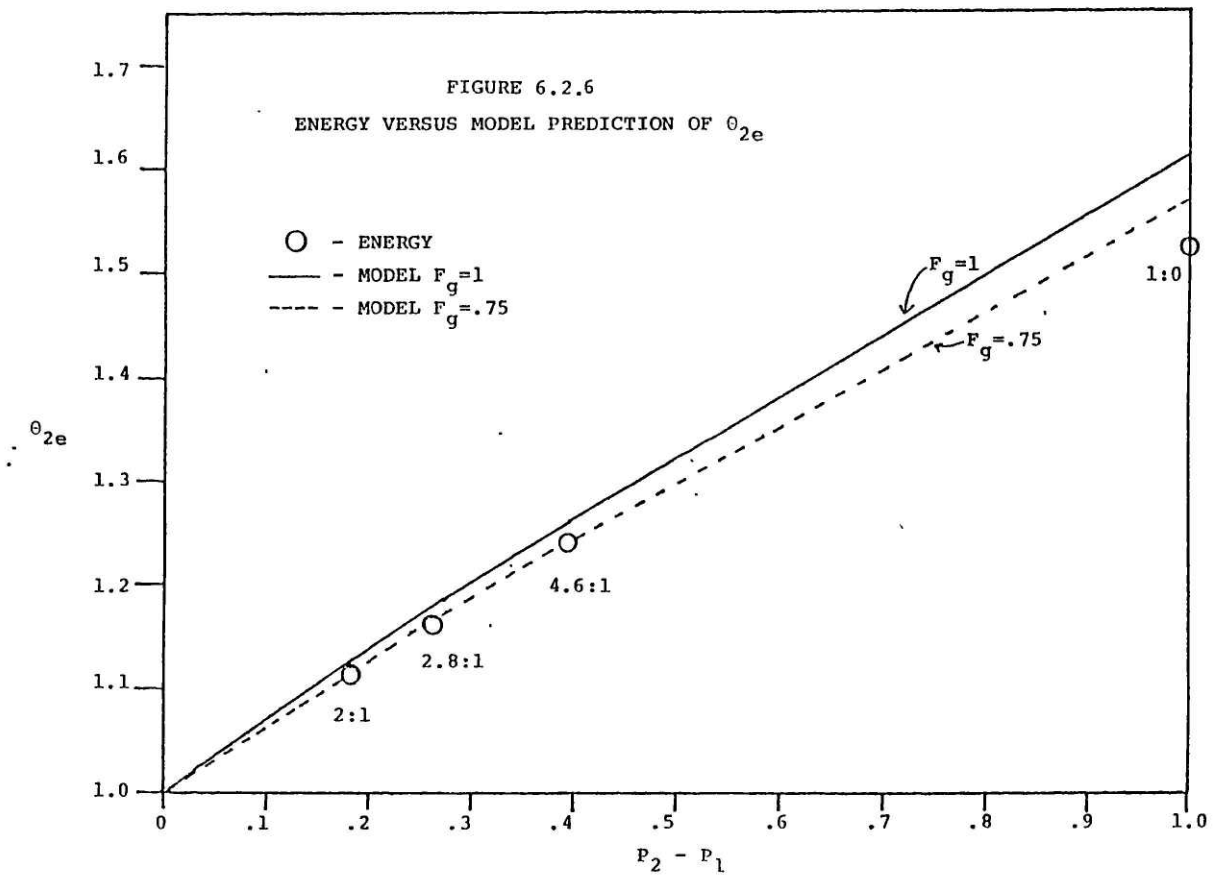
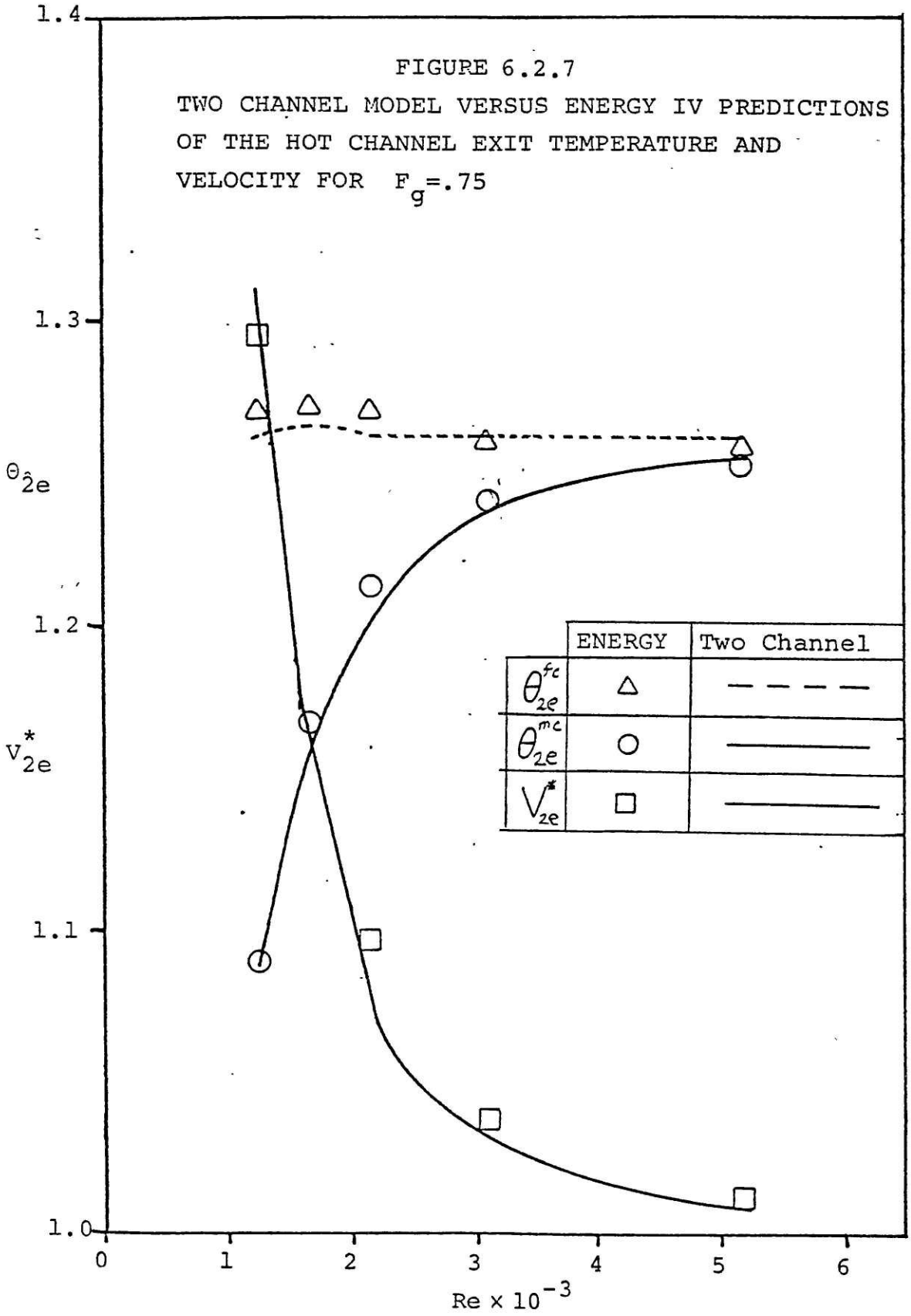

FIGURE 6.2.6
ENERGY VERSUS MODEL PREDICTION OF θ_{2e}
O - ENERGY
—— - MODEL F_g=1
---- - MODEL F_g=.75
F_g=1
F_g=.75
1:0
4.6:1
2.8:1
2:1
θ_{2e}
1.7
1.6
1.5
1.4
1.3
1.2
1.1
1.0
0
.1
.2
.3
.4
.5
.6
.7
.8
.9
1.0
$P_2 - P_1$

FIGURE 6.2.7

TWO CHANNEL MODEL VERSUS ENERGY IV PREDICTIONS OF THE HOT CHANNEL EXIT TEMPERATURE AND VELOCITY FOR $F_g = .75$



For the five mixed convection ENERGY runs of Figure 6.2.7 the hot channel axial velocity and crossflow was plotted as a function of axial distance in Figures 6.2.8 and 6.2.9. The axial velocity profile function (obtained from the ENERGY results from Equation 6.1.1) for the same 5 runs are plotted in Figure 6.2.10. As the Reynolds number decreased, and the buoyancy induced crossflow increased the crossflow profile becomes skewed toward the inlet. For run #9 the crossflow reversed sign near the outlet of the bundle. This was also observed in the COBRA results given earlier in this chapter.

Since the two channel model will be used as an onset of mixed convection criterion, run #4 (which is close to the onset of mixed convection) will be given further consideration. For the ENERGY and two channel model results presented so far in this section a 1.38 peak to mean chopped cosine axial power profile was used, since that is what exists in LMFBR applications. Run #4 was rerun with a uniform axial power profile. Figure 6.2.11 shows θ_{2e} plotted as a function of x^* for run #4. It is observed that the uniform axial power case gives the same exit temperature ($x^* = 1.0$) and midplane temperature ($x^* = .5$) as the chopped cosine power profile. The results differ at other axial locations due to the different axial power profiles. The ENERGY predicted temperatures agree very well with the model prediction with a chopped cosine. For the onset of mixed convection criteria only the exit temperature is needed, hence the uniform axial power profile ($g(x^*) = 1$) does equally well.

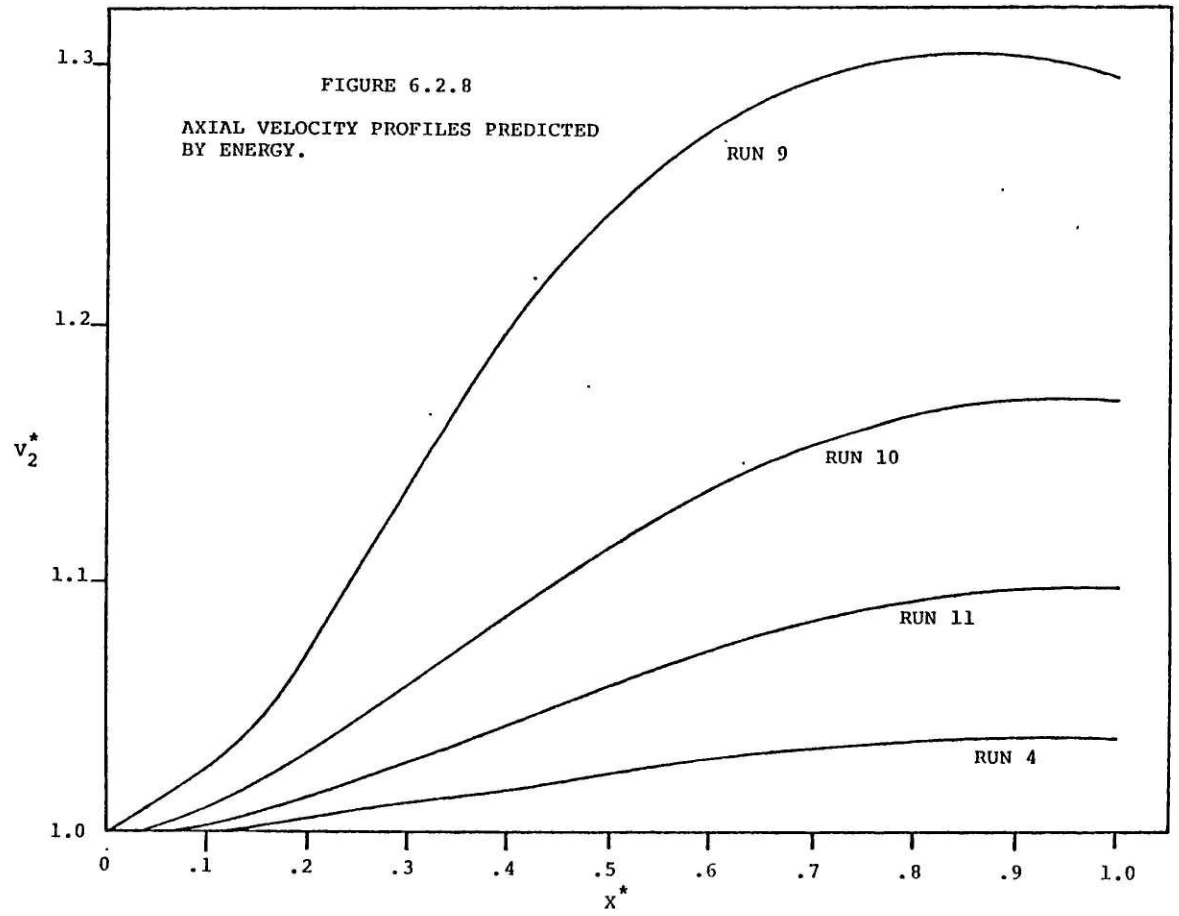


FIGURE 6.2.8

AXIAL VELOCITY PROFILES PREDICTED BY ENERGY.

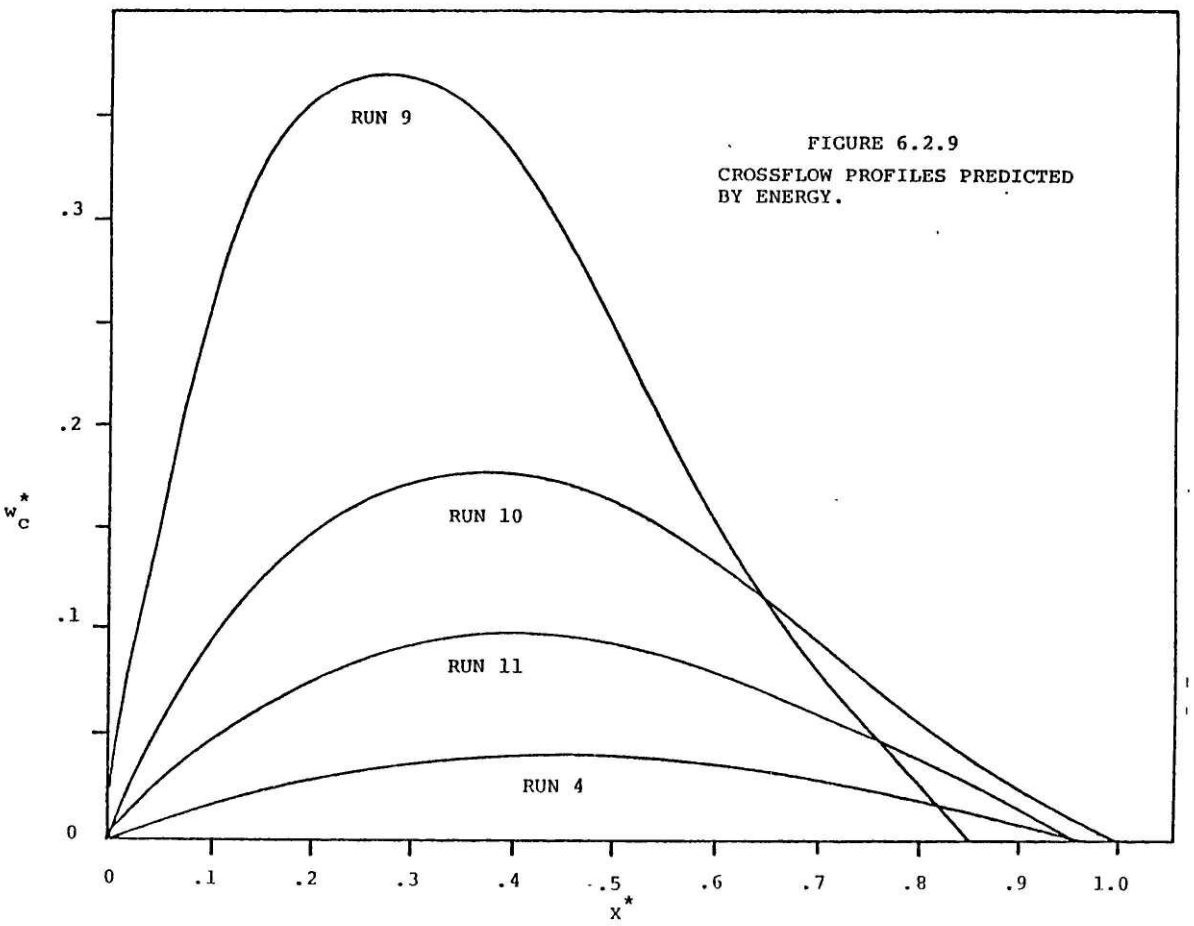


FIGURE 6.2.9

CROSSFLOW PROFILES PREDICTED BY ENERGY.

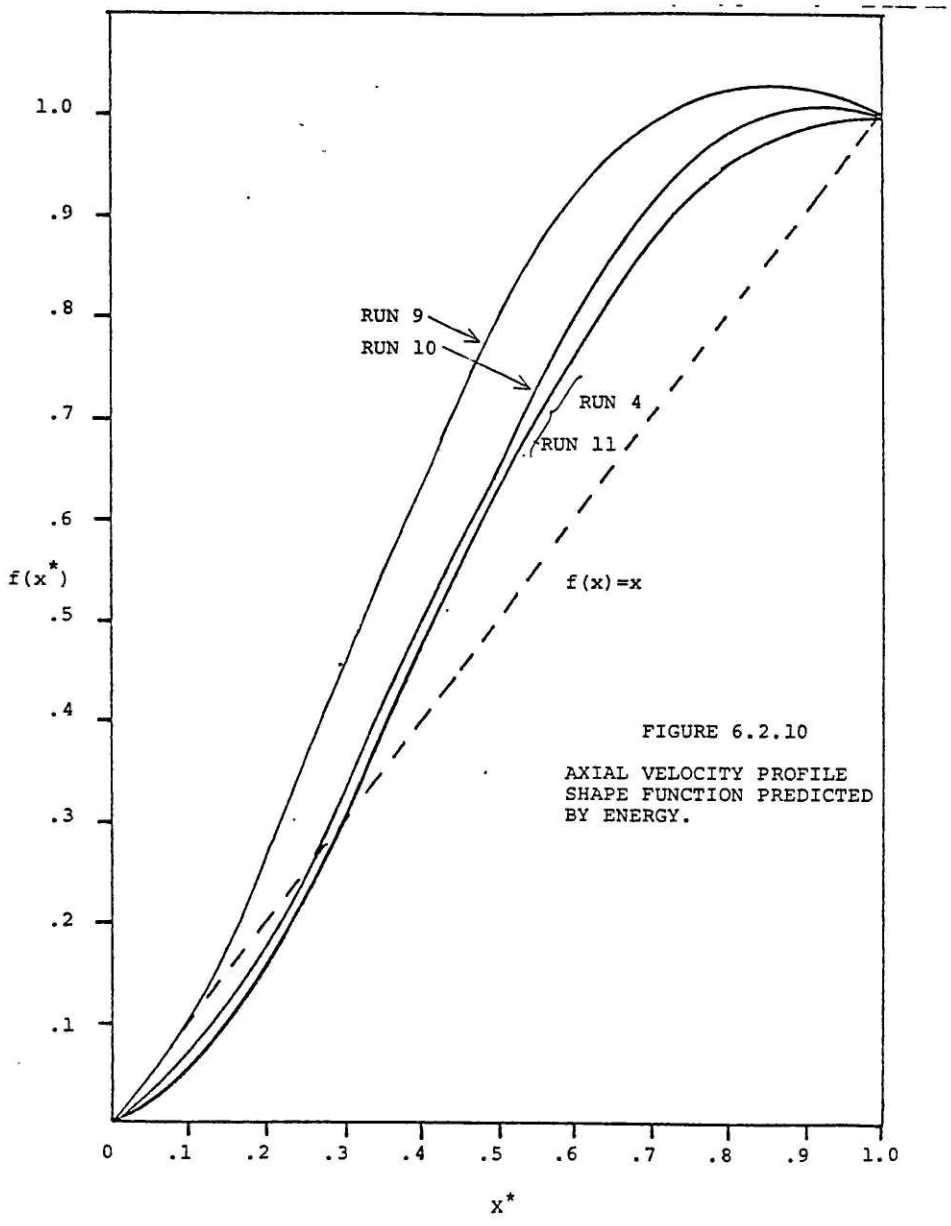
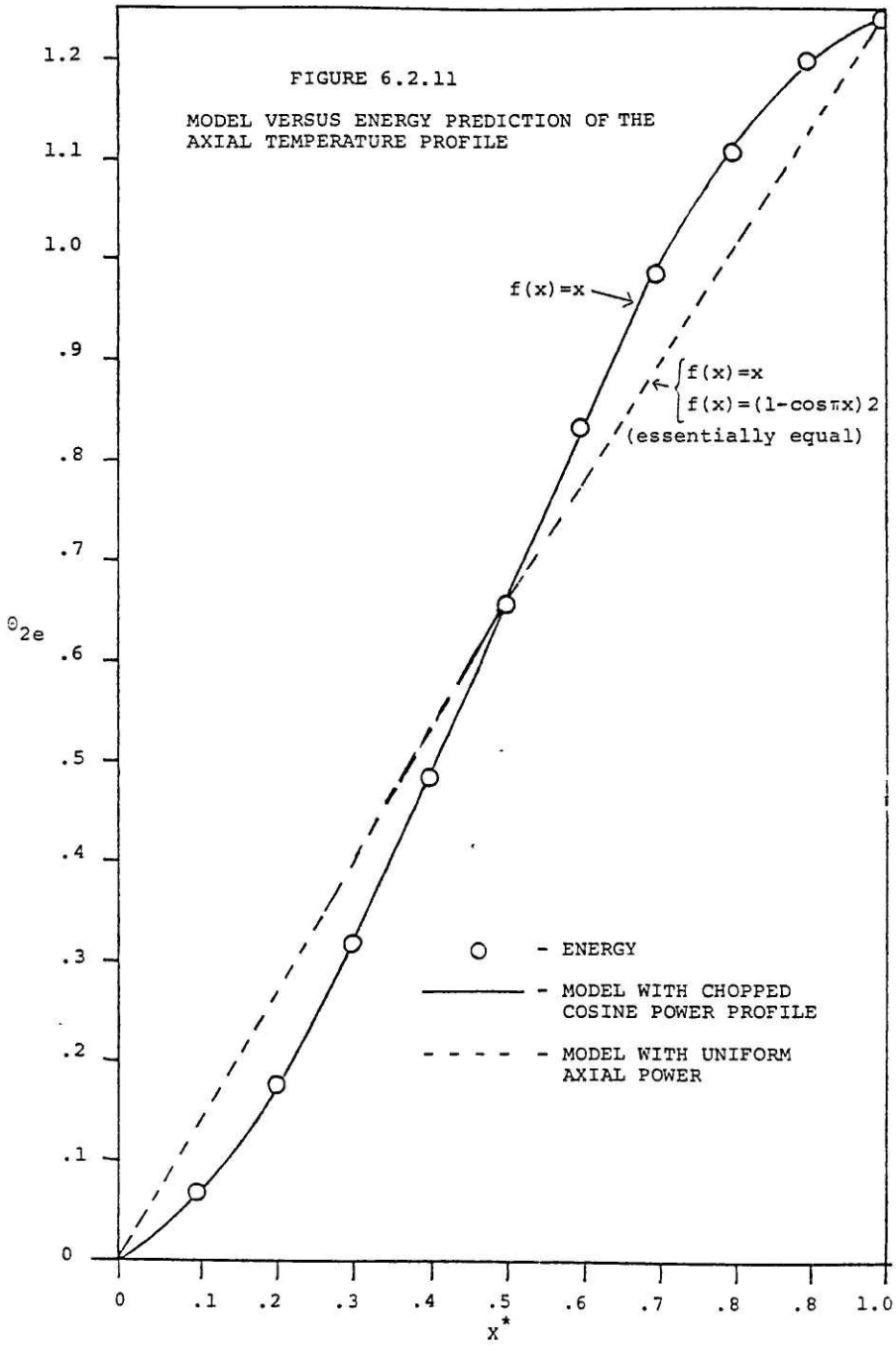


FIGURE 6.2.10

AXIAL VELOCITY PROFILE SHAPE FUNCTION PREDICTED BY ENERGY.


FIGURE 6.2.11
MODEL VERSUS ENERGY PREDICTION OF THE AXIAL TEMPERATURE PROFILE
f(x)=x
f(x)=x
f(x)=(1-cosπx)2
(essentially equal)
- ENERGY
- MODEL WITH CHOPPED COSINE POWER PROFILE
- MODEL WITH UNIFORM AXIAL POWER
Θ2e
X*
0
.1
.2
.3
.4
.5
.6
.7
.8
.8
1.0
1.2
1.1
1.0
.9
.8
.7
.6
.5
.4
.3
.2
.1
0

It was also found that there is essentially no difference between using $f(x^*) = \frac{1}{2}(1 - \cos \pi x^*)$ and $f(x^*) = x^*$ at onset of mixed convection conditions. Hence for future calculations $f(x^*) = x^*$ and $g(x^*) = 1$ will be used.

CHAPTER 7

CRITERIA FOR ONSET OF FLOW RECIRCULATION IN VERTICAL ROD BUNDLES

The onset of recirculation criterion may be used to identify when reverse flow may exist in a rod bundle with a forced upward flow. Flow reversal occurs in cooler regions of the rod bundle where the fluid has a higher density if the forced flow is not sufficient to counteract the downward buoyancy forces.

There are several reasons why a recirculation criterion is needed. First, it identifies a regime which should be avoided in design since the accuracy of numerical predictions of the temperature field are suspect for recirculating flows, and the potential for local overheating exists. Second, it gives a means of determining what type of numerical tool is needed for detailed analysis of the rod bundle. If no recirculation exists, explicit (marching) methods may be employed, where reverse flows require implicit methods.

Whether flow recirculation will occur in a bundle for the conditions which exist in a reactor is an open question which should be resolved by this work. In an LMFBR the power gradients are large enough for recirculation to be of concern, but radial conduction and wire induced mixing tend

to reduce buoyancy effects. In a water reactor the power gradients are not very large, so flow recirculation may not be a problem.

7.1 LITERATURE REVIEW

Flow recirculation in rod bundles has been observed experimentally by several investigators. In Reference 59 recirculation was observed in a water cooled 2 x 6 rod bundle for controlled flow transients for a step change in power with half the bundle unheated. Flow recirculation existed in one of the three steady state runs in the 2 x 6 rod bundle in Reference 58 . Recirculation was also observed by Wang (Reference 1) in a 4 rod bundle, but no data was given to indicate under what conditions the recirculation occurred. Namekawa (Reference 71) observed flow recirculation under natural convection conditions in a 37 pin hexagonal bundle but no recirculation was observed, for single phase mixed convection, recirculation in rod bundles can be predicted by the COBRA-IV and COBRA-WC codes with an implicit solution scheme.

An experimental study is underway at Westinghouse to determine if flow recirculation will occur in the LMFBR blanket bundle, but no data is available yet.

7.2 EXPERIMENTAL DETERMINATION OF THE ONSET OF FLOW RECIRCULATION IN THE MIT 4 x 4 ROD BUNDLE

7.2.1 Bundle Instrumentation

The MIT 4 x 4 rod bundle was used to experimentally determine the onset of recirculation over a wide range of bundle power inputs and radial power profiles. The bundle was instrumented as shown in Figures 7.2.1 and 7.2.2. A dye injection probe was used to inject a dye tracer near the outlet of the bundle in any of the five gaps. The dye was observed through the top window, and indicated whether upflow or downflow existed in the injection subchannel. The top window was used because recirculation starts at the top of the bundle. For a given power input and radial power profile, the bundle flow rate was varied until the onset of recirculation condition was observed; that is, the transition from upflow to downflow. In all of the cases investigated, downflow occurred first in the edge subchannel most distant from the high power side of the bundle. The bundle was also instrumented with five thermocouples at the end of the heated length. The thermocouples could also be used to detect recirculation since hot fluid from the upper plenum enters the cold side of the bundle when reverse flow occurs.

The six radial power profiles which were employed are shown in Figures 7.2.3 and 7.2.4. Power profiles 1, 2, and 3 were with 1, 2 and 3 rows uniformly heated. Profile #4

FIGURE 7.2.1
UPPER REGION OF BUNDLE

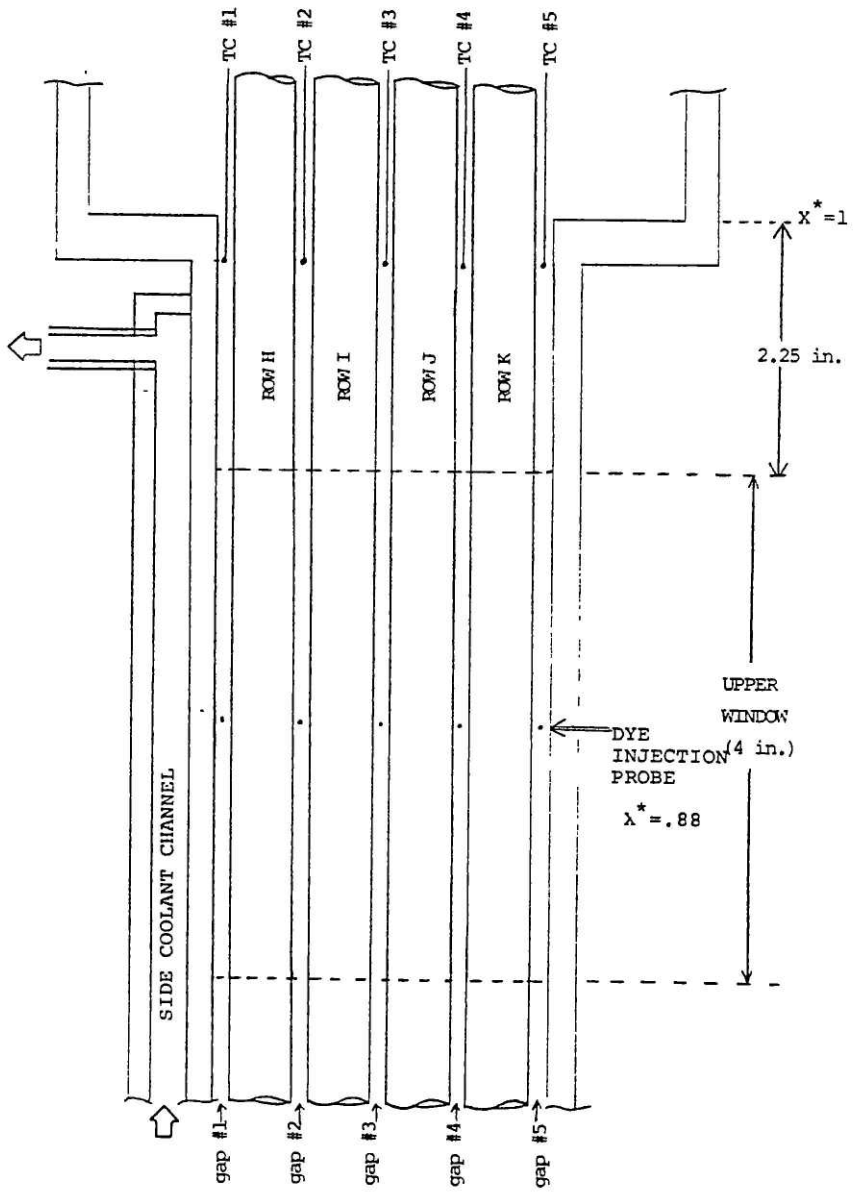


FIGURE 7.2.2

CROSS SECTION OF TEST SECTION

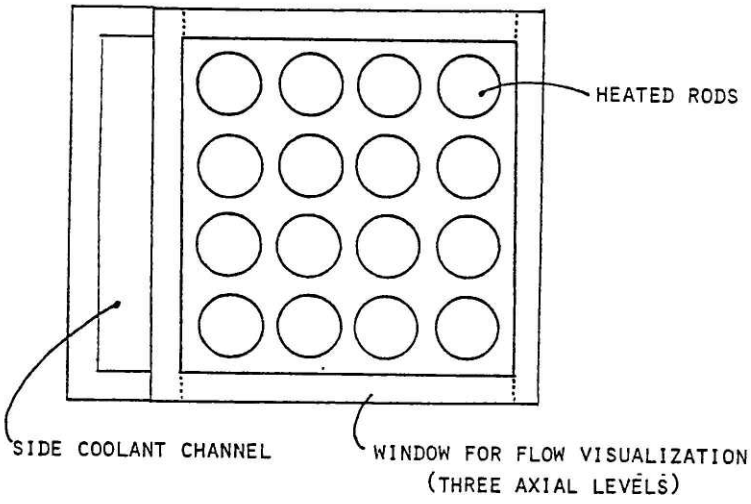


FIGURE 7.2.3

POWER GRADIENTS USED IN RECIRCULATION EXPERIMENTS

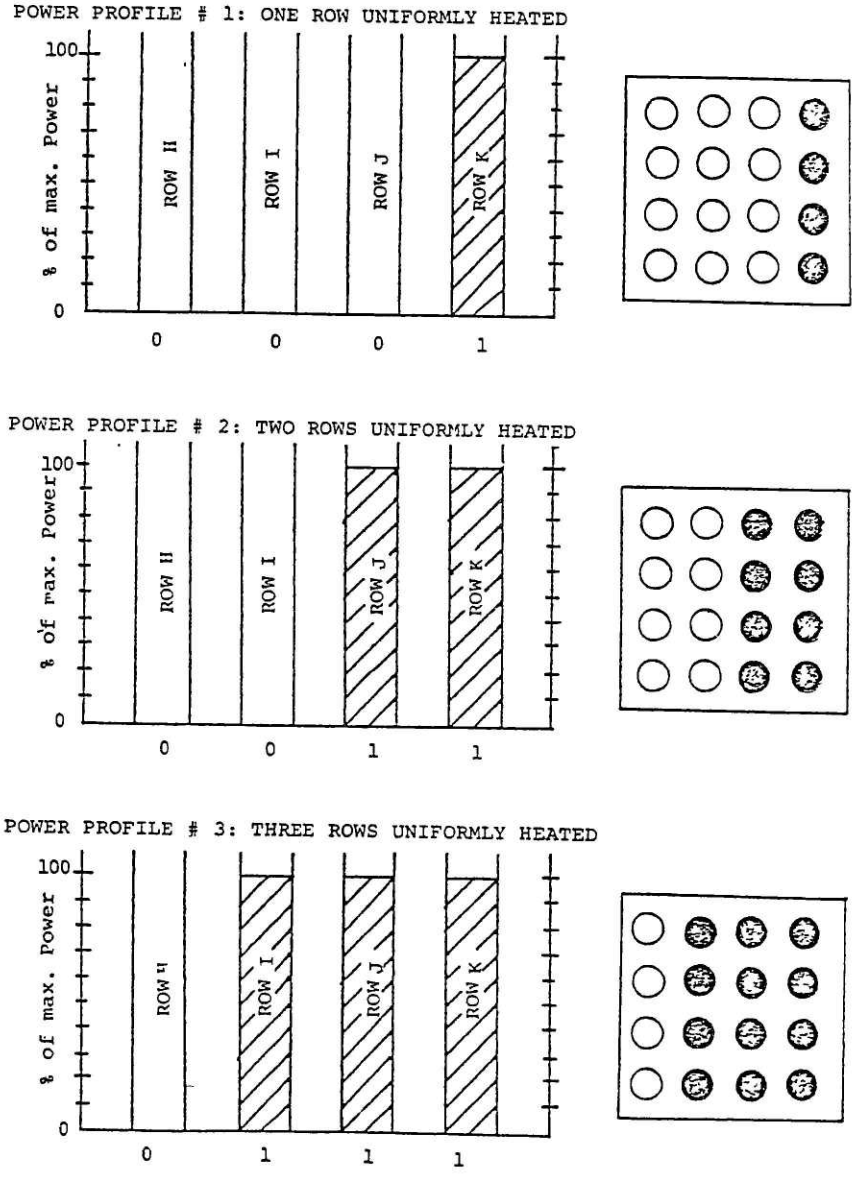
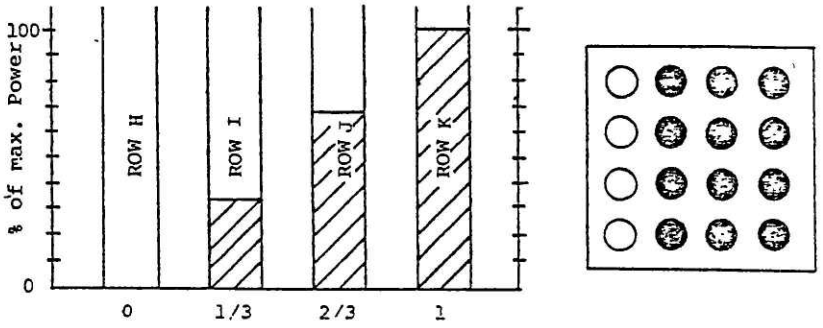


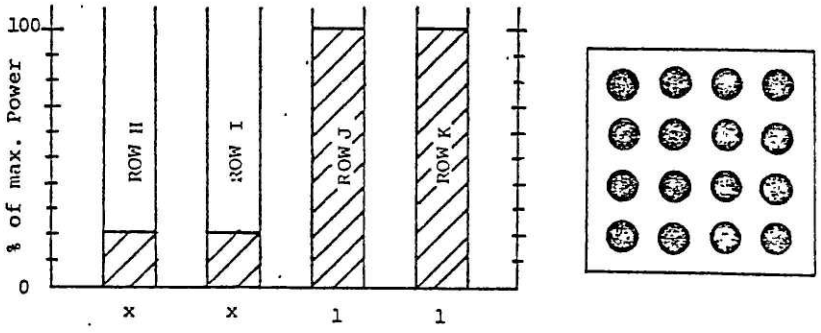
FIGURE 7.2.4

POWER GRADIENTS USED IN RECIRCULATION EXPERIMENTS

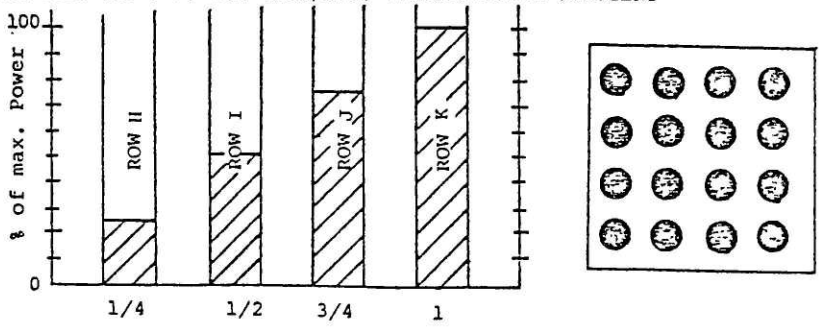
POWER PROFILE # 4: LINEAR GRADIENT WITH ROW H UNHEATED



POWER PROFILE # 5: STEP CHANGE IN POWER



POWER PROFILE # 6: 4:1 (max/min) LINEAR POWER GRADIENT



is a linear power gradient with one row unheated. Profile #5 is a step change in power with all rods heated. Profile #6 is a 4:1 linear power gradient with all rods heated. The power skew for profile #6 is 4:1 (max to min) which is typical of the LMFBR radial blanket assembly.

A plexiglass side wall coolant channel is located on one wall of the bundle. Cold water can be passed through this channel to simulate the effect of interassembly heat transfer. As seen in Figure 7.2.2 the bundle was wrapped with fiberglass insulation and a vapor barrier to prevent heat loss. The coolant flow to both the bundle and the side channel could be controlled, and the bulk inlet and outlet temperatures could be measured.

7.2.2 Dye Injection Method Versus Outlet Thermocouple Technique for Determining the Onset of Recirculation

In this section, typical onset of recirculation data points will be discussed, and an analysis of errors presented. The first case considered is two rows uniformly heated at 500 w/rod. Dye injection data and temperature profiles were obtained over a range of bundle flow rates. The data is given in Table 7.2.1, and the temperature profiles are shown in Figure 7.2.5. Ten temperature readings were taken for each thermocouple, and the mean and standard deviation was calculated. At the initial flow rate of 70% full scale (1.372 GPM) the dye injection results showed upflow in all channels. The corresponding temperature profile is shown in Figure 7.2.5 with the symbol (⊡). Note

FIGURE 7.2.5

DYE INJECTION AND THERMOCOUPLE DATA WITH TWO ROWS HEATED AT 500 WATTS PER ROD

% G_{max}	SYMBOL	DYE	T.C.
.70	□	↑	↑
.51	⬡	↑	↑
.46	△	↑	↓
.41	○	↓	↓
.38	▽	↓	↓

G_{max}=1.96 GPM

↑ Indicates upflow
↓ Indicates downflow

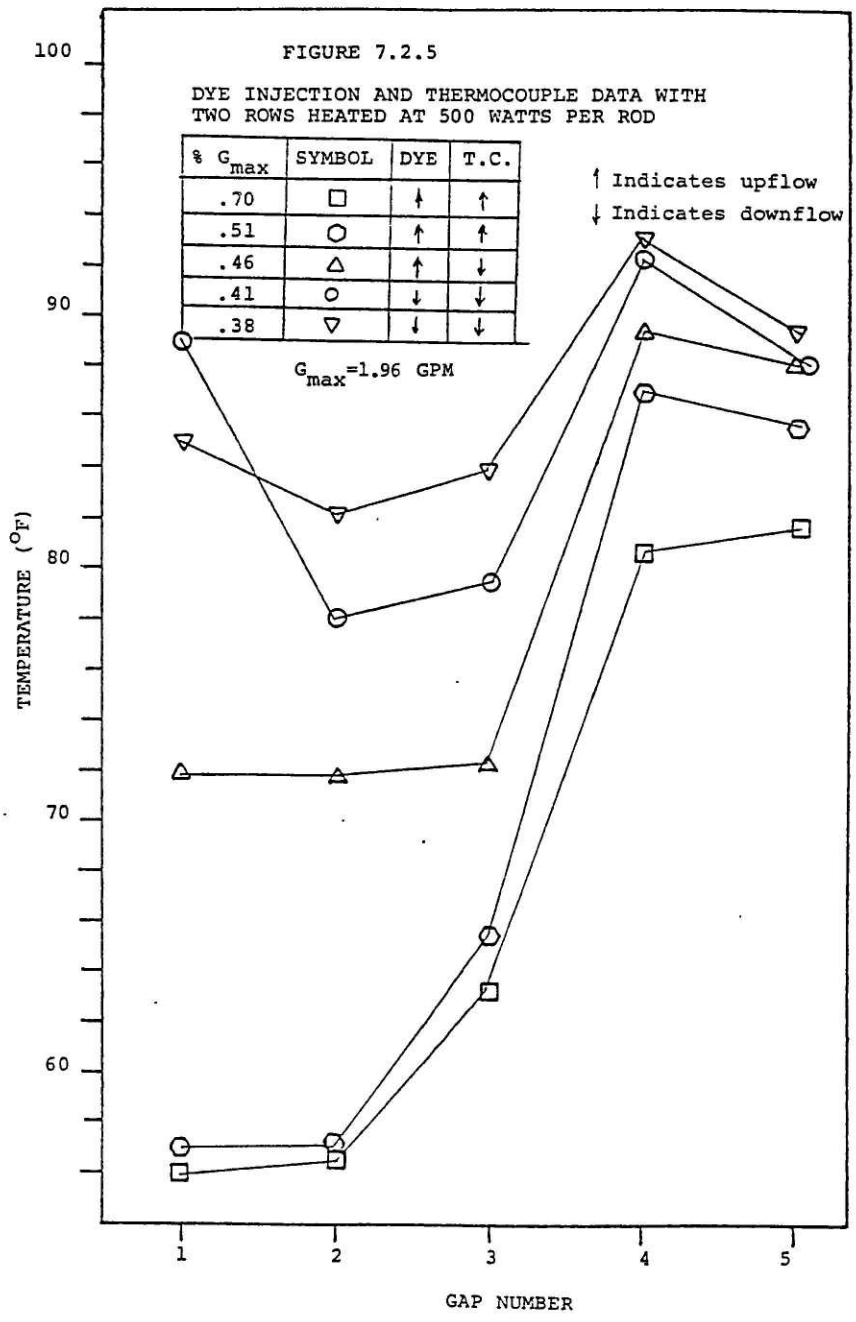


TABLE 7.2.1

DATA FOR DETERMINING ONSET OF RECIRCULATION
FOR TWO ROWS HEATED AT 500 W/ ROD

Bundle Flow		Bulk Temperature Rise (F)		Mean Temperature/Standard Deviation						
% Full Scale (1.96)	GPM	Measured	Calculated	T_1/S_1	T_2/S_2	T_3/S_3	T_4/S_4	T_5/S_5	Dye	Symbol
70	1.372	19.0	20.1	56.0 -	56.5 -	63.2 2.7	80.7 1.3	81.7 1.8	↑	□
51	1.00	25.5	27.6	57.0 -	57.0 -	65.5 3.4	87.0 3.2	85.7 1.4	↑	+
46	.902	31.0	30.6	72.0 -	71.8 1.7	72.3 2.3	89.6 3.0	88.2 1.9	↑	△
41	.804	33.0	34.3	89.0 -	78.0 -	79.5 2.4	92.3 2.3	88.1 1.5	↓	○
38	.747	36.0	37.0	85.0 1.8	82.1 1.3	83.8 5.5	93.0 1.3	89.4 1.7	↓	▽

that at the unheated side of the bundle (gaps 1 and 2), the exit temperatures are the same as the inlet temperature to the bundle ($56^{o}F$), indicating no recirculation. This also indicates that transverse energy transport due to conduction and coolant mixing can be neglected.

The bundle flow rate was then reduced to 51% full scale, and the flow was allowed to reach a steady state condition before any measurements were taken. Both the dye injection and thermocouple results indicated no recirculation was occurring. Reducing the flow rate to 46% full scale caused the thermocouples in gaps 1 and 2 to read $16^{o}F$ higher than the inlet temperature, indicating that flow near the bundle exit in gaps 1 and 2 has reversed, causing the hot fluid in the upper plenum to contact the thermocouples. However, the dye injection results indicated that the flow was still going upward at the injection location, though it moves toward the heated side of the bundle due to the buoyancy induced crossflow. This occurs because the recirculation zone starts at the bundle exit ($x^{*} = 1.00$). Further reductions in the bundle flow are required before the recirculation zone moves down to the dye injection location ($x^{*} = .88$). Further reducing the flow to 41% full scale caused the injected dye to flow downward.

Similar results are presented in Table 7.2.2 and Figure 7.2.6 for one row heated at 1500 w/rod (profile #1). For the 85% full scale run the thermocouple measurements indicate

FIGURE 7.2.6

DYE INJECTION AND THERMOCOUPLE DATA
WITH ONE ROW HEATED AT 1500 WATTS PER ROD

% G_{max}	SYMBOL	DYE	T.C.
.90	□	↑	↑
.88	⬡	↑	↑
.85	△	↓	↑
.80	○	↓	↓

G_{max}=1.96 GPM

↑ Indicates upflow

↓ Indicates downflow

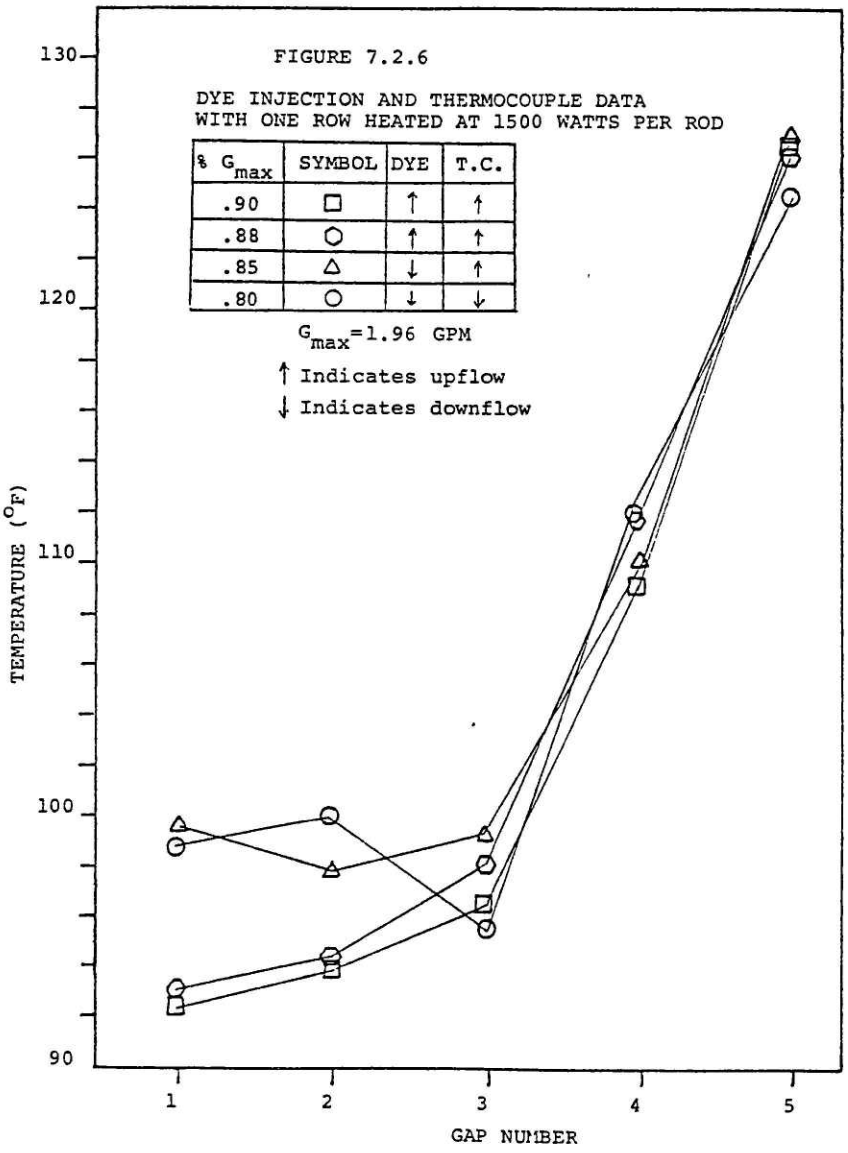


TABLE 7.2.2

DATA FOR DETERMINING ONSET OF RECIRCULATION
FOR ONE ROW HEATED AT 1500 W/ROD

Bundle Flow		Bulk Temperature Rise (F)		Mean Temperature/Standard Deviation						
% Full Scale (1.96)	GPM	Measured	Calculated	T_1/S_1	T_2/S_2	T_3/S_3	T_4/S_4	T_5/S_5	Dye	Symbol
90	1.764	25.5	23.5	92.3 1.0	94.0 1.3	96.4 2.7	109.1 4.1	126.5 3.0	↑	□
88	1.725	25.5	24.1	93.0 .7	94.1 .7	98.1 2.4	112.1 6.3	126.7 2.3	↑	+
85	1.666	26.0	24.9	99.6 1.1	97.8 1.2	99.3 3.1	110.1 7.0	126.8 4.0	↑	△
80	1.568	26.0	26.5	98.9 1.4	100.0 1.2	95.5 2.5	112.1 6.6	124.5 5.0	↓	○

that recirculation has occurred near the outlet, while at the dye injection location upflow still exists. Further reduction in flow to 80% full scale causes the flow recirculation zone to move down to the dye injection location.

These results indicate that the flow rate at the onset of recirculation as measured by the dye injection technique is about 5% less than the flow rate at the onset of recirculation given by the outlet thermocouple measurements. The drawback of the outlet thermocouple technique is that it fails to identify recirculation for power gradients where all of the rods are heated. We will therefore adopt the dye injection method, and include the 5% difference in the error bar of the data.

7.2.3 Onset of Recirculation Data

Onset of recirculation data was obtained for the six power profiles of Figures 7.2.3 and 7.2.4. For each power profile, a number of runs were taken over a range of bundle powers. Several data points were taken with side channel cooling for power profiles 2 and 6.

The results of the dye injection experiments are given in Figures 7.2.7 and 7.2.11 for the six power profiles. The flowmeter reading (% of full scale) is plotted against run number for each power profile. For each run, the flowrate was varied, and the results of the dye injection are indicated as pure upflow (Δ), pure downflow (∇), stagnant flow (O),

FIGURE 7.2.7

DYE INJECTION DATA FOR PROFILE #1

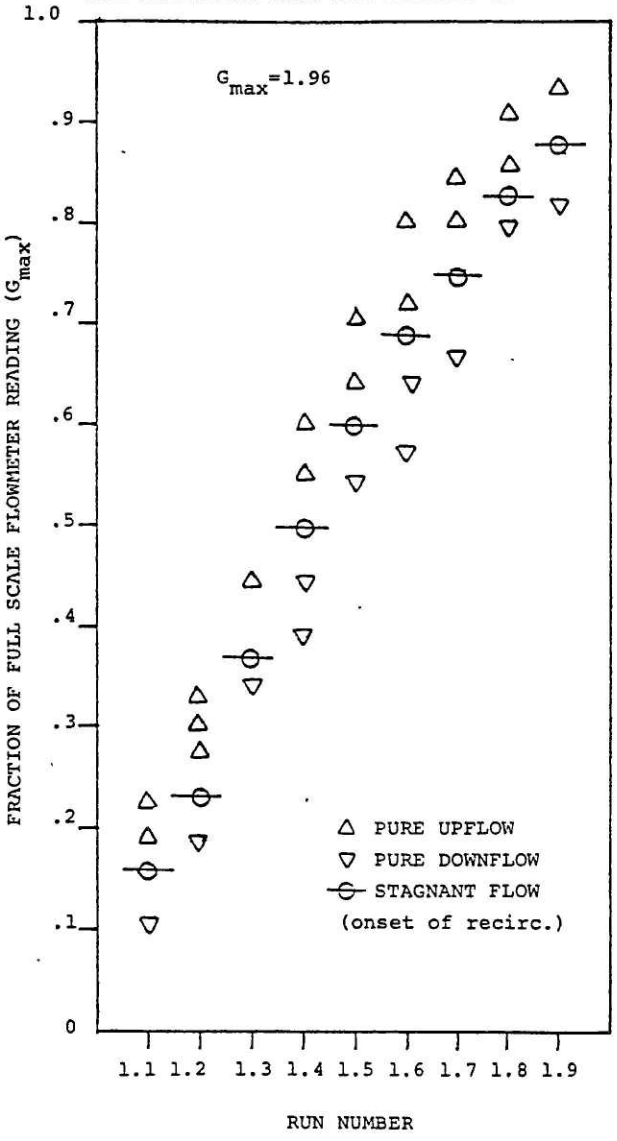


FIGURE 7.2.8

DYE INJECTION DATA FOR PROFILE #2

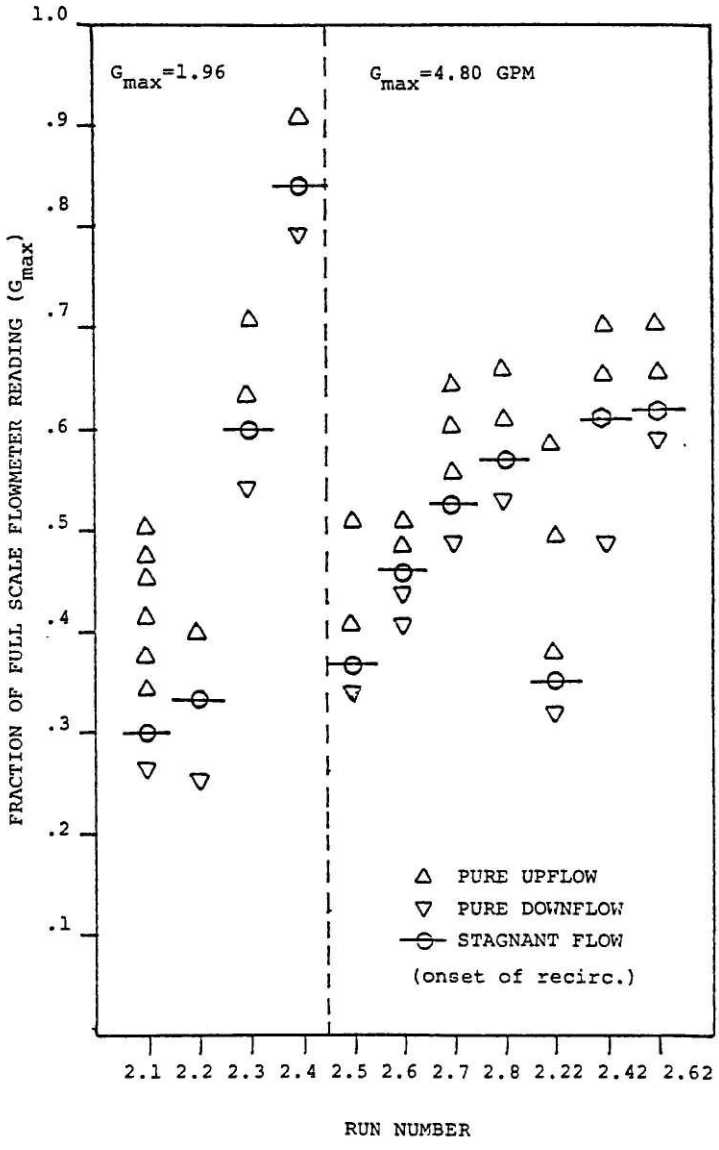


FIGURE 7.2.9

DYE INJECTION DATA FOR PROFILE #3

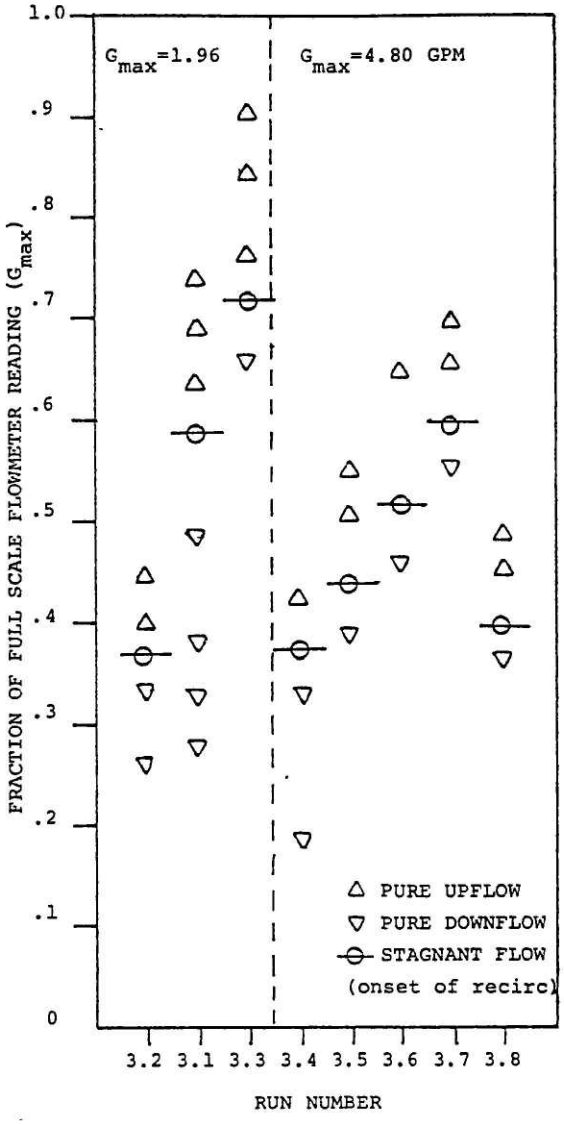


FIGURE 7.2.10

DYE INJECTION DATA FOR PROFILE #5

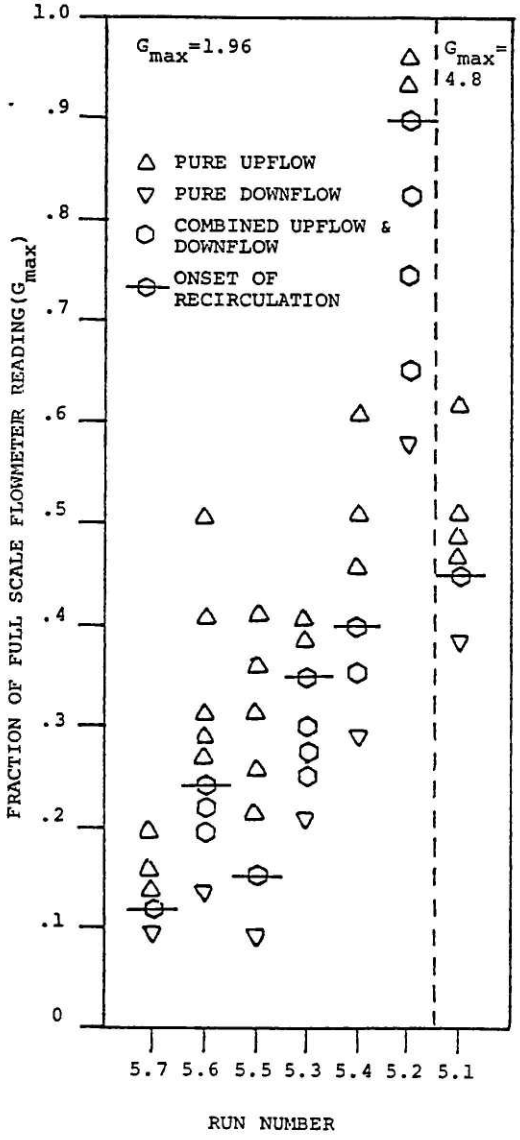
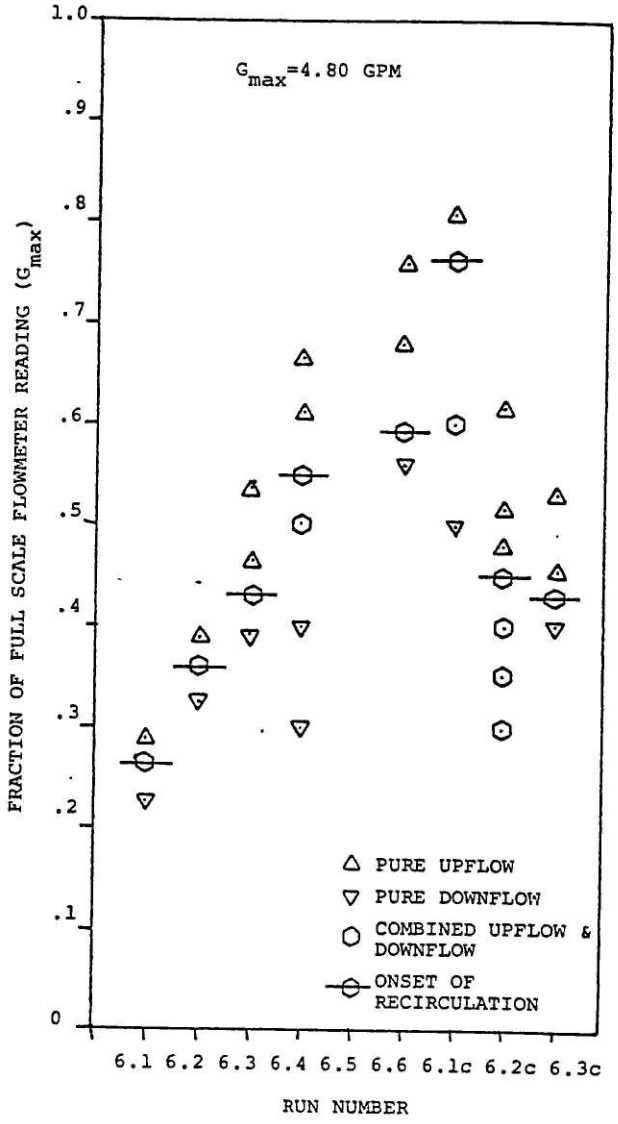


FIGURE 7.2.11

DYE INJECTION DATA FOR PROFILE #6



combined upflow and downflow (○), and onset of recirculation (-•-). The flowmeter employed is also indicated. Flow meter #1 (FM1) has a full scale reading of 1.96 GPM, and flowmeter 2 (FM2) has a full scale reading of 4.80 GPM.

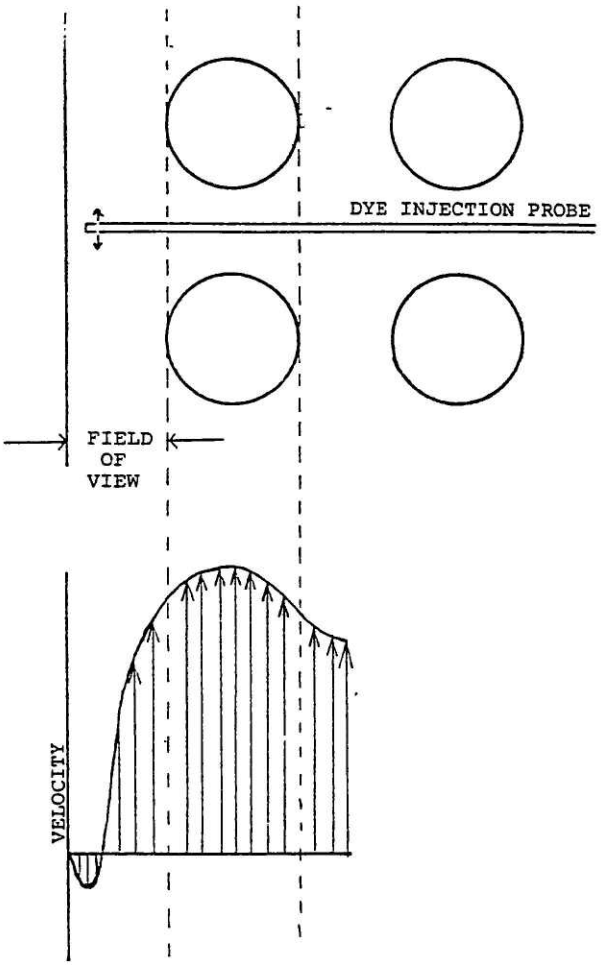
For profiles 1-4 the left row of rods was unheated, and the onset of recirculation was observed as a flow stagnation at the dye injection location. For profiles 5 and 6 the left row of rods was heated so combined upflow and downflow was observed in the injection subchannel. This was caused by local buoyancy effects within the subchannel which maintained upflow near the rod surface while downflow occurred in the rest of the subchannel as illustrated in Figure 7.2.12. For this case, the onset was taken as the first appearance (at highest bundle flow) of downflow.

In addition to providing a presentation of the raw dye injection data, Figures 7.2.7 to7.2.11 indicate how sharp the transition from upflow to downflow is, and what the maximum expected error is on the flow rate at the onset. It is roughly the distance between the lowest appearance of upflow, and the onset of recirculation point.

Once the total bundle power, inlet temperature and flowrate at the onset are known, key flow paramters such as Re, Gr_q and Pr can be calculated. In Appendix F1 a means of calculating these parameters is presented which evaluates the fluid properties at the mean temperature in the bundle. The mean temperature is used because it is believed that recirculation

FIGURE 7.2.12

COMBINED UPFLOW AND DOWNFLOW



depends upon integrated effects, not local effects. The raw data for the recirculation test (measured rod powers, flowrates, temperatures, etc.) is presented in Appendix F2. A summary of the recirculation data is given in Table 7.2.3

For each run the bundle bulk temperature rise was calculated from a steady state energy balance. For many runs the bulk temperature rise was also measured. The measured and calculated results are plotted in Figure 7.2.13. The results fall along the 45^{o} line indicating good agreement. These results suggest that:

1) steady state conditions were achieved
2) the bundle was well insulated against heat loss
3) measurement of powers, flows and temperatures were of reasonable accuracy ($\pm$ 5%)

Note that for cases where there was power loss through the cold wall, the power loss was calculated as $P_{loss} = \dot{m}_x C_p \Delta T$, and subtracted from the bundle power to obtain the net power. The calculated temperature rise was then obtained from

$$\Delta T_B = \frac{P_{bundle} - P_{loss}}{C_p \dot{m}_{bundle}}$$

In Appendix F2, an analysis is made of the errors involved in the onset of flow recirculation experiment. It was estimated that the maximum expected total error in the critical Reynolds number is about 26% for the lowest flow run, and 9% for the highest flow run. The error in Gr_q is about 6%.

TABLE 7.2.3

ONSET OF RECIRCULATION DATA

Run #	Parameters at Onset			Nominal Power (w/rod)				Bulk Temp. Rise (^{O}F)	
	Gr_q	Re	Pr	Q_H	Q_I	Q_J	Q_K	Meas.	Calc.
1.1	4.02E4	125	4.65	0	0	0	50	-	4.0
1.2	9.16E4	185	4.50	0	0	0	100	-	6.1
1.3	3.10E5	327	4.05	0	0	0	250	-	9.5
1.4	7.06E5	454	3.90	0	0	0	500	-	14.5
1.5	9.64E5	545	3.90	0	0	0	750	-	16.5
1.6	1.40E6	632	3.85	0	0	0	1000	-	20.0
1.7	1.86E6	694	3.80	0	0	0	1250	-	23.7
1.8	1.60E6	695	4.30	0	0	0	1500	-	-
1.9	2.88E6	822	3.80	0	0	0	2000	-	30.0
2.1	8.34E4	204	4.65	0	0	50	50	-	4.9
2.2	1.84E5	267	4.45	0	0	100	100	-	8.3
2.3	4.48E5	478	4.55	0	0	250	250	12	11.8
2.4	8.46E5	686	4.40	0	0	500	500	14	14.7
2.5	1.92E6	808	4.00	0	0	750	750	-	23.4
2.6	2.79E6	1033	3.85	0	0	1000	1000	-	24.5
2.7	4.58E6	1201	3.75	0	0	1500	1500	-	32.3
2.8	6.47E6	1356	3.65	0	0	2000	2000	38	38.1
2.2c	1.27E5	740	3.85	-112	0	100	100		
2.4c	2.20E6	1709	3.00	-174	0	500	500		
2.6c	2.08E6	1284	4.25	-110	0	1000	1000		
3.1	1.25E5	290	4.65	0	50	50	50	-	5.2
3.2	2.18E5	444	4.85	0	100	100	100	-	7.1
3.3	6.09E5	578	4.05	0	250	250	250	-	13.0
3.4	1.57E6	769	4.30	0	500	500	500	23	22.8
3.5	2.46E6	935	3.70	0	750	750	750	-	28.1
3.6	3.47E6	1105	4.10	0	1000	1000	1000	-	32.1
3.7	6.05E6	1334	3.90	0	1500	1500	1500	45	42.6

TABLE 7.2.3 (Continued)

Run #	Parameters at Onset			Nominal Power (w/rod)				Bulk Temp. Rise (^{o}F)	
	Gr_q	Re	Pr	Q_H	Q_I	Q_J	Q_K	Meas.	Calc
4.1	5.50E5	463	4.45	0	100	200	300	14.5	14.6
4.2	1.29E6	649	4.30	0	200	400	600	22.5	22.0
4.3	2.09E6	783	4.20	0	300	600	900	29.0	28.1
4.4	2.57E6	953	4.25	0	400	800	1200	31.0	29.3
4.5	3.73E6	1046	4.10	0	500	1000	1500	37.0	35.9
5.1	7.05E6	1071	3.65	100	100	1500	1500	42.0	40.9
5.2	3.34E6	841	3.80	100	100	1000	1000	36.0	34.2
5.3	2.73E6	378	3.20	100	100	500	500	50.0	47.9
5.4	2.22E6	399	3.50	100	100	500	500	43.0	42.5
5.5	1.47E6	164	3.15	100	100	200	200	56.5	57.4
5.6	9.52E5	226	3.75	100	100	200	200	36.0	35.5
5.7	4.20E5	101	4.30	100	100	100	100	46.0	46.3
6.1	6.51E5	239	3.95	50	100	150	200	-	25.2
6.2	1.53E6	343	3.80	100	200	300	400	-	38.4
6.3	5.70E6	502	2.90	200	400	600	800	65.0	65.1
6.4	7.60E6	614	3.07	300	600	900	1200	83.5	76.2
6.5	1.58E7	799	2.75	500	1000	1500	1800	100.0	102.8
6.6	1.50E7	763	2.85	500	1000	1500	2000	108.8	107.4
6.1c	3.81E5	637	4.30	-62	100	150	200	7.0	6.7
6.2c	1.31E6	1020	3.85	-15	200	300	400	11.0	10.5
6.3c	3.72E6	1189	3.45	+ 4	400	600	800	22.5	21.5

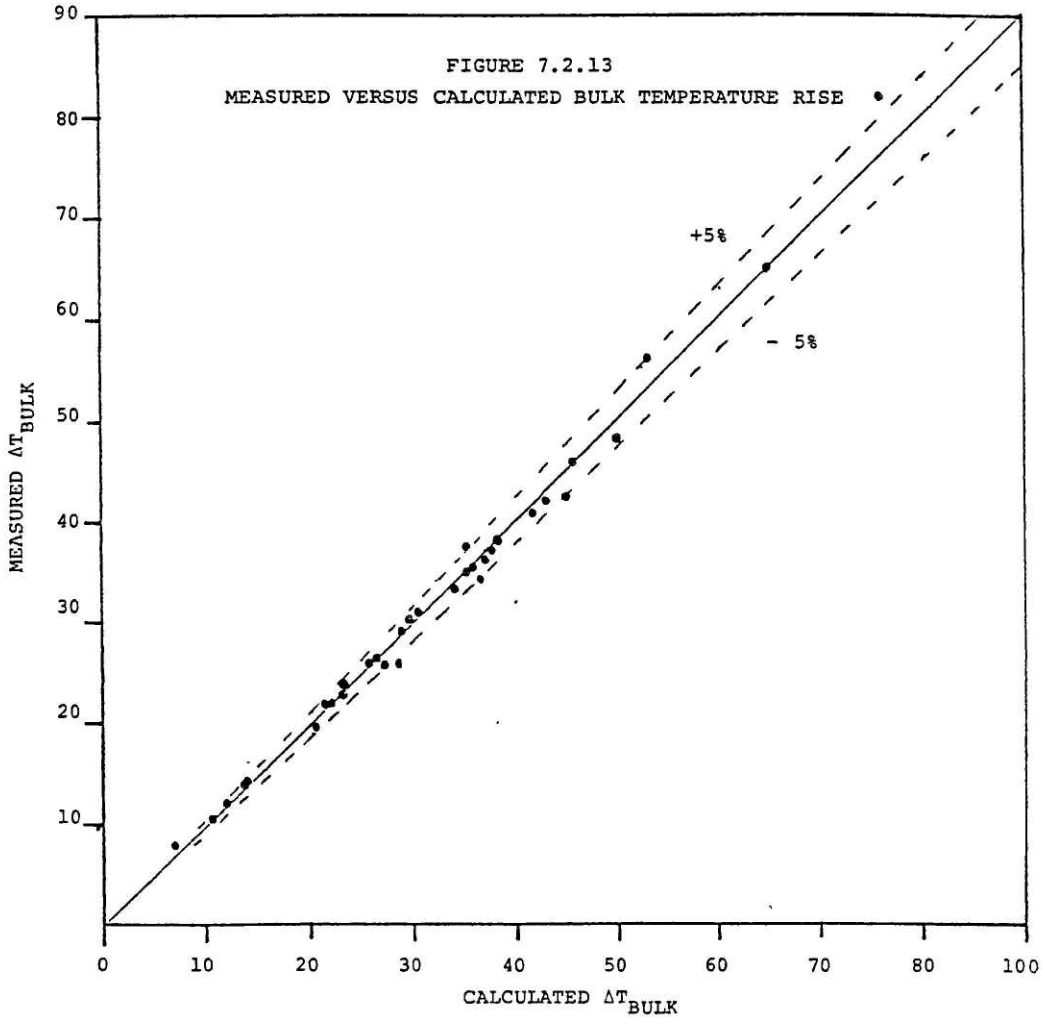


FIGURE 7.2.13
MEASURED VERSUS CALCULATED BULK TEMPERATURE RISE

7.3 ONSET OF RECIRCULATION CRITERION BASED ON A TWO CHANNEL MODEL OF THE ROD BUNDLE

7.3.1 Equations and Solution Method

Equation 5.3.1 is the governing equation for the recirculation criterion. With C fixed at the value at which we expect recirculation to occur, the corresponding critical Reynolds number may be calculated by iteration given the bundle operating conditions. These calculations were performed by program RECIRC wich is discussed in Appendix D

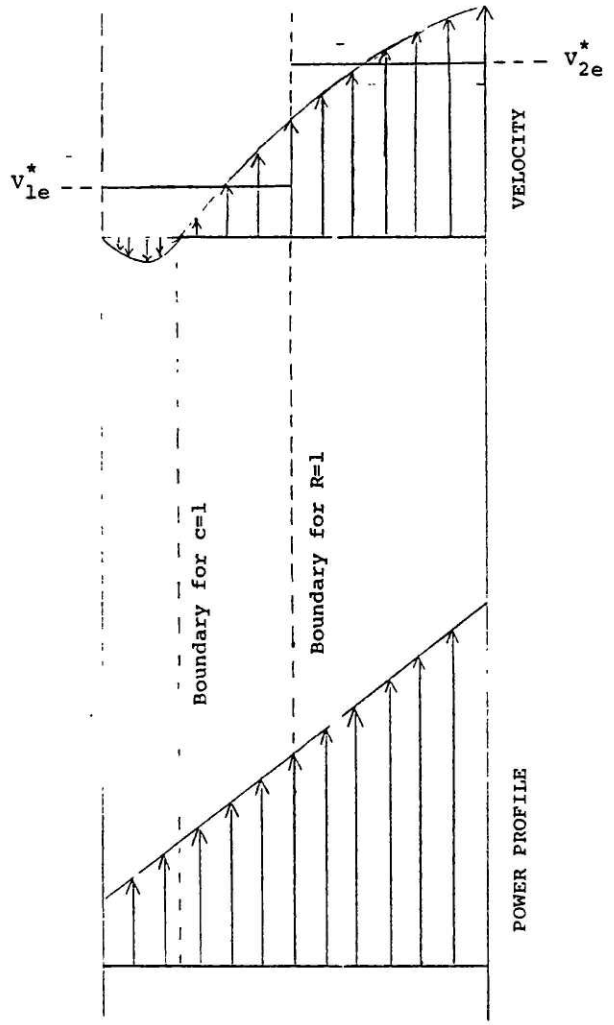
7.3.2 Alternate Approaches for Specification of the Onset of Recirculation

As exhibited in Figure 7.3.1 two options exist for specifying the onset of recirculation within the context of the two channel model. Both methods will be developed and tested initially.

For the first method (variable R approach) the channel boundary is fixed such that channel #1 contains the subchannels which are expected to first experience flow reversal, and R ($=A_1/A_2$) is specified. Accordingly, as shown in Figure 7.3.1, this implies that the bulk exit velocity for channel #1 is zero at the onset of recirculation so that $C_{crit} = 1.0$. If local buoyancy effects within channel #1 are significant, recirculation will occur while the bulk exit velocity for channel #1 is nonzero, as shown in Figure 7.2.12. For this case C at the onset will be less than one, but the detailed velocity field in the subchannel is needed

FIGURE 7.3.1

ALTERNATE APPROACHES FOR SPECIFYING THE ONSET OF RECIRCULATION



to fix C. For now the local buoyancy effects will be neglected.

For the second approach the bundle is divided along a plane of symmetry perpendicular to the power gradient so that R = 1. Then an appropriate value for C at the onset must be specified.

Model for C Neglecting Local Buoyancy Effects

For the variable R approach, selecting the appropriate value of R requires some engineering judgement (we expect recirculation to occur first in the subchannels with the least power input). For the R = 1 approach it is much less obvious what to specify for C, unless all the rods in channel #1 are unheated in which case C = 1. In Appendix F4 a model is developed to estimate C at the onset of recirculation allowing for a nonuniform power in channel #1. This model gives the critical value of C as:

$$C_{crit} = 1 - 2\frac{\sum_{ch\#1} A_i^*(Q_i^* - Q_{min}^*)}{\sum_{b} A_i^*(Q_i^* - Q_{min}^*)} \qquad (7.3.1)$$

The model is based on the assumption that at the onset of recirculation the flow field roughly follows the power distribution.

7.4 COMPARISON OF ONSET OF RECIRCULATION CRITERION WITH DATA

In this section the onset of recirculation criterion will be compared against available data. The effect of the input parameters on the predictions will be discussed, and the model results will be compared with the data from the MIT 4 x 4 rod bundle and the BNWL 2 x 6 rod bundle.

7.4.1 Discussion of Effect of Input Parameters on the Onset of Recirculation

Velocity Profile Shape Function

As discussed previously, the correct velocity profile shape function ($f(x^*)$ must be determined from the results of multichannel codes which numerically solve the full set of conservation equations. From the predicted flow field, we can compute $f(x^*)$ at each axial level.

In sections 6.1.1 and 6.1.2 COBRA predictions for $f(x^*)$ were presented for the BNWL 2 x 6 bundle. Figures 6.1.24 and 6.1.25 show two channel COBRA predictions for flow transients for a 1:0 and a 4:1 power gradient, respectively. Figure 6.1.15 shows 25 channel COBRA predictions for 3 steady state runs. Each of the three figures has one curve for $f(x^*)$ representative of the onset of recirculation. These three predictions are plotted together in Figure 7.4.1, along with $f(x^*) = x^*$ (uniform crossflow).

The validity of employing the uniform crossflow approximation may be determined from the COBRA predictions

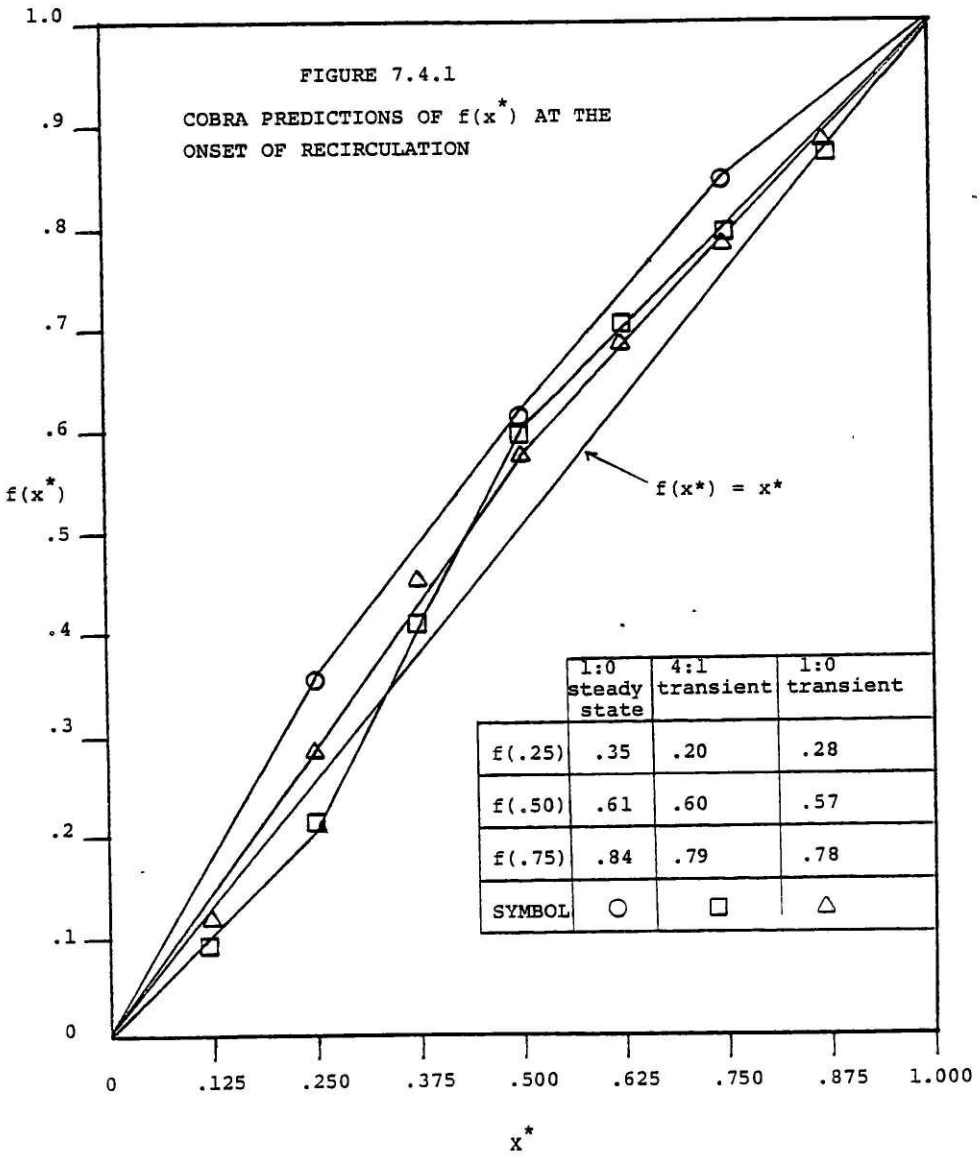


FIGURE 7.4.1

COBRA PREDICTIONS OF $f(x^*)$ AT THE ONSET OF RECIRCULATION

	1:0 steady state	4:1 transient	1:0 transient
f(.25)	.35	.20	.28
f(.50)	.61	.60	.57
f(.75)	.84	.79	.78
SYMBOL	○	□	△

of $f(x^*)$. Table 7.4.1 gives Re the onset of recirculation calculated with the two channel model by inputing the COBRA predicted $f(x^*)$. The model results with $f(x^*) = x^*$ are also shown. The COBRA predicted crossflow was input to the two channel model by employing a piecewise linear $f(x^*)$ as discussed in Section 6.1. The results in Table 7.4.1 indicate that the maximum error which will be incurred by employing $f(x^*) = x^*$ rather than the "true" (COBRA predicted) $f(x^*)$ is at most 8% for the three runs. It is also noted that employing $f(x^*) = x^*$ gives a conservative estimate of the onset of recirculation. Based on these results $f(x^*) = x^*$ will be used in all future recirculation calculations.

Turbulent Interchange Parameter

Turbulent interchange causes lateral energy transport which reduces the radial temperature difference at any axial location. This in turn reduces the buoyancy term, and causes the onset of recirculation to occur at a lower Reynolds number. Many correlations are available for turbulent interchange in bare and wire wrapped rod bundles for forced convection (72). For bare rod bundles COBRA employs:

$$w_t' = \beta s \bar{G} \qquad (7.4.1)$$

where $\bar{G}$ is the average mass flux. Converting to w_t^* gives:

$$w_t^* = \beta \frac{sL}{A_b} \qquad (7.4.2)$$

TABLE 7.4.1

MODEL PREDICTIONS OF RECIRCULATION
REYNOLDS NUMBER FOR IVP=4

INPUTS: $w_t^* = 0$, $f = \frac{88}{Re}$, $Pr = 4.15$, $P_2 = 1.0$, $C = 1.0$, $R = 1$

Gr_q	$f(x^*) = x^*$	1:0 S.S.	4:1 Transient	1:0 Transient
1E4	88.8	88.5	85.1	95.1
3E4	149.2	138.2	145.6	143.7
1E5	262.8	242.6	257.3	253.6
3E5	433.0	403.7	423.9	420.2
1E6	729.7	687.6	715.0	711.4
3E6	1149.0	1092.2	1130.7	1125.2
1E7	1850.3	1771.5	1823.7	1815.5
3E7	2804.3	2705.4	2771.3	2762.1
1E8	4358.8	4228.8	4314.9	4303.9
f(.25)	.25	.35	.20	.28
f(.50)	.50	.61	.60	.57
f(.75)	.75	.84	.79	.78

In Reference 59 it was observed that mixing occurred at low Reynolds numbers due to the effect of interacting thermal plumes. The mixing was empirically correlated as:

$$w' = .01 \frac{Gr_{\Delta T}}{Re^2} \hat{Q}_p \qquad (7.4.3)$$

$\hat{Q}_p$ is the ratio of the local to average power, and the constant .01 has units of lb_m/ft-sec. Note that in unheated regions of the bundle the mixing is zero (since $\hat{Q}_p = 0$). This is consistent with the notion that it is the thermal plumes which generate the turbulence, since there are no thermal plumes on unheated rods. Since Equation 7.4.3 is empirically based, it may only be valid under the test conditions of the BNWL experiment. It should be noted that Re did not go below 320 in the 2 x 6 test.

The correlation given above can be expressed in terms of the nomenclature of this study by multiplying w' by $L/\rho V_b A_b$ and converting $Gr_{\Delta T}$ to Gr_q to give

$$w_c^* = \frac{.04L}{\mu A_b} \frac{Gr_q}{Re^4 Pr} \hat{Q}_p \qquad (7.4.4)$$

The effect that these correlations have on the prediction of onset of recirculation will be discussed in Section 7.4.2.

Friction Factor Correlations

Many forced convection correlations exist for fully developed flow in rod bundles. For a square rod array of P/D = 1.25 with laminar flow, the friction factor correlations

of Reference 1 will be used. For interior subchannels:

$$f = \frac{89.4}{Re} \tag{7.4.5}$$

while for edge channels,

$$f = \frac{86.4}{Re} \tag{7.4.6}$$

For turbulent flow with $Re = 10^5$, it follows from Equation 3.1.3 that for an interior channel of a rod array of P/D = 1.25 the $f/f_{ct} = 1.055$. If we employ the circular tube result of $f_{ct} = \frac{.316}{Re^{.25}}$ it follows that:

$$f = \frac{.329}{Re^{.25}} \tag{7.4.7}$$

No correlations were found for edge channels, but it appears from the laminar flow correlations that the difference between edge and interior friction factors is small. Hence the same correlation will be employed for interior and edge subchannels by taking a weighted average of the friction factors of Equation 7.4.5 and 7.4.6.

$$f = \frac{9(89.4) + 12(86.4)}{(9+12)\,Re} = \frac{88}{Re} \tag{7.4.8}$$

In mixed convection fewer correlations exist, particularly for rod bundles. In Reference 1 correlations were given

for laminar mixed convection in triangular rod arrays, but not square arrays. Circular tube correlations are available for both laminar (25) and turbulent (16) mixed convection with aiding flow. Browns laminar flow correlation (Reference 25) is:

$$\frac{f}{f_o} = .1\left(\frac{Gr_q}{Re}\right)^{.475} \tag{7.4.9}$$

where $f_o = \frac{64}{Re}$ (7.4.10)

and Petukhov's turbulent flow correlation may be expressed as (by eliminating Ra_A in favor of Gr_q):

$$\frac{f}{f_o} = \left[1 + 3.5\left(\frac{D_e}{D_H}\right)^2 \frac{Gr_q^2}{Re^5}\right]^{.4} \tag{7.4.11}$$

where $f_o = \frac{.316}{Re^{.25}}$ (7.4.12)

These mixed convection correlations will be used for the rod bundle geometry by employing Equations 7.4.7 and 7.4.8 for f_o rather than their circular tube counterparts, Equations 7.4.12 and 7.4.10.

7.4.2 COMPARISON OF CRITERIA WITH MIT DATA

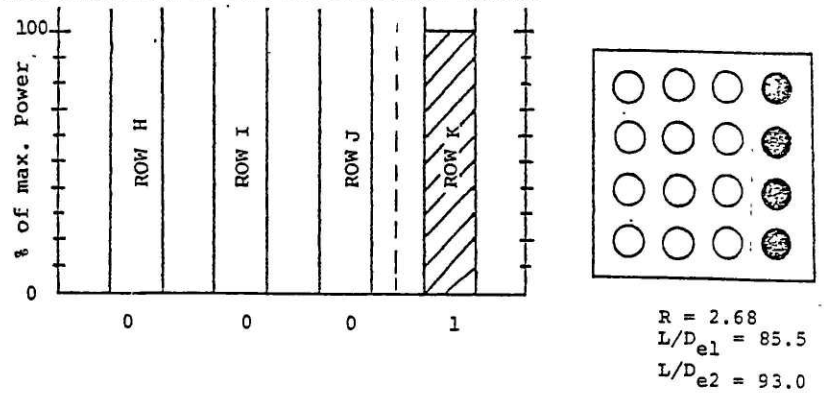
Recirculation Prediction for Profile #2

For power profile #2, the bundle is modeled as shown in Figure 7.4.2. For this profile, the noding scheme and the prediction of onset of recirculation is identical for the

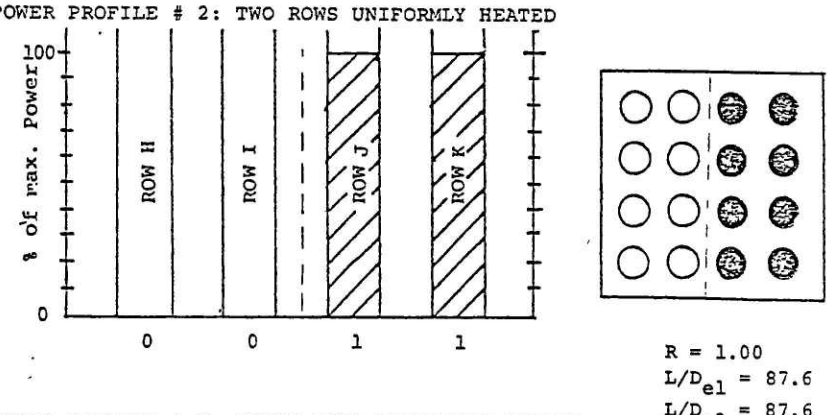
FIGURE 7.4.2

BUNDLE NODING FOR VARIABLE R APPROACH

POWER PROFILE # 1: ONE ROW UNIFORMLY HEATED



POWER PROFILE # 2: TWO ROWS UNIFORMLY HEATED



POWER PROFILE # 3: THREE ROWS UNIFORMLY HEATED

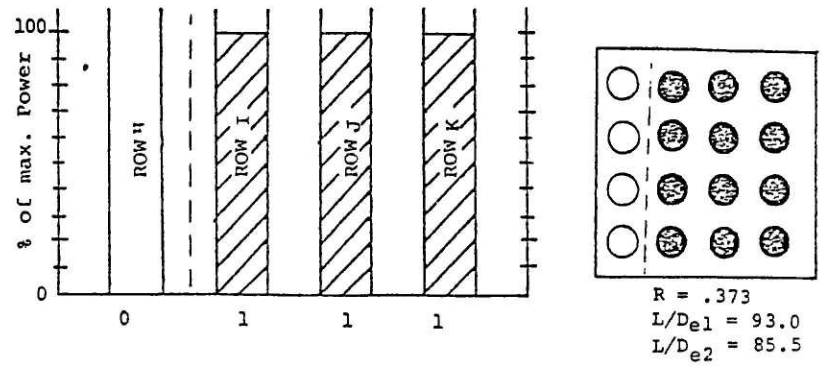
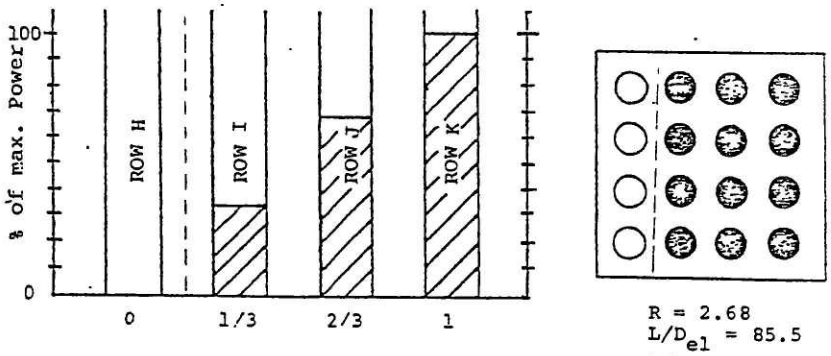


FIGURE 7.4.3

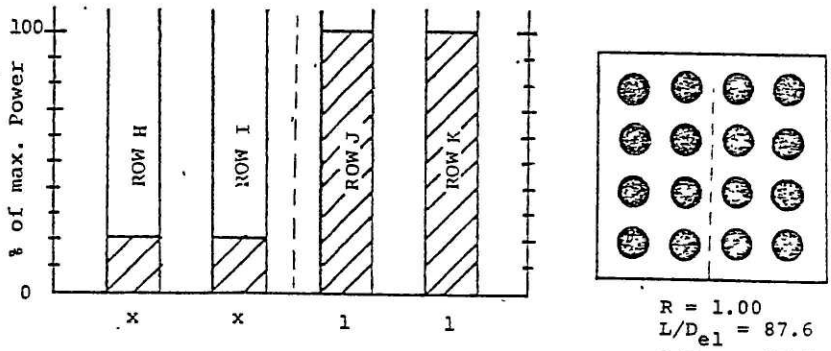
BUNDLE NODING FOR VARIABLE R APPROACH

POWER PROFILE # 4: LINEAR GRADIENT WITH ROW H UNHEATED



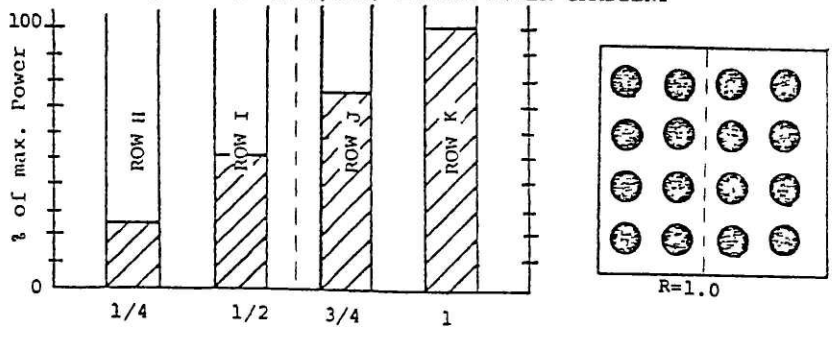
R = 2.68
L/D_{e1} = 85.5
L/D_{e2} = 93.0

POWER PROFILE # 5: STEP CHANGE IN POWER



R = 1.00
L/D_{e1} = 87.6
L/D_{e2} = 87.6

POWER PROFILE # 6: 4:1 (max/min) LINEAR POWER GRADIENT



R=1.0

R=1 approach and the C=1 approach. Recirculation predictions were performed for all four of the friction factor correlations discussed in Section 7.4.1 and the results are presented in Figure 7.4.4 and Table 7.4.2. The onset of recirculation for the data with side channel cooling occurs at a significantly higher Re than with no cooling. Model predictions of the cold wall data will be given later. It is observed from the table that the turbulent flow forced convection and mixed convection (Petukhov) correlations give essentially identical results for the entire range investigated. The value of $\frac{f}{f_o}$ from Equation 7.4.11 varies from 1.001 to 1.003 along the onset of recirculation line, indicating that local buoyancy does not significantly effect the friction factor at the onset of recirculation.

Comparison of the recirculation prediction for laminar forced and mixed convection friction factor correlations shows a significant difference between the two. The mixed convection correlation causes a decrease in the critical Reynolds number for a given Gr_q. This is because buoyancy in the hot channel is increasing the friction factor, which opposes flow redistribution. The difference between the forced and mixed convection predictions increases with Gr_q. The value of f/f_o is 2.02 for $Gr_q = 10^5$ and goes up to 8.5 for $Gr_q = 10^7$.

It is observed in Figure 7.4.4 that the predictions of the onset of flow recirculation for the forced convection laminar ($f = 88/Re$) and turbulent ($f = .329/Re^{.25}$) friction

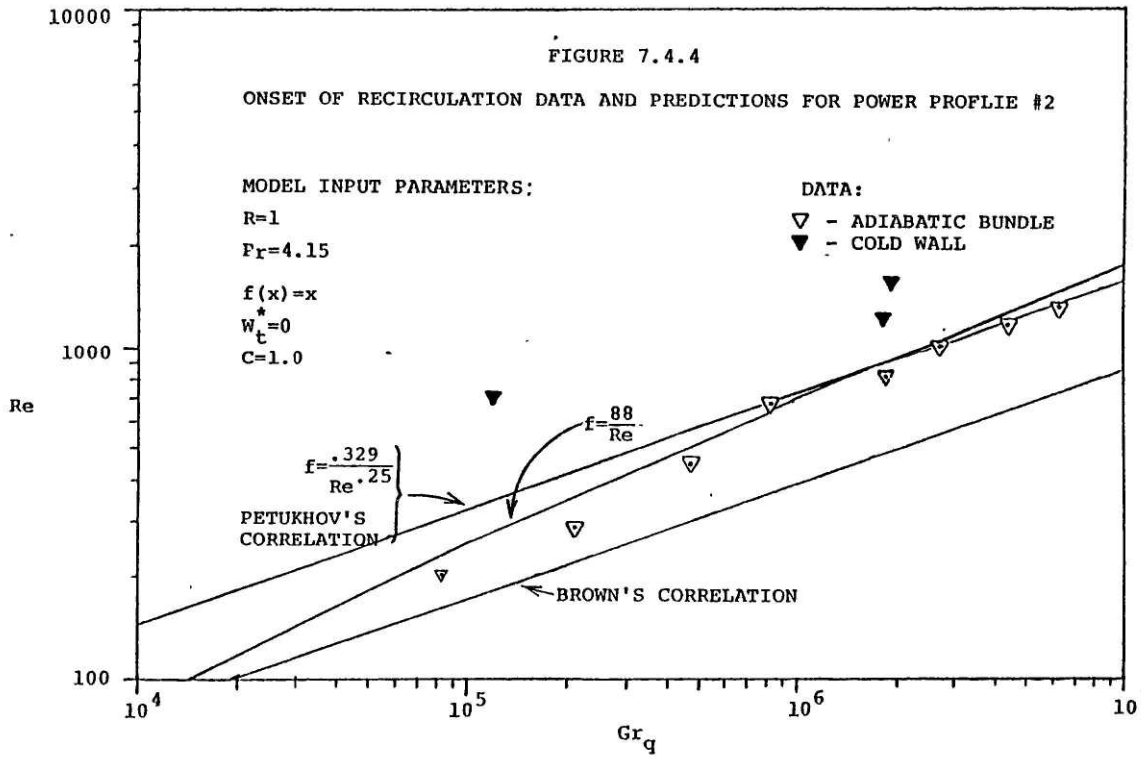


FIGURE 7.4.4

ONSET OF RECIRCULATION DATA AND PREDICTIONS FOR POWER PROFLIE #2

TABLE 7.4.2

ONSET OF RECIRCULATION PREDICTIONS FOR PROFILES 1 TO 4

	Profile #2				Profile #4			Profile #3			Profile #1
Gr_q	$f = \frac{88}{Re}$	$f = \frac{.329}{Re^{.25}}$	Petukhov	Brown	R=1	R = .373	R=1 w/ mixing model	R=1	R = .373	R=1 w/ mixing model	R = 2.68
1E4	89	147	145	-	-	112	-	-	112	-	64
3E4	150	217	214	119	142	190	123	138	190	102	108
1E5	263	331	328	178	251	334	221	244	334	184	187
3E5	433	488	483	260	415	552	367	405	552	309	306
1E6	729	747	738	393	704	935	622	693	935	527	510
3E6	1149	1097	1036	573	1116	1480	983	1105	1480	834	795
1E7	1850	1672	1655	865	1807	2392	1580	1800	2392	1334	1266
P_1	0.0	0.0	0.0	0.0	.167	0	.167	.333	0	.333	0
P_2	1.0	1.0	1.0	1.0	.833	1.0	.833	.667	1.0	.667	1.0
C	1.0	1.0	1.0	1.0	.696	1.0	.696	.374	1.0	.374	1.0
w_t^*	0	0	0	0	0.0	0.0	Eq.7.4.2	0.0	0.0	Eq.7.4.2	0

factor correlations intersect at Re ≃ 800. For Re < 800, the turbulent forced convection correlation overpredicts the data, while for Re > 800 the turbulent flow correlation does slightly better than the laminar flow forced convection correlation, though only a small difference exists between the two. For Re > 3,000 (not shown in Figure) a large difference exists between the laminar and turbulent flow results. It is expected that the recirculation data for large Re will follow the turbulent flow correlation, but such data was not obtained due to the power limits of the heater rods. Considering the range of Re of this study, f = 88/Re will be used for future comparisons.

Recirculation Prediction for Profile #1.

For the variable R approach, the bundle is noded as shown in Figure 7.4.2 for profile #1. The results presented in Figure 7.4.5 show that excellent agreement between the model and the data exists.

For the R=1 approach it follows from Equation 7.3.1 that the critical value for C is 1.00. As seen in Figure 7.4.5 this leads to an overprediction of the data.

Recirculation Prediction for Profile #3.

For the variable R approach, the bundle is divided as shown in Figure 7.4.2, and C=1 is used with the power skew given by $P_1 = 0.0$ and $P_2 = 1.0$. For the R=1 approach the power skew is given by $P_1 = .333$ and $P_2 = .667$. It follows

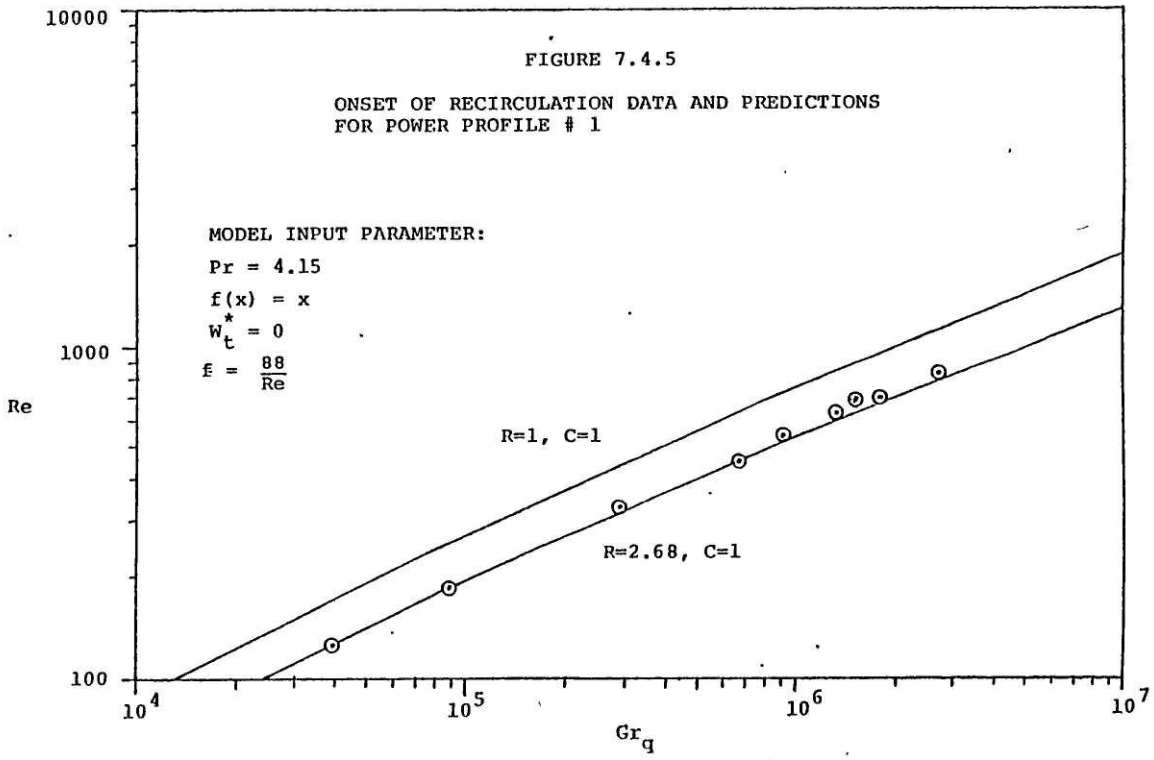


FIGURE 7.4.5

ONSET OF RECIRCULATION DATA AND PREDICTIONS
FOR POWER PROFILE # 1

from Equation 7.3.1 that C = .325. A comparison of the two predictions is given in Figure 7.4.6. The variable R approach overpredicts the data slightly, while good results are given by the R=1 method.

Recirculation Data and Predictions for Profile #4.

For the variable R approach, the onset of recirculation prediction for power profile #4 is identical to the prediction for profile #3. As seen in Figure 7.4.7 the model overpredicts the data. For the R=1 approach it follows from Equation 7.3.1 that C = .660, and from Figure F4.3 it can be seen that P_1 = 1/6 and P_2 = 5/6. Figure 7.4.7 shows that a significant improvement in the prediction occurs for the R=1 approach.

Recirculation Predictions for Profile #6

Profile # 6 is a 4:1 (max:min) linear radial power profile. The data and predictions for both the R=1 approach and variable R appraoch are shown in Figure 7.4.8. For the variable R case, P_1 = .111, P_2 = .889 and C=1. For the R=1 case P_1 = .30 P_2 = .70 and C = .660 from Equation 7.3.1. Both methods overpredict the data considerably.

A likely reason for the overprediction of the data for this power profile is the effect of coolant mixing induced by thermal plumes. As discussed in Section 7.4.1, mixing will only occur in heated regions of the bundle since the plumes develop on the heated rods only. It follows that the

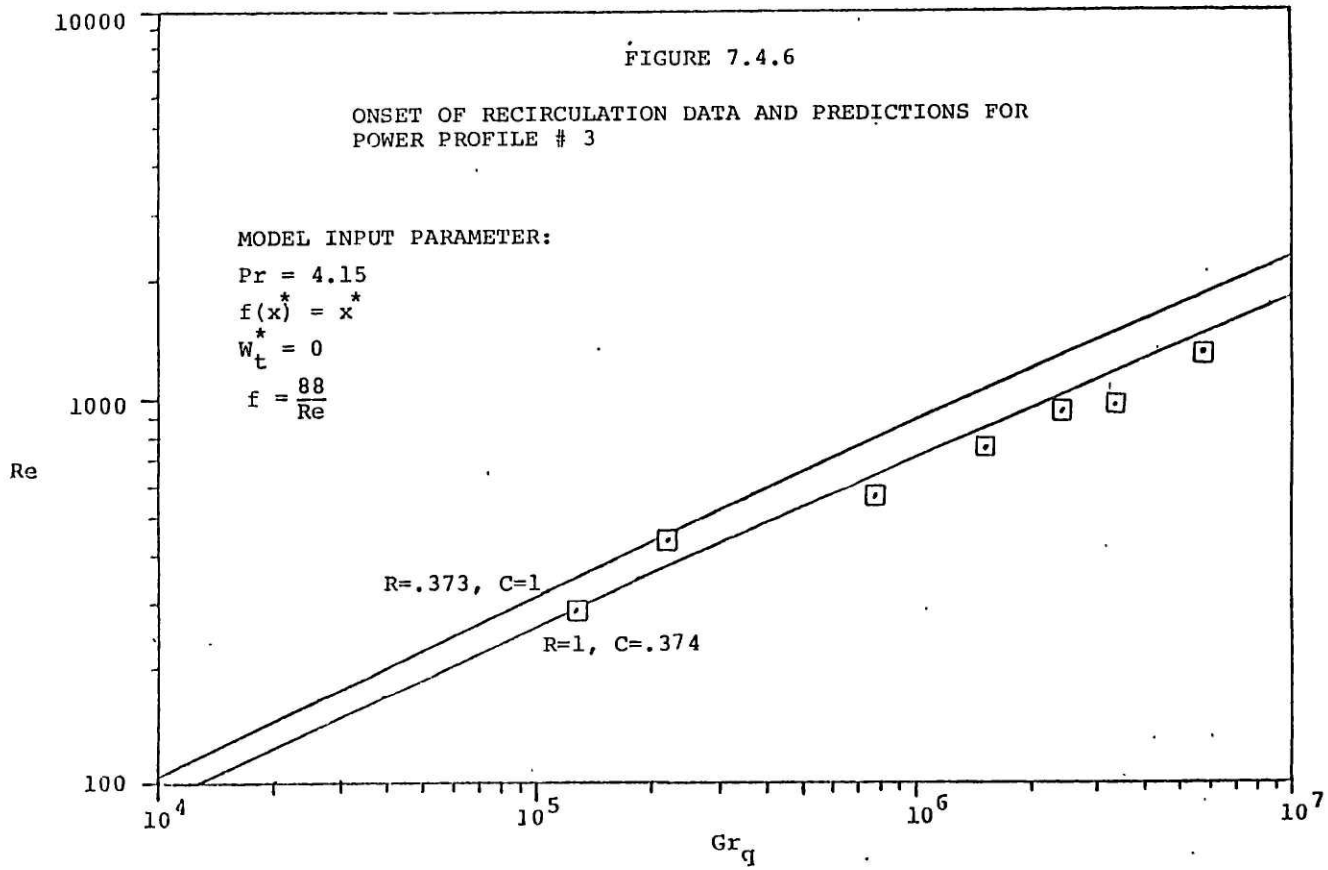


FIGURE 7.4.6

ONSET OF RECIRCULATION DATA AND PREDICTIONS FOR POWER PROFILE # 3

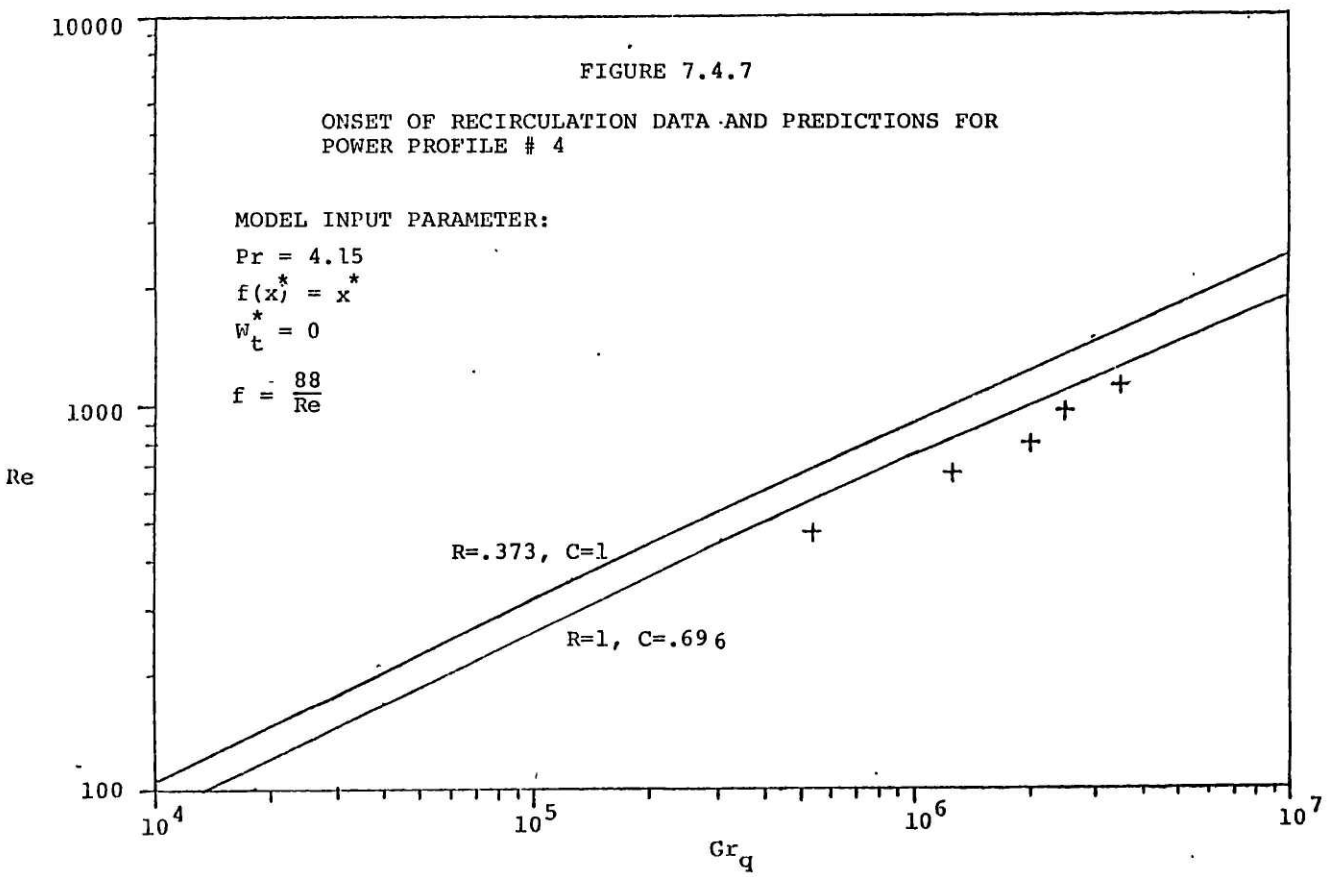


FIGURE 7.4.7

ONSET OF RECIRCULATION DATA AND PREDICTIONS FOR POWER PROFILE # 4

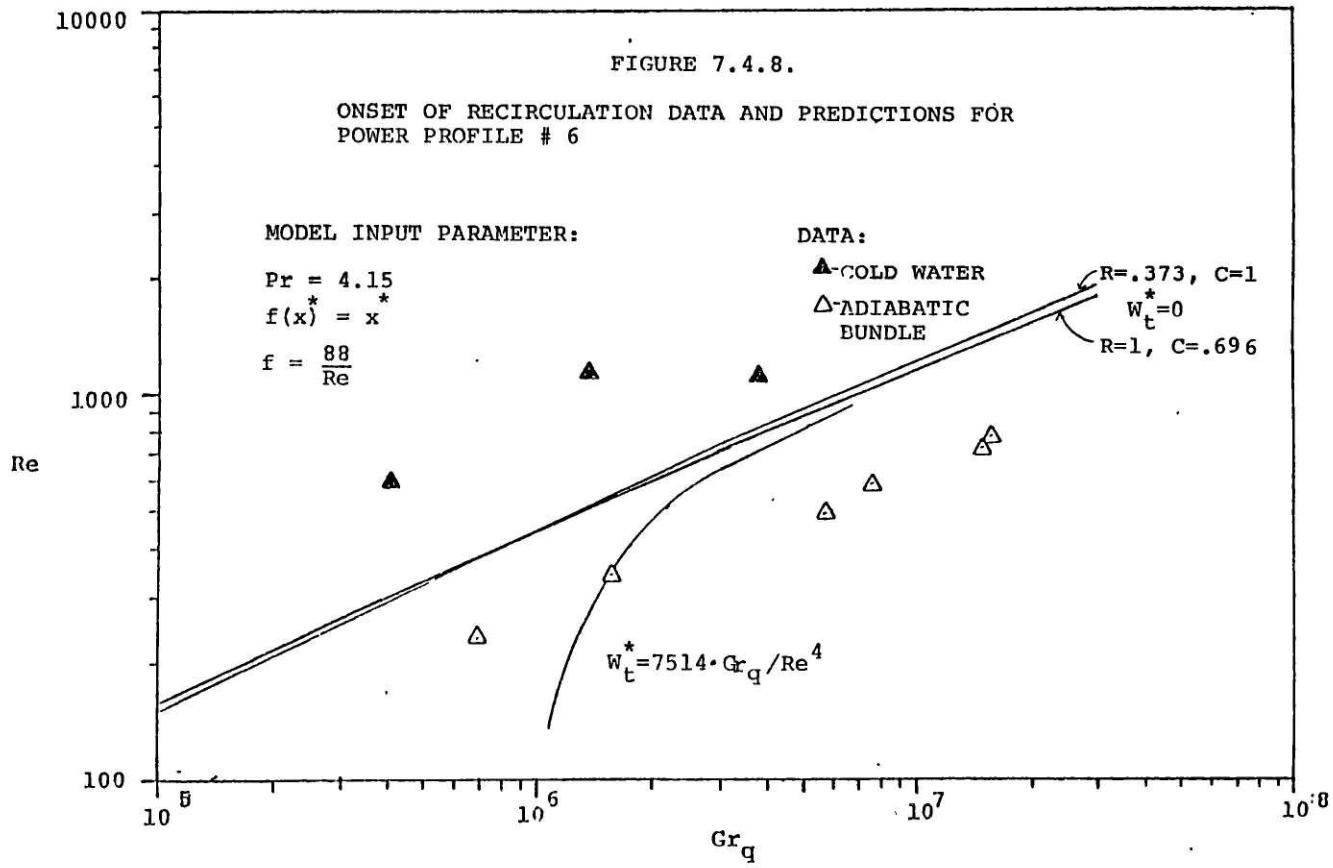


FIGURE 7.4.8.

ONSET OF RECIRCULATION DATA AND PREDICTIONS FOR POWER PROFILE # 6

effect of coolant mixing may be significant in runs where some rods are heated in channel # 1 (profiles 3, 4, 5 and 6 for the R=1 noding scheme).

To account for buoyancy induced mixing, Equation 7.4.4 was used to calculated w_t^* in program RECIRC. It is necessary to place the correlation in the iterative loop since w_t^* changes with Reynolds number. The results of the calculation are given in Figure 7.4.8. For large Re the effect of w_t^* is negligible, though as Re decreases w_t^* becomes large and delays the onset of recirculation. For Re=300, w_t^* grows so large that the critical Reynolds number drops rapidly. This unusual behavior is due to the exponent of 4 on the Reynolds number of the BNWL mixing correlation (Equation 7.4.4). It is obvious that this correlation gives unreasonable results in the recirculation criteria. This may be expected since the correlation is purely empirical. It may only apply to the BNWL 2x6 geometry in the Re range of that test. The Reynolds number did not go below 320 in the 2x6 test, so the large increase in mixing may not have been encountered.

In Appendix F6, a model is developed for w_t^* based on a modification of the mixing length hypothesis. The predictions with this model will be presented in Section 7.4.3.

Recirculation Data and Predictions for Profile #5

For profile # 5 (Figure F4.2) the R=1 approach and variable R approach lead to identical results since for the R=1 approach Equation 7.3.1 gives C=1, which is also the

case for the variable R approach. For Profile # 5 the rods in the left hand side of the bundle were heated at 100 Watts per rod, and the power level for the right half of the bundle was set at 1500, 1000, 500, 200 and 100 Watts per rod, giving power gradiens of 15:1, 10:1, 5:1, 2:1 and uniform power. It is observed in figure 7.4.9 that the data for profile number 5 and the two channel model prediction, the prediction for profile # 2 (zero power in left half of bundle, or a 1:0 skew) is also drawn in for comparison. The vertical lines link data with prediction. The predictions are also given in Table 7.4.3. As the power skew decreases from 15:1 to 5:1, the prediction of the recirculation Reynolds number decreases, as do they recirculation data points. As for profile #6, the model overpredicts the data, because mixing is not included. However for the 2:1 gradient and uniform power case, the model has no solution (i.e. there is no positive Re which satisfies Equation 5.3.1 for C=1) while the data indicates that recirculation exists. For the uniform power case we do not expect the model to predict recirculation, since no crossflow is predicted for the uniform power case (C=0). However, recirculation was observed experimentally and is believed to be caused by local buoyancy effects. To demonstrate why no solution exists for the 2:1 and 1:1 skew, program TWOCHAN was used to determine C as a function of Re for runs 5.4 (5:1 skew) 5.5 (2:1 skew) and 5.6 (2:1 skew). As exhibited in Figure 7.4.10, the value of C increases with decreasing Re for all cases.

FIGURE 7.4.9

RECIRCULATION DATA AND PREDICTIONS FOR POWER PROFILE # 5

POWER GRADIENT:	15:1	10:1	5:1	2:1	1:1
DATA:	□	△	○	⬡	▽
MODEL ($w_t^*=0$):	■	▲	◕	no solution	

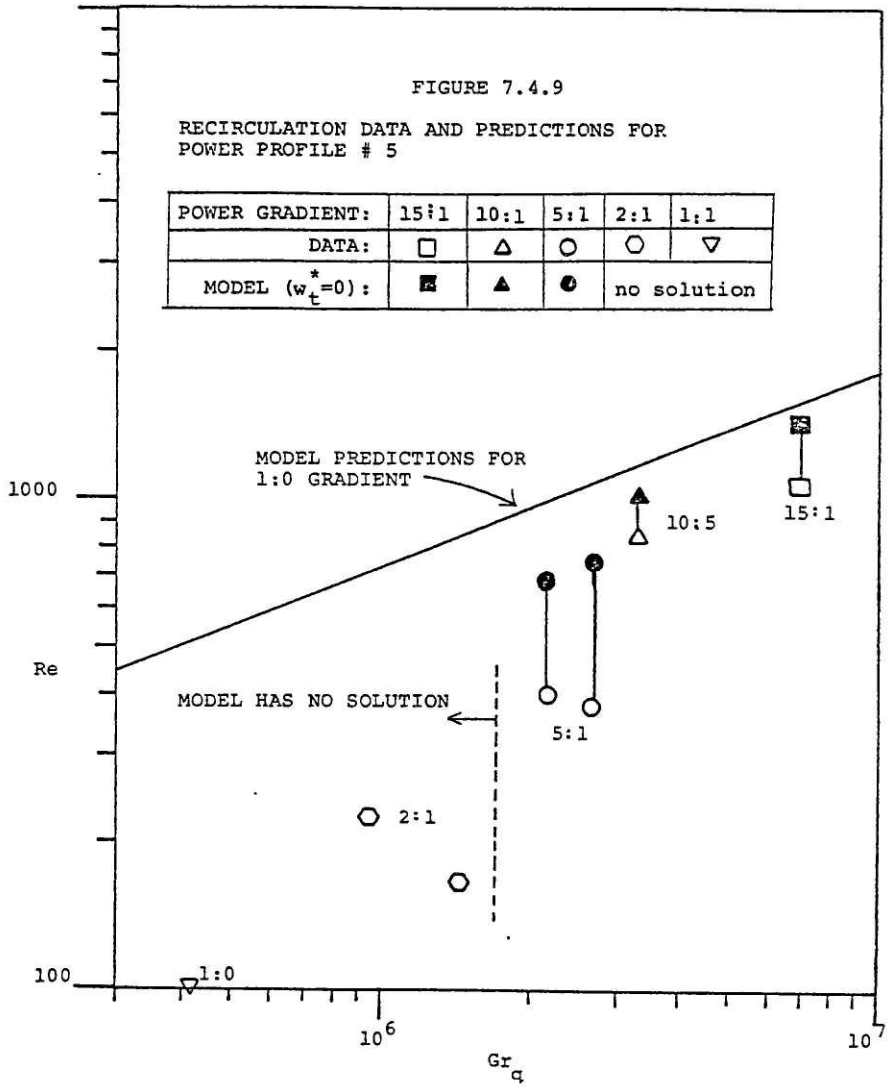


TABLE 7.4.3

RECIRCULATION DATA AND PREDICTIONS FOR POWER PROFILE #5

	DATA			POWER SKEW		PREDICTED Re_{crit}			
Run	Gr_q	Re	Symbol	P_1	P_2	$w_t^*=0$	Mixing Model	Local Buoyancy $F_D = 1.0$	Local Buoyancy $F_D = .30$
5.1	7.05E6	1071	□	.0625	.9375	1457	1370	N.N.	N.N.
5.2	3.34E6	841	△	.091	.909	1017	923	N.N.	N.N.
5.3	2.73E6	378	○	.167	.833	745	571	N.N.	N.N.
5.4	2.22E6	399	○	.167	.833	683	524	N.N.	N.N.
5.5	1.47E6	164	○	.333	.667	N.S.	N.S.	790	360
5.6	9.52E5	226	○	.333	.667	N.S.	N.S.	555	260
5.7	4.20E5	101	▽	.50	.50	N.S.	N.S.	286	80

N.S. - model has no solution

N.N. - local buoyancy not needed

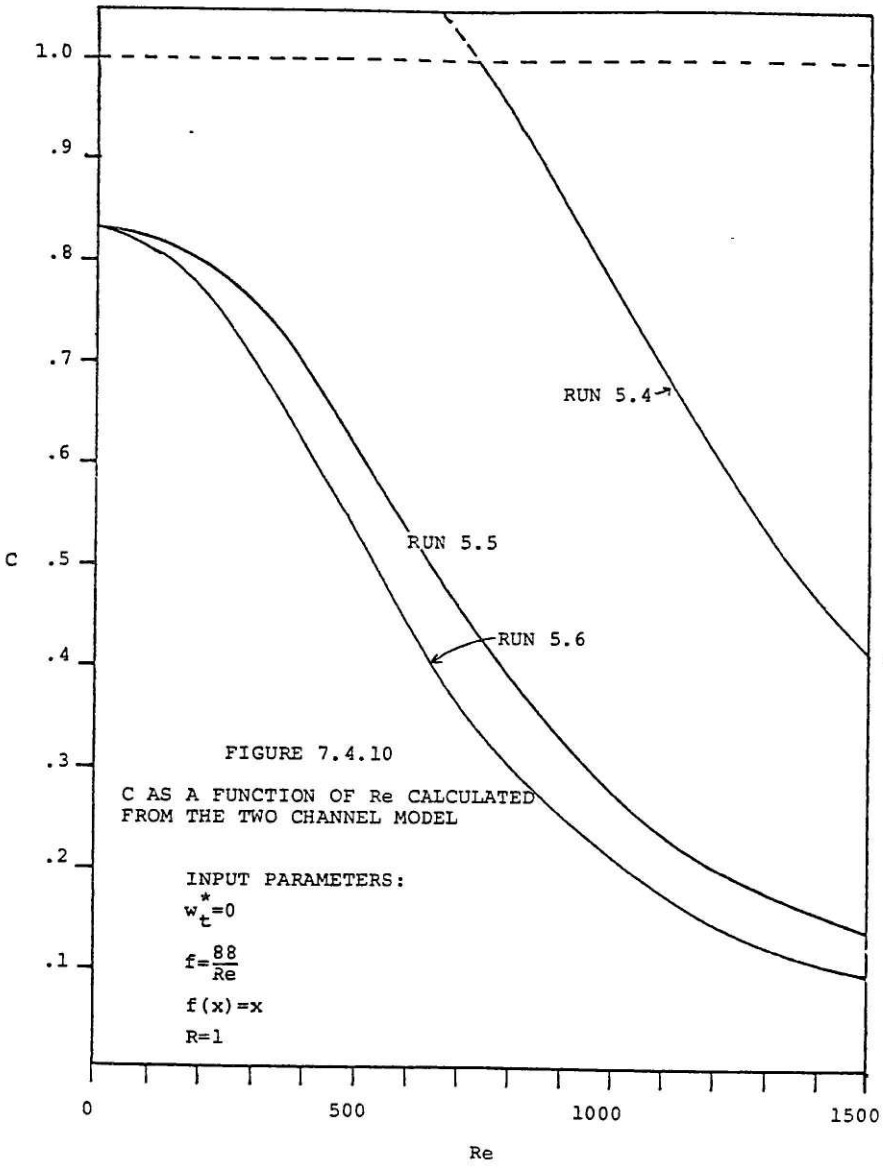


FIGURE 7.4.10

C AS A FUNCTION OF Re CALCULATED FROM THE TWO CHANNEL MODEL

INPUT PARAMETERS:

$w_t^* = 0$

$f = \frac{88}{Re}$

$f(x) = x$

$R = 1$

For the 5:1 skew C becomes 1.0 when Re = 745, indicating the onset of recirculation. For the 2:1 gradient, even for Re=0, the value of C remains less than one, suggesting that the buoyancy induced crossflow is not large enough to cause flow recirculation. For the uniform power case, the model predicts C=0 for all Re. Why then is recirculation observed experimentally?

The answer is that the recirculation is in part determined by the local buoyancy effects within the subchannel. This is supported by the experimental observation of combined upflow and downflow in the dye injection subchannel, as shown in Figure 7.2.10. Recirculation may exist since there is net upflow in the edge subchannel, a smaller value for C must be used to specify the onset of recirculation. For the uniform power run, recirclation is dominated by the local buoyancy effect.

In Appendix F5 a model is presented which couples the two channel model with a distributed parameter solution (Reference 1) of the edge subchannel velocity field, allowing the onset of recirculation to be obtained for runs 5.5, 5.6 and 5.7. The predictions based on this model, and the predictions based on the mixing model will be discussed in Section 7.4.3.

Recirculation Predictions for Runs With Side Channel Cooling

Six runs were made to examine the effect of side channel cooling on the onset of recirculation. Three data points were for profile #2 and three were for profile #6. These data points are labeled with a "C" in Table 7.2.3. For example, run 6.2C had the same power distribution as run 6.2, but had coolant flowing through the side channel.

As seen in Figures 7.4.4 and 7.4.8, the effect of the cold wall was to cause recirculation to occur at a higher Reynolds number than the corresponding adiabatic bundle case. To model the effect of side channel cooling with the two channel model, the power lost through the cold wall was subtracted from the power in the 4 rods closest to the cold wall. The power skew parameters P_1 and P_2 were calculated accordingly. The Grashof number was calculated from the net bundle power (rod power - power lost through cold wall). The model predictions for this case are presented in Table 7.4.4. Note that for some cases P_1 is negative, indicating the the power lost to the side channel exceeds the power input due to the rods in channel #1. The model results for profile #2 were all within 21% of the data, while the results for power profile # 6 were all within 32% for both the R=1 approach and the variable R method. The data and predictions are given in Figure 7.4.11

TABLE 7.4.4

RECIRCULATION DATA AND PREDICTIONS WITH COLD WALL

	Run #	Gr_q	Re	Symbol	$-P_1$	P_2	C	Re_{crit}	% Error	Symbol
R = 1	2.2C	2.20E6	1709	○	- .311	1.211	1.00	1454	- 15	●
	2.4C	2.08E6	1284	□	- .058	1.058	1.00	1061	- 21	■
	2.6C	1.27E6	738.9	△	-1.279	2.279	1.00	657	- 11	▲
R = .373	6.1C	3.81E5	637	⬡	- .064	1.064	1.00	690	+ 8	⬢
	6.2C	1.31E6	1020	▽	- .017	1.017	1.00	1070	+ 5	▼
	6.3C	3.72E6	1189	▷	.002	.998	1.00	1571	+ 32	▶
R = 1	6.1C	3.81E5	637	⬡	.099	.901	.696	525	- 18	◐
	6.2C	1.31E6	1020	▽	.209	.791	"	715	- 30	▼
	6.3C	3.72E6	1189	▷	.224	.776	"	1550	+ 30	▶

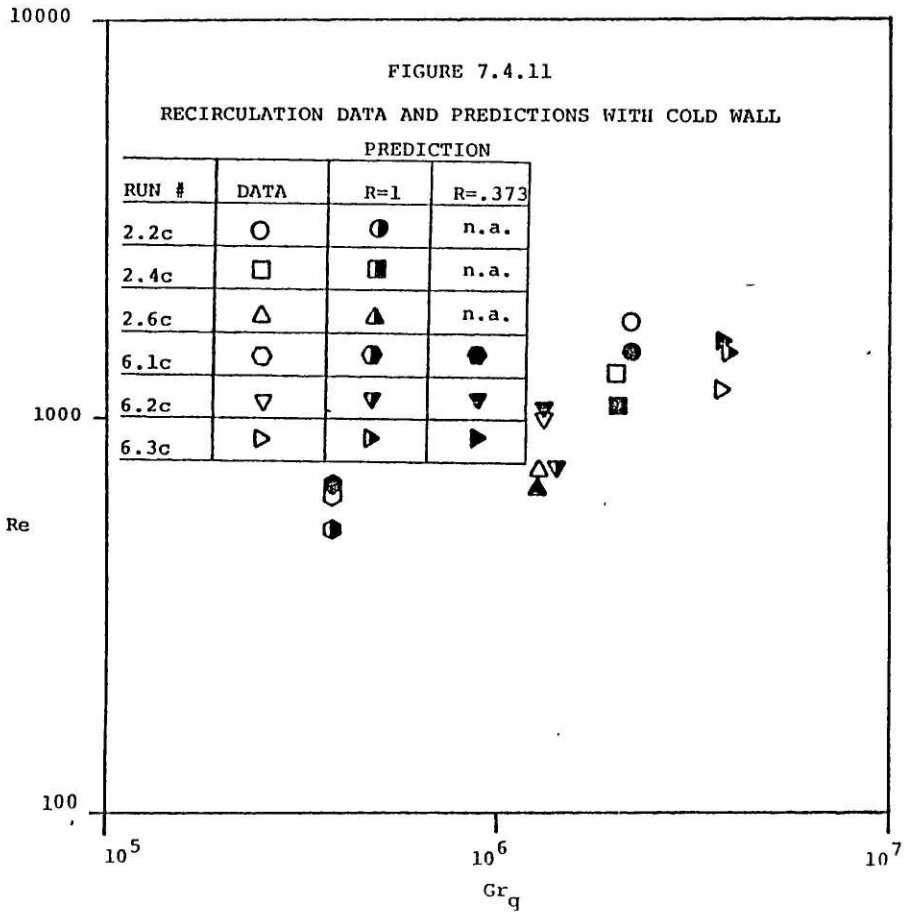


FIGURE 7.4.11

RECIRCULATION DATA AND PREDICTIONS WITH COLD WALL

7.4.3 Improved Predictions Based on a Mixing Model, and A Model for Local Buoyancy Effects

It was determined in Section 7.4.2 that the effects of coolant mixing and localized buoyancy effects become important in predicting the onset of flow recirculation. Models were developed to account for these two phenomena in Appendices F5 and F6, respectively. In this section two channel model predictions will be presented which include the effects of mixing and local buoyancy. The mixing model will be considered first, and will be calibrated against the recirculation data. Then local buoyancy effects will be considered. Only the R=1 approach will be employed.

Calibration of the Mixing Model

As discussed in Section 7.4.2, the effects of mixing caused by buoyancy induced turbulence at low Reynolds number may be important for cases in which some rods in channel #1 are heated. In appendeix F5 a model was developed to calculate the mixing parameter w_t^* under these conditions, and is given by:

$$w_t^* = K \cdot P_1 \cdot \frac{\sqrt{Gr}}{Re^m} \qquad (7.4.1)$$

where K and m are constants to be determined from the experimental data. Actually K depends on geometry and Prandtl number, but since only one geometry and one coolant will be considered, K may be treated as a constant.

The power profiles where mixing may be important are profiles number 3, 4, 5 and 6. These profiles were selected because hot rods existed in channel #1. It was determined that K = 2.0 and m = 1.2 gave a reasonably good fit to the data. Hence Equation 7.4.1 becomes:

$$w_t^* = 2.0\ P_1 \frac{\sqrt{Gr_q}}{Re^{1.2}} \qquad 7.4.2$$

The above equation was incorporated into program RECIRC to calculate the onset of recirculation for profiles 3, 4, 5 and 6.

The predictions for profile # 6 are given in Figure 7.4.12 and in Table 7.4.5. Significant improvement in the prediction occurs. The R=1 prediction with no mixing ($w_t^* = 0$) from Figure 7.4.8 is included, along with a prediction with $w_t^* = .6$ (selected arbitrarily for comparative purposes). It is observed that the prediction with w_t^* given by Equation 7.4.2 is parallel to the $w_t^* = .6$ result, indicating that the quantity $\sqrt{Gr_q}/Re^{1.2}$ is nearly constant along the onset of recirculation curve.

The predictions for power profile #5 with the new mixing model are given in Figure 7.4.13 and Table 7.4.3. The results are improved though the model still overpredicts the data somewhat. As was observed in Figure 7.4.9, the model still has no solution for the 2:1 and 1:1 power skews. This issue will be taken up in the section on local buoyancy effects.

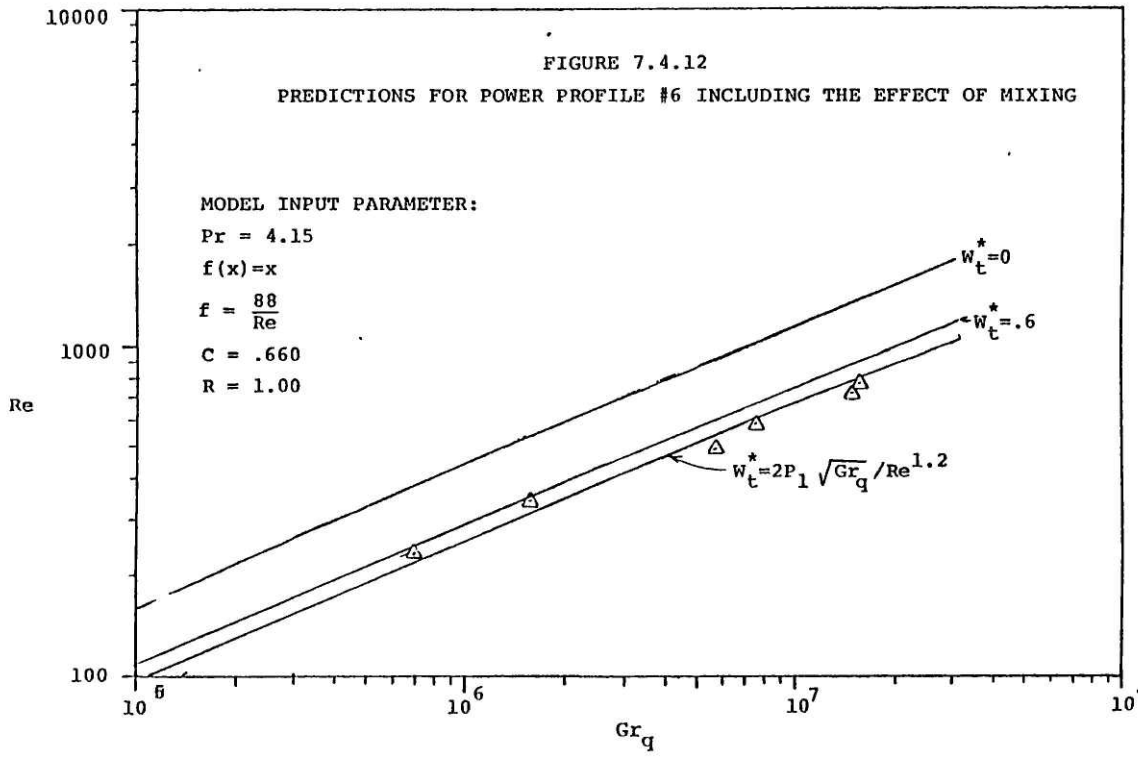


FIGURE 7.4.12
PREDICTIONS FOR POWER PROFILE #6 INCLUDING THE EFFECT OF MIXING

TABLE 7.4.5

ONSET OF RECIRCULATION PREDICTIONS FOR POWER PROFILE 6

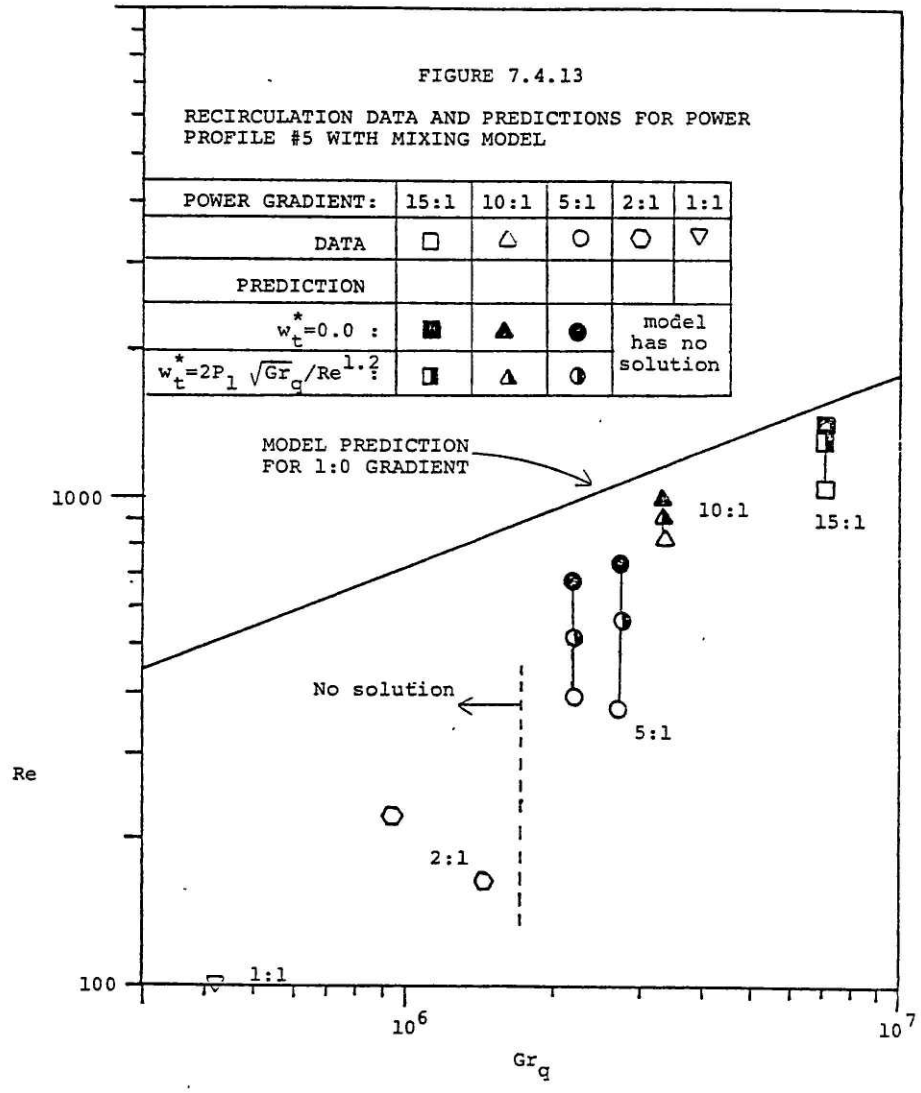
	Reynolds Number at Onset of Recirculation				
Gr_q	R = .373	R = 1	BNWL Mixing Model	$w_t^* = .6$	M.I.T. Mixing Model
1E4	-	-	-	-	-
3E4	-	-	-	-	-
1E5	160	150	-	103	-
3E5	269	252	-	155	120
1E6	472	438	113.8	266	221
3E6	772	710	691	429	363
1E7	1293	1173	1213	705	591
3E7	N.C.	N.C.	1909	N.C.	N.C.
1E8	N.C.	N.C.	3044	N.C.	N.C.
R	.373	1.0	1.0	1.0	1.0
C	1.0	.696	.696	.696	.696
P_1	.111	.30	.30	.30	.30
P_2	.889	.70	.70	.70	.70
w_t^*	0	0	$7514 \frac{Gr_q}{Re^4}$	.6	$2P_1 \frac{\sqrt{Gr}}{Re^{1.2}}$

N.C. -R_e not calculated at this G_{rq}

FIGURE 7.4.13

RECIRCULATION DATA AND PREDICTIONS FOR POWER PROFILE #5 WITH MIXING MODEL

POWER GRADIENT:	15:1	10:1	5:1	2:1	1:1
DATA	□	△	○	⬡	▽
PREDICTION					
$w_t^*=0.0$:	■	▲	●	model has no solution	
$w_t^*=2P_1\sqrt{Gr_q}/Re^{1.2}$:	◨	◭	◑		



The results for profile # 4 are given in Figure 7.4.14. It is observed that the prediction improves when the mixing model is utilized.

The results for power profile # 3 are given in Figure 7.4.15 and Table 7.4.2. The predictions are slightly better without the mixing model, though the error is quite small. For power profiles 1 and 2 the predictions of Figure 7.4.4 and 7.4.5 are unchanged, since Equation 7.4.2 gives $w_t^* = 0$ (since $P_1 = 0$) for these cases.

In summary, the mixing model given by Equation 7.4.2 results in an improvement of the prediction of the onset of recirculation. A significant improvement occurred for profile #6 (where Equation 7.4.2 gives $w_t^* = .76$ at the onset) while $w_t^*=0$ does better for profile #3 (where Equation 7.4.2 gives $w_t^* = .25$ at the onset).

Application of the Model Accounting for Local Buoyancy Effects

In Appendix F5 a model was developed to calculate the critical value of C at the onset of recirculation when local buoyancy effects in the recirculation subchannel are significant. This model will be used to predict the onset of recirculation for runs 5.5, 5.6 and 5.7, but in a form modified to account for flow development empirically.

It is well known that the fully developed flow assumption causes the buoyancy effect to be overestimated. For developing flow, a larger Rayleigh number is required to induced recirculation. This concept may be expressed as:

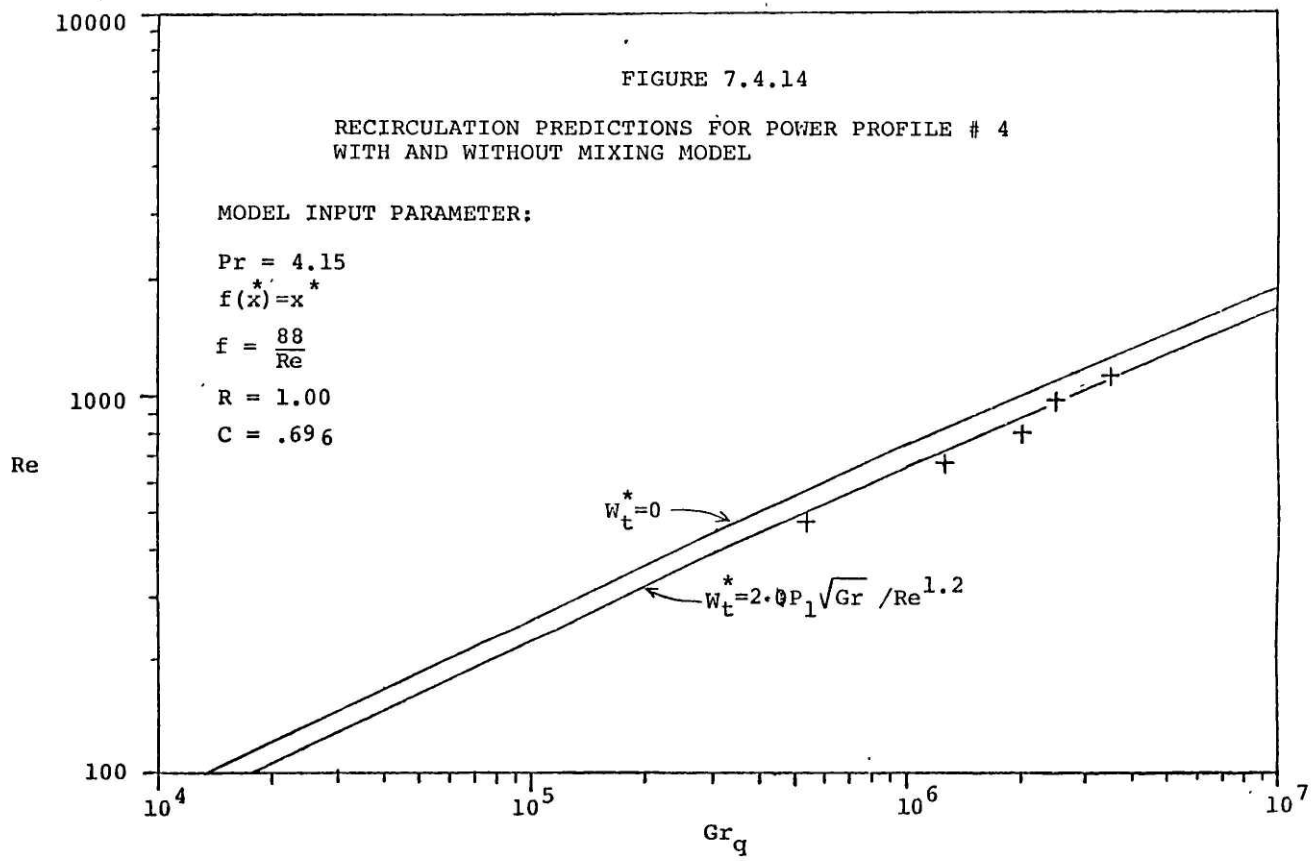


FIGURE 7.4.14

RECIRCULATION PREDICTIONS FOR POWER PROFILE # 4
WITH AND WITHOUT MIXING MODEL

MODEL INPUT PARAMETER:

Pr = 4.15

$f(x^*)=x^*$

$f = \frac{88}{Re}$

R = 1.00

C = .696

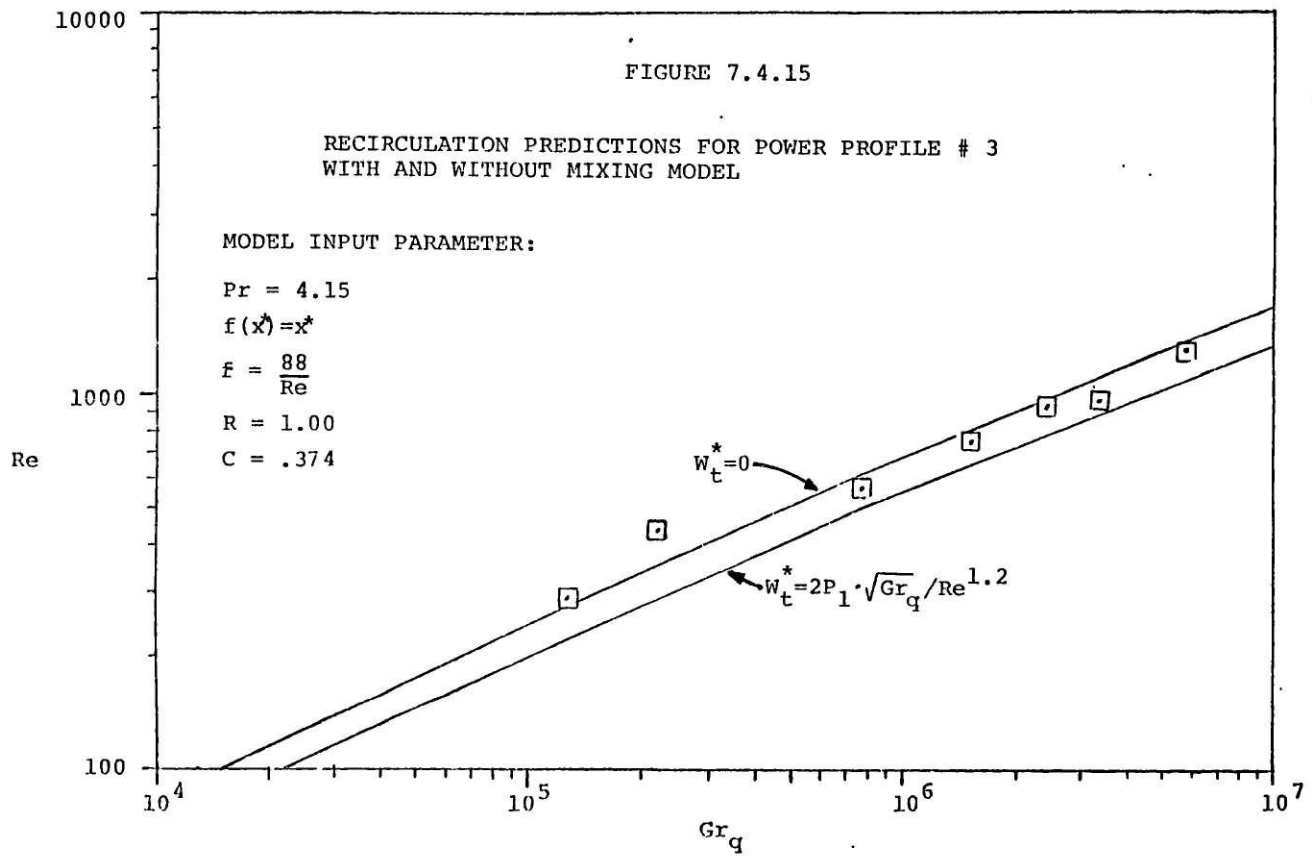


FIGURE 7.4.15

RECIRCULATION PREDICTIONS FOR POWER PROFILE # 3
WITH AND WITHOUT MIXING MODEL

$$Ra_D^C\Big|_{\substack{\text{developing}\\\text{flow}}} = \left(1/F_D\right) Ra_D^C\Big|_{\substack{\text{fully}\\\text{developed}}} \qquad (7.4.3)$$

where F_D is a flow development factor which depends on L/D_e. For fully developed flow $F_D = 1$ while for developing flow $F_D<1$. Substituting Ra_D^C for developing flow from Equation 7.4.3 into Equation F5.9 gives

$$V_{edg}^* = 4 \left[\frac{D_{rod}}{D_{eb}}\right]^4 \frac{D_{eb}}{D_H} \frac{F_D}{Ra_D^C} \frac{Gr_q}{Re} \frac{Q_{min}}{Q_b} \qquad (7.4.4)$$

Equation F5.1 gives the critical Rayleigh number for the square array edge subchannel with P/D = 1.25.

$$Ra_D^C = 10^4 \qquad (7.4.5)$$

Substituting this result into Equation 7.4.4, along with the geometry of the MIT 4x4 rod budnle gives:

$$V_{edg}^* = 6.82E\text{-}4 \frac{Gr_q}{Re} \frac{Q_{min}}{Q_b} F_D \qquad (7.4.6)$$

For power profile #5, Equation F5.20 gives for C_{crit}:

$$C_{crit} = 1 - 2 V_{edg}^* \qquad (7.4.7)$$

Hence the critical value of C is

$$C_{crit} = 1 - 1.364E\text{-}3 \frac{Gr_q}{Re} \frac{Q_{min}}{Q_b} F_D \qquad (7.4.8)$$

Predictions for Fully Developed Flow

The above equation is plotted in Figure 7.4.16 for runs 5.5, and 5.6 as a function of Re for $F_D = 1.0$ (fully developed flow). The intersection of Equation 7.4.8 with the curve of C vs Re predicted by the two channel medel (with w_t^* given by Equation 7.4.2) gives the values of C and Re at the onset of recirculation. It can be seen from Figure 7.4.16 that the value of Re_{crit} for runs 5.5 and 5.6 are 790 and 555, respectively. These points are given in Table 7.4.3 and are observed to overpredict the experimental data considerably (i.e., 790 versus 164 for run 5.4). This overprediction of the onset of recirculation is due to the assumption of fully developed flow.

For the uniform power recirculation data (run 5.7) the two channel model predicts C=0 for all Re, so no recirculation occurs. Considering the local buoyancy effects, we put $V_{edg}^* = 1$ and $Q_{min}/Q_b = 1$ in Equation 7.4.6 and solve for the critical Reynolds number:

$$Re_{crit} = 6.82 \times 10^{-4} Gr_q F_D \qquad (7.4.9)$$

For fully developed flow ($F_D = 1$) this gives $Re_{crit} = 286$ for run 5.7, which far exceeds the experimentally determined value of $Re_{crit} = 101$. Clearly, the assumption of fully

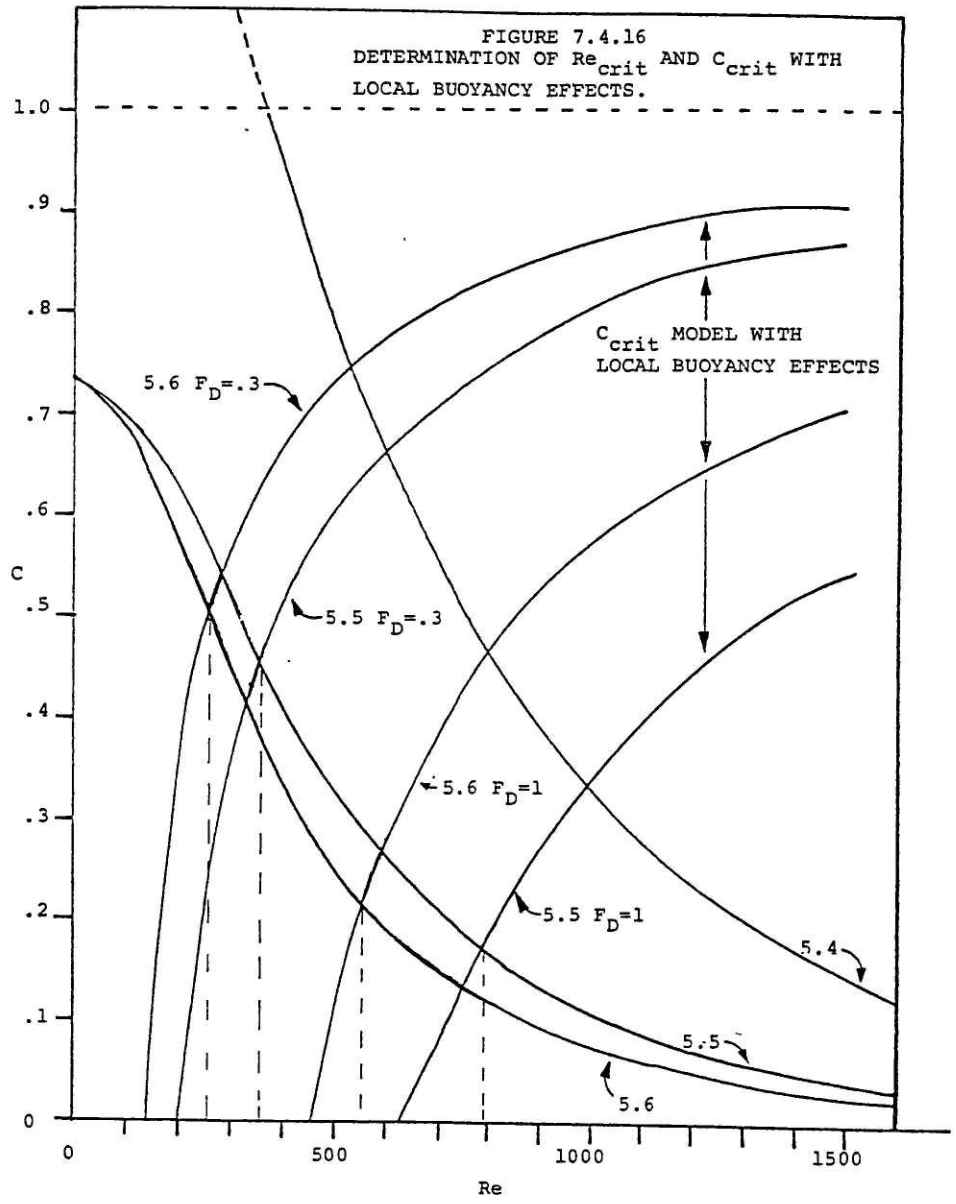


FIGURE 7.4.16
DETERMINATION OF Re_{crit} AND C_{crit} WITH
LOCAL BUOYANCY EFFECTS.

developed flow leads to an over conservative prediction of the onset of recirculation.

Prediction Allowing for the Effects of Flow Development

As discussed earlier the empirical factor F_D of Equation 7.4.4 may be used to account for the effects of flow development. In general F_D will depend on L/D_e. Here, F_D will be calibrated for one value of L/D_e with a limited data base (runs 5.5, 5.6 and 5.7).

It was found that if $F_D = .30$, significant improvement in the predictions occurred. Equation 7.4.8 was used to calculate C_{crit} for runs 5.5 and 5.6 with $F_D = .30$. The results are drawn in Figure 7.4.16. As before, the intersection points give Re_{crit} for runs 5.5 and 5.6 as 360 and 260, respectively. For the case of uniform power (run 5.7) Equation 7.4.9 gives $Re_{crit} = 80$. As shown in Table 7.4.3, this is a significant improvement over the results for $F_D = 1$. The data and final predictions for profile # 5 are given in Figure 7.4.17. The mixing model (Equation 7.4.2) was used for all the runs. The local buoyancy model (Equation 7.4.6) was used for runs 5.5, 5.6 and 5.7 with $F_D = .3$.

7.4.4 Comparison With BNWL Recirculation Data

Flow recirculation was observed to occur in the BNWL 2x6 rod bundle during flow transients in three runs reported in Reference 59, and in one steady state run in Reference 58. Table 7.4.6 lists the conditions under which recirculation

FIGURE 7.4.17

RECIRCULATION DATA WITH MODEL PREDICTIONS
FOR POWER PROFILE # 5

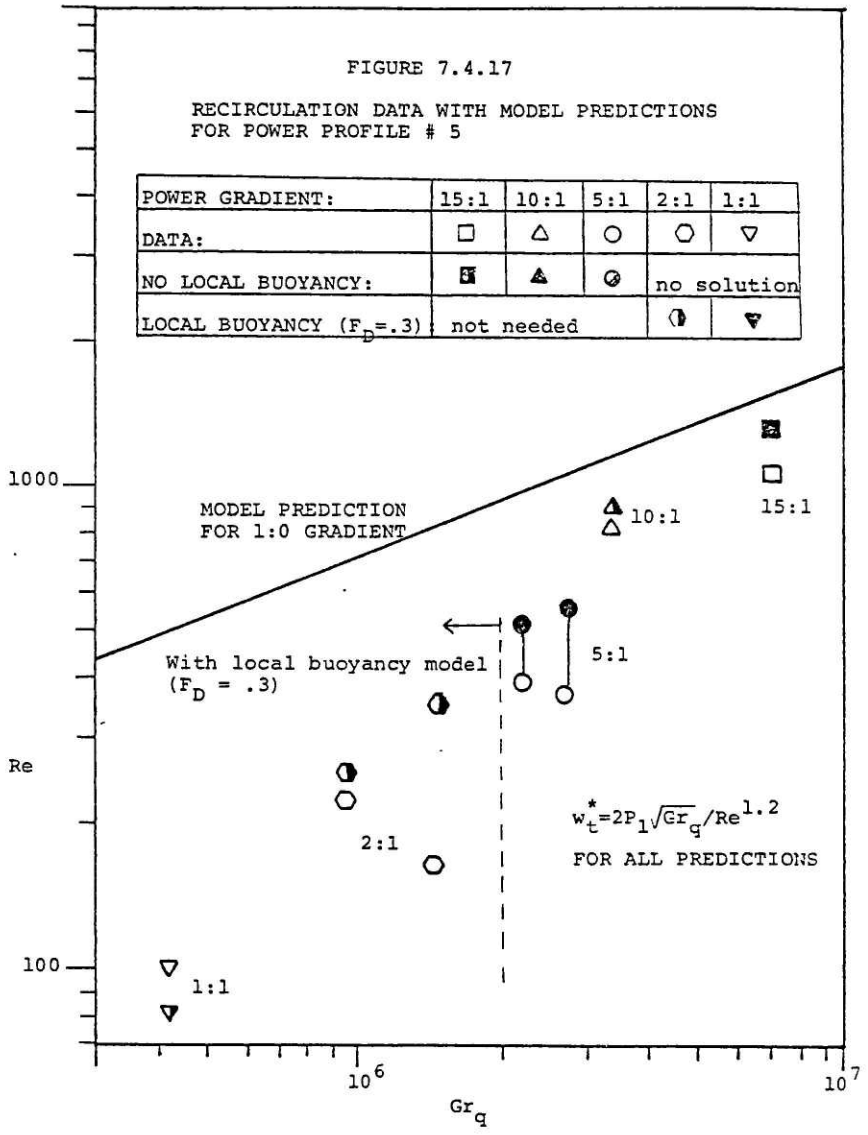


TABLE 7.4.6

ONSET OF RECIRCULATION DATA FROM BNWL 2x6
TRANSIENT AND STEADY STATE RUNS

					At Inception of Recirculation				
	Case #	$\frac{\Delta Re}{\Delta t}$	Transient Time	Power Skew $P_2:P_1$	$\frac{Gr^*}{Re^2}$	Time	Re	Gr_q	Symbol
Transients (59)	4	- 5.13	150	1:0	.20	160[1]	520	5.05×10^5	□
	6	-17.10	45	1:0	.23	55[1]	520	5.81×10^5	○
	9	- 9.11	45	1:0	.29	30	457	4.97×10^5	△
S.S. (58)	2	0	55	1:0	not given	-	480	3.49×10^5	⬡

[1]Recirculation occurred after end of flow coastdown

occurred for the four cases.

The two channel model was employed to predict the onset of recirculation for the four cases. As discussed in Section 6.1.2 the quasi-steady state approximation will be used. Since all of the BNWL recirculation data was for one side of the bundle unheated (1:0 power skew, $P_1 = 0$) it follows that $C_{crit} = 1.0$ and $w_t^* = 0$. The bundle was divided into geometrically identical channels (R=1) for the calculation. The prediction and data are given in Figure 7.4.18. Note that local buoyancy effects are unimportant since there was no heating in the low power side.

It is observed that the model prediction overestimates the onset of recirculation by as much as 41% for case 9. The emperical onset of flow recirculation criteria of Reference 59 is also shown. Their criteria is:

$$\frac{Gr_{\Delta T}}{Re^2} > .2$$

or in the nomenclature of this work,

$$4 \frac{L}{D_H} \frac{Gr_q}{Re^3 Pr} > .2$$

Note that the Prandtl number appears due to the conversion of $Gr_{\Delta T}$ to Gr_q (see Table 2.1.2). The two criteria give similar results over the range of Gr_q considered, though the criterion based on the two channel model has a slightly larger slope.

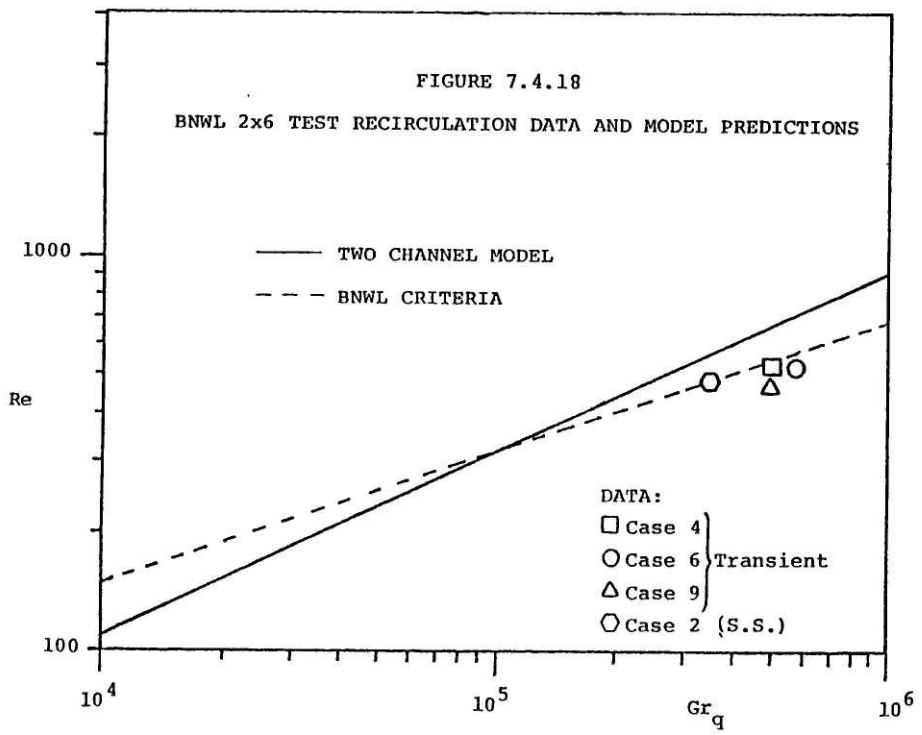


FIGURE 7.4.18

BNWL 2x6 TEST RECIRCULATION DATA AND MODEL PREDICTIONS

It was shown from the analysis of Appendix B2 that the quasi-steady approximation is probably not valid for the transients used in the BNWL tests. The criterion is seen to conservatively predict the transient recirculation data.

7.5 FLOW REGIME MAP AND HAND CALCULATION FOR THE ONSET OF RECIRCULATION

In Section 7.4 the onset of recirculation criteria was compared with experimental data from this work, and data from BNWL. It was found that the criteria predicted the experimental data quite well. However this data was for bare rod bundles with water flow. It is desired to predict recirculation in wire wrapped bundles with sodium flow, where no data presently exists. Since the model includes pertinent geometrical parameters, and the effects of lateral energy transport due to mixing and conduction, it should work for LMFBR bundles as well provided reliable correlations are available for the input parameters.

In this section the onset of recirculation criterion will be represented as a flow regime map. First the dominant dimensionless parameters governing the onset of mixed convection must be identified. It was shown in Appendix F7 that the balance of frictional forces and buoyancy forces is the primary physical mechanism governing flow recirculation. It was also shown that if the frictional and buoyancy forces are in balance, two key dimensionless parameters appear, Re

and B_L^* where B_L^* may be expressed as:

$$B_L^* = \frac{L}{D_H} \frac{Gr_q}{Pr} \frac{K_2P_2-K_1P_1}{C_{fL}C} = \frac{L}{D_H} \frac{\beta g q'' D_e^4}{\mu C_p \nu^2} \frac{K_2P_2-K_1P_1}{C_{fL}C}$$

Note that thermal conductivity does not appear in Gr_q/Pr. The effect of heat conduction is incorporated in K_1 and K_2. The two channel model equation can then be written as Equation F7.16 for laminar flow ($f = C_{fL}/Re$):

$$B_L^* = \frac{Re^3}{4} \left[A^* + \frac{1}{2Re} \right] \tag{7.5.1}$$

and as Equation F7.17 for turbulent flow ($f = C_{fT}/Re^m$):

$$B_L^* = \frac{Re^3}{4} \left[A^* + \frac{1}{2Re^m} \frac{F_C}{C} \frac{C_{fT}}{C_{fL}} \right] \tag{7.5.2}$$

where:

$$A^* = \frac{2+C+4w_t^*}{C_{fL}L/D_e} \tag{7.5.3}$$

$$\frac{F_C}{C} = \frac{(1+C)^{3-m} + (1-C)^{3-m} - 2}{(3-m)\ C^2} \tag{7.5.4}$$

It was shown that though C_{fT} and C_{fL} depend on geometry, the ratio C_{fT}/C_{fL} is nearly constant for different geometries. It was also found the F_C/C is nearly constant for a given m for the range of C of interest (F_C/C varies from 1.75 to 1.72 as C varies from .01 to 1). With the quantities F_C/C

and C_{fT}/C_{fC} taken as constants, Equations 7.5.1 and 7.5.2 may be written functionally as:

$$B_L^* = f_n(Re, A^*, m) \qquad (7.5.5)$$

It was also found that for the rod bundle geometries of interest, the effect of A^* was not strong (see Figure F7.2). Hence it is concluded that Re and B_L^* are the dominant dimensionless parameters governing flow recirculation in rod bundles. The case where $A^* = 0$ represents the limiting situation where inertia and momentum transported by cross-flow and mixing are negligible so that only friction and buoyancy exist (large L/D). The fact that the A* effect is small is important. It means that the onset of recirculation criteria for different geometries and coolants will correlate well in terms of Re and B_L^*.

7.5.1 Onset of Recirculation Criteria Expressed as a Flow Regime Map

The data which was presented in Section 7.4 will next be plotted on Re - B_L^* coordinates. The data is expected to correlate in terms of these parameters because:

1) These are the dominant dimensionless parameters in the model, as shown in Appendix F7

2) The model predicts the data well as shown in Section 7.4.

For comparative purposes, all of the recirculation data is plotted in uncorrelated form (Re versus Gr_q) in Figure 7.5.1.

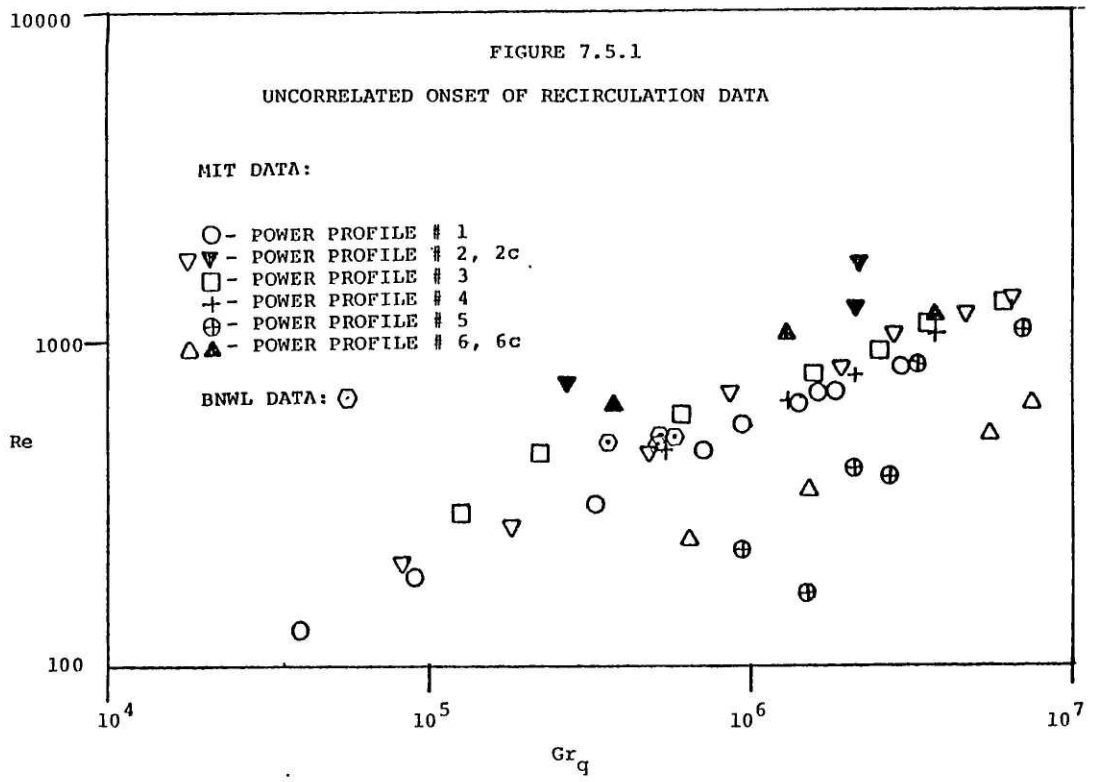


FIGURE 7.5.1

UNCORRELATED ONSET OF RECIRCULATION DATA

Considerable scatter in the data is observed because of the wide range of power skews used, and the existance of a cold wall for some of the runs. The correlated data is shown in Figure 7.5.2. The data is observed to correlate very well in terms of these parameters. Equation 7.4.2 was used to calculate w_t^* (upon which K_1 and K_2 depend) and Equation 7.3.1 was used to calculate the critical value of C, except for runs 5.5 and 5.6 where Equation 7.4.8 with $F_D = .3$ was used to account for local buoyancy effects. Run 5.7 is not included since recirculation was produced by local effects only.

The onset of recirculation predicted by the model (Equation 7.5.2) is also drawn in for the MIT 4x4 bundle ($A^*=5.51 \times 10^{-4}$) and for $A^* = 0$ (friction and buoyancy only. The prediction for the WARD blanket bundle ($A^* = 1.16 \times 10^{-4}$) lies between the two curves given.

The onset of recirculation criterion shown in Figure 7.5.2 included only the laminar flow ($f = C_{fL}/Re$) prediction, since all of the data is in the laminar friction factor region. The criteria is plotted in Figure 7.5.3 with a wider range of B_L^* to include the turbulent friction factor prediction (Equation 7.5.2) of the onset of recirculation. It is observed that at the laminar-turbulent transition, a change in slope occurs due to the change in the friction factor. This causes recirculation to occur at even higher values of Gr_q for a given Re. Both the result for friction and buoyancy only ($A^*=0$) and the prediction for the MIT

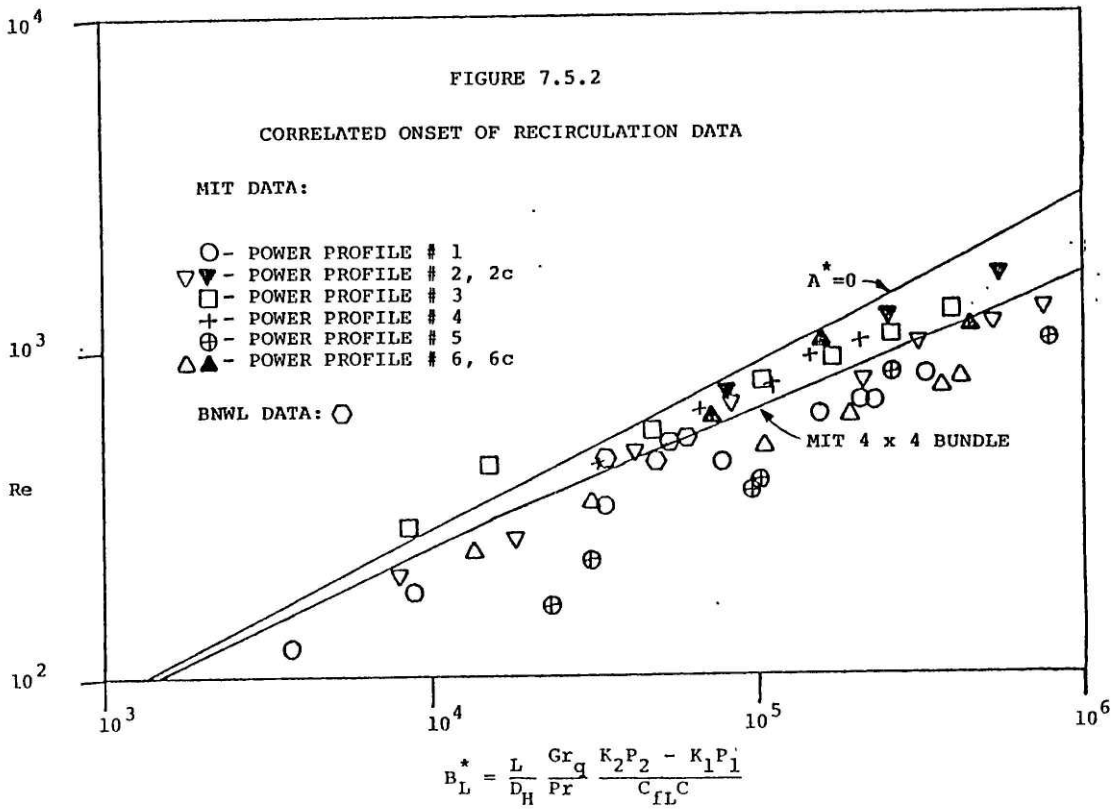


FIGURE 7.5.2

CORRELATED ONSET OF RECIRCULATION DATA

$$B_L^* = \frac{L}{D_H} \frac{Gr_q}{Pr} \frac{K_2P_2 - K_1P_1}{C_{fL}C}$$

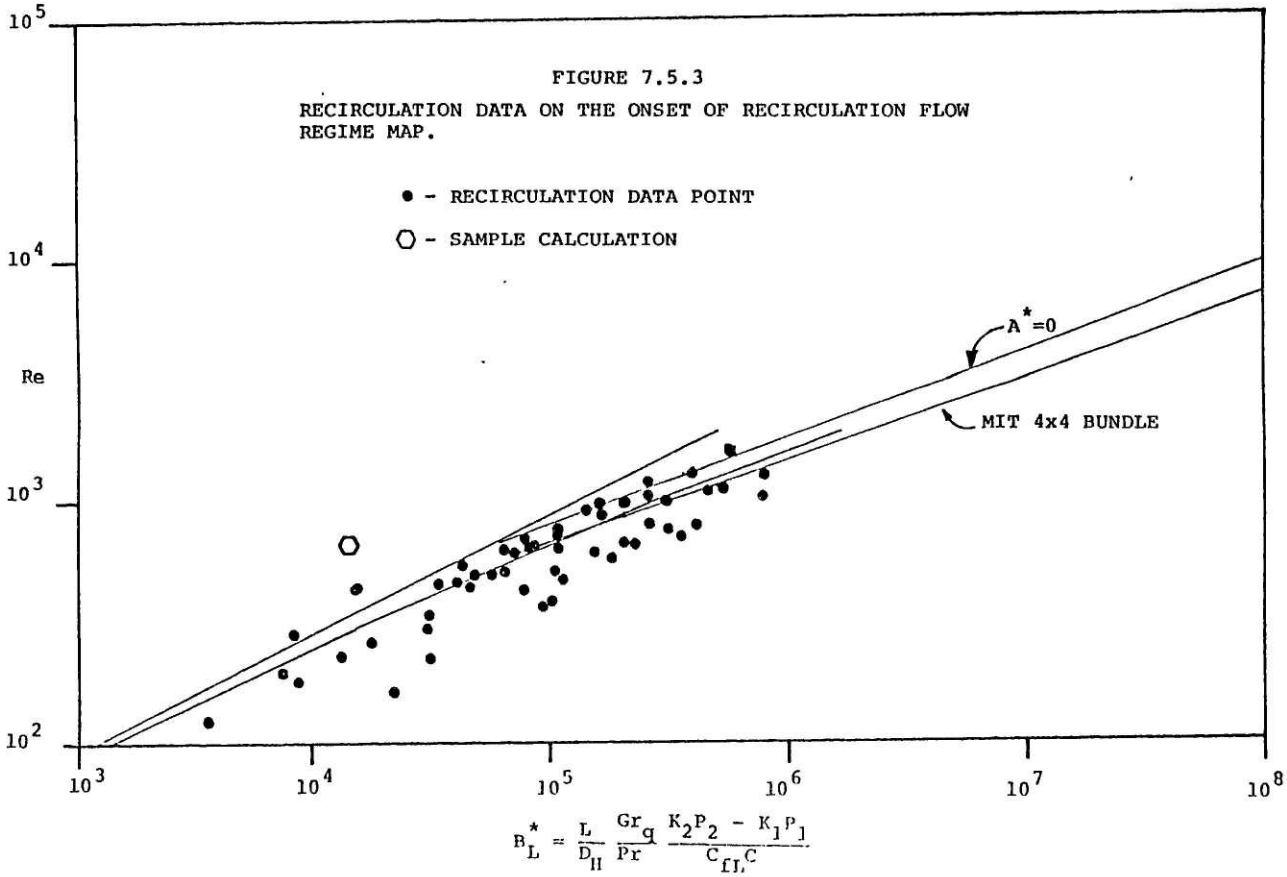


FIGURE 7.5.3

RECIRCULATION DATA ON THE ONSET OF RECIRCULATION FLOW REGIME MAP.

● - RECIRCULATION DATA POINT

⬡ - SAMPLE CALCULATION

4x4 bundle ($A^*=5.51 \times 10^{-4}$) is given, along with the experimental data.

Figure 7.5.3 is the flow regime map for the onset of recirculation in rod bundles. From the bundle operating conditions, Re and B_L^* can be calculated to identify a point on the map, and hence determine if recirculation exists. If the point lies in the region between $A^*=0$ and $A^* = 5.51 \times 10^{-4}$, it may also be necessary to calculate A^* to determine if the recirculation condition exists. However, the dependence of the criteria on A^* is quite weak, and may be neglected in the application of the criteria. In the region of the laminar - turbulent transition, it is recommended that the curve which gives the lower Re_{crit} be used, since the data of Figure 7.4.4 seemed to follow this trend.

7.5.2 Hand Calculation Procedure for the Onset of Recirculation

If one only needs to know if a bundle with given operating conditions is in the recirculation regime or not, a simple hand calculation may be performed to obtain the answer. Since Equations 7.5.1 and 7.5.2 define the onsets, the recirculation condition will exist if:

$$B_L^* > \frac{Re^3}{4}\left[A^* + \frac{1}{2Re}\right] \quad \text{For laminar flow } (Re < 800) \quad (7.5.6)$$

$$B_L^* > \frac{Re^3}{4}\left[A^* \frac{1}{2Re^m} \frac{F_C}{C} \frac{C_{fT}}{C_{fL}}\right] \text{For turbulent flow } (Re > 800) \quad (7.5.7)$$

where A^* and F_C/C are given by Equations 7.5.3 and 7.5.4

respectively. Note that Re = 800 was taken as the transition Reynolds number since the curves of Figure 7.5.3 intersect there .

7.5.3 Recommended Input Parameters and Sample Calculation

The input parameters for the onset of mixed convection criterion are C_{crit}, w_t^*, SF and $f = C_f/Re^m$.

The critical value of C at the onset of recirculation must be obtained from Equation 7.3.1 if local buoyancy effects are neglected and Equation 7.4.7 if they are included. Presently no criterion exists for when the local effects become important. An indication that they must be included is when the power skew term $(K_2P_2 - K_1P_1)$ becomes negative. Physically, this means that the critical value of C specified by Equation 7.3.1 is too large, and temperature reversal occurs (the high power side of the bundle is at a lower temperature than the low power side). If this occurs, the local effects must certainly be considered. Then the additional input parameter F_D must be considered. Until F_D is calibrated against a larger data base, it is recommended that $F_D = 1$ be used to be conservative.

For the mixing parameter (w_t^*) it is recommended that the best available mixing correlations are used. For LMFBR geometries, only forced convection correlations exist. They were used to evaluate w_t^* (Equation 6.2.1) which is plotted in Figure 8.3.1 for the blanket geometry and 8.3.2 for the fuel geometry. The forced convection correlation will provide a conservative estimate of the onset of recirculation. Mixed convection correlations should be developed in the future. In Appendix F6 a model for buoyancy induced

mixing was developed, but was calibrated against a limited data base so is not recommended for general use. Employing $w_t^* = 0$ will yield conservative results.

For the predictions presented here it was found that reasonable agreement is obtained if forced convection friction factor correlations are used in the model; however, mixed convection correlations may be needed if the model is used for higher values of Gr_q. Little information is available on the shape factor, so the user's best estimate should be employed.

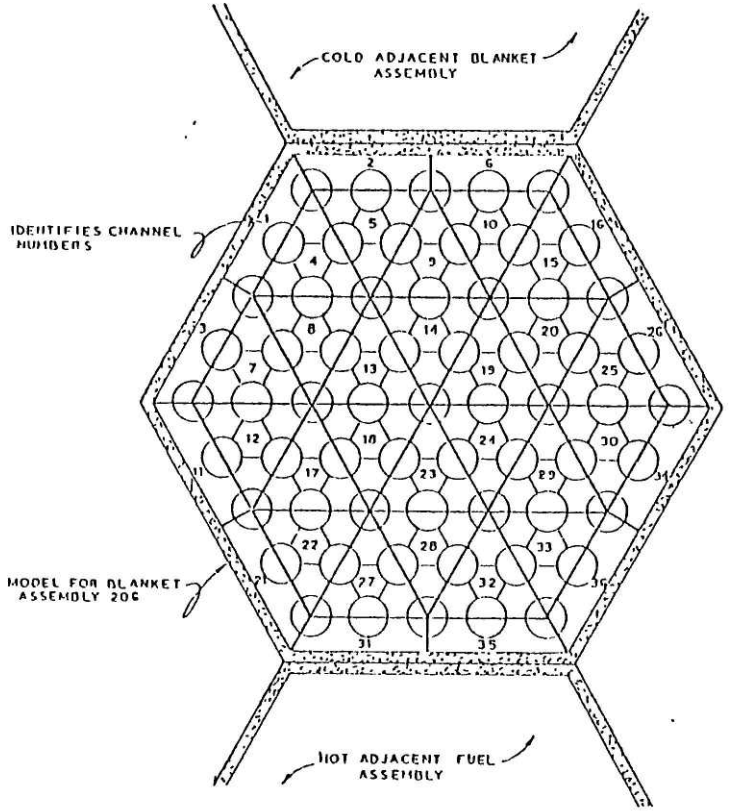
A sample calculation for use of the criterion will next be given. Consider a blanket bundle with the rod power factors shown in Figure 7.5.4 operating at 2.5 GPM (Re = 670) and 18.2 kW (Gr_q = 520). For this power profile, the critical value of C can be found (with a lengthy calculation) from Equation 7.3.1 to be .43. For Re = 670 it can be found from Figure 8.3.1 that K^* = .12, w_t^* = .10 and E* = .22. It then follows from Figure 5.2.2 that K_2 = .60 and K_1 = .85. From the bundle power distribution it is found that P_1 = .40 (Equation 6.2.4) and P_2 = .60 (Equation 6.2.5). For a heated length of 64 inches, B_L^* can then be calculated using Equation F7.15 as:

$$B_L^* = \frac{L}{D_H} \frac{Gr_q}{Pr} \frac{K_2P_2 - K_1P_1}{C_{fL}C}$$

$$= \frac{64}{.18} \frac{520}{.0055} \frac{.6(.6)-.85(.4)}{(110)(.43)}$$

$$= 1.42 \times 10^4$$

FIGURE 7.5.4
POWER DISTRIBUTION IN A BLANKET BUNDLE



.700 .692 .681 .667 .652

.757 .748 .737 .723 .707 .689

.828 .819 .808 .794 .778 .759 .738

.914 .905 .893 .879 .863 .844 .822 .798

1.015 1.006 .995 .980 .963 .944 .922 .897 .870

1.123 1.112 1.097 1.080 1.060 1.038 1.012 .985

1.244 1.231 1.214 1.193 1.170 1.144 1.116

1.382 1.364 1.344 1.320 1.293 1.264

1.533 1.512 1.488 1.460 1.430

NORMALIZED ROD POWERS

The point Re = 670, $B_L^* = 1.42 \times 10^4$ may then be plotted on Figure 7.5.3, where it is found that no recirculation exists. For the hand calculation Equation 7.5.6 is used:

$$1.42 \times 10^4 > \frac{670^3}{4}\left[\frac{2.43 + 4(.10)}{110\quad(308)} + \frac{1}{2(670)}\right]$$

$$1.42 \times 10^4 > 6.24 \times 10^4$$

Since the inequality does not hold, the recirculation condition does not exist.

CHAPTER 8

CRITERIA FOR THE ONSET OF MIXED CONVECTION IN VERTICAL ROD BUNDLES

The purpose of developing a criterion for onset of mixed convection in rod bundles is to be able to predict when buoyancy forces have a significant effect on the bundle temperature and flow field. The criterion can be used to determine if a forced convection code, or a code with mixed convection capability is required in a given situation. The mixed convection code will certainly be valid in the forced convection regime, but the computing cost will be significantly more than that of the forced convection code. This is because the momentum and energy equations are coupled in mixed convection. They can be solved separately in forced convection.

8.1 LITERATURE REVIEW AND PREVIOUS WORK IN CRITERIA DEVELOPMENT

It was suggested by Khan (73) that the inception of mixed convection in a rod bundle could be predicted using the dimentionless parameter Gr^*, defined by:

$$Gr^* = \frac{Gr_{\Delta T}}{fRe^2} X \qquad (8.1.1)$$

where:

$$X = \frac{1}{M} \frac{(Q_p - 1)}{2\gamma L} \qquad (8.1.2)$$

$$M = \frac{1.034}{(P/D)^{.124}} \left[\frac{29.7 (P/D)^{6.94} Re^{.086}}{(H/D)^{2.24}} \right]^{.885} \qquad (8.1.3)$$

$$\gamma = \frac{P/D-1}{D} \frac{16}{\pi} \varepsilon^* \frac{\bar{\lambda}a}{\lambda_{Ll}} + K\alpha^* \bar{\lambda}_a \qquad (8.1.4)$$

when $Gr^* > .025$, the buoyancy effects are important, while if $Gr^* < .025$ they can be neglected. This critical value of Gr^* was determined by comparing the results of ENERGY III (mixed convection code) with ENERGY I (forced convection code) to ascertain when buoyancy affects the peak temperature by 5% of the bulk temperature rise.

It was shown by Greene (67) that Khan's onset of mixed convection parameter represented the ratio of the axial buoyancy force to the axial friction force. It was stated by Greene that the quantity of interest is the temperature field, suggesting that the criterion should be based on thermal effects rather than momentum related effects. Greene went on to develop a criterion by considering the three principal mechanisms which contribute to the transverse energy transport. He considered the energy transport due to enhanced mixing Q_M, buoyancy induced crossflow Q_B and transverse heat conduction Q_C. In his approach the energy transport due to the buoyancy induced crossflow was neglected if:

$$\frac{Q_B}{Q_B+Q_M+Q_C} \simeq \frac{Q_B}{Q_M+Q_C} << 1 \qquad (8.1.5)$$

from which he showed that:

$$\frac{\eta U_T}{S^{K_{Nl}\alpha+\varepsilon_{HNl}/\lambda_{Ll}}} << 1 \qquad (8.1.6)$$

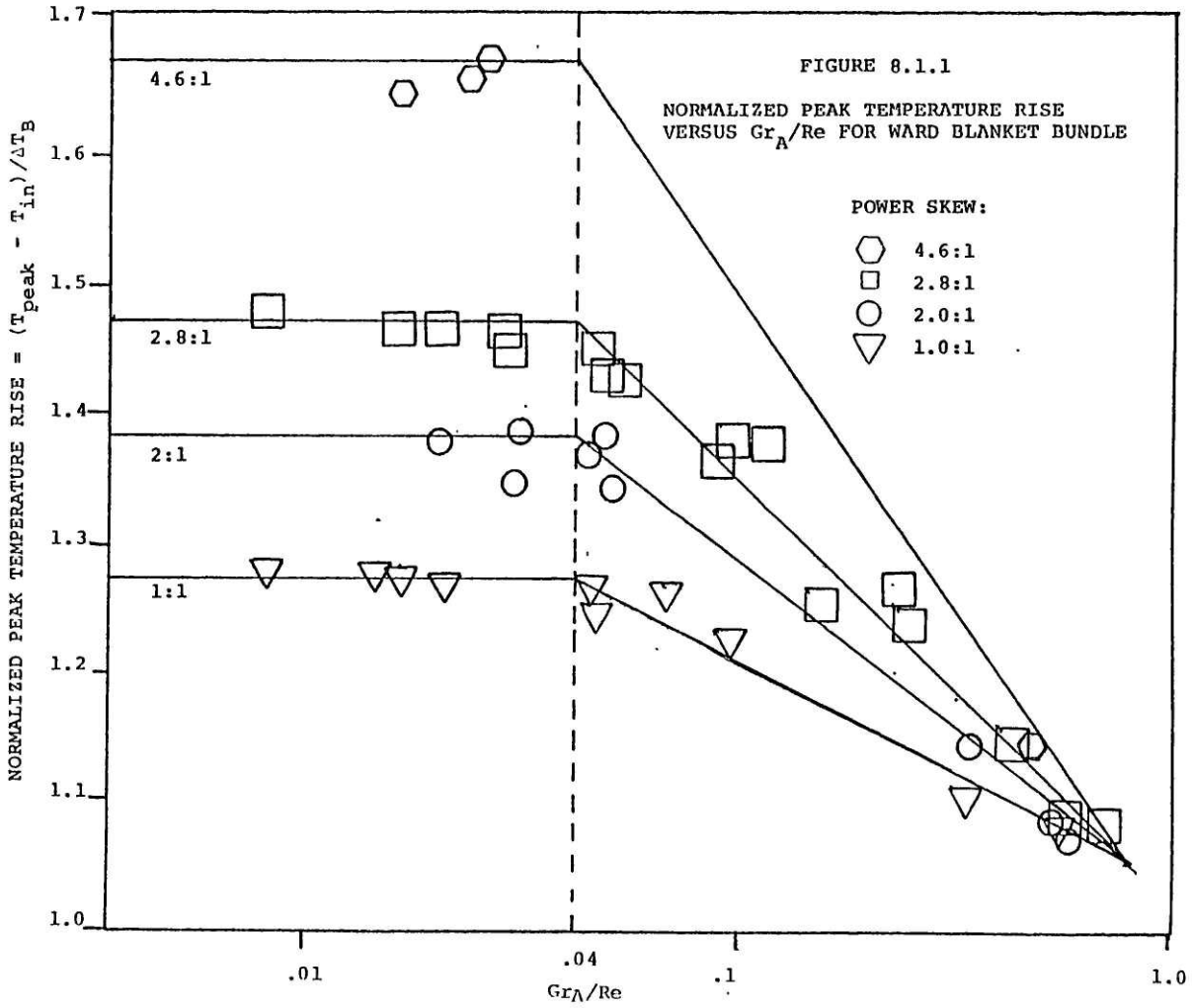
where η is the centroidal distance between interior subchannels, U_T is the transverse velocity, $_S K_{N1}$ is the conduction shape factor, ε_{HN1} is an enhanced eddy diffusivity and λ_{L1} is a lateral porosity.

The transverse velocity U_T was obtained from a two channel model, to give

$$\phi_B = \frac{\eta[g\beta L\Delta T(P/D-1)]^{\frac{1}{2}}}{\varepsilon_{HN1}/\lambda_{L1} + {}_S K_{N1}\alpha} << \frac{K_{ij}\pi}{2\gamma} \qquad (8.1.7)$$

where ϕ_B was proposed as the predictor of the onset of recirculation. The quantity $K_{i\gamma}\pi/2\gamma$ was then calibrated from ENERGY code predictions of the onset of mixed convection, which was defined to be when the maximum difference between the forced and mixed convection solutions is 5^oF. The critical value of ϕ_B was plotted as a function of Re and power skew for the blanket geometry with a heated length of 64 inches. However, Greene's criteria does not include an L/D_e effect.

More recently, a purely empirical criterion has been developed by Engel et al. (74) for the Westinghouse blanket bundle. Engel found that when the normalized peak temperature rise (NPTR) was plotted against the parameter Gr_A/Re, the NPTR started to decrease at a constant value of Gr_A/Re of .04 for a range of powers and power skews shown in Figure 8.1.1. Hence their criterion for the onset of mixed convection is simply:


FIGURE 8.1.1
NORMALIZED PEAK TEMPERATURE RISE VERSUS Gr_A/Re FOR WARD BLANKET BUNDLE
POWER SKEW:
4.6:1
2.8:1
2.0:1
1.0:1
4.6:1
2.8:1
2:1
1:1
NORMALIZED PEAK TEMPERATURE RISE = $(T_{peak} - T_{in})/\Delta T_B$
1.7
1.6
1.5
1.4
1.3
1.2
1.1
1.0
.01
.04
.1
1.0
Gr_A/Re

$$\frac{Gr_A}{Re} > .04 \qquad (8.1.8)$$

for the blanket geometry. In general the constant .04 would depend on geometry (P/D and H/D). Engel indicated (74) that a similar analysis of the ORNL fuel bundle dam gave the onset of mixed convection at $Gr_A/Re \simeq .01$. A lower value for the fuel is expected since the coolant mixing is lower, which allows larger buoyancy forces to develop.

It is surprising that the data for all four power skews begin to decrease at the same value of Gr_A/Re. One would expect a stronger buoyancy influence for larger power skews. Their method may also fail if radial conduction is significant. The decrease in NPTR which they observed may be due to the effects of radial conduction rather than buoyancy induced crossflow.

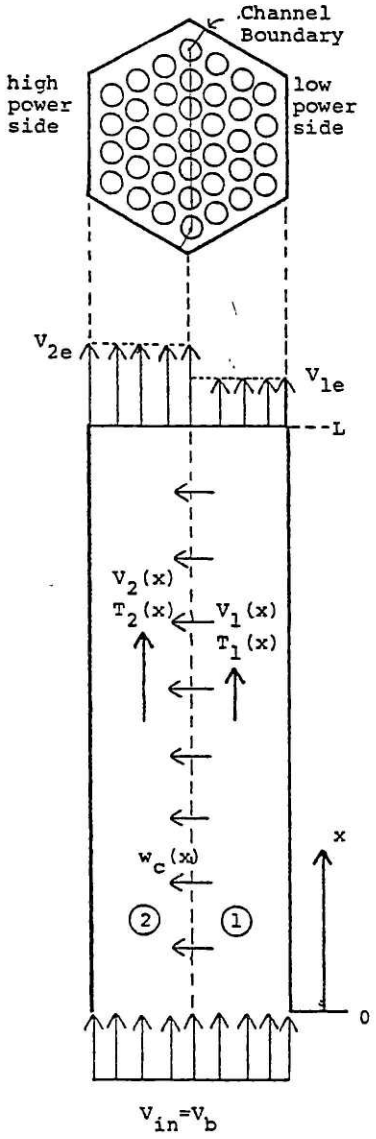
8.2 ALTERNATE APPROACHES FOR PREDICTING THE ONSET OF MIXED CONVECTION

In this section three options for predicting the onset of mixed convection will be given, and the merits of each discussed. The two channel model will be employed for all three methods. Figure 8.2.1 shows the noding scheme employed for an LMFBR rod bundle along with the nomenclature used in the two channel approach. The two channels are of identical geometry so that R=1, and $D_{e1} = D_{e2} = D_{eb}$.

The validation of the two channel model was discussed in detail in Chapter 6. It was concluded that at the onset of mixed convection, $f(x^*) = x^*$ (uniform crossflow) and $g(x^*) = 1$

FIGURE 8.2.1

TWO CHANNEL MODEL OF AN LMFBR ROD BUNDLE



(uniform axial power) gave good agreement to the ENERGY IV predictions. The error in the hot channel exit temperature that is made by employing a uniform crossflow rather than the crossflow which is predicted by ENERGY IV is less than 1%. Hence $f(x^*) = x^*$ and $g(x^*) = 1$ will be employed in the onset of mixed convection calcuations.

In the first approach, inception of mixed convection occurs when the buoyancy induced crossflow becomes significant. A better term for this may be onset of flow redistribution, since the criteria is based on the effect of buoyancy on the flow field. In the second approach, Greene's method will be adopted, but the buoyancy induced crossflow will be obtained from the two channel model. The final method is based on the hot channel exit temperature calculated from the two channel model. This approach bears some similarity to the WARD emprical method, but the effects of conduction and mixing on the reduction of the peak temperature will be considered.

8.2.1 Predictor of the Onset of Mixed Convection Based on the Buoyancy Induced Crossflow

With this approach the onset occurs when buoyancy has a significant effect on the flow field. Within the context of the two channel model, this may be written:

$$\frac{\Delta V_{mc}}{V_b} = \frac{V_{2e} - V_{1e}}{V_b} = V^*_{2e} - V^*_{1e} > 2\alpha \qquad (8.2.1)$$

where α is some constant which is small at the onset of mixed convection. Substituting Equations 5.2.5 and 5.2.10 (with S=1 for uniform inlet velocity) gives:

$$(R+1)\ C > 2\alpha \qquad (8.2.2)$$

For R=1, this becomes

$$C > \alpha \qquad (8.2.3)$$

The criteria for onset of flow redistribution requires C to be a constant. This is the same as the onset of flow recirculation criteria, but with a different value of C. We will use C = .01 for the onset of mixed convection criteria.

8.2.2 Criteria for Onset of Mixed Convection Based on Buoyancy Induced Energy Transport

With this approach, the onset of mixed convection occurs when the buoyancy induced transverse energy transport becomes significant with respect to other transverse energy transport mechanisms (turbulence and wire induced mixing, and conduction). This is the two channel equivalent of Greene's method. The three energy transport mechanisms may be written:

Buoyancy Induced Crossflow: $$dE_C = w_C C_p (T_2-T_1)dx \qquad (8.2.4)$$

Mixing Due to Turbulence or Wire Induced Mixing: $$dE_M = w_t C_p (T_2-T_1)dx \qquad (8.2.5)$$

Heat Conduction: $$dE_K = \frac{w}{\ell}\ SF\ K(T_2-T_1)dx \qquad (8.2.6)$$

Define ϕ as a measure of the relative importance of buoyancy induced energy transport:

$$\phi = \frac{E_C}{E_M + E_K} \tag{8.2.7}$$

For onset of mixed convection, ϕ is fixed at a constant, but small value of α. Integrating equations 8.2.4, 8.2.5 and 8.2.6 and substituting them into Equation 8.2.7 gives:

$$\phi = \frac{\int_0^L w_C C_p (T_2 - T_1) dx}{(w_t C_p + \frac{w}{\ell} K\ SF) \int_0^L (T_2 - T_1) dx} \tag{8.2.8}$$

or, in dimensionless form:

$$\phi = \frac{\int_0^1 w_C^* y\ dx^*}{(w_t^* + \frac{w}{\ell} \frac{LD_e}{A_b} \frac{SF}{RePr}) \int_0^1 Y\ dx^*} \tag{8.2.9}$$

define $\bar{w}_C^*$ as:

$$\bar{w}_C^* \equiv \frac{\int_0^1 w_C^* y\ dx^*}{\int_0^1 y\ dx^*} \tag{8.2.10}$$

so that:

$$\phi = \frac{\bar{w}_C^*}{w_t^* + \frac{w}{\ell} \frac{LD_e}{A_b} \frac{SF}{RePr}} = \frac{\bar{w}_C^*}{E^*} \tag{8.2.11}$$

For the case that w_C^* is not a function of x* (constant cross-flow, or $f(x^*) = x^*$) the integrals cancel out of Equation 8.2.10,

and $\bar{w}_C^* = w_C^* = RC/(1+R)$. Then, with R=1 Equation 8.2.11 becomes:

$$\phi = \frac{C}{2E^*} \tag{8.2.12}$$

Alternately, we can define Φ as the ratio of buoyance induced transverse energy transport to the total transverse energy transport:

$$\Phi = \frac{E_C}{E_C + E_M + E_K} \tag{8.2.13}$$

From Equation 8.2.7, ϕ and Φ can be related by

$$\Phi = \frac{\phi}{1+\phi} \tag{8.2.14}$$

For uniform crossflow, Equation 8.2.12 can be substituted into 8.2.14 to give:

$$\Phi = \frac{C}{2E^* + C} \tag{8.2.15}$$

At the onset of mixed convection the buoyancy induced energy transport is becoming significant, so the onset may be defined as

$$\phi = \alpha \tag{8.2.16}$$

or in terms of Φ:

$$\Phi = \frac{\alpha}{1+\alpha} \simeq \alpha \qquad (8.2.17)$$

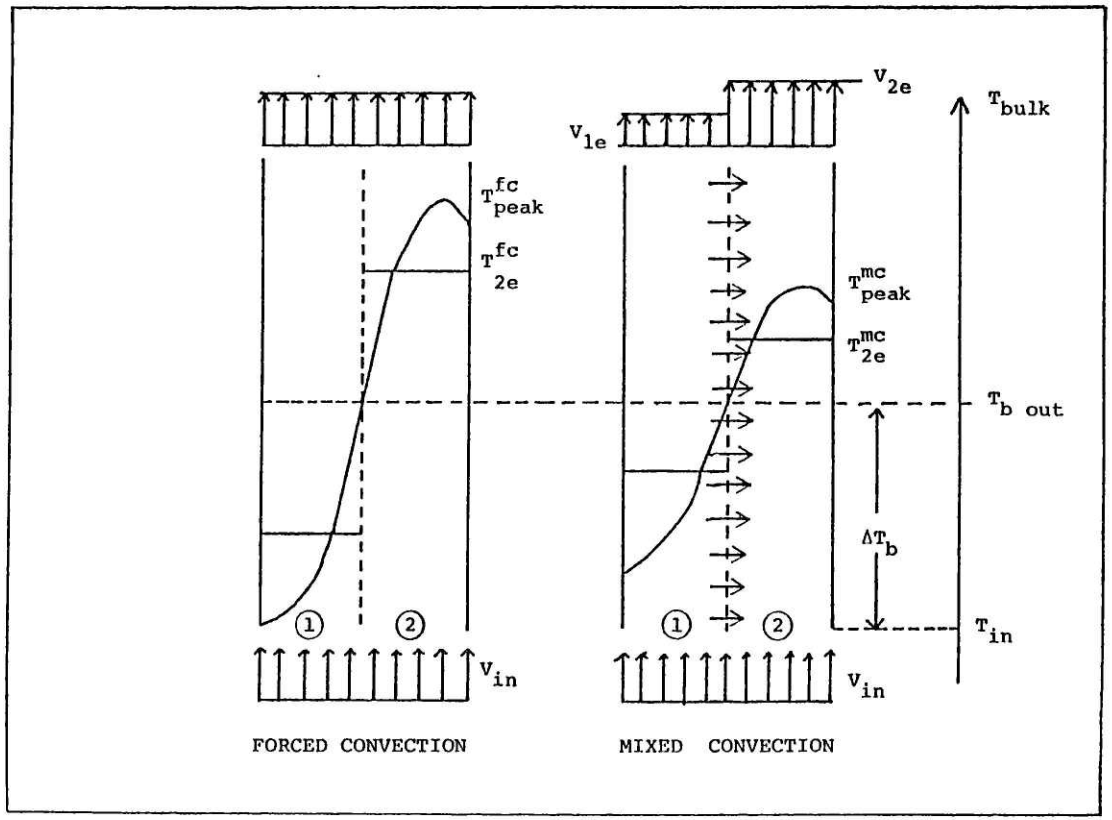
where α is a constant which is small at the onset of mixed convection.

8.2.3 Criterion for Onset of Mixed Convection Based on the Peak Temperature Rise

From the LMFBR designers point of view, the bundle peak temperature is of most interest since it is one of the design limitations. As indicated in Figure 8.2.2 the peak temperature is higher for the forced convection solution than the mixed convection solution. As the mixed convection regime is approached, the difference between the forced convection peak temperature and the mixed convection peak temperature increases. The criteria of Engel et al. (74) was based on this peak bundle temperature, which was determined experimentally. For the two channel model, the hot channel exit temperature T_{2e} can be considered to represent the peak bundle temperature. As shown in Figure 8.2.2 T_{2e} is smaller than the actual peak temperature since it is a channel average temperature, but its numerical value is not of importance here. We are primarily interested in determining when the peak temperature calculated from a mixed convection analysis of the rod bundle begins to differ from the peak temperature calculated from a forced convection analysis. Within the context of the two channel model this may be expressed as:

FIGURE 8.2.2

TEMPERATURE AND FLOW FIELDS FOR FORCED CONVECTION AND MIXED CONVECTION WITH TWO CHANNEL MODEL APPROXIMATIONS.



$$\psi = \frac{T_{2e}^{mc} - T_{2e}^{mc}}{\Delta T_B} = \theta_{2e}^{fc} - \theta_{2e}^{mc} = \alpha \qquad (8.2.18)$$

At the onset of mixed convection α is small. We will employ $\alpha = .01$, so the onset of mixed convection is defined by

$$\psi = \theta_{2e}^{fc} - \theta_{2e}^{mc} = .01 \qquad (8.2.19)$$

In the above equations fc indicates forced convection solution and mc indicates mixed convection solution. To calculate the onset of mixed convection we require the forced convection hot channel temperature, θ_{2e}^{fc}. The forced convection solution has been obtained in Appendix C1, and for R=1 it may be expressed in the following normalized form:

$$\frac{\theta_{2e}^{fc} - 1}{P_2 - P_1} = \frac{1-e^{-4E^*}}{4E^*} \qquad (8.2.20)$$

where E* is given by Equation 5.2.42, and is the sum of the dimensionless coolant mixing (w_t^*) and the dimensionless radial conduction (K*). As discussed in Section 6.2.2, for LMFBR bundles w_t^* may be expressed in terms of the mixing and flow-split parameters, and bundle geometry by Equation 6.2.1. For bare rod bundles w_t^* is considerably smaller. It may be determined from bare rod mixing correlations, or in some instances it may be neglected. For water-cooled bundles, the conduction term (K^*) may be neglected. If both w_t^* and K^* are negligible E* is close to zero and Equation 8.2.20

reduces to:

$$\frac{\theta_{2e}^{fc} - 1}{P_2 - P_1} = 1 \qquad (8.2.21)$$

so that the forced convection solution depends on the power skew only (no radial energy transport).

8.2.4 Discussion of the Three Approaches

Three predictors for the onset of mixed convection have been discussed. The first predictor based on the buoyancy induced crossflow will be called the C = constant approach. The second predictor based on the lateral energy transport will be called the ϕ = constant approach or Φ = constant approach depending on whether Equation 8.2.7 or Equation 8.2.13 is used to define the predictor. The final method based on the peak temperature rise will be called the ψ = constant approach.

Of the three methods discussed, the one based on the lateral energy transport has definite shortcomings. The ϕ = constant approach is similar to the method employed by Greene for LMFBR geometries. A problem arises if the mixing and conduction terms are zero, because E* becomes zero. If $E^* = 0$, Equation 8.2.12 becomes $\phi = \infty$, and Equation 8.2.15 becomes $\Phi = 1$. Hence for $E^* = 0$, the ϕ = constant approach tells us that buoyancy is always important while the Φ = constant approach tells us that buoyancy is never

important. The problem is due to the definitions of ϕ and Φ. The buoyancy induced energy transport is being compared to other lateral energy transport mechanisms. If there are no other lateral energy transport mechanisms ($E^* = 0$, as may be the case in bare rod bundles with water coolant) the definition is meaningless. Though the ϕ and Φ approaches may give meaningful results for LMFBR geometries, they will be rejected because they lack general application.

Thus we are left with the C = constant and ψ = constant formulations, which both give meaningful results when the buoyancy induced crossflow is the only mechanism for lateral energy transport ($E^*=0$). In fact, for $E^*=0$ or E^* = constant it follows from the energy equation that ψ is a function of C only. Therefore C = constant implies that ψ must be constant also, though the numerical values of the constants will differ.

In the section which follows the C = constant and ψ = constant approaches will be examined in detail for LMFBR geometries where $E^* \neq 0$.

8.3 CALCULATION OF THE ONSET OF MIXED CONVECTION IN LMFBR BUNDLES

In this section determination of the onset of mixed convection in LMFBR bundles will be discussed. As indicated earlier, for bare rod bundles with a coolant of higher Pr, the effects of mixing and conduction may be negligible ($E^*=0$) so the calculations are simplified considerably. For the

LMFBR case, we must first determine w_t^* and K^*.

8.3.1 Input Parameters for LMFBR Rod Bundles

The mixing and flowsplit parameters from the correlations of reference 69 are plotted as a function of Reynolds number in Figures 6.2.1 and 6.2.2 for the blanket geometry, and in Figures 6.2.3 and 6.2.4 for the fuel geometry (the geometry of the two bundles is given in Table 6.2.1). Equation 6.2.1 with F_g=.75 (determined in Section 6.2.3 for the blanket bundle) was then used to calculate w_t^* as a function of Reynolds number for the two bundles. The parameter F_g is not believed to be geometry dependent. The results are given in Figures 8.3.1 and 8.3.2 for the fuel and blanket geometries, respectively. Also shown is the dimensionless conduction term, which is given by

$$K^* = \frac{SF}{RePr} \frac{w}{\ell} \frac{D_e L}{A_b} \qquad (8.3.1)$$

The value for E^* was then calculated as $w_t^* + K^*$, and Equation 8.2.20 was used to evaluate the normalized forced convection hot channel temperature. These results are also given in Figure 8.3.1 for the blanket geometry, and Figure 8.3.2 for the fuel geometry. For comparative purposes the fuel and blanket results are plotted together in Figure 8.3.3.

For turbulent flow, it is observed in Figure 8.3.3 that the mixing term (w_t^*) is about twice as large for the blanket bundle due to the tighter wire wrap pitch. For laminar

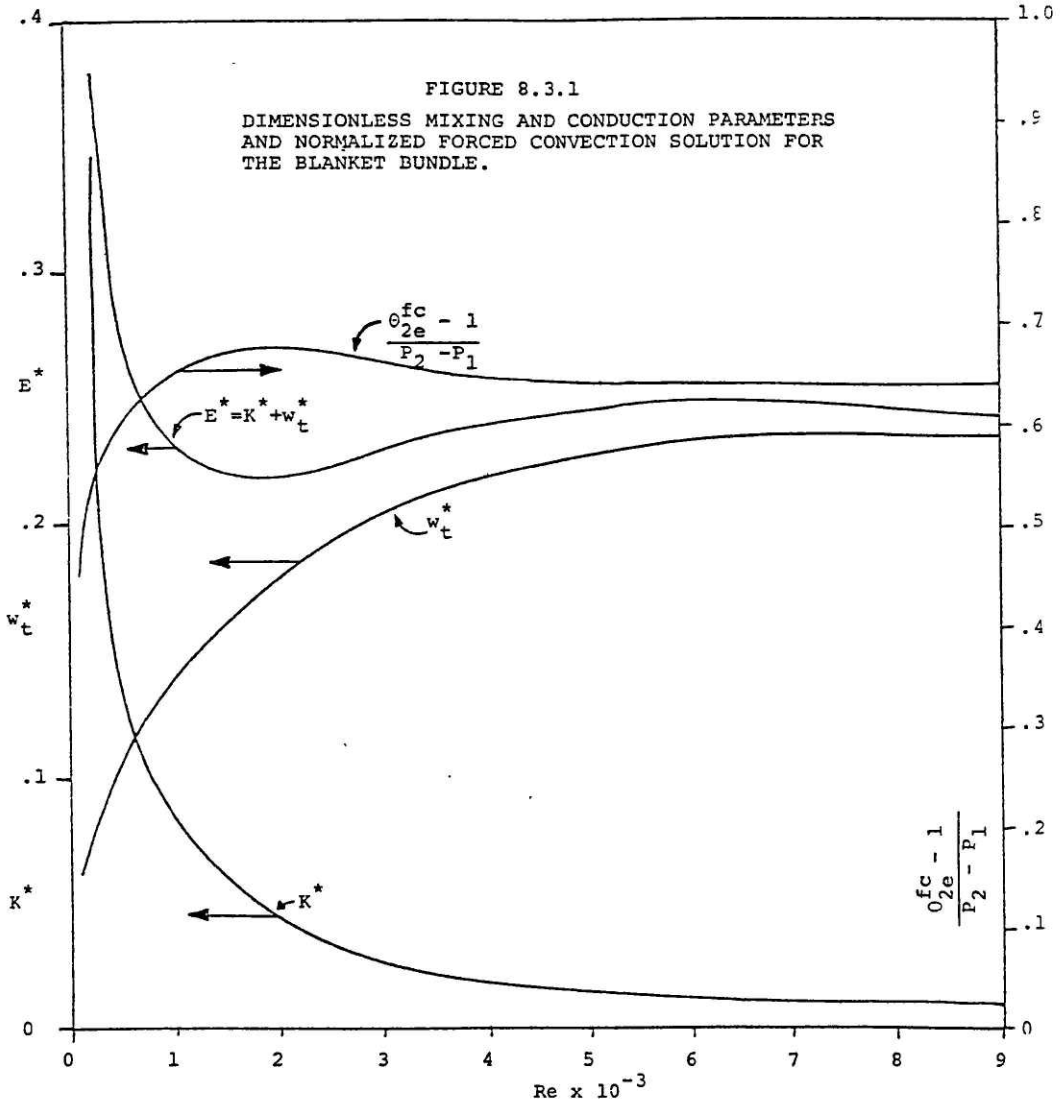
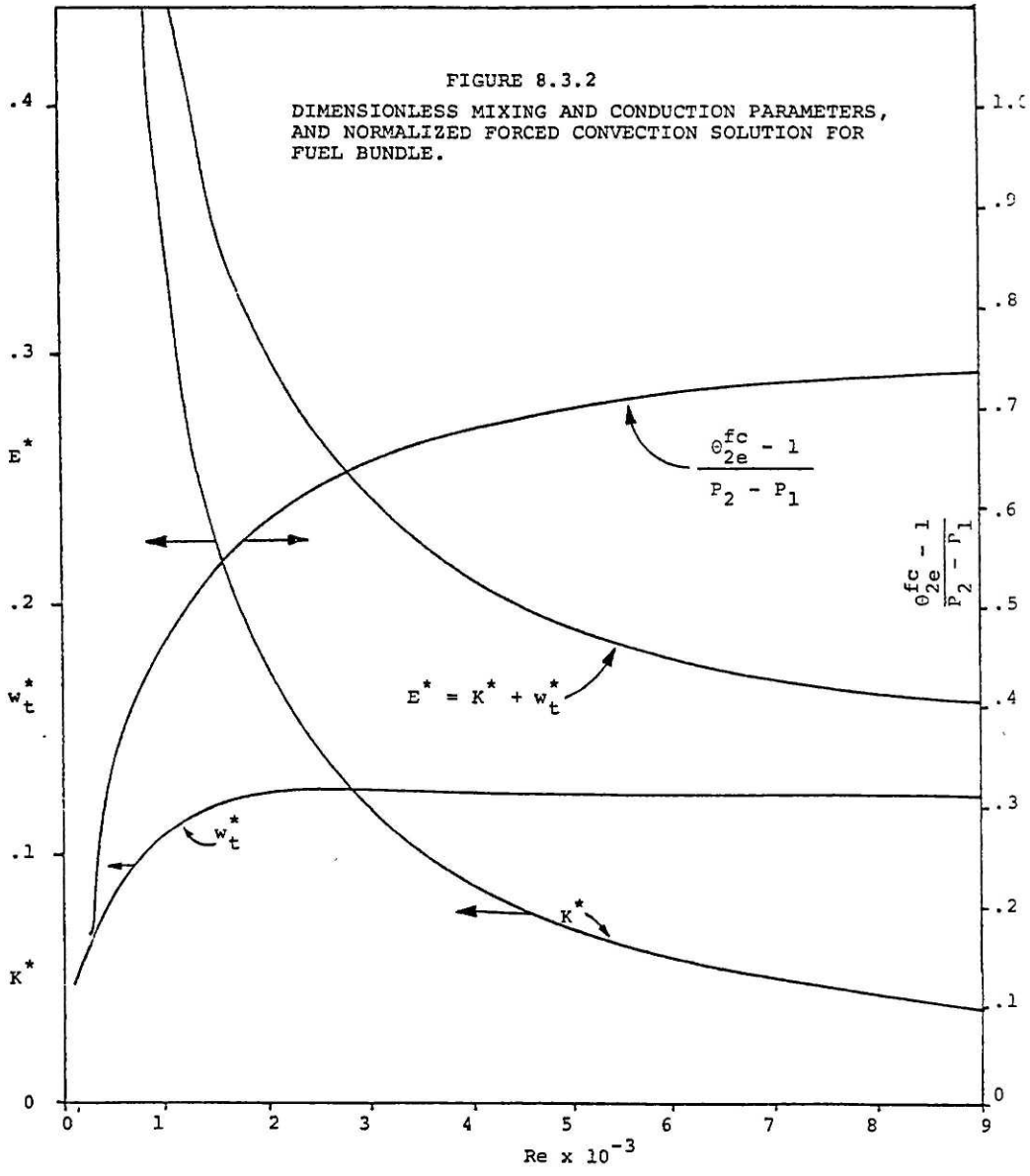


FIGURE 8.3.1

DIMENSIONLESS MIXING AND CONDUCTION PARAMETERS AND NORMALIZED FORCED CONVECTION SOLUTION FOR THE BLANKET BUNDLE.

FIGURE 8.3.2
DIMENSIONLESS MIXING AND CONDUCTION PARAMETERS, AND NORMALIZED FORCED CONVECTION SOLUTION FOR FUEL BUNDLE.



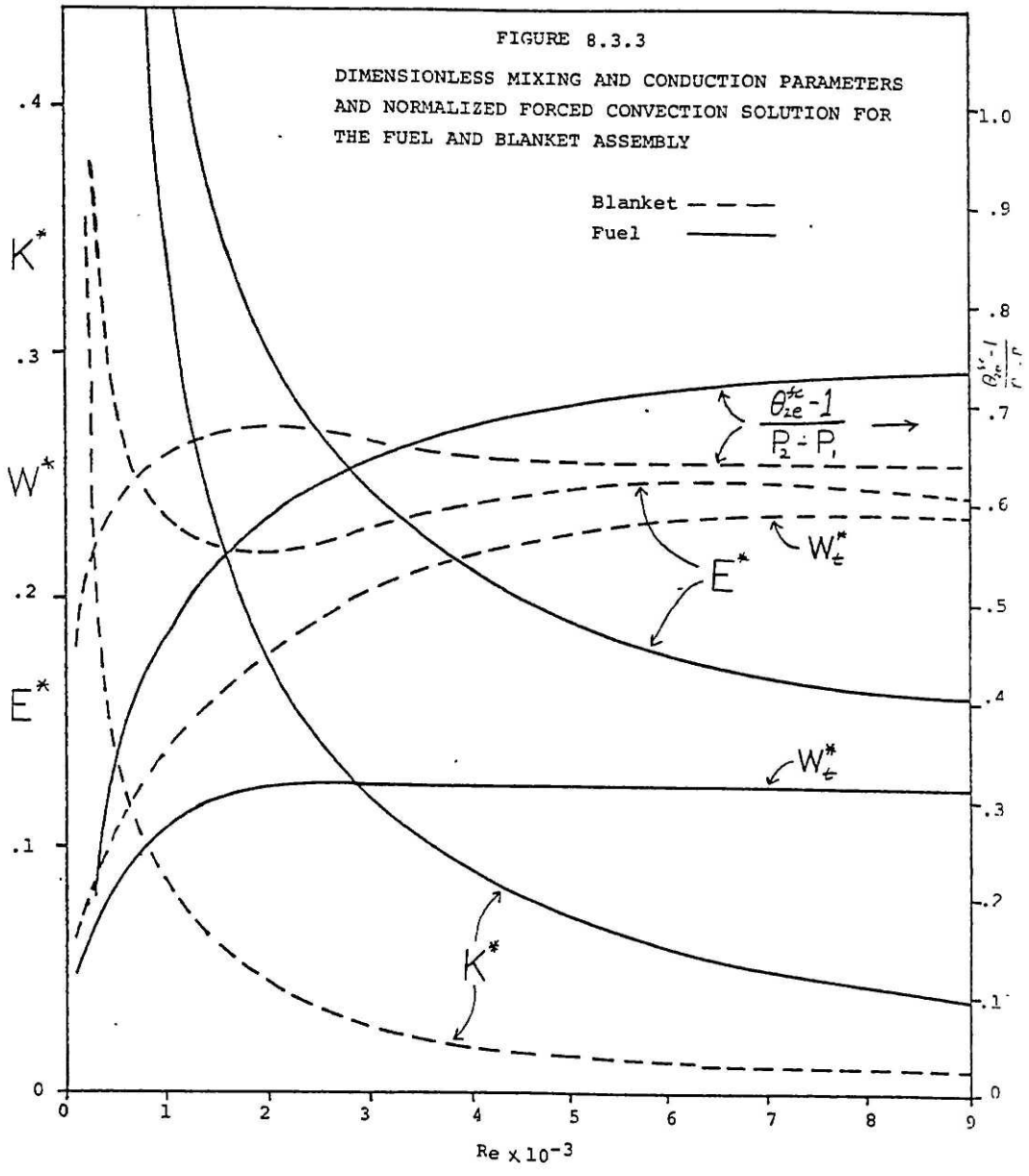


FIGURE 8.3.3

DIMENSIONLESS MIXING AND CONDUCTION PARAMETERS AND NORMALIZED FORCED CONVECTION SOLUTION FOR THE FUEL AND BLANKET ASSEMBLY

flow, w_t^* decreases with Re for both cases, though w_t^* starts to drop at a higher Re for the blanket bundle. The dimensionless conduction term (Equation 8.3.1) varies inversely with Re, and is about 4 times as large for the fuel bundle since the gap between rods, and hence the conduction width (w) is larger. The sum of w_t^* and K^* is E^*, the total forced convection lateral energy transport term. Significantly different behavior in E^* is observed for the fuel and blanket assemblies. E^* decreases monotonically with Re for the fuel bundle, but a local minima occurs at Re = 1500 for the blanket assembly.

With E^* known in Figures 8.3.1 and 8.3.2 the forced convection solution θ_{2e}^{fc} can be calculated from Equation 8.2.20. The results given in 8.3.5 indicate that for the blanket assembly, θ_{2e}^{fc} is nearly constant with Re down to Re = 1500 due to the cancelling effects of decreasing mixing (w_t^*) and increasing conduction (K^*). A maxima occurs at Re = 1500. Then θ_{2e}^{fc} decreases rapidly with Re as the conduction dominates. This local peak is also predicted by ENERGY-IV-FC (Figure 6.2.3) for forced convection. For the fuel (Figure 8.3.2) assembly no such peak exists, and θ_{2e}^{fc} decreases continuously with Re, as shown in Figure 8.3.2.

The results presented in Figures 8.3.1 to 8.3.3 for w_t^* are based on the latest forced convection correlations for ε_{1L}^* and C_{1L}. For low Re, local buoyancy effects may be important, causing a distortion of the subchannel velocity profile, and an enhancement of the effect of the wire wrap.

These results should be revised when mixed convection correlations become available. Also, the results for K^* should be considered preliminary until more information is available on the shape factor. In the Westinghouse blanket test, conduction through the heater pins was significant at low Re. If large enough, this shunting effect could eliminate the peak temperature at Re = 1500 of Figure 8.3.1.

8.3.2 Calculation of the Onset of Mixed Convection

Determination of the onset of mixed convection with the constant ψ approach requires repetitive calculation of θ_{2e}^{mc} and θ_{2e}^{fc} for decreasing Re. When ψ, the difference between the two is .01, Equation 8.2.19 is satisfied and the onset has been found. These calculations were performed by program TWOCHAN discussed in Appendix D. For a given set of operating conditions TWOCHAN solves Equation 5.3.2 for C with the bisection method. For the constant C approach, if $C = \alpha$ (Equation 8.2.3) the onset has been found. For the constant ψ approach, the hot channel exist temperature θ_{2e} must be calculated from Equation 5.1.77 where y is given by Equation 5.2.50. Ideally, it would be desirable to solve for the value of Re at which ψ or $C = \alpha$, but the equations generally do not allow such a simple solution. The only exception is the $c = \alpha$ approach, which for $f = \frac{C_f}{Re}$ leads to a cubic equation which has an analytical solution, albeit complicated.

Figures 8.3.4 and 8.3.5 show the results of this calculation for the blanket and fuel assemblies, respectively

FIGURE 8.3.4

DETERMINATION OF THE ONSET OF MIXED CONVECTION FOR THE BLANKET BUNDLE

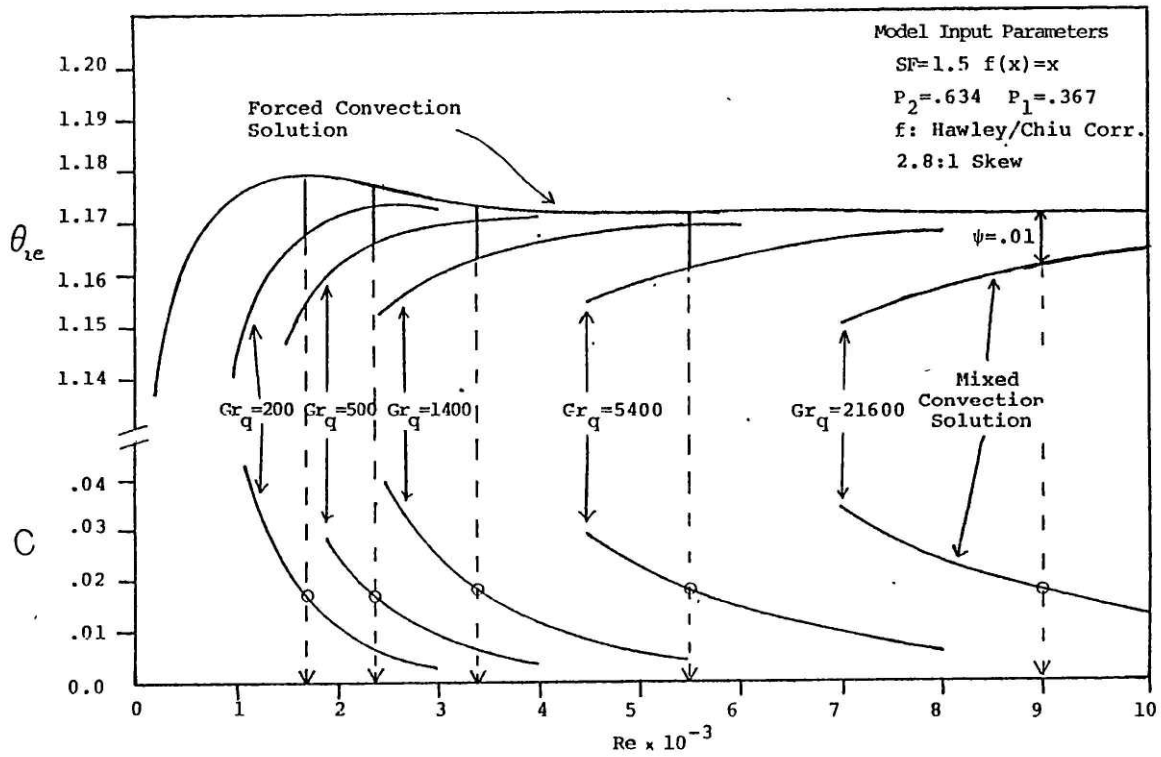
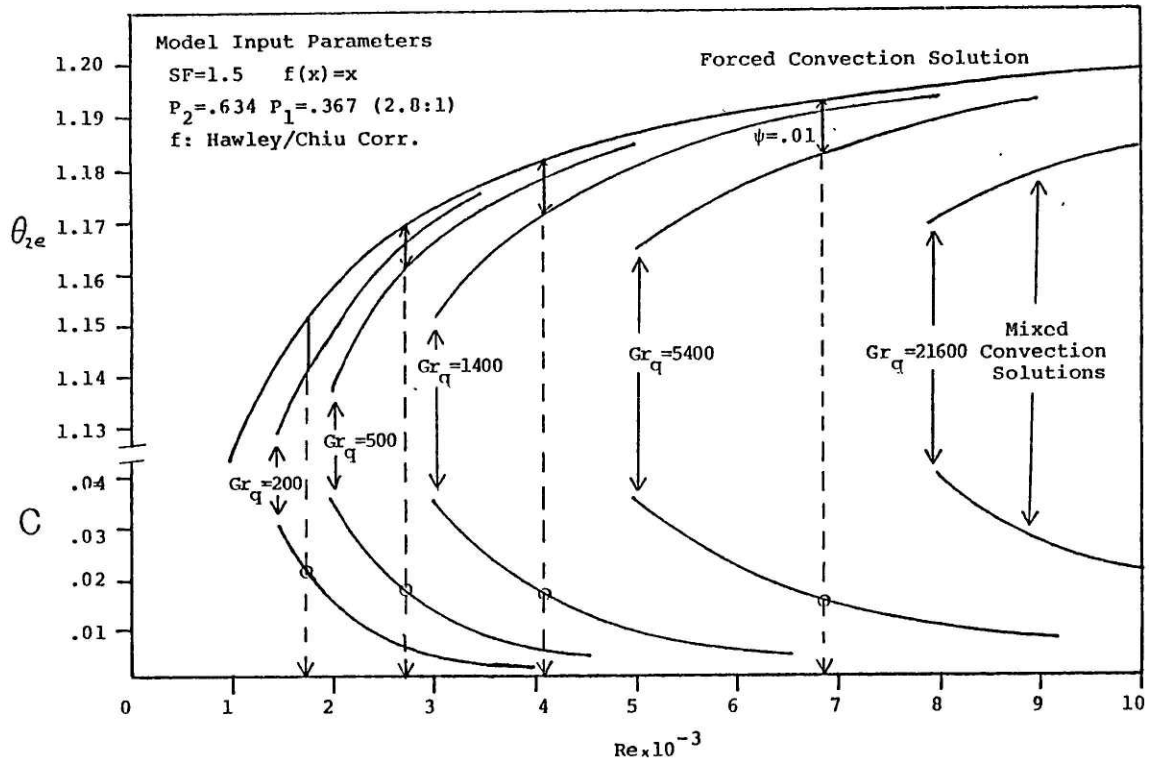


FIGURE 8.3.5

DETERMINATION OF THE ONSET OF MIXED CONVECTION FOR THE FUEL BUNDLE



with a 2.8:1 maximun/minimum power gradient for Gr_q = 200, 500, 1400, 5400 and 21600. This range in Gr_q corresponds to a power range of 10 to 800 kW. The vertical lines drawn between theforced convection and mixed convection solutions indicate the onset of mixed convection (ψ = .01) for each Gr_q. Looking directly below the vertical lines, the corresponding value for C can be found, along with the Reynolds number at the onset of mixed convection. It is observed that the value of C corresponding to ψ = .01 is nearly constant at a value of .015 to .020 for all the runs.

Figure 8.3.6 shows the effect of power skew on the onset of mixed convection. The values of Re and C at the onset are also given in Table 8.3.1. The larger the power skew, the hgher the Reynolds number at the onset of mixed convection, and the smaller the value of C. The results of Figures 8.3.4 to 8.3.6 are summarized in Table 8.3.1, which gives the values of Re and C at which ψ = .01. Values for the parameters B* and Gr_A/Re are also given, and will be discussed at a later time.

8.3.3 Comparison of Model Results to the Westinghouse Criterion

In this section the onset of mixed convection criterion based on the two channel model will be compared to the Westinghouse empirical criterion of Reference 74.

It follows form Figures 8.3.4 and 8.3.5 that the fuel bundle enters the mixed convection regime at a higher Re than

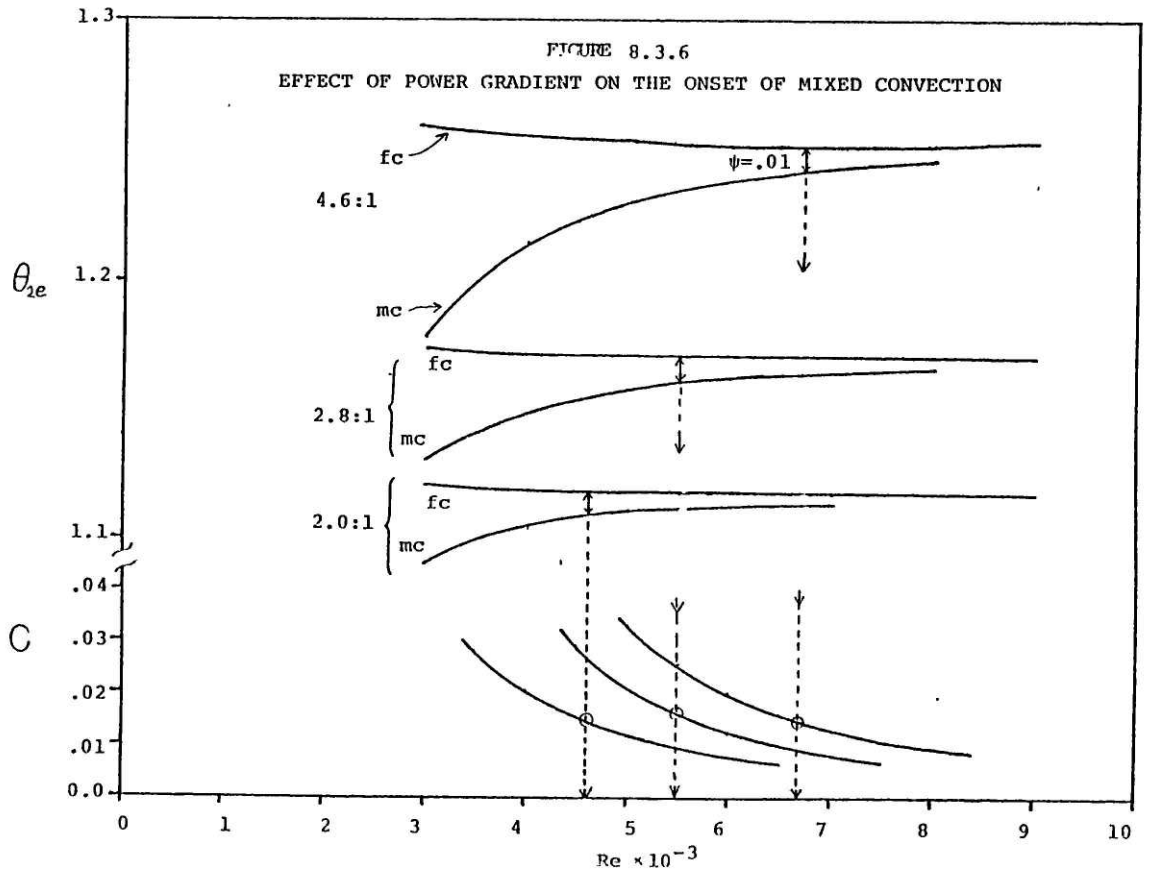

FIGURE 8.3.6
EFFECT OF POWER GRADIENT ON THE ONSET OF MIXED CONVECTION
θ_{2e}
C
fc
mc
ψ=.01
4.6:1
2.8:1
2.0:1
1.3
1.2
1.1
.04
.03
.02
.01
0.0
0
1
2
3
4
5
6
7
8
9
10
Re ×10⁻³

TABLE 8.3.1

ONSET OF MIXED CONVECTION
RESULTS FOR $\psi = .01$ APPROACH

Gr_q	Skew	Re	C	Gr_A/Re	B*
200	2.8:1	1747	.0168	.039	1.68E4
500	2.8:1	2399	.0169	.051	4.15E4
1400	2.8:1	3430	.0171	.070	1.15E5
5400	2.8:1	5500	.0173	.105	4.36E5
21600	2.8:1	9000	.0173	.157	1.75E6
5400	4.6:1	6700	.0149	.071	6.55E5
5400	2.0:1	4593	.0195	.151	2.97E5
200	2.8:1	1853	.0194	.030	1.96E4
500	2.8:1	2732	.0176	.035	5.27E4
1400	2.8:1	4121	.0187	.043	1.55E5
5400	2.8:1	6875	.0156	.059	6.25E5
21600	2.8:1	11500	.0151	.085	2.55E6
1.50E7	1:0	16000	.0050	N.A.	2.53E6
1.50E7	4:1	9220	.0091	N.A.	1.01E6
2.16E4	4:1	944	.0092	N.A.	1.45E3
6.51E6	4:1	3080	.0092	N.A.	4.36E4

the blanket bundle, a result in agreement with the findings of Westinghouse. This is primarily due to two effects. First, the blanket bundle has a larger friction factor, which tends to oppose flow redistribution. Also, lateral energy transport due to mixing and conduction (E*) is larger in the blanket bundle for Re>3000 (from Figure 8.3.7). This causes a reduction in the buoyancy forces. Conversely for Re<3000 the fuel bundle has higher E*, so a reversal in this trend could be anticipated, but the effect of the friction factor dominates for the range of Gr_q investigated.

It was observed in Figure 8.3.10 that the mixed convection regime is entered at a higher Re for larger power skews. This is in disagreement with the Westinghouse criteria, which suggests that the onset is independent of power skew.

In Table 8.3.1 the value of Gr_A/Re at the onset of mixed convection obtained with the constant ψ method (Figures 8.3.8 to 8.3.10) is given. Unlike the Westinghouse approach, the value of Gr_A/Re at the onset of mixed convection varies from .039 to .157 for the blanket bundle, and from .030 to .085 for the fuel bundle for a range of power skews and power levels. It was shown in Appendix F7 that if it is assumed that the friction and buoyancy forces are in balance, and if $f = \frac{C_f}{Re^m}$ it follows that

$$\frac{1}{2}\frac{C_f}{Re^m} F_C = 4\frac{L}{D_H}\frac{Gr_q}{Re^3 Pr}(K_2P_2 - K_1P_1)$$

Expressing Gr_q in terms of Gr_A (Table 2.1.2) this may be

written as

$$\frac{Gr_A}{Re} = \frac{1}{2}\frac{D_e}{L}\frac{C_f F_C}{K_2P_2 - K_1P_1}\,Re^{1-m}$$

where F_C is given by Equation F7.2. It follows from this result that the parameter Gr_A/Re holds no special significance in the two channel model. It will always depend on the power skew, and for turbulent flow (m=.25) will depend on Re also. For laminar flow (m=1), Gr_A/Re becomes independent of Re.

It is not clear that the experimental technique employed by Westinghouse determined the onset of mixed convection. The decrease in the normalized peak temperature rise in Figure 8.1.1 was attributed to buoyancy effects. However the observed decrease in NPTR may be due to an increase in radial conduction which occurs as Re decreases. They are in effect assuming that the normalized peak temperature rise for forced convection is independent of Re, which is not the case for small Re. Their experimental technique is valid where $E^* \simeq$ constant, or for Re > 1500 from Figure 8.3.5.

An experimental technique (albeit an impractical one) for determining the onset of mixed convection follows, First, an experiment like the one performed by WARD is made at the surface of the earth. The experimental apparatus is then transported to a zero gravity environment where the same experimental runs are made again, but now the buoyancy effects have been removed. The data points obtained in space may be considered the forced convection results, and the data on

earth, the mixed convection results. The onset of mixed convection occurs when the mixed convection data begins to deviate from the forced convection data.

The above argument suggests that the onset of mixed convection for low Re cannot be obtained from experiment alone (on earth), since buoyancy effects cannot be totally eliminated from the data with samll Re, though they can be made small by running tests at low power. However in a computer code or analytical model, the buoyancy effect is easily eliminated by using a constant for the density. Both an experiment and an analysis are needed to determine the onset of mixed convection. The experiment is needed to validate the analysis, then the buoyancy effects can be easily eliminated from the analysis to determine their importance.

8.4 CALCULATION OF THE ONSET OF MIXED CONVECTION IN A BARE ROD WATER COOLED BUNDLE

For demonstrative purposes the onset of mixed convection will next be calculated for the MIT 4x4 bundle. The radial conduction and turbulent interchange will be neglected. The friction factor correlations discussed in Section 7.4.1 will be used.

A plot of C and θ_{2e} versus Re for the 4x4 bundle is given in Figure 8.4.1 for a 4:1 power skew (Profile #6 of Figure 7.2.4) with Gr_q = 2.16 x 10^4, 6.51 x 10^6 and 1.50 x 10^7. For the Gr_q = 2.16 x 10^4 run, the laminar flow friction factor was used, since the onset occurred at low Re. The

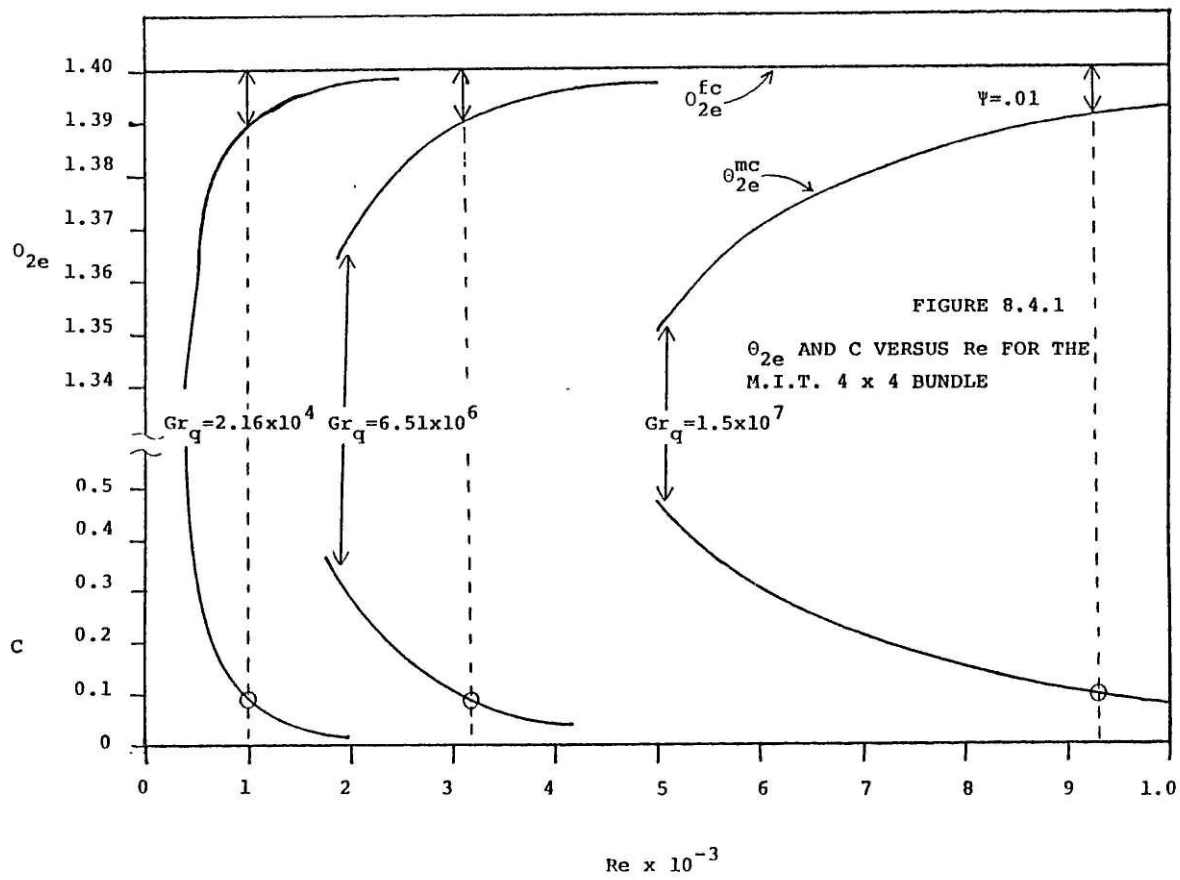


FIGURE 8.4.1

θ_{2e} AND C VERSUS Re FOR THE M.I.T. 4 x 4 BUNDLE

turbulent flow friction factor was used for the other calculations. Note that the forced convection solution θ_{2e}^{fc} is independent of Re. The results of the calculation are summarized in Table 8.3.1. For the 4:1 power gradient the $\psi = .01$ criteria gives a constant value of C at the onset of .009. Included in Table 8.3.1 is an additional run which was made with $Gr_q = 1.50 \times 10^7$ for a 1:0 power skew, and the onset occurred at a significantly higher Re.

For the 1:0 gradient the value of C at which $\psi = .01$ is .005. As was the case for the Westinghouse blanket bundle, the value of C at which $\psi = .01$ decreases for increasing power skew.

8.5 DISCUSSION OF THE ALTERNATE APPROACHES FOR SPECIFYING THE ONSET OF MIXED CONVECTION

Two methods of predicting the onset of mixed convection have been discussed. The constant ψ approach is based on the effect of buoyancy on the temperature field, and the constant C approach is based on the effect of buoyancy on the flow field. The constant ψ approach is preferred since the temperature field is of greater interest, but the constant C approach leads an easy to use formulation, as will be seen shortly.

It is therefore desirable to use $\psi = .01$ as the criteria definition, but for computational purposes employ an equivalent C = constant calculation. This involves determining the critical value of C ($C_{\psi=.01}$) at which $\psi = .01$. This is a dif-

ficult task since the equations are highly implicit in C, but it may be expressed in functional form as

$$C_{\psi=.01} = f_n(E^*, P_2, P_1)$$

As was observed in Section 8.4, if E* = constant $C_{\psi=.01}$ depends on power skew only.

To avoid the need of obtaining $C_{\psi=.01}$, the criteria may be approximately expressed as C=.01. This follows from examination of Figures 8.3.8, 8.3.9, 8.3.10 and 8.4.1, where it was found that there is not a significant difference between specifying ψ = .01, and C = constant. As exhibited in Table 8.3.1 the value of $C_{\psi=.01}$ varied from .0149 to .0194 for LMFBR geometries over a wide rnage of power skews and Grashof numbers. For a bare rod water cooled bundle, the value of $C_{\psi=.01}$ decreased with increasing power skew, and was .009 for a 4:1 power gradient, and .005 for a 1:0 gradient. Rejecting the step change in power since it will not occur in practice, the ψ=.01 criteria may be expressed approximately as

$$C = .01$$

8.6 FLOW REGIME MAP AND HAND CALCULATION FOR THE ONSET OF MIXED CONVECTION

Considerable simplication in the criteria results if the onset of mixed convection can be stated as C = constant rather than ψ = constant. In this section two practical methods will be presented for determining the onset of mixed convection. One is by means of a flow regime map, and the other is a simple hand calculation procedure.

At the onset of mixed convection C is small, and the power skew term can be simplified. For $C \simeq 0$, $K_1 \simeq K_2 \simeq K_0$ where K_0 is the value of K_1 or K_2 at C=0 (see Figure 5.2.2) Hence the power skew term can be written:

$$K_2P_2 - K_1P_1 \simeq K_0(P_2 - P_1) \tag{8.6.1}$$

where K_0 is given by:

$$K_0 = 2\left[1 + \frac{e^{-4E^*}-1}{4E^*}\right] \tag{8.6.2}$$

This eliminates the need to evaluate K_1 and K_2 numerically.

It was shown in Appendix F7 that the dominant dimensionless parameters of the model could be determined by balancing the friction and buoyancy forces, which yields the parameters Re and B* where B* may be expressed as:

$$B^* = \frac{L}{D_H}\frac{Gr_q}{Pr}\frac{K_2P_2 - K_1P_1}{C_{fL}} \tag{8.6.3}$$

The two channel model equation can then be written as Equation F7.20 for laminar flow:

$$B^* = \frac{Re^3}{4}\left[A^* + \frac{1}{2Re}\right] C \qquad (8.6.4)$$

and for turbulent flow:

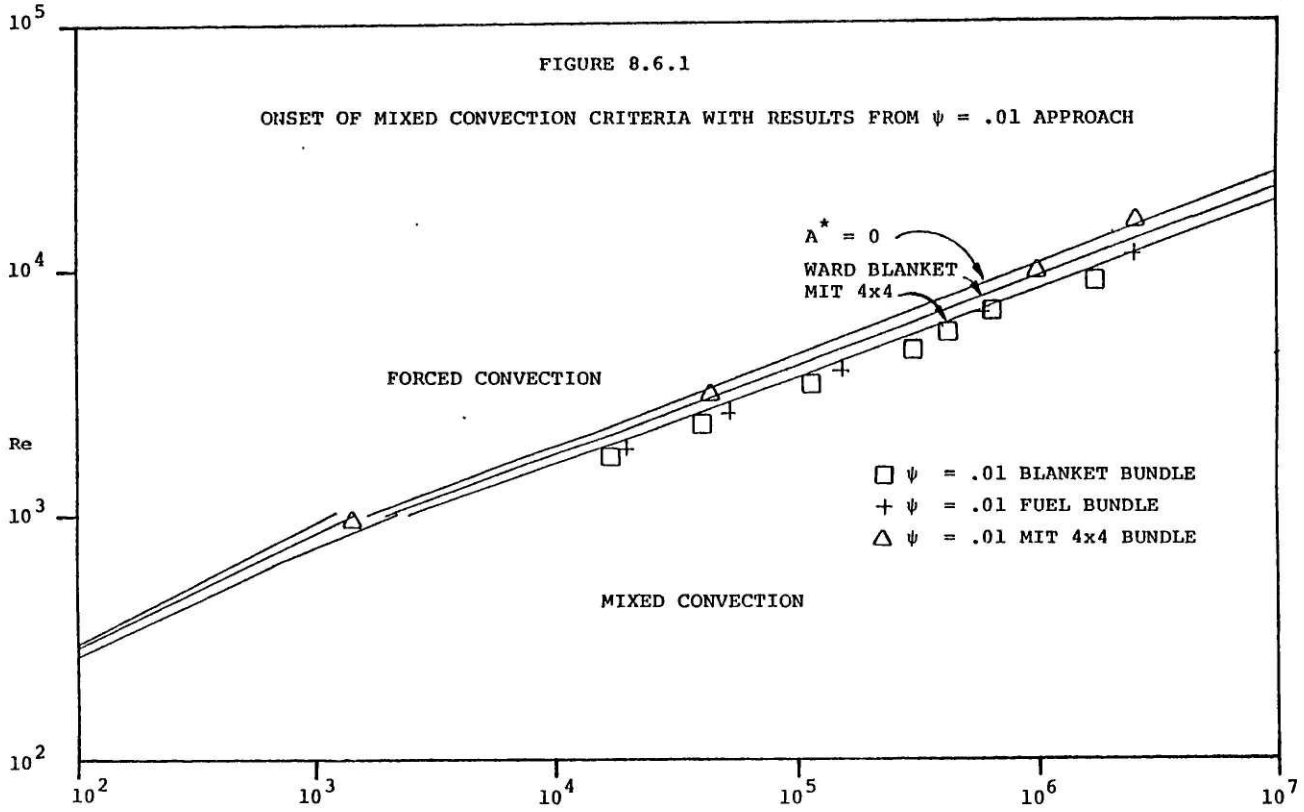
$$B^* = \frac{Re^3}{4}\left[A^* + \frac{1}{2Re^m}\frac{F_C}{C}\frac{C_{fT}}{C_{fL}}\right] C \qquad (8.6.5)$$

where A* is given by Equation F7.18. It was found that the dependence on A* is weak, and that C_{fT}/C_{fL} is nearly a constant for geometries of interest. Hence Re and B* are the dominant dimensionless parameters governing the onset of mixed convection.

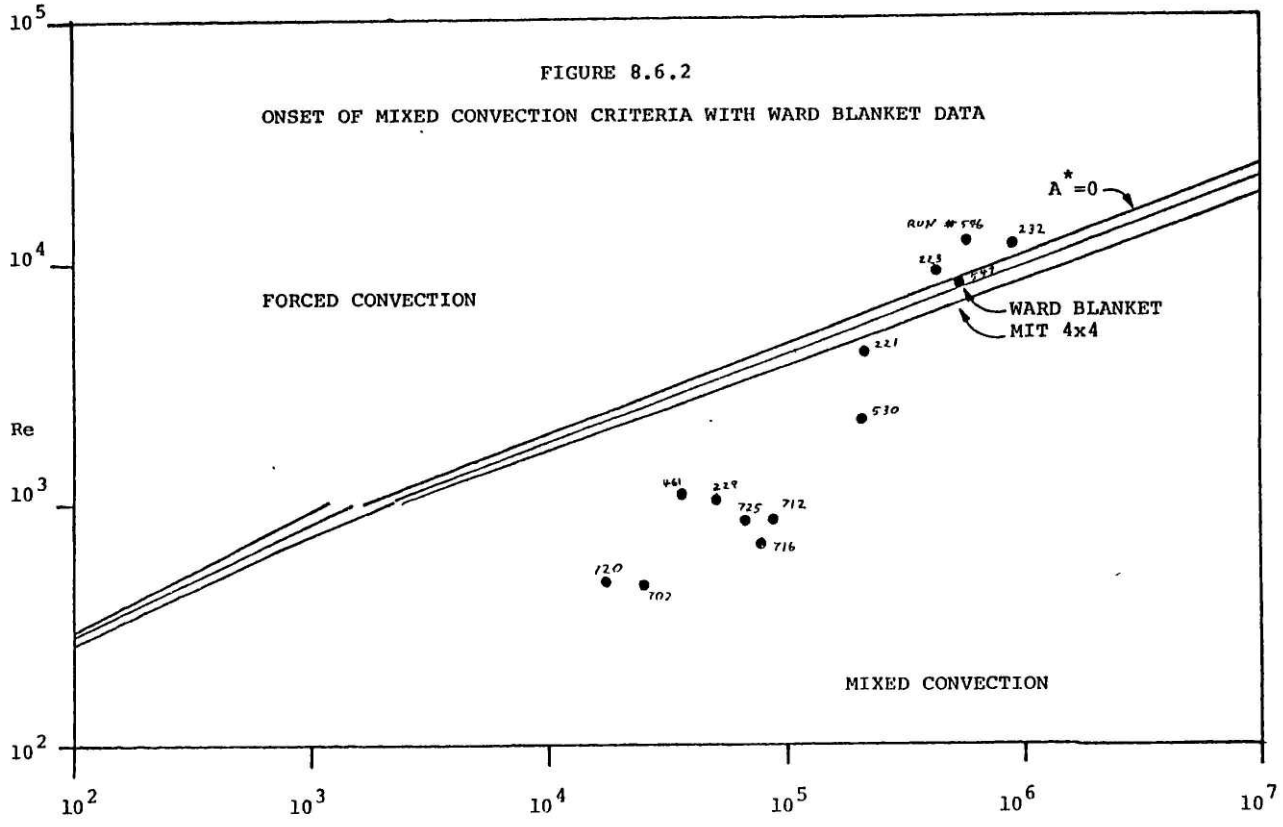
8.6.1 Flow Regime Map for the Onset of Mixed Convection

The prediction of the onset of mixed convection from Equations 8.6.4 and 8.6.5 are given in Figure 8.6.1 for the WARD blanket bundle and the MIT 4x4 bundle. The A* = 0 result (friction and buoyancy only) is also shown. The onset of mixed convection points for the ψ = .01 approach from Table 8.3.1 are also plotted. As expected, the criteria based on the C=.01 approach conservatively predicts the $\psi \geq .01$ results, with the exception of the 1:0 power gradient (for this case, C corresponding to ψ = .01 was .005, hence it falls above the C=.01 line). However, the 1:0 power gradient does not occur in practice.

In Appendix E3 comparisons were made between the ENERGY code predictions and WARD blanket bundle data. The Westinghouse data points of Table E4.1 are plotted on Figure 8.6.2



$$B^* = \frac{L}{D_H} \frac{Gr_q}{Pr} \frac{K_2P_2 - K_1P_1}{C_{fL}}$$



$$B^* = \frac{L}{D_H} \frac{Gr_q}{Pr} \frac{K_2P_2 - K_1P_1}{C_{fL}}$$

along with the onset of mixed convection criteria. It is observed that runs 223, 232, 546 and 547 are in the forced convection regime, while the rest are in mixed convection. It can be seen from the comparisons of Appendix E4 that the model correctly predicts the onset of mixed convection. Compare, for example, runs 221 and 223. Clearly run 221 (Figure E4.3) is in mixed convection since the forced convection and mixed convection energy results differ significantly. For run 223 (Figure E4.4) they are quite close, indicating forced convection. Similar conclusions can be drawn by comparing runs 546 and 530 (Figures E4.16 and E4.18).

8.6.2 Hand Calculation of the Onset of Mixed Convection

If one need only determine if a bundle operating under given conditions is in forced or mixed convection, a simple hand calculation will suffice. Since Equations 8.6.2 and 8.6.3 define the onsets, the mixed convection condition will exist if:

$$B^* > \frac{Re^3}{4}\left[A^* + \frac{1}{2Re}\right]C \qquad \text{For } Re < 800 \qquad (8.6.4)$$

$$B^* > \frac{Re^3}{4}\left[A^* + \frac{1}{2Re^m}\frac{F_C}{C}\frac{C_{fT}}{C_{fL}}\right]C \quad \text{For } Re > 800 \qquad (8.6.5)$$

where A^* and F_C/C are given by Equations 7.5.3 and 7.5.2, respectively.

8.6.3 Recommended Input Parameters and Sample Calculation of the Onset of Mixed Convection.

To calculate the onset of mixed convection, input parameters or correlations are needed for mixing (w_t^*), conduction shape factor (SF), and friction factor ($f = C_f/Re^m$). For LMFBR geometries Equation 6.2.1 allows w_t^* to be expressed in terms of the mixing and flowsplit parameters, and can be obtained from Figures 8.3.1 and 8.3.2 for the blanket and fuel bundle. These figures are based on the latest forced convection correlations, and should be revised when mixed convection correlations become available. No correlations are available for the shape factor, so the users best estimate of SF should be used. A friction factor correlation of the form $f = C_f/Re^m$ must also be available for the geometry under consideration.

For purposes of providing a sample calculation of the onset of mixed convection, consider WARD run # 221. For run # 221, Re = 4380 and Gr_q = 2764. From Figure 8.3.1 it can be found that w_t^* = .22 and E* = .24. From Equation 8.6.2 it follows that $K_1 \simeq K_2 \simeq K_0 = .71$. For a 2.8:1 linear power gradient P_1 = .367 and P_2 = .635 from Equations 6.2.4 and 6.2.5. The friction factor correlations are f = 110/Re for laminar flow and $f = .48/Re^{.25}$ for turbulent flow. With L/D_H = 250 and Pr = .0055, B* (Equation 8.6.1) can be calculated:

$$B^* = \frac{L}{D_H} \frac{Gr_q}{Pr} \frac{K_2P_2 - K_1P_1}{C_{fL}}$$

$$B^* = 250 \frac{2764}{.0055} \quad \frac{.71(.635-.367)}{110} = 2.18 \times 10^5$$

The point Re = 4380, $B^* = 2.18 \times 10^5$ can then be plotted on the flow regime map, and as shown in Figure 8.6.2, it is in the mixed convection regime.

For the hand calculation it is also necessary to calculate A^* (Equation 7.5.3), F_C/C (Equation 7.5.4) and C_{fT}/C_{fL}

$$A^* = \frac{2.01 + .22}{110\ (308)} = 6.58 \times 10^{-5}$$

$$\frac{F_C}{C} = \frac{1.01^{2.75} - .99^{2.75} - 2}{2.75\ (.01)^2} = 1.75$$

$$C_{fT}/C_{fL} = .48/110 = 4.36 \times 10^{-3}$$

Then it follows from Equation 8.6.5 that:

$$2.18 \times 10^5 > \frac{4380^3}{4} \left[6.58 \times 10^{-5} + \frac{1.75\ 4.36 \times 10^{-3}}{2(4380)^{.25}} \right] .01$$

or

$$2.18 \times 10^5 > 1.12 \times 10^5$$

Therefore the point is in the mixed convection regime.

CHAPTER 9

FLOW REGIME MAP FOR MIXED CONVECTION IN ROD BUNDLES

In Chapters 7 and 8 criteria were developed for the onset of mixed convection and onset of flow recirculation in rod bundles. In this chapter a flow regime map will be presented which combines the results of the previous two chapters.

It was shown in Section 7.5 that the onset of recirculation criterion could be expressed as a flow regime map in terms of the parameters Re and B_L^* where B_L^* is defined by Equation 7.5.2. In Section 8.6 it was found that the onset of mixed convection criterion could be expressed in terms of the parameters Re and B*, where B* is given by Equation 8.6.1. The two parameters are related by $B^* = B_L^* \cdot C$. To plot both the onset of mixed convection and onset of recirculation criterion on the same set of coordinates, we must choose between the Re versus B* representation and the Re versus B_L^* representation. The Re versus B_L^* representation has the disadvantage that the onset of mixed convection criterion and onset of recirculation criterion nearly coincide, as was observed in Figure F.7.2. Though technically justified, this representation leads to a confusing flow regime map. The disadvantage of the Re versus B* representation is that

the onset of recirculation criterion does not collapse into a single line as it does on Re versus B_L^* coordinates. Hence the onset of recirculation must be expressed as a family of curves of different values of C_{crit}. The last choice is considered to have the lesser disadvantage, so the Re versus B* representation will be employed in the flow regime map.

The flow regime map expressed in terms of Re and B* is given in Figure 9.2.1. The Westinghouse blanket geometry was employed in the calculation of the onsets, along with the onset for friction and buoyancy only A* = 0. Three flow regimes are identified - the forced convection regime, the mixed convection regime and the recirculation regime. Note that the onset of recirculation is given by a family of curves with different values of C (C = 1.00, .6 and .4 are shown).

It should be noted that Gr_q/Pr can be written as:

$$\frac{Gr_q}{Pr} = \frac{\beta g q'' D_e^4}{\mu C_p \nu^2}$$

The above parameter is somewhat deceptive since the Prandtl number appears, but it is independent of the thermal conductivity. The effect of thermal conduction is incorporated in $K_2P_2 - K_1P_1$ since it resulted from integrating the energy equation. Increasing thermal conductivity of the coolant reduces $K_2P_2 - K_1P_1$, and hence reduces the buoyancy effects.

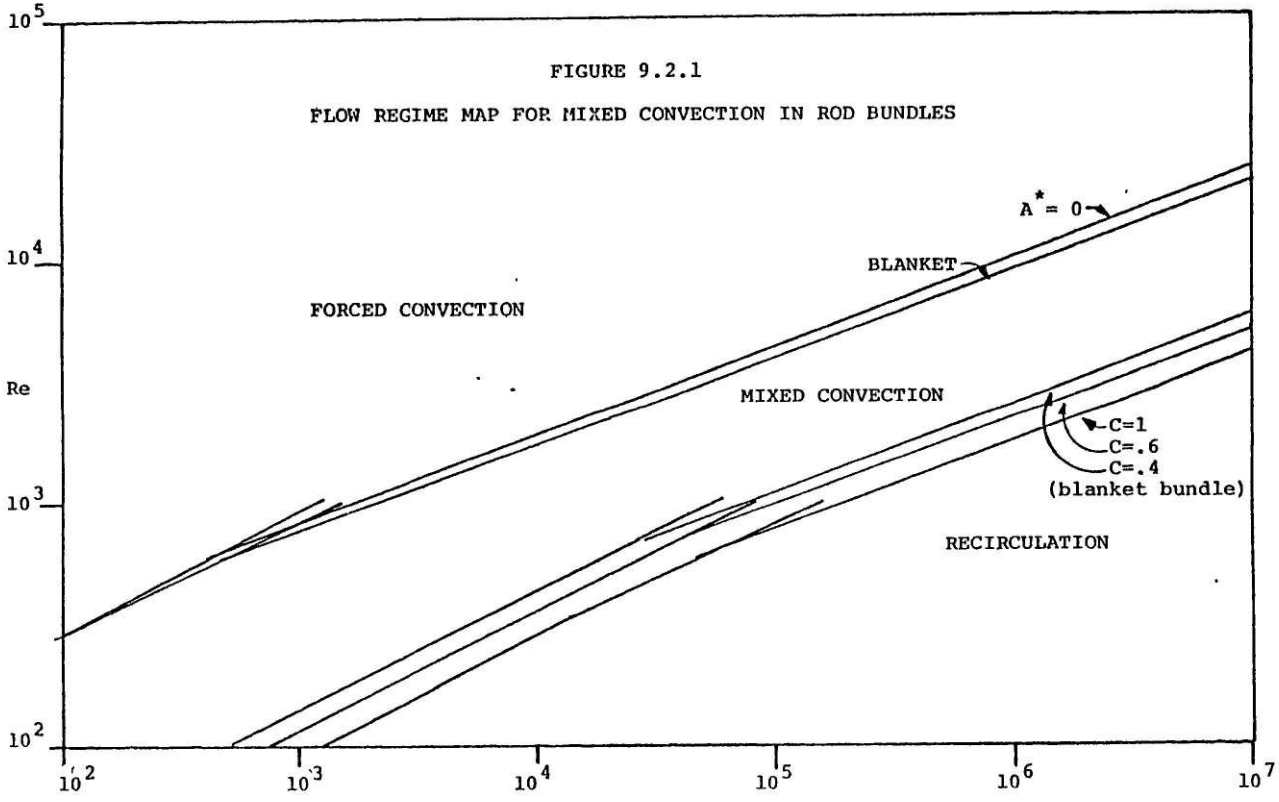


FIGURE 9.2.1

FLOW REGIME MAP FOR MIXED CONVECTION IN ROD BUNDLES

$$B^* = \frac{L}{D_H} \frac{Gr_q}{Pr} \frac{K_2 P_2 - K_1 P_1}{C_{fL}}$$

CHAPTER 10

SUMMARY, CONCLUSIONS, AND RECOMMENDATIONS FOR FUTURE WORK

10.1 SUMMARY AND LIMITATIONS OF THE MODEL

Figure 10.1.1 summarizes the development of the two channel model, highlights some of the restrictions which were imposed, and reviews the auxiliary models which were developed. In Section 5.1 the governing equations were derived. The axial conduction terms and transient terms were neglected, and the conditions under which these assumptions are valid were discussed in Appendix B1 and B2. The resulting equations were solved by trial solution with undetermined parameters. The two undetermined parameters were C (the buoyancy induced crossflow) and $f(x^*)$ (the axial velocity profile shape). It was determined that the model results were not highly sensitive to $f(x^*)$, and that $f(x^*) = x^*$ gave a good approximation to the actual profile shape. Employing $f(x^*) = x^*$ rather than the "true" (ENERGY or COBRA predicted) $f(x^*)$ leads to less than 1% error in Re_{crit} at onset of mixed convection conditions, and at most 8% error in Re_{crit} at onset of recirculation conditions.

The resulting model is given by Equation 5.3.1. It can be used in two ways. First as a model to calculate the velocity and temperature distribution in a rod bundle with a lumped subchannel approximation. For this case the Reynolds

number and other bundle operating conditions are input, and the value of C is calculated. Second, as a criterion where C is set at an appropriate value; and the corresponding critical Reynolds number is found. The model was validated by using it as a predictive model, and comparing its results to channel averaged results obtained from COBRA and ENERGY.

For the onset of mixed convection criteria, it was found that using C = .01, (criteria based on the buoyancy induced crossflow) was nearly the same as using ψ = .01 (criterion based on the temperature field).

For the onset of recirculation criteria, an auxiliary model is required to specify the critical value of C at the onset. A model for C_{crit} neglecting local buoyancy effects was developed in Appendix F4. It was found that for flatter power skews, the local buoyancy effects had to be considered. This was done in Appendix F5 by coupling the two channel model to a fully developed isolated cell distributed parameter analysis of local flow recirculation. The assumption of fully developed flow lead to highly conservative results, so a flow development factor (F_D) was used to account for flow development. It was found that F_D = .3 gave a good fit to the data. In general F_D will depend on L/D, so employing F_D = .3 for other bundles is not recommended. However, conservative results may be obtained by using F_D = 1.0.

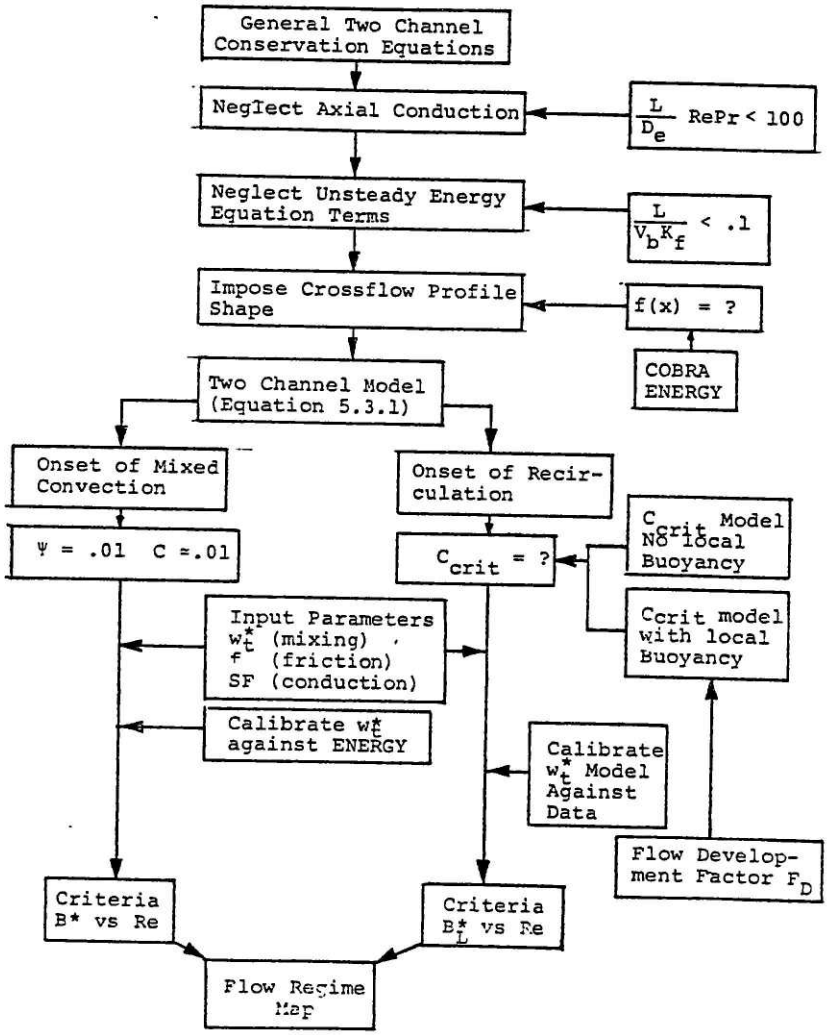
Near onset of recirculation conditions, it was found that buoyancy induced mixing (thermal plumes) was significant.

A model for buoyancy induced mixing was developed in Appendix F6, and the model constants were calibrated against the data. General use of this model is not recommended until it is calibrated with data from bundles of different geometries. Until more data is available, $w_t^*=0$ is recommended since it will give conservative results.

It was found in Appendix F7 that the dominant dimensionless parameters in the model were Re and some form of the parameter B* (B* or B_L^*). The onset of mixed convection criterion was presented as a plot of Re versus B*, and the onset of recirculation criterion was in terms of Re and B_L^*.

FIGURE 10.1.1

SUMMARY OF MODEL DEVELOPMENT



10.2 CONCLUSIONS

In this thesis criteria were developed for the onset of recirculation and onset of mixed convection in vertical rod bundles. It was concluded that the dominant mechanisms governing mixed convection in rod bundles are the frictional and buoyancy forces. By balancing these two terms, the key dimensionless parameters were identified as Re and B*. The criteria was expressed in terms of a flow regime map of Re versus B*. It was found that the onset of mixed convection could be predicted with forced convection input parameters, but for the onset of recirculation the effect of buoyancy on mixing was important.

10.3 RECOMMENDATIONS FOR FUTURE WORK

During the course of this work, several areas where more research is needed have been identified. They are summarized in the following sections.

Mixed Convection in Tubes

(1) It was found in Chapter 2 that no correlation exists which adequately predicts Nusselt numbers for turbulent aiding flow. A specific recommendation was made in Chapter 2 which would account for flow development effects.

(2) A recommendation was made to employ Gr_A rather than Ra_A in the Metais-Eckert flow regime map to properly account for the effect of Pr. The effect of L/D should also be given more careful consideration.

Onset of Recirculation and Onset of Mixed Convection Criteria

(3) The onset of recirculation should be checked against liquid sodium recirculation data when it becomes available.

(4) The model for C_{crit} allowing for local buoyancy effects should be improved upon if a local subchannel recirculation criteria which accounts for flow development becomes available. In liu of such a criteria, F_D should be calibrated against a broader data base to account for L/D. Alternately, Bodyfit predictions could be used to determine F_D as a function of L/D.

(5) A simple model for buoyancy induced mixing was developed in Appendix F6. It should be calibrated against a broader data base before being used for other geometries.

(6) Wire induced mixing models should be developed for mixed convection flows. These new models should then replace the forced convection mixing models used in this work, particularly for the recirculation criteria.

REFERENCES

1. S. F. Wang, "Natural Convection Effects in Isolated and Interconnecting Subchannels of a Reactor Fuel Assembly", Ph.D. Thesis, MIT, January 1981.

2. Physical Fluid Dynamics, D. J. Tritton, Van Nostrand Reinhold Company, 1977.

3. Natural Convection Heat and Mass Transfer, Y. Jaluria, Pergamon Press, 1980.

4. Boundary Layer Theory, H. Schlichting, McGraw Hill, 1969.

5. W. Hall and J. Jackson, "Laminarization of a Turbulent Pipe Flow by Buoyancy Forces", ASME paper 69-HT-55, 1969.

6. G. Caldwell and R. Seban, "Flow and Heat Transfer in a Laminarizing Turbulent Boundary Layer", ASME paper 69-HT-10, 1969.

7. W. Hall, "Heat Transfer Near the Critical Point", Advances in Heat Transfer, Volume 7,

8. D. Kenning, "Local Reductions in Heat Transfer Due to Buoyancy Effects in Upward Turbulent Flow", Fifth International Heat Transfer Conference, Tokyo (1974).

9. M. Connor and A. Carr, "Heat Transfer in Vertical Tubes under Conditions of Mixed Free and Forced Convection", Sixth International Heat Transfer Conference (1978).

10. J. Jackson and W. Hall, "Influences of Buoyancy on Heat Transfer to Fluids Flowing in Vertical Tubes Under Turbulent Conditions" from "Turbulent Forced Convection in Channels and Bundles" by KaKac and Spalding, 1979.

11. W. P. Jones and B. E. Launder, "The Prediction of Laminarization with a Two-Equation Model of Turbulence", International Journal of Heat and Mass Transfer, 1972.

12. Abdelmeguid and Spalding, "Turbulent Flow and Heat Transfer in Pipes with Buoyancy Effects", Journal of Fluid Mechanics (1979).

13. Buhr, Horsten, and Carr, "The Distortion of Turbulent Velocity and Temperature Profiles on Heating for Mercury in a Vertical Pipe", J. Heat Transfer, May 1974.

14. Oosthuizen, "Turbulent Combined Convective Flow Over a Vertical Plane Surface", 5th International Heat Transfer Conference, Tokyo 1974.

15. Buhr, Carr, and Balzhieser, "Temperature Profiles in Liquid Metals and the Effect of Superimposed Free Convection in Turbulent Flow", International Journal of Heat and Mass Transfer, 1967.

16. Petukhov, "Turbulent Flow and Heat Tansfer in Pipes under Considerable Effect of Thermogravitational Forces", Heat Transfer and Turbulent Buoyant Convection, 1977.

17. Petukhov and Strigin, "Experimental Investigation of Heat Transfer with Viscous-Inertial-Gravitational Flow of a Liquid in Vertical Tubes", High Temperatures, Vol. 6, 1968.

18. R. Greif, "An Experimental and Theoretical Study of Heat Transfer in Vertical Tube Flows", ASME J. Heat Transfer 100, 86-91 (1978).

19. R. Greif, "Laminar Convection with Radiation Experimental Results", International Journal of Heat and Mass Transfer, 1977.

20. Byrne and Ejiogu, "Combined Free and Forced Convection Heat Transfer in a Vertical Pipe", Heat and Mass Transfer by Combined Forced and Natural Convection, 1971.

21. N. S. Alferov, R. A. Rybin, and B. F. Balunov, "Heat Transfer with Turbulent Flow in a Vertical Tube under Conditions of Appreciable Influence of Free Convection", Thermal Engineering 16 (12), 66-70 (1969).

22. A. A. Bishop, J. M. Willis, and R. A. Marklev, "Effects of Buoyancy on Laminar Vertical Upward Flow Friction Factor in Cylindrical Tubes", Nuclear Engineering and Design 62, 365-369 (1980).

23. H. L. Greene and G. F. Sheele, "Effect of Fluid Viscosity on Combined Free Forced Convection Flow Phenomena in Vertical Pipes", A.I.Ch.E. Journal 16, No.6, November 1970.

24. G. A. Kemeny and E. V. Somers, "Combined Free and Forced-Convection Flow in Vertical Tubes - Experiments with Water and Oil", Trans. ASME, Series C, J. Heat Transfer 84, 339-346 (1962).

25. W. G. Brown, "Forsschung auf dem Gebiete des Ingenieurwesens" 26 VDI, Forschumgsheft 480 (1960).

26. J. P. Easby, "The Effect of Buoyancy on Flow and Heat Transfer for a Gas Passing Down a Vertical Pipe at Low Turbulent Reynolds Number", International Journal of Heat and Mass Transfer 21, 791-801 (1978).

27. M. W. Collins, "Combined Convection in Vertical Tubes", Heat and Mass Transfer by Combined Forced and Natural Convection, 1971.

28. Khosla, Hoffman and Pollok, "Combined Forced and Natural Convective Heat Transfer to Air in a Vertical Tube", 5th International Heat Transfer Conference, Tokyo, 1974.

29. B. P. Axcell and W. B. Hall, "Mixed Convection to Air in a Vertical Pipe", 6th IHIC, p.p. 37-42, 1978.

30. L. S. Herbert and V. J. Sterns, "Heat Transfer in Vertical Tubes - Interaction of Forced and Free Convection", Chem. Eng. J. 4, 46-52 (1972).

31. J. D. Jackson and J. Fewster, "Enhancement of Heat Transfer due to Buoyancy for Downward Flow in H_2O in Vertical Tubes", International Seminar on Turbulent Buoyant Convection, Dubrovnik, Yugoslavia (1976).

32. J. R. Lloyd and E. M. Sparrow, "Combined Forced and Free Convection Flow on Vertical Surfaces", International J. of Heat and Mass Transfer 13, 434-438 (1970).

33. Sparrow and Minkowycz, International Journal of Heat and Mass Transfer 5 (1962).

34. M. J. Hommel, "Mixed Convection Heat Transfer from a Vertical Plate: Prandtl Number Effects", ASME Paper 76-WA/HT-17.

35. A. A. Szewczyk, "Combined Free and Forced Convection Laminar Flow", J. of Heat Transfer, November 1964

36. Polyakov, "Transient Effects Due to Thermogravity in Turbulence and Heat Transfer", High Temperatures, Vol. 11, 1973.

37. Wendling, Ricque, and Martin, "Mixed Convection with Sodium", Progress in Heat and Mass Transfer, Dwyer, Vol. 7, 1973.

38. S. R. Husain, L. C. Chow, and A. Campo, "Free Convection Effects on Forced Flow Inside a Vertical Channel at Low Peclet Numbers", ASME Paper #81-WA/HT-66, 1981.

39. Metias and Eckert, "Forced, Mixed, and Free Convection Regimes", J. Heat Transfer, May 1964.

40. Metias and Eckert report "Criteria for Mixed convection" University of Minnesota, Heat Transfer Laboratory Report #HTLTR No.51, 1963.

41. Viscous Fluid Flow,Frank M. White, McGraw Hill, 1974.

42. B. Gebhart, "Natural Convection Flow, Instability, and Transition", J. Heat Transfer, August 1969.

43. G. F. Sheele and T. J. Hanratty, "Effect of Natural Convection Instabilities on Rates of Heat Transfer at Low Reynolds Number", AIChE Journal 9, 183-185 (1963).

44. Sherwin and Wallis, "Combined Natural and Forced Laminar Convection for Upflow Through Heated Vertical Annuli", Heat and Mass Transfer in Combined Forced and Natural Convection, 1971.

45. W. T. Lawrence, "Entrance Flow and Transition from Laminar to Turbulent Flow in Vertical Tubes with Combined Free and Forced Convection", Sc.. Thesis, MIT, February 1965.

46. M. W. Collins, "Heat Transfer by Laminar Combined Convection in a Vertical Tube - Prediction for Water", 6th International Heat Transfer Conference, Paper MC-5, 1978.

47. R. Shah and A. London, "Laminar Flow Forced Convection in Ducts", Advances in Heat Transfer, 1978.

48. K. Rehme, "Simple Method of Predicting Friction Factors of Turbulent Flow in Non-Circular Channels", International Journal of Heat and Mass Transfer 16, 933-950 (1973).

49. Marek, Maubach, and Rehme, "Heat Transfer and Pressure Drop Performance of Rod Bundles Arranged in Square Arrays", International Journal of Heat and Mass Transfer 16, 2215 (1973).

50. J. W. Yang, "Analysis of Combined Convection Heat Transfer in Infinite Rod Arrays", Heat Transfer 1978, National Research Council of Canada, Ottawa (1978), Volume 1, pp. 49-54.

51. J. W. Yang, "Heat Transfer and Fluid Flow in Regular Rod Arrays with Opposing Flow", in Fluid Flow and Heat Transfer Over Rod or Tube Bundles, S. C. Yao and P. A. Pfund, Editors, ASME, New York (1979), pp. 149-153.

52. L. R. Davis and J. J. Perona, "Development of Free Convection Axial Flow Through a Tube Bundle", International Journal of Heat and Mass Transfer 16, 1425-1438 (1973).

53. J. C. Dutton and J. R. Welty, "An Experimental Study of Low Prandtl Number Natural Convection in an Array of Uniformly Heated Vertical Cylinders", ASME J. Heat Transfer 97, 372-377 (1975).

54. S. F. Wang, W. M. Rohsenow, and N. E. Todreas, "Sub-channel Friction Factor for Bare Rod Arrays under Mixed Convection Conditions", Decay Heat Removal and Natural Convection in Fast Breed Reactors, Hemisphere Publishing Corporation, 1981.

55. C. Tsai, "Effects of Buoyancy Force on the Velocity and Temperature Distributions in an LMFBR Radial Blanket Fuel Rod Assembly", ASME Paper #73-HT-58 (1973).

56. S. D. Savkar, "Developing Forced and Free Convective Flows Between Two Semi-Infinite Parallel Plates", 4th International Heat Transfer Conference, Paris, France (1970).

57. H. Ramm and K. Johannsen, "Combined Forced and Free Laminar Convection in Vertical Rod Bundles with Longitudinal Flow", ASME Paper #77-Ht-44.

58. M. Quigley, C. McMonagle and J. Bates, "Investigation of Combined Free and Forced Convection in a 2x6 Rod Bundle", BNWL-2216, 1977.

59. J. Bates and E. Kahn, "Investigation of Combined Free and Forced Convection in a 2x6 od Bundle During Controlled Flow Transients", 1980 AIChE paper, Orlando.

60. A. Efthimiadis, W. M. Rohsenow, N. E. Todreas, and S-F Wang, "Investigating of Developing Vertical Mixed Convection Flow in a Square Array of Cylindrical Rods", 7th International Heat Transfer onference, Munich, Germany, September 1982.

61. Chen, Sha, Doria, Schmitt and Thompson, Bodyfit, a computer code for 30 steady state/transient single phase rod bundle thermal hydraulic analysis, ANL Report Nureg/Cr-1874 (1980).

62. ENERGY - IV , J. Robinson and N. E. Todreas, DOE/ET/37240 18TR, Revision 2, August 1982.

63. COBRA, T. L. George, "Cobra-WC: A Version of Cobra for Single-Phase Multiassembly Thermal Hydraulic Transient Analysis, PNL 3259, July 1980.

64. C. Chiu, W. M. Rohsenow and N. E. Todreas, "Turbulent Sweeping Flow Mixing Model for Wire Wrapped LMFBR Assemblies", COO-2245-55TR, Rev. 1, MIT, 1978.

65. K. J. Burns, W. M. Rohsenow, N. E. Todreas, "Laminar/ Transition Sweeping Flow Mixing Model for Wire Wrapped LMFBR Assemblies", DOE/ET/37240-81TR, July 1980.

66. J. T. Hawley, C. Chiu, M. M. Rohsenow and N. E. Todreas, "Correlations for Subchannel and Bundle Friction Factors and Flowsplit Parameters for Laminar, Transition, and Turbulent Longitudinal Flows in Wire Wrap Spaced Hexagonal Arrays", DOE/ET/37240-79TR, December 1980.

67. "Development and Evaluation of Techniques for Thermal-Hydraulic Analysis of LMFBR Fuel Assemblies", T. E. Greene, SM Thesis, MIT, July 1980.

68. "LMFBR Thermal Hydraulic Code Development and Evaluation", S. N. Kim, S.M. Thesis, MIT, October 1981.

69. S. F. Wang, N. E. Todreas, "Computer Model for MIT Correlations for Friction Factors, Flow Split, and Mixing Parameters in LMFBR Wire-Wrapped Rod Assemblies", DOE/ET/37240-87TR, February 1981.

70. Engineering Analysis, Stephen H. Crandell, McGraw-Hill Book Company, 1956.

71. E. Namekawa, "Out of Pile Experiments for Natural Circulation Decay Heat Removal in LMFBR Fuel Assembly - Power Skew Effects upon Intra-Assembly Hydraulic Characteristics", BNL, 1980.

72. Thermal Analysis of LMFBR, Tang, Coffield, and Markley, ANS, 1978.

73. E. Khan, W. Rohsenow, A. Sonin, and N. Todreas, "A Porous Body Model for Predicting Temperature Distribution in Wire-Wrapped Rod Assemblies Operating in Combined Forced and Free Convection", Nuclear Engineering and Design 35, 199-211 (1975).

74. Engel, Markley and Bishop, "The Effects of Heat Flux Gradients and Flow Regimes on the Peak Sodium Temperature Rise in a Wire-Wrapped Rod Bundle", ANS Topical Meeting, Kiamesha Lake, N.Y., 1982.

75. Theories of Engineering Experimentation, Schenck, McGraw Hill, 1968.

76. S.F. Wang and N.E. Todreas "Input Parameters to Codes Which Analyse LMFBR Wire Wrapped Bundles", COO - 2245 - 17TR Revision 1, May 1979.

77. A First Course In Turbulence, H Tennekes and J Lumey, M.I.T. Press, 1972.

APPENDIX A

KENNING'S DATA FOR MIXED CONVECTION IN A VERTICAL TUBE

This appendix contains the experimental data of Kenning (8) for mixed convection in a vertical tube. This data was used to help evaluate the Nusselt number correlations presented in section 2.3.

In Table A.1 the raw data is given in the following order: run #, average velocity (ft/sec), inlet temperature (^{o}C), heat transfer coefficient at x/D = 9.2, 18.4, 27.6, 36.8, 46.0, 55.3, 64.5 and 73.7 (w/m^2 ^{o}C), and average heat flux (kw/m^2).

A listing is given of a program which reads in the raw data and calculates Re, Gr, Pr, Nu/Nu_T, and other parameters of interest at 8 axial locations for each run.

TABLE A.1 KENNING'S DATA FOR MIXED CONVECTION IN A VERTICAL TUBE

#	U	T_{in}	h_1	h_2	h_3	h_4	h_5	h_6	h_7	h_8	q"
1	0.400	60.4	3484.0	13709.0	6870.0	4575.0	6875.0	2829.0	6821.0	4498.0	1.7
2	0.400	60.4	1348.0	1774.0	1672.0	1344.0	1507.0	1446.0	1909.0	1745.0	2.2
3	0.400	60.4	1419.0	1413.0	1415.0	1276.0	1291.0	1303.0	1557.0	1380.0	3.3
4	0.400	60.2	1168.0	1183.0	1126.0	1005.0	1032.0	943.0	998.0	986.0	4.1
5	0.400	60.4	1212.0	1168.0	1018.0	825.0	730.0	617.0	583.0	531.0	4.8
6	0.400	60.0	1127.0	1054.0	882.0	755.0	619.0	527.0	496.0	481.0	5.5
7	0.400	60.4	1182.0	1034.0	865.0	702.0	588.0	517.0	502.0	508.0	6.3
8	0.400	60.0	1024.0	870.0	698.0	582.0	516.0	518.0	594.0	667.0	7.9
9	0.400	60.4	898.0	738.0	614.0	566.0	661.0	712.0	716.0	667.0	9.8
10	0.591	17.4	959.0	918.0	882.0	898.0	901.0	893.0	882.0	911.0	9.3
11	0.591	17.6	935.0	898.0	865.0	854.0	821.0	823.0	813.0	842.0	12.0
12	0.591	18.1	948.0	863.0	785.0	735.0	680.0	650.0	601.0	564.0	18.0
13	0.591	18.7	958.0	849.0	750.0	682.0	594.0	565.0	538.0	526.0	24.4
14	0.591	18.1	962.0	827.0	721.0	659.0	619.0	618.0	647.0	711.0	34.5
15	0.591	19.4	929.0	782.0	619.4	636.0	643.0	757.0	703.0	748.0	36.5
16	0.591	18.2	976.0	840.0	732.0	688.0	679.0	735.0	793.0	805.0	42.7
17	0.591	20.5	962.0	817.0	741.0	739.0	823.0	875.0	853.0	862.0	47.8
18	0.591	18.9	1002.0	852.0	767.0	755.0	822.0	878.0	891.0	878.0	51.9
19	0.591	19.6	1067.0	961.0	1029.0	1128.0	1135.0	1156.0	1187.0	1229.0	85.0
20	0.591	19.4	1196.0	1193.0	1338.0	1405.0	1409.0	1468.0	1540.0	1645.0	123.3
21	0.591	60.1	2476.0	2652.0	2566.0	2312.0	3612.0	1819.0	2380.0	2443.0	3.5
22	0.591	56.2	1835.0	1866.0	1794.0	1731.0	2216.0	1515.0	1774.0	1841.0	5.0
23	0.591	57.5	1686.0	1624.0	1575.0	1526.0	1699.0	1390.0	1521.0	1592.0	7.2
24	0.591	56.1	1510.0	1363.0	1426.0	1406.0	1549.0	1606.0	1415.0	1475.0	8.9
25	0.591	59.5	1478.0	1335.0	1257.0	1168.0	1122.0	936.0	843.0	746.0	12.7
26	0.591	58.8	1371.0	1198.0	1018.0	840.0	705.0	621.0	624.0	722.0	16.8
27	0.591	61.3	1399.0	1183.0	965.0	771.0	681.0	692.0	742.0	875.0	18.4
28	0.591	61.8	1303.0	1024.0	812.0	716.0	810.0	912.0	959.0	920.0	24.6
29	0.591	61.5	1336.0	1042.0	839.0	765.0	892.0	995.0	1006.0	929.0	28.5
30	0.591	60.4	1218.0	974.0	805.0	766.0	857.0	929.0	930.0	890.0	29.1
31	0.591	60.8	1148.0	923.0	817.0	873.0	962.0	990.0	941.0	946.0	33.6
32	0.591	60.7	1148.0	941.0	869.0	995.0	1046.0	1022.0	986.0	1021.0	39.3
33	0.591	60.7	1253.0	971.0	882.0	1048.0	1137.0	1083.0	1053.0	1084.0	41.8
34	0.667	19.4	1097.0	1069.0	1076.0	1079.0	1077.0	1074.0	1084.0	1088.0	9.8
35	0.667	19.2	1085.0	1076.0	1044.0	1059.0	1065.0	1060.0	1049.0	1076.0	13.0
36	0.667	19.3	1111.0	1057.0	1052.0	1039.0	1048.0	1042.0	1054.0	1069.0	15.1
37	0.667	19.2	1088.0	1034.0	1017.0	1008.0	1000.0	1002.0	1011.0	1023.0	18.6
38	0.667	19.1	1019.1	1010.0	960.0	973.0	903.0	852.0	820.0	799.0	24.9
39	0.667	17.7	1131.0	1049.0	1004.0	970.0	902.0	894.0	835.0	794.0	29.9
40	0.667	17.6	1183.0	1042.0	977.0	910.0	843.0	783.0	707.0	667.0	33.7
41	0.667	17.5	1150.0	1012.0	907.0	811.0	732.0	702.0	673.0	704.0	44.0
42	0.667	17.4	1173.0	1016.0	885.0	803.0	750.0	761.0	826.0	886.0	54.5
43	0.667	17.5	1198.0	1012.0	899.0	827.0	818.0	904.0	965.0	988.0	64.7
44	0.667	17.4	1220.0	1047.0	938.0	944.0	1037.0	1133.0	1130.0	1122.0	84.8
45	0.667	59.0	1945.0	2037.0	2068.0	2007.0	2350.0	1915.0	2163.0	2213.0	9.0
46	0.667	60.3	1983.0	1917.0	1908.0	1880.0	2080.0	1830.0	1952.0	2035.0	14.5
47	0.667	60.3	1808.0	1754.0	1729.0	1732.0	1795.0	1646.0	1691.0	1788.0	21.4
48	0.667	61.2	1659.0	1567.0	1506.0	1446.0	1392.0	1317.0	1267.0	1215.0	25.1
49	0.667	61.4	1790.0	1677.0	1630.0	1596.0	1642.0	1498.0	1487.0	1507.0	25.6
50	0.667	58.0	1668.0	1597.0	1473.0	1370.0	1233.0	1105.0	923.0	809.0	27.5
51	0.667	56.0	1744.0	1592.0	1484.0	1376.0	1256.0	1075.0	941.0	833.0	29.9
52	0.667	58.6	1671.0	1505.0	1324.0	1082.0	860.0	795.0	826.0	989.0	33.0
53	0.667	60.0	1661.0	1416.0	1141.0	905.0	807.0	882.0	1090.0	1152.0	36.9
54	0.667	58.3	1609.0	1330.0	1031.0	867.0	878.0	1052.0	1166.0	1106.0	41.2
55	0.667	58.9	1679.0	1457.0	1200.0	955.0	820.0	898.0	1122.0	1192.0	40.9
56	0.667	62.1	1682.0	1380.0	2465.0	1673.0	2481.0	3404.0	3165.0	43.5	58.0
57	0.667	61.2	1552.0	1266.0	986.0	870.0	999.0	1167.0	1186.0	1103.0	44.4
59	0.667	61.4	1570.0	1193.0	954.0	903.0	1110.0	1218.0	1177.0	1114.0	48.3
60	0.667	61.1	1532.0	1192.0	955.0	909.0	1102.0	1210.0	1185.0	1132.0	49.1
61	0.667	60.0	1505.0	1185.0	970.0	943.0	1131.0	1234.0	1183.0	1140.0	53.4

TABLE A.1 (continued)

#	U	T_{in}	h_1	h_2	h_3	h_4	h_5	h_6	h_7	h_8	q"
62	0.667	61.4	1501.0	1162.0	943.0	989.0	1200.0	1252.0	1178.0	1141.0	54.7
63	0.667	62.0	1498.0	1139.0	960.0	1085.0	1266.0	1283.0	1198.0	1201.0	57.0
64	0.667	60.1	1464.0	1138.0	1039.0	1242.0	1319.0	1319.0	1263.0	1316.0	60.8
65	0.667	60.4	1496.0	1162.0	978.0	1078.0	1255.0	1269.0	1213.0	1212.0	68.6
67	0.716	60.4	1698.0	1630.0	1539.0	1450.0	1409.0	1342.0	1188.0	984.0	29.4
66	0.716	60.7	1696.0	1650.0	1566.0	1481.0	1422.0	1441.0	1368.0	1351.0	29.3
68	0.716	60.4	1724.0	1678.0	1604.0	1545.0	1499.0	1470.0	1396.0	1366.0	29.7
69	0.716	60.4	1757.0	1622.0	1571.0	1377.0	1129.0	915.0	810.0	865.0	32.6
70	0.716	60.4	1689.0	1582.0	1514.0	1415.0	1377.0	993.0	855.0	844.0	32.7
71	0.716	60.4	1698.0	1591.0	1461.0	1322.0	1094.0	1033.0	936.0	864.0	32.8
72	0.716	60.4	1660.0	1497.0	1328.0	1101.0	866.0	809.0	896.0	1111.0	35.8
73	0.716	60.4	1672.0	1539.0	1362.0	1103.0	895.0	822.0	890.0	1099.0	36.1
74	0.716	60.4	1569.0	1400.0	1226.0	992.0	848.0	791.0	886.0	1123.0	36.3
75	0.716	60.4	1653.0	1468.0	1237.0	971.0	845.0	876.0	1084.0	1225.0	39.3
76	0.716	60.4	1640.0	1477.0	1223.0	978.0	840.0	898.0	1119.0	1254.0	39.3
77	0.716	60.7	1589.0	1423.0	1219.0	970.0	816.0	879.0	1102.0	1191.0	39.3
78	0.716	60.9	1746.0	1481.0	1154.0	933.0	881.0	1035.0	1225.0	1195.0	42.8
79	0.716	60.7	1643.0	1421.0	1139.0	925.0	886.0	1035.0	1233.0	1240.0	42.9
80	0.716	60.7	1838.0	1689.0	1663.0	1303.0	1031.0	937.0	1034.0	1377.0	45.5
81	0.716	60.7	1595.0	1281.0	1017.0	935.0	1183.0	1313.0	1276.0	1208.0	52.4
82	0.716	60.4	1632.0	1287.0	1028.0	964.0	1243.0	1335.0	1277.0	1214.0	55.1
83	0.716	60.4	1764.0	1497.0	1201.0	973.0	1095.0	1319.0	1442.0	1386.0	55.4
84	0.716	60.2	1580.0	1251.0	1011.0	993.0	1282.0	1351.0	1255.0	1219.0	57.2
85	0.838	60.7	1827.0	1849.0	1818.0	1776.0	1785.0	1758.0	1795.0	1794.0	22.6
86	0.838	60.0	1815.0	1692.0	1641.0	1568.0	1491.0	1454.0	1363.0	1244.0	41.3
87	0.838	60.3	1809.0	1662.0	1553.0	1455.0	1278.0	1067.0	903.0	895.0	45.9
88	0.838	60.0	1832.0	1600.0	1379.0	1092.0	913.0	941.0	1152.0	1315.0	52.7
89	0.838	61.3	1888.0	1457.0	1152.0	1055.0	1230.0	1586.0	1733.0	1755.0	66.6
90	0.838	61.6	1802.0	1361.0	1137.0	1272.0	1472.0	1714.0	1598.0	1491.0	78.7
91	0.838	60.7	1796.0	1384.0	1159.0	1302.0	1488.0	1558.0	1420.0	1483.0	91.3
92	0.838	61.3	1778.0	1351.0	1296.0	1444.0	1565.0	1561.0	1487.0	1608.0	103.2
93	0.954	60.3	2080.0	2039.0	2034.0	2014.0	2020.0	1999.0	2009.0	1989.0	35.0
94	0.954	60.1	2176.0	2061.0	2037.0	2005.0	1999.0	1975.0	1983.0	2006.0	43.4
95	0.954	60.9	2149.0	1998.0	1957.0	1911.0	1851.0	1873.0	1842.0	1841.0	54.5
96	0.954	60.1	2096.0	1910.0	1820.0	1731.0	1573.0	1431.0	1220.0	1172.0	66.4
97	0.954	60.8	2071.0	1810.0	1530.0	1264.0	1330.0	1433.0	1878.0	2064.0	81.5
98	1.086	59.8	2484.0	2372.0	2358.0	2340.0	2371.0	2374.0	2351.0	2351.0	48.3
99	1.086	60.1	2538.0	2400.0	2374.0	2372.0	2346.0	2321.0	2344 0	2362.0	54.8
100	1.086	60.6	2602.0	2439.0	2417.0	2413.0	2369.0	2360.0	2362.0	2364.0	62.1
101	1.086	60.0	2490.0	2318.0	2293.0	2264.0	2266.0	2260.0	2241.0	2248.0	75.5
102	1.086	60.6	2446.0	2268.0	2239.0	2206.0	2143.0	2144.0	2124.0	2164.0	84.2
103	1.086	60.8	2464.0	2288.0	2233.0	2190.0	2118.0	2111.0	2159.0	2233.0	103.9
104	1.086	60.1	2436.0	2170.0	2042.0	1927.0	1747.0	1583.0	1738.0	2262.0	117.0
105	1.086	61.4	2447.0	2139.0	1827.0	1651.0	1670.0	1879.0	2121.0	2292.0	128.3
106	1.086	61.3	1751.0	2073.0	1715.0	1738.0	1841.0	2110.0	2135.0	2271.0	138.0
0	0 000	0.0	0.0	0.0	0.0	0.0	0.0	0.0	0.0	0.0	0.0

PROGRAM TO REDUCE KENNING'S DATA

```
      real t,k,nut1,nut2,nut3,pr,nnn
      real h(8)
      g=32.2
      cp=1.00
      dh=.109
      axs=9.33e-3
      den=62.4
      pi=3.14159
3     format(v)
2     continue
      read (5,3) n,u,tin,(h(i),i=1,8),q
      tin=tin*1.8+32.
      if (n.eq.0) go to 50
      q=q*317.
      do 5 i=1,8
      delt=(q*float(i)*pi*dh)/(den*u*axs*cp*3600.)
      tbulk=tin+delt
      t=tbulk
      r=rho(t)
      v=visc(t)
      k=cond(t)
      b=beta(t)
      pr=cp*v/k
      re=3600.*r*dh*u/v
      raresq=4.*dh*(g*b*v/(r*k))*(q/u**3.)/3600.
      gr1=raresq/pr
      grq=raresq*re**3/4.

      nut1=.023*re**.8*pr**.4
      twall=q/h(i)+tbulk
      y=.495-.0225*alog(pr)
      nnn=(re/870000.)**.84
      visctb=visc(tbulk)
      visctw=visc(twall)
      nut2=.0225*re**.795*pr**y*(visctb/visctw)**nnn
      f=(1.82*alog(re)-1.64)**-2.
      kkk=1.+900./re
      nut3=(f/8.)*re*pr/kkk+12.7*(f/8.)**.5*(pr**.6667-1.)


      h(i)=h(i)*.1716
      nu=h(i)*dh/k
      ratio=nu/nut1
      xtod=10.*float(i)
      p1=grq*xtod/(re**3*pr**1.2)
      fdfac=1.+1.e-5*(re*pr)/xtod
      ratio2=nu/(fdfac*nut1)
10    format(3x,i4,2x,i3,2x,f7.0,2x,f4.2,2x,f4.2,2x,5e10.3)
      write(6,10) n,i,re,pr,ratio,ratio2,gr1,grq,p1
5     continue
      write(6,20)
20    format('0')
      go to 2
50    continue
      stop
      end
      function cond(t)
      c1=.2903
      c2=9.559e-4
      c3=-2.199e-6
```

```
      cond=c1+c2*t+c3*t**2
      return
      end
      function rho(t)
      c4=62.505
      c5=2.146e-3
      c6=-7.285e-5
      rho=c4+c5*t+c6*t**2
      return
      end
      function visc(t)
      c7=.67
      c8=1.702
      c9=-.01848
      visc=c7+c8*exp(c9*(t-70.))
      return
      end
      function beta(t)
      c4=62.505
      c5=2.146e-3
      c6=-7.285e-5
      beta=-(c5+2.*c6*t)/(c4+c5*t+c6*t**2)
      return
      end
```

APPENDIX B1

ASSESSMENT OF THE IMPORTANCE OF THE AXIAL CONDUCTION TERM

To obtain an upper estimate of the effects of axial conduction on the hot channel temperature profile, we will neglect transverse energy transport, so the hot channel axial temperature gradient is at its maximum possible value. For this case, Equation 5.1.33 is (for steady flow):

$$- \frac{K}{C_p} \frac{d^2T_2}{dx^2} + \rho V_b \frac{dT_2}{dx} = \frac{q_2'}{A_2 C_p} \qquad \text{(B1.1)}$$

To make dimensionless multiply by $L/\Delta T_B$ where:

$$\Delta T_B = \frac{q_t' L}{\rho V_b A_b C_p} \qquad \text{(B1.2)}$$

In dimensionless form, Equation 1 is:

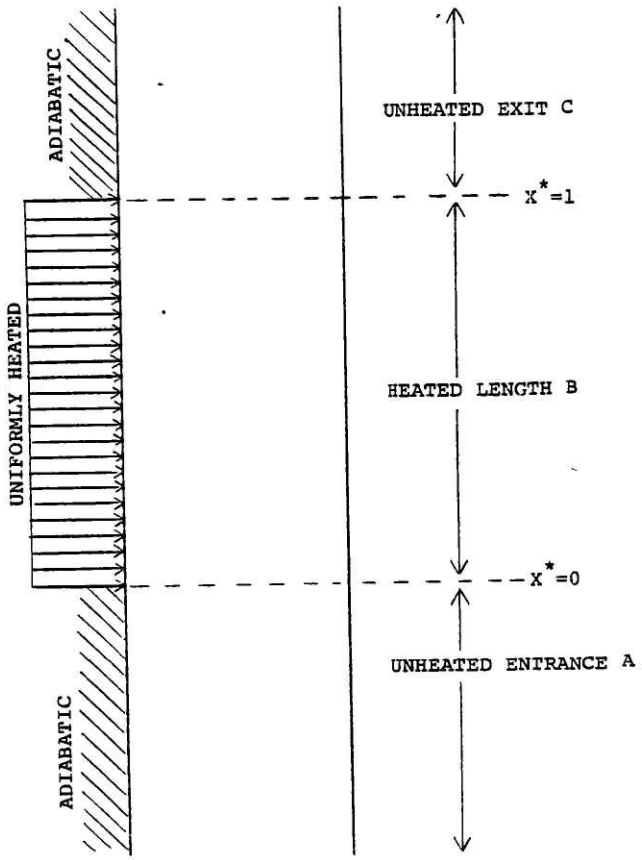
$$- \frac{1}{\frac{L}{D_e} RePr} \frac{d^2\theta_2}{dx^{*2}} + \frac{d\theta_2}{dx^*} = P_2 \qquad \text{(B1.3)}$$

This equation is valid over the heated length. For unheated regions simply set P_2 equal to zero. As shown in Figure B1.1, the solution domain is broken up into three regions. The heated length (B), the unheated entrance (A), and the unheated exit region (C). The dimensionless equations are:

$$- \frac{1}{K_3} \theta_A'' + \theta_A' = 0 \qquad - \infty \leq x^* \leq 0 \qquad \text{(B1.4)}$$

$$- \frac{1}{K_3} \theta_B'' + \theta_B' = P_2 \qquad 0 \leq x^* \leq 1 \qquad \text{(B1.5)}$$

FIGURE B1.1
AXIAL CONDUCTION IN A HEATED CHANNEL



$$-\frac{1}{K_3}\theta_C'' + \theta_C' = 0 \qquad 1 \leq x^* \leq +\infty \qquad \text{(B1.6)}$$

where: $K_3 = \frac{L}{D_e} RePr = \frac{L}{D_e} Pe$

$$\theta = \frac{T_2 - T_{IN}}{\Delta T_B}$$

$$P_2 = \frac{q_2'}{q_t'}$$

$$x^* = \frac{x}{L}$$

The solutions to the above equations are:

$$\theta_A = C_1 + C_2 e^{K_3 x^*} \qquad \text{(B1.7)}$$

$$\theta_B = C_3 + C_4 e^{K_3 x^*} + P_2 x^* \qquad \text{(B1.8)}$$

$$\theta_C = C_5 + C_6 e^{K_3 x^*} \qquad \text{(B1.9)}$$

From the boundary conditions:

$$\theta_A(-\infty) = 0$$

$$\theta_C(+\infty) = \text{finite}$$

it follows that $C_1 = C_6 = 0$. For a continuous temperature across the region boundaries, the following equations must be satisfied:

$$\theta_A(0) = \theta_B(0) \quad \text{gives} \quad C_2 = C_3 + C_4$$

$$\theta_A'(0) = \theta_B'(0) \quad \text{gives} \quad K_3 C_2 = P_2 + K_3 C_4$$

$$\theta_B(1) = \theta_C(1) \quad \text{gives} \quad P_2 + C_3 + C_4 e^{K_3} = C_5$$

$$\theta_B'(1) = \theta_C'(1) \quad \text{gives} \quad P_2 + K_3 C_4 e^{K_3} = 0$$

Solving for the C's gives:

$$C_4 = -\frac{P_2}{K_3} e^{-K_3}$$

$$C_2 = \frac{P_2}{K_3} (1 - e^{-K_3})$$

$$C_3 = \frac{P_2}{K_3}$$

$$C_5 = P_2$$

The region of most interest is the heated length. There the solution is:

$$\theta_B(x^*) = P_2\left[x^* + \frac{1}{\frac{L}{D_e}Pe}\left(1 - e^{\frac{L}{D_e}Pe(x^*-1)}\right)\right] \qquad \text{(B1.10)}$$

If axial conduction is negligible, the solution is:

$$\theta_B(x^*) = P_2 x^* \qquad \text{(B1.11)}$$

For the unheated inlet length, the solution is:

$$\theta_A(x^*) = \frac{P_2}{K_3}\left(e^{K_3 x^*} - e^{K_3(x^*-1)}\right) \qquad \text{(B1.12)}$$

If axial conduction is negligible, the solution is simply $\theta_A(x^*) = 0$. For the unheated exit length the solution is $\theta_C(x^*) = P_2$, and the temperature is constant.

In Figure B1.2 the solutions are plotted for $\frac{L}{D_e}RePr$ of 2, 4, and 10 along with the solution for zero axial conduction. The effect of axial conduction is to increase the

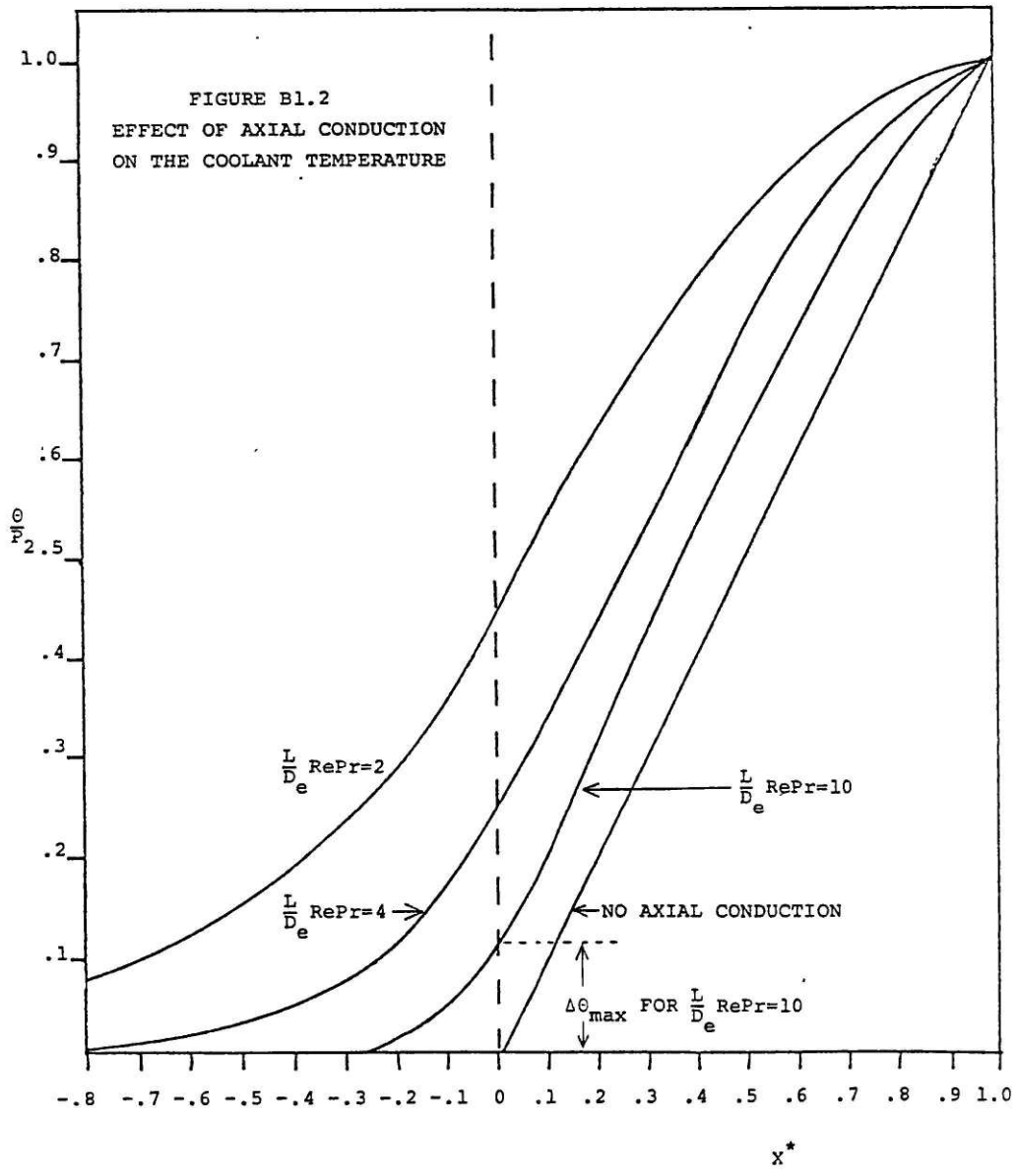


FIGURE B1.2
EFFECT OF AXIAL CONDUCTION
ON THE COOLANT TEMPERATURE

normalized temperature over the entire channel length including the unheated inlet region. The maximum increase in temperature occurs at x = 0 and is given by:

$$\Delta\theta_{MAX} = \frac{P_2}{K_3}\left(1 - e^{-K_3}\right) \qquad \text{(B1.13)}$$

If we define the onset of significant axial conduction as $\Delta\theta_{MAX} = .01$, Equation B1.13 gives $K_3 = \frac{L}{D_e} RePr = 100$ for a 1:0 power skew ($P_2 = 1.0$). For the blanket geometry ($\frac{L}{D_e} = 308$), and Pr = .004 this gives Re = 81.3, while for the fuel geometry ($\frac{L}{D_e} = 284$) Re = 88. We expect axial conduction to become important below this Reynolds number.

Since axial conduction causes the normalized temperature to increase, we expect axial conduction to enhance buoyancy effects under conditions with radial power gradients. This is because the increased hot side temperature in the unheated portion of the bundle will set up a radial temperature difference which will produce a buoyancy induced cross-flow in the unheated length. Therefore neglecting axial conduction in our analysis will cause the criteria to become nonconservative.

APPENDIX B2

ASSESSMENT OF THE IMPORTANCE OF THE TRANSIENT TERM

An estimate of the importance of the transient term can be made by solving the bundle energy equation for ΔT_B. The energy equation is

$$\rho V_b(t) A_b C_P (T_{OUT} - T_{IN}) - q'_t L + \frac{d}{dt}[\rho L_H A C_V \bar{T}] = 0 \quad \text{(B2.1)}$$

The average temperature in the bundle is:

$$\bar{T} = \frac{1}{2}[T_{OUT} + T_{IN}] \quad \text{(B2.2)}$$

The energy equation becomes:

$$\rho V_b A C_P \Delta T_B - q'_t L + \frac{1}{2}\rho L A C_v \frac{d\Delta T_B}{dt} = 0 \quad \text{(B2.3)}$$

or; for $C_P = C_V$

$$V_b \Delta T_B + \frac{1}{2} L \frac{d\Delta T_B}{dt} = \frac{q'_t L}{\rho A C_p} \quad \text{(B2.4)}$$

Dividing by V_{b0}, the initial bundle velocity prior to the flow transient:

$$V_b^* \Delta T_b + \frac{1}{2} \frac{L}{V_{b0}} \frac{d\Delta T_B}{dt} = \frac{q'_t L}{\rho V_{b0} A C_p} = \Delta T_{B0} \quad \text{(B2.5)}$$

where $\Delta T_{B0} = \dfrac{q'_t L}{\rho V_{b0} A C_p}$ is the initial bulk temperature rise. Dividing by ΔT_{B0} and rearranging:

$$\frac{L}{V_{b0}} \frac{dT^*}{dt} + 2 V_b^* T^* = 2 \quad \text{(B2.6)}$$

where:

$$T^* = \Delta T_B / \Delta T_{B0} \tag{B2.7}$$

Note that when the transient term is small ($\frac{dT^*}{dt} = 0$) Equation B2.6 gives:

$$T^*_{QS} = \frac{1}{V^*} \tag{B2.8}$$

or

$$\Delta T_B = \frac{q'_t L}{\rho V_b(t) A C_P} \tag{B2.9}$$

This is the quasi-steady state bulk temperature rise which is used in the two channel model. By studying Equation B2.6 we can determine under what conditions the quasi-steady state approach is valid. Equation B2.6 can be written as:

$$\frac{dT^*}{dt} + V_b^* \frac{2V_{b0}}{L} T^* = 2 \frac{V_{b0}}{L} \tag{B2.10}$$

The solution is given by:

$$T^*(t) = \frac{1}{\mu(t)} \left[\frac{2V_{b0}}{L} \int_0^t \mu(t)\,dt + \mu(0) \right] \tag{B2.11}$$

where:

$$\mu(t) = \exp\left[\int_0^t \frac{2V_{b0}}{L} V_b^*\,dt \right] \tag{B2.12}$$

In Reference [72], it is suggested that a typical flow coast-down can be expressed as:

$$\frac{w(t)}{w(0)} = V_b^* = 1 - \frac{t}{t+K_t} = \frac{1}{1+t^*} \tag{B2.13}$$

t is the dimensionless transient time:

$$t^* = \frac{t}{K_t} \tag{B2.14}$$

and K_t is a time constant for the flow coastdown. The initial flow is reduced by 50% when $t = K_t$. With the bulk velocity given by Equation B2.13, Equation B2.12 becomes:

$$\mu(t) = (1 + t^*)^P \tag{B2.15}$$

where:

$$P = \frac{2V_{b0}K_t}{L} \tag{B2.16}$$

Integrating $\mu(t)$ gives:

$$\int_0^t \mu(t)dt = \frac{K_t}{P+1}\left[(1 + t^*)^{P+1} - 1\right] \tag{B2.17}$$

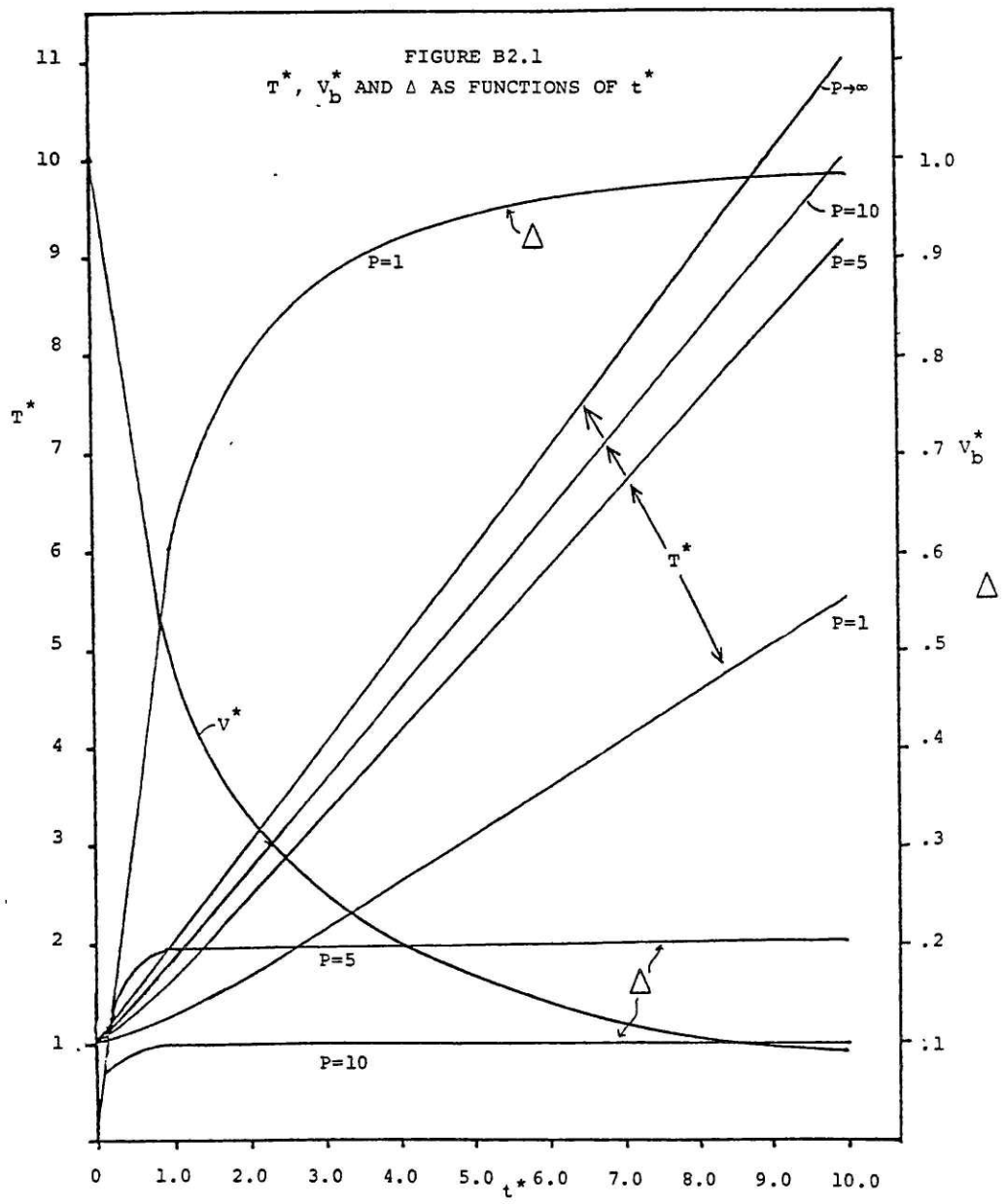
Substituting B2.17 and B2.15 into B2.11 gives:

$$T^* = (1 + t^*)^{-P}\left\{\frac{P}{P+1}\left[(1 + t^*)^{P+1} - 1\right] + 1\right\} \tag{B2.18}$$

The dimensionless bulk temperature rise depends on the two dimensionless parameters, t* and P. In Figure B2.1 a comparison is made between the quasi-steady T* (Equation B2.8) and T* from Equation B2.18 for P=1, 5 and 10. The bulk velocity as a function of dimensionless time is also shown. The difference between the quasi-steady T* and transient T* increases with t*, but decreases with P. For large P, Equation B2.18 reduces to the quasi-steady result (Equation B2.8). This can be shown by taking the limit of Equation B2.17 as P approaches infinity:

$$\lim_{P\to\infty} T^* = (1 + t^*) = \frac{1}{V_b^*} = T^*_{QS} \tag{B2.19}$$

If we are not concerned about errors in the bulk temperature


FIGURE B2.1
T*, V*b AND Δ AS FUNCTIONS OF t*
P→∞
P=10
P=5
P=1
P=1
P=5
P=10
T*
V*
Δ
T*
V*b
Δ
t*
0
1.0
2.0
3.0
4.0
5.0
6.0
7.0
8.0
9.0
10.0
1
2
3
4
5
6
7
8
9
10
11
.1
.2
.3
.4
.5
.6
.7
.8
.9
1.0

rise of less than 10%, then if the parameter:

$$\Delta = \frac{\Delta T_B(\text{quasi-steady}) - \Delta T_B(\text{transient})}{\Delta T_B(\text{transient})} = \frac{T^*_{QS} - T^*}{T^*} \leq .1 \tag{B2.20}$$

the quasi-steady approach is valid. Substituting Equation B2.8 and Equation B2.18 into the above result gives:

$$\Delta = \frac{T^*_{QS} - T^*}{T^*} = (1+t^*)^{P+1} \left\{ \frac{P}{P+1} \left[(1+t^*)^{P+1} - 1 \right] + 1 \right\}^{-1} - 1 \leq .1 \tag{B2.21}$$

Equation B2.21 gives a criterion for when the quasi-steady approach is valid. The quantity Δ is also plotted in Figure B2.1 for P = 1, 5, and 10. For P = 5 or 10, Δ is observed to increase rapdily, and reach a steady state value. By taking the limit of Equation B2.21, the steady state value is:

$$\Delta_{ss} = \lim_{t^* \to \infty} \Delta = 1/P \tag{B2.22}$$

so that if P>10, the above criteria (B2.21) is satisfied at all times. If P<10, the above criteria will be satisfied for a short time after the initiation of the transient of about one tenth of a time constant. Neglecting this short time period, the criteria can be stated simply as:

$$\Delta_{ss} = 1/P = \frac{L}{2V_0 K_t} \leq .1 \tag{B2.23}$$

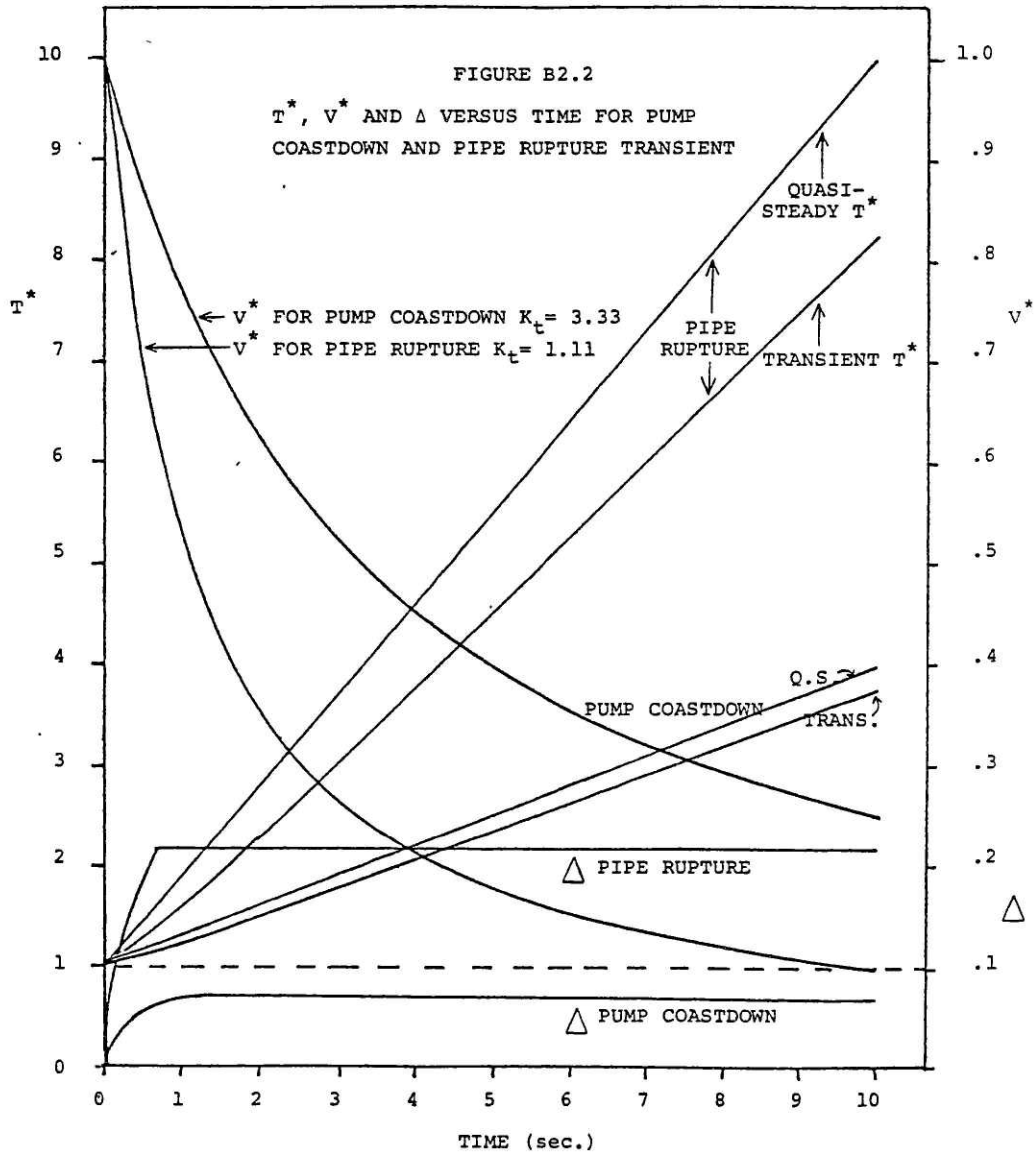
Physically, Δ_{ss} is the ratio of the fluid particle residence time in the heated length to twice the coastdown time constant.

In Reference 72, p. 156, figures were given for the core flow rate versus time for typical LMFBR transients.

For a pump coastdown, the flow is reduced to 25% of its initial value in 10 seconds, so $K_t = 3.33$ from Equation B2.13 (this coastdown is for a U.S. design, with no flywheel on the pump). For a pipe rupture the core flow is reduced to 10% of its initial value in 10 seconds so $K_t = 1.11$. For the radial blanket assembly, the coolant velocity is 11 ft/sec for normal operation (Reference 72, p.52). With a heated length of 64 in., the value of P is 13.74 for the pump coastdown, and P = 4.58 for the pipe rupture.

Figure B2.2 gives V* and T* for the two transients described above. Both the quasi-steady T* (Equation B2.19) and the transient T* are included. The quantity Δ from Equation B2.21 is also plotted versus time. It can be seen that our criteria (Equation B2.21) is satisfied for the pump coastdown during the entire transient since P>10. However, for the pipe rupture Δ exceeds .1 at about .2 sec into the transient, and reaches a steady state value of 1/P = .22. These results suggest that the quasi-steady approach is valid for a pump coastdown transient, but not for a pipe rupture transient. For the fuel geometry, with a heated length of 36" and the same initial velocity, the same conclusions are obtained.

For the BNWL transient experiments, the flow coastdown was linear in time, so can not be expressed in the form of Equation B2.13. The linear coastdown is expressed as:


FIGURE B2.2
T*, V* AND Δ VERSUS TIME FOR PUMP COASTDOWN AND PIPE RUPTURE TRANSIENT
QUASI-STEADY T*
V* FOR PUMP COASTDOWN Kt= 3.33
V* FOR PIPE RUPTURE Kt= 1.11
PIPE RUPTURE
TRANSIENT T*
Q.S.
TRANS.
PUMP COASTDOWN
PIPE RUPTURE
PUMP COASTDOWN
T*
V*
Δ
TIME (sec.)
0
1
2
3
4
5
6
7
8
9
10
.1
.2
.3
.4
.5
.6
.7
.8
.9
1.0

$$V^*(t) = \begin{cases} 1 - mt & 0 \leq t \leq t_{et} \\ V^*_{et} & t \geq t_{et} \end{cases} \qquad \text{(B2.24)}$$

where V_{et} is the velocity at the end of the transient at time t_{et}, and m is the rate of decrease of the bulk velocity. It follows that:

$$m = (1 - V^*_{et})/t_{et} \qquad \text{(B2.25)}$$

With Equation B2.23 representing the flow transient, the author was unable to obtain an analytical expression for Equation B2.11. A numerical scheme, such as the Euler method, must be employed for this case.

Figure B2.3 gives the results of the numerical solution for two flow transients. The first transient is representative of the BNWL case 9 45 second transient. The second is the same run, but a 150 second transient. The parameter L/V_0 is 20 sec for each run. This is the fluid particle residence time in the heated length at the initiation of the transient. V^*_{et} is .337 for each run, while t_{et} is 45 sec for the first run, and 150 sec for the second run.

The results of Figure B2.3 indicate that transient effects are important for both cases. The maximum error in T* caused by employing the quasi-steady approach occurs at t_{et}, and is 1.17 for the 45 sec transient and .63 for the 150 sec transient.

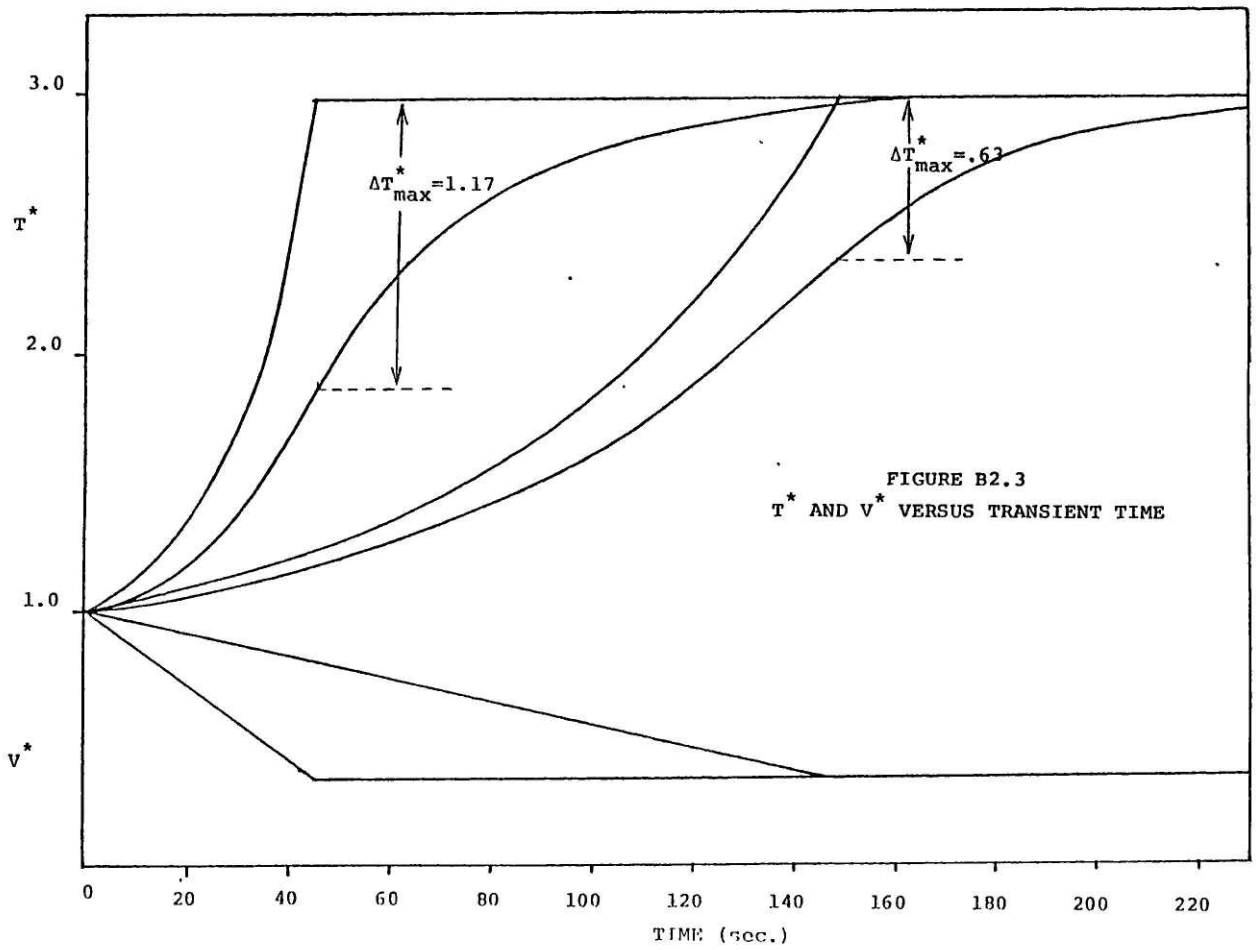


FIGURE B2.3
T^* AND V^* VERSUS TRANSIENT TIME

APPENDIX C1

In this Appendix, analytical solutions for the energy equation are found by the method discussed in Section 5.2.3. We first consider the case where $E^* = 0$ (Energy transport due to conduction and mixing are negligible), then C=0 (negligible crossflow).

For the first case we neglect energy transport due to coolant mixing and thermal conduction by setting E^* equal to zero in Equation 5.2.44:

$$f_1(X^*) = \frac{1}{V_2^*} \frac{dV_2^*}{dx^*} \tag{C1.1}$$

For this case, the integration for $\mu(x^*)$, (Equation 5.2.49), is then straightforward:

$$\mu(x^*) = \exp\left[\int^{x} \frac{dV_2^*}{V_2^*}\right] = V_2^* \tag{C1.2}$$

The equations for $Y_1(x^*)$ and $Y_2(x^*)$ become:

$$Y_1(x^*) = \frac{1+1/R}{V_2^*} \int_0^{x^*} \frac{gV_2^*}{V_1^*} \, dx^* \tag{C1.3}$$

$$Y_2(x^*) = \frac{1+R}{V_2^*} \int_0^{x^*} g \, dx^* \tag{C1.4}$$

then K_1 and K_2 are found by integrating the above equations from zero to one, as in Equations 5.2.56 and 5.2.57:

$$K_1 = (1+1/R) \int_0^1 \left[\frac{1}{V_2^*} \int_0^{x^*} \frac{V_2^*}{V_1^*} \, g \, dx^* \right] dx^* \tag{C1.5}$$

$$K_2 = (1+R)\int_0^1 \left[\frac{1}{V_2^*} \int_0^{x^*} g \, dx^* \right] dx^* \qquad (C1.6)$$

Recall that V_1^* and V_2^* are given by:

$$V_1^* = (1 - Cf(x^*))V_{1i}^* \qquad (C1.7)$$

$$V_2^* = (1 + RCSf(x^*))V_{2i}^* \qquad (C1.8)$$

The above integrals may or may not be expressed in closed form depending on the functional dependence of f and g on x*. Table 5.2.3 summarizes the known integrations.

For the case that C=0, the solution is straight forward. This case is the forced convection limit where the buoyancy induced crossflow can be neglected. For this case $f_1(x^*)$ of Equation 5.2.44 is constant, and is given by:

$$f_1 = E^* \left(\frac{1+R}{V_2^*} + \frac{1+1/R}{V_1^*} \right) \qquad (C1.9)$$

Equation 5.2.49 becomes:

$$\mu(x^*) = e^{f_1 x^*} \qquad (C1.10)$$

Equations 5.2.52 and 5.2.53 give for $Y_2(x)$ and $Y_1(x)$:

$$Y_2(x^*) = \frac{1+R}{V_2^*} e^{-f_1 x^*} \int_0^{x^*} e^{f_1 x^*} g(x^*) \, dx^* \qquad (C1.11)$$

$$Y_1(x^*) = \frac{1+1/R}{V_1^*} e^{-f_1 x^*} \int_0^{x^*} e^{f_1 x^*} g(x^*) \, dx^* \qquad (C1.12)$$

For uniform axial power ($g(x^*) = 1$) Equations C1.11 and

C1.12 integrate to:

$$Y_2(x^*) = \frac{1+R}{V_2^*}\left[1 - e^{-f_1 x^*}\right]\frac{1}{f_1} \qquad \text{(C1.13)}$$

$$Y_1(x^*) = \frac{1+1/R}{V_1^*}\left[1 - e^{-f_1 x^*}\right]\frac{1}{f_1} \qquad \text{(C1.14)}$$

K_2 and K_1 are obtained by integrating the above equations (C1.13 and C1.14) from zero to one as in Equations 5.2.56 and 5.2.57:

$$K_2 = \frac{1+R}{V_2^* f_1}\left[1 + \frac{1}{f_1}\left(e^{-f_1} - 1\right)\right] \qquad \text{(C1.15)}$$

$$K_1 = \frac{1+1/R}{V_1^* f_1}\left[1 + \frac{1}{f_1}\left(e^{-f_1} - 1\right)\right] \qquad \text{(C1.16)}$$

For a chopped cosine axial power profile with a peak to mean ratio of α, $g(x^*)$ is given by:

$$g(x^*) = \alpha \cos \gamma (x^* - .5) \qquad \text{(C1.17)}$$

where γ is obtained by requiring that Equation 5.1.62 is satisfied [$\int_0^1 g(x^*)dx^* = 1$], which gives the implicit relation:

$$\alpha \sin(\tfrac{1}{2}\gamma) - \tfrac{1}{2}\gamma = 0 \qquad \text{(C1.18)}$$

With $g(x^*)$ given by Equation C1.17, integration of Equations C1.11 and C1.12 gives:

$$Y_2(x) = \frac{1+R}{V_2} \frac{\alpha}{f_1^2+\gamma^2} \left\{ \left[f_1 \cos\gamma(x - \tfrac{1}{2}) + \gamma \sin\gamma(x - \tfrac{1}{2}) \right] \right.$$

$$\left. - e^{-f_1 x} \left[f_1 \cos(\tfrac{1}{2}\gamma) - \gamma \sin(\tfrac{1}{2}\gamma) \right] \right\} \qquad \text{(C1.19)}$$

$$Y_1(x) = \frac{1+1/R}{V_1} \frac{\alpha}{f_1^2+\gamma^2} \left\{ \left[f_1 \cos\gamma(x - \tfrac{1}{2}) + \gamma \sin\gamma(x - \tfrac{1}{2}) \right] \right.$$

$$\left. - e^{-f_1 x} \left[f_1 \cos(\tfrac{1}{2}\gamma) - \gamma \sin(\tfrac{1}{2}\gamma) \right] \right\} \qquad \text{(C1.20)}$$

To obtain K_2 and K_1, the above equations are integrated from zero to one. Upon performing these integrations, the same results as Equation C1.15 and C1.16 are obtained.

APPENDIX C2

NUMERICAL SOLUTION OF THE ENERGY SOLUTIONS

It was shown in Appendix C1 that an analytical solution for the energy equation can be obtained for certain simple cases only. Neglecting E* (transverse energy transport due to turbulence and conduction) may not be an acceptable approximation, particularly for LMFBR applications where conduction is significant due to the high conductivity coolant, and coolant mixing is large due to the wire wrap. In this section a numerical technique will be employed to calculate K_1 and K_2.

The energy equation can be written:

$$\frac{dY}{dx^*} + f_1(x^*)Y = f_2(x^*) = a_2(x^*)P_2 - a_1(x^*)P_1 \qquad (C2.1)$$

where $a_1(x^*)$ and $a_2(x^*)$ are given by Equations 5.2.47 and 5.2.46, respectively, and $f_1(x^*)$ is given by Equation 5.2.44. Since the differential equation is linear, the superposition principal may be used to obtain two linearly independent solutions, $Y_1(x^*)$ and $Y_2(x^*)$ such that:

$$Y(x^*) = Y_2(x^*)P_2 - Y_1(x^*)P_1 \qquad (C2.2)$$

$Y_2(x^*)$ is found from:

$$\frac{dY_2}{dx^*} + f_1(x^*)Y_2 = a_2(x^*) \; ; \quad Y_2(0) = 0 \qquad (C2.3)$$

and $Y_1(x^*)$ is found from:

$$\frac{dY_1}{dx^*} + f_1(x^*)Y_1 = a_1(x^*) ; \qquad Y_1(0) = 0 \tag{C2.4}$$

Hence we must solve:

$$\frac{dY_K}{dx^*} + f_1(x^*)Y_K = a_K(x^*) ; \qquad K = 1, 2 \tag{C2.5}$$

If forward differencing is employed, the derivative of Y is approximated as:

$$\frac{dY}{dx^*} \simeq \frac{Y_{i+1} - Y_i}{\Delta x^*} \tag{C2.6}$$

Substituting this into Equation C2.5 gives the finite difference expression:

$$\frac{Y_{i+1} - Y_i}{\Delta x^*} + f_1(x_i^*)Y_i = a_K(x_i^*) \qquad K = 1, 2 \tag{C2.7}$$

or:

$$Y_{i+1} = (1 - f_1(x_i^*)\Delta x^*)Y_i + a_K(x_i^*)\Delta x^* \qquad K = 1, 2 \tag{C2.8}$$

This is the Euler method for solving differential equations. This method allows the solution for Y_i to be marched out. The numerical results can be improved by using the average value of $f_1(x_i^*)$ and $a_K(x_i^*)$ over the interval from x_i^* to x_{i+1}^*.

$$Y_{i+1} = (1 - \bar{f}_1(x_{i+1/2}^*)\Delta x^*)Y_i + \bar{a}_K(x_{i+1/2}^*)\Delta x^* \qquad K = 1,2 \tag{C2.9}$$

Once the solutions for $\bar{Y}_1$ and $\bar{Y}_2$ are obtained, K_1 and K_2 are found by numerically integrating $\bar{Y}_K$. Subroutine EULER was written to perform these calculations. The numerical integrations were performed using Simpsons method. Listings of subroutines EULER and SIMPINT are given at the end of this appendix.

LISTING OF SUBROUTINE EULER

```
c  subroutine to numerically calculate coefficients of buoyancy term
c
      subroutine euler(c,r,n,y1,y2,k1,k2)
      common/ax/estar,ivp,nn,indg,v1in,v2in,w,f25,f50,f75
      dimension f1(100),f2(100),b(100),y(100),a1(100),a2(100)
      dimension y1(100),y2(100),g(100),f1ave(100),bave(100)
      real k1,k2
      real nn
      n=100
      w=.5*c
      dx=1./float(n)
c  calculate f1 and f2
      do 100 i=1,n
      x=float(i)/float(n)
      a2(i)=(1.+r)/(v2in+v1in*r*c*fx(x,ivp,nn,r,c,w,f25,f50,f75))
      if(c.eq.1.0) go to 50
      a1(i)=(1.+1./r)/(v1in-v1in*c*fx(x,ivp,nn,r,c,w,f25,f50,f75))
50    continue
      if(c.eq.1.0) a1(i)=(1.+1./r)/(v1in-.99*v1in*fx(x,ivp,nn,r,c,
     1     w,f25,f50,f75))
      a3=(r*c*v1in*dfx(x,ivp,nn,r,c,w,f25,f50,f75))/(v2in+v1in*r*c*
     1     fx(x,ivp,nn,r,c,w,f25,f50,f75))
      f1(i)=a3+estar*(a1(i)+a2(i))
100   continue
c  indic indicates which coefficient is to be calculated
      indic=1
246   continue
      do 247 i=1,n
      x=float(i)/float(n)
      if (indic.eq.1) f2(i)=a1(i)
      if (indic.eq.2)  f2(i)=a2(i)
      if(indg.eq.1) g(i)=1.0
      if(indg.eq.2) g(i)=1.38*cos(2.689*(x-.5))
      xstart=.33333
      if((indg.eq.3).and.(x.le.xstart)) g(i)=0.0
      if((indg.eq.3).and.(x.gt.xstart)) g(i)=1./(1.-xstart)
      b(i)=f2(i)*g(i)*dx
247   continue
      y(1)=b(1)
      do 250 i=1,n-1
      f1ave(i)=(f1(i)+f1(i+1))/2.
      bave(i)=(b(i)+b(i+1))/2.
      y(i+1)=y(i)*(1.-dx*f1ave(i))+bave(i)
250   continue
      call simpint(y,n,yint)
      do 252 i=1,n
      if(indic.eq.1) y1(i)=y(i)
      if(indic.eq.2) y2(i)=y(i)
252   continue
      if(indic.eq.1) k1=yint
      if(indic.eq.2) k2=yint
      if(indic.eq.2) go to 290
      indic=2
      go to 246
290   continue
      return
      end
      function fx(x,ivp,nn,r,c,w,f25,f50,f75)
c  ivp=1 for constant or linear crossflow
c  ivp=2 for half sine crossflow
```

SUBROUTINE EULER (continued)

```
c  ivp=3 for full cosine crossflow
c   ivp=4 for ramp crossflow
      real nn
      fx=x**nn
      if(ivp.eq.1) go to 10
      pi=3.14159
      fx=(1.-cos(pi*x))/2.
      if(ivp.eq.2) go to 10
      fx=x-sin(2.*pi*x)/(2.*pi)
      if(ivp.eq.3) go to 10
      fx=x+(1.+1./r)*.5*w*(x-x**2)/c
      if(ivp.eq.4)go to 10
      if(x.le.0.25) fx=4.0*f25*x
      if((x.ge.0.25).and.(x.le.0.5)) fx=f25+4.*(x-.25)*(f50-f25)
      if((x.le.0.75).and.(x.ge.0.5)) fx=f50+4.*(x-.5)*(f75-f50)
      if((x.le.1.0).and.(x.ge.0.75)) fx=f75+4.*(x-.75)*(1.-f75)
10    continue
      return
      end
      function dfx(x,ivp,nn,r,c,w,f25,f50,f75)
      real nn
      dfx=nn*x**(nn-1.)
      if(ivp.eq.1) go to 20
      pi=3.14159
      dfx=pi*sin(pi*x)/2.
      if(ivp.eq.2) go to 20
      dfx=1.-cos(2.*pi*x)
      if(ivp.eq.3) go to 20
      dfx=1.+(1.+1./r)*.5*w*(1.-2.*x)/c
      if(ivp.eq.4)go to  20
      if(x.le.0.25) dfx=4.*f25
      if((x.ge.0.25).and.(x.le.0.5)) dfx=4.*(f50-f25)
      if((x.le.0.75).and.(x.ge.0.5)) dfx=4.*(f75-f50)
      if((x.le.1.0).and.(x.ge.0.75)) dfx=4.*(1.0-f75)
20    continue
      return
      end
```

LISTING OF SUBROUTINE SIMPINT

```
      subroutine simpint(y,n,yint)
      dimension y(100)
      n=100
      dx=1./float(n)
      sum=0.0
      do 10 i=1,n-1
      iodd=mod(i,2)
      mult=2.
      if(iodd.eq.1) mult=4.
10    sum=sum+mult*y(i)
      sum=sum+y(n)
      yint=(dx/3.)*sum
      return
      end
```

APPENDIX D

COMPUTER PROGRAMS FOR SOLUTION OF THE TWO CHANNEL MODEL EQUATIONS

In this appendix programs are given to solve Equation 5.3.1 by numerical iteration. Program RECIRC solves for the critical Reynolds number, and program TWOCHAN solves for C. Both programs use the bisection root finding method.

For purposes of performing the numerical iteration Equation 5.3.1 may be written as Equation 5.2.15.

$$RES = \text{Term 1} + \text{Term 2} + \text{Term 3} + \text{Term 4} - \text{Term 5} \quad (D.1)$$

where RES is the residual, Term 1 is the inertia and cross-flow term (Equation 5.2.23), Term 2 is the mixing term (Equation 5.2.28, Term 3 is the friction term (Equation 5.2.30), Term 4 is the transient term (Equation 5.2.40), and Term 5 is the buoyancy term (Equation 5.1.55). The solution has been found when:

$$RES = 0 \quad (D.2)$$

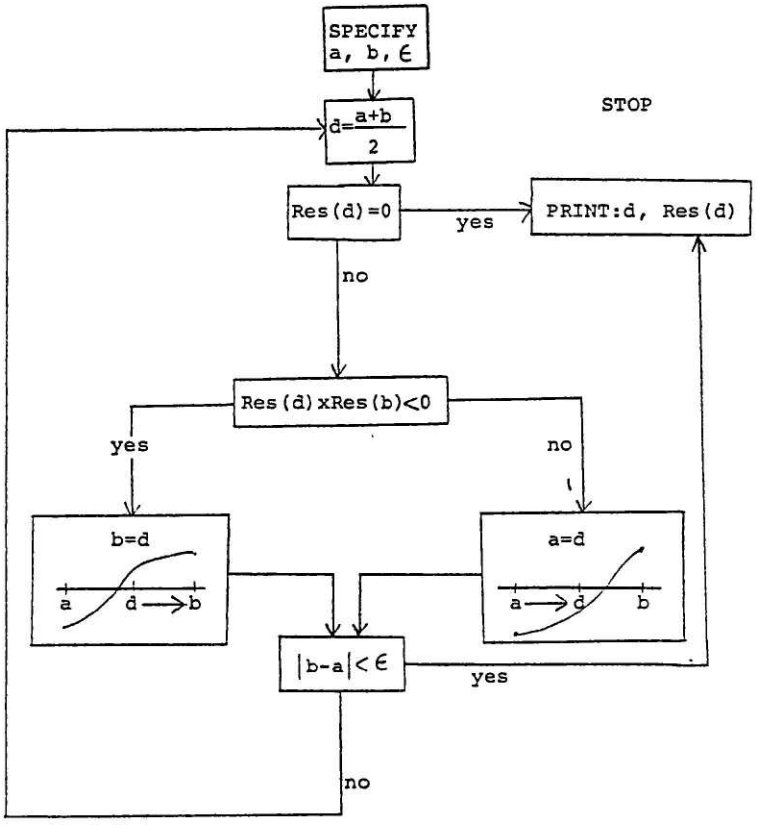
Subroutine RESCALC was written to evaluate the residual defined by Equation D.1. It contains all of the friction factor correlations of Table 5.2.2, which are required to evaluate the friction term (Term 3). A listing of subroutine RESCALC is given at the end of this appendix.

With subroutine RESCALC available to calculate the

residual, the bisection method can easily be implemented. A flowchart for the bisection method is given in Figure D.1. The interval where the solution lies [a,b] must be specified. For program RECIRC it is a range of Reynolds numbers and for program TWOCHAN, it is a range for C. The interval is bisected until the root is found within the accuracy specified by ε Both RECIRC and TWOCHAN call subroutine EULER to evaluate K_1 and K_2, and subroutine RESCALC to evaluate the residual at each iteration. Listings of TWOCHAN and RECIRC are given at the end of this appendix, along with a sample run for each.

FIGURE D.1

FLOWCHART FOR BISECTION ALGORITHM



LISTING OF SUBROUTINE RESCALC

```
      subroutine rescalc(res)
      common/ax/estar,ivp,nn,indg,v1in,v2in,w,f25,f50,f75
      common/resid/c,r,wtstar,ifx,ltod2,ltod1,ltod,ltodh,
     1     dredt,ldtonew,re,pr,k1,k2,p1,p2,m1,m2,n1,n2,cf1,cf2,
     2     grq,ifric,cfl1,cfl2,cft1,cft2
      common/term/term1,term2,term3,term4,term5
      real k1,k2,ifx,nn,ifxsq
      real ltod,ltod1,ltod2,ltodh,ldtonew
      real m1,m2,n1,n2
      if(ivp.eq.1) ifx=1./(nn+1.)
      if(ivp.eq.1) ifxsq=1./(2.*nn+1.)
      if(ivp.ne.1) ifx=.5
      if(ivp.eq.2) ifxsq=3./8.
      const4=w*(1.+r)/(c*2.*r)
      if(ivp.eq.4) ifx=.5+const4/6.
      if(ivp.eq.4) ifxsq=.3333+const4/6.+const4**2/30.
      if(ivp.eq.5) ifx=(2.*f25+2.*f50+2.*f75+1.0)/8.
      term1=2.*r*c*v1in*v2in+(r*c*v1in)**2+(r-1.)*c*v1in**2*(.5*c-1.)
      term2=(1.+r)**2*wtstar*((v2in-v1in)+c*(1.+r)*v1in*ifx)/r
c  evaluate friction term
      if(ivp.eq.1) ifxsq=1./(1.+2.*nn)
      if(ifric.ne.1) go to 100
      f1=v1in*(1.-c*ifx)
      f2=v2in+r*c*v1in*ifx
      f2=f2*(ltod2/ltod)
      f1=f1*(ltod1/ltod)
      fb1=cf1/re
      fb2=cf2/re
      if(ifric.eq.1) go to 1000
100   continue
      f1=((1.-(1.-c)**(3.-m1))/((3.-m1)*c))*v1in**(2-m1)
      f2=((v2in+r*c*v1in)**(3-m2)-v2in**(3-m2))
     1     /((3-m2)*r*c*v1in)
      f1=f1*(ltod1/ltod)**m1
      f2=f2*(ltod2/ltod)**m2
      if(ifric.ne.2) go to 200
      fb1=cf1/re**m1
      fb2=cf2/re**m2
      if(ifric.eq.2) go to 1000
200   continue
      if(ifric.ne.3) go to 300
      fb2=(cf2/re**m2)*(grq*p2)**n2
      if(p1.ne.0.0)  fb1=(cf1/re**m1)*(grq*p1)**n1
      if(p1.eq.0.0)  fb1=(cf1/re**m1)
      if(ifric.eq.3) go to 1000
300   continue
      re1=re*(1.-c*ifx)*v1in*(ltod1/ltod)
      re2=re*(1.+r*c*ifx)*v2in*(ltod2/ltod)
      f2=v2in**2+2.*r*c*v1in*v2in*ifx+(r*c*v1in)**2*ifxsq
      f1=(1.-2.*c*ifx+c**2*ifxsq)*v1in**2
      if(ifric.ne.4) go to 400
      fb1=((cfl1/re1)**1.49+(cft1/re1**.18)**1.49)**.671
      fb2=((cfl2/re2)**1.49+(cft2/re2**.18)**1.49)**.671
400   continue
      if(ifric.eq.4) go to 1000
c  westinghouse test bundle friction factor
      if(ifric.ne.5) go to 500
      sigh1=(re1-400)/4600.
      sigh2=(re2-400)/4600.
      if(sigh1.le.0.0) fb1=110./re1
```

SUBROUTINE RESCALC (continued)

```
      if(sigh2.le.1.0) fb2=110./re2
      if(sigh1.ge.1.0) fb1=.48/re**.25
      if(sigh2.ge.1.0) fb2=.48/re**.25
      if((sigh1.gt.0.0).and.(sigh1.lt.1.0))  fb1=
     1     (110./re1)*(1.-sigh1)**.5+(.48/re1**.25)*sigh1**.5
      if((sigh2.gt.0.0).and.(sigh2.lt.1.0))  fb2=
     1     (110./re2)*(1.-sigh2)**.5+(.48/re2**.25)*sigh2**.5
      if(ifric.eq.5) go to 1000
500   continue
      if(ifric.ne.6) go to 600
      grq1=grq*p1
      grq2=grq*p2
      fb1=((1+3.5*(ltodh/ltod)**2*grq1**2/re1**5)**.4)*(.329/re1**.25)
      fb2=((1+3.5*(ltodh/ltod)**2*grq2**2/re2**5)**.4)*(.329/re2**.25)
      if(ifric.eq.6) go to 1000
600   continue
1000  continue
      term3=.5*(ltod2*fb2*f2-ltod1*fb1*f1)
      term4=ldtonew*((1+r)*v1in*ifx*c*dredt+(v2in-v1in)*dredt)/re**2
      xstart=0.0
      if(indg.eq.3) xstart=.3333
      term5=ltod*ltodh*(1.-xstart)*grq*4.*(k2*p2-k1*p1)/(pr*re**3)
      res=term1+term2+term3+term4-term5
      return
      end
```

LISTING OF PROGRAM TWOCHAN

```
      commonn/ax/estar,ivp,nn,indg,v1in,v2in,w,f25,f50,f75
     .common/resid/c,r,wtstar,ifx,ltod2,ltod1,ltod,ltodh,
     1   dredt,ldtonew,re,pr,k1,k2,p1,p2,m1,m2,n1,n2,cf1,cf2,
     2   grq,ifric,cf11,cf12,cft1,cft2
      common/term/term1,term2,term3,term4,term5
      dimension y1(100),y2(100),y(100)
      dimension theta1(100),theta2(100)
      dimension dfx(100),wcstar(100),wcy1(100),wcy2(100)
      real nn,n1,n2,m1,m2
      real ldtoa,ltodh,ltod,ltod1,ltod2,dredt,ldtonew,stol
      n=100
      real k1,k2,ifx
      indg=1
      iwt=1
      iprint=2
      v1in=1.0
      v2in=1.0
c  read input data
      read(5,2) ldtoa,ltodh,ltod,ltod1,ltod2,dredt,ldtonew,stol
      read(5,2) sf,r,pr,ivp,nn,m1,m2,n1,n2,cf1,cf2,ifric
      if(ifric.eq.4) read(5,2) cf11,cf12,cft1,cft2
      if(ivp.eq.5) read(5,2) f25 f50 f75
2     format(v)
      write(6,3) ldtoa,ltod,dredt,ldtonew,sf,pr,ivp,nn
      continue
3     format(3x,'  ld/a=',f6.2,'  1/d=',f6.1,'  dre/dt=',f6.1,
     1     '  ld/v=',f6.1,
     1   ' sf=',f4.2,'  pr=',f7.4,'  ivp=',i1,'  nn=',f3.1,/)
      write(6,4) ifric,indg
4     format(3x,'ifric=',i1,'  indg=',i1)
5     read(5,2) re,grq,wtstar,p1,p2
      if(re.eq.0.0) go to 70
      write(6,6)
6     format(/,'  ****************************************************')
      write(6,8) re,grq,wtstar,p1,p2
8     format(3x,' re=',f10.1,'    grq=',e8.3,
     1     '  wtstar=',f5.3,'  p1=',f5.3,'  p2=',f5.3/)
      if(iprint.eq.1) write(6,9)
9     format(7x,'  c(b)',3x,' c(c)  ',3x,'resb',5x,'resc')
      estar=(sf/(re*pr))*stol*ldtoa+wtstar
      cata=.99
      catb=-.30
c
c  calculate the residual at b
c
10    c=catb
      if(iwt.eq.2) wtstar=2.*p1*grq**.5/re**1.2
      call euler(c,r,n,y1,y2,k1,k2)
      call rescalc(res)
c
c  residual has been calculated
c
      resb=res
      catc=(cata+catb)/2.
c
c  calculate the residual at c
c
      c=catc
      if(iwt.eq.2) wtstar=2.*p1*grq**.5/re**1.2
      call euler(c,r,n,y1,y2,k1,k2)
```

PROGRAM TWOCHAN (continued)

```
      call rescalc(res)
c
c residual has been calcualted
c
      resc=res
      if(iprint.eq.1) write(6,15) catb,catc,resb,resc
15    format(3x,2f10.4,2f10.4)
      if(abs(resc).le..0002) go to 16
      if(resb*resc.lt.0.0) go to 16
      catb=catc
      go to 18
16    cata=catc
18    if(abs(catb-cata).lt.0.0002) go to 20
      go to 10
20    c=catc
      do 25 i=1,n
      x=float(i)/float(n)
      y(i)=y2(i)*p2-y1(i)*p1
      pi=3.14159
      if(ivp.eq.1) fx=x**nn
      if(ivp.eq.2)  fx=(1-cos(pi*x))/2.
      if(ivp.eq.3)  fx=x-sin(2*pi*x)/(2*pi)
      if(indg.eq.1) pf=x
      if(indg.eq.2) pf=.5132*(sin(2.689*(x-.5))+.9745)
      theta2(i)=(pf+y(i)*(1.-c*fx)*v1in/(1.+1./r))*
     1   ((1.+r)/(v2in+r*v1in))
      theta1(i)=theta2(i)-y(i)
25    continue
      write(6,7)
7     format(/)
      write(6,26) (y(i),i=10,100,10)
26    format(3x,'y(i)=  ',10f7.3)
      write(6,28) (theta1(i),i=10,100,10)
28    format(3x,'theta1=',10f7.3)
      write(6,29) (theta2(i),i=10,100,10)
29    format(3x,'theta2=',10f7.3)
      write(6,7)
      write(6,27) k1,k2,c
27    format(3x,'  k1=',f6.3,'  k2=',f6.3,'   c=',f6.4)
      write(6,7)
      write(6,33) term1,term2,term3,term4,term5
33    format(3x,'term1=',f7.4,'  term2=',f7.4,'  term3=',f7.4,'  term4='
     1   ,f7.4,'  term5=',f7.4,/)
      if(c.le.0.998) go to 40
      write(6,7)
      write(6,31)
31    format(3x,'recirculation is predicted')
      write(6,7)
40    continue
c  forced convection solution for indg=1:
      a=(1.+r)*p2/v2in-(1.+1./r)*p1/v1in
      b=((1+r)/v2in+(1+1./r)/v1in)*estar
      if(b.eq.0.0) go to 41
      yfc=a*(1.-exp(-b))/b
41    if(b.eq.0.0) yfc=a
      th2fc=1.+.5*yfc
      sigh=th2fc-theta2(100)
      write(6,32) th2fc,sigh
32    format(3x,'fc theta2e = ',f6.3,'  sigh = ',f6.4/)
43    continue
```

PROGRAM TWOCHAN (continued)

```
c
c  next determine phi
c
      pi=3.14159
      do 50 i=1,n
      x=float(i)/float(n)
      if(ivp.eq.1) dfx(i)=nn*x**(nn-1.)
      if(ivp.eq.2) dfx(i)=pi*(sin(pi*x))/2.
      if(ivp.eq.3)  dfx(i)=1.-cos(2.*pi*x)
      wcstar(i)=r*c*dfx(i)/(1.+r)
      wcy2(i)=wcstar(i)*y2(i)
50    wcy1(i)=wcstar(i)*y1(i)
      n=100
      call simpint(wcy2,n,yint)
      d2=yint
      call simpint(wcy1,n,yint)
      d1=yint
      wcbar=(p2*d2-p1*d1)/(p2*k2-p1*k1)
      if(estar.eq.0.0) go to 55
      phi=wcbar/estar
55    continue
      buoy=1todh*grq*(k2*p2-k1*p1)/pr
      write(6,60) wcbar,estar,phi,buoy
60    format(3x,'wcstarbar = ',f10.3,5x,'estar = ',f10.3,5x,
     1     'phi = ',f6.3,' buoy=',e9.3,/)
      go to 5
70    continue
      stop
      end
```

SAMPLE PROBLEM FOR PROGRAM TWOCHAN

INPUT FILE:

```
1.47 249.5 307.8 307.8 307.8 0.0 0.0 .211
1.5 1.0 .0054 1 1.0 1.0 1.0 0.0 0.0 64. 64. 4
118.5 118.5 .283 .283
6000. 5400. .138 .408 .592
10000. 5400. .158 .408 .592
0.0
```

OUTPUT FILE:

```
 ld/a=  1.47  l/d= 307.8  dre/dt=   0.0  ld/v=   0.0 sf=1.50  pr= 0.0054  ivp=1  nn=1.0

ifric=4  indg=1

**************************************************
 re=    6000.0    grq=.540E+04  wtstar=0.138  p1=0.408  p2=0.592


y(i)=    0.036  0.069  0.100  0.129  0.156  0.181  0.205  0.227  0.247  0.266
theta1=  0.082  0.165  0.250  0.335  0.421  0.509  0.597  0.686  0.775  0.866
theta2=  0.118  0.234  0.350  0.464  0.578  0.690  0.802  0.912  1.022  1.132


  k1= 0.827  k2= 0.821   c=0.0107

term1= 0.0215  term2= 0.0059  term3= 0.1849  term4= 0.0000  term5= 0.2112

fc theta2e =  1.138  sigh = 0.0062

wcstarbar =      0.005     estar =      0.152     phi =  0.035 buoy=0.371E+08

**************************************************
 re=   10000.0    grq=.540E+04  wtstar=0.158  p1=0.408  p2=0.592


y(i)=    0.036  0.069  0.100  0.129  0.156  0.182  0.205  0.227  0.248  0.267
theta1=  0.082  0.165  0.250  0.335  0.422  0.509  0.597  0.686  0.776  0.866
theta2=  0.118  0.234  0.350  0.465  0.578  0.691  0.802  0.913  1.024  1.133


  k1= 0.813  k2= 0.811   c=0.0025

term1= 0.0050  term2= 0.0016  term3= 0.0387  term4= 0.0000  term5= 0.0457

fc theta2e =  1.134  sigh = 0.0012

wcstarbar =      0.001     estar =      0.167     phi =  0.008 buoy=0.371E+08
```

LISTING OF PROGRAM RECIRC

```
c program to calculate recirculation reynolds number
      common/ax/estar,ivp,nn,indg,v1in,v2in,w,f25,f50,f75
      common/resid/c,r,wtstar,ifx,ltod2,ltod1,ltod,ltodh,
     1    dredt,ldtonew,re,pr,k1,k2,p1,p2,m1,m2,n1,n2,cf1,cf2,
     2    grq,ifric,cf11,cf12,cft1,cft2
      common/term/term1,term2,term3,term4,term5
      dimension y1(100),y2(100)
      dimension y(100),theta1(100),theta2(100)
      dimension dfx(100),wcstar(100),wcy1(100),wcy2(100)
      real nn,n1,n2,m1,m2
      real ldtoa,ltodh,ltod,ltod1,ltod2,dredt,ldtonew,stol
      real ifx,k1,k2
c   hard wired input parameters:
      nn=1.0
      indg=1
      iopt=1
      iprint=2
      iwt=2
      n=100
      v1in=1.00
      v2in=1.00
c  read input data
      read(5,2) ldtoa,ltodh,ltod,ltod1,ltod2,dredt,ldtonew,stol
      read(5,2) sf,r,pr,ivp,nn,m1,m2,n1,n2,cf1,cf2,ifric,c
      if(ifric.eq.4) read(5,2) cf11,cf12,cft1,cft2
      if(ivp.eq.5) read(5,2) f25,f50,f75
2     format(v)
      write(6,2)ldtoa,ltodh,ltod,ltod1,ltod2,dredt,ldtonew,stol
      write(6,2) sf,r,pr,ivp,nn,m1,m2,n1,n2,cf1,cf2,ifric,c

      if(ivp.eq.5) write(6,2) f25,f50,f75
5     read(5,2) re,grq,wtstar,p1,p2
      write(6,6)
6     format(/,' ***********************************************',/)
      if(re.eq.0.0) go to 70
      write(6,8) grq,wtstar,p1,p2
8     format(3x,'grq  = ',e10.3,'wtstar =',f4.2,' p1 = ',f5.3,' p2 = ',
     1     f5.3,/)
      rea=100.
      reb=3000.
      re=reb
      ifx=.5
      if(iopt.eq.2) estar=wtstar
      if(ivp.eq.1) ifx=1./(nn+1.)
      if(iopt.eq.2) call euler(c,r,n,y1,y2,k1,k2)
c calculate residual at b
c
10    re=reb
      if(iwt.eq.2) wtstar=2.0*p1*grq**.5/re**1.2
      estar=(sf/(re*pr))*ldtoa*stol+wtstar
      if(iopt.eq.1) call euler(c,r,n,y1,y2,k1,k2)
      call rescalc(res)
c
c  residual has been calculated
c
      resb=res
      rec=(rea+reb)/2.
c  calculate the residual at c
c
      re=rec
```

PROGRAM RECIRC (continued)

```
      if(iwt.eq.2) wtstar=2.0*pi*grq**.5/re**1.2
      estar=(sf/(re*pr))*ldtoa*stol+wtstar
      if(iopt.eq.1) call euler(c,r,n,y1,y2,k1,k2)
      call rescalc(res)
c
c residual has been calcualted
c
      resc=res
      if(iprint.eq.1) write(6,15) reb,rec,resb,resc
15    format(3x,2f10.1,2f10.4)
      if(abs(resc).le..001) go to 20
      if(resb*resc.lt.0.0) go to 16
      reb=rec
      go to 18
16    rea=rec
18    if(abs(reb-rea).lt.1.0) go to 20
      go to 10
20    re=rec
      write(6,30) k1,k2,re
30    format(3x,'  k1=',f6.3,'  k2=',f6.3,'  recrit=',f8.1,/)
      write(6,33) term1,term2,term3,term4,term5
33    format(3x,'  term1=',f10.4,'  term2=',f10.4,'  term3=',f10.4,
     1     '  term4=',f10.4,'  term5=',f10.4,/)
      do 25 i=1,n
      x=float(i)/float(n)
      y(i)=y2(i)*p2-y1(i)*p1
      pi=3.14159
      if(ivp.eq.1) fx=x**nn
      if(ivp.eq.2)  fx=(1-cos(pi*x))/2.
      if(ivp.eq.3)  fx=x-sin(2*pi*x)/(2*pi)
      if(indg.eq.1) pf=x
      if(indg.eq.2) pf=.5132*(sin(2.689*(x-.5))+.9745)
      theta2(i)=pf+y(i)*(1.-c*fx)/(1.+1./r)
      theta1(i)=theta2(i)-y(i)
25    continue
      write(6,7)
7     format(/)
      write(6,26) (y(i),i=10,100,10)
26    format(3x,'y(i)=  ',10f7.3)
      write(6,28) (theta1(i),i=10,100,10)
28    format(3x,'theta1=',10f7.3)
      write(6,29) (theta2(i),i=10,100,10)
29    format(3x,'theta2=',10f7.3,/)
c
c  next determine phi
c
      pi=3.14159
      do 50 i=1,n
      x=float(i)/float(n)
      if(ivp.eq.1) dfx(i)=nn*x**(nn-1.)
      if(ivp.eq.2) dfx(i)=pi*(sin(pi*x))/2.
      if(ivp.eq.3)  dfx(i)=1.-cos(2.*pi*x)
      wcstar(i)=r*c*dfx(i)/(1.+r)
      wcy2(i)=wcstar(i)*y2(i)
50    wcy1(i)=wcstar(i)*y1(i)
      call simpint(wcy2,n,yint)
      d2=yint
      call simpint(wcy1,n,yint)
      d1=yint
      wcbar=(p2*d2-p1*d1)/(p2*k2-p1*k1)
```

PROGRAM RECIRC (continued)

```
      if(estar.eq.0.0) go to 55
      phi=wcbar/estar
55    continue
      buoy=ltodh*grq*(k2*p2-k1*p1)/pr
      write(6,60) wcbar,estar,phi,buoy
60    format(3x,'wcstarbar = ',f10.3,5x,'estar = ',f10.3,5x,
     1     'phi = ',f6.3,'  buoy=',e7.2,/)
      go to 5
70    continue
      stop
      end
```

SAMPLE PROBLEM FOR PROGRAM RECIRC

INPUT FILE FOR PROGRAM RECIRC

```
4.08 61.9 87.6 93.0 85.5 0.0 0.0 0.0
0.0 .373 4.15 1 1.0 1.0 1.0 0.0 0.0 88. 88. 1 1.0
 100. 1e4 0.0 0.0 1.0
 100. 3e4 0.0 0.0 1.0
0.0
```

OUTPUT FILE FOR PROGRAM RECIRC

```
4.0799999 61.9 87.6 93. 85.5 0. 0. 0.
0. 0.37299999 4.1499999 1 1. 1. 1. 0. 0. 88. 88. 1 1.

*********************************************

 grq  =  0.100E+05wtstar =0.00 p1 = 0.000 p2 = 1.000

   k1= 3.289  k2= 0.553  recrit=   112.0

   term1=    1.1986  term2=    0.0000  term3=   19.4980  term4=    0.0000  term5=   20.5697


 y(i)=    0.133  0.256  0.371  0.479  0.579  0.674  0.763  0.847  0.926  1.001
 theta1= -0.000 -0.000 -0.000 -0.001 -0.001 -0.001 -0.001 -0.001 -0.001 -0.001
 theta2=  0.132  0.256  0.371  0.478  0.579  0.673  0.762  0.846  0.925  1.000

 wcstarbar =      0.272     estar =      0.000     phi =  0.000  buoy=.83E+05

*********************************************

 grq  =  0.300E+05wtstar =0.00 p1 = 0.000 p2 = 1.000

   k1= 3.289  k2= 0.553  recrit=   189.9

   term1=    1.1986  term2=    0.0000  term3=   11.5023  term4=    0.0000  term5=   12.6687


 y(i)=    0.133  0.256  0.371  0.479  0.579  0.674  0.763  0.847  0.926  1.001
 theta1= -0.000 -0.000 -0.000 -0.001 -0.001 -0.001 -0.001 -0.001 -0.001 -0.001
 theta2=  0.132  0.256  0.371  0.478  0.579  0.673  0.762  0.846  0.925  1.000

 wcstarbar =      0.272     estar =      0.000     phi =  0.000  buoy=.25E+06
```

APPENDIX E1

COBRA PREDICTIONS FOR THE 2x6 ROD BUNDLE STEADY STATE TEST

In this appendix the COBRA predicted velocities and temperatures are given for the three steady state runs of Reference 58, which were taken from a preprint of Reference 58. These three cases were used to validate the two channel model in section 6.1. In Tables E1.1, E1.2, and E1.3 the subchannel velocities are given and in E1.4, E1.5, and E1.6 the subchannel temperatures are given.

TABLE E1.1 CASE 1 COBRA SUBCHANNEL VELOCITIES

Subchannel Number	Window 1 U (ft/sec)	Window 1 U/UB	Window 3 U (ft/sec)	Window 3 U/UB	Window 5 U (ft/sec)	Window 5 U/UB	Window 7 U (ft/sec)	Window 7 U/UB	Window 9 U (ft/sec)	Window 9 U/UB
1	0.2219	0.6786	0.2285	0.6988	0.2479	0.7581	0.2741	0.8382	0.3019	0.9232
2	0.3013	0.9214	0.3186	0.9743	0.3393	1.0376	0.3655	1.1177	0.3975	1.2156
3	0.3032	0.9272	0.3156	0.9651	0.3294	1.0073	0.3446	1.0538	0.3637	1.1122
4	0.3030	0.9266	0.2937	0.8982	0.2873	0.8786	0.2807	0.8584	0.2768	0.8465
5	0.3027	0.9257	0.2728	0.8343	0.2495	0.7630	0.2313	0.7073	0.2113	0.6462
6	0.3001	0.9177	0.2693	0.8235	0.2486	0.7602	0.2320	0.7095	0.2129	0.6511
7	0.2210	0.6758	0.1882	0.5755	0.1729	0.5287	0.1611	0.4927	0.1496	0.4575
8	0.3017	0.9226	0.3175	0.9709	0.3415	1.0443	0.3734	1.1419	0.4104	1.2550
9	0.4087	1.2498	0.4550	1.3914	0.4828	1.4765	0.5032	1.5388	0.5241	1.6028
10	0.4110	1.2569	0.4545	1.3899	0.4791	1.4651	0.4945	1.5122	0.5095	1.5581
11	0.4106	1.2557	0.4309	1.3177	0.4392	1.3431	0.4343	1.3281	0.4274	1.3070
12	0.4103	1.2547	0.4061	1.2419	0.3887	1.1887	0.3646	1.1150	0.3313	1.0131
13	0.4078	1.2471	0.4026	1.2312	0.3853	1.1783	0.3620	1.1070	0.3296	1.0080
14	0.3008	0.9199	0.2727	0.8339	0.2489	0.7612	0.2292	0.7009	0.2084	0.6373
15	0.2219	0.6786	0.2286	0.6991	0.2468	0.7547	0.2726	0.8336	0.3002	0.9180
16	0.3025	0.9251	0.3187	0.9746	0.3393	1.0376	0.3658	1.1187	0.3982	1.2177
17	0.3032	0.9272	0.3156	0.9651	0.3297	1.0083	0.3457	1.0572	0.3664	1.1205
18	0.3030	0.9266	0.2937	0.8982	0.2873	0.8786	0.2807	0.8584	0.2783	0.8511
19	0.3027	0.9257	0.2728	0.8343	0.2488	0.7609	0.2297	0.7024	0.2102	0.6428
20	0.3015	0.9220	0.2697	0.8248	0.2462	0.7529	0.2274	0.6954	0.2085	0.6376
21	0.2207	0.6749	0.1882	0.5755	0.1740	0.5321	0.1625	0.4969	0.1500	0.4587

y = -0.531 (rows 1–4) y = 0.0 (rows 5–16) y = -0.531 (rows 17–21)

TABLE E1.2 CASE 2 COBRA SUBCHANNEL VELOCITIES

	Window Number									
	1		3		5		7		9	
Subchannel Number	U (ft/sec)	U/UB	U (ft/sec)	U/UB	U (ft/sec)	U/UB	U (ft/sec)	U/UB	U (ft/sec)	U/UB
1	0.1166	0.7110	0.1746	1.0646	0.2270	1.3841	0.2807	1.7116	0.3006	1.8329
2	0.1565	0.9543	0.2184	1.3317	0.2686	1.6378	0.3176	1.9366	0.3576	2.1805
3	0.1557	0.9494	0.1897	1.1567	0.2089	1.2738	0.2165	1.3201	0.2379	1.4506
4	0.1523	0.9287	0.1365	0.8323	0.1190	0.7256	0.0982	0.5988	0.0779	0.4750
5	0.1495	0.9116	0.0951	0.5799	0.0549	0.3348	0.0203	0.1238	0.0000	0.0000
6	0.1464	0.9049	0.0928	0.5659	0.0536	0.3268	0.0198	0.1207	-0.0000	0.0000
7	0.1084	0.6610	0.0649	0.3957	0.0377	0.2299	0.0139	0.0848	-0.0000	0.0000
8	0.1574	0.9598	0.2315	1.4116	0.3045	1.8567	0.3810	2.3232	0.4299	2.6213
9	0.2205	1.3445	0.3085	1.8811	0.3973	2.4226	0.4707	2.8701	0.5171	3.1530
10	0.2203	1.3433	0.2889	1.7616	0.3685	2.1250	0.4057	2.4738	0.4439	2.7067
11	0.2174	1.3255	0.2240	1.3659	0.2219	1.3530	0.2135	1.3018	0.1851	1.1287
12	0.2146	1.3085	0.1546	0.9427	0.0894	0.5451	0.0328	0.2000	-0.0027	-.0165
13	0.2134	1.3012	0.1515	0.9238	0.0873	0.5323	0.0319	0.1945	-0.0027	-.0159
14	0.1495	0.9116	0.0940	0.5732	0.0536	0.3268	0.0198	0.1207	-0.0000	0.0000
15	0.1169	0.7128	0.1749	1.0665	0.2273	1.3860	0.2810	1.7134	0.2998	1.8280
16	0.1568	0.9561	0.2187	1.3335	0.2689	1.6396	0.3176	1.9366	0.3552	2.1659
17	0.1560	0.9512	0.1900	1.1585	0.2092	1.2756	0.2155	1.3140	0.2312	1.4098
18	0.1526	0.9305	0.1368	0.8341	0.1197	0.7268	0.0985	0.6006	0.0773	0.4713
19	0.1498	0.9134	0.0955	0.5823	0.0551	0.3360	0.0203	0.1238	0.0000	0.0000
20	0.1488	0.9073	0.0932	0.5683	0.0538	0.3280	0.0199	0.1213	-0.0000	0.0000
21	0.1088	0.6634	0.0652	0.3976	0.0378	0.2305	0.0139	0.0849	-0.0000	0.0000

TABLE E1.3 CASE 3 COBRA SUBCHANNEL VELOCITIES

	Window Number									
	1		3		5		7		9	
Subchannel Number	U (ft/sec)	U/UB	U (ft/sec)	U/UB	U (ft/sec)	U/UB	U (ft/sec)	U/UB	U (ft/sec)	U/UB
1	0.2235	0.6836	0.2877	0.8798	0.3615	1.1055	0.4409	1.3483	0.5078	1.5529
2	0.3028	0.9260	0.3696	1.1303	0.4419	1.3514	0.505[illegible]	1.5459	0.5533	1.6920
3	0.3041	0.9300	0.3474	1.0624	0.3787	1.1581	0.4063	1.2425	0.4392	1.3431
4	0.3032	0.9272	0.2873	0.8786	0.2655	0.8119	0.2420	0.7401	0.2218	0.6783
5	0.3022	0.9242	0.2296	0.7021	0.1726	0.5278	0.1258	0.3847	0.0856	0.2618
6	0.2990	0.9144	0.2241	0.6853	0.1690	0.5168	0.1244	0.3804	0.0860	0.2630
7	0.2200	0.6728	0.1570	0.4801	0.1153	0.3541	0.0834	0.2550	0.0573	0.1752
8	0.3033	0.9275	0.3785	1.1575	0.4717	1.4425	0.5488	1.6783	0.6074	1.8575
9	0.4094	1.2520	0.5030	1.5382	0.5807	1.7758	0.6542	2.0006	0.7213	2.2058
10	0.4112	1.2575	0.4753	1.4535	0.5495	1.6804	0.6007	1.8370	0.6467	1.9777
11	0.4101	1.2541	0.4317	1.3202	0.4369	1.3361	0.4312	1.3187	0.4223	1.2914
12	0.4092	1.2514	0.3529	1.0792	0.2813	0.8602	0.2072	0.6336	0.1397	0.4272
13	0.4063	1.2425	0.3463	1.0587	0.2744	0.8391	0.2014	0.6159	0.1356	0.4147
14	0.2999	0.9171	0.2293	0.7012	0.1696	0.5187	0.1212	0.3706	0.0817	0.2498
15	0.2739	0.6847	0.2878	0.8801	0.3609	1.1037	0.4403	1.3465	0.5076	1.5523
16	0.3039	0.9294	0.3697	1.1306	0.4420	1.3517	0.5064	1.5486	0.5555	1.6988
17	0.3042	0.9303	0.3473	1.0621	0.3788	1.1584	0.4084	1.2489	0.4454	1.3621
18	0.3032	0.9272	0.2872	0.8783	0.2648	0.8098	0.2421	0.7404	0.2255	0.6896
19	0.3022	0.9242	0.2295	0.7018	0.1707	0.5220	0.1228	0.3755	0.0834	0.2550
20	0.3004	0.9187	0.2242	0.6856	0.1658	0.5070	0.1189	0.3636	0.0806	0.2465
21	0.2197	0.6719	0.1522	0.4807	0.1176	0.3596	0.0855	0.2615	0.0586	0.1792

$y = -0.531$ ⟵ $y = 0.0$ ⟵ $y = -0.531$

TABLE E1.4 CASE 1 SUBCHANNEL TEMPERATURES

Window Number	Data Type	T_{in} (°F)	T_{out} (°F)	ΔT_B (°F)	Subchannel Temperature (°F)						
					8	9	10	11	12	13	14
1	Measured	55.6	87.2	21.6	55.5	55.6	55.7	55.9	56.1	56.1	56.3
	COBRA	59.62	88.04	28.42	59.62	59.62	59.62	59.62	59.62	59.62	59.62
3	Measured	56.2	88.0	31.8	58.0	66.0	64.1	61.9	60.7	60.7	58.2
	COBRA	59.62	88.04	28.42	68.65	69.13	68.95	66.72	64.56	64.59	64.38
5	Measured	61.7	95.6	33.9	66.0	78.8	79.5	74.5	71.3	71.3	71.5
	COBRA	59.62	88.04	28.42	77.19	77.84	77.44	73.46	69.66	69.73	69.65
7	Measured	61.8	92.1	30.3	68.9	89.1	85.6	81.9	78.2	78.4	74.2
	COBRA	59.62	88.04	28.42	85.14	86.15	85.43	80.04	75.03	75.14	75.40
9	Measured	60.1	88.6	28.5	72.3	94.0	96.2	89.4	82.7	82.8	80.0
	COBRA	59.62	88.04	28.42	92.41	94.08	93.00	86.55	80.84	80.99	81.71

TABLE E1.5 CASE 2 SUBCHANNEL TEMPERATURES

Window Number	Data Type	T_{in} (°F)	T_{out} (°F)	ΔT_B (°F)	Subchannel Temperature (°F)						
					8	9	10	11	12	13	14
1	Measured	60.2	93.1	32.9	59.1	59.1	59.1	59.3	59.4	59.4	59.6
	COBRA	60.4	89.5	29.1	60.40	60.40	60.40	60.40	60.40	60.40	60.40
3	Measured	60.6	93.1	32.5	60.8	61.77	69.2	60.8	60.9	60.9	61.1
	COBRA	60.4	89.5	29.1	72.65	73.17	71.67	65.79	60.40	60.40	60.40
5	Measured	59.3	92.4	33.1	60.5	68.2	73.3	59.7	59.4	59.4	59.9
	COBRA	60.4	89.5	29.1	81.45	81.95	78.99	69.58	60.40	60.40	60.40
7	Measured	59.5	92.6	33.1	65.6	77.6	88.2	68.3	59.8	60.0	60.6
	COBRA	60.4	89.5	29.1	88.06	88.85	85.39	72.67	60.40	60.40	60.40
9	Measured	62.6	96.1	33.5	89.9	99.5	99.7	88.5	74.7	69.2	69.3
	COBRA	60.4	89.5	29.1	93.50	94.93	90.79	76.88	67.98	68.56	67.54

TABLE E1.6 CASE 3 SUBCHANNEL TEMPERATURES

Window Number	Data Type	T_{in} (°F)	T_{out} (°F)	ΔT_B (°F)	Subchannel Temperature (°F)						
					8	9	10	11	12	13	14
1	Measured										
	COBRA	60.9	91.01	30.11	60.90	60.90	60.90	60.90	60.90	60.90	60.90
3	Measured	61.1	93.3	32.2	63.5	74.4	72.1	64.5	61.3	61.4	61.6
	COBRA	60.9	91.01	30.11	74.44	75.32	74.14	67.27	60.90	60.90	60.90
5	Measured	61.9	97.5	35.6	68.1	84.1	87.6	67.1	62.1	62.1	62.3
	COBRA	60.9	91.01	30.11	85.31	87.04	84.11	72.04	60.90	60.90	60.90
7	Measured	61.8	92.3	30.5	74.5	95.1	96.4	69.6	61.9	62.0	62.3
	COBRA	60.9	91.01	30.11	94.32	96.97	92.23	75.98	60.90	60.90	60.90
9	Measured	59.7	88.7	29.1	81.5	106.1	105.3	81.0	61.0	59.9	60.6
	COBRA	60.9	91.01	30.11	102.29	105.69	99.35	79.56	60.90	60.90	60.90

APPENDIX E2

THE VERSION OF ENERGY EMPLOYED IN THIS STUDY

The ENERGY code and the correlations for the input parameters are presently in a stage of development. The purpose of this appendix is to identify the version of the code which was used in this study. The version of Reference 68 was used with one change.

In Reference 68 several modifications were made in the code which included incorporating the latest input parameters, and modifying the energy equation to include a term (named ZZJ in the program) which caused the peak bundle temperature to be shifted slightly in the direction of the swirl flow. It was found that including this term caused the matrix inverter in energy not to converge. The term was removed in this work by setting:

```
ZZJ = 0
```

after the statement:

```
151 CONTINUE
```

in subroutine BUOYAN.

APPENDIX E3

DETERMINATION OF w_t^* FOR AN LMFBR WIRE WRAPPED BUNDLE

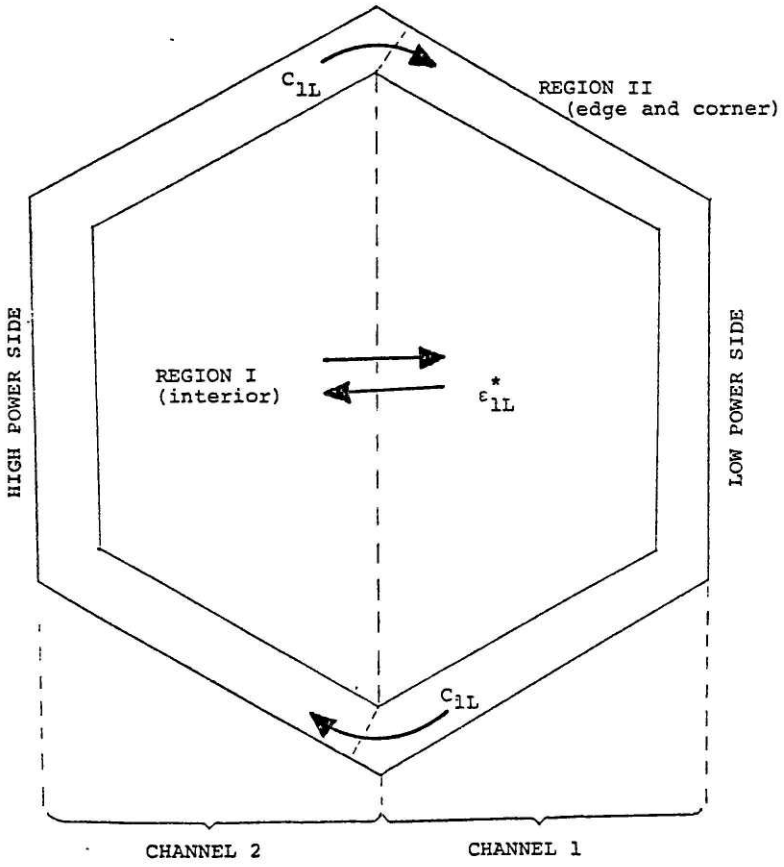
In the appendix a method is developed to determine the coolant mixing between channels (w_t^*) for various noding schemes for an LMFBR bundle, in terms of the ENERGY code mixing parameters. The porous body formulation discussed in Reference 76 will be employed.

Generally speaking, when it is desired to model the buoyancy induced crossflow in a rod bundle with the two channel approach, the bundle is separated into two channels such that the boundary line between the channels is normal to the direction of the buoyancy induced crossflow. If a strong radial power gradient exists, the buoyancy induced crossflow goes parallel to the power gradient. For the case of uniform power, the buoyancy induced crossflow goes from the edge region to the interior region.

Figures E3.1 shows a noding scheme with equal channel areas for a flat to flat power gradient. Note that each channel contains both Region I (interior) subchannels, and Region II (edge and corner) subchannels. The energy transport equation for Region I of channel 1 is equation 1a of reference 76.

FIGURE E3.1

MIXING ACROSS THE CHANNEL BOUNDARY FOR AN LMFBR ROD BUNDLE



$$P^{A}_{I}\rho C_{p}U_{AI}\left[\frac{T_{out}-T_{in}}{\Delta Z}\right]_{I1} = \left(\rho C_{p}\ \varepsilon_{H_{NI}} + P^{K}_{NI}K\ P^{P}_{I}\right)\nabla T_{I1-I2}$$

$$- \left(\rho C_{p}\ \varepsilon_{H_{NII}} + P^{K}_{NII}K\ P^{P}_{NII}\right)\nabla T_{I1=II1} + P^{Q}_{I}\ P^{A}_{I} \qquad \text{(E3.1)}$$

and for Region II of channel 1,

$$P^{A}_{II}\ C_{pA}U_{II}\ \frac{T_{out}-T_{in}}{\Delta Z}_{II1} = \rho C_{p}U_{SII}\ P^{P}_{SII}\left(T_{i} - T_{j}\right)_{II}$$

$$- \left(\rho C_{p}\varepsilon_{H_{NII}} + P^{K}_{NII}K\ \ P^{P}_{NII}\right)\nabla T_{I1-II1}$$

$$- \left(\rho C_{p}\varepsilon_{H_{SII}} + P^{K}_{SII}K\ \ P^{P}_{SII}\right)\nabla T_{II1-II2} + P^{Q}_{II}P^{A}_{II} \qquad \text{(E3.2)}$$

The second term on the right hand side of Equations E3.1 and E3.2 are both zero because for the two channel approach, no lateral gradients exist within either channel, so that:

$$T_{I1=II1} = 0 \qquad \text{(E3.3)}$$

The axial temperature gradients in Regions I and II of channel 1 are identical for the two channel approach:

$$\left[\frac{T_{out}-T_{in}}{\Delta x}\right]_{I1} = \left[\frac{T_{out}-T_{in}}{\Delta x}\right]_{II1} \simeq \frac{dT_{1}}{dx} \qquad \text{(E3.4)}$$

In Region II, the energy transport due to conduction and diffusion is neglected with respect to the swirl flow, so that:

$$\varepsilon_{H_{SII}} = 0 \; ; \quad {}_{P}K_{SII} = 0 \tag{E3.5}$$

We need to estimate the temperature gradient between regions, i.e. ∇T_{I1-I2} of the interior mixing term and the temperature difference $(T_i - T_j)_{II}$ of the edge region swirl term from the two bulk temperatures calculated by the two channel model. Figure E3.2 illustrates how these estimates are made. The two channel model is formulated in terms of $T_1(x)$ and $T_2(x)$, the bulk temperature in each channel as a function of the axial coordinate. The lateral energy transport depends on the local temperature gradient at the channel boundary. This temperature gradient can be estimated as:

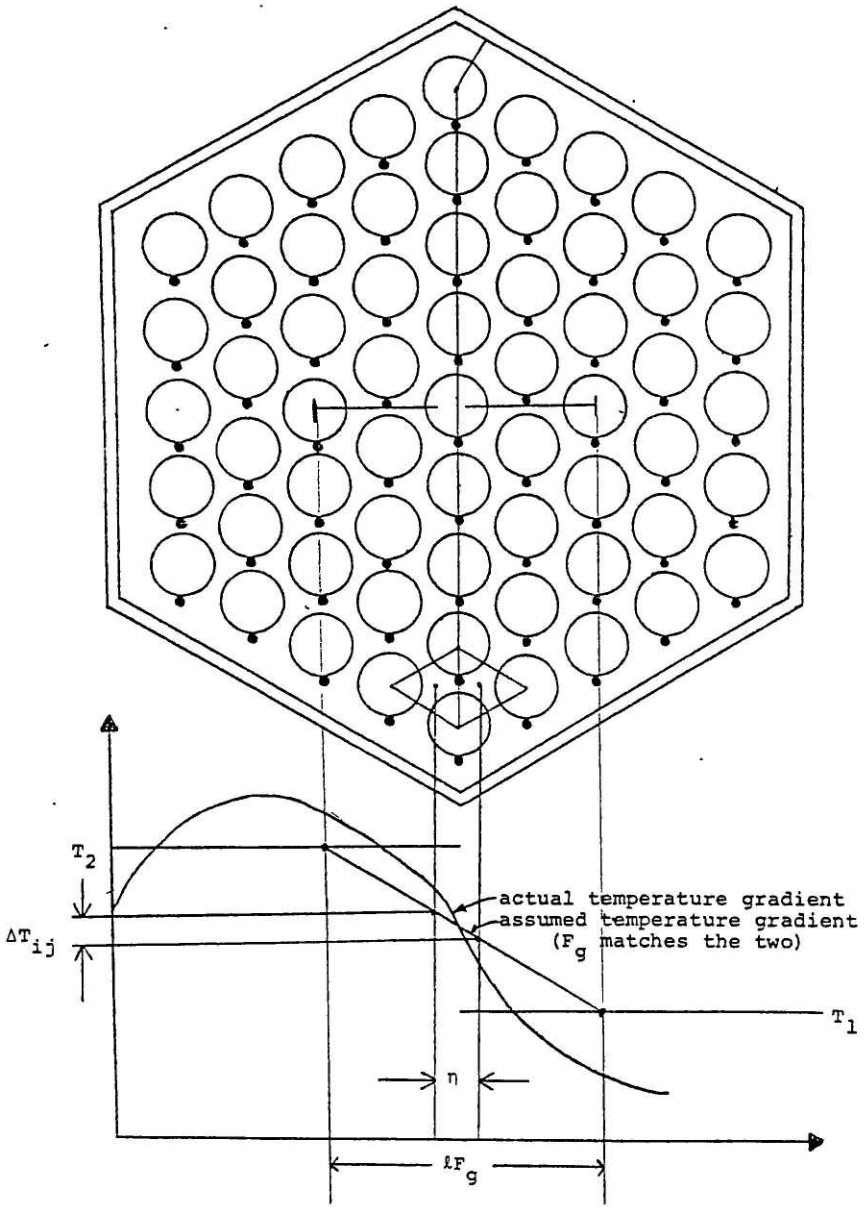
$$\nabla T_{I1=I2} = \frac{T_2 - T_1}{\ell \cdot F_g} \tag{E3.6}$$

where ℓ is the centroid to centroid distance between the two channels. For the bundle noding of Figure E3.1, it can be shown that $\ell_C = \frac{4}{9} D_F$ where D_F is the bundle flat to flat distance. F_g is a factor which may be employed to match the estimated gradient based on the two bulk temperatures with the local gradient. The ENERGY code can be employed to obtain the local gradient, which it calculates as:

$$\nabla T_{ij} = \frac{T_i - T_j}{\eta_1} \tag{E3.7}$$

FIGURE E3.2

PHYSICAL SIGNIFICANCE OF F_g



where T_i and T_j are the temperatures of adjacent interior subchannels, and η_1 is the centroid to centroid distance between interior subchannels.

Neglecting the corner subchannel, the ΔT in the swirl term is the temperature difference between adjacent edge subchannels. As shown in Figure E3.2, this local temperature difference can be estimated from the two bulk temperatures as:

$$T_i - T_j = (T_2 - T_1) \frac{\eta_2}{\ell F_g} \tag{E3.8}$$

where η_2 is the centroid to centroid distance between the edge subchannels:

$$\eta_2 = P^2 + (g + \frac{1}{2}D)^2 \tag{E3.9}$$

and F_g is a correction factor for the ΔT in the swirl term. Adding Equations E3.1 and E3.2, and applying relations E3.5, E3.6, and E3.8 gives:

$$\rho C_p ({}_pA_I U_{AI} + {}_pA_{II} A U_{II}) \frac{dT_1}{dx} = (\rho C_p \varepsilon_{H_{NI}} + {}_pK_{NI} K)_p P_I \frac{T_2 - T_1}{\ell F_g}$$

$$- \rho C_{pS} U_{II} P_{SII} (T_2 - T_1) \frac{\eta_2}{\ell F_g} + {}_pQ_I \, {}_pA_I + {}_pQ_{II} \, {}_pA_{II} \tag{E3.10}$$

Rearranging terms, Equation E3.10 becomes:

$$\rho C_p \left(A_I U_{AI} + P^A_{II} U_{AII} \right) \frac{dT_1}{dx} = - \quad C_p \varepsilon_{H_{NI}} \quad \frac{P^P_I}{\ell F_g}$$

$$\rho C_p U_{SII} P^P_{SII} \frac{\eta_2}{\ell F_g} + P^K_{NI} P^P_I \frac{K}{\ell F_g} \quad (T_2 - T_1)$$

$$+ \quad P^Q_I P^A_I + P^Q_{II} P^A_{II} \qquad \text{(E3.11)}$$

To transform this to the subchannel presentation the following relations (taken from Reference 76) must be employed:

Enhanced eddy diffusivity:

$$\varepsilon_{H_{NI}} = \frac{\lambda_{LI}}{\lambda_A} D_{el} U_A S^X_I \varepsilon^*_{1L}$$

Velocities:

$$U_{AI} = V_{AI} \lambda_{AI} \; ; \quad U_{AII} = V_{AII} \lambda_{AII}$$

$$U_{SII} = V_{SII} \lambda_{LII} \; ; \; U_A = V_A \lambda_A$$

Perimeters for heat transfer:

$$P^P_I = S^P_I \frac{1}{\lambda_{Ll}}$$

$$P^P_{II} = S^P_{II} \frac{1}{\lambda_{LII}}$$

Volumetric heat sources:

$$P^{Q}_{I} = \lambda_{AI} \; S^{Q}_{I}$$

$$P^{Q}_{II} = \lambda_{AII} \; S^{Q}_{II}$$

Flow areas:

$$P^{A}_{I} = S^{A}_{I} \frac{1}{\lambda_{AI}}$$

$$P^{A}_{II} = S^{A}_{II} \frac{1}{\lambda_{LII}}$$

Employing the above relations, Equation E3.11 becomes:

$$\rho C_p (S^{A}_{I} V_{AI} + S^{A}_{II} V_{AII}) \frac{dT_1}{dx} = - \rho C_p D_{el} V_A S^{X}_{I} \varepsilon^{*}_{1L} \frac{S^{P}_{I}}{\ell F_g}$$

$$+ \rho C_p V_S S^{P}_{SII} \frac{\eta_2}{\ell F_g} + P^{K}_{NI} P^{P}_{I} \frac{K}{F_g \ell} \quad (T_2 - T_1)$$

$$+ S^{Q}_{I} S^{A}_{I} + S^{Q}_{II} S^{A}_{II} \qquad \text{(E3.12)}$$

A mass balance for channel 1 gives:

$$V_1 A_1 = S^{A}_{I} V_{AI} + S^{A}_{II} V_{AII} \qquad \text{(E3.13)}$$

The total heat input per unit length to channel 1 is the sum of the Region I and Region II heat inputs:

$$q'_1 = S^{Q}_{I} S^{A}_{I} + S^{Q}_{II} S^{A}_{II} \qquad \text{(E3.14)}$$

Substituting Equations E3.13 and E3.14 into Equation E3.10 gives:

$$\rho C_p V_1 A_1 \frac{dT_1}{dx} = - \left[\rho C_p D_{el} V_A S^{X_I} \varepsilon^*_{1L} \frac{S^{P_I}}{\ell F_g} \right.$$

$$\left. + \rho C_p V_S S^{P_{SII}} \frac{\eta_2}{\ell F_g} + P^{K_{NI}} S^{P_I} \frac{K}{\ell F_g} \right] (T_2 - T_1) + q_1' \qquad \text{(E3.15)}$$

For comparison, the channel 1 energy Equation derived in Section 5.1.2 is:

$$\rho C_p V_1 A_1 \frac{dT_1}{dx} = - (C_p w_t + SF K \frac{w}{\ell})(T_2 - T_1) + q_1' \qquad \text{(E3.16)}$$

Comparison of E3.15 and E3.16 gives the mixing term for the two channel model:

$$C_p w_t = \rho C_p D_{ei} V_A S^{X_I} \varepsilon^*_{1L} \frac{S^{P_I}}{\ell F_g} + \rho C_p V_S S^{P_{II}} \frac{\eta_2}{\ell F_g} \qquad \text{(E3.17)}$$

For the half bundle noding scheme of Figure E3.1, the perimeters for heat transfer are:

$$S^{P_{II}} = 2g \qquad \text{(E3.18)}$$

$$S^{P_I} = 2N_R (P-D) \equiv w \qquad \text{(E3.19)}$$

The swirl velocity ratio is:

$$C_{1L} = \frac{1}{S^{X_{II}}} \frac{V_S}{V_b} \qquad \text{(E3.20)}$$

Employing E3.18, E3.19, and E3.20, Equation E3.17 gives the dimensionless mixing as:

$$w_t^* = \frac{w_t L}{\rho V_b A_b} = \frac{D_{ei}}{\ell F_g} 2N_R \frac{(P-D)L}{A_b} X_1 \varepsilon_{1L}^* + \frac{2gL\eta_2}{A_b \ell F_g} X_2 C_{1L} \quad \text{(E3.21)}$$

For the channel geometry of Figure E3.1, the centroid to centroid distance is:

$$\ell = \frac{4}{9} D_F \quad \text{(E3.22)}$$

Equation E3.21 gives the mixing between channels for the noding scheme of Figure E3.1, which is the scheme employed for the criteria developed in this study. The mixing for other noding schemes may be found by substituting suitable relations for the perimeters for heat transfer in Equations E3.18 and E3.19.

APPENDIX E4

COMPARISON OF ENERGY RESULTS WITH THE WESTINGHOUSE BLANKET BUNDLE DATA

As discussed in Section 6.2, the mixing model in the two channel model was calibrated against the ENERGY results of the code. In this Appendix comparisons will be made with the ENERGY results and the Westinghouse blanket data. This completes the two step validation procedure for the two channel model (data compared to code results, and code results compared to model results).

Table E4.1 outlines the WARD blanket data which has been compared to the ENERGY code results. Some comparisons were made in Greene's thesis (67) and Kims thesis (68). Several comparisons were also made in the present study.

The results of Greene were near the transition from forced convection to mixed convection, and the mixed convection predictions were in good agreement with the WARD data. Kim gave only the mixed convection ENERGY results since most of his comparisons were well into the mixed convection regime. It is observed that the code prediction is more peaked than the data. This can be attributed to heat conduction through the pins and enhances wire wrap mixing due to buoyancy. The three comparisons made in this work also include the predictions of the velocity field.

TABLE E4.1

WESTINGHOUSE DATA COMPARISONS WITH ENERGY

Run #	Power (kW)	Flow (GPM)	T_{in} (^{o}F)	Skew	Re	Gr_q	B*	Figure
218	127	18.1	603	1:1	4370	2701	0	E4.2
221	130	18.2	603	2.8:1	4380	2764	2.18E5	E4.3
223	258	36.8	605	2.8:1	8890	5487	4.36E5	E4.4
224	259	36.9	596	1:1	8780	5508	0	E4.5
232	362	69.8	616	2.8:1	11600	7699	9.21E5	E4.6
227	33.3	4.9	602	1:1	1200	708	0	E4.7
719	15.4	2.3	618	1:1	500	328	0	E4.8
401	33.1	4.9	605	2:1	1067	704	3.74E4	E4.9
725	59.6	4.2	572	2:1	865	1267	6.93E4	E4.10
720	14.1	2.3	581	2:1	480	300	1.82E4	E4.11
229	31.4	4.8	598	2.8:1	1025	668	5.16E4	E4.12
702	15.2	2.2	588	2.8:1	460	323	2.49E4	E4.13
716	32.1	3.3	680	4.6:1	680	683	8.38E4	E4.14
712	56.3	4.1	589	2.8:1	860	1197	9.24E4	E4.15
546	430.0	61.8	503	2.8:1	11758	7050	5.60E5	E4.16
547	431.8	40.5	503	2.8:1	7677	7081	5.62E5	E4.17
530	129.7	11.7	508	2.8:1	2237	2122	2.11E5	E4.18

FIGURE E4.1

SUBCHANNEL NUMBERING SCHEME USED IN WARD-ENERGY COMPARISON

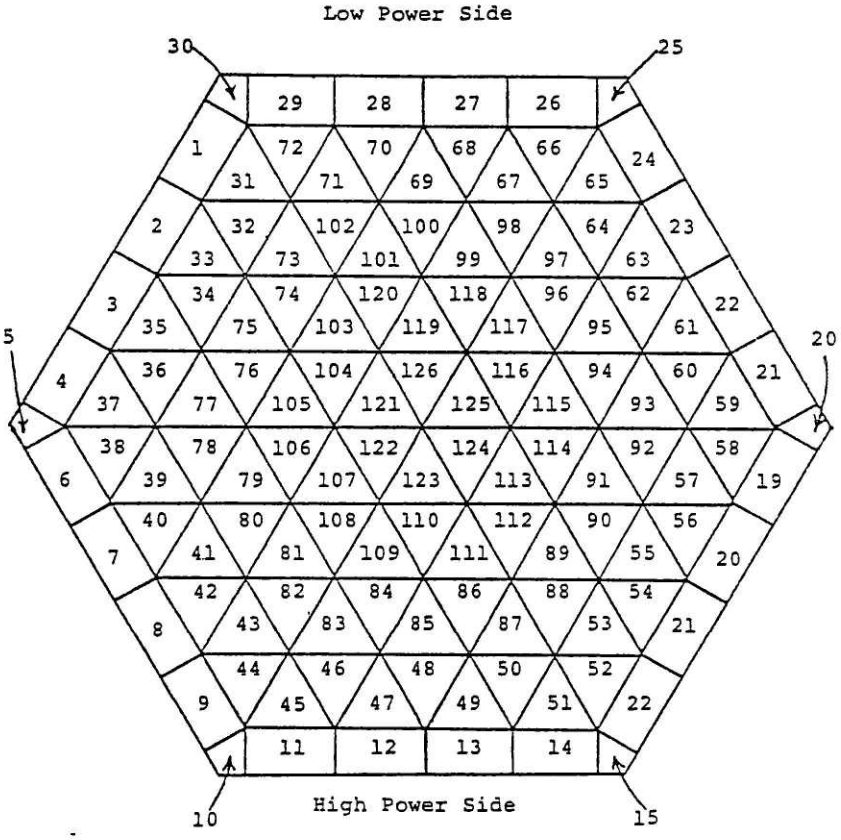


FIGURE E4.2
COMPARISON OF ENERGY PREDICTIONS TO WARD DATA - RUN 218

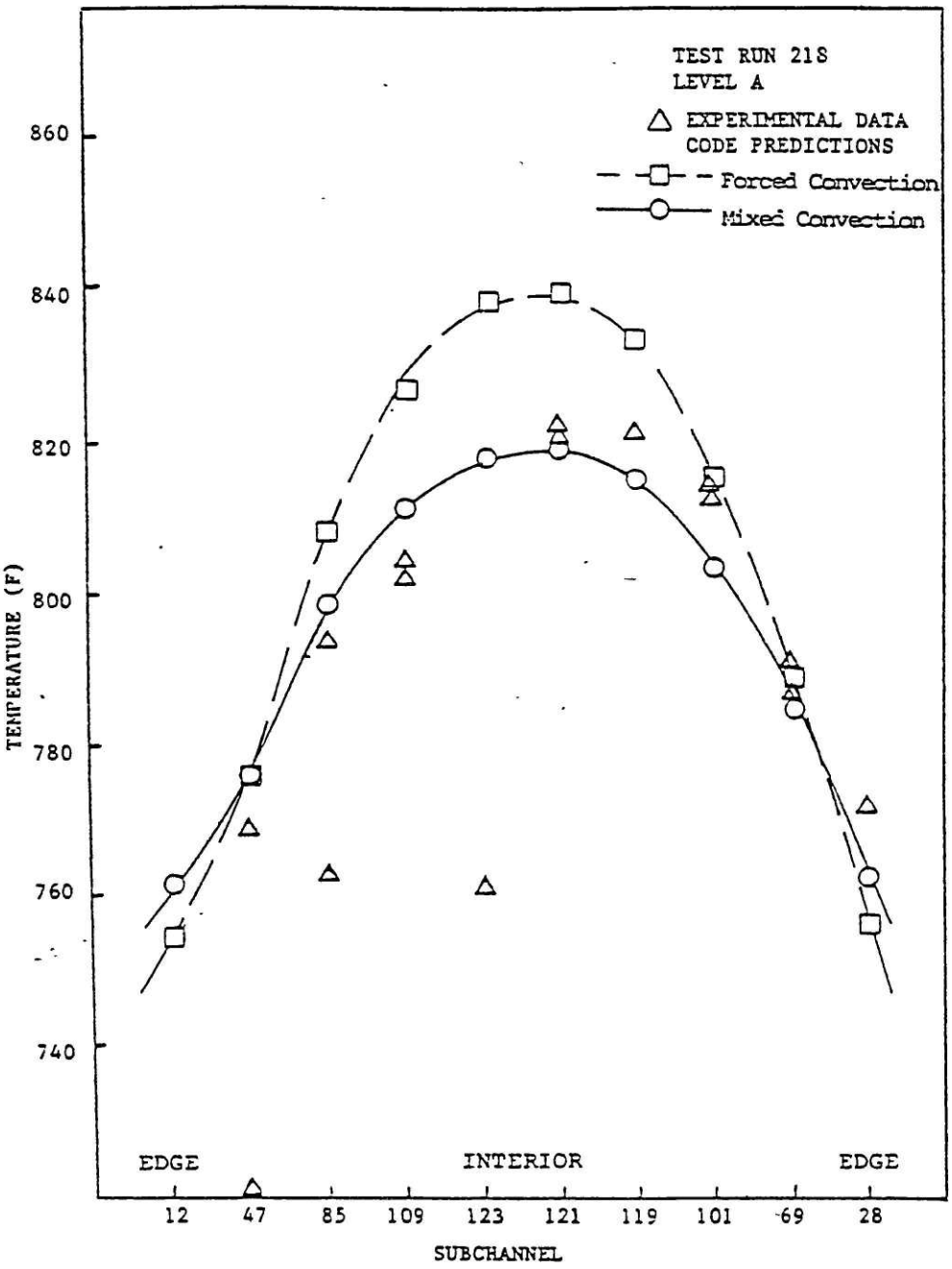


FIGURE E4.3

COMPARISON OF ENERGY PREDICTIONS TO WARD DATA - RUN 221

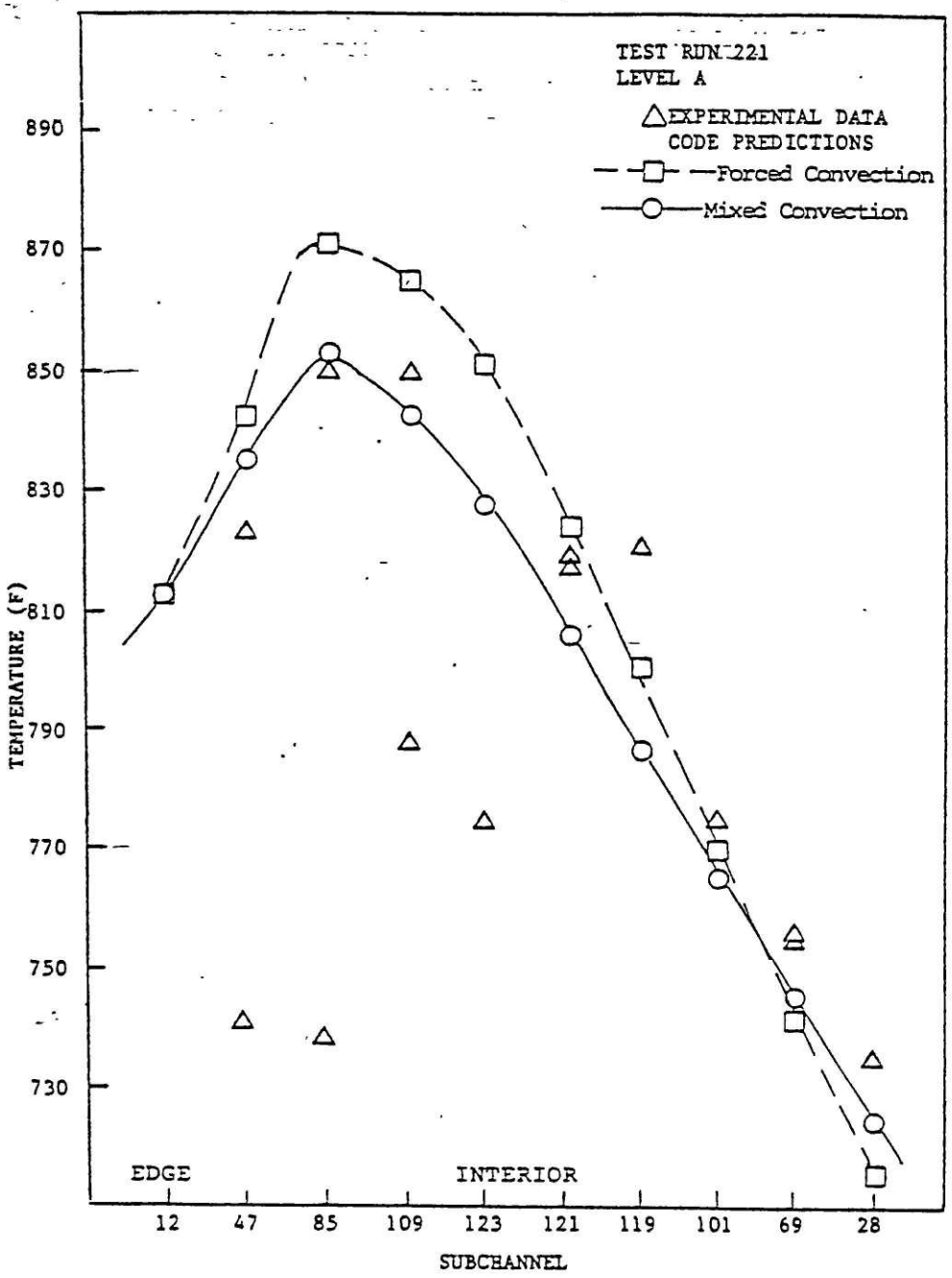


FIGURE E4.4

COMPARISON OF ENERGY PREDICTIONS TO WARD DATA - RUN 223

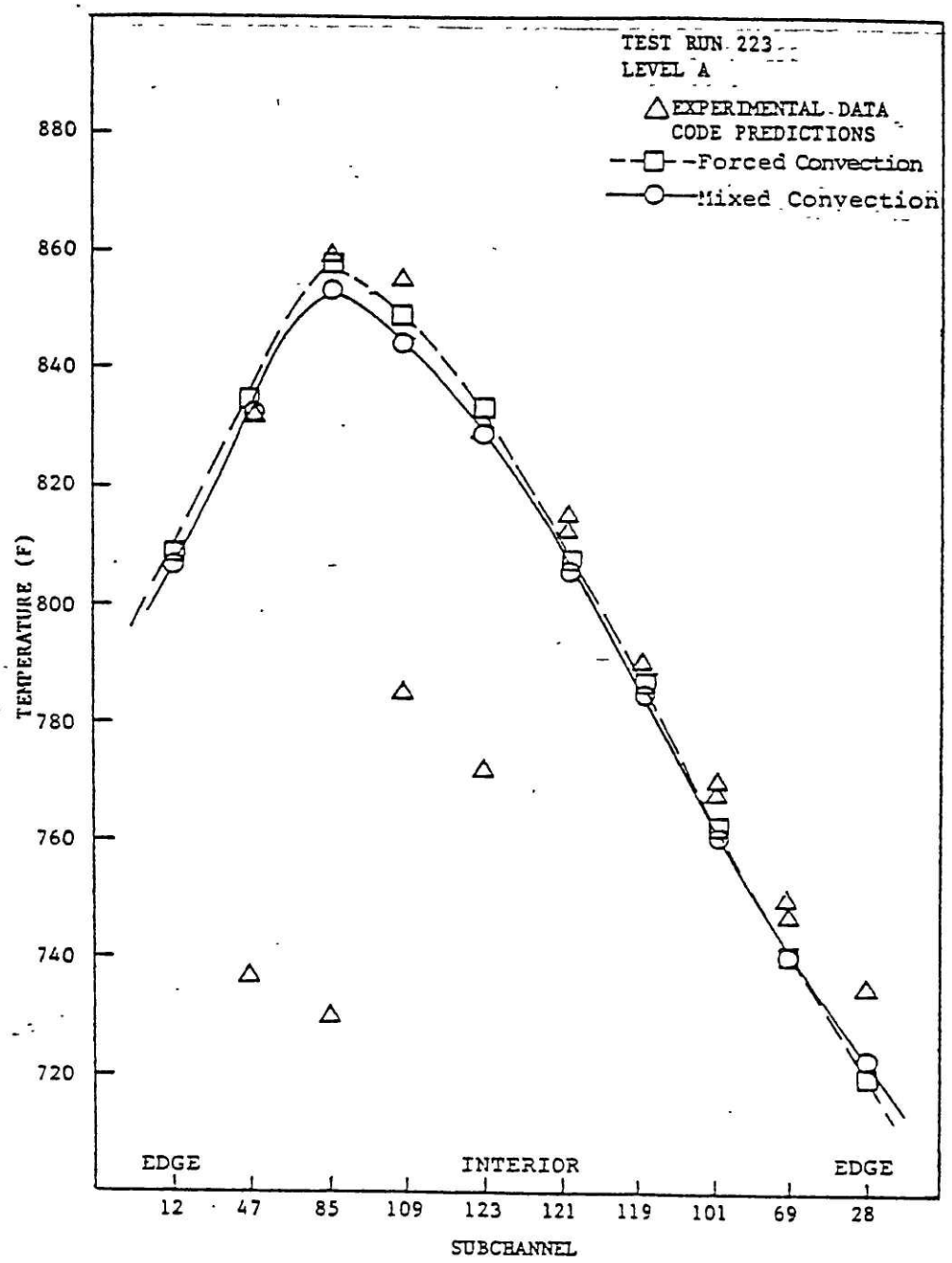


FIGURE E4.5

COMPARISON OF ENERGY PREDICTIONS TO WARD DATA - RUN 224

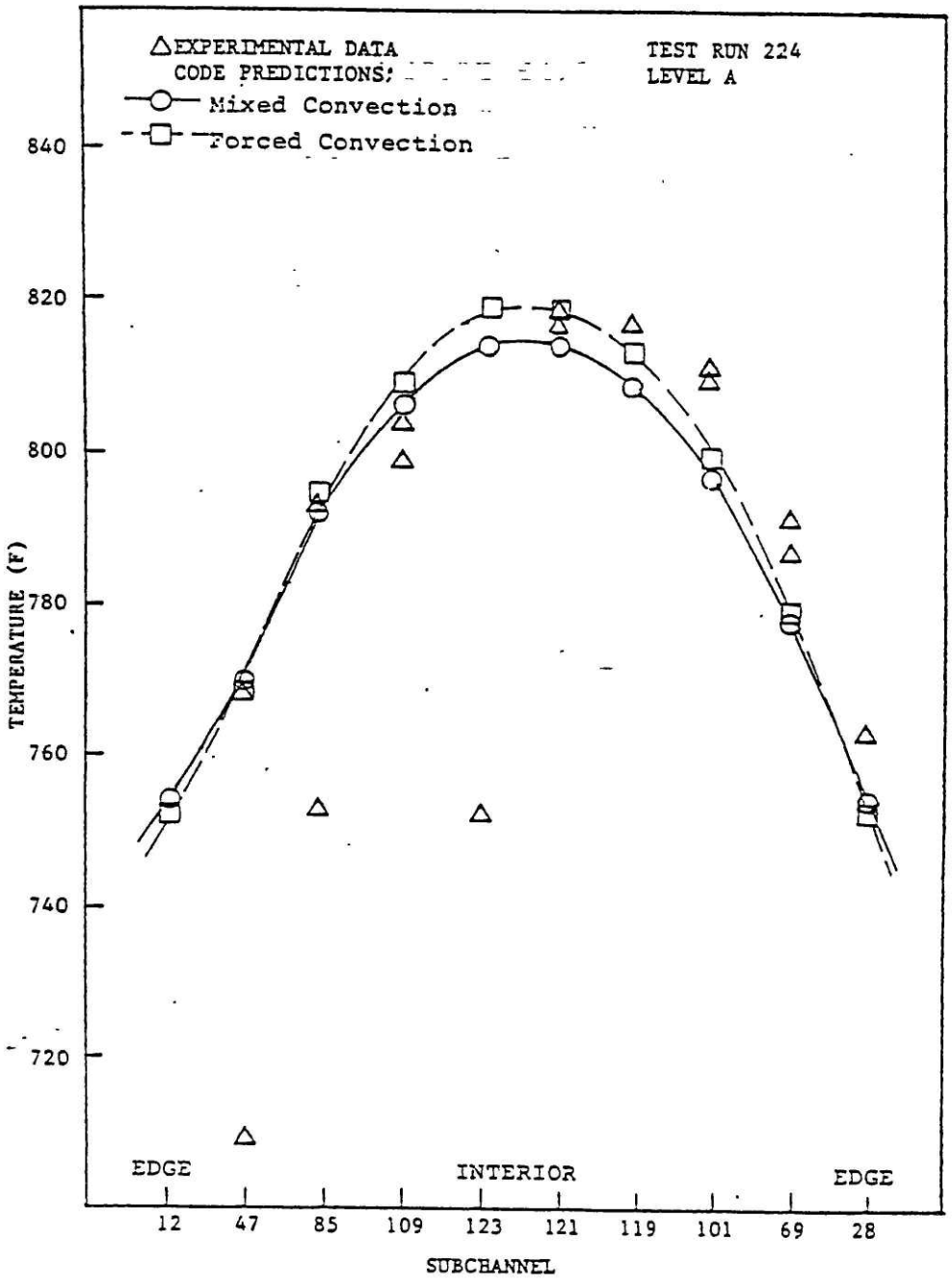
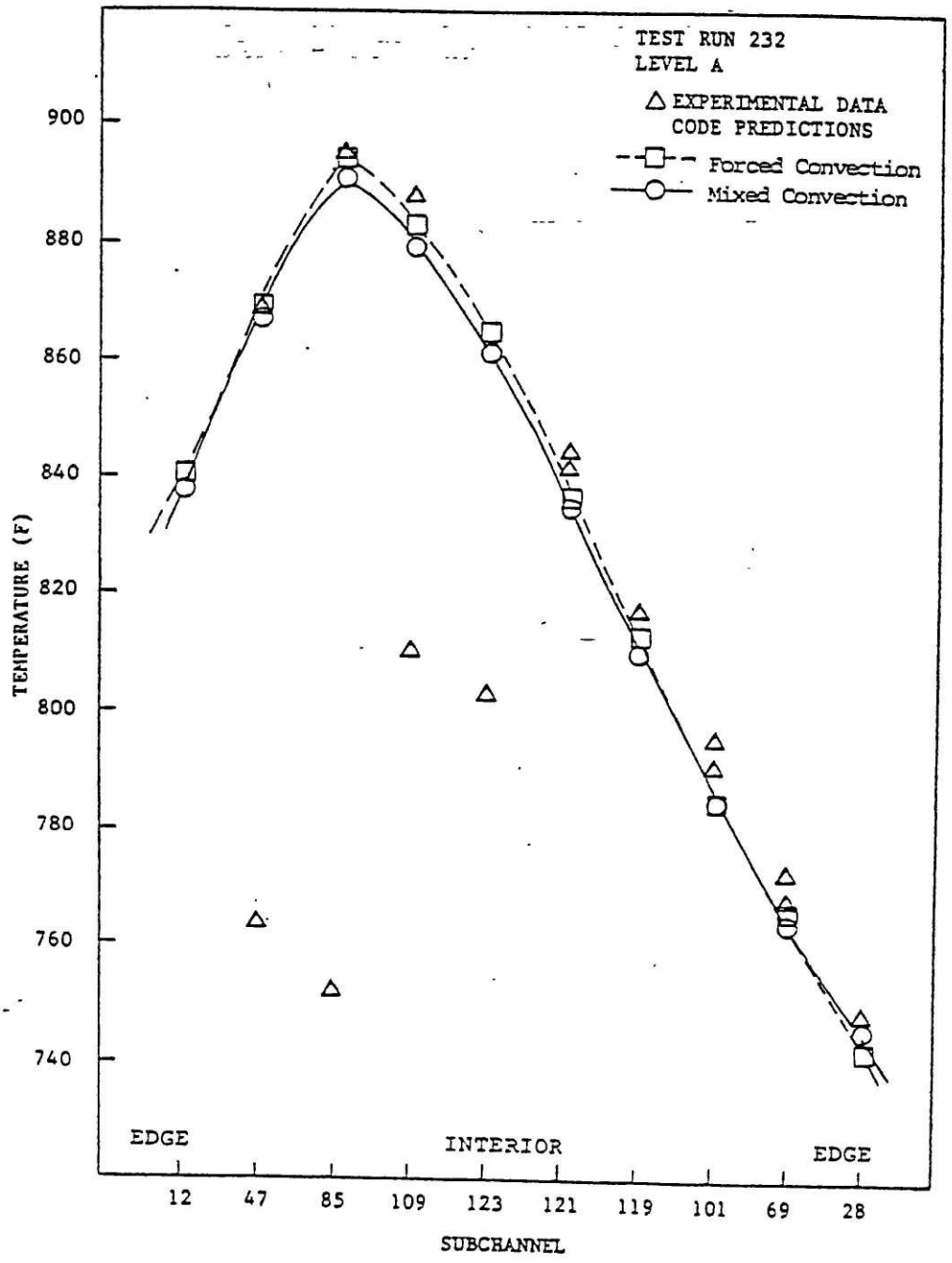
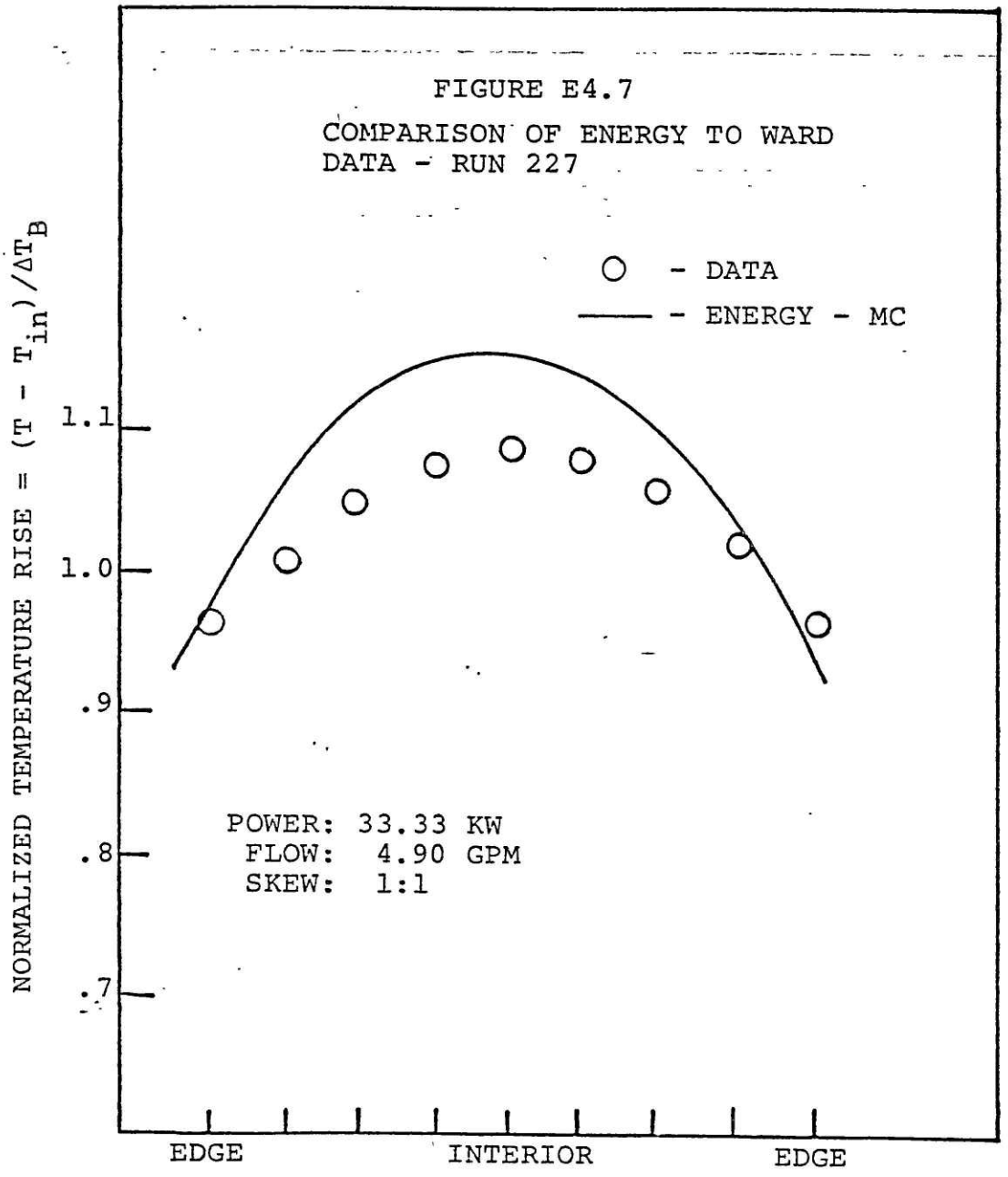
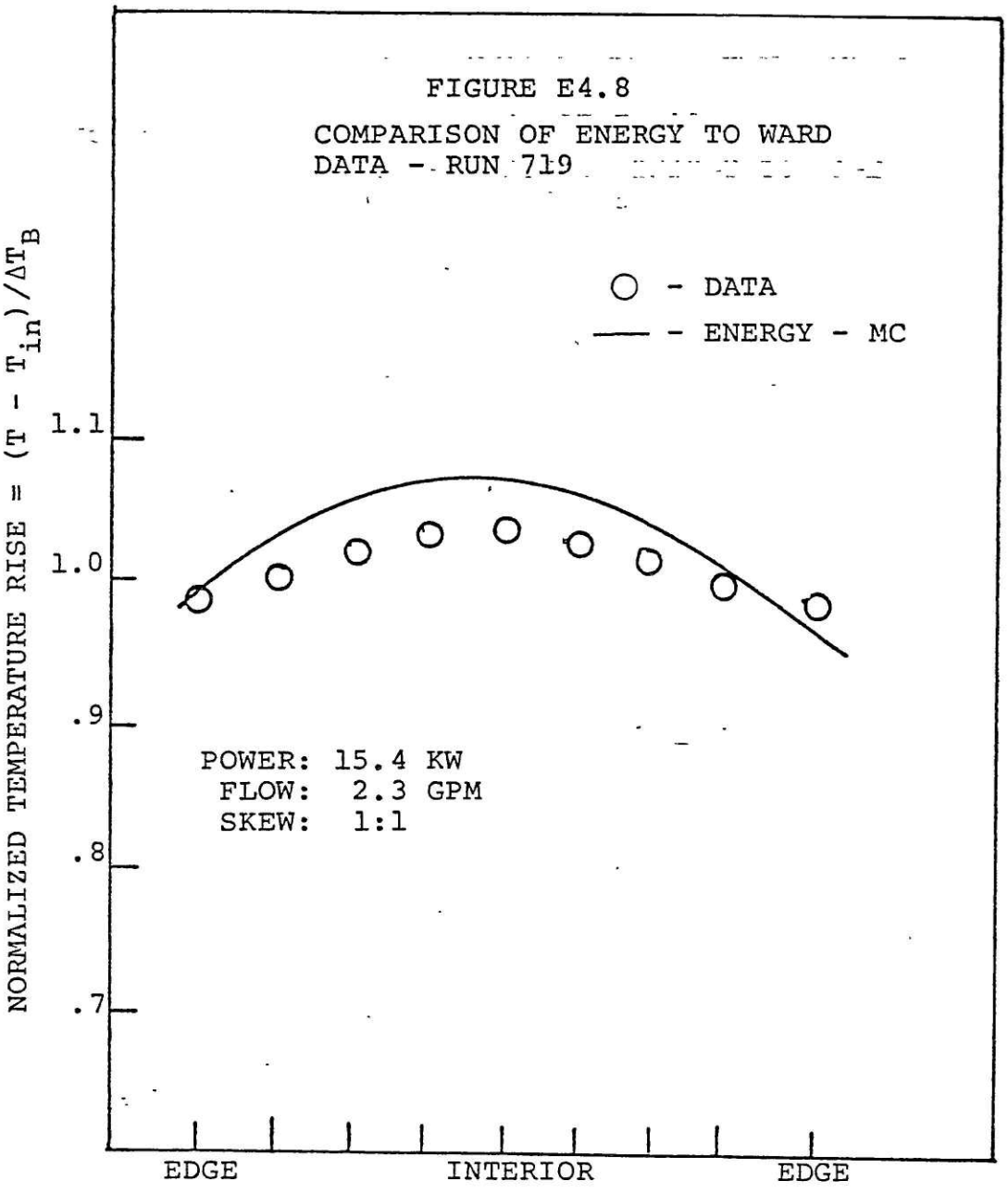


FIGURE E4.6

COMPARISON OF ENERGY PREDICTIONS TO WARD DATA - RUN 232




FIGURE E4.7
COMPARISON OF ENERGY TO WARD DATA - RUN 227
○ - DATA
—— - ENERGY - MC
NORMALIZED TEMPERATURE RISE = $(T - T_{in})/\Delta T_B$
1.1
1.0
.9
.8
.7
POWER: 33.33 KW
FLOW: 4.90 GPM
SKEW: 1:1
EDGE
INTERIOR
EDGE


FIGURE E4.8
COMPARISON OF ENERGY TO WARD
DATA - RUN 719
○ - DATA
—— - ENERGY - MC
NORMALIZED TEMPERATURE RISE = $(T - T_{in})/\Delta T_B$
1.1
1.0
.9
.8
.7
POWER: 15.4 KW
FLOW: 2.3 GPM
SKEW: 1:1
EDGE
INTERIOR
EDGE

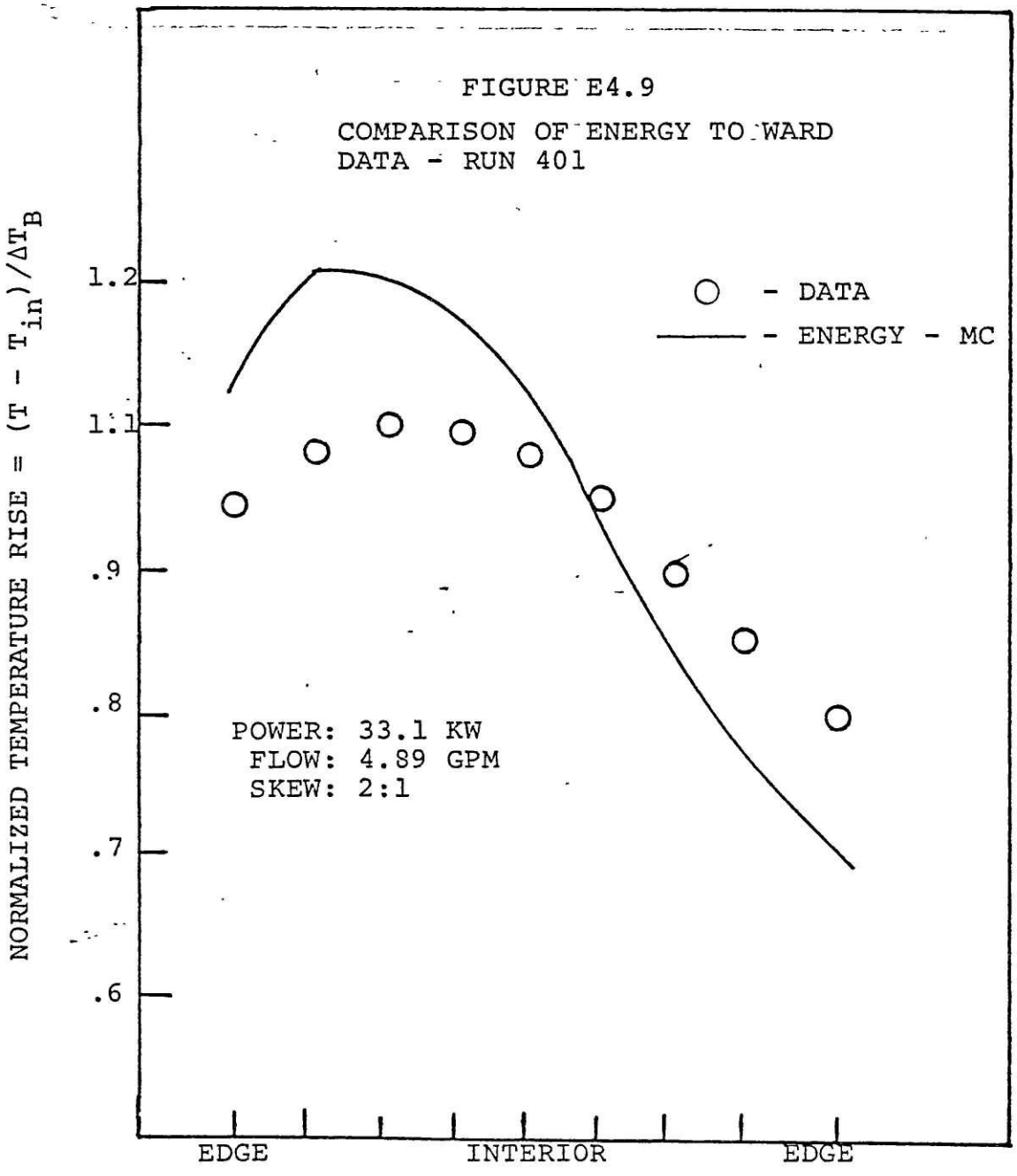
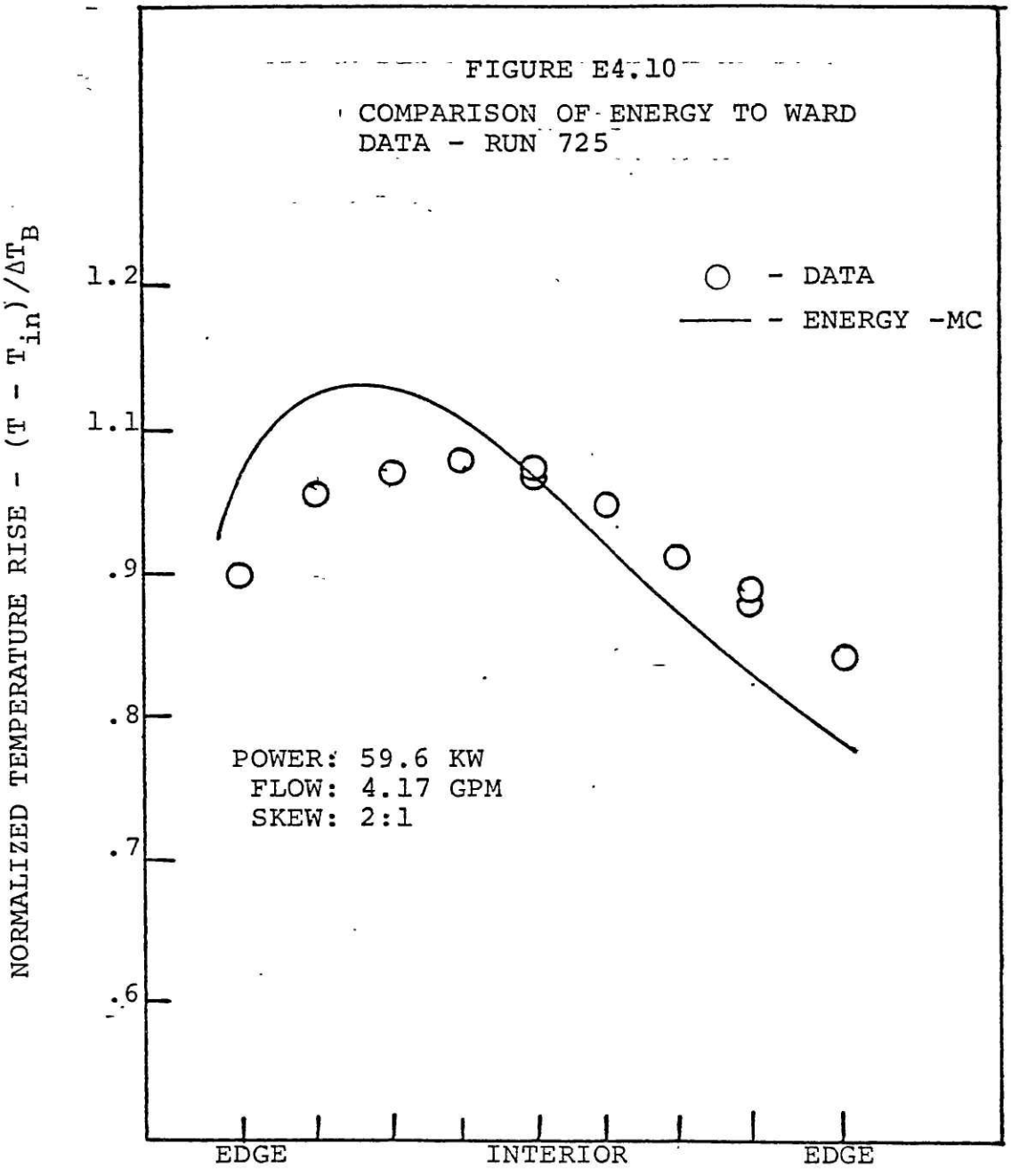

FIGURE E4.9
COMPARISON OF ENERGY TOWARD DATA - RUN 401
NORMALIZED TEMPERATURE RISE = $(T - T_{in})/\Delta T_B$
1.2
1.1
.9
.8
.7
.6
○ - DATA
——— - ENERGY - MC
POWER: 33.1 KW
FLOW: 4.89 GPM
SKEW: 2:1
EDGE
INTERIOR
EDGE

FIGURE E4.10

COMPARISON OF ENERGY TO WARD DATA - RUN 725



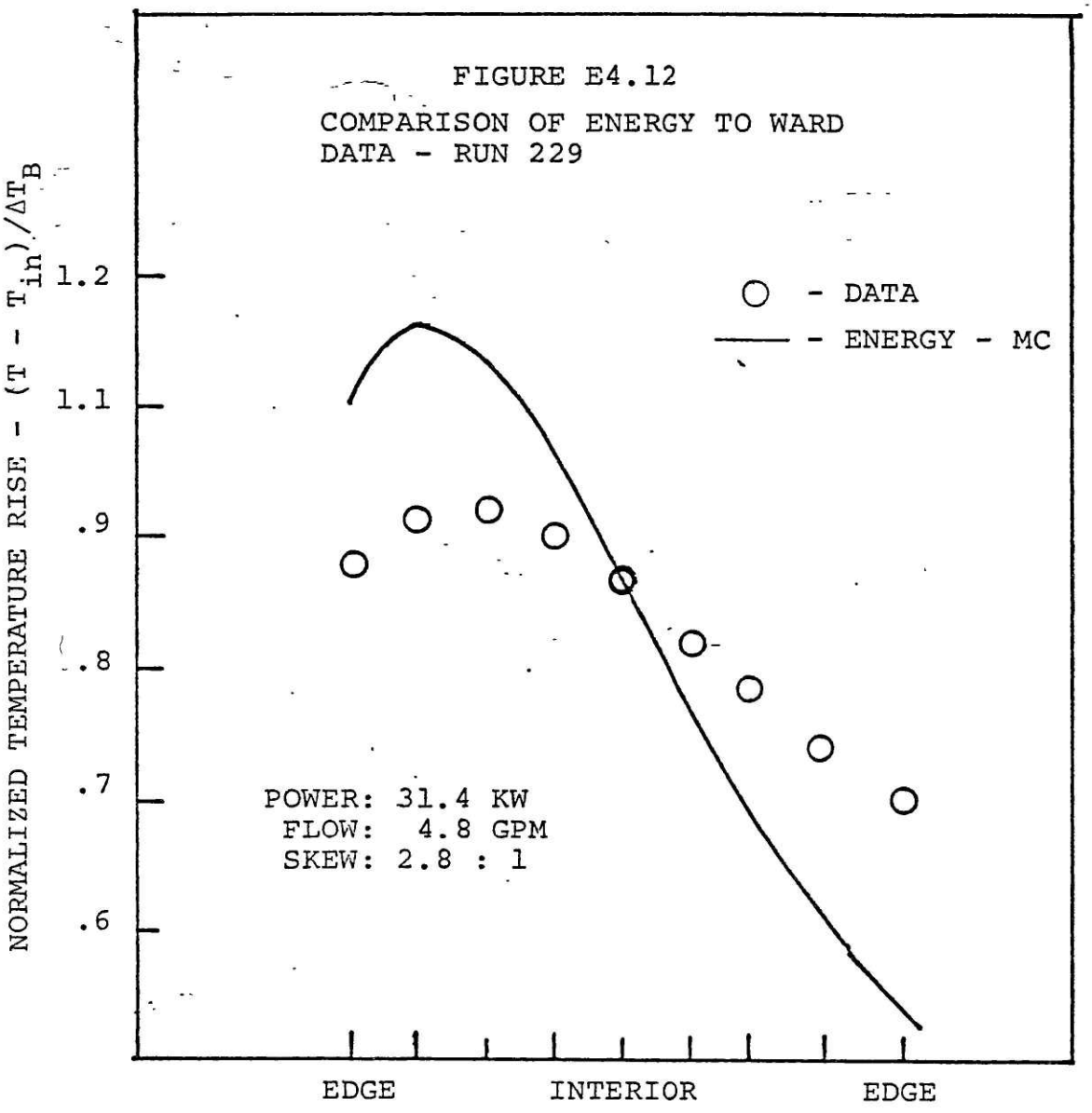


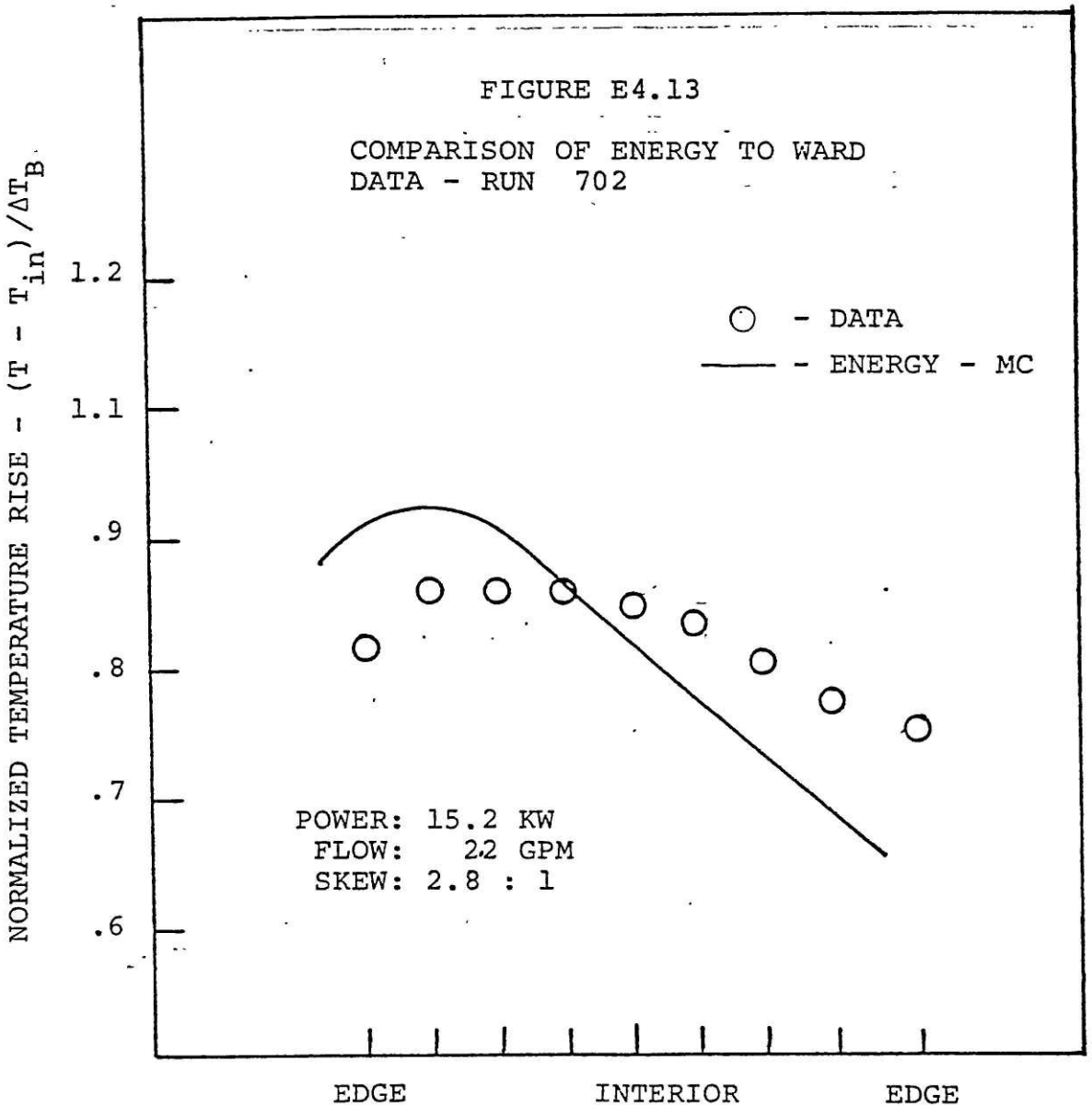
The Libraries
Massachusetts Institute of Technology
Cambridge, Massachusetts 02139

Institute Archives and Special Collections
Room 14N-118
(617) 253-5688

This is the most complete text of the thesis available. The following page(s) were not included in the copy of the thesis deposited in the Institute Archives by the author:

p. 425


FIGURE E4.12
COMPARISON OF ENERGY TO WARD
DATA - RUN 229
NORMALIZED TEMPERATURE RISE - $(T - T_{in})/\Delta T_B$
1.2
1.1
.9
.8
.7
.6
○ - DATA
—— - ENERGY - MC
POWER: 31.4 KW
FLOW: 4.8 GPM
SKEW: 2.8 : 1
EDGE
INTERIOR
EDGE


FIGURE E4.13
COMPARISON OF ENERGY TO WARD
DATA - RUN 702
NORMALIZED TEMPERATURE RISE - $(T - T_{in})/\Delta T_B$
1.2
1.1
.9
.8
.7
.6
○ - DATA
—— - ENERGY - MC
POWER: 15.2 KW
FLOW: 2.2 GPM
SKEW: 2.8 : 1
EDGE
INTERIOR
EDGE

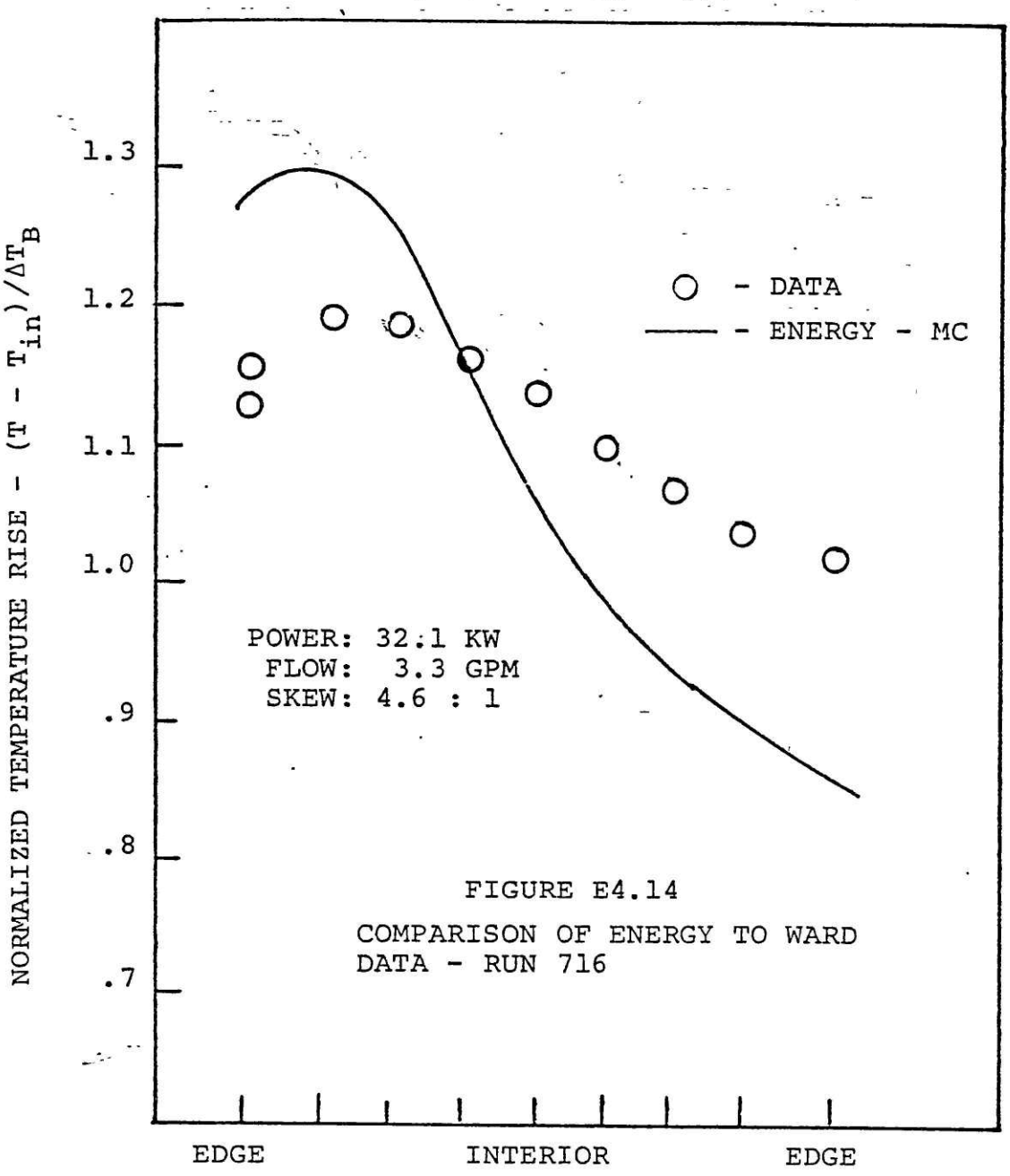
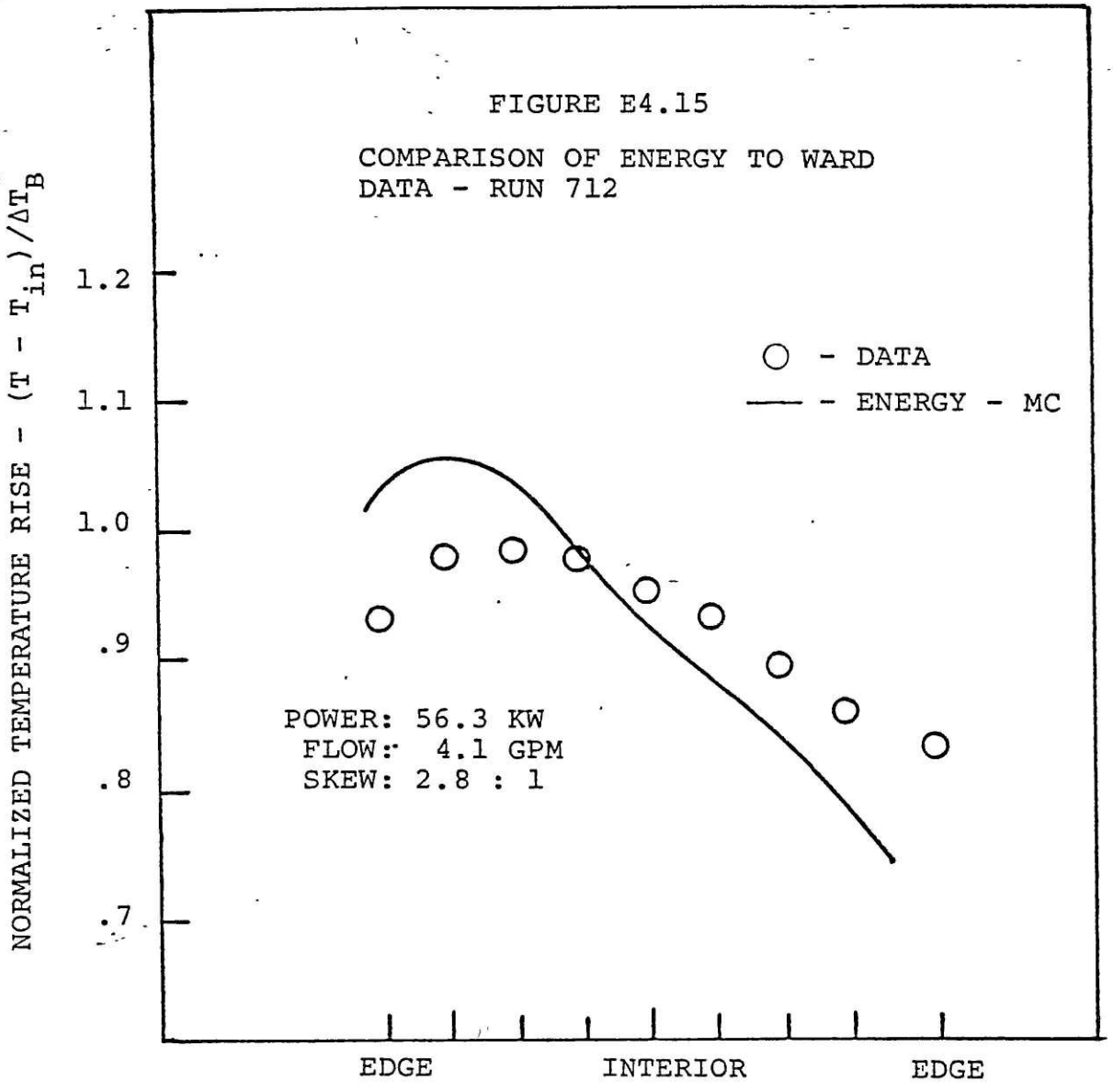


FIGURE E4.14

COMPARISON OF ENERGY TO WARD DATA - RUN 716

FIGURE E4.15

COMPARISON OF ENERGY TO WARD DATA - RUN 712



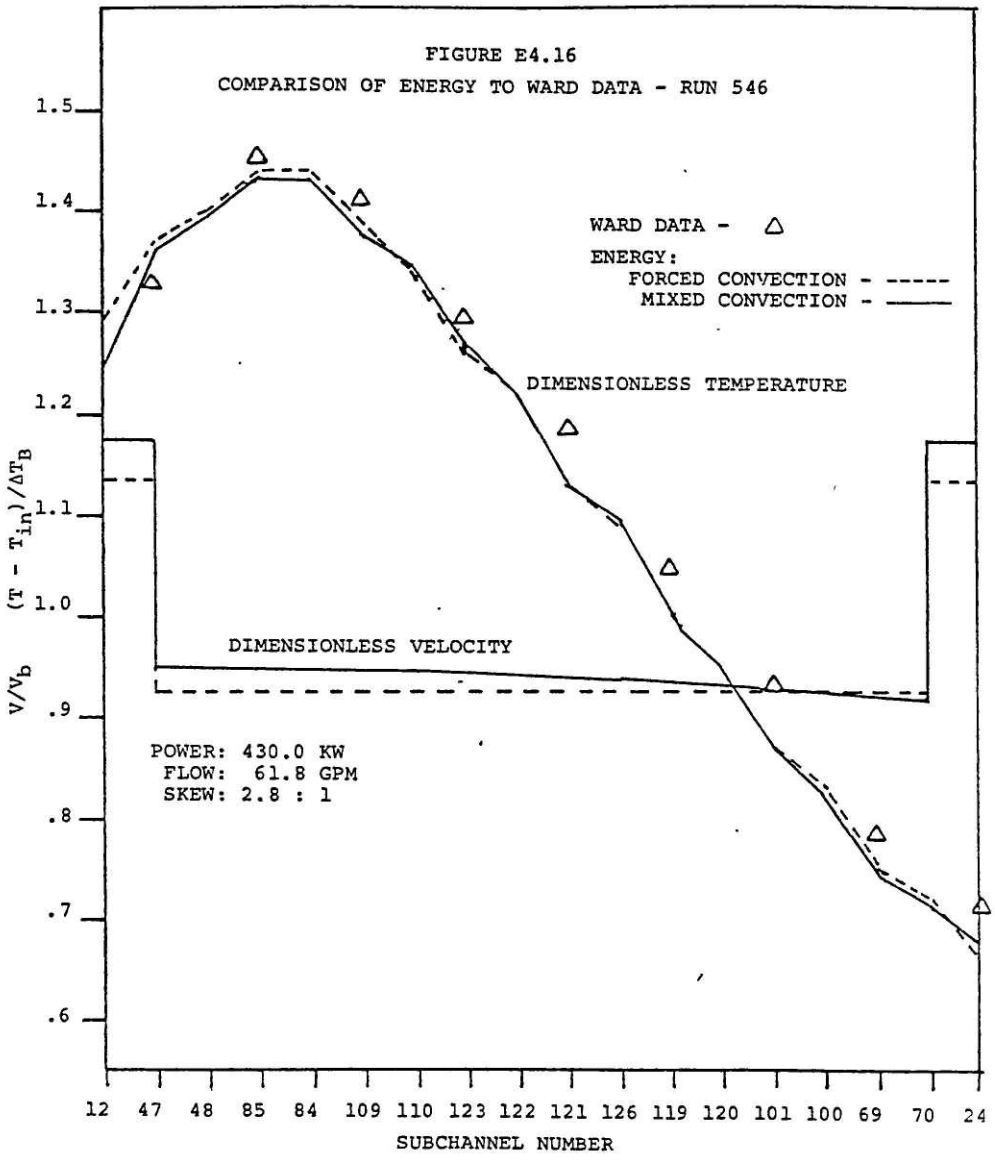

FIGURE E4.16
COMPARISON OF ENERGY TO WARD DATA - RUN 546
WARD DATA - Δ
ENERGY:
FORCED CONVECTION - -----
MIXED CONVECTION - ——
DIMENSIONLESS TEMPERATURE
DIMENSIONLESS VELOCITY
POWER: 430.0 KW
FLOW: 61.8 GPM
SKEW: 2.8 : 1
(T - T_in)/ΔT_B
V/V_b
1.5
1.4
1.3
1.2
1.1
1.0
.9
.8
.7
.6
12 47 48 85 84 109 110 123 122 121 126 119 120 101 100 69 70 24
SUBCHANNEL NUMBER

FIGURE E4.17

COMPARISON OF ENERGY TO WARD DATA - RUN 547

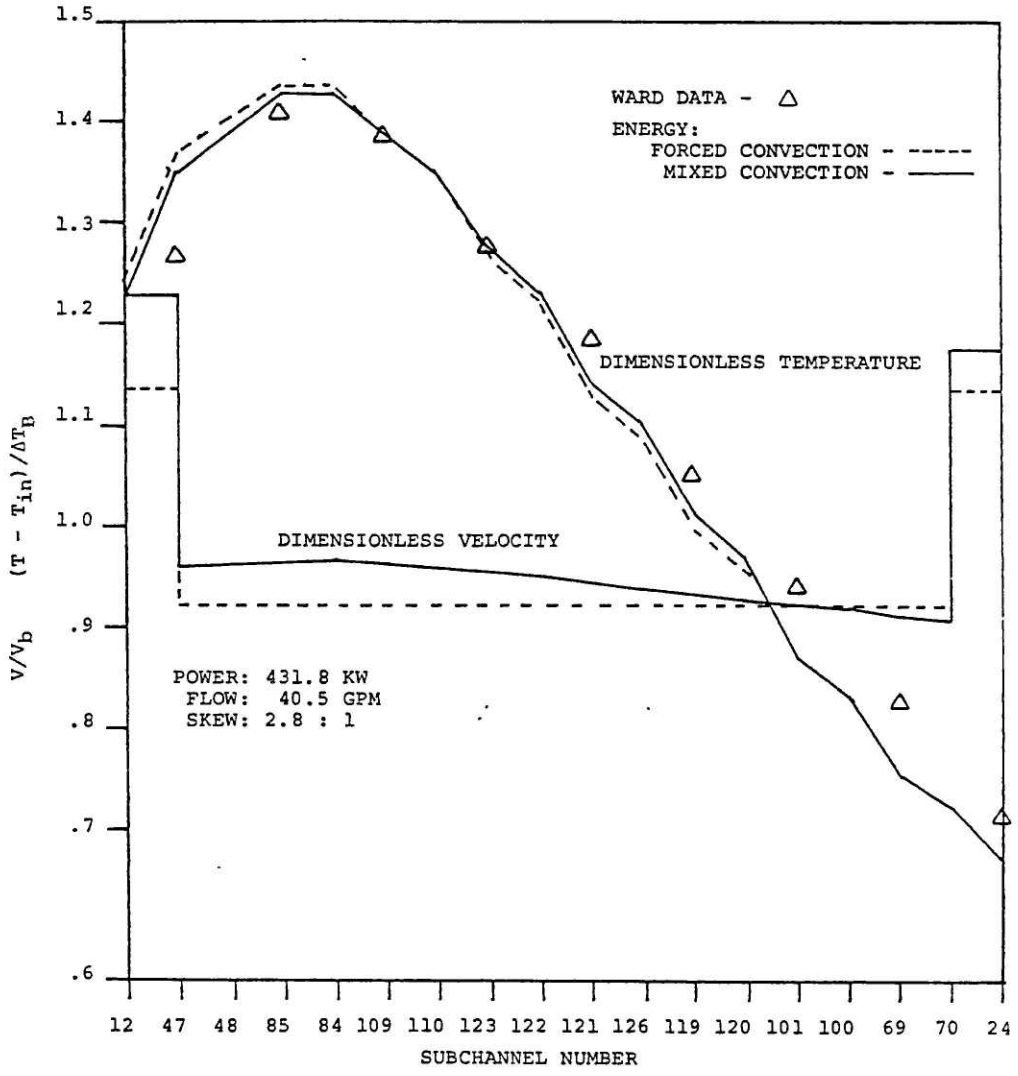
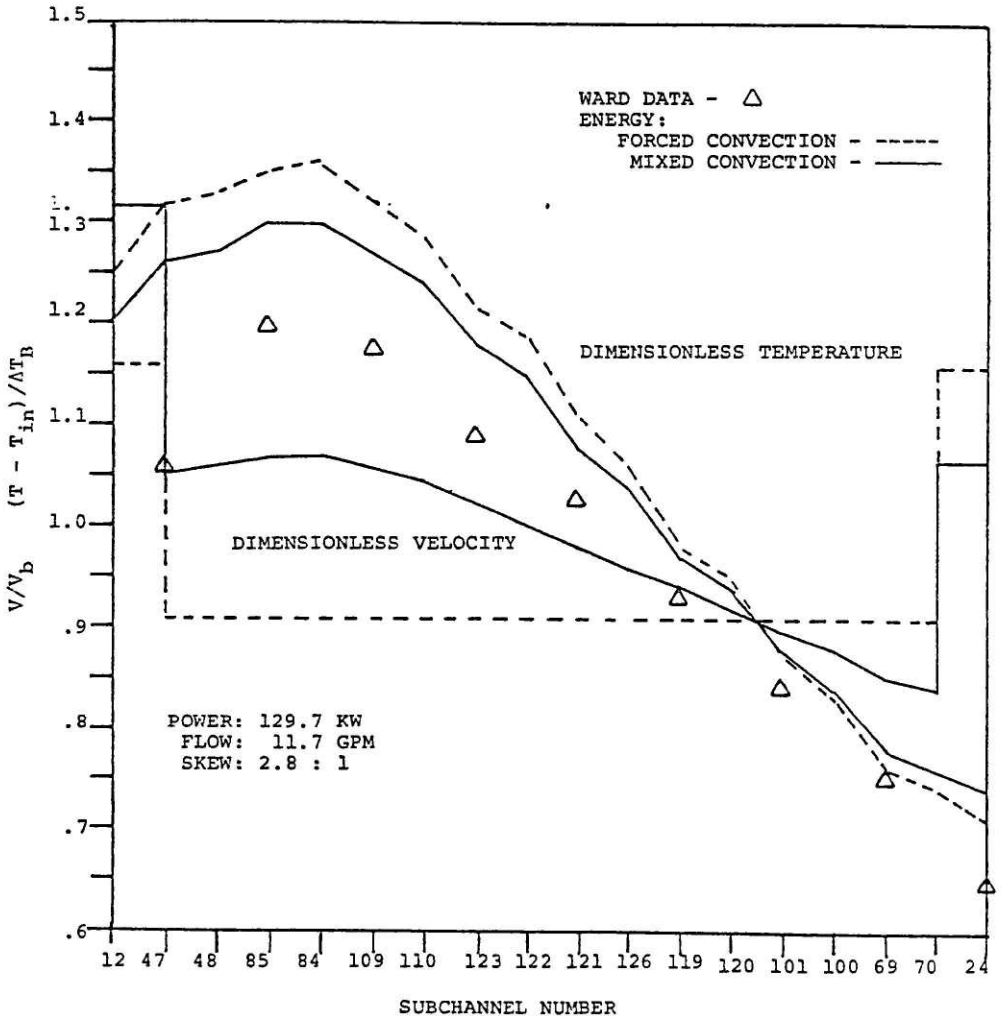


FIGURE E4.18
COMPARISON OF ENERGY TO WARD DATA - RUN 530



APPENDIX F1

DETERMINATION OF TEMPERATURE DEPENDENT FLOW PARAMETERS FOR THE 4x4 ROD BUNDLE

In this appendix, equations will be developed which allow calculation of Re and Gr_q for the 4x4 rod bundle, along with the bulk temperature rise. The Prandtl number will also be plotted as a function of temperature.

The Grashof number is defined as:

$$Gr_q = \frac{g\beta D_e^4 q''}{K\nu^2} \qquad \text{(F1.1)}$$

for the 16 rod bundle, the average heat flux may be written as:

$$q'' = \frac{Q_b}{16\pi D_R L} \qquad \text{(F1.2)}$$

where Q_b is the bundle power. Substituting F1.2 into F1.1 gives:

$$Gr_q = \frac{gD_e^4}{16\pi D_R L_H} Q_b \qquad \text{(F1.3)}$$

where ϕ is defined as:

$$\phi = \frac{\beta}{K\nu^2} \qquad \text{(F1.4)}$$

The parameter ϕ gives the temperature dependence of the

Grashof number. If ϕ_o is the value of ϕ at a reference temperature of 60°F, Equation F1.3 may be written as:

$$Gr_q = \frac{\phi}{\phi_o} \cdot \phi_o \frac{gD_e^4}{16\pi D_R L_H} Q_b \qquad \text{(F1.5)}$$

Substituting in water properties evaluated at 60°F, and the bundle geometry along with appropriate conversion factors Equation F1.5 becomes:

$$Gr_q = 50.24 \left(\frac{\phi}{\phi_o}\right) Q_b$$

where Q_b is the bundle power in watts. The quantity ϕ/ϕ_o is plotted in Figure F1.1 as a function of temperature.

The bundle Reynolds number may be expressed as:

$$Re = \frac{V_e D_e}{\nu} = \frac{D_e \dot{m}}{\nu \rho A} = \frac{\nu_o D_e \dot{m}}{\rho A (\nu/\nu_o)} \qquad \text{(F1.6)}$$

where changes in density are neglected. Converting the mass flow rate to gallons per minute, substituting in the bundle geometry and water viscosity at 60°F gives:

$$Re = 247.9 \frac{G}{(\nu/\nu_o)} \qquad \text{(F1.7)}$$

where G is the bundle flow rate in GPM and ν/ν_o is plotted in Figure F1.1 as a function of temperature. An additional fluid property of interest is the Prandtl number, which is

also given in Figure F1.1.

The bundle bulk temperature rise is given by:

$$\Delta T_B = \frac{Q_b}{\dot{m} C_p} \qquad \text{(F1.8)}$$

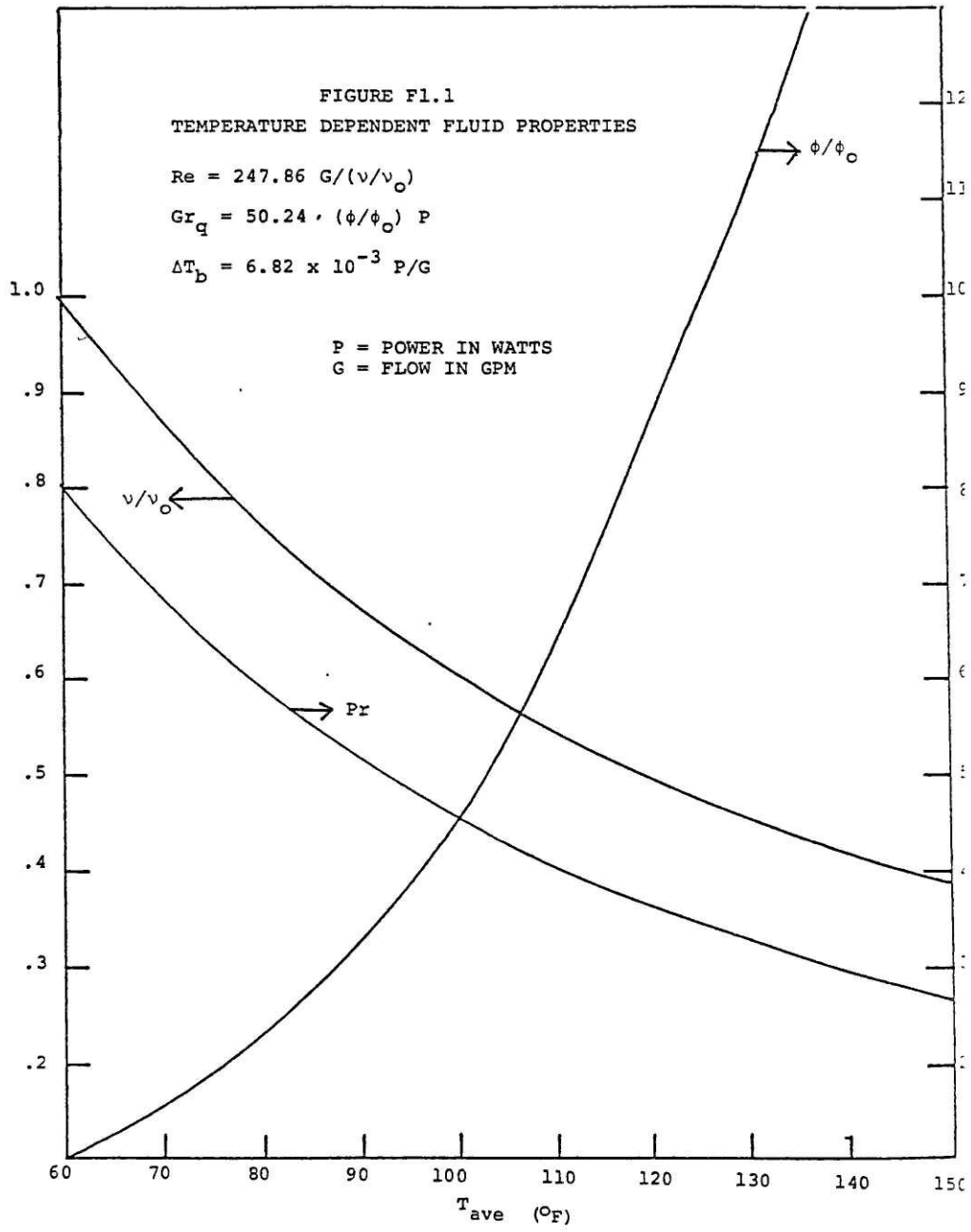
converting $\dot{m}$ to GPM, substituting the heat capacity of water, and employing appropriate conversion factors gives:

$$\Delta T_B = 6.82 \times 10^{-3} \frac{Q_b}{G} \qquad \text{(F1.9)}$$

where ΔT_B is in degrees Farenheit, Q_b is the bundle power in watts, and G is the bundle flow rate in GPM. It follows that the average temperature in the bundle is:

$$T_{ave} = T_{in} + \frac{1}{2} \Delta T_B$$

For calculation of Re, Gr_q and Pr, the above temperature will be used.


FIGURE F1.1
TEMPERATURE DEPENDENT FLUID PROPERTIES
Re = 247.86 G/(ν/ν_o)
Gr_q = 50.24 · (φ/φ_o) P
ΔT_b = 6.82 x 10^-3 P/G
P = POWER IN WATTS
G = FLOW IN GPM
φ/φ_o
ν/ν_o
Pr
1.0
.9
.8
.7
.6
.5
.4
.3
.2
60
70
80
90
100
110
120
130
140
T_ave (°F)

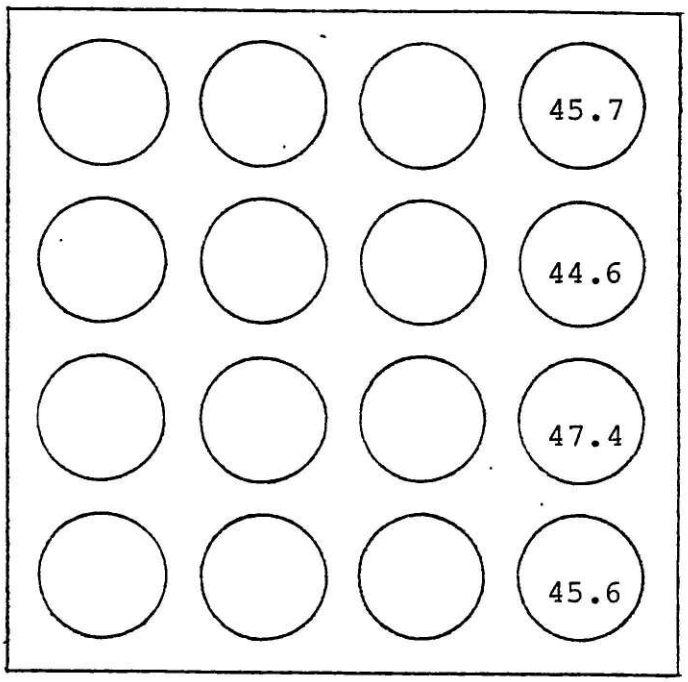
APPENDIX F2

ONSET OF RECIRCULATION DATA

The onset of recirculation data was outlined in Table 7.2.3. In this Appendix the raw onset of recirculation data is given. For each run the bundle power distribution is given, along with the flow parameters at the onset of recirculation.

RUN 1.1

BUNDLE POWER DISTRIBUTION (W/ROD):



BUNDLE OPERATING CONDITIONS:

Flow rate at onset=	.314 Gpm	Total rod power	= 183.3 W
Measured ΔT_{bulk}	=	Calculated ΔT_{bulk}	= 4.0°F
Inlet Temperature	= 95°F	Average Temp.	= 97°F

TEMPERATURE DEPENDENT FLUID PROPERTIES:

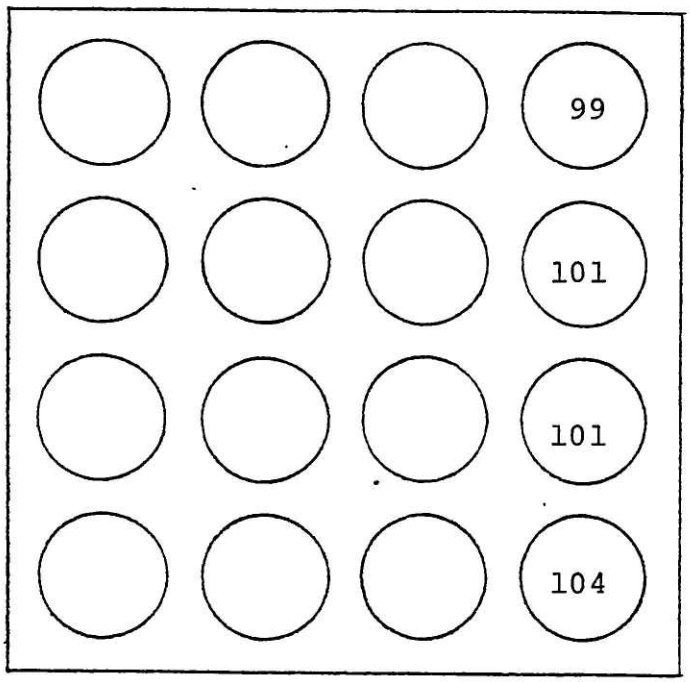
Pr= 4.65 ϕ/ϕ_o= 4.0 ν/ν_o= .625

FLOW PARAMETERS AT ONSET OF RECIRCULATION:

Re= 125 Gr_q= 4.02E4

RUN 1.2

BUNDLE POWER DISTRIBUTION (W/ROD):



BUNDLE OPERATING CONDITIONS:

Flow rate at onset= .451 Gpm Total rod power = 405 W
Measured ΔT_{bulk} = Calculated ΔT_{bulk}= 6.1°F
Inlet Temperature = 97°F Average Temp. = 100°F

TEMPERATURE DEPENDENT FLUID PROPERTIES:

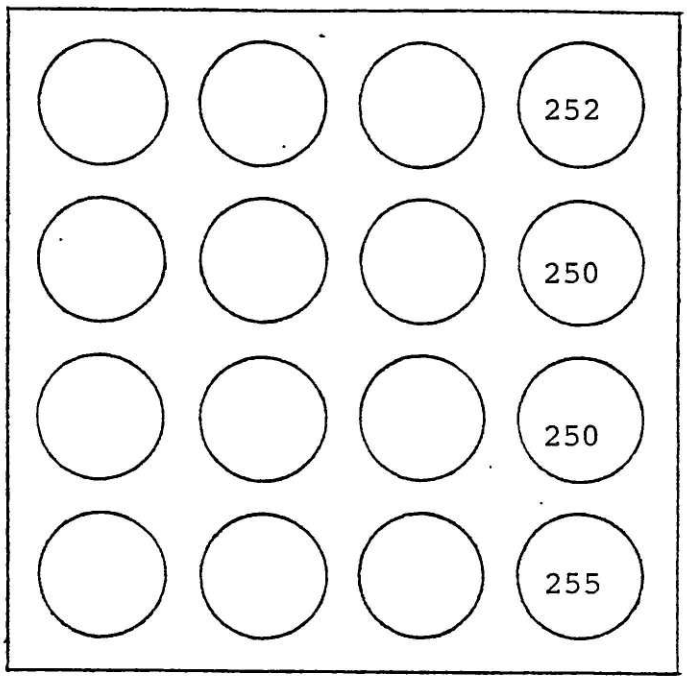
Pr= 4.50 ϕ/ϕ_o= 4.5 ν/ν_o= .605

FLOW PARAMETERS AT ONSET OF RECIRCULATION:

Re= 185 Gr_q= 9.16E4

RUN 1.3

BUNDLE POWER DISTRIBUTION (W/ROD):



BUNDLE OPERATING CONDITIONS:

Flow rate at onset=.725 Gpm Total rod power = 1007 W
Measured ΔT_{bulk} = Calculated ΔT_{bulk}= 9.5°F
Inlet Temperature = 104°F Average Temp. = 109°F

TEMPERATURE DEPENDENT FLUID PROPERTIES:

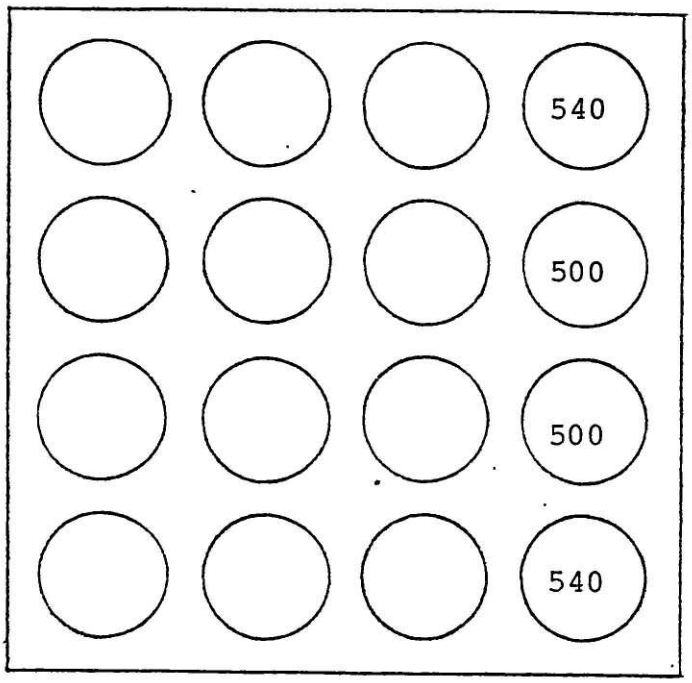
Pr= 4.05 ϕ/ϕ_o= 6.13 ν/ν_o= .55

FLOW PARAMETERS AT ONSET OF RECIRCULATION:

Re= 327. Gr_q= 3.10E5

RUN 1.4

BUNDLE POWER DISTRIBUTION (W/ROD):



BUNDLE OPERATING CONDITIONS:

Flow rate at onset= .980 Gpm Total rod power = 2080 W

Measured ΔT_{bulk} = Calculated ΔT_{bulk} = 14.5°F

Inlet Temperature = 105°F Average Temp. = 112°F

TEMPERATURE DEPENDENT FLUID PROPERTIES:

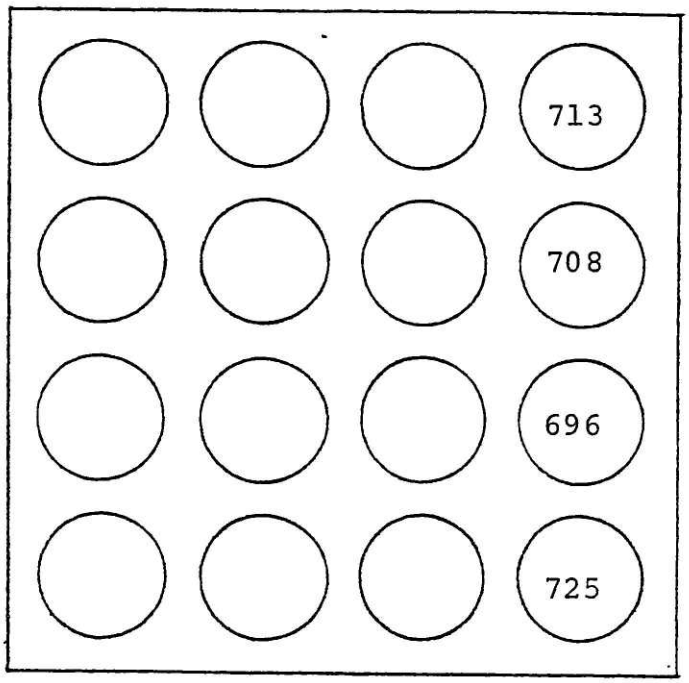
Pr= 3.90 ϕ/ϕ_o= 6.75 ν/ν_o= .535

FLOW PARAMETERS AT ONSET OF RECIRCULATION:

Re= 454 Gr_q= 7.06E5

RUN 1.5

BUNDLE POWER DISTRIBUTION (W/ROD):



BUNDLE OPERATING CONDITIONS:

Flow rate at onset=1.176 Gpm Total rod power = 2841 W
Measured ΔT_{bulk} = Calculated ΔT_{bulk}= 16.5
Inlet Temperature = 104°F Average Temp. = 112°F

TEMPERATURE DEPENDENT FLUID PROPERTIES:

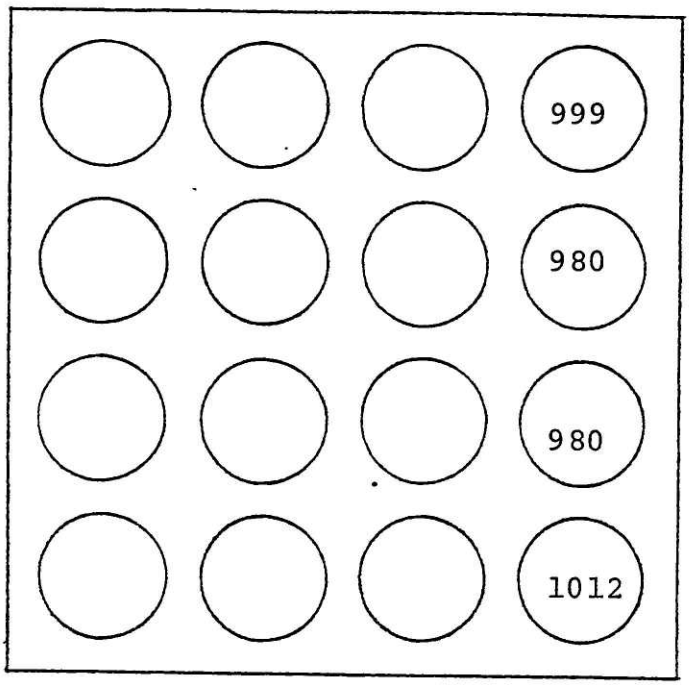
Pr= 3.9 ϕ/ϕ_o= 6.75 ν/ν_o= .535

FLOW PARAMETERS AT ONSET OF RECIRCULATION:

Re= 545 Gr_q= 9.64E5

RUN 1.6

BUNDLE POWER DISTRIBUTION (W/ROD):



BUNDLE OPERATING CONDITIONS:

Flow rate at onset= 1.352 Gpm Total rod power = 3971 W
Measured ΔT_{bulk} = Calculated ΔT_{bulk} = 20.0°F
Inlet Temperature = 103°F Average Temp. = 113°F

TEMPERATURE DEPENDENT FLUID PROPERTIES:

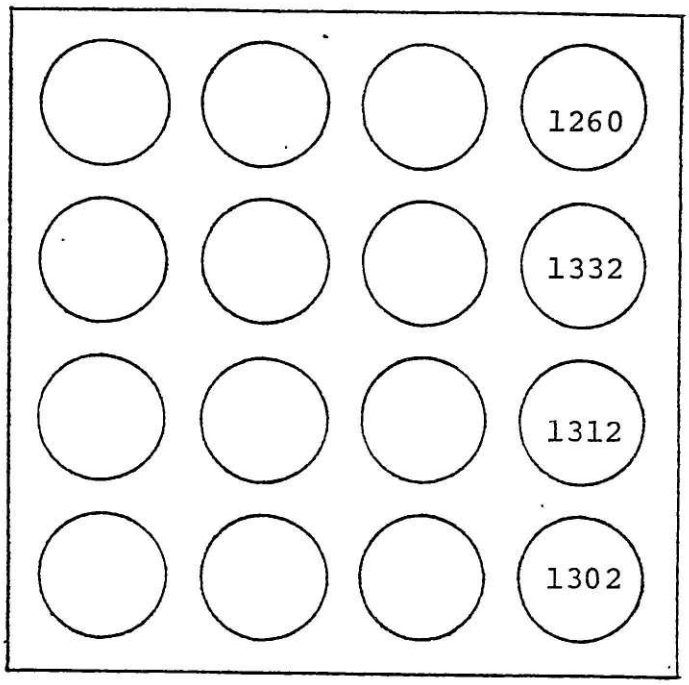
Pr= 3.85 ϕ/ϕ_o= 7.00 ν/ν_o= .53

FLOW PARAMETERS AT ONSET OF RECIRCULATION:

Re= 623 Gr_q= 1.40E6

RUN 1.7

BUNDLE POWER DISTRIBUTION (W/ROD):



BUNDLE OPERATING CONDITIONS:

Flow rate at onset= 1.47 Gpm Total rod power = 5106 W

Measured ΔT_{bulk} = Calculated ΔT_{bulk}= $23.7^{o}F$

Inlet Temperature = $102.5^{o}F$ Average Temp. = $114^{o}F$

TEMPERATURE DEPENDENT FLUID PROPERTIES:

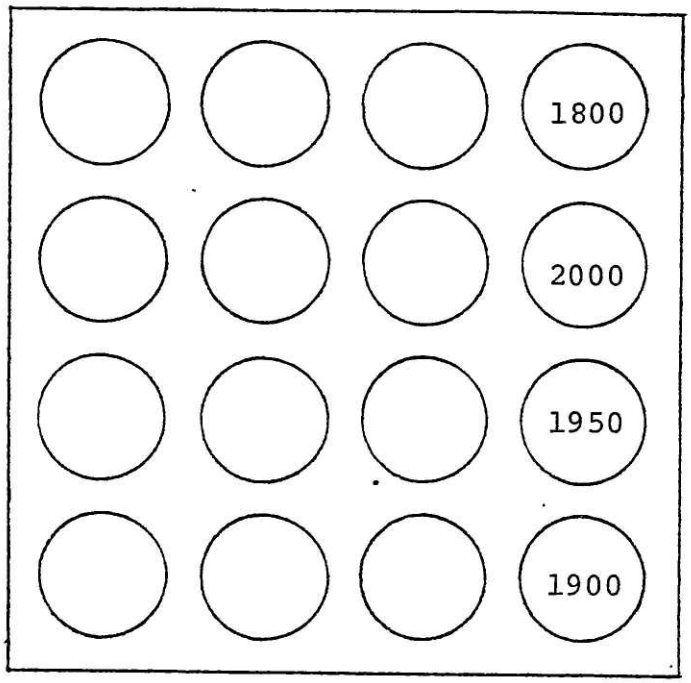
Pr= 3.80 ϕ/ϕ_o= 7.25 ν/ν_o= .525

FLOW PARAMETERS AT ONSET OF RECIRCULATION:

Re= 694 Gr_q= 1.86E6

RUN 1.9

BUNDLE POWER DISTRIBUTION (W/ROD):



BUNDLE OPERATING CONDITIONS:

Flow rate at onset= 1.725 Gpm Total rod power = 7650 W

Measured ΔT_{bulk} = Calculated ΔT_{bulk} = 30.0°F

Inlet Temperature = 100°F Average Temp. = 115°F

TEMPERATURE DEPENDENT FLUID PROPERTIES:

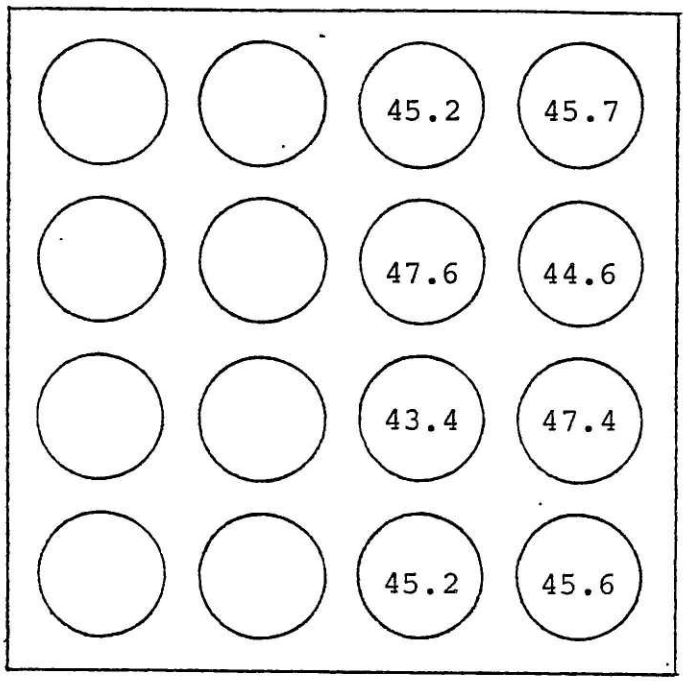
Pr= 3.80 ϕ/ϕ_o= 7.50 ν/ν_o= .520

FLOW PARAMETERS AT ONSET OF RECIRCULATION:

Re= 822 Gr_q= 2.88E6

RUN 2.1

BUNDLE POWER DISTRIBUTION (W/ROD):



BUNDLE OPERATING CONDITIONS:

Flow rate at onset=	.51 Gpm	Total rod power =	364.8 W
Measured ΔT_{bulk} =		Calculated ΔT_{bulk} =	$4.9^{o}F$
Inlet Temperature =	$95^{o}F$	Average Temp. =	$97.4^{o}F$

TEMPERATURE DEPENDENT FLUID PROPERTIES:

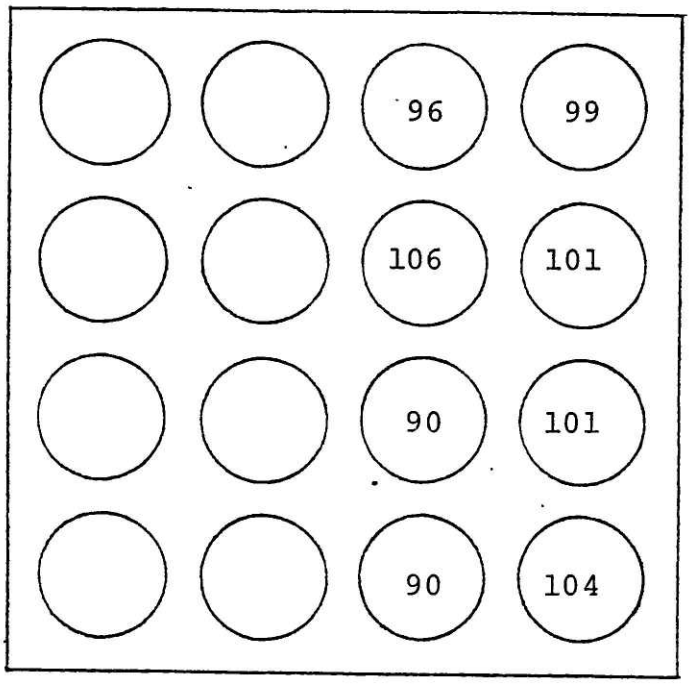
Pr= 4.65 ϕ/ϕ_o= 4.15 ν/ν_o= .62

FLOW PARAMETERS AT ONSET OF RECIRCULATION:

Re= 204 Gr_q= 8.34E4

RUN 2.2

BUNDLE POWER DISTRIBUTION (W/ROD):



BUNDLE OPERATING CONDITIONS:

Flow rate at onset=.647 Gpm Total rod power = 789 W
Measured ΔT_{bulk} = Calculated ΔT_{bulk}= 8.3°F
Inlet Temperature = 97°F Average Temp. = 101°F

TEMPERATURE DEPENDENT FLUID PROPERTIES:

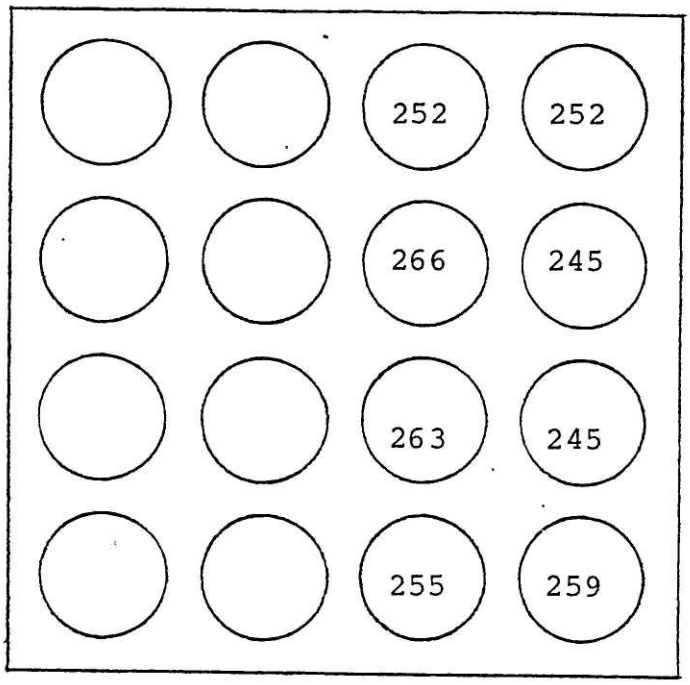
Pr= 4.45 ϕ/ϕ_o= 4.65 ν/ν_o= .60

FLOW PARAMETERS AT ONSET OF RECIRCULATION:

Re= 267 Gr_q= 1.84E5

RUN 2.3

BUNDLE POWER DISTRIBUTION (W/ROD):



BUNDLE OPERATING CONDITIONS:

Flow rate at onset=1.176 Gpm Total rod power = 2037 W

Measured ΔT_{bulk} = 12°F Calculated ΔT_{bulk} = 11.8°F

Inlet Temperature = 93°F Average Temp. = 91°F

TEMPERATURE DEPENDENT FLUID PROPERTIES:

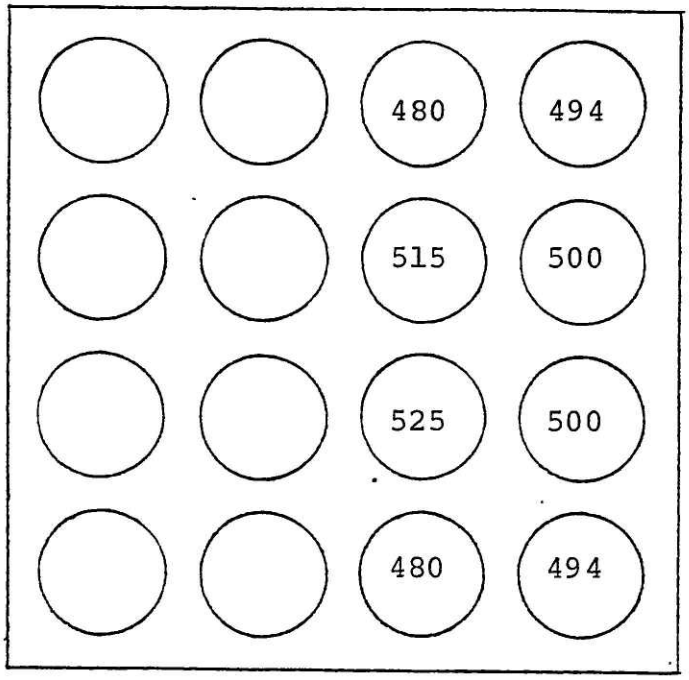
Pr= 4.55 ϕ/ϕ_o= 4.40 ν/ν_o= .61

FLOW PARAMETERS AT ONSET OF RECIRCULATION:

Re= 478 Gr_q= 4.48E5

RUN 2.4

BUNDLE POWER DISTRIBUTION (W/ROD):



BUNDLE OPERATING CONDITIONS:

Flow rate at onset=	1.646 Gpm	Total rod power	= 3543 W
Measured ΔT_{bulk}	= 14°F	Calculated ΔT_{bulk}	= 14.7°F
Inlet Temperature	= 95°F	Average Temp.	= 102°F

TEMPERATURE DEPENDENT FLUID PROPERTIES:

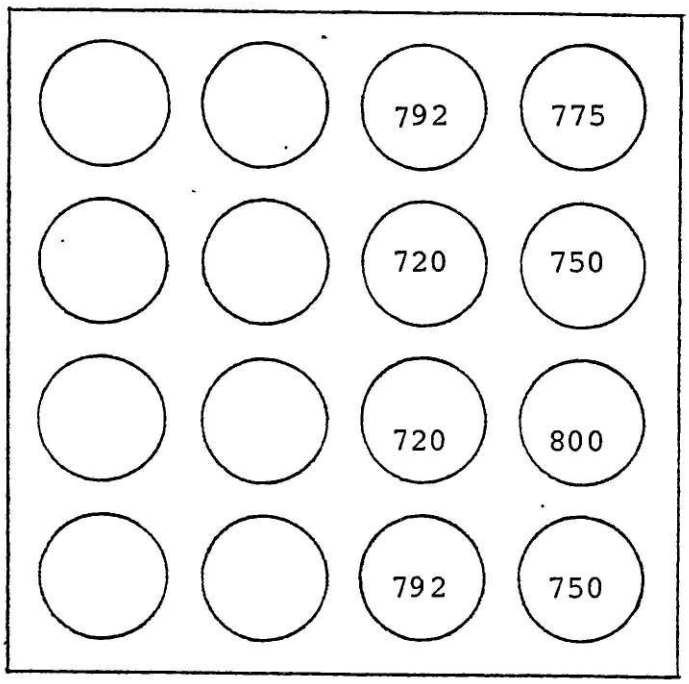
Pr= 4.40 ϕ/ϕ_o= 4.75 ν/ν_o= .595

FLOW PARAMETERS AT ONSET OF RECIRCULATION:

Re= 686 Gr_q= 8.46E5

RUN 2.5

BUNDLE POWER DISTRIBUTION (W/ROD):



BUNDLE OPERATING CONDITIONS:

Flow rate at onset= 1.776 Gpm Total rod power = 6099 W

Measured ΔT_{bulk} = Calculated ΔT_{bulk} = $23.4^{o}F$

Inlet Temperature = $98^{o}F$ Average Temp. = $110^{o}F$

TEMPERATURE DEPENDENT FLUID PROPERTIES:

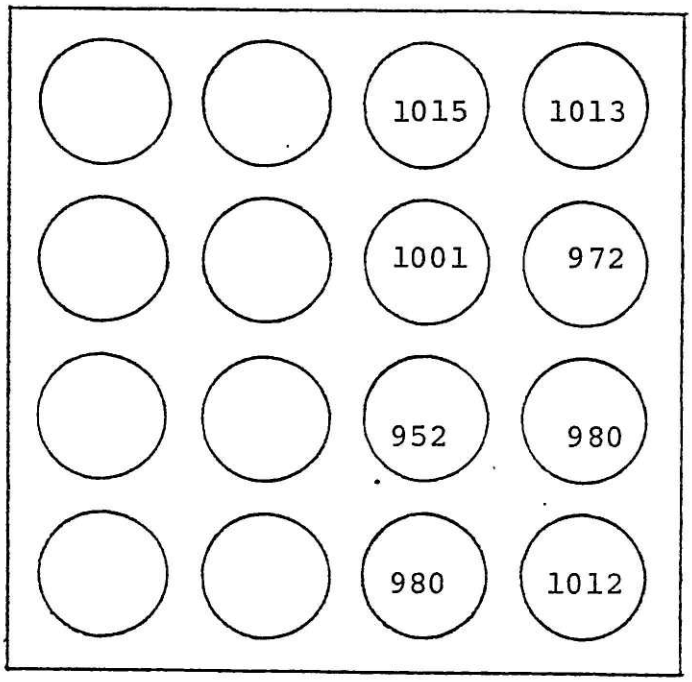
Pr= 4.00 ϕ/ϕ_o= 6.25 ν/ν_o= .545

FLOW PARAMETERS AT ONSET OF RECIRCULATION:

Re= 808 Gr_q= 1.92E6

RUN 2.6

BUNDLE POWER DISTRIBUTION (W/ROD):



BUNDLE OPERATING CONDITIONS:

Flow rate at onset=2.208 Gpm Total rod power = 7928 W
Measured ΔT_{bulk} = Calculated ΔT_{bulk}= 24.5°F
Inlet Temperature = 101°F Average Temp. = 113°F

TEMPERATURE DEPENDENT FLUID PROPERTIES:

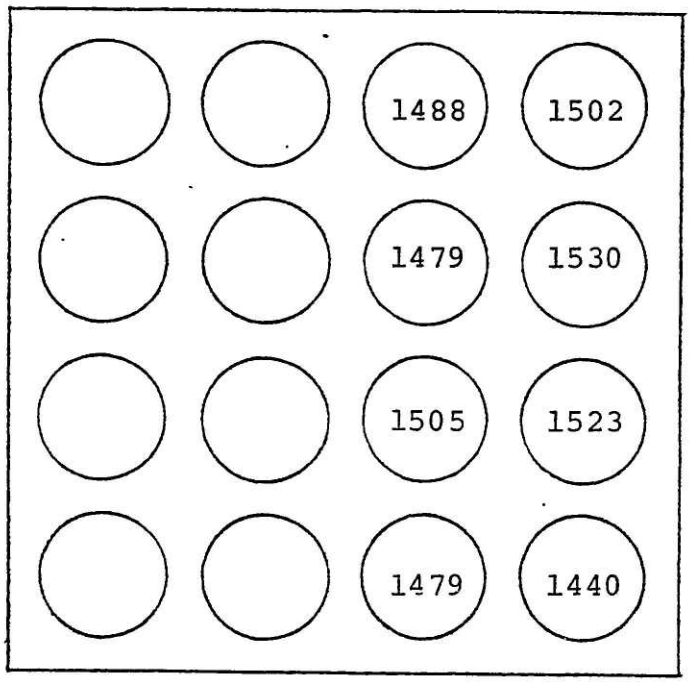
Pr= 3.85 ϕ/ϕ_o= 700 ν/ν_o= .53

FLOW PARAMETERS AT ONSET OF RECIRCULATION:

Re= 1033 Gr_q= 2.79E6

RUN 2.7

BUNDLE POWER DISTRIBUTION (W/ROD):



BUNDLE OPERATING CONDITIONS:

Flow rate at onset=2.52 Gpm Total rod power = 11945 W
Measured ΔT_{bulk} = Calculated ΔT_{bulk} = 32.3°F
Inlet Temperature = 100°F Average Temp. = 116°F

TEMPERATURE DEPENDENT FLUID PROPERTIES:

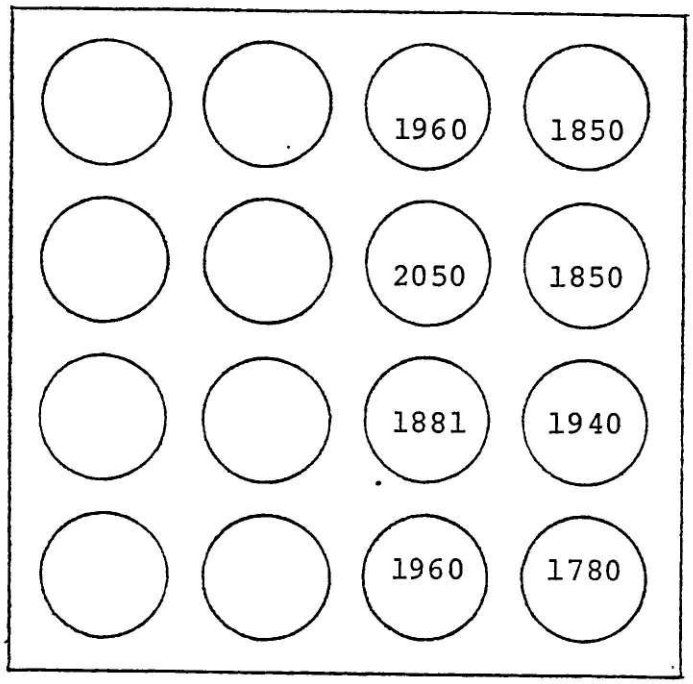
Pr= 3.75 ϕ/ϕ_o= 7.60 ν/ν_o= .52

FLOW PARAMETERS AT ONSET OF RECIRCULATION:

Re= 1201 Gr_q= 4.58E6

RUN 2.8

BUNDLE POWER DISTRIBUTION (W/ROD):



BUNDLE OPERATING CONDITIONS:

Flow rate at onset=2.736 Gpm Total rod power = 15271 W
Measured ΔT_{bulk} = 38°F Calculated ΔT_{bulk} = 38.1°F
Inlet Temperature = 100°F Average Temp. = 119°F

TEMPERATURE DEPENDENT FLUID PROPERTIES:

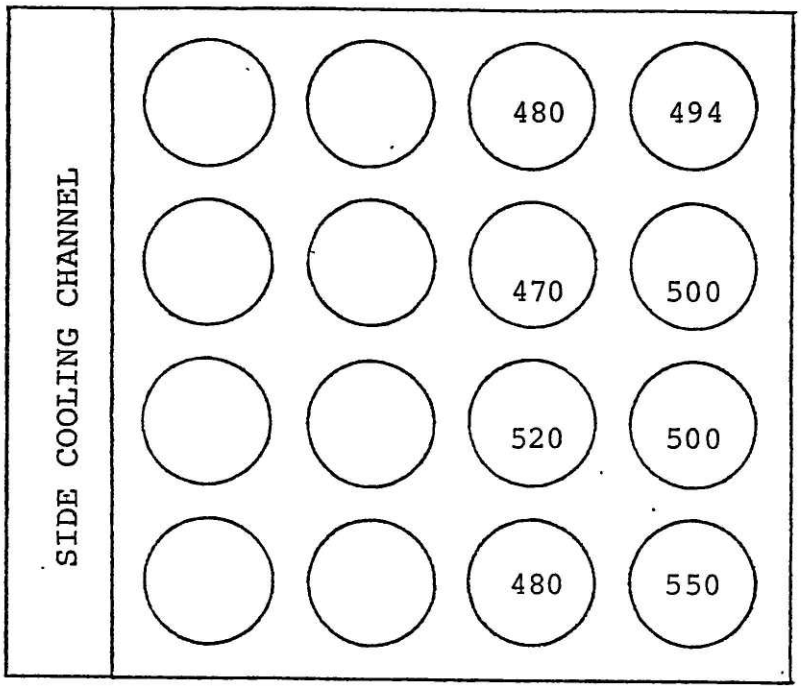
Pr= 3.65 ϕ/ϕ_o= 8.45 ν/ν_o= .50

FLOW PARAMETERS AT ONSET OF RECIRCULATION:

Re= 1356 Gr_q= 6.47E6

RUN 2.2 C

BUNDLE POWER DISTRIBUTION (W/ROD):



BUNDLE OPERATING CONDITIONS:

Flow rate at onset=	2.93 GPM	Total rod power	= 3994 W
Measured ΔT_{bulk}	= 8.0°F	Calculated ΔT_{bulk}	= 9.3°F
Inlet Temperature	= 134°F	Average Temp.	= 138°F

SIDE CHANNEL COOLANT FLOW:

Inlet Temperature	= 41°F	Outlet Temperature	= 82°F
Flow rate	= .116 GPM	Power from bundle	= 559 W

TEMPERATURE DEPENDENT FLUID PROPERTIES:

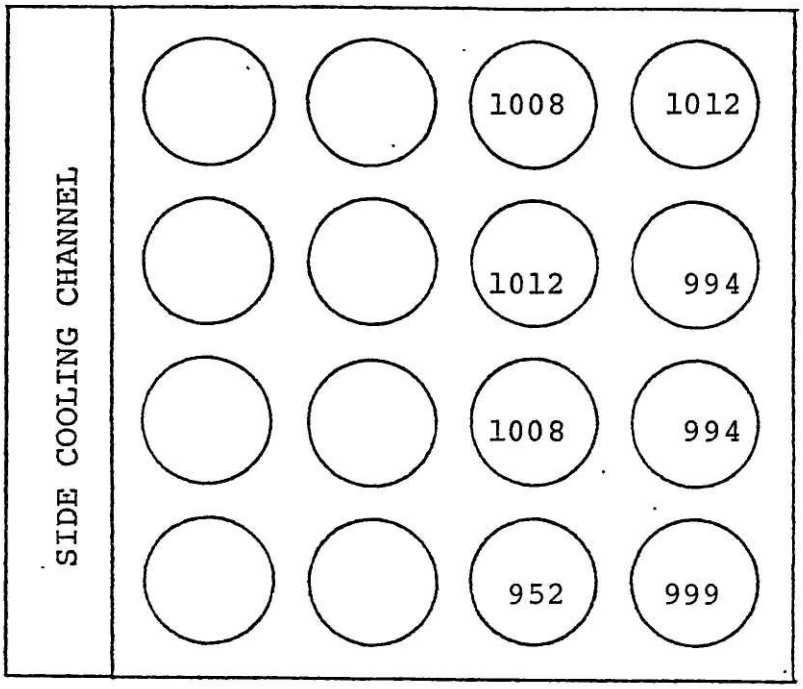
Pr= 3.0 $\quad \phi/\phi_o$= 13.3 $\quad \nu/\nu_o$= .425

FLOW PARAMETERS AT ONSET OF RECIRCULATION:

Re= 1709 $\quad Gr_q = 2.20 \times 10^6$

RUN 2.4 C

BUNDLE POWER DISTRIBUTION (W/ROD):



BUNDLE OPERATING CONDITIONS:

Flow rate at onset= 2.98 GPM Total rod power = 7980 W
Measured ΔT_{bulk} = 18.0°F Calculated ΔT_{bulk} = 18.6°F
Inlet Temperature = 96°F Average Temp. = 105°F

SIDE CHANNEL COOLANT FLOW:

Inlet Temperature = 34°F Outlet Temperature = 67°F
Flow rate = .091 GPM Power from bundle = 271 W

TEMPERATURE DEPENDENT FLUID PROPERTIES:

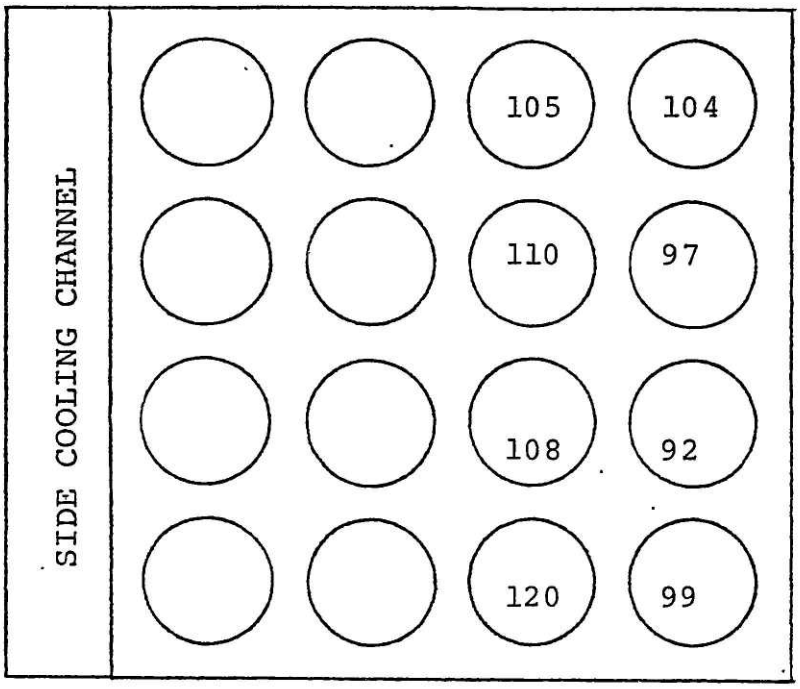
Pr= 4.25 ϕ/ϕ_o= 5.5 ν/ν_o= .575

FLOW PARAMETERS AT ONSET OF RECIRCULATION:

Re= 1284 Gr_q= 2.08 x 10^6

RUN 2.6 C

BUNDLE POWER DISTRIBUTION (W/ROD):



BUNDLE OPERATING CONDITIONS:

Flow rate at onset= 1.58 GPM Total rod power = 805 W
Measured ΔT_{bulk} = 3.5°F Calculated ΔT_{bulk} = 1°F
Inlet Temperature = 113°F Average Temp. = 113.5°F

SIDE CHANNEL COOLANT FLOW:

Inlet Temperature = 40°F Outlet Temperature = 70°F
Flow rate = .102 GPM Power from bundle = 573 W

TEMPERATURE DEPENDENT FLUID PROPERTIES:

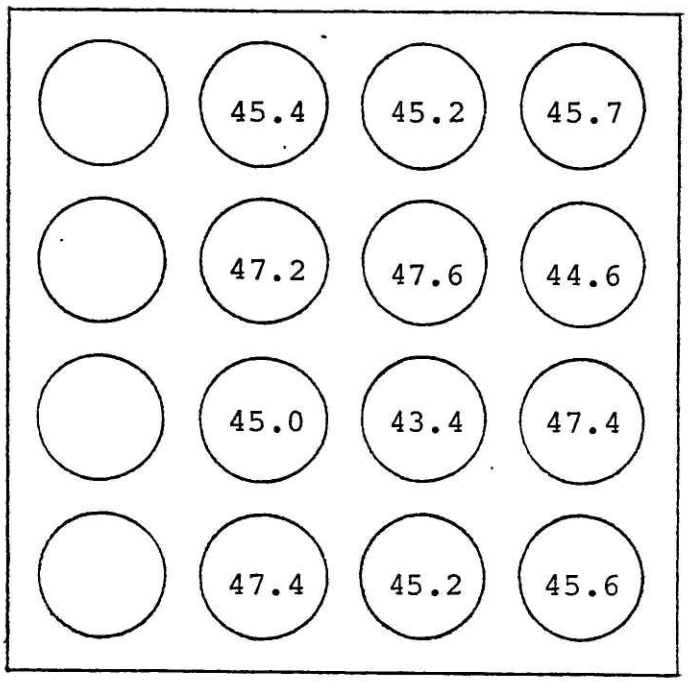
Pr= 3.90 ϕ/ϕ_o= 7.1 ν/ν_o= .53

FLOW PARAMETERS AT ONSET OF RECIRCULATION:

Re= 739 Gr_q= 2.87×10^5

RUN 3.1

BUNDLE POWER DISTRIBUTION (W/ROD):



BUNDLE OPERATING CONDITIONS:

Flow rate at onset= .725 Gpm Total rod power = 549.8 W
Measured ΔT_{bulk} = Calculated ΔT_{bulk} = $5.2^{o}F$
Inlet Temperature = $95^{o}F$ Average Temp. = $97.6^{o}F$

TEMPERATURE DEPENDENT FLUID PROPERTIES:

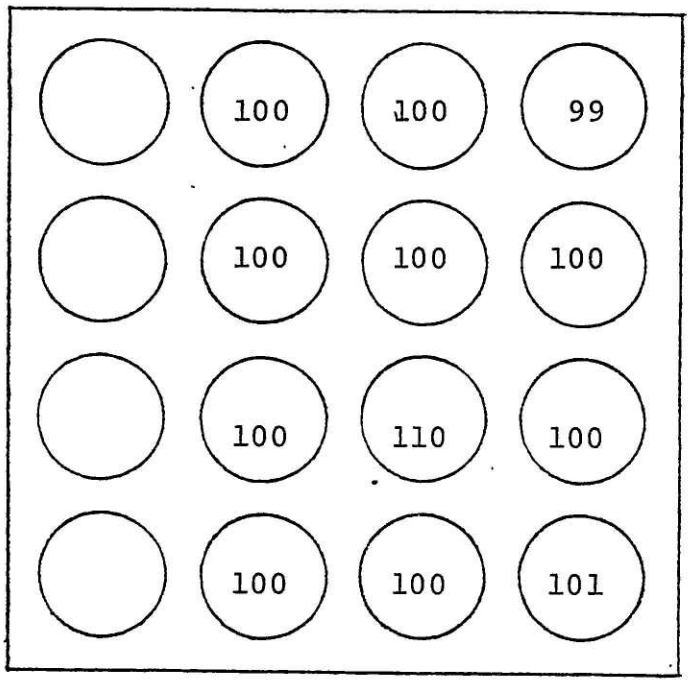
Pr=4.65 ϕ/ϕ_o= 4.15 ν/ν_o= .62

FLOW PARAMETERS AT ONSET OF RECIRCULATION:

Re= 290 Gr_q= 1.25E5

RUN 3.2

BUNDLE POWER DISTRIBUTION (W/ROD):



BUNDLE OPERATING CONDITIONS:

Flow rate at onset= 1.156 Gpm Total rod power = 1210 W

Measured ΔT_{bulk} = Calculated ΔT_{bulk} = $7.1^{o}F$

Inlet Temperature = $90^{o}F$ Average Temp. = $93.5^{o}F$

TEMPERATURE DEPENDENT FLUID PROPERTIES:

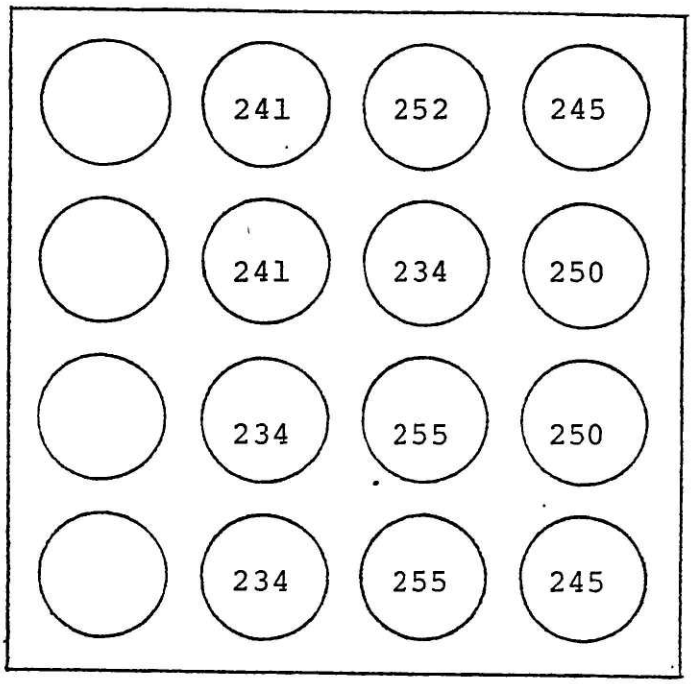
Pr= 4.85 ϕ/ϕ_o= 3.65 ν/ν_o= .645

FLOW PARAMETERS AT ONSET OF RECIRCULATION:

Re= 444 Gr_q= 2.18E5

RUN 3.3

BUNDLE POWER DISTRIBUTION (W/ROD):



BUNDLE OPERATING CONDITIONS:

Flow rate at onset= 1.411 Gpm Total rod power = 2694 W
Measured ΔT_{bulk} = Calculated ΔT_{bulk} = 13.0°F
Inlet Temperature = 94°F Average Temp. = 100.5°F

TEMPERATURE DEPENDENT FLUID PROPERTIES:

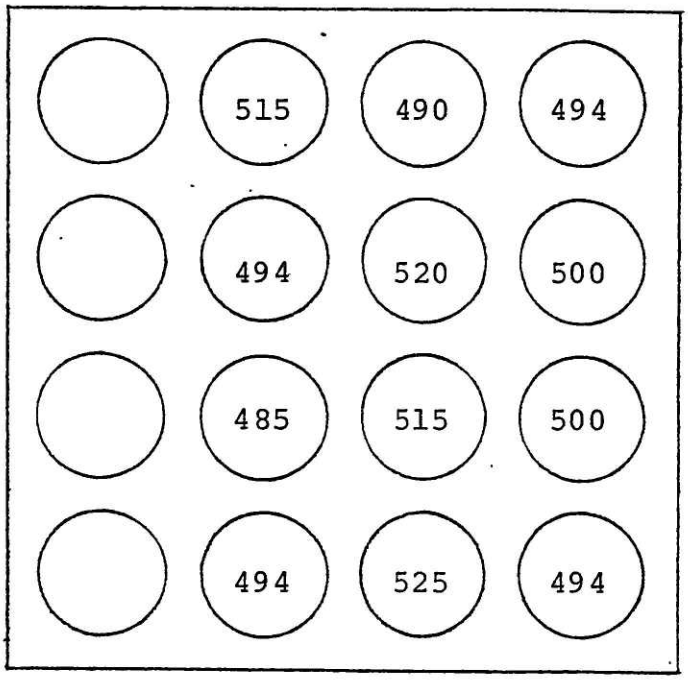
Pr= 4.05 ϕ/ϕ_o = 4.50 ν/ν_o = .605

FLOW PARAMETERS AT ONSET OF RECIRCULATION:

Re= 578 Gr_q = 6.09E5

RUN 3.4

BUNDLE POWER DISTRIBUTION (W/ROD):



BUNDLE OPERATING CONDITIONS:

Flow rate at onset= 1.80 Gpm Total rod power = 6025 W
Measured ΔT_{bulk} = 23°F Calculated ΔT_{bulk} = 22.8°F
Inlet Temperature = 93°F Average Temp. = 104.5°F

TEMPERATURE DEPENDENT FLUID PROPERTIES:

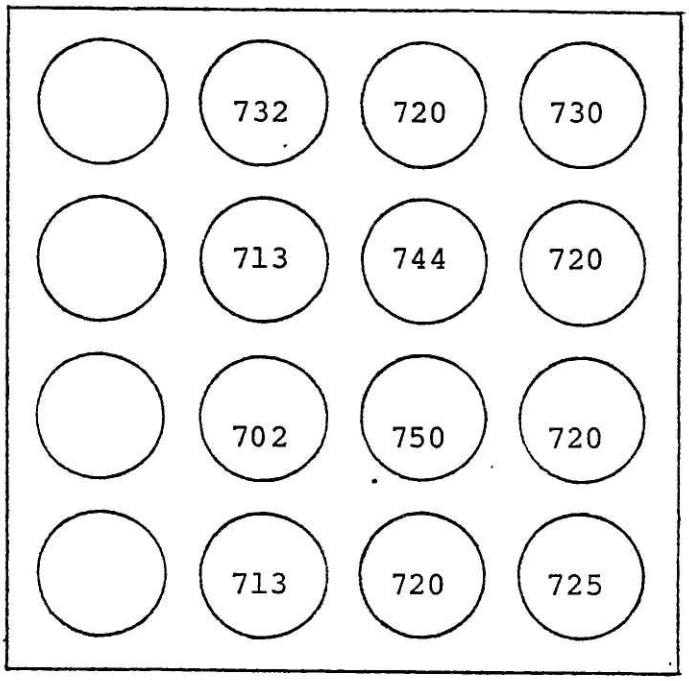
Pr= 4.30 ϕ/ϕ_o= 5.20 ν/ν_o= .58

FLOW PARAMETERS AT ONSET OF RECIRCULATION:

Re= 769 Gr_q= 1.57E6

RUN 3.5

BUNDLE POWER DISTRIBUTION (W/ROD):



BUNDLE OPERATING CONDITIONS:

Flow rate at onset=2.112 Gpm Total rod power = 8688 W

Measured ΔT_{bulk} = Calculated ΔT_{bulk}= 28.1°F

Inlet Temperature = 93°F Average Temp. = 107°F

TEMPERATURE DEPENDENT FLUID PROPERTIES:

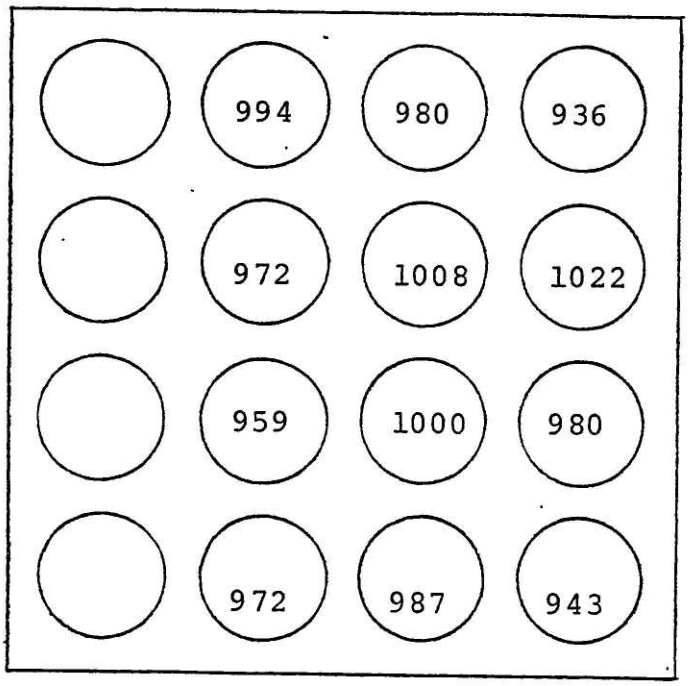
Pr= 3.70 ϕ/ϕ_o= 5.65 ν/ν_o= .56

FLOW PARAMETERS AT ONSET OF RECIRCULATION:

Re= 935 Gr_q= 2.46E6

RUN 3.6

BUNDLE POWER DISTRIBUTION (W/ROD):



BUNDLE OPERATING CONDITIONS:

Flow rate at onset=2.496 Gpm Total rod power = 11753 W

Measured ΔT_{bulk} = Calculated ΔT_{bulk} = 32.1°F

Inlet Temperature = 92°F Average Temp. = 108°F

TEMPERATURE DEPENDENT FLUID PROPERTIES:

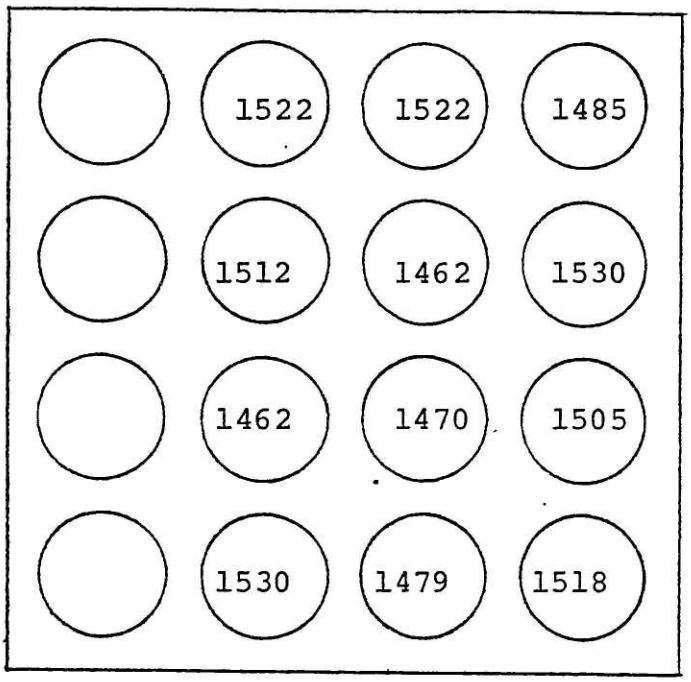
Pr= 4.10 ϕ/ϕ_o= 5.90 ν/ν_o= .56

FLOW PARAMETERS AT ONSET OF RECIRCULATION:

Re= 1105 Gr_q= 3.47E6

RUN 3.7

BUNDLE POWER DISTRIBUTION (W/ROD):



BUNDLE OPERATING CONDITIONS:

Flow rate at onset= 2.88 Gpm Total rod power = 17998 W
Measured ΔT_{bulk} = 45°F Calculated ΔT_{bulk} = 42.6°F
Inlet Temperature = 91°F Average Temp. = 112°F

TEMPERATURE DEPENDENT FLUID PROPERTIES:

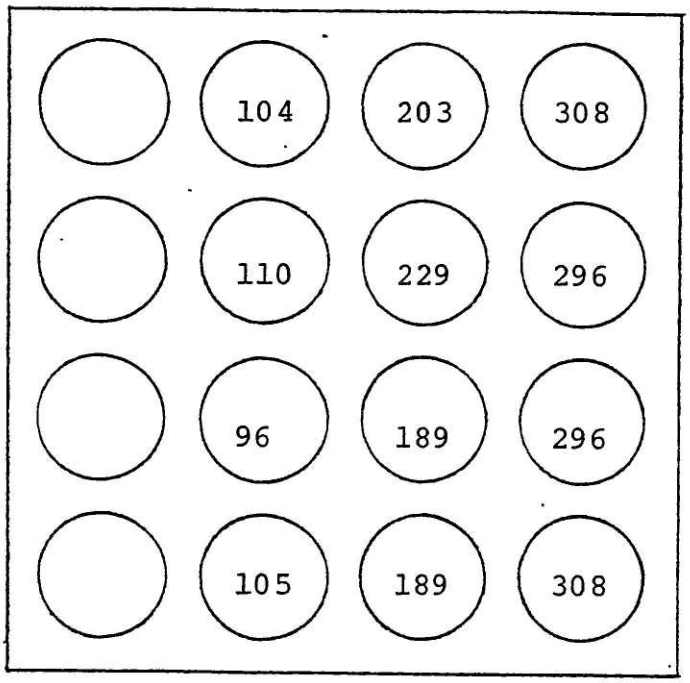
Pr= 3.90 ϕ/ϕ_o= 6.70 ν/ν_o= .535

FLOW PARAMETERS AT ONSET OF RECIRCULATION:

Re= 1334 Gr_q= 6.05E6

RUN 4.1

BUNDLE POWER DISTRIBUTION (W/ROD):



BUNDLE OPERATING CONDITIONS:

Flow rate at onset= 1.14 Gpm Total rod power = 2433 W
Measured ΔT_{bulk} = 14.5°F Calculated ΔT_{bulk} = 14.6°F
Inlet Temperature = 94°F Average Temp. = 101.3°F

TEMPERATURE DEPENDENT FLUID PROPERTIES:

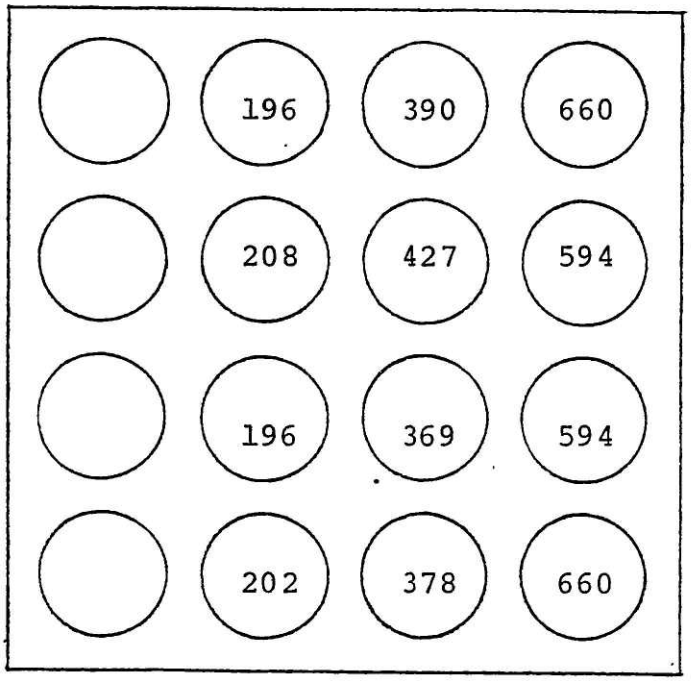
Pr= 4.45 ϕ/ϕ_o= 4.5 ν/ν_o= .61

FLOW PARAMETERS AT ONSET OF RECIRCULATION:

Re= 463 Gr_q= 5.50 X 10^5

RUN 4.2

BUNDLE POWER DISTRIBUTION (W/ROD):



BUNDLE OPERATING CONDITIONS:

Flow rate at onset= 1.51 Gpm Total rod power = 4874 W
Measured ΔT_{bulk} = 22.6°F Calculated ΔT_{bulk} = 22.0°F
Inlet Temperature = 93°F Average Temp. = 104.0°F

TEMPERATURE DEPENDENT FLUID PROPERTIES:

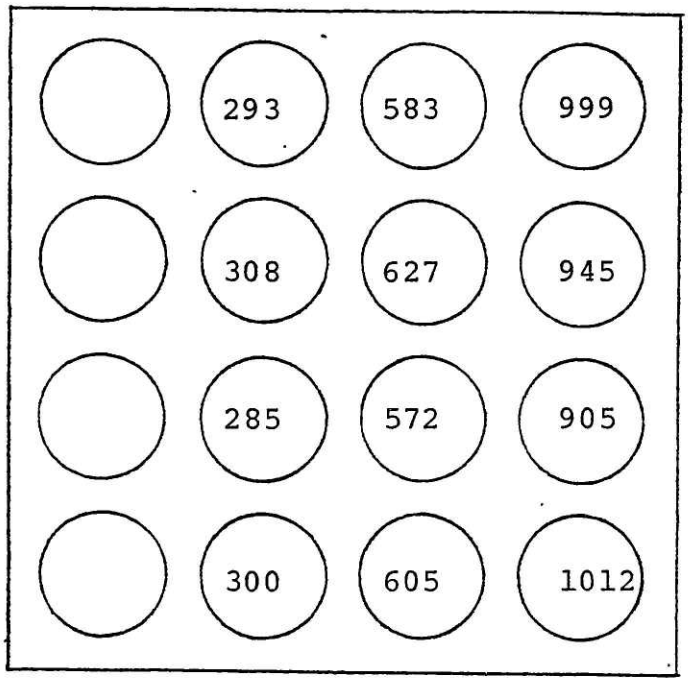
Pr= 4.30 ϕ/ϕ_o= 5.25 ν/ν_o= .58

FLOW PARAMETERS AT ONSET OF RECIRCULATION:

Re= 649 Gr_q= 1.29E6

RUN 4.3

BUNDLE POWER DISTRIBUTION (W/ROD):



BUNDLE OPERATING CONDITIONS:

Flow rate at onset= 1.80 Gpm Total rod power = 7434 W
Measured ΔT_{bulk} = 29.0°F Calculated ΔT_{bulk} = 28.1°F
Inlet Temperature = 92°F Average Temp. = 106°F

TEMPERATURE DEPENDENT FLUID PROPERTIES:

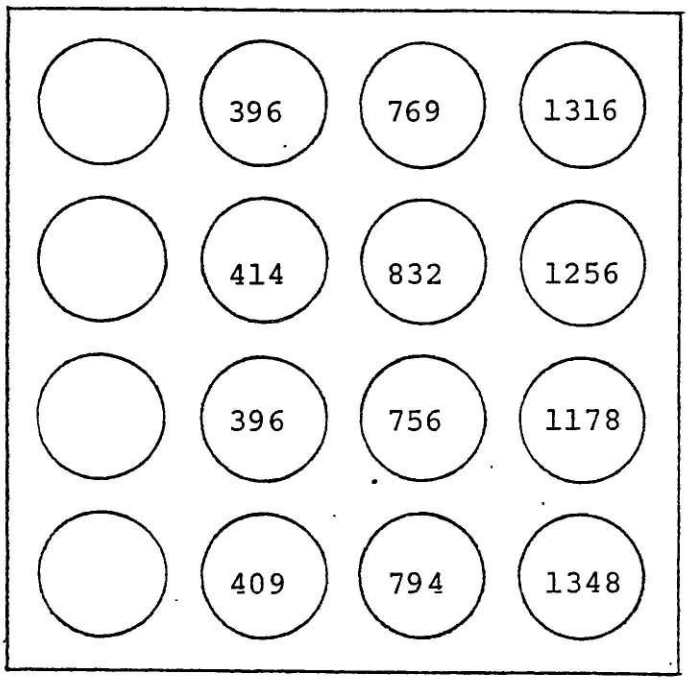
Pr= 4.20 ϕ/ϕ_o= 5.6 ν/ν_o= .57

FLOW PARAMETERS AT ONSET OF RECIRCULATION:

Re= 783 Gr_q= 2.09E6

RUN 4.4

BUNDLE POWER DISTRIBUTION (W/ROD):



BUNDLE OPERATING CONDITIONS:

Flow rate at onset= 2.21 Gpm Total rod power = 9481 W
Measured ΔT_{bulk} =31.0°F Calculated ΔT_{bulk}= 29.3°F
Inlet Temperature =90.0°F Average Temp. =105.1°F

TEMPERATURE DEPENDENT FLUID PROPERTIES:

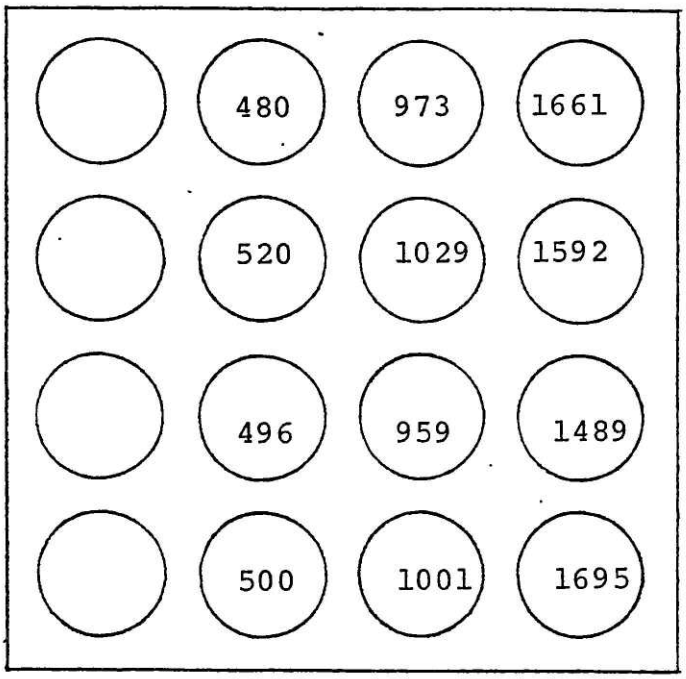
Pr= 4.25 ϕ/ϕ_o= 5.4 ν/ν_o= .575

FLOW PARAMETERS AT ONSET OF RECIRCULATION:

Re= 953 Gr_q= 2.57E6

RUN 4.5

BUNDLE POWER DISTRIBUTION (W/ROD):



BUNDLE OPERATING CONDITIONS:

Flow rate at onset= 2.35 Gpm Total rod power = 12388 W
Measured ΔT_{bulk} = 37°F Calculated ΔT_{bulk}= 35.9°F
Inlet Temperature = 90°F Average Temp. = 108°F

TEMPERATURE DEPENDENT FLUID PROPERTIES:

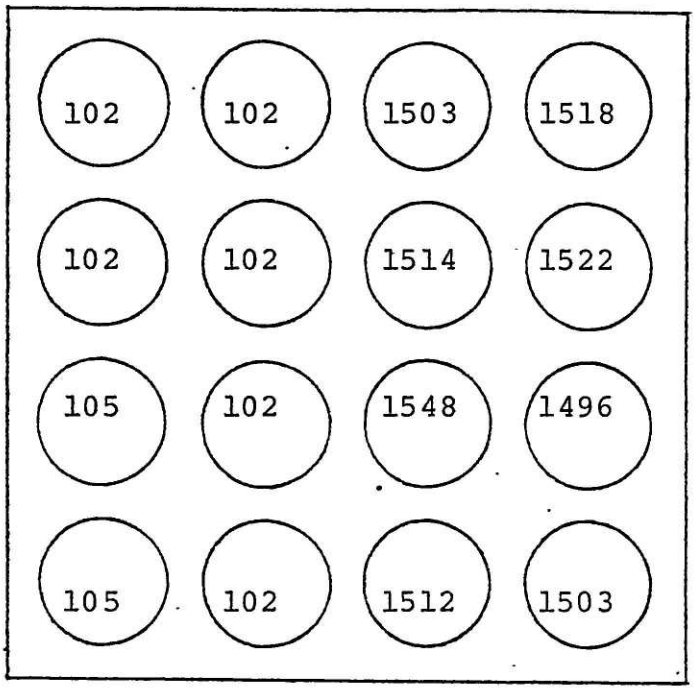
Pr= 4.10 ϕ/ϕ_o= 6.0 ν/ν_o= .555

FLOW PARAMETERS AT ONSET OF RECIRCULATION:

Re= 1046 Gr_q= 3.73E6

RUN 5.1

BUNDLE POWER DISTRIBUTION (W/ROD):



BUNDLE OPERATING CONDITIONS:

Flow rate at onset= 2.16GPM Total rod power = 12939 W
Measured ΔT_{bulk} = 42°F Calculated ΔT_{bulk} = 40.9°F
Inlet Temperature = 98°F Average Temp. = 119°F

TEMPERATURE DEPENDENT FLUID PROPERTIES:

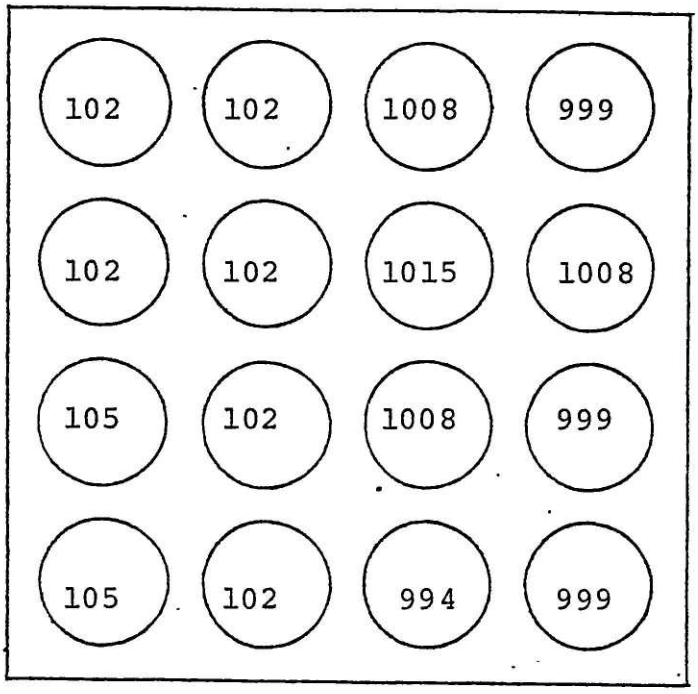
Pr= 3.65 ϕ/ϕ_o= 10.85 ν/ν_o= .50

FLOW PARAMETERS AT ONSET OF RECIRCULATION:

Re= 1071 $Gr_q = 7.05 \times 10^6$

RUN 5.2

BUNDLE POWER DISTRIBUTION (W/ROD):



BUNDLE OPERATING CONDITIONS:

Flow rate at onset= 1.764 GPM Total rod power = 8853 W
Measured ΔT_{bulk} = 36°F Calculated ΔT_{bulk} = 34.2°F
Inlet Temperature = 98°F Average Temp. = 115°F

TEMPERATURE DEPENDENT FLUID PROPERTIES:

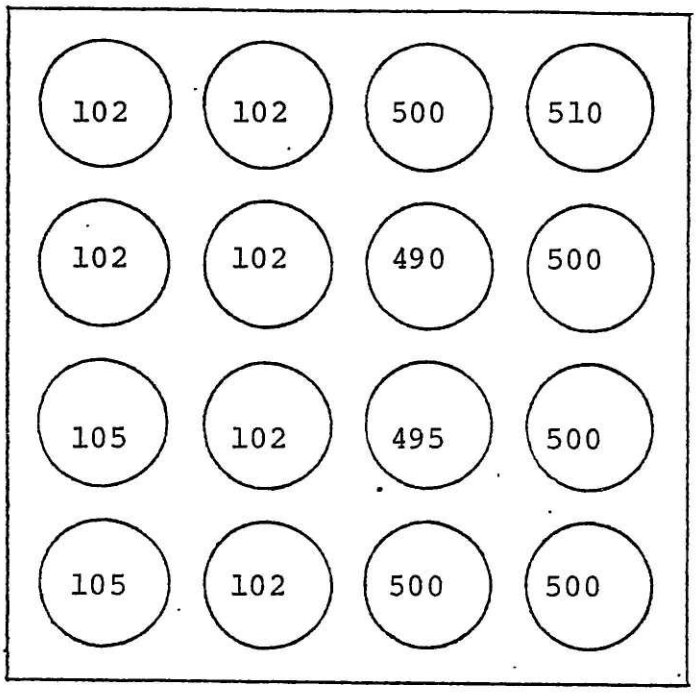
Pr= 3.80 ϕ/ϕ_o = 7.5 ν/ν_o = .52

FLOW PARAMETERS AT ONSET OF RECIRCULATION:

Re= 841 $Gr_q = 3.34 \times 10^6$

RUN 5.3

BUNDLE POWER DISTRIBUTION (W/ROD):



BUNDLE OPERATING CONDITIONS:

Flow rate at onset= .686 GPM
Total rod power = 4817 W
Measured ΔT_{bulk} = $50^{o}F$
Calculated ΔT_{bulk} = $47.9^{o}F$
Inlet Temperature = $107^{o}F$
Average Temp. = $131^{o}F$

TEMPERATURE DEPENDENT FLUID PROPERTIES:

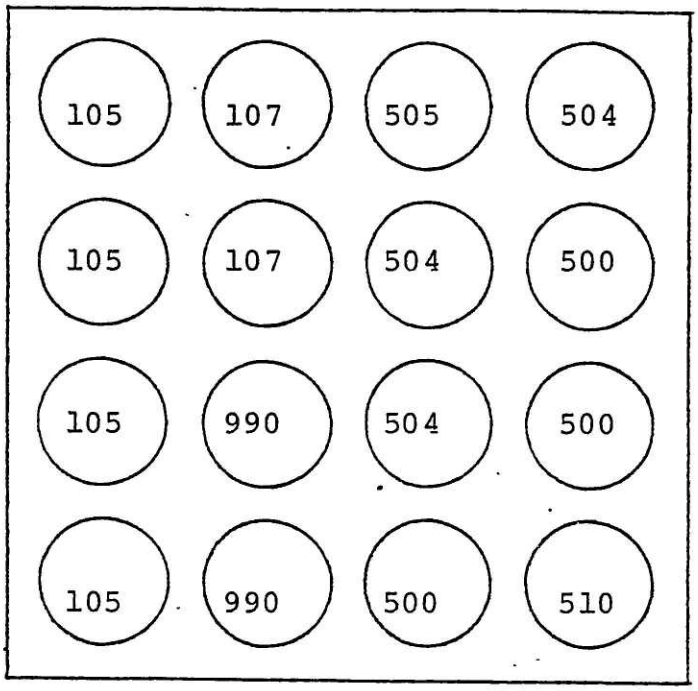
Pr= 3.20 ϕ/ϕ_o= 11.3 ν/ν_o= .45

FLOW PARAMETERS AT ONSET OF RECIRCULATION:

Re= 378 $Gr_q = 2.73 \times 10^6$

RUN 5.4

BUNDLE POWER DISTRIBUTION (W/ROD):



BUNDLE OPERATING CONDITIONS:

Flow rate at onset= .78 GPM Total rod power = 4859.9 W
Measured ΔT_{bulk} = 43.0°F Calculated ΔT_{bulk} = 42.5°F
Inlet Temperature = 100.5°F Average Temp. = 122°F

TEMPERATURE DEPENDENT FLUID PROPERTIES:

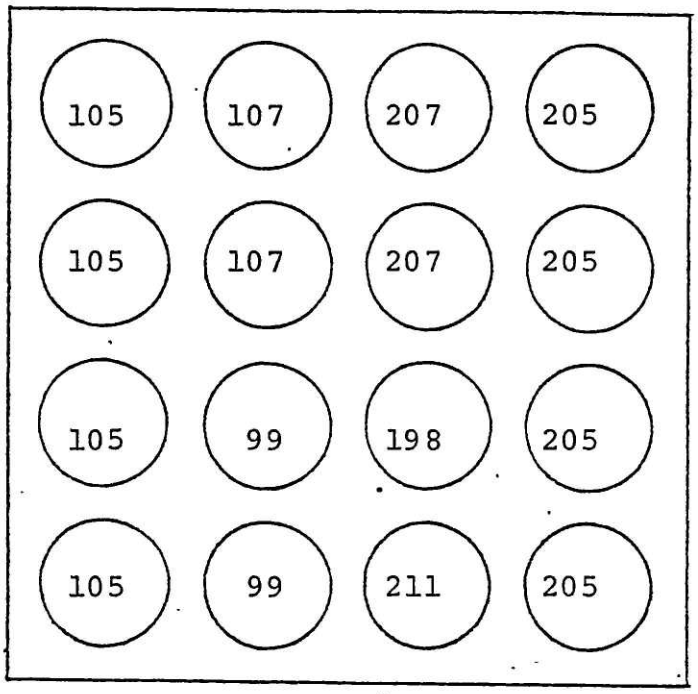
Pr= 3.50 ϕ/ϕ_o= 9.1 ν/ν_o= .485

FLOW PARAMETERS AT ONSET OF RECIRCULATION:

Re= 399 $Gr_q = 2.22 \times 10^6$

RUN 5.5

BUNDLE POWER DISTRIBUTION (W/ROD):



BUNDLE OPERATING CONDITIONS:

Flow rate at onset=	.294GPM	Total rod power	= 2474 W
Measured ΔT_{bulk}	= 56.5°F	Calculated ΔT_{bulk}	= 57.4°F
Inlet Temperature	= 102°F	Average Temp.	= 133°F

TEMPERATURE DEPENDENT FLUID PROPERTIES:

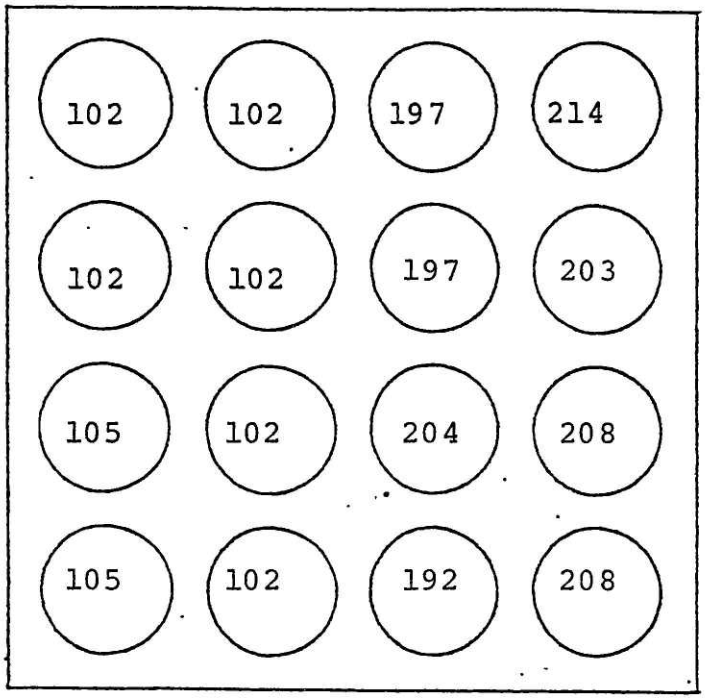
Pr= 3.15 $\quad \phi/\phi_o$= 11.85 $\quad \nu/\nu_o$= .445

FLOW PARAMETERS AT ONSET OF RECIRCULATION:

Re= 164 $\quad Gr_q = 1.47 \times 10^6$

RUN 5.6

BUNDLE POWER DISTRIBUTION (W/ROD):



BUNDLE OPERATING CONDITIONS:

Flow rate at onset= .470 GPM
Total rod power = 2446 W
Measured ΔT_{bulk} = $36^{o}F$
Calculated ΔT_{bulk} = $35.5^{o}F$
Inlet Temperature = $98^{o}F$
Average Temp. = $116^{o}F$

TEMPERATURE DEPENDENT FLUID PROPERTIES:

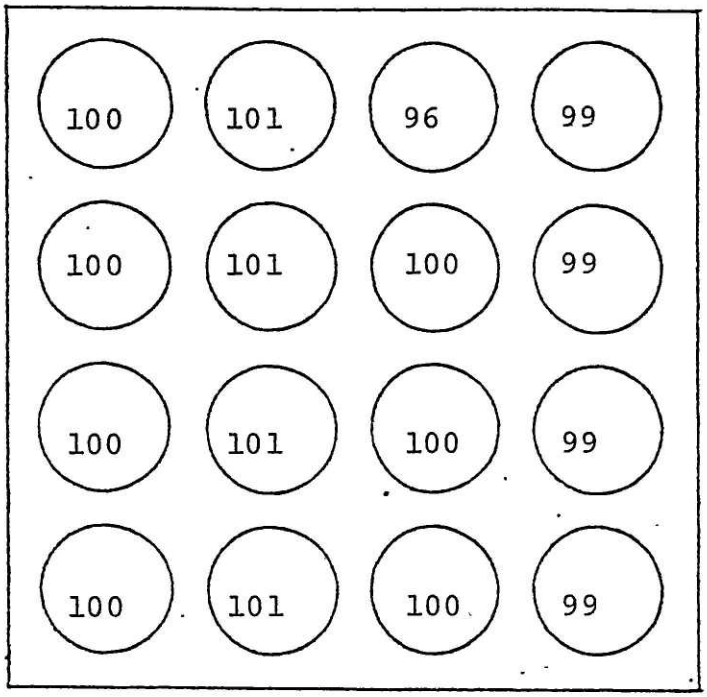
Pr= 3.75 ϕ/ϕ_o= 7.75 ν/ν_o= .515

FLOW PARAMETERS AT ONSET OF RECIRCULATION:

Re= 226 $Gr_q = 9.52 \times 10^5$

RUN 5.7

BUNDLE POWER DISTRIBUTION (W/ROD):



BUNDLE OPERATING CONDITIONS:

Flow rate at onset=.235 GPM Total rod power = 1597 W
Measured ΔT_{bulk} = 46°F Calculated ΔT_{bulk} = 46.3°F
Inlet Temperature = 81°F Average Temp. = 104°F

TEMPERATURE DEPENDENT FLUID PROPERTIES:

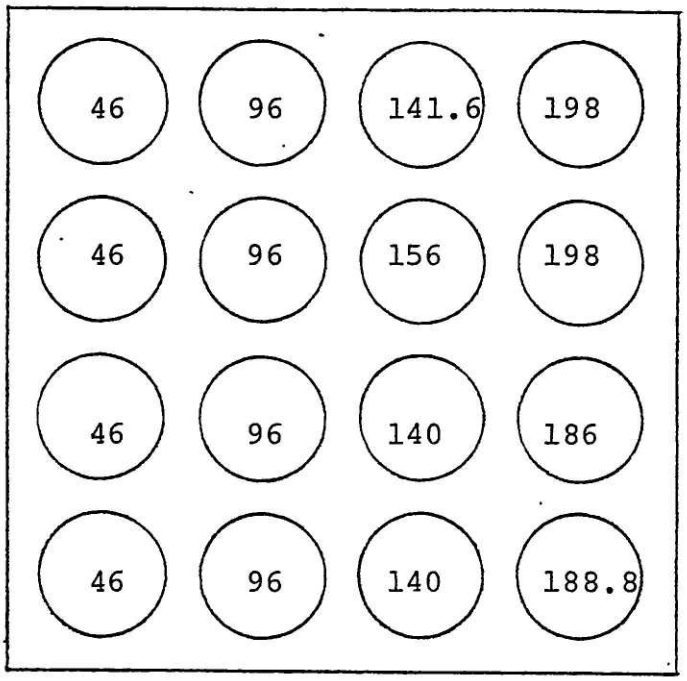
Pr= 4.30 ϕ/ϕ_o= 5.25 ν/ν_o= .58

FLOW PARAMETERS AT ONSET OF RECIRCULATION:

Re= 101 $Gr_q = 4.2 \times 10^5$

RUN 6.1

BUNDLE POWER DISTRIBUTION (W/ROD):



BUNDLE OPERATING CONDITIONS:

Flow rate at onset=0.52 GPM Total rod power = 1918.7 W

Measured ΔT_{bulk} = Calculated ΔT_{bulk}= 25.2^{o}F

Inlet Temperature =99^{o}F Average Temp. = 111.6^{o}F

TEMPERATURE DEPENDENT FLUID PROPERTIES:

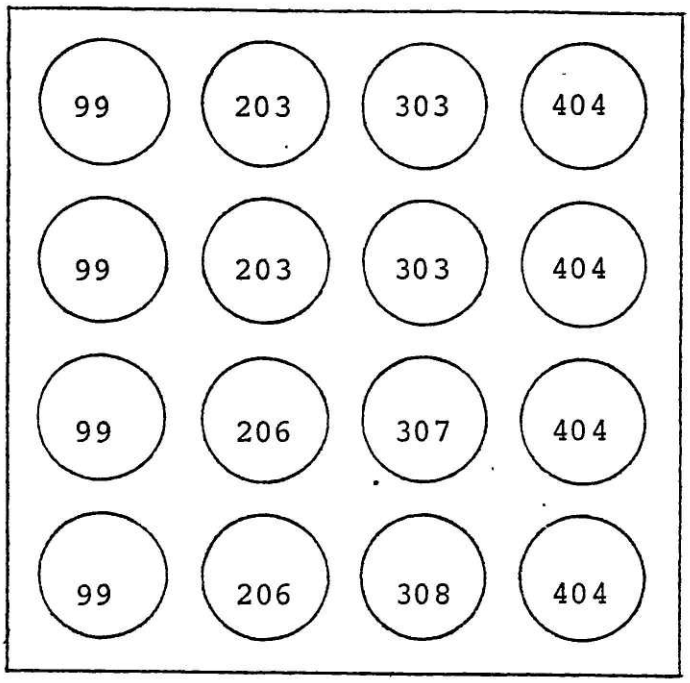
Pr= 3.95 ϕ/ϕ_o= 6.75 ν/ν_o= 0.54

FLOW PARAMETERS AT ONSET OF RECIRCULATION:

Re= 239 $Gr_q = 6.51 \times 10^5$

RUN 6.2

BUNDLE POWER DISTRIBUTION (W/ROD):



BUNDLE OPERATING CONDITIONS:

Flow rate at onset= 0.72 GPM Total rod power = 4054.8 W

Measured ΔT_{bulk} = Calculated ΔT_{bulk} = 38.41°F

Inlet Temperature = 96°F Average Temp. = 115.2°F

TEMPERATURE DEPENDENT FLUID PROPERTIES:

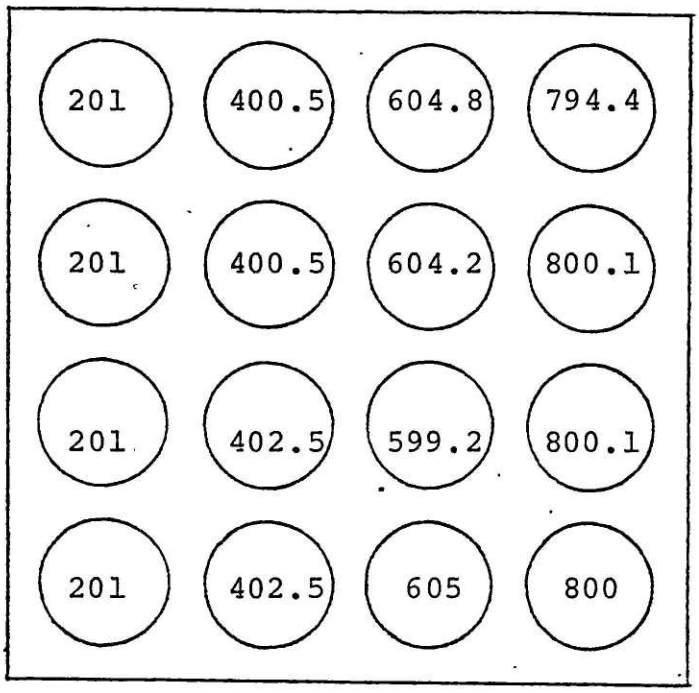
Pr= 3.80 ϕ/ϕ_o= 7.50 ν/ν_o= .520

FLOW PARAMETERS AT ONSET OF RECIRCULATION:

Re= 343 $Gr_q = 1.53 \times 10^6$

RUN 6.3

BUNDLE POWER DISTRIBUTION (W/ROD):



BUNDLE OPERATING CONDITIONS:

Flow rate at onset=0.84 GPM
Measured ΔT_{bulk} =65°F
Inlet Temperature =109°F
Total rod power = 8019.8 W
Calculated ΔT_{bulk} = 65.1°F
Average Temp. = 141.6°F

TEMPERATURE DEPENDENT FLUID PROPERTIES:

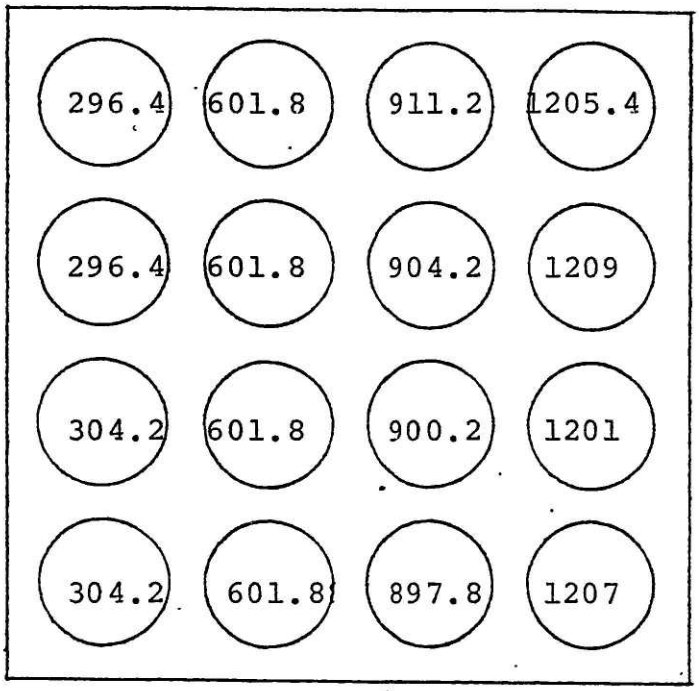
Pr= 2.90 ϕ/ϕ_o= 14.24 ν/ν_o=0.415

FLOW PARAMETERS AT ONSET OF RECIRCULATION:

Re= 502 $Gr_q = 5.70 \times 10^6$

RUN 6.4

BUNDLE POWER DISTRIBUTION (W/ROD):



BUNDLE OPERATING CONDITIONS:

Flow rate at onset= 1.078GPM Total rod power = 12044.5 W

Measured ΔT_{bulk} = 83.5°F Calculated ΔT_{bulk} = 76.2°F

Inlet Temperature = 98°F Average Temp. = 136.1°F

TEMPERATURE DEPENDENT FLUID PROPERTIES:

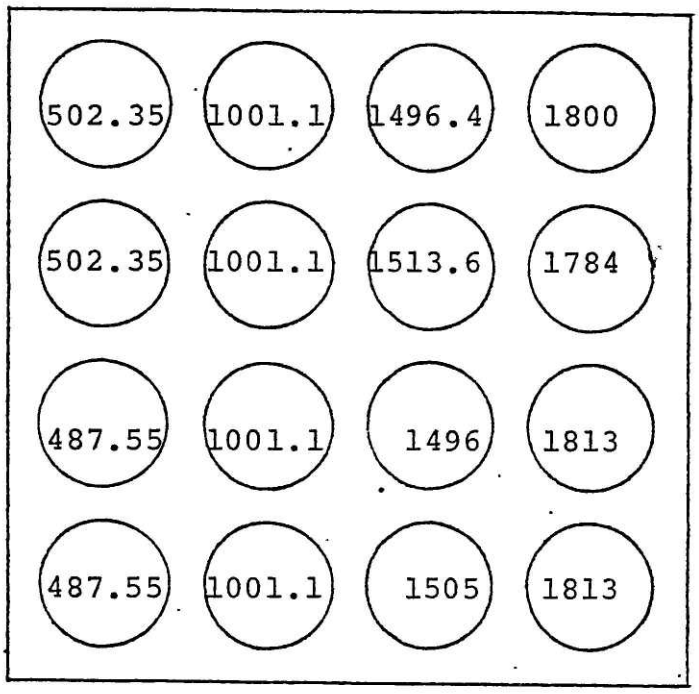
Pr= 3.07 ϕ/ϕ_o= 12.6 ν/ν_o=0.435

FLOW PARAMETERS AT ONSET OF RECIRCULATION:

Re= 614 $Gr_q = 7.60 \times 10^6$

RUN 6.5

BUNDLE POWER DISTRIBUTION (W/ROD):



BUNDLE OPERATING CONDITIONS:

Flow rate at onset= 1.274GPM Total rod power =19206 W
Measured ΔT_{bulk} = 100°F Calculated ΔT_{bulk} =102.8°F
Inlet Temperature = 97°F Average Temp. =148.4°F

TEMPERATURE DEPENDENT FLUID PROPERTIES:

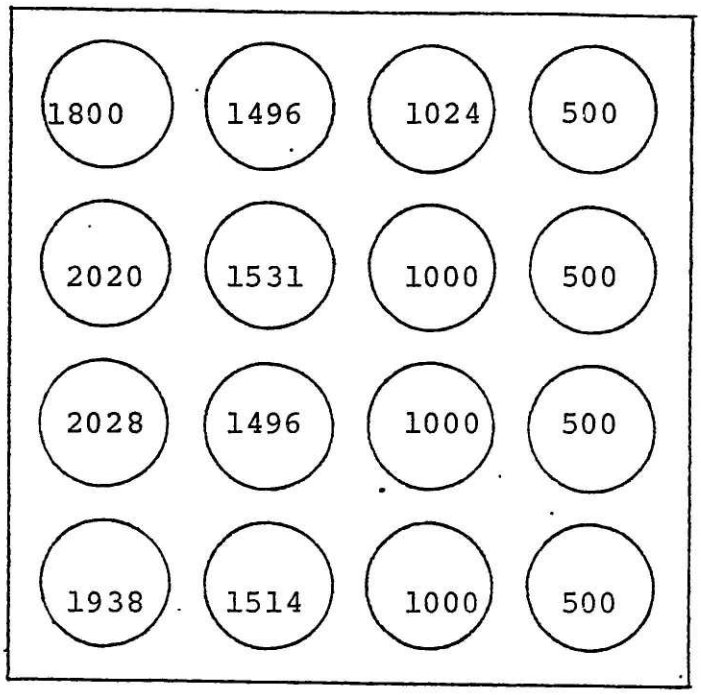
Pr= 2.75 ϕ/ϕ_o= 16.33 ν/ν_o= 0.395

FLOW PARAMETERS AT ONSET OF RECIRCULATION:

Re= 799 $Gr_q = 1.58 \times 10^7$

RUN 6.6

BUNDLE POWER DISTRIBUTION (W/ROD):



BUNDLE OPERATING CONDITIONS:

Flow rate at onset= 1.254GPM Total rod power = 19755 W
Measured ΔT_{bulk} = 109°F Calculated ΔT_{bulk} = 107.4°F
Inlet Temperature = 90°F Average Temp. = 144°F

TEMPERATURE DEPENDENT FLUID PROPERTIES:

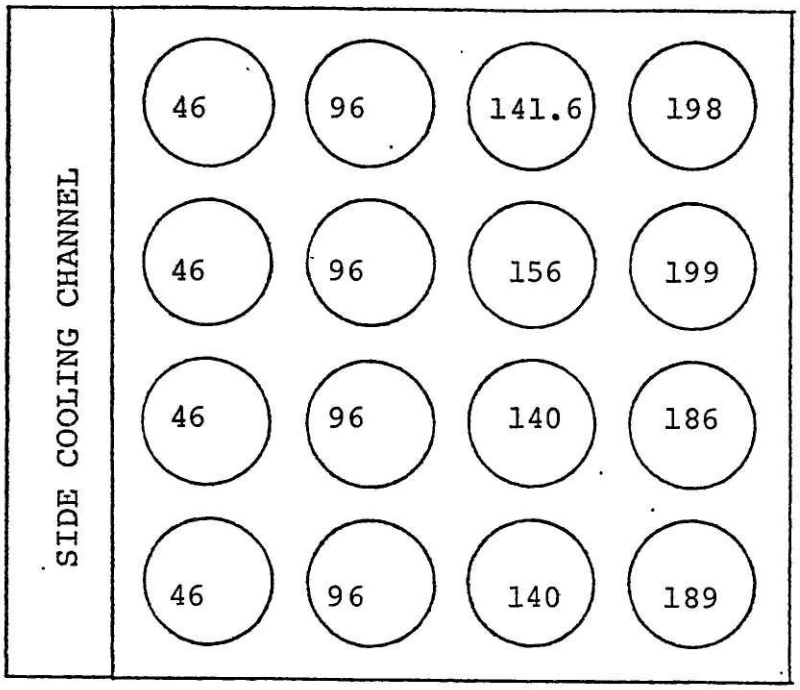
Pr= 2.85 ϕ/ϕ_o= 15.10 ν/ν_o= .408

FLOW PARAMETERS AT ONSET OF RECIRCULATION:

Re= 763 $Gr_q = 1.50 \times 10^7$

RUN 6.1 C

BUNDLE POWER DISTRIBUTION (W/ROD):



BUNDLE OPERATING CONDITIONS:

Flow rate at onset= 1.49 GPM Total rod power = 1919 W
Measured ΔT_{bulk} = 7.0°F Calculated ΔT_{bulk} = 6.74°F
Inlet Temperature = 99°F Average Temp. = 103.5°F

SIDE CHANNEL COOLANT FLOW:

Inlet Temperature = 38°F Outlet Temperature = 50°F
Flow rate = .254 Power from bundle = 448 W

TEMPERATURE DEPENDENT FLUID PROPERTIES:

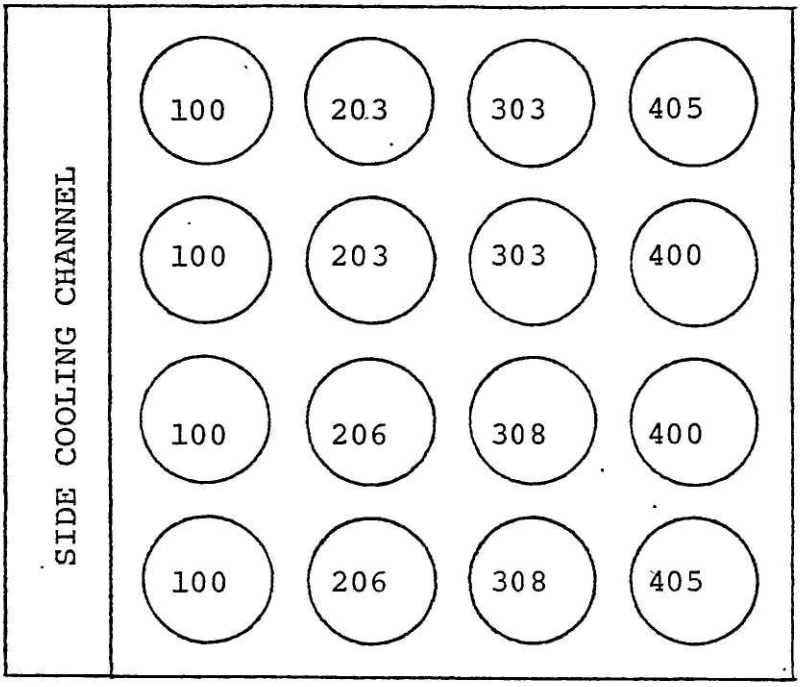
Pr= 4.30 ϕ/ϕ_o= 5.15 ν/ν_o= ,58

FLOW PARAMETERS AT ONSET OF RECIRCULATION:

Re= 637 $Gr_q = 3.81 \times 10^5$

RUN 6.2 C

BUNDLE POWER DISTRIBUTION (W/ROD):



BUNDLE OPERATING CONDITIONS:

Flow rate at onset= 2.16 GPM Total rod power = 4055 W
Measured ΔT_{bulk} = 11°F Calculated ΔT_{bulk} = 10.5°F
Inlet Temperature = 108°F Average Temp. = 113.5°F

SIDE CHANNEL COOLANT FLOW:

Inlet Temperature = 42°F Outlet Temperature = 54°F
Flow rate = .262 GPM Power from bundle = 460 W

TEMPERATURE DEPENDENT FLUID PROPERTIES:

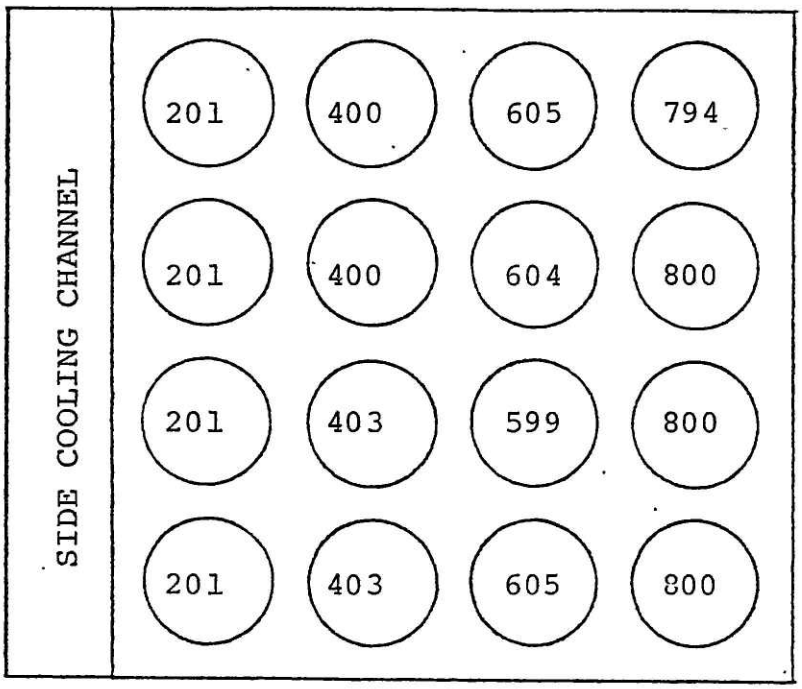
Pr= 3.85 ϕ/ϕ_o= 7.25 ν/ν_o= .525

FLOW PARAMETERS AT ONSET OF RECIRCULATION:

Re= 1020 $Gr_q = 1.31 \times 10^6$

RUN 6.3 C

BUNDLE POWER DISTRIBUTION (W/ROD):



BUNDLE OPERATING CONDITIONS:

Flow rate at onset= 2.30 GPM Total rod power = 8020 W
Measured ΔT_{bulk} = 22.5°F Calculated ΔT_{bulk} = 21.5°F
Inlet Temperature = 113°F Average Temp. = 124°F

SIDE CHANNEL COOLANT FLOW:

Inlet Temperature = 37.5°F Outlet Temperature = 60.0°F
Flow rate = .238 GPM Power from bundle = 783.8 W

TEMPERATURE DEPENDENT FLUID PROPERTIES:

Pr= 3.45 ϕ/ϕ_o= 9.0 ν/ν_o= .48

FLOW PARAMETERS AT ONSET OF RECIRCULATION:

Re= 1189 Gr_q= 3.72 x 10^6

APPENDIX F3

ANALYSIS OF ERRORS IN THE ONSET OF RECIRCULATION EXPERIMENT

To estimate the errors involved in the recirculation experiment, the methods of Schenck (Reference 75) will be used. It was shown in Reference 75 that if a result R is a function of measured quantitites X, Y, and Z such that:

$$R = K \frac{XY}{Z} \tag{F3.1}$$

then it follows that:

$$\left(\frac{w_R}{R}\right)^2 = \left(\frac{w_X}{X}\right)^2 + \left(\frac{w_Y}{Y}\right)^2 + \left(\frac{w_Z}{Z}\right)^2 \tag{F3.2}$$

where w is a deviation limit for the subscripted quantity. The quantity w_R/R may be considered the percentage error in R. Equation F3.2 is a mathematical form of the rule "when the result is a function of quotients and/or products of a series of measurements, the square of the percent error of the result is equal to the sum of the squares of the percent errors of the individual measurements." Equation F3.2 will be used to estimate the maximum expected error for the determination of Gr_q and Re at the onset of recirculation. Two estimates will be made, one for low power and flow and the other for high power and flow.

The Reynolds number can be expressed as:

$$Re = K \frac{G}{\nu/\nu_o} \tag{F3.3}$$

From Equation F3.2 it follows that:

$$\left(\frac{w_{Re}}{Re}\right)^2 = \left(\frac{w_G}{G}\right)^2 + \left(\frac{w_{\nu/\nu_o}}{\nu/\nu_o}\right)^2 \tag{F3.4}$$

The maximum expected error in G (the bundle flow rate) is composed of three components which are estimated as follows:

1) Error due to flow meter reading which is half the smallest division, or $\pm$ .005 G_{max} where G_{max} is the full scale flow rate.

2) Error due to uncertainty in determining the flow rate at which recirculation begins. From Figures 7.2.7 to 7.2.11, this may be estimated as $\pm$ .025 G_{max}

3) Error due to dye injection location. The thermocouple measurements of Figures 7.2.5 and 7.2.6 indicate that recirculation may exist at the bundle exit plane at a flow + 6% higher than when recirculation is observed at the dye injection location.

The first two errors are random, while the third is systematic. Equation F3.2 is valid for normally distributed random

errors only. The systematic error must be treated separately.

$$\frac{w_G}{G} = .005 \frac{G_{max}}{G} + .025 \frac{G_{max}}{G} \qquad \text{(F3.5)}$$

For the low flow case, the minimum value for G was .15 G_{max} from Figure 7.2.7 which gives:

$$\frac{w_G}{G} = \frac{.03}{.15} = .20 \qquad \text{(F3.6)}$$

while for the high flow case, G obtained a maximum of $.9G_{max}$ so:

$$\frac{w_G}{G} = \frac{.03}{.9} = .03$$

The maximum expected error in ν is due to error in the determination of the mean bundle temperature, which is estimated as $\pm$ 1°F. The error in ν due to this uncertainty in temperature is

$$w_{\nu/\nu_o} = \frac{d(\nu/\nu_o)}{dT} \Delta T \qquad \text{(F3.7)}$$

where $\frac{d(\nu/\nu_o)}{dT}$ is the slope of Figure F1.1. Over the temperature range from 100 to 150°F the slope is nearly constant at

$$\frac{\Delta(\nu/\nu_o)}{\Delta T} = .0043 \quad 1/^oF \qquad \text{(F3.8)}$$

With $\Delta T = 1^{o}F$ Equation F3.7 gives

$$w_{\nu/\nu_o} = .0043 \qquad \text{(F3.9)}$$

The mean value of ν/ν_o over the temperature range of interest is .35. It follows that:

$$\frac{w_{\nu/\nu_o}}{\nu/\nu_o} = .012 \qquad \text{(F3.10)}$$

It then follows from Equation F3.4 that for the lowest flow rate

$$\frac{w_{Re}}{Re} = \sqrt{.20^2 + .012^2} = .20 \qquad \text{(F3.11)}$$

while for high flows

$$\frac{w_{Re}}{Re} = \sqrt{.03^2 + .012^2} = .03 \qquad \text{(F3.12)}$$

the error in ν/ν_o is negligible. We therefore expect the percent error in Re_{crit} to vary from $\pm$ 20% for low flow recirculation to $\pm$ 3% for high flow recirculation.

The error due to dye injection location is systematic since it causes an underestimation of the critical Reynolds number. Since errors due to uncertainty in fluid properties were found to be negligible, the +6% error in the bundle flow rate (error #3 discussed above) leads directly to a +6% error in the Reynolds number.

In summary, for high flow recirculation the random error in Re_{crit} is $\pm$ 3% while the systematic error is +6% giving a maximum expected total error of 9%. Similarly for low flow recirculation, the maximum expected total error is 26%. The experimental error in determination of the Grashof number will be considered next.

The Grashof number may be expressed as:

$$Gr_q = K\left(\frac{\phi}{\phi_o}\right) Q_b \qquad \text{(F3.13)}$$

so from F3.2 the percent error in the Grashof number is:

$$\left(\frac{w_{Gr}}{Gr}\right)^2 = \left(\frac{w_{\phi/\phi_o}}{(\phi/\phi_o)}\right)^2 + \left(\frac{w_Q}{Q}\right)^2 \qquad \text{(F3.14)}$$

From Figure 7.2.13 the error in the bundle power may be estimated as 5% since the bulk temperature calculated from a heat balance differs by at most 5% from the measured bulk temperature rise. From Figure F1.1 the error due to graphical determination of ϕ/ϕ_o is:

$$\frac{w_{\phi/\phi_o}}{\phi/\phi_o} = \frac{d(\phi/\phi_o)}{dT} \cdot \frac{\Delta T}{\phi/\phi_o} \qquad \text{(F3.15)}$$

With $\Delta T = 1^oF$ and a mean temperature of 120^oF Figure F1.1 can be used to obtain:

$$\frac{d(\phi/\phi_o)}{dT} \equiv .22$$

$$\phi/\phi_o = 8.5$$

Substituting into Equation F3.15 gives

$$\frac{w_{\phi/\phi_o}}{\phi/\phi_o} = .22 \frac{1}{8.5} = .027$$

It follows from Equation F3.14 that the error in Gr_q is

$$\frac{w_{Gr}}{Gr} = \sqrt{(.027)^2 + (.05)^2} = .057$$

so the maximum expected error in Gr_q is 6%.

APPENDIX F4

MODEL FOR THE CRITICAL VALUE OF C AT THE ONSET OF RECIRCULATION ALLOWING FOR NONUNIFORM POWER

For the R=1 approach, the bundle is divided into two identical channels and C is fixed at an appropriate value to indicate onset of recirculation. In what follows, a simple model is developed to calculate the critical value of C at the onset of recirculation when nonuniform power conditions exist in channel #1.

For uniform inlet velocity, C is given by:

$$C = 1 - V_{le}^{*} \tag{F4.1}$$

Under certain conditions (zero power, or uniform power in channel #1) $V_{le}^{*} = 0$ at the onset of recirculation, giving $C_{crit} = 1.0$. In general V_{le}^{*} at the onset of recirculation will depend on the velocity distribution within channel #1, which the two channel model neglects entirely. Therefore auxillary models will be developed for V_{le}^{*} at the onset of recirculation. In this appendix, differing subchannel flow rates within channel #1 will be considered. In Appendix F5 the local buoyancy effects within the recirculation subchannel will be allowed for.

To model V_{le}^{*} at the onset of recirculation, it is assumed that buoyancy effects dominate to the extent that at the exit plane, the bundle velocity field follows the power dis-

tribution. First, divide the bundle into a number of subchannels which contain rows of rods at the same power as shown in Figure F4.1 for the 4 x 4 rod bundle. Then, for each channel, we define a dimensionless power input as the ratio of the power input to that subchannel to the bundle average power input:

$$Q_i^* = \frac{Q_i}{Q_b} \tag{F4.2}$$

Recirculation will occur first in the subchannel with smallest Q_i^*, so at the onset of recirculation, the velocity in this subchannel will be zero. If we assume the velocity field follows the power distribution, the channel velocities will be:

$$V_i^* = \frac{V_i}{V_b} = K(Q_i^* - Q_{min}^*) \tag{F4.3}$$

so that $V_i^* = 0$ in the subchannel with Q_{min}^*, and V_i^* is proportional to $Q_i^* - Q_{min}^*$ in all other subchannels. The continuity equation in dimensionless form is:

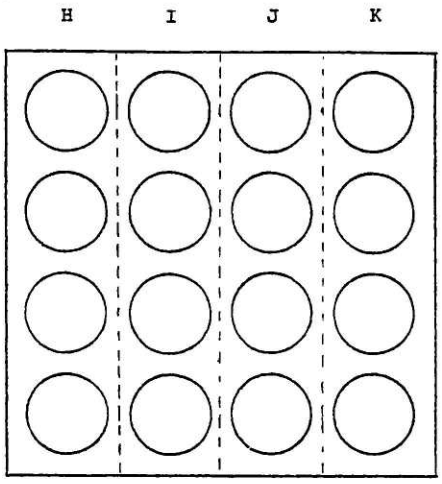
$$\sum_b V_i^* A_i^* = 1 \tag{F4.4}$$

where $\sum_b$ indicates the sum is taken over all of the subchannels in the bundle, and $A_i^* = A_i/A_b$. Substituting F4.3 into F4.4 allows the constant to be calculated:

$$K = \frac{1}{\sum_b A_i^*(Q_i^* - Q_{min}^*)} \tag{F4.5}$$

FIGURE F4.1

BUNDLE GEOMETRY - LUMPED SUBCHANNELS



CHANNEL:	H,K	I,J
AREA, (in^2)	.9851	.8277
WETTED PERIMETER, (in)	10.181	7.4679
HEATED PERIMETER, (in)	6.233	6.233
HYDRAULIC DIAMETER, (in)	.3870	.4433

Substituting this result back into F4.2 gives the subchannel velocities:

$$V_i^* = \frac{Q_i^* - Q_{min}^*}{\sum_b A_i^*(Q_i^* - Q_{min}^*)} \qquad \text{(F4.6)}$$

Now the exit velocity for channel #1 (V_{1e}^*) can be found by area averaging the subchannel exit velocities in channel #1:

$$V_{1e}^* \frac{A_1}{A_b} = \sum_{ch\#1} V_i^* A_i^* \qquad \text{(F4.7)}$$

where $\sum_{ch\#1}$ indicates the sum is taken over channel #1, and $A_1/A_b = 1/2$ since the bundle is divided into equal halves. Combining F4.1, F4.6 and F4.7 allows C_{crit} to be found:

$$C_{crit} = 1 - 2\Gamma \qquad \text{(F4.8)}$$

where:

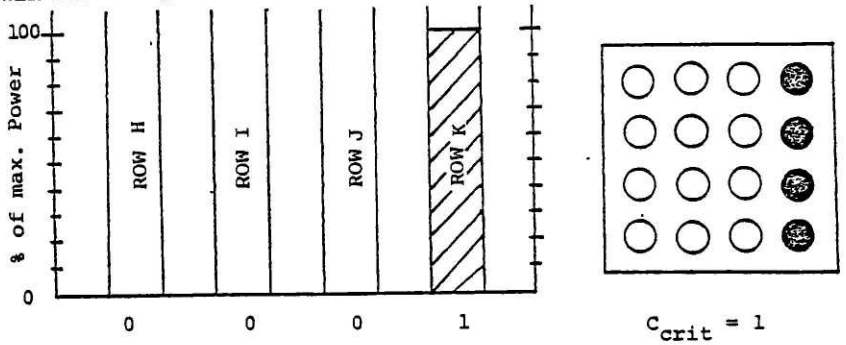
$$\Gamma = \frac{\sum_{ch\#1} A_i^*(Q_i^* - Q_{min}^*)}{\sum_b A_i^*(Q_i^* - Q_{min}^*)} \qquad \text{(F4.9)}$$

We next employ this model to the six power profiles to determine the critical value of C. The power distributions, along with the assumed velocity distributions are shown in Figures F4.2 and F4.3. The bundle consists of the four subchannels shown in Figure F4.1, each containing 4 rods at the same power. It is obvious that $C_{crit} = 1$ for profiles 1 and

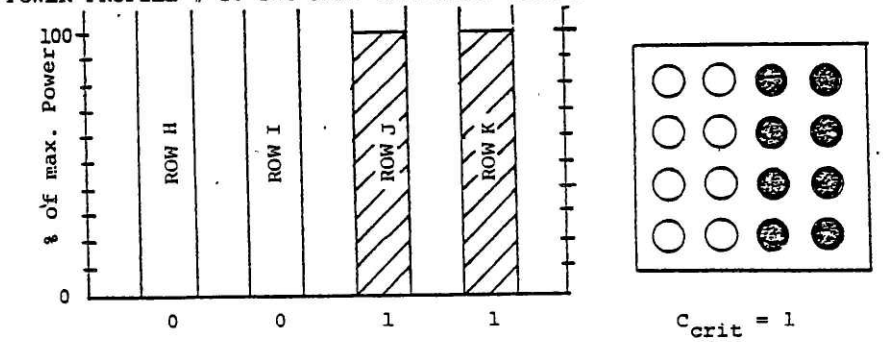
FIGURE F4.2

ASSUMED EXIT VELOCITY PROFILES AT THE ONSET OF RECIRCULATION FOR POWER PROFILES 1 TO 3

POWER PROFILE # 1: ONE ROW UNIFORMLY HEATED



POWER PROFILE # 2: TWO ROWS UNIFORMLY HEATED



POWER PROFILE # 3: THREE ROWS UNIFORMLY HEATED

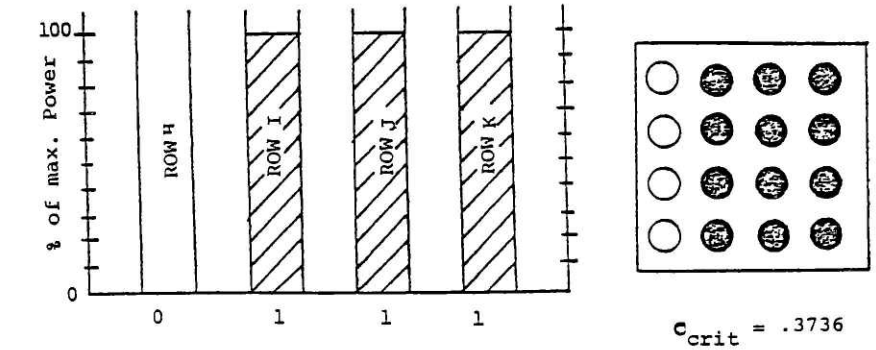
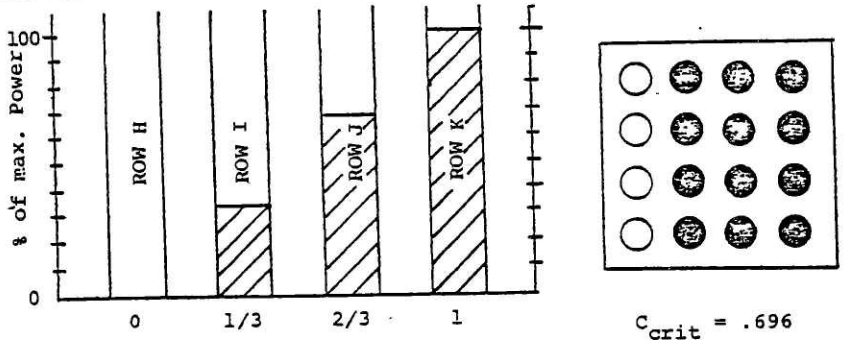


FIGURE F4.3

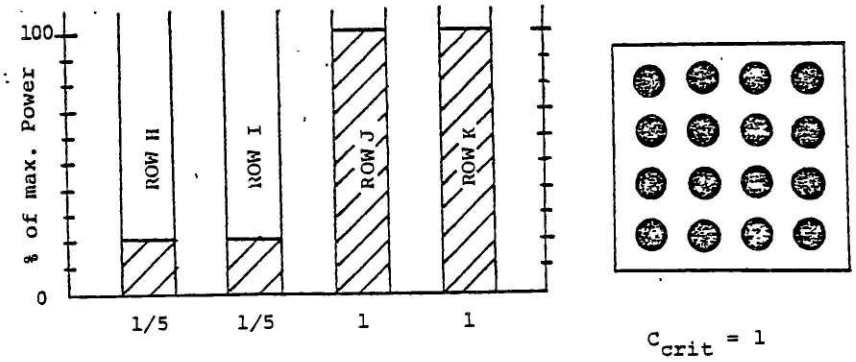
ASSUMED EXIT VELOCITY PROFILES AT THE ONSET OF RECIRCULATION FOR POWER PROFILES 4 TO 6

POWER PROFILE # 4: LINEAR GRADIENT WITH ROW H UNHEATED



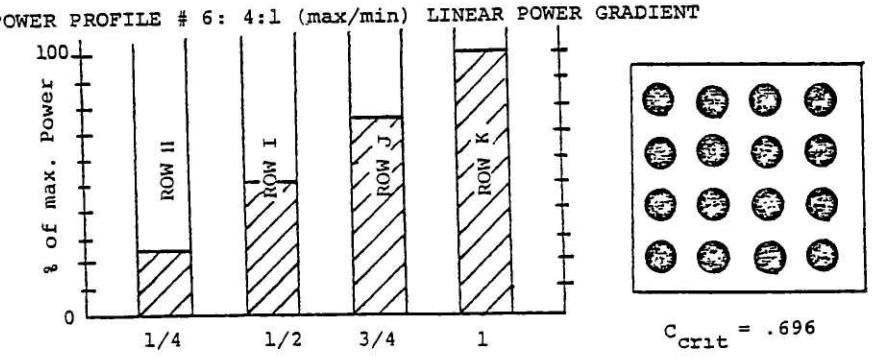
C_{crit} = .696

POWER PROFILE # 5: STEP CHANGE IN POWER



C_{crit} = 1

POWER PROFILE # 6: 4:1 (max/min) LINEAR POWER GRADIENT



C_{crit} = .696

2, since there are no heated rods in channel #1, so $V^*_{le} = 0$. For profiles 3 through 6 Equation F4.8 will be used to find C_{crit}. For profile #3, $Q^*_{min} = 0$, and Equation F4.8 gives

$$C_{crit} = 1 - 2\left[\frac{.272(0)+.228(1)}{.272(0)+.228(1)+.228(1)+.272(1)}\right] = .3736$$

Similarly for profile #4

$$C_{crit} = 1 - 2\left[\frac{.272(0)+.228(1/3)}{.272(0)+.228(1/3)+.228(2/3)+.272(1)}\right] = .696$$

For profile #5, $Q_{min} \neq 0$, but the Q^*_i in channel #1 are equal to Q_{min}, so that:

$$C_{crit} = 1 - 2\left[\frac{0}{\sum_b A^*_i (Q^*_i - Q^*_{min})}\right] = 1$$

For profile #6, $Q^*_{min} = 1/4$, so the equation for C is:

$$C_{crit} = 1 - 2\left[\frac{.272(0)+.228(1/4)}{.272(0)+.228(1/4)+.228(1/2)+.272(3/4)}\right]$$

$$= 1 - 2(.152) = 0.696$$

which is the same as for profile #4.

APPENDIX F5

MODEL FOR THE CRITICAL VALUE OF C AT THE ONSET OF RECIRCULATION ALLOWING FOR LOCAL BUOYANCY EFFECTS

For cases in which the subchannel where recirculation starts to occur is heated, local buoyancy effects may become important, causing a reduction in the value of C_{crit}. Figure F5.1 exhibits a case where recirculation exists while there is net upflow in a subchannel. Wang (1) has performed a numerical study to determine under what conditions local flow recirculation occurs in various types of subchannels for fully developed laminar flow. He expressed the onset of recirculation in terms of a critical Rayleigh number. For aiding flow in an edge subchannel of a square rod array:

$$\log_{10} Ra_D^c = 10.80 - 7.53(P/D)+1.61(P/D)^2 \qquad (F5.1)$$

while for a triangular array:

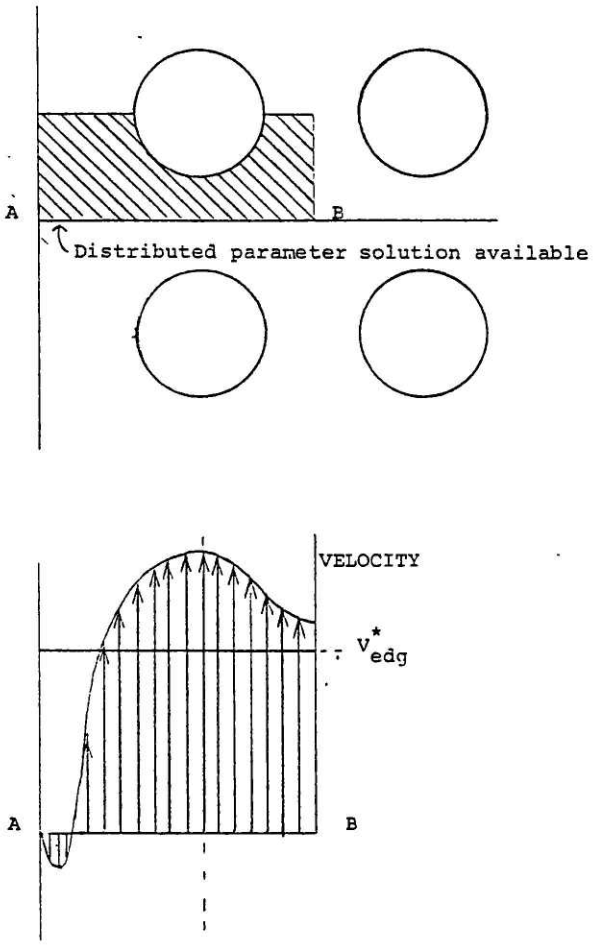
$$\log_{10} Ra_D^c = 12.56 - 9.87(P/D)+2.39(P/D)^2 \qquad (F5.2)$$

Both equations are valid for $1.05 \leq P/D \leq 1.50$. The recirculation first occurs at point A of Figure F5.1.

In order to couple Wang's distributed parameter analysis with the two channel model, we must first obtain the dimensionless edge subchannel velocity at the onset of recircula-

FIGURE F5.1

LOCAL FLOW RECIRCULATION IN
AN EDGE SUBCHANNEL



tion, $V^*_{edg} = V_{edg}/V_b$. Wang defined Ra_D as:

$$Ra_D = \left[\frac{D_{rod}}{D_e}\right]^4 Gr_A Pr \qquad \text{(F5.3)}$$

which for edge subchannels can be written as:

$$Ra_D = 4\left(\frac{D_{rod}}{D_{edg}}\right)^4\left(\frac{D_e}{D_H}\right)_{edg} \left.\frac{Gr_{q''}}{Re}\right|_{edg} \qquad \text{(F5.4)}$$

The Grashof number for edge subchannels is:

$$\left.Gr_{q''}\right|_{edg} = \left.Gr_{q''}\right|_b \left(\frac{D_{edg}}{D_{eb}}\right)^4 \frac{q''_{edg}}{q''_b} \qquad \text{(F5.5)}$$

and the edge subchannel Reynolds number can be expressed as:

$$\left.Re\right|_{edg} = Re_b \frac{D_{edg}}{D_{eb}} V^*_{edg} \qquad \text{(F5.6)}$$

Substituting Equations F5.5 and F5.6 into Equation F5.4 gives:

$$Ra_D = 4\left(\frac{D_{rod}}{D_{eb}}\right)^4\left(\frac{D_e}{D_H}\right)_b \left.\frac{Gr_{q''}}{Re}\right|_b \frac{1}{V^*_{edg}} \frac{q''_{edg}}{q''_b} \qquad \text{(F5.7)}$$

Recirculation will first occur in an edge subchannel next to the row of rods at minimum power, so we can write

$$\frac{q''_{edg}}{q''_b} = \frac{Q_{min}}{Q_b} \qquad \text{(F5.8)}$$

At the onset of recirculation the critical value of Ra_D is given by Equations F5.1 or F5.2. Solving F5.7 for V^*_{edg} gives:

$$V^*_{edg} = 4\left[\frac{D_{rod}}{D_{eb}}\right]^4 \frac{D_{eb}}{D_H} \frac{1}{Ra_D^c} \frac{Gr_q}{Re} \frac{Q_{min}}{Q_b} \qquad \text{(F5.9)}$$

This is the dimensionless edge subchannel velocity at which flow recirculation will occur for fully developed laminar flow. This result can be used to obtain the critical value of C at the onset of recirculation. Both the variable R approach and R=1 approach will be considered.

For the variable R approach, the bundle is noded such that channel #1 contains the row of rods at minimum power. Neglecting the effect of corner subchannels, V^*_{edg} can be written as follows for uniform inlet velocity:

$$V^*_{edg} \simeq V^*_{le} = 1 - C \qquad \text{(F5.10)}$$

So the critical value of C is simply:

$$C_{crit} = 1 - V^*_{edg} \qquad \text{(F5.11)}$$

where V^*_{edg} is given by Equation F5.9.

For the R=1 approach, the model of Appendix F4 can be modified to allow for a nonzero velocity in the recirculation

subchannel. The logic of this approach is exhibited in Figure F5.2. From Wang's analysis, we know V^*_{edg} at the onset of recirculation. As before we assume the subchannel velocities are proportional to Q^*_i, but now subtract λ instead of Q^*_{min} to allow V^*_i to be nonzero in the channel with minimum power.

$$V^*_i = K(Q^*_i - \lambda) \tag{F5.12}$$

To obtain λ, employ the condition that the subchannel of minimum power has velocity V^*_{edg} :

$$V^*_{edg} = K(Q^*_{min} - \lambda) \tag{F5.13}$$

which gives:

$$\lambda = Q_{min} - \frac{V^*_{edg}}{K} \tag{F5.14}$$

Substituting this result back into Equation F5.12 gives:

$$V^*_i = K(Q^*_i - Q_{min}) + V^*_{edg} \tag{F5.15}$$

The dimensionless continuity equation is:

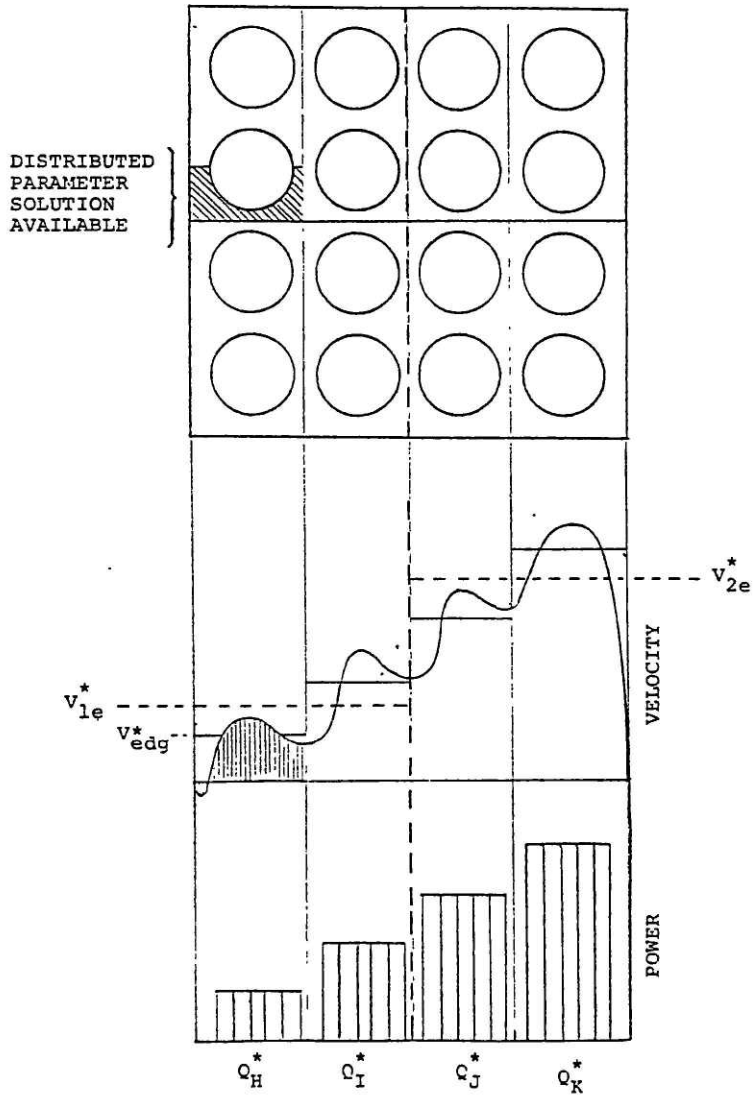
$$\sum_b V^*_i A^*_i = 1 \tag{F5.16}$$

Substituting F5.15 into F5.16 gives:

$$K \sum_b (Q^*_i - Q_{min})A^*_i + V^*_{edg} = 1 \tag{F5.17}$$

FIGURE F5.2

VELOCITY FIELD AT ONSET OF RECIRCULATION



Solving for K:

$$K = \frac{1 - V^*_{edg}}{\sum_b (Q_i - Q_{min}) A^*_i} \qquad \text{(F5.18)}$$

Substituting this result back into F5.15 gives the velocities as:

$$V^*_i = \frac{(1-V^*_{edg})(Q^*_i - Q^*_{min})}{\sum_b (Q^*_i - Q^*_{min}) A_i} + V^*_{edg} \qquad \text{(F5.19)}$$

With the subchannel velocity field given by Equation F5.19, as in Appendix F4, C_{crit} can be obtained by combining F4.1, F4.7 and F5.19 to give:

$$C_{crit} = 1 - 2\,(1 - V^*_{edg})\,\Gamma - 2\,V^*_{edg} \qquad \text{(F5.20)}$$

where Γ is given by Equation F4.9.

Equation F5.20 is a general expression for determining the critical value of C at the onset of recirculation. Two limiting cases of F5.20 will next be discussed. In one case the local buoyancy effects dominate, and for the other case bundle buoyancy effects dominate.

For uniform power $Q_i = Q_{min}$, so Γ is of the form 0/0. This indeterminate form may be resolved by returning to Equation F5.17 which gives $V^*_{edg}=1$ for $Q_i = Q_{min}$, and C=0 from Equation F4.1. Under these conditions flow recirculation is determined entirely by local (subchannel) buoyancy

effects, and is given by Equation F5.9 with $V^*_{edg} = 1$ and $Q_{min} = Q_b$.

Bundle buoyancy effects dominate when $V^*_{edg} = 0$. Under these conditions Equation F5.20 reduces to Equation F4.8. There are two situations where V^*_{edg} will be zero. First, if one row of rods is unheated $Q_{min} = 0$, and it follows from Equation F5.9 that $V^*_{edg} = 0$. The second situation is if $Q_{min} \neq 0$ but Gr_q/Re in Equation F5.9 is small yielding $V^*_{edg} \simeq 0$.

APPENDIX F6

DEVELOPMENT OF A MIXING MODEL FOR BUOYANCY DOMINATED FLOWS THROUGH ROD BUNDLES

In Reference 14 a mixing length model was developed which accounted for the effect of buoyancy on the turbulence terms. This model will be modified for use in the two channel model to account for mixing which has been observed near onset of recirculation conditions.

The turbulent shear stress and heat transfer rate are given by:

$$\tau_t = - \rho \overline{u'v'} \tag{F6.1}$$

$$q_t = \rho C_p \overline{v'T'} \tag{F6.2}$$

where primes indicate fluctuating quantities, and the bar indicates time averaging. It can be shown through physical arguments that $\overline{u'v'}$ is negative. It is then assumed that

$$\tau_t = C_t \rho |\overline{u'}||\overline{v'}| \tag{F6.3}$$

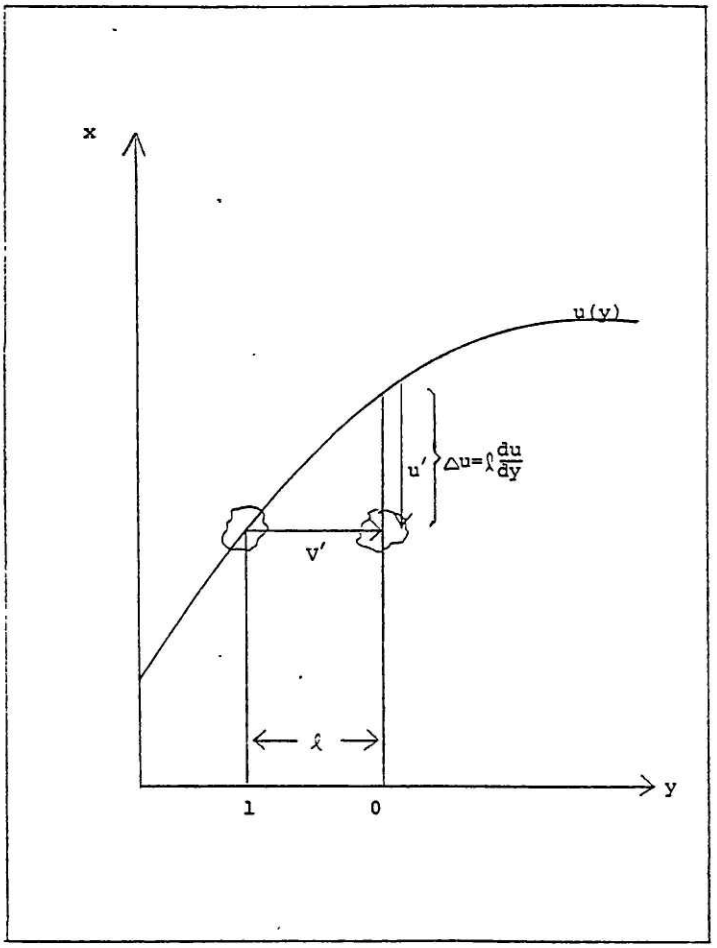
$$q_t = C_q \rho C_p |\overline{v'}||\overline{T'}| \tag{F6.4}$$

The quantities $|\overline{u'}|, |\overline{v'}|$ and $|\overline{T'}|$ are obtained from the mixing length model. The bars will be omitted for simplicity.

Consider the classical mixing length model in which buoyancy effects are ignored. Figure F6.1 illustrates the logic of the model. As a fluid particle moves a distance ℓ from point 1 to point 0 due to some velocity fluctuation v',

FIGURE F6.1

MIXING LENGTH TURBULENCE MODEL



its momentum is assumed to be conserved, so it arrives at point 0 with a velocity difference given by:

$$\Delta u_1 = u_0 - u_1 \simeq \ell \left(\frac{du}{dy}\right)_0 \tag{F6.5}$$

It is assumed that the magnitude of the x velocity fluctuation is:

$$|u'| = |\Delta u_1| = \ell \left|\frac{du}{dy}\right|_0 \tag{F6.6}$$

where ℓ is the mixing length. Similarly if the fluid particles conserve their temperature, the magnitude of the temperature fluctuation is given by:

$$|T'| = \ell \left|\frac{dT}{dy}\right|_0 \tag{F6.7}$$

The model is completed by assuming that the magnitude of the x and z velocity fluctuations are proportional;

$$|V'| = c|u'| \tag{F6.8}$$

Substituting equations F6.6, F6.7 and F6.8 into F6.3 and F6.4 gives:

$$\tau_t = \rho \ell^2 \frac{du}{dy}\left|\frac{du}{dy}\right| \tag{F6.9}$$

$$q_t = \ell^2 C_p \frac{dT}{dy}\left|\frac{du}{dy}\right| \tag{F6.10}$$

where the constant c has been incorporated in the mixing length. This is the classical mixing length theory which does not include buoyancy.

It was suggested in Reference 77 that the mixing length

model is closer to reality for the turbulent heat transfer than for the turbulent shear stress, because the fluid particles conserve their temperature more so than their momentum. This may not be the case for fluids of low Pr where fluid particles may experience heat transfer during a fluctuation.

Now the effects of buoyancy will be considered. Since the fluid particle conserves its temperature, when it arrives at 0 it will experience a buoyancy force per unit mass of $-\beta g \Delta T$. The average force on the fluid particle as it moves from 1 to 0 may be estimated as:

$$\frac{\text{Buoyant Force}}{\text{Mass}} = -\frac{1}{2}\beta g\left(\frac{dT}{dy}\right)_0 \ell \qquad \text{(F6.11)}$$

From Newton's Law, $\frac{\text{Force}}{\text{Mass}} = \frac{\Delta u_B}{\Delta t}$. The force acts for the time Δt required for the particle to travel from 1 to 0. This time may be estimated as:

$$\Delta t = \ell/|v'| \qquad \text{(F6.12)}$$

The change in velocity due to buoyancy is then:

$$\Delta u_B = -\frac{1}{2}\beta g \frac{dT}{dy}\frac{\ell}{|v'|} \qquad \text{(F6.13)}$$

and the total change in velocity is:

$$\Delta u = \ell\left(\frac{du}{dy}\right) + \frac{1}{2}\beta g\left(\frac{dT}{dy}\right)\frac{\ell^2}{|v'|} \qquad \text{(F6.14)}$$

from which it follows that:

$$|u'| = \ell\left|\frac{du}{dy}\right| + \frac{1}{2}\beta g\left|\frac{dT}{dy}\right|\frac{\ell^2}{|v'|} \qquad \text{(F6.15)}$$

It will again be assumed that $|u'| = c|v'|$, which upon substitution into Equation F6.15 yields a quadratic equation in $|v'|$. In Reference 14 it was assumed that the effect of the buoyancy term in Equation F6.15 is small. We will assume that at the onset of recirculation the buoyancy term in Equation F6.15 dominates. This gives $|v'|$ as:

$$|v'| = \sqrt{\frac{\ell^2}{2c}\beta g\left|\frac{dT}{dy}\right|} \tag{F6.16}$$

Substituting Equation F6.16 and F6.7 into Equation F6.4 gives the turbulent heat flux as

$$q_t = C_q \rho C_p \ell^2 \frac{dT}{dy}\sqrt{\frac{1}{2c}\beta g \frac{dT}{dy}} \tag{F6.17}$$

To convert to w_t' we use the definition:

$$w_t' = \frac{q_t w}{\ell C_p \, dT/dy} \tag{F6.18}$$

which gives:

$$w_t' = C_q \rho \ell w \sqrt{\frac{1}{2c}\beta g \frac{dT}{dy}} \tag{F6.19}$$

or in dimensionless form:

$$w_t^* = \frac{w_t' L}{\rho V_b A_b} = \frac{C_q w \ell L}{V_b A_b}\sqrt{\frac{1}{2c}\beta g \frac{dT}{dy}} \tag{F6.20}$$

The temperature gradient may be estimated from the two channel model:

$$\frac{dT}{dy} \simeq \frac{T_2-T_1}{\ell} = \frac{T_2-T_1}{\Delta T_B} \cdot \frac{\Delta T_B}{\ell} = Y \frac{\Delta T_B}{\ell} \qquad \text{(F6.21)}$$

where: $Y \equiv \frac{T_2-T_1}{\Delta T_B}$

Substituting Equation F6.21 into Equation F6.20 gives with some rearranging:

$$w_t^* = \frac{K''}{Re} \frac{D_e}{D_H} \frac{SL}{A_b} \sqrt{\frac{\ell}{D_H}} \sqrt{Gr_{\Delta T} \, Y} \qquad \text{(F6.22)}$$

where all constants have been combined into K''. Eliminating $Gr_{\Delta T}$ in favor of Gr_q:

$$w_t^* = K'' \frac{D_e}{D_H} \frac{SL}{A_b} \sqrt{\frac{\ell}{D_H}} \sqrt{\frac{Gr_q}{Re^3 Pr} \, Y} \qquad \text{(F6.23)}$$

As it stands now, the correlation is difficult to apply since Y is a function of x which is not known a priori. We will therefore insert a simple expression for Y in terms of the parameters upon which it depends:

$$Y = K_3 (P_2-P_1)^q \, Re^n \qquad \text{(F6.24)}$$

where K_3, q and n are parameters which are to be determined. Y is expected to increase with both power skew and Reynolds number. For buoyancy dominated flows, the effect of increasing Reynolds number is to reduced the buoyancy induced crossflow,

and hence increase the radial temperature difference (Y). The extent to which this occurs is accounted for by the parameter n. The influence of the power skew (P_2-P_1) on Y is due to two effects. First, as the power skew increases Y increases simply because one channel receives more power than the other. But for buoyancy dominated flows an increase in power skew will be accompanied by an increase in the buoyancy induced crossflow, which tends to reduce Y. These two competing effects may be accounted for by the parameter q. It will be assumed that the two competing effects cancel each other out, so that q = 0. Equation 6.2.4 is then given by:

$$Y = K_3 \, Re^n \qquad \text{(F6.25)}$$

Substituting this into Equation F6.23, and combining the constants gives:

$$w_t^* = K' \, \frac{D_e}{D_H} \, \frac{wL}{A_b} \, \sqrt{\frac{\ell}{D_H}} \, \sqrt{\frac{Gr_q}{Re^{3-n} Pr}} \qquad \text{(F6.26)}$$

It has been experimentally observed in this study and in work done at BNWL that the buoyancy induced turbulence goes to zero in unheated regions of the bundle. This is reflected in Equation F6.26 if Gr_q is considered a local Grashof number, but the formulation is in terms of the bundle Grashof number. Equation F6.26 will be multiplied by P_1 so that the mixing between channels goes to zero if one channel is unheated:

$$w_t^* = K' P_1 \frac{D_e}{D_H} \frac{wL}{A_b} \sqrt{\frac{\ell}{D_H}} \sqrt{\frac{Gr_q}{Re^{3-n} Pr}} \qquad \text{(F6.27)}$$

This may also be expressed as:

$$w_t^* = K\ P_1 \frac{\sqrt{Gr}}{Re^m} \qquad \text{(F6.28)}$$

where:

$$K = K' \frac{D_e}{D_H} \frac{wL}{A_b} \sqrt{\frac{\ell}{D_H Pr}} \qquad \text{(F6.29)}$$

$$m = \frac{1}{2}(3-n)$$

For a given geometry and coolant, K is a constant. The mixing model is in terms of two undetermined coefficients, K and m, which will be obtained from the experimental recirculation data.

Equation F6.28 bears similarity to the empirical mixing correlation developed at BNWL, which in terms of Gr_q is

$$w_t^* = K \frac{Gr_q}{Re^4} \hat{Q}_p \qquad \text{(F6.30)}$$

APPENDIX F7

DETERMINATION OF THE DOMINANT DIMENSIONLESS PARAMETERS FOR THE ONSET OF MIXED CONVECTION AND ONSET OF RECIRCULATION CRITERIA

It can be seen from the governing equation of the two channel model (Equation 5.3.1) that many dimensionless parameters are involved. It is the purpose of this appendix to identify the two dominant dimensionless parameters to allow construction of a flow regime map.

For R=1, $f = \frac{C_f}{Re^m}$, quasi steady flow, uniform crossflow ($f(x)=x$, $\overline{f(x)} = 1/2$) and uniform inlet velocity the two channel model equation (Equation 5.3.1) becomes:

$$0 = C(2+C) + 4Cw_t^* + \frac{1}{2}\frac{L}{D_e}\frac{C_f}{Re^m}F_C - 4\frac{L}{D_e}\frac{L}{D_H}(K_2P_2-K_1P_1)\frac{Gr_q}{Re^3Pr} \qquad (F7.1)$$

where

$$F_C = \frac{(1+C)^{3-m} + (1-C)^{3-m} - 2}{(3-m)C} \qquad (F7.2)$$

For laminar flow (m=1) F_C is given by:

$$F_C = \frac{(1+C)^2 + (1-C)^2 - 2}{2C} = \frac{2C^2}{2C} = C \qquad (F7.3)$$

To identify the key dimensionless parameters in the model, it is assumed that frictional forces and buoyancy forces are dominant. This assumption will be checked later. Balancing the friction and buoyancy terms of Equation F7.1 gives:

$$\frac{1}{2}\frac{L}{D_e}\frac{C_f}{Re^m}F_C = 4\frac{L}{D_e}\frac{L}{D_H}\frac{Gr_q}{Re^3 Pr}(K_2P_2 - K_1P_1) \qquad (F7.4)$$

Selecting Re as one key parameter, the other can be identified by isolating Re to one side:

$$\frac{1}{8}Re^{3-m} = \frac{L}{D_H}\frac{Gr_q}{Pr}\frac{K_2P_2 - K_1P_1}{F_C C_f} \qquad (F7.5)$$

The right hand side is defined as B_D^*, the dimensionless buoyancy parameter:

$$B_D^* \equiv \frac{L}{D_H}\frac{Gr_q}{Pr}\frac{K_2P_2 - K_1P_1}{F_C C_f} \qquad (F7.6)$$

We next test the hypothesis that Re and B_D^* are dominant by returning to the governing two channel equation. Substituting the dimensionless buoyancy parameter into Equation F7.1 gives

$$0 = C(2+C) + 4Cw_t^* + \frac{1}{2}\frac{L}{D_e}\frac{C_f}{Re^m}F_C - 4\frac{L}{D_e}\frac{B^*}{Re^3}F_C C_f \qquad (F7.7)$$

Solving for B_D^* gives:

$$B_D^* = \frac{Re^3}{4}\left[\frac{C(2+C) + 4\,C\,w_t^*}{C_f\,F_C\,\frac{L}{D_e}} + \frac{1}{2Re^m}\right] \qquad (F7.8)$$

The above equation is equivalent to Equation 7.1, but many of the dimensionless parameters have been lumped into B_D^*. It may be expressed in functional form as:

$$B_D^* = f_n(Re,\ C_f,\ m,\ C,\ w_t^*,\ \frac{L}{D_e}) \qquad (F7.9)$$

If our assumption that frictional forces and buoyancy forces are dominant (Equation F7.4) is correct, it follows from Equation F7.5 that:

$$B_D^* = f_n(Re,\ m) \qquad (F7.10)$$

which reflects the assumption that B_D^* and Re are indeed the dominant dimensionless parameters. However, since B_D^* depends on m we must also know if the flow is laminar (m=1) or turbulent (m=.25) to determine B_D^*. If we define A_D^* as:

$$A_D^* = \frac{C(2+C) + 4\ C\ w_t^*}{C_f F_C\ L/De} \qquad (F7.11)$$

Then F7.8 may be written:

$$B_D^* = \frac{Re^3}{4}\left[A_D^* + \frac{1}{2Re^m}\right] \qquad (F7.12)$$

There are two conditions under which F7.10 holds true. The first is that A_D^* must be small:

$$A_D^* << \frac{1}{2Re^m} \qquad (F7.13)$$

This is the case for long bundles, and low Reynolds numbers. The second is that A_D^* must be constant:

$$A_D^* \simeq \text{constant} \qquad (F7.14)$$

As defined by Equation F7.12 B_D^* actually has two values, one for laminar flow ($C_f = C_{fL}$, $F_C = C$) and one for turbulent flow ($C_f = C_{fT}$, F_C given by Equation F7.2). This leads to several alternate representations, which will be discussed in the following sections.

F7.1 PRESENTATION OF RESULTS IN TERMS OF THE DUAL VALUED B_D^*

Equation F7.12 was used to calculate B_D^* as a function of Re for laminar and turbulent flow for C=.01 (onset of mixed convection) and C=1 (onset of recirculation) for the water cooled MIT 4x4 rod bundle ($\frac{L}{D_e} = 61.9$), and the sodium cooled WARD blanket bundle ($\frac{L}{D_e} = 308$). Coolant mixing will be neglected in the 4x4 bundle ($w_t^* = 0$), and the fully turbulent mixing value ($w_t^* = .23$ from Figure 8.3.5) for the WARD bundle. The results are given in Figure F7.1. Equation F7.8 with $A_D^* = 0$ (friction and buoyancy only) is also plotted, and gives a straight line on the log-log plot.

It is observed in Figure F7.1 that the lines for onset of mixed convection and onset of recirculation for a given geometry and flow condition nearly coincide. This does not suggest that the two onsets occur at the same time. It occurs because the crossflow parameter C is included in B_D^*, and C changes by roughly two orders of magnitude from the onset of mixed convection to the onset of recirculation. It follows from Figure F7.1 that A^* is nearly independent of C, and that the effect of C is almost totally incorporated into B_D^*.

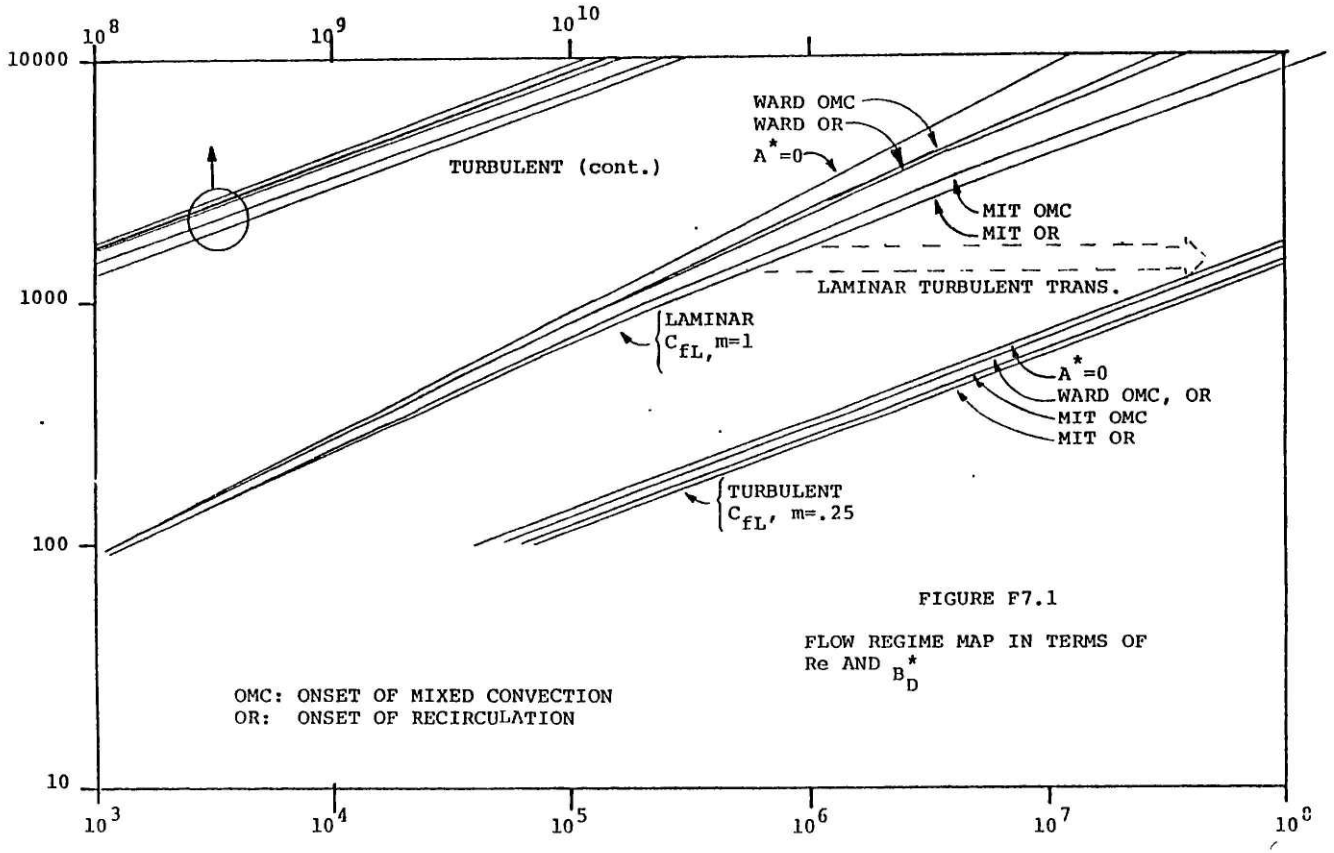


FIGURE F7.1

FLOW REGIME MAP IN TERMS OF Re AND B_D^*

OMC: ONSET OF MIXED CONVECTION
OR: ONSET OF RECIRCULATION

$$B_D^* = \frac{L}{D_H} \quad \frac{Gr_q}{Pr} \quad \frac{K_2P_2 - K_1P_1}{C_1 F}$$

For laminar flow (m=1) at low Re, all 5 curves merge into one because A_D^* is dominated by $\frac{1}{2Re}$ in Equation F7.12. As Re increases, the effect of A_D^* becomes significant, and the curves for the WARD and MIT geometries depart from the $A_D^*=0$ result. Note that the A_D^* effect is less for the Westinghouse geometry since L/D_e is larger. For the turbulent flow result, the curves do not spread out as rapidly because with m=.25 in F7.12 the term $1/2Re^m$ does not decrease as rapidly.

From the results presented above it appears that A_D^* depends very weakly on C, but does depend on L/D_e. However, the region where this dependence is significant (high Re laminar flow) will not be encountered in practice since the turbulent flow prediction will be used for high Re. It is therefore concluded that Re and B_D^* are the dominant dimensionless parameters.

F7.2 PRESENTATION OF RESULTS IN TERMS OF THE LAMINAR FLOW VALUE OF B_D^*

As discussed earlier, B_D^* given by Equation F7.6 has two values, one for laminar flow and one for turbulent flow. As seen in Figure F7.1, this leads to separate groups of curves for laminar and turbulent flow with a jump discontinuity at the laminar /turbulent transition (see dotted line in Figure F7.1 at Re≈2,000).

To avoid this awkward representation of the transition region, let B_D^* be given by its laminar flow value:

$$B_L^* = \frac{L}{D_H} \frac{Gr_q}{Pr} \frac{K_2P_2 - K_1P_1}{C_{fL}C} \qquad \text{(F7.15)}$$

For laminar flow (m=1, $C_f = C_{fL}$, $F_C = C$) Equation F7.12 becomes:

$$B_L^* = \frac{Re^3}{4}\left[A^* + \frac{1}{2Re}\right] \qquad (F7.16)$$

Substituting F7.15 into F7.1 for turbulent flow ($C_f = C_{fT}$) gives:

$$B_L^* = \frac{Re^3}{4}\left[A_L^* + \frac{1}{2Re^m}\frac{F_C}{C}\frac{C_{fT}}{C_{fL}}\right] \qquad (F7.17)$$

where:

$$A_L^* = \frac{2 + C + 4w_t^*}{C_{fL}\ L/D_e} \qquad (F7.18)$$

The equation for turbulent flow has two additional terms which do not appear in the laminar flow equation. These terms are F_C/C and C_{fT}/C_{fL}. If these two terms depend strongly on geometry or C, Equation F7.17 would no longer approximate the simplified functional dependence of B_D^* reflected by Equation F7.10, so Re and B_D^* would not be the dominant parameters. It turns out the F_C/C (with m=.25) varies from 1.72 for C=1 to 1.75 for C=.01, so it depends very weakly on C. The value of C_{fT}/C_{fL} is a function of geometry, but only weakly so. For a circular tube, $C_{fT}/C_{fL} = .316/64 = 4.94 \times 10^{-3}$, for the blanket bundle $C_{fT}/C_{fL} = .329/88 = 3.74 \times 10^{-3}$. It follows from these results that the laminar flow B_L^* (Equation F7.15) can serve as the dominant dimensionless parameter for both laminar and turbulent flow.

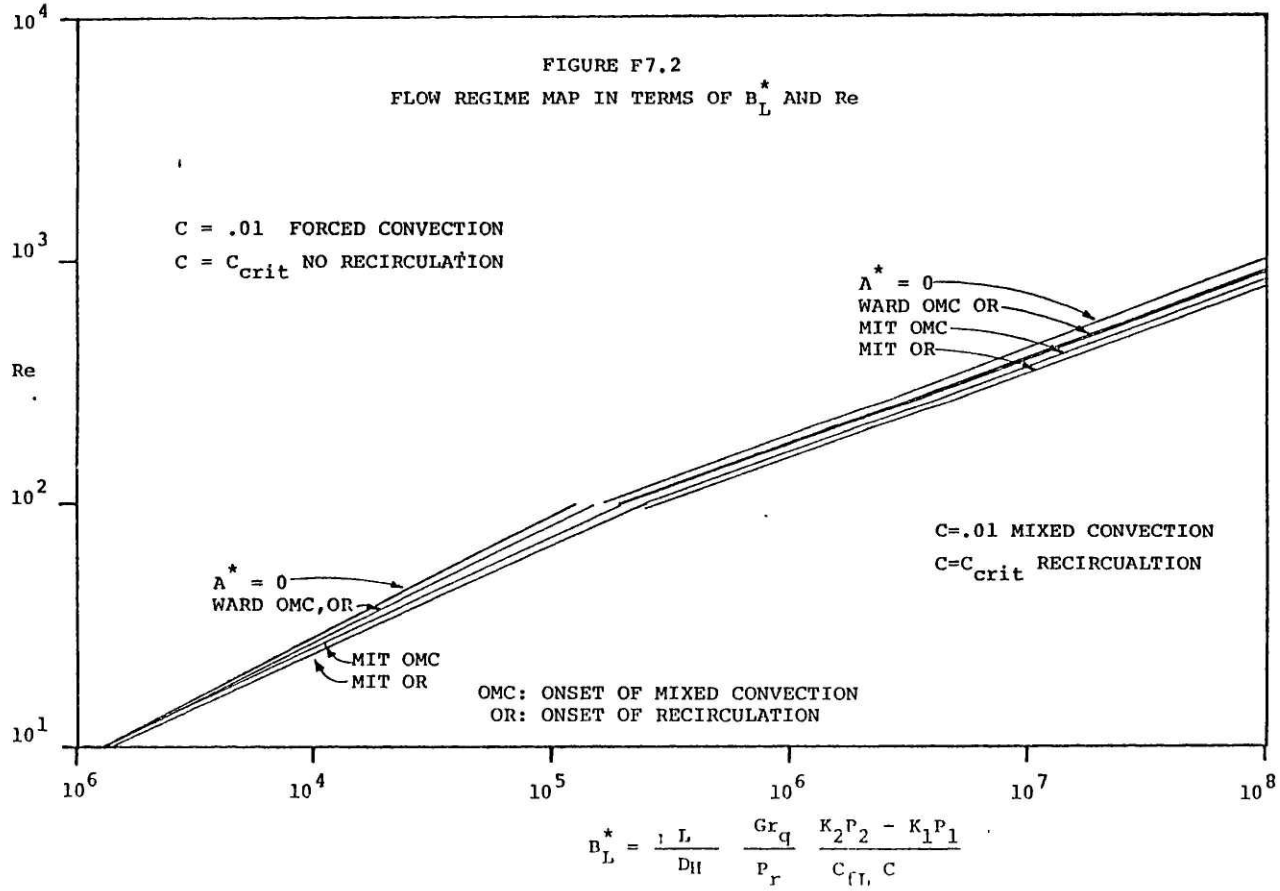
The onset of mixed convection and onset of recirculation for the MIT 4x4 bundle and the WARD blanket bundle were then replotted in terms of Re vs B_L^*. The onsets for laminar flow are as before. For turbulent flow Equation F7.17 was employed to calculate the onsets. The results are plotted in Figure F7.2. The curves for turbulent flow are observed to shift to the left so they intersect the curves for laminar flow in the transition region, providing for a smooth transition rather than a discontinuous one. Thus B_L^* gives a much more convenient representation of the onsets than B_D^* since the laminar/turbulent transition is reflected in the model equations (F7.16 and F7.17) rather than in the definition in B_D^* (Equation F7.8).

It is interesting that the curves for a wide range of C (.01 to 1) nearly coincide. This is because the C dependence has been almost entirely incorporated into B_D^* or B_L^*. This is desireable for the onset of recirculation, since recirculation can occur for a range of values of C.

F7.3 PRESENTATION OF RESULTS IN TERMS OF $B_L^* \cdot C$

If it is desired to plot both the onset of mixed convection and the onset of recirculation on the same set of coordinates, the two onsets will nearly coincide if B_D^* or B_L^* are used. This makes it difficult to visualize the boundaries between the forced, mixed and recirculation flow regimes.

This problem can be alleviated by removing C from B_L^*, and allowing the C dependence to be seen on the flow regime


FIGURE F7.2
FLOW REGIME MAP IN TERMS OF B_L^* AND Re
C = .01 FORCED CONVECTION
C = C_{crit} NO RECIRCULATION
A^* = 0
WARD OMC OR
MIT OMC
MIT OR
C=.01 MIXED CONVECTION
C=C_{crit} RECIRCUALTION
A^* = 0
WARD OMC,OR
MIT OMC
MIT OR
OMC: ONSET OF MIXED CONVECTION
OR: ONSET OF RECIRCULATION
Re
10^4
10^3
10^2
10^1
10^6
10^4
10^5
10^6
10^7
10^8
$B_L^* = \frac{L}{D_H} \frac{Gr_q}{P_r} \frac{K_2P_2 - K_1P_1}{C_{fL}\, C}$

map. Now B^* is defined as:

$$B^* = B_L^* \cdot C = \frac{L}{D_H} \frac{Gr_q}{Pr} \frac{K_2P_2 - K_1P_1}{C_{fL}} \tag{F7.19}$$

Then Equation F7.16 becomes for laminar flow:

$$B^* = \frac{Re^3}{4} \left[A_L^* + \frac{1}{2Re} \right] C \tag{F7.20}$$

and for turbulent flow, Equation F7.17 gives:

$$B^* = \frac{Re^3}{4} \left[A_L^* + \frac{1}{2Re^m} \frac{F_C}{C} \frac{C_{fT}}{C_{fL}} \right] C \tag{F7.21}$$

where A_L^* is given by Equation F7.18.

The results are given in Figure F7.3, where the forced, mixed, and recirculation regimes have been identified. Actually the onset of recirculation must be exhibited as a family of curves for various values of C, where the critical value of C is calculated from Equation F4.8 or F5.20.

F7.4 SUMMARY OF RESULTS

In summary, three alternate definitions for B^* have been found. When B_D^* is defined by Equation F7.8, the flow regime map takes the form of Figure F7.8. The jump discontinuity in the laminar turbulent transition made this approach unattractive. If B_L^* is defined in terms of the laminar friction coefficient (Equation F7.15) the flow regime map is given by Figure F7.2. If it is desired to separate the onset of mixed

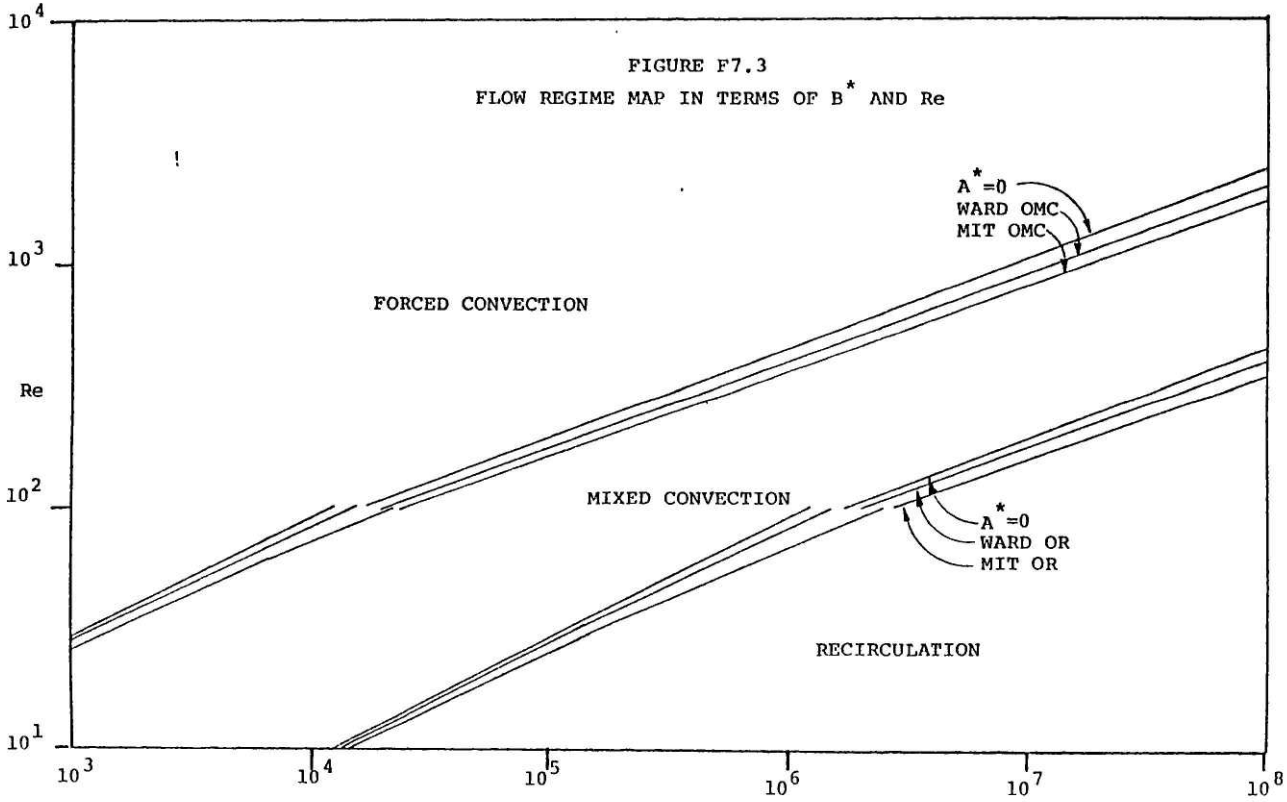


FIGURE F7.3
FLOW REGIME MAP IN TERMS OF B^* AND Re

$$B^* = \frac{L}{D_H} \frac{Gr_q}{Pr} \frac{K_2 P_2 - K_1 P_1}{C_{fL}}$$

convection curves on the map, B^* should be defined by Equation F7.19.

Regardless of which presentation is used, the dominant dimensionless parameters have been identified as Re and some form of B^*. An additional parameter A^* has been found which is important under certain conditions.